AD-A143 301 PROCEEDINGS OF THE INTERNATIONAL CONFERENCE ON RECENT ADVANCES IN STRUCTU..(U) SOUTHAMPTON UNIV (ENGLAND) INST OF SOUND AND VIBRATION RESEAR.. H PETYT ET AL. 1/6

UNCLASSIFIED 1984 F/G 20/11 NL

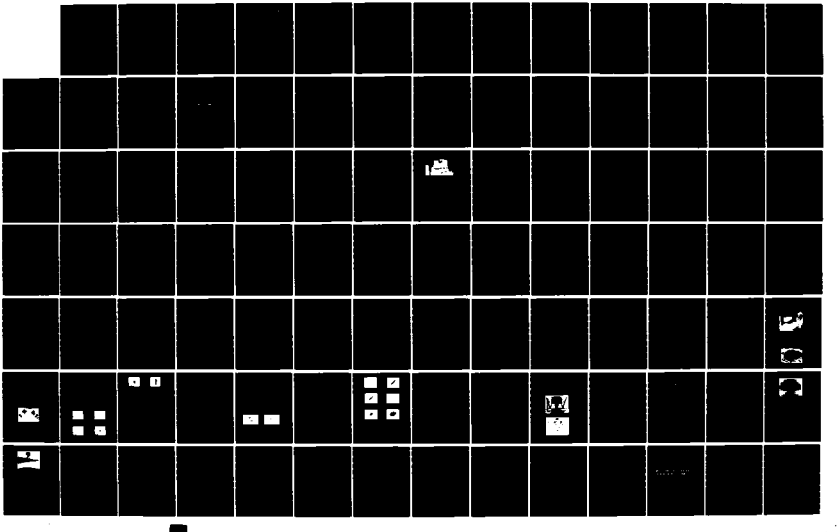

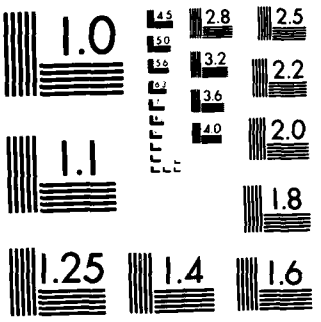

MICROCOPY RESOLUTION TEST CHART
NATIONAL BUREAU OF STANDARDS-1963-A

PROCEEDINGS OF THE

SECOND INTERNATIONAL CONFERENCE

ON

RECENT ADVANCES

IN

STRUCTURAL DYNAMICS

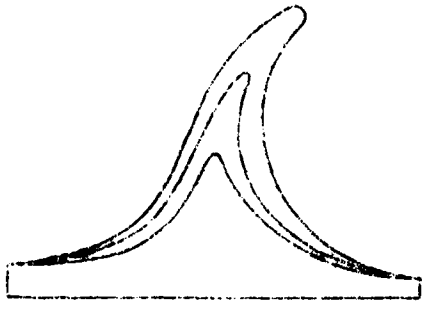

VOLUME II

INSTITUTE OF SOUND & VIBRATION RESEARCH

UNIVERSITY OF SOUTHAMPTON

COMPONENT PART NOTICE

THIS PAPER IS A COMPONENT PART OF THE FOLLOWING COMPILATION REPORT:

(TITLE): Proceedings of the International Conference on Recent Advances in Structural Dynamics (2nd) held at the University of Southampton (England) on 9-13 April 1984. Volume 2.

(SOURCE): Southampton Univ. (England) Inst. of Sound and Vibration Research

TO ORDER THE COMPLETE COMPILATION REPORT USE AD-A143 301.

THE COMPONENT PART IS PROVIDED HERE TO ALLOW USERS ACCESS TO INDIVIDUALLY AUTHORED SECTIONS OF PROCEEDINGS, ANNALS, SYMPOSIA, ETC. HOWEVER, THE COMPONENT SHOULD BE CONSIDERED WITHIN THE CONTEXT OF THE OVERALL COMPILATION REPORT AND NOT AS A STAND-ALONE TECHNICAL REPORT.

THE FOLLOWING COMPONENT PART NUMBERS COMPRISE THE COMPILATION REPORT:

AD#:	TITLE:
AD-P003 674	Application of Modal Synthesis Concepts to Spacecraft Design Verification.
AD-P003 675	A Flexible Multichannel Measurement System for Dynamic Analysis.
AD-P003 676	Limitations on the Identification of Discrete Structural Dynamic Models.
AD-P003 677	Foolproof Methods for Frequency Response Measurements.
AD-P003 678	An Investigation of the Behavior of the Simultaneous Three Axis Vibration System.
AD-P003 679	Recent Experimental Devices to Obtain the Dynamic Parameters of Bridges.
AD-P003 680	The Experimental Measurement of Flexural Wave Power Flow in Structures.
AD-P003 681	Recent Advances in Reduction Methods in Non Linear Structural Dynamics.
AD-P003 682	Feasibility of Using Modal Analysis Techniques for Nonlinear Multidegree of Freedom Systems.
AD-P003 683	Modal Analysis and Identification of Structural Non-Linearity.
AD-P003 684	Time Domain Analysis of Nonlinear Vibration Data.
AD-P003 685	Extended Damping Models for Vabration Data Analysis.
AD-P003 686	Non-Stationary Responses of Non-Linear Rectangular Plates During Transition Through Parametric Resonances. Part 1. Theory.
AD-P003 687	Non-Stationary Responses of Non-Linear Rectangular Plates During Transition through Parametric Resonances. Part 2. Experiment.
AD-P003 688	Non-Linear Dynamic Analysis of Anisotropic Rectangular Plates by a New Method.
AD-P003 689	Large Amplitude Vibrations of Initially Stressed Bimodulus Thick Plates.
AD-P003 690	Non-Linear Multimode Response of Clamped Rectangular Plates to Acoustic Loading.

COMPONENT PART NOTICE (CON'T)

A

AD#:	TITLE:
AD-P003 691	Steel Fibrous Concrete Under Seismic Loading.
AD-P003 692	Inelastic Analysis of Short Highway Bridges Subjected to Strong Ground Motions.
AD-P003 693	Elastic-Plastic Response of Rooftop Frames to Distributed and Concentrated Shock Load Experimental Results and Theoretical Predictions.
AD-P003 694	Researches in Random Vibration.
AD-P003 695	Some Closed-From Solutions in Random Vibration of Timoshenko Beams.
AD-P003 696	Random Vibration of Discrete, Periodic Coupled Frame-Wall Systems.
AD-P003 697	Dynamic Analysis of Vehicles with Nonlinear Suspension Properties.
AD-P003 698	A State Space Approach to the Analysis of Nonstationary, Nonlinear Random Vibration With Particular Application to the Problem of Vehicles on Rough Ground.
AD-P003 699	Dynamic Modelling of Railway Track and Wheelsets.
AD-P003 700	Two Theoretical Models for Wave Propagation in Rails.
AD-P003 701	Dynamics and Stability of Train-Track-Systems.
AD-P003 702	Assessment of the Generating Mechanisms and Characteristics of Whedel/Rall Noise Via Study of a Rolling Disc.
AD-P003 703	On the Acoustically Optimal Design of Railway Whels.
AD-P003 704	Galileo Spacecraft Modal Test and Evaluation of Testing Techniques.
AD-P003 705	Acoustic Fatigue Life of Adhesive Bonded Structures Subjected to Acoustic Loads.
AD-P003 706	Dynamic Response and Acoustic Fatigue of Stiffened Composite Structure.
AD-P003 707	Sonic Fatigue Design Method for the Response of CFRP (Carbon-Fibre Reinforced Plastic) Stiffened-Skin Panels.
AD-P003 708	Prediction of the Dynamic Properties of Carbon-Glass Fibre Sandwich Hybrid Laminated Composites.
AD-P003 709	Life Time Prediction Based on the Combined Use of Finite Element and Modal Analysis Data.
AD-P003 710	Noise Energy Radiated from Rod-Like Structures.
AD-P003 711	Using a Scale Model to Investigate the Post Fracture Structural Vibrations and Noise of a 200 Tonne Power Press.
AD-P003 712	Active Force Control in Machinery Noise.
AD-P003 713	Modeling the Relation Between Structural Vibrations And Radiated Sound.
AD-P003 714	Development of the Aerospace Structures Technology Damping Design Guide.
AD-P003 715	Continuum Modelling of Damping in Large Space Structures.
AD-P003 716	Determination of Receptances of Locally Damped Structures.

Unclassified

SECURITY CLASSIFICATION OF THIS PAGE

REPORT DOCUMENTATION PAGE

1a. REPORT SECURITY CLASSIFICATION Unclassified	1b. RESTRICTIVE MARKINGS
2a. SECURITY CLASSIFICATION AUTHORITY	3. DISTRIBUTION/AVAILABILITY OF REPORT Approved for public release; distribution unlimited
2b. DECLASSIFICATION/DOWNGRADING SCHEDULE	
4. PERFORMING ORGANIZATION REPORT NUMBER(S)	5. MONITORING ORGANIZATION REPORT NUMBER(S)
6a. NAME OF PERFORMING ORGANIZATION University of Southampton 6b. OFFICE SYMBOL (If applicable)	7a. NAME OF MONITORING ORGANIZATION Acoustics and Sonic Fatigue Group
6c. ADDRESS (City, State and ZIP Code) Southampton, SO9 5NH England	7b. ADDRESS (City, State and ZIP Code) AFWAL/FIBED Wright-Patterson AFB, OH 45433
8a. NAME OF FUNDING/SPONSORING ORGANIZATION 8b. OFFICE SYMBOL (If applicable)	9. PROCUREMENT INSTRUMENT IDENTIFICATION NUMBER
8c. ADDRESS (City, State and ZIP Code)	10. SOURCE OF FUNDING NOS. PROGRAM ELEMENT NO. / PROJECT NO. / TASK NO. / WORK UNIT NO.
11. TITLE (Include Security Classification) Recent Advances in Structural Dynamics, Vol II	
12. PERSONAL AUTHOR(S)	
13a. TYPE OF REPORT Conference Proceedings 13b. TIME COVERED FROM _____ TO _____	14. DATE OF REPORT (Yr., Mo., Day) 15. PAGE COUNT 500
16. SUPPLEMENTARY NOTATION No Air Force designated number was used	
17. COSATI CODES FIELD / GROUP / SUB. GR.	18. SUBJECT TERMS (Continue on reverse if necessary and identify by block number)

19. ABSTRACT (Continue on reverse if necessary and identify by block number)

This report contains the Second International Conference proceedings on Recent Advances in Structural Dynamics held 9-13 April 1984 at the Institute of Sound and Vibration Research, The University of Southampton, England.

20. DISTRIBUTION/AVAILABILITY OF ABSTRACT UNCLASSIFIED/UNLIMITED ☒ SAME AS RPT. ☐ DTIC USERS ☐	21. ABSTRACT SECURITY CLASSIFICATION Unclassified
22a. NAME OF RESPONSIBLE INDIVIDUAL Howard F. Wolfe	22b. TELEPHONE NUMBER (Include Area Code) (513) 255-5229 22c. OFFICE SYMBOL AFWAL/FIBED

DD FORM 1473, 83 APR EDITION OF 1 JAN 73 IS OBSOLETE.

Unclassified
SECURITY CLASSIFICATION OF THIS PAGE

PROCEEDINGS OF THE SECOND INTERNATIONAL CONFERENCE ON

RECENT ADVANCES IN STRUCTURAL DYNAMICS

9-13 April, 1984

University of Southampton, England

Edited by

M. Petyt and H.F. Wolfe

VOLUME II

ORGANISATION

The Conference was organised by the

Institute of Sound and Vibration Research

in collaboration with the

Air Force Wright Aeronautical Laboratories,
Wright-Patterson Air Force Base

and the

European Office of Aerospace Research and Development,
London, England.

ORGANISING COMMITTEE

Local Members

Dr. M. Petyt	Dr. J.K. Hammond	Dr. J.G. Walker
Professor R.G. White	Dr. R.J. Pinnington	Mrs. M.Z. Strickland
Dr. F.J. Fahy	Mr. K.T. Brown	

International Members

H.F. Wolfe	Professor B.L. Clarkson	Mr. D.C.G. Eaton
Major J.E. Marsh	Professor M. Heckl	Dr. C. Mei
Colonel C.F. Fisher	Professor M. Lalanne	Mr. J. Soovere
	Professor A.C. Nilsson	

PREFACE

This conference follows the very successful first event in the series organised by the Institute of Sound and Vibration Research in July 1980. The second conference has support from the Air Force Wright Aeronautical Laboratories in the USA, the European Office of Aerospace Research and Development and has the continuing objective of reviewing advances which have been made in theoretical and experimental structural dynamics.

Dynamic structural analysis now benefits greatly from the availability of large computational facilities, either for theoretical work or signal processing. Most work is, however, based upon the assumption of linear behaviour, an assumption which is often not valid in practice. Although the balance of the conference is biased towards linear vibration, a section on nonlinear vibration is included which has attracted contributions on a variety of problems.

Generally, the conference papers cover a wide range of topics and it is hoped that this will stimulate discussion and promote liaison between the participants.

I hope that you enjoy the conference both technically and socially.

R. G. White

Editors' Preface

We should like to thank all authors for their contributions. Due to the high stand[illegible]d of the papers we accepted more than for the previous Confere[illegible]. Many were suitable for more than one session. In selecting which one, we have tried to establish an interesting and well balanced programme.

Our thanks also go to the members of the organizing committees for their help in many ways.

M. Petyt.
H. F. Wolfe

CONTENTS

		Page No.
	1. ANALYTICAL METHODS	
1.	Wave propagation in circularly curved beams and rings *C.A. Fettahlioglu and G.M. Vehodian*	1
2.	Calculation of natural frequencies of specially orthotropic multilayered thin circular cylinders *C.B. Sharma and M. Darvizeh*	15
3.	Dynamic response of layered orthotropic cylindrical shells subjected to pressure and axial loadings *O.A. Fettahlioglu and A.M. Sayed*	25
4.	Amplitude growth in vibrations of arms with increasing length *S. Bergamaschi, A. Sinopoli and A. Repaci*	37
5.	Seismic stress fields for nuclear elbows using toroidal elasticity theory *H.A. Lang*	47
6.	Vibrational power transmission from a short source beam to a long finite receiver beam via a vibration isolator *R.J. Pinnington*	55
7.	Prediction of smoothed frequency responses using general orthogonal polynomials *M.E. Gaylard*	65
8.	Dynamic analysis of systems of bars encased in elastic medium *S.M. Aljaweini and J.J. Tuma*	73
9.	Invited paper - Transmission of waves through localized discontinuities; evaluation of two approaches *G. Maidanik*	83
	2. VIBRATION CONTROL	
10.	Auxiliary mass damper for Cardan suspended gyro *J. Rosenberg and A. Kahana*	87
11.	Alleviation of observation spillover in continuous structures *A.V. Metcalfe and J.S. Burdess*	97

3. FINITE ELEMENT AND BOUNDARY ELEMENT METHODS

12. A new beam finite element with seven degrees of freedom at each node for the study of coupled bending-torsion vibrations — 109
A. Potiron, D. Gay and C. Czekajski

13. A boundary element program for the calculation of coupled flexure torsion constants for beams of any cross section shape — 119
C. Czekajski, D. Gay and A. Potiron

14. A comparative study of soil spring and finite element models application to nuclear power station — 127
K.M. Ahmed

15. Dynamic response of crane structure — 139
Chen Wei-zhang

16. State space approach to mechanical vibration — 151
Hu Zongwu and Yan Junqi

17. Non-stationary division by the space time finite element method in vibration analysis — 161
C.I. Bajer

18. Application of the method of integral equations to the vibration of plates — 171
J. Scheuren

19. Use of strain energy density as a basis for finite element model development — 179
A.H. Patel and R. Ali

20. Analysis of dynamic stress characteristics of hollow shell type blades — 189
J. Thomas and S.H. Abdulrahman

21. Some recent advances in dynamic response of shells — 199
R.K. Kapania and T.Y. Yang

4. COMPONENT MODE SYNTHESIS TECHNIQUES

22. Calculation of eigenvalues using substructures and dynamic condensation — 211
N. Petersmann

23. The improvement of free-mode methods in component mode synthesis techniques and its accuracies — 221
Z.W. Wang and M. Petyt

24. Locality principle in structural dynamics — 229
A.K. Belyaev and V.A. Palmov

5. NON LINEAR ANALYSIS TECHNIQUES

25. Invited paper - Nonlinear analysis of plate and shell vibrations — 241
A. Leissa

26. Nonstationary random response of nonlinear structures to nonstationary random excitation — 261
C.W.S. To

27. Extension of transfer-matrix methodology to nonlinear problems — 271
J.W. Davis and L.D. Mitchell

28. Modal synthesis of large structures with nonlinear joints from vibration tests — 281
L. Jezequel

29. An averaging technique for the analysis of oscillations in abruptly non-linear systems — 297
R.K. Miller and M.A. Heidari

30. The numerical solution of discontinuous structural systems — 307
W.K.D. Borthwick

6. NON LINEAR DYNAMICS OF BEAMS

31. A finite element method for nonlinear forced vibrations of beams — 319
C. Mei and K. Decha-Unphai

32. Snap-through of initially buckled beams under uniform random pressure — 329
P. Seide

33. Accurate nonlinear equations and a perturbation solution for the free nonplanar vibrations of inextensional beams — 341
A. Luongo, G. Rega and F. Vestroni

34. Parametric vibration in large blades rotating in a gravitational field — 351
A.D.S. Barr and T. Webster

35. Damped vibrations of a jointed cantilever beam — 361
H. Wissbrok

36. The effects of small clearances on friction loaded constrained points on bending wave energy transmission in a long beam — 373
M.J.H. Fox

37. Review of air-blast response of beams and plates — 383
J. Ari-Gur, D.L. Anderson and M.D. Olson

7. TESTING TECHNIQUES

38. Invited paper - Application of modal synthesis concepts to spacecraft design verification 395
A. Bertram

39. A flexible multichannel measurement system for dynamic analysis 415
H. Van der Auweraer, P. Van Herck, R. Snoeys

40. Limitations on the identification of discrete structural dynamic models 427
A. Berman

41. Foolproof methods for frequency response measurements 437
H.G.D. Goyder

42. An investigation of the behaviour of the simultaneous three axis vibration system 447
G.K. Hobbs

43. Recent experimental devices to obtain the dynamic parameters of bridges 457
W.C. McCarthy, K.R. White and A.G. Arroyo

44. The experimental measurement of flexural wave power flow in structures 467
W. Redman-White

8. MODAL AND DATA ANALYSIS OF NON LINEAR SYSTEMS

45. Recent advances in reduction methods in nonlinear structural dynamics 475
S.R. Idelsohn and A. Cardona

46. Feasibility of using modal analysis techniques for nonlinear multi-degree of freedom systems 483
C. Nopporn, R. Singh and H. Busby

47. Modal analysis and identification of structural non-linearity 495
G.R. Tomlinson and N.E. Kirk

48. Time domain analysis of nonlinear vibration data 511
S.F. Masri, R.K. Miller, H. Sassi and T. Caughey

49. Extended damping models for vibration data analysis 521
J.A. Fabunmi

9. NON LINEAR DYNAMICS OF PLATES

50. Non-stationary responses of non-linear rectangular plates during transition through parametric resonance, Part I: Theory 535
G. Ostiguy

51. Non-stationary responses of non-linear rectangular plates during transition through parametric resonance, Part II: Experiment 547
G. Ostiguy

52. Nonlinear dynamic analysis of anisotropic rectangular plates by a new method 559
M. Sathyamoorthy

53. Large amplitude vibration of an initially stressed bimodulus thick plate 567
L.W. Chen and C.J. Lin

54. Nonlinear multimode response of clamped rectangular plates to acoustic loading 577
C. Mei and D.B. Paul

10. RESPONSE TO SEISMIC EXCITATION

55. Steel fibrous concrete under seismic loading 589
L. Minnetyan and G.B. Batson

56. Inelastic analysis of short highway bridges subjected to strong ground motions 599
M. Saiidi, J.D. Hart and B.M. Douglas

57. Elastic-plastic response of rooftop frames to distributed and concentrated shock load: experimental results and predictions using a numerical technique 609
M.S.J. Hashmi

11. RANDOM VIBRATION

58. Invited paper - Researches in random vibration 621
J.D. Robson

59. Some closed-form solutions in random vibration of Timoshenko beams 639
I. Elishakoff and D. Livshits

60. Random vibration of discrete, periodic coupled frame-wall systems 649
G. Oliveto and A. Santini

12. ROAD VEHICLES

61. Dynamic analysis of vehicles with nonlinear suspension properties 665
J.A. Lyons and L. Minnetyan

62. A state space approach to the analysis of non-stationary, nonlinear random vibration with particular application to the problem of vehicles on rough ground 673
R.F. Harrison and J.K. Hammond

13. RAILWAY VEHICLES

63. Invited paper - Dynamic modelling of railway track and wheelsets 681
S.L. Grassie

64. Two theoretical models for wave propagation in rails 699
W. Scholl

65. Dynamics and stability of train-track systems 709
R. Bogacz and K. Popp

66. Assessment of the generating mechanisms and characteristics of wheel/rail noise via study of a rolling disc 723
N.S. Ferguson and R.G. White

67. On the acoustically optimal design of railway wheels 731
H. Irretier and O. Mahrenholtz

14. AEROSPACE STRUCTURES AND/OR FATIGUE

68. Galileo spacecraft modal test and evaluation of testing techniques 749
Jay-Chung Chen

69. Acoustic fatigue life of adhesive bonded structures subjected to acoustic loads 763
H.F. Wolfe and I. Holehouse

70. Dynamic response and acoustic fatigue of stiffened composite structures 775
J. Soovere

71. Sonic fatigue design method for the response of CFRP stiffened-skin panels 787
I. Holehouse

72. Prediction of the dynamic properties of carbon-glass fibre sandwich hybrid laminated composites 799
R.D. Adams, R.G. Ni and D.X. Lin

73. Life time prediction based on the combined use of finite element and modal analysis data 809
E. Verdonck and R. Snoeys

15. MACHINERY

74. Noise energy radiated from rod-like structures 825
L.C. Chow and J.M. Cuschieri

75. Using a scale model to investigate the post fracture structural vibrations and noise of a 200 tonne power press 835
G. Stimpson

76. Active force control in machinery noise 845
J.M. Cuschieri

77. Modelling the relation between structural vibrations and radiated sound 853
P. Sas, P. Vandeponseele, R. Snoeys

16. DAMPING

78. Development of the aerospace structures technology damping design guide 867
J. Soovere, M.L. Drake, V.R. Miller and L.C. Rogers

79. Continuum modelling of damping in large space structures 877
S. Abrate and C.T. Sun

80. Determination of receptances of locally damped structures 887
H.N. Ozguven

7. TESTING TECHNIQUES

APPLICATION OF MODAL SYNTHESIS CONCEPTS TO SPACECRAFT DESIGN VERIFICATION+

A. Bertram

DFVLR/AVA Göttingen
Institut für Aeroelastik

1. INTRODUCTION

A spacecraft never will be subjected to the flight environment for which it was designed until it is launched. To ensure safety and reliability of the structure, one is left to demonstrate that it can withstand all loads to be expected during launch and during its life in orbit prior one will risk to put it onto a launcher.

The only argument the structural engineer is endowed with is a calculation of the dynamic response and of internal loads under certain specified dynamic environments. This is done using a mathematical model representing the dynamic characteristics of the structure - and certainly more or less realistically.

The general way to model a complex structural system is the method to discretize it by means of large finite-element (FE) program systems. The dynamic behaviour of the structure is described in discrete physical degrees of freedom (DOF), which correspond to the nodal point displacements of the FE mesh. The physical distribution of mass and stiffness is represented in discrete matrices. It is commonly known that the mass-matrix can be evaluated very correctly by the FE method, whereas the stiffness matrix is infected with certain inaccuracies depending on the effort which is spent on modelling the structure. Concerning the description of the damping characteristics, generally no information can be obtained by means of the finite-element method; one is left to perform experimental investigations.

FE-models are a very efficient tool to study the dynamic behaviour of a structure already in a very early phase of its development. A mathematical model, however, is a reliable tool only when it is verified by means of the dynamic behaviour of a realistic structure. In doing so, a number of selected experiments is performed. To minimize both experimental and analytical effort in the design verification procedure, a combined procedure is our aim. To identify the basic conditions we must see this in the light of the spacecraft development in recent years. Namely, the trend to interchangeable payload modules and the technology of the future large spacecraft which renders experimental investigation of the complete structure impossible. This is the reason it becomes necessary to separate it into substructures (see also [1] and [2]. Furthermore, small structural modifications may be the result

---

+The paper is based on work conducted under several ESA/ESTEC Contracts

of design changes with the consequence of extensive work and costs in order to update the mathematical model if it should not be possible to find a way on which we can pass a new test or a renewed FE analysis.

In the light of these problems, concepts for structural analysis and of appropriate experimental techniques were elaborated in recent years. An extensive literature search [3] highlights a large number of publications dealing with methods for the solution of the structural analysis tasks described above. Based on these sources, suitable procedures were selected and described in this work, all fulfilling the following criteria:

- o applicability to spacecraft structures,
- o use of experimental data, and
- o use of modal data.

As already said above, the general way to describe the elastic behaviour of any structural system is by discretizing it. In doing so, the equations for a dynamic system with n discrete DOFs read

$$\underline{\underline{m}}\,\ddot{\underline{u}} + \underline{\underline{c}}\,\dot{\underline{u}} + \underline{\underline{k}}\,\underline{u} = \underline{f} \qquad (1)$$

assuming linearity and viscous-type damping, where $\underline{\underline{m}}$, $\underline{\underline{c}}$ and $\underline{\underline{k}}$ are quadratic matrices (of order n) of mass, damping and stiffness, and $\underline{u}$ and $\underline{f}$ are the independent vectors of the nodal point displacements and of the external forces, respectively. These equations may be transformed into energy equations by writing the discrete coordinates $\underline{u}(x,t)$ in a series expansion of the orthogonal mode shape matrix

$$\underline{u}(x,t) = \underline{\underline{\phi}}\,\underline{q}(t) \qquad (2)$$

where vector $\underline{q}$ contains the generalised or modal coordinates as weighting factors of the series expansion. Equation (2) is strictly valid only for an infinite number of modes; in practical cases, however, only a truncated set of modes can be considered. The convergence of this series expansion depends on the selection of mode shapes. The sufficient fulfillment of this equation is of significance in using modal methods. Its accomplishment is the most important objective in all what is described in the following.

2. MODAL DESCRIPTION OF STRUCTURAL DYNAMICS

It can be derived that a condition called the orthogonality of the mode shapes related to the mass matrix exists, such as

$$\underline{\phi}_p^T\,\underline{\underline{m}}\,\underline{\phi}_q = \begin{cases} 1 & \text{for } p = q \\ 0 & \text{for } p \neq q \end{cases} . \qquad (3)$$

The orthogonality condition is the second fundamental basis for the applicability of modal methods. According to Equation (3) there is a diagonal matrix $\underline{\underline{M}}$, called the matrix of generalised masses

$$\underline{\underline{\phi}}^T\,\underline{\underline{m}}\,\underline{\underline{\phi}} = \underline{\underline{M}} . \qquad (4)$$

Analogue to $\underline{\underline{M}}$ the matrices of generalised stiffness $\underline{\underline{K}}$ and generalised damping $\underline{\underline{C}}$ can be built, whereas the generalised forces $\underline{F}$ read

$$\underline{\underline{\phi}}^T \underline{f} = \underline{F} \quad . \tag{5}$$

Matrices $\underline{\underline{M}}$ and $\underline{\underline{K}}$ both become diagonal too; the generalised damping matrix $\underline{\underline{C}}$ is assumed for the sake of simplicity to be also diagonal, although it is not necessarily so. In modal description, the dynamic equations given in (1) yield to

$$\underline{\underline{M}}\,\ddot{\underline{q}} + \underline{\underline{C}}\,\dot{\underline{q}} + \underline{\underline{K}}\,\underline{q} = \underline{F} \tag{6}$$

with the order m, the number of modes taken into account.

The decoupling of the equations due to the diagonality of the system's matrices together with the reduction of the system's order from the discrete to the generalised DOFs are two important advances in numerical treatment of structural dynamics analyses. Moreover, the modal system is very suitable for the structural engineer, to obtain an improved insight into the dynamics of the structure, owing to the direct description of structural characteristics by means of mode shapes.

2.1 Modal Synthesis Methods

The elasto-dynamic behaviour of any structural system is defined by a combination of inertial, stiffness and damping forces and, additionally, external forces. For simplification reasons, damping and external forces are neglected in the following. Based on these assumptions, the elastic behaviour can be described completely when the following modal parameters are known: eigenfrequencies $\underline{\underline{\omega}}$, mode shapes $\underline{\underline{\phi}}$ and generalised masses $\underline{\underline{M}}$. With this, the dynamic equations read

$$\underline{\underline{M}}\,\ddot{\underline{q}} + \underline{\underline{K}}\,\underline{q} = \underline{0} \tag{7a}$$

or

$$\underline{\underline{M}}\,\ddot{\underline{q}} + \underline{\underline{\omega}}\,\underline{\underline{M}}\,\underline{\underline{\omega}}\,\underline{q} = \underline{0} \tag{7b}$$

These modal data have to fulfill the additional conditions, as specified above, namely:

- o orthogonality of the modes and
- o sufficient convergence in the modal approach within the interesting frequency range.

A typical application of modal synthesis methods is presented in Figure 1, where the mathematical model of an assembled structure is analytically determined from the dynamic data of its substructures. The mathematical models of both substructures are obtained in an experimental way - by means of modal survey tests e. g. The antenna module is tested with its interface to the other substructure being fixed. When testing the lower substructure, it is fixed at its base; the interface to the antenna is "loaded" by means of a rigid dummy mass. The procedure in this particular case of modal coupling will be described later on. First, the basical procedures of modal synthesis are briefly outlined.

2.2 Dynamic Equations of a Coupled System

According to (7a), the equations of motion of a structure assembled from the substructures A and B read:

$$\begin{bmatrix} \underline{\underline{M}}^{A} & \\ & \underline{\underline{M}}^{B} \end{bmatrix} \begin{bmatrix} \ddot{\underline{q}}^{A} \\ \ddot{\underline{q}}^{B} \end{bmatrix} + \begin{bmatrix} \underline{\underline{K}}^{A} & \\ & \underline{\underline{K}}^{B} \end{bmatrix} \begin{bmatrix} \underline{q}^{A} \\ \underline{q}^{B} \end{bmatrix} = \begin{bmatrix} \underline{0} \\ \underline{0} \end{bmatrix} \tag{8a}$$

or

$$\begin{bmatrix} & \underline{\underline{M}} & \end{bmatrix} \begin{bmatrix} \ddot{\underline{q}} \end{bmatrix} + \begin{bmatrix} & \underline{\underline{K}} & \end{bmatrix} \begin{bmatrix} \underline{q} \end{bmatrix} = \begin{bmatrix} \underline{0} \end{bmatrix} \tag{8b}$$

The system is of order $m = m^{A} + m^{B}$, i. e. the number of modes taken into account for both substructures. In Equation (8) both subsystems are still uncoupled. The coupling is performed by additionally considering the specific coupling conditions. These are expressed by the stiffness relations in the interface between both substructures.

2.3 Coupling conditions

A destinction must be made between two special cases of interface condition: rigid coupling and elastic coupling. In the case of elastic coupling by means of an elastic coupling element with the discrete physical stiffness matrix $\underline{\underline{k}}^{AB}$, the additional potential energy U in the springs yields (as described in [4])

$$U = \frac{1}{2} \underline{u}_{e}^{T} \underline{\underline{k}}^{AB} \underline{u}_{e} \quad . \tag{9}$$

Applying Lagrange's operation, the additional stiffness in generalised description is obtained by

$$\underline{\underline{\Delta K}} = \begin{bmatrix} \underline{\phi}_{e}^{A^{T}} & \\ & \underline{\phi}_{e}^{B^{T}} \end{bmatrix} \begin{bmatrix} \underline{\underline{k}}^{AB} \end{bmatrix} \begin{bmatrix} \underline{\phi}_{e}^{A} & \\ & \underline{\phi}_{e}^{B} \end{bmatrix} \tag{10}$$

and may then be introduced into Equation (8)

$$\begin{bmatrix} & \underline{\underline{M}} & \end{bmatrix} \begin{bmatrix} \ddot{\underline{q}} \end{bmatrix} + \left\{ \begin{bmatrix} & \underline{\underline{K}} & \end{bmatrix} + \begin{bmatrix} \underline{\underline{\Delta K}} \end{bmatrix} \right\} \begin{bmatrix} \underline{q} \end{bmatrix} = \begin{bmatrix} \underline{0} \end{bmatrix} \quad . \tag{11}$$

The case of rigid coupling is defined by a compatibility condition between corresponding DOFs in the common interface as shown in

$$\underline{u}_r^A - \underline{u}_r^B = \underline{0} \tag{12}$$

Using modal description, it yields

$$\left[\underline{\phi}_r^A \;\vdots\; -\underline{\phi}_r^B\right] \begin{bmatrix} \underline{q}^A \\ \underline{q}^B \end{bmatrix} = \left[\underline{0}\right] \tag{13a}$$

or

$$\underline{\phi}_r \, \underline{q} = \underline{0} \quad . \tag{13b}$$

Compatibility implies a reduction in the number of DOFs by r, the number of constraints. Vector $\underline{q}$ in Equation (13b) containing m independent DOFs decreases to $\underline{\bar{q}}$. The reduction to m-r DOFs is caused by a transformation according to

$$\underline{q} = \underline{\underline{T}} \, \underline{\bar{q}} \quad . \tag{14}$$

To generate $\underline{\underline{T}}$, a set of r independent vectors $\underline{\phi}_i$ out of matrix $\underline{\phi}_r$ of Equation (13b) must be found; a set of dependent vectors $\underline{\phi}_d$ is kept. The elemination of the r DOFs is performed by means of the following relation

$$\underline{\phi}_r \, \underline{q} = \left[\underline{\phi}_d \;\vdots\; \underline{\phi}_i\right] \begin{bmatrix} \underline{q}_d \\ \underline{q}_i \end{bmatrix} = \underline{0} \quad , \tag{15}$$

and consequently

$$\underline{q}_i = -\underline{\phi}_i^{-1} \, \underline{\phi}_d \, \underline{q}_d \tag{16}$$

is obtained for the transformation given in Equation (14)

$$\underline{q} = \begin{bmatrix} \underline{\underline{I}} \\ - - - - \\ -\underline{\phi}_i^{-1} \, \underline{\phi}_d \end{bmatrix} \underline{\bar{q}} = \underline{\underline{T}} \, \underline{\bar{q}} \quad . \tag{17}$$

The requirement to select a number of r independent vectors out of $\underline{\phi}_r$ may be difficult in an automatic process of a computer programme. To escape this inconvenience, a computer suitable process for automatic generation of the independent coordinates $\underline{\bar{q}}$ is presented now, using the so called "zero-eigenvalue theorem", presented in [5].

Here a routine can be employed, whereby an eigenvalue analysis has to be solved instead of a matrix inversion. $\underline{\underline{T}}$ is generated by means of the special eigenvalue problem

$$\underline{\underline{\phi}}_r^T \, \underline{\underline{\phi}}_r \, \underline{y} = \underline{0} \quad , \tag{18}$$

whereby $\underline{\underline{T}}$ is produced from the eigenvectors belonging to zero eigenvalues.

Applying the transformation of Equation (14) on Equation (8b) yields

$$\underline{\underline{T}}^T \, \underline{\underline{M}} \, \underline{\underline{T}} \, \ddot{\underline{q}} + \underline{\underline{T}}^T \, \underline{\underline{K}} \, \underline{\underline{T}} \, \underline{q} = \underline{0} \quad . \tag{19}$$

2.4 Structural Modifications

An experimentally determined mathematical model, however, has the disadvantage of being inflexible, i.e. the elastomechanical parameters obtained are only valid for the particular configuration tested. The modal formulation of the equations of motion is the basis for the application of a simple correction procedure. Structural modifications can be handled with the following method when they result in dynamic properties that can be sufficiently described by superimposing the normal modes of the basic structure (see e.g. [4] and [6]). This is done by considering some structural changes involving the distribution of physical masses $\underline{\underline{\Delta m}}$ or physical stiffness $\underline{\underline{\Delta k}}$ in the modal mathematical model.

Proceeding from (7) the equations of motion of the basic configuration (a) yield

$$\underline{\underline{M}}^a \, \ddot{\underline{q}}^a + \underline{\underline{K}}^a \, \underline{q}^a = \underline{0} \quad . \tag{20}$$

After some structural modifications $\underline{\underline{\Delta m}}$ and $\underline{\underline{\Delta k}}$, the changed configuration (b) reads

$$\underline{\underline{M}}^b \, \ddot{\underline{q}}^b + \underline{\underline{K}}^b \, \underline{q}^b = \underline{0} \quad , \tag{21}$$

where

$$\underline{\underline{M}}^b = \underline{\underline{M}}^a + \underline{\underline{\Delta M}} \tag{22a}$$

and

$$\underline{\underline{K}}^b = \underline{\underline{K}}^a + \underline{\underline{\Delta K}} \quad . \tag{22b}$$

Modifications of the discrete mass distribution result in an alteration of the kinetic energy of the system by

$$T = \frac{1}{2} \, \underline{u}_m^T \, \underline{\underline{\Delta m}} \, \underline{u}_m \quad . \tag{23}$$

Again applying Lagrange's operation, the mass modification yields in generalised description

$$\underline{\underline{\Delta M}} = \underline{\underline{\phi}}_m^T \, \underline{\underline{\Delta m}} \, \underline{\underline{\phi}}_m \quad . \tag{24}$$

Accordingly, a discrete stiffness modification leads to an alteration in the potential energy

$$U = \frac{1}{2} \underline{u}_k^T \underline{\underline{\Delta k}} \underline{u}_k \tag{25}$$

and thereby to a change in the generalised stiffness

$$\underline{\underline{\Delta K}} = \underline{\Phi}_k^T \underline{\underline{\Delta k}} \underline{\Phi}_k \cdot \tag{26}$$

Assembling Equations (24), (26) and (22), the dynamic behaviour of the modified structure is described by means of the modal data of the basic configuration and the discrete structural changes.

3. ACCOMPLISHING THE ORTHOGONALITY CONDITION AND A SUFFICIENT CONVERGENCE

As examined above, modal transformation is a series expansion which leads to an exact description of the structural deformations if and only if an infinite number of orthogonal mode shapes is taken into account. A great variety of mode shapes are described in papers dealing with modal synthesis methods. They are different in the kind of the boundary conditions taken as a basis in determining the corresponding modes. The present paper is limited to those modes that can be determined experimentally.

3.1 Selection of Suitable Modes

In References [1] and [7] detailed reviews of the different types of mode shapes are given. In Figure 2 [7] a selected number of modes is summarised together with the appropriate coupling methods.

Rigid body modes and elastic normal modes are the most common ones, and within this category free-interface and loaded-interface normal modes. It is not only useful but mandatory to consider the effect of neighbouring structures as the mass and/or stiffness properties of adjacent structures act dynamically at the joint interface. In cases of statically determinate coupling, an interface loading of the main structure considering only the inertial properties is sufficient in many cases.

Beyond these types of normal modes, there are several other kinds of modes. Fixed-interface normal modes can, in general, only be determined analytically. Constraint modes may be used to complement fixed-interface normal modes and attachment modes to complement a set of free-interface normal modes.

Let us now consider to what extent the requisite orthogonality of the different mode sets used in the example of Figure 1 is fulfilled. The mode set of the upper substructure is composed of rigid-body modes and fixed-interface normal modes

$$\underline{\underline{\Phi}} = \left[\underline{\underline{\Phi}}_R \,\vdots\, \underline{\underline{\Phi}}_E \right] \cdot \tag{27}$$

Due to the various boundary conditions, these two mode sets are not mutually orthogal, resulting in off-diagonal elements in the matrix of generalised masses $\underline{\underline{M}}$

$$\underline{\underline{M}} = \underline{\underline{\Phi}}^T \underline{\underline{m}} \underline{\underline{\Phi}} = \begin{bmatrix} \underline{\underline{M}}_{RR} & \underline{\underline{M}}_{RE} \\ \underline{\underline{M}}_{ER} & \underline{\underline{M}}_{EE} \end{bmatrix} , \tag{28}$$

where

$$\underline{\underline{M}}_{RR} = \underline{\underline{\Phi}}_R^T \underline{\underline{m}} \underline{\underline{\Phi}}_R \tag{29a}$$

$$\underline{\underline{M}}_{EE} = \underline{\underline{\Phi}}_E^T \underline{\underline{m}} \underline{\underline{\Phi}}_E \tag{29b}$$

$$\underline{\underline{M}}_{RE} = \underline{\underline{\Phi}}_R^T \underline{\underline{m}} \underline{\underline{\Phi}}_E = \underline{\underline{M}}_{ER}^T . \tag{29c}$$

Whereas $\underline{\underline{M}}_{RR}$ and $\underline{\underline{M}}_{EE}$ are diagonal matrices, $\underline{\underline{M}}_{RE}$ and $\underline{\underline{M}}_{ER}$ are fully occupied. It can be shown (see [20] and [21]), however, that the corresponding matrix of generalised stiffness

$$\underline{\underline{K}} = \underline{\underline{\Phi}}^T \underline{\underline{k}} \underline{\underline{\Phi}} = \begin{bmatrix} \underline{\underline{K}}_{RR} & \underline{\underline{K}}_{RE} \\ \underline{\underline{K}}_{ER} & \underline{\underline{K}}_{EE} \end{bmatrix} \tag{30}$$

generated by means of the semi-definite matrix $\underline{\underline{k}}$ yields

$$\underline{\underline{K}} = \begin{bmatrix} \underline{\underline{0}} & \underline{\underline{0}} \\ \underline{\underline{0}} & \underline{\underline{K}}_{EE} \end{bmatrix} , \tag{31}$$

whereby $\underline{\underline{K}}_{EE}$ is diagonal according to

$$\underline{\underline{K}}_{EE} = \underline{\underline{\Phi}}_E^T \underline{\underline{k}} \underline{\underline{\Phi}}_E = \underline{\underline{\omega}}_E^T \underline{\underline{M}}_{EE} \underline{\underline{\omega}}_E . \tag{32}$$

The result of this derivation is that, despite the nonorthogonality of both mode sets $\underline{\underline{\Phi}}_R$ and $\underline{\underline{\Phi}}_E$, modal synthesis can be performed when the off-diagonal elements in the matrix of generalised masses are taken into account.

The fulfillment of the second specified condition, the convergence of the modal transformation requires among others an attentive selection of the used modes. For both modal synthesis methods, it is evident that accurate results can only be obtained when the structures are described by a complete set of modes. For structures with a limited number of modal DOFs, where only a truncated set of modes can be taken into account, the result depends on the suitability of the experimental data. In the modal correction analyses, the modes obtained analytically are produced from the modes of the measured structural configuration in the form of a series expansion, even including significant changes in mode shapes. With this condition, the applicability of correction methods is evidently defined.

Successful application of the modal coupling approach is apparently highly dependent on the authenticity of the description and simulation of the actual coupling conditions. In a later section of this paper the importance of a realistic description of the coupling conditions in the interface is outlined. It is anticipated here, that this may be due to an interface loading of the substructures as shown in the former example. The rigid dummy mass on top of the lower substructure when determining its modes has a convergence improving effect in the coupling approach. The realistic inertial properties of the antenna module are introduced into the analysis in considering its rigid body modes, whereas the dummy mass is removed by means of the modal correction method being proved as a very efficient tool in modal synthesis procedures.

3.2 Test Data Requirements

Design verification procedures are dependent on the performance of reliable and realistic tests with high accuracy. Due to the high modal density of spacecraft structures and the presence of structual non-linearities, modal survey tests using appropriate excitation is up to now the most reliable way to determine a complite set of real normal modes. Poor orthogonality may occur as a result of insufficient exciter accessibility to internal parts of the structure. Further development of modal survey test methods led to procedures described in References [22] and [23], which improve test results even in such cases.

In summary, the following guidelines for the preparation and performance of modal survey tests can be laid down:

- The measuring points must be appropriate to describe all modes in the frequency range of interest.
- The mass matrix must accurately simulate the mass distribution of the real structure.
- The number of measuring points must be adequate to describe the modes, especially at the interfaces.
- The excitation must be well appropriated.
- Good accessibility to inner parts of the structure should be considered a spacecraft design requirement.
- Test methods and procedures should be continuously improved and adapted to the latest state of the art.

3.3 Improving the Convergence

Convergence improving procedures have the aim to introduce into the modal approach certain flexibilities which are characterised by producing deformations at frequencies above the range taken into account. In the following, two different ways are outlined; both consider additional information which would have got lost due to the truncation of modes.

3.3.1 Considering Residual Terms

In the literature a number of methods to improve convergence by means of residual terms are known. They may be traced back to mainly two works, presented by Mac Neal [15] and Rubin [16]. The common aim is to increase the accuracy of the classical modal approach by means of globally approximating the contributions of the neglected modes, without detailly knowing what's what (see [24]). The common modal survey test delivers the modal matrices $\underline{\underline{M}}$, $\underline{\underline{K}}$, and $\underline{\underline{\phi}}$, completely describing the structural dynamics of the structure in the investigated range of frequency, as generally known

$$\underline{\underline{M}}\,\underline{\ddot{q}} + \underline{\underline{K}}\,\underline{q} = \underline{0} \quad . \tag{33}$$

Additionally, the complex response $\underline{\hat{u}}$ of the structure due to harmonic excitation $\underline{\hat{p}}$ is recorded for a number of discrete exciter frequencies Ω_j

$$\underline{\hat{u}} = \underline{\underline{Y}}\,\underline{\hat{p}} \quad . \tag{34}$$

The steps for the discrete frequencies Ω_j should be spaced closely enough, to describe a continuous relation between $\underline{\hat{u}}$ and $\underline{\hat{p}}$. Considering the results of the modal survey test, it yields for the remaining admittance $\underline{\underline{Y}}_c$ (Ω_j) for the discrete frequencies Ω_j

$$\underline{\underline{Y}}_c(\Omega_j) = \underline{\underline{Y}}(\Omega_j) - \underline{\underline{\phi}}^T \left\{-\Omega_j^2\,\underline{\underline{M}} + \underline{\underline{K}}\right\}^{-1} \underline{\underline{\phi}} \quad . \tag{35}$$

In Equation (35) the contribution of the measured modes is subtracted from the complete admittance of the structure. The parts of the higher modes now can be approximated by the following quadratic approach

$$\underline{\underline{Y}}_c = \underline{\underline{A}}_c + \Omega^2\,\underline{\underline{B}}_c \tag{36}$$

delivering the constant auxiliary matrices $\underline{\underline{A}}_c$ and $\underline{\underline{B}}_c$ and finally the residual terms for generalised stiffness

$$\underline{\underline{K}}_c = \underline{\underline{A}}_c^{-1} \tag{37a}$$

and generalised masses

$$\underline{\underline{M}}_c = \underline{\underline{K}}_c\,\underline{\underline{B}}_c\,\underline{\underline{K}}_c \quad , \tag{37b}$$

respectively. In a first order approach, only $\underline{\underline{K}}_c$ is evaluated. The complete equations of motion yield

$$\begin{bmatrix} \underline{\underline{M}}_{11} & \underline{\underline{M}}_{12} \\ \underline{\underline{M}}_{21} & \underline{\underline{M}}_{22} \end{bmatrix} \begin{bmatrix} \underline{\ddot{v}} \\ \end{bmatrix} + \begin{bmatrix} \underline{\underline{K}}_{11} & \underline{\underline{K}}_{12} \\ \underline{\underline{K}}_{21} & \underline{\underline{K}}_{22} \end{bmatrix} \begin{bmatrix} \underline{v} \\ \end{bmatrix} = \begin{bmatrix} \underline{w} \\ \end{bmatrix} \quad , \tag{38}$$

with

$$\underline{\underline{M}}_{11} = \underline{\underline{M}} + \underline{\underline{\phi}}^T\,\underline{\underline{M}}_c\,\underline{\underline{\phi}} \tag{39a}$$

$$\underline{\underline{M}}_{12} = -\underline{\underline{\phi}}^T\,\underline{\underline{M}}_c = \underline{\underline{M}}_{21}^T \tag{39b}$$

$$\underline{\underline{M}}_{22} = \underline{\underline{M}}_c \tag{39c}$$

and analogous

$$\underline{\underline{K}}_{11} = \underline{\underline{K}} + \underline{\underline{\Phi}}^T \underline{\underline{K}}_c \underline{\underline{\Phi}} \tag{40a}$$

$$\underline{\underline{K}}_{12} = -\underline{\underline{\Phi}}^T \underline{\underline{K}}_C = \underline{\underline{K}}_{21}^T \tag{40b}$$

$$\underline{\underline{K}}_{22} = \underline{\underline{K}}_c \quad . \tag{40c}$$

The vectors $\underline{v}$ and $\underline{w}$ read

$$\underline{v} = \begin{bmatrix} \underline{q} \\ \underline{u} \end{bmatrix} , \qquad \underline{w} = \begin{bmatrix} \underline{0} \\ \underline{p} \end{bmatrix} . \tag{41a,b}$$

The examples in [15], [16] and [24] verify that global approximations of the modes which are not considered improve the accuracy of dynamic analyses. Particularly in the modal coupling approach the engineer is interested in representing the local effects in some discrete coupling points also at very high frequencies. In the "classical" approach, a large number of higher modes has to be taken into account to get the same results as the method of residual terms is producing with a relatively small number of experimentally well-determinable modes.

3.3.2 Realistic Description of the Interface

The method of using residual terms is a more global one, whereas the method of utilizing interface loading is aimed to generate deformations in the interface of the substructures similar to those found in the common interface of the assembled structure.

Evidently, in the case of mode truncation, this method will assure the necessary convergence and thus improve modal coupling, bearing in mind that, according to the modal approach, the mode set of the complete system is composed of the mode sets of the single substructures. Whereas the mode shapes of the substructures are intentionally modified by additional stiffness and masses, changes in the frequencies and generalised masses are undesirable. According to the procedure presented in Figure 1, the effect of interface loading on frequencies and generalised masses has to be corrected. This is done by means of the modal correction method derived above. The correction terms are introduced into the equations of motion of the coupled system as given in Equation (8b).

$$\left\{\underline{\underline{M}} - \underline{\underline{\Delta M}}\right\} \ddot{\underline{q}} + \left\{\underline{\underline{K}} - \underline{\underline{\Delta K}}\right\} \underline{q} = \underline{0} \quad . \tag{42}$$

As given in Equation (24)

$$\underline{\underline{\Delta M}} = \underline{\underline{\Phi}}_m^T \underline{\underline{\Delta m}} \underline{\underline{\Phi}}_m \tag{43}$$

for correction of inertia-loading, and in (26)

$$\underline{\underline{\Delta K}} = \underline{\phi}_k^T \underline{\underline{\Delta k}} \underline{\phi}_k \qquad (44)$$

for correction of stiffness-loading.

Taking advantage of interface loading, especially in cases of redundant interfaces it is necessary to realistically describe the coupling conditions during the performance of the substructure tests and in the coupling approach. Figure 3 taken from [25] shows the example of two parallel beam-type structures, coupled at five discrete points. In Figure 3a the bolted connection is described by means of rigidly coupled, translational DOFs vertical to the interface. The frequency discrepancy related to an FE analysis of the assembled structure amounts up to 21%, which is not satisfactory. A more exact description is obtained by considering the coupling of DOFs in the plane of the interface, producing an additional stiffness, which approximates better to the real conditions. This leads to the application of mixed coupling, whereby some DOFs are coupled rigidly and some elastically. The frequency discrepancy decreases to about 12 %. The interface considering these lateral constraints is given in Figure 3b.

In most practical cases, the interface between different spacecraft structures is highly redundant, e. g. the connection between two modules of a satellite (Figure 4). The results of a modal coupling analysis depend on the extent to which compatibility in the common iterface is fulfilled. As experience has shown ([26]), the coupling analyses considering a great number of constraints generally yield unsatisfactory results because, evidently, many more than the available modes are necessary to obtain good convergence. It is therefore worth optimizing the coupling conditions and keeping the number of constraints a minimum.

In the course of a contract funded by ESTEC ([27]), analytical studies were performed to obtain information for optimizing modal-coupling procedures for satellite structures. For this purpose, a simple satellite type structure SIMOD (Figure 5) consisting of two modules was built. To obtain information for optimizing substructure modal survey test conditions, various modal coupling analyses were performed using FE modal models. Among others the appropriation of free interface normal modes and fixed interface normal modes of the upper substructure were investigated; 36 constraints were considered. With both mode sets no satisfactory result could be obtained; but the understanding was established that the highly redundant coupling conditions could not be realised realistically enough by means of a large number of constraints. As a first step towards improved results, inertia loading was applied on the interface of the lower module. To achieve further advancement, the following assumptions concerning interface conditions were made. The lower substructure interface will not be deformed elastically within the frequency range of interest, but will perform only rigid body motions, due to the perpendicular connection of the side walls to the horizontal floor. The upper substructure interface is forced to deform in the same way when connected to the lower substructure. As rigid body deformations are described by only six discrete displacements, it is sufficient -indeed mandatory- to introduce two pairs of six constraints whereby the condition that the interfaces deform rigidly must be fulfilled in both substructure tests. To produce a mode set for the upper substructure, where out-of-plane deformations in the interface are suppressed while rigid body motions are made possible, stiff-

ness loading on the interface was introduced. Following these assumptions, modal survey tests were performed with the following boundary conditions (as shown in Figure 6):

Lower substructure: clamped at its base and upper interface equipped with rigid lumped masses.

Upper substructure: soft suspension; lower interface stiffened by means of two aluminum tubes.

Complete structure: clamped at its base.

With these modal data the modal coupling analysis was performed with 15 elastic normal modes of the lower substructure, 15 elastic normal modes of the upper one, and six additional rigid body modes. Figure 7 shows mode A-3 of the lower substructure, mode B-6 of the upper one and two corresponding mode shapes of the complete structure at about 32 Hz, presenting a comparison between the modal coupling analysis and the reference measurement. All resulting frequencies and generalised masses are correlated with the reference data in Figure 8. Evaluation of the correlated frequencies up to about 130 Hz indicates satisfactory correspondence. Two further pairs of correlated mode shapes are presented in Figure 9 and 10.

As a general result of this example, it can be stated that the interface conditions specified for the individual substructures must simulate the deformation conditions of the assembled configuration. Thus, the interface loading need not necessarily be of the same magnitude as the actual conditions, as long as it represents a reasonable approximation.

4. CORRELATION BETWEEN ANALYSIS AND TEST

Modal data obtained by tests are never identical to the results of finite element analyses. This is the argument for performing tests in design verification procedure. Study of the reasons for the discrepancies is no subject of this paper. Certainly, a description of the various methods for correlating the mode sets and updating the discrete mathematical models would exceed the scope of this work. Currently a large number of investigations and studies is dealing with the problem of updating and correcting FE stiffness matrices. In this paper, only two very simple procedures are presented having the common objective to support the engineering judgement in correlating measured to calculated data.

A correlation matrix $\underline{\underline{Z}}$ presented in [26] is composed of two independently determined mode sets $\underline{\underline{\phi}}_p$ and $\underline{\underline{\phi}}_q$ and the discrete mass matrix $\underline{\underline{m}}$

$$\begin{bmatrix} \underline{\underline{\phi}}_p^T \\ \hline \underline{\underline{\phi}}_q^T \end{bmatrix} \left[\underline{\underline{m}} \right] \left[\underline{\underline{\phi}}_p \;\vdots\; \underline{\underline{\phi}}_q \right] = \begin{bmatrix} \underline{\underline{Z}}_{pp} & \underline{\underline{Z}}_{pq} \\ \underline{\underline{Z}}_{qp} & \underline{\underline{Z}}_{qq} \end{bmatrix} . \tag{45}$$

Considering the orthogonality condition derived in Equation (3)

$$\underline{\underline{\phi}}_p^T \, \underline{\underline{m}} \, \underline{\underline{\phi}}_q = \begin{cases} 1.0 & \text{if } p = q \\ 0.0 & \text{if } p \neq q \end{cases} \tag{46}$$

the submatrices $\underline{\underline{Z}}_{pq}$ and $\underline{\underline{Z}}_{qp}$ of the correlation matrix are occupied by figures between 1 and 0, expressing qualitative and quantitative correlation of both mode sets $\underline{\Phi}_p$ and $\underline{\Phi}_q$. A value near to 1 is a criterion for good conformity between two modes from the different mode sets.

The second procedure is a support for the comparison of the graphics of corresponding mode shapes. As is well known the uncondensed FE model has a larger number of physical DOFs than a measured mode shape. To produce still fully comparable graphics, use of the following procedure is proposed in [28]. The measured deformations are introduced into a static computer run as "prescribed freedoms" and the deformations of the complete FE net are calculated in this way mode by mode. Even, bearing in mind that the discrete FE stiffness matrix is imperfect, the resultant graphics will be better than those obtained by using pure geometric spline functions. All graphics of mode shapes presented in this paper were produced by means of this procedure.

5. CONCLUSION

Modal synthesis methods can be very efficient and useful tools in the design verification procedure of spacecraft. The general applicability of the methods presented here make them suitable for even complex and large spacecraft structures. It turns out, however, that the quality of the results depends greatly on the level of individual experience.

Thus, in preparing the tests, special attention must be given in order to obtain the particular kind of modes the analysist needs in his approach.

Concerning the modal correction method, its applicability is limited to cases where the mode shapes of the modified structure can sufficiently be described by the modes of the measured configuration. The modal correction method enables modal coupling results to be improved by making use of special test techniques.

The successful application of the modal coupling approach is apparently dependent on how realistic the coupling conditions were simulated in the test and in the coupling approach.

6. REFERENCES

1. A. BERTRAM 1980 Acta Astronautica 7, 1179-1190. Dynamic Qualification of Large Space Structures by Means of Modal Coupling Techniques.

2. A. BERTRAM and P. CONRAD 1982/1983 ESA-Journal 6(4), 449-462 and 7(1), 45-61. Dynamic Qualification of Spacecraft by Means of Modal Synthesis, Parts 1 and 2.

3. A. BERTRAM, M. DEGENER and R. FREYMANN 1977 DFVLR Report 1B 253-77 C 05 ESTEC/Contract No. 2998/76/NL/PP(SC). Development of Modal Techniques Using Experimental Modal Data. End of Phase I Report.

4. E. BREITBACH, M. DEGENER and N. NIEDBAL 1976 ESTEC, ESA SP-121. Modal Survey, Lectures and Discussions.

5. W.C. WALTON and E.C. STEEVES 1969 NASA TR R-362 A New Matrix Theorem and its Application for Establishing Independent Coordinates for Complex Dynamical Systems with Constraints.

6. R. FREYMANN 1977 DLR-FB 77-21, also ESA TT-463 (1978). Structural Modifications on a Swept Wing Model with Two External Stores by Means of Modal Perturbation and Modal Correction Methods.

7. A. GIRARD and M. RAGAB 1982 Conference held in Sophia-Antipolis, France. Interet et aspects pratiques de la synthese modal pour l'analyse dynamique des structures, Tendances Actuelles en Calcul de Structures.

8. W.C. HURTY 1965 AIAA Journal, 3(4), 678-585. Dynamic Analysis of Structural Systems Using Component Modes.

9. R.R. CRAIG, Jr. and M.C.C. BAMPTON 1968 AIAA Journal, 6(7), 1313-1319. Coupling of Substructures for Dynamic Analyses.

10. W.A. BENFIELD and R.F. HRUDA 1971 AIAA Journal 9(7), 1255-1261. Vibration Analysis of Structures by Component Mode Substitution.

11. G.M.L. GLADWELL 1971 Journal of Sound and Vibration 1, 41-59. Branch Mode Analysis of Vibrating Systems.

12. J.F. IMBERT 1978 Note Technique CNES 78/CT/PRT/SST/SM/155. Validation d'une methode de couplage modal pour l'analyse couplee ARIANE/Charge utile.

13. R.L. GOLDMAN 1969 AIAA Journal, 7(6), 1152-1154. Vibration Analysis by Dynamic Partitioning.

14. S.-N HOU 1969 Bellcomm. Inc. Technical Memorandum 69-2031-5, presented at 40th Shock and Vibration Symposium, Hampton, Virginia. Review of Modal Synthesis Techniques and a New Approach.

15. R.H. MACNEAL 1971 Journal of Computers and Structures 1,(4), 581-601. A Hybrid Method of Component Mode Synthesis.

16. S. RUBIN 1975 AIAA Journal, 13(8), 995-1006. Improved Component-Mode Representation for Structural Dynamic Analysis.

17. R.M. HINTZ 1975 AIAA Journal, 13(8), 1007-1016. Analytical Methods in Component Modal Synthesis.

18. R.R. CRAIG, Jr. and Ch.-J. CHANG 1976 Advances in Engineering Science, vol. 2, 13th Annual Meeting of the Society of Engineering Science, Hampton, Virginia, 393-408. A Review of Substructure Coupling Methods for Dynamic Analysis.

19. R.R. CRAIG, Jr. and Ch.-J. CHANG 1977 AIAA/ASME/SAE 18th Structures, Structural Dynamics and Materials Conference. On the Use of Attachment Modes in Substructure Coupling for Dynamic Analysis.

20. E. BREITBACH 1980 Advanced School on Identification of Vibrating Structures, CISM, Udine, Italy. Modal Synthesis.

21. E. BREITBACH 1981 Proc. 53rd Meeting SMP "Dynamic Environmental Qualification Techniques", Noordwijkerhout, Netherlands. Application of Modal Synthesis Techniques for the Dynamic Qualification of Wings with Stores.

22. H. HUENERS and N. NIEDBAL 1982 ESA Journal 6(1), 21-43. Using Ground Vibration Tests for System Identification and for the Dynamic Qualification of Spacecraft Structures.

23. N. NIEDBAL and M. KNORR 1983 Presented at EUROMECH 168, Manchester, England. An Analytical Method to Determine Normal Mode Parameters Out of Measured Complex Responses.

24. F. KIESSLING 1977/1978 ESA-TT-467. Translation of DLR-FB 73-33. Improvement of Modal Methods for Dynamic Response Problems of Linear Elastic Structures.

25. A. BERTRAM and E. KLUSOWSKI 1981 DFVLR Report 1B 232-81 C 17, ESTEC/Contract No. 3690/78/NL/MS. Evaluation of Modal Survey Techniques Using Experimental Modal Data, Final Report, Part 1 - Modal Synthesis.

26. A. BERTRAM and P. CONRAD 1981 DFVLR Report 1B 232-81 C 06, ESTEC/ Contract No. 3347/77/NL/PP(SC). Structural Dynamic Analyses of a Spacecraft Using Experimental Modal Data, Final Report.

27. A. BERTRAM and P. CONRAD 1982 DFVLR Report IB 232-82 C 09, ESTEC/ Contract No. 4350/80/NL/PP. Development of Procedures for Component Mode Synthesis, Final Report.

28. H. HUENERS 1980 DFVLR Report IB 253-80 C 24, ESTEC/Contract No. 3825/79/NL/PP. Modal Survey Test on the FLECS Structure, Final Report.

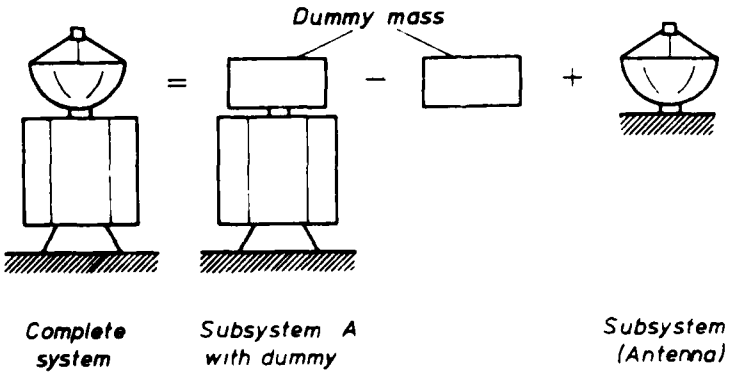

Figure 1: Coupling of the Antenna Module onto the Main Structure.

Sub-Structures	Methods of Modal Coupling						
	[8], [9]	[10],[11] [12]	[13],[14]	[15],[16]	[17]	[18],[19]	[3]
Constraint Modes	x	x	x	x	x	x	x
Attachment Modes	x			x	x	x	x
Fixed Interface Normal Modes	x	x		x			
Free Interface Normal Modes		x	x	x	x	x	x
Loaded Interface Normal Modes		x					x

Figure 2: Modal Coupling Methods.

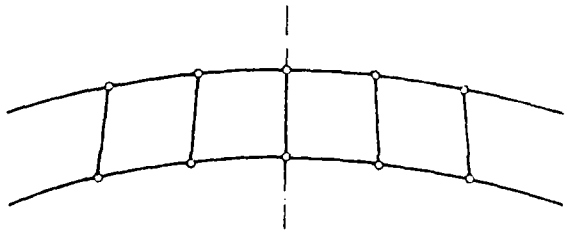

Figure 3a: Interface without Consideration of Lateral Constraints.

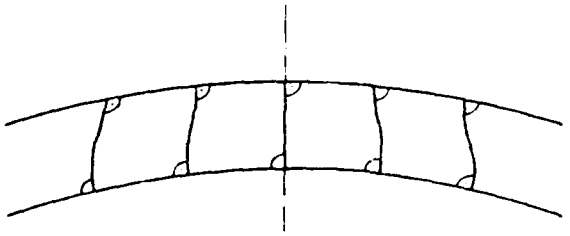

Figure 3b: Interface with Consideration of Lateral Constraints.

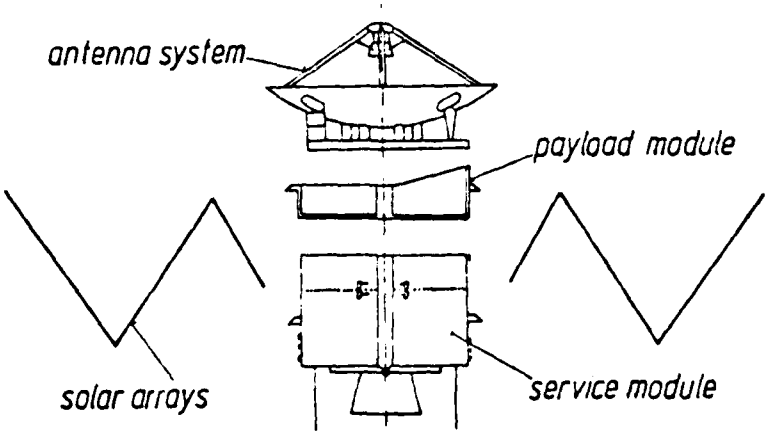

Figure 4: Structural Modules of a Satellite.

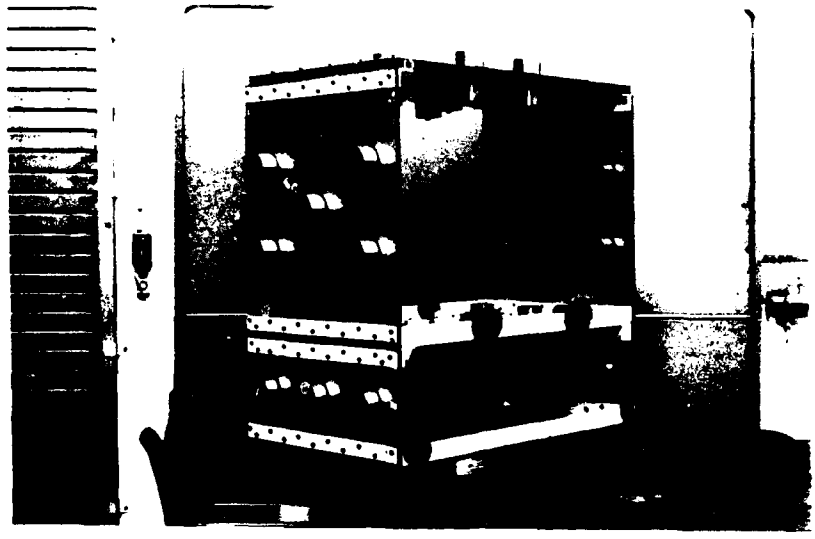

Figure 5: SIMOD Structure.

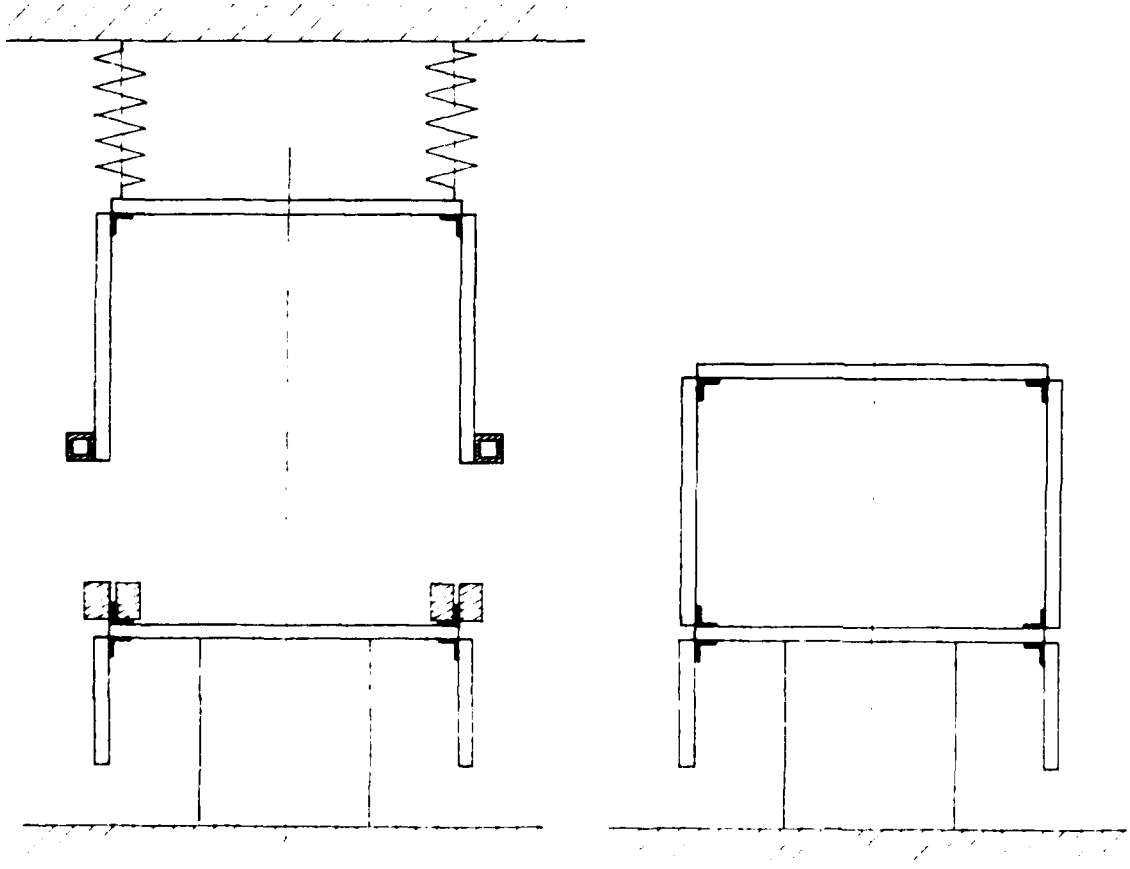

Figure 6: Boundary Conditions for the Modal Survey Tests on SIMOD.

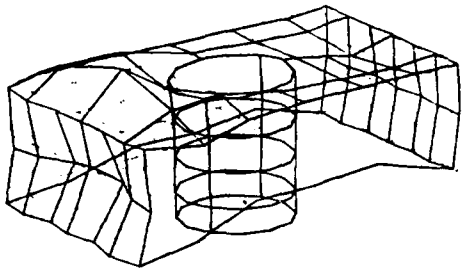

129.45 Hz Measurement

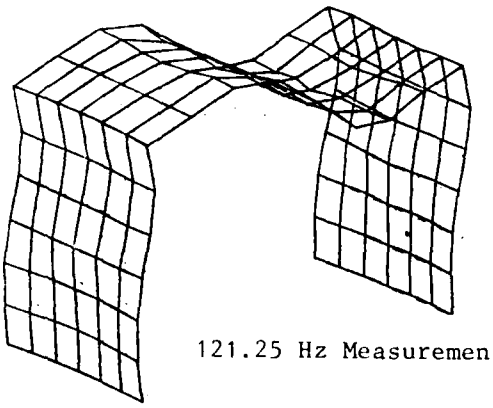

121.25 Hz Measurement

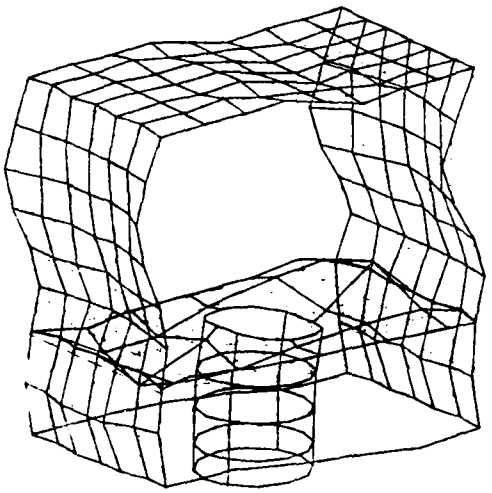

129.23 Hz Measurement

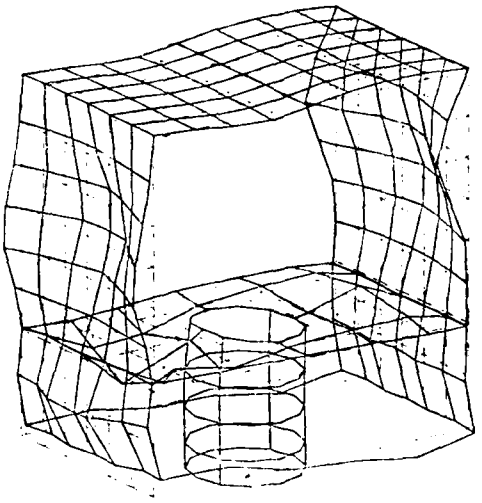

130.45 Hz Modal Coupling

Figure 7: Mode Shapes of SIMOD.

Measurement FREQ. Hz	Measurement GEN. MASS Kg*m**2	MODAC-Analysis FREQ. Hz	MODAC-Analysis GEN. MASS Kg*m**2
5.34	53.832	5.58	74.377
9.02	52.351	8.33	65.989
13.40	107.457	13.24	59.984
16.76	74.124	15.97	85.641
18.06	44.048	16.99	55.720
32.52	37.837	31.94	30.778
33.26	31.681	33.64	32.338
52.48	17.567	54.80	17.757
		60.22	15.158
59.91	87.659	62.07	27.424
65.90	82.102	65.98	39.112
71.44	27.213	75.64	11.344
73.77	23.107	79.29	6.826
83.02	25.710	81.97	25.924
		85.76	23.460
		88.06	21.523
96.73	22.521	94.18	12.781
99.01	9.893	99.45	6.351
101.32	42.852		
107.78	4.097	110.02	3.341
118.35	27.211	114.33	32.250
110.99	9.257	120.08	13.119
127.45	24.224	126.36	20.906
129.23	29.080	130.45	26.704
		137.21	8.930

Figure 8: Frequencies and Generalised Masses of the Assembled Structure

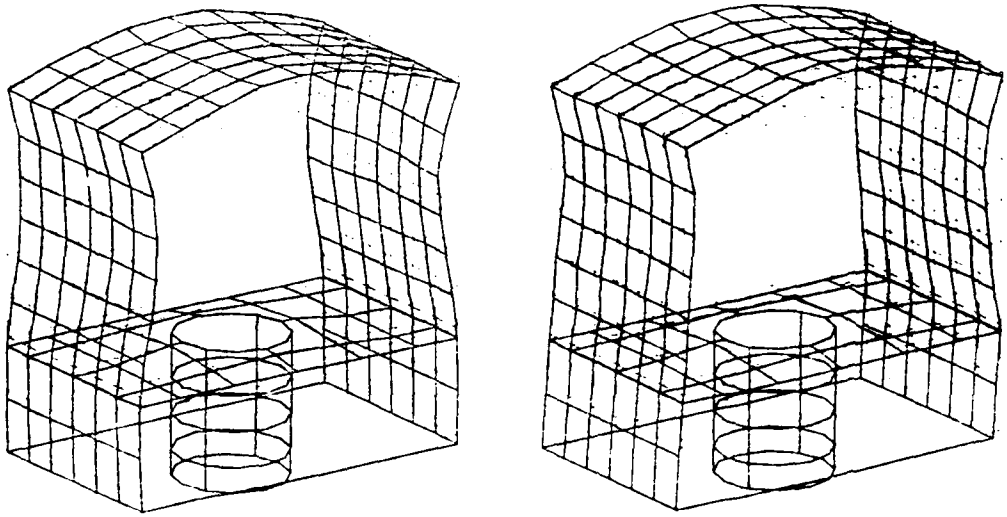

32.52 Hz Measurement

31.94 Hz Modal Coupling

Figure 9: Mode Shapes of SIMOD at 30 Hz.

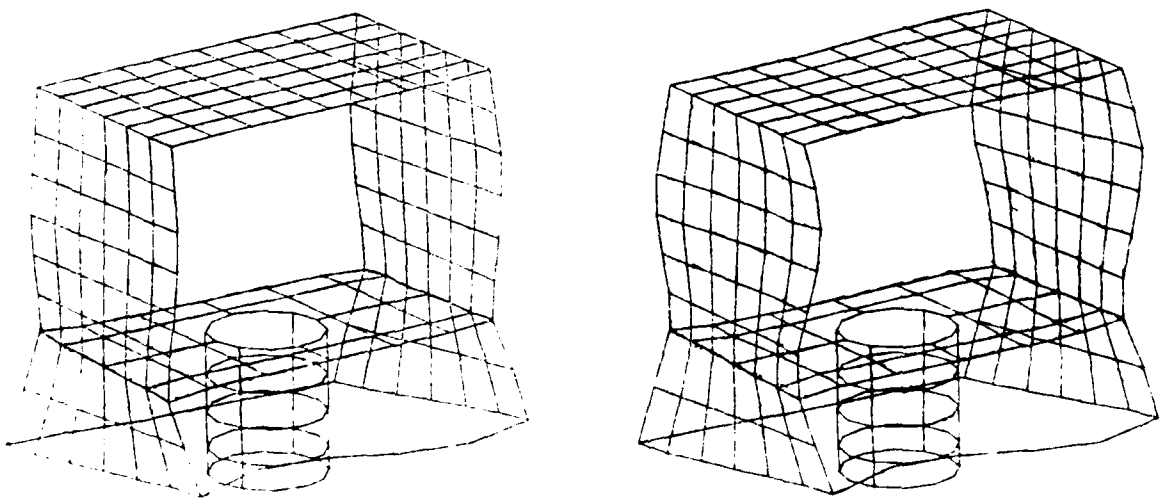

83.02 Hz Measurement

81.97 Hz Modal Coupling

Figure 10: Mode Shapes of SIMOD at 80 Hz.

A FLEXIBLE MULTICHANNEL MEASUREMENT SYSTEM FOR DYNAMIC ANALYSIS

ir. H. Van der Auweraer, ing. P. Van Herck, prof.dr.ir. R. Snoeys

Katholieke Universiteit Leuven
Departement Werktuigkunde

1. INTRODUCTION

Modal analysis is a widely used tool for the analysis of the vibrational and noise behaviour of mechanical structures.
In experimental modal analysis, the dynamic behaviour is studied by means of a model, based on transfer function measurements. One of the main limitations of the experimental technique in a lot of applications is the highly specialised equipment and the corresponding investment.

Our aim was to design a multichannel data-acquisition system front-end for our H.P.1000 computer (Digital Data Harvester). This system should be easily expandable and flexible enough to be used with a wide range of mini and micro computers. Although the original design purpose was to develop such a system for Modal Analysis, its application area is likely to be much wider.
The design of this system is related to the evolution of Fourier Analysis equipment into two directions :

*The small, but powerful systems, based on a microcomputer or even a microprocessor, with a limited number of channels, will remain a good solution for many problems.

*The 'big' systems, which are expensive as they are inflexible to be used for other purposes, will be more and more replaced by general purpose computers with a data-acquisition front-end and eventually upgraded by a preprocessing unit or an array processor.

As the expandability to a great number of channels was the most important design requirement, some attention will be paid to the reasons for this demand. After a summary of the other requirements, our solution proposals will be discussed in some more detail.

2. MULTICHANNEL MODAL ANALYSIS.

The reasons for multichannel measurements fall into three major classes, which are all, directly or indirectly, related to the system parameter accuracy.

* The measurement time.
* The consistency of the calculated parameters.
* The use of inherently multichannel analysis techniques.

2.1. Measurement time

When a Modal Analysis is performed, the total time Tp, spent on the project, is a summation of :

* The set-up time Ts (geometry definition, exciter location, equipment set-up and testing).

* The measurement time Tm (acquisition and processing of the data).

* The analysis time Ta (curve-fitting, interpretation, further analysis).

Tp = Ts + Tm + Ta

The significance of the measurement time can vary widely depending on many factors. When this time becomes important, it can be reduced sharply by measuring a lot of channels simultaneously.

Tm = (N/C)*Av*Acquisition time + N*Av*Recovery time

N = number of measurement points * number of exciter locations.
C = number of parallel measured channels.
Av = number of averages.
Acquisition time = time to take the measurement samples.
Recovery time = delay time before the next acquisition can be made.

2.2. Consistency of the parameters.

In some applications, the structural characteristics being measured may change during the test, depending on parameters such as temperature... The influence of nonstationary noise signals may also affect the consistency.
It should be investigated if multichannel acquisition gives a better, more consistent set of parameters in such cases, or that, contrary, it gives parameters which are more biased by the momentary, maybe system dependent noise.

2.3. Inherently multichannel techniques.

A lot of new techniques are coming up, based on multiple input / multiple output system modelling (1), where the acquisition of, at least all the input channels, should be simultaneous.
Some concrete research topics are :

* Multiple point excitation of systems, where different columns of the transfer function matrix are measured at the same time (2).
The advantages of this technique are : better energy distribution in the system, excitation of local modes, increased accuracy of the results because of the information redundancy.

* The use of coherence techniques in source localisation and identification.

* The use of microphone array's in acoustic measurements.

3. MULTICHANNEL MEASUREMENT SYSTEM.

The system is built up around a central controller module. Around this module, a number of acquisition channels and a signal generator will compose the concrete system.
The link with the computer is an interface module, which passes the computer commands to the controller and the generator, and the measured data from each channel to the computer (Fig.1).

3.1. Acquisition modules.

Each acquisition channel contains a transducer interface, an autoranging amplifier, an anti-aliasing filter, a sample-and-hold, an analog-to-digital convertor and a buffer memory (Fig.2).
The choice of an ADC on each channel module is based on following reasons :

* Once the signal is digitised, it can't be affected by noise, and the data-flow is much easier to control.

* The price of N ADC's with a maximum sample-rate i is about the same as for one ADC with a sample-rate N*i (for i=25000).

* The expandability is better because of the greater autonomy of each module.

3.1.1. Transducer inputs.

The first stage is an accelerometer compatible input, with an adjustable current source and a pre-amplifier which can be set in correspondence with the transducer sensitivity. If an open circuit or short circuit is detected at the transducer input, an indication is given. This allows for an impedance check before each measurement. This stage can only be used with accelerometers with a built-in FET-amplifier.

3.1.2. Amplifiers.

The amplifier is a programmable gain amplifier (*1 to *800), with autoranging capabilities. The autoranging procedure takes place during a test phase preceeding the actual acquisition, and is based on overload information from the AD convertor.
During the actual measurement, this overload status is monitored and a count is made. After the measurement, the gain settings and the number of overload's during the measurement, are read-out to the computer. Depending on the number of overloads, the measurement data are accepted or rejected, taking into acount the type of excitation signal.

3.1.3. Anti-aliasing filters.

The anti-aliasing filters are single-chip switched-capacitor filters which can be programmed by means of a control clock.
The choice of those switched capacitor filters, which are analog, but time-discreet ('sampled-data') components, was one of the most crucial points in the design process.

Old-fashioned analog filters become very expensive if they have to be programmable, accurate, and steep (72 db/oct.) at the same time. Therefore, recent developments in digital filters are used in most

modern Fourier Analysers, mostly based on the oversampling and decimation principle (4). The arrival of low-priced digital filters may expand their use to general data acquisition systems, but besides of the cost of the filters themself, the oversampling principle implies a much more expensive Sample / Hold and ADC circuitery.
As these developments will take some years, the only choice for low-priced programmable filters were the switched capacitor filters. Their roll-off is very high (100 db/oct.), (Fig.4), the phase accuracy is better than 2%, but for those 7-pole, 6-zero elliptic filters, this still means 0.02*630=12 degrees. A software correction is possible as their monolithic design guarantees a high stability.

3.1.4. Sampling and AD-conversion.

The design specifications were :

* 12 bit resolution

* Consequent accuracy of the SH and ADC components.
This means for Fmax = maximum signal frequency = 10 kHz, and Amax = maximum signal amplitude = 5 V. :

Aperture jitter LT 2^{-12} /(2πFmax) = 3 nanosec.

Droop rate LT 2^{-11} .Amax/Tadc = 0.1 V./millisec.

Feedthrough LT 2^{-11} .Amax = 2 mV.

Slew rate GT 2πFmax.Amax = 0.3 V./microsec.

Tadc = AD conversion time + SH acquisition time LT 1/max.sample rate = 40 microsec.

3.1.5. Buffer memory.

To avoid sample-rate reduction by interface limitations, each channel has its own buffer memory. At this moment, this is a 1 K * 12 bit memory, but an extension to a 4 K or even a 64 K memory is very easy.

3.2. Signal generator module.

So far, a programmable function generator has been developed, with pre-programmed signal types.
This generator has following characteristics :

Signal types : continuous sine, single shot sine, cosine, ramp.

Signal frequency ranging from 0.01000 to 9999. Hz

Amplitude : 0 to 5 V., step 1mV.

Offset : -5 to +5 V., step 2mV.

Sample-rate output f = F(sin) * 2^i (i = 3 to 10)

The generator is built-up around a 1024 point, 12 bit wide ROM table (Fig.3). An extension to a general DAC system, based on a RAM-buffer, is under study.

The number of points and the wordlength were defined following the design criteria in (5), pp 42-48 and pp 207-241.

A variable clock generator, based on a Phase-Locked-Loop (P.L.L.) circuit is applied to the ROM-addres counter and defines as such the resulting sine frequency. A divided output signal from this P.L.L. can be used as a sample-rate generator in order to permit leakage free measurements.

Due to this way of generating a sine-wave, the signal has a very high spectral purity.
The settling time of the generator is defined by the response time of the P.L.L. This time is limited by the response capabilities of the phase comparator. A special design for this comparator was made, in order to obtain a maximum response time of 5 ms, while maintaining a frequency stability better than one digit.

3.3. System control module.

The task of this module can be divided in following parts :

* Derivation of the timing signals for filter, SH, ADC, data buffers from an internal clock ,from the generator related clock or from an external input.

* Supervision of the data-flow from the measurement modules to the computer and from the computer to the generator and the control modules.

* Triggering of the signal acquisition (with possibility for pre-triggering with a user definable amount of pre-trigger.)

As each measurement channel contains as much logic as possible, the global system control task is greatly reduced and the system becomes easily expandable to more measurement channels. A maximum of 64 channels is standard, but an extension to a higher number is straightforward.

3.4. Interface.

The interface with the computer is a 16-bit parallel interface with a 3-wire handshake (Computer Command, System Flag, I/O-Status) The Digital Data Harvester has already been connected to a HP.9845, HP.9816 and HP.9826 desk-top computer and to a HP.1000F minicomputer. In the case of the H.P.12566 microcircuit interface card of the H.P.1000, the I/O line is not present. Due to this fact, 2 interface cards are needed (one for input, the other for output). A solution to this problem may be to use the 05451-60025 Interface Card from the H.P.5451 systems, which has two sets of two-wire handshake lines, and which is backward compatible to the 125666 card (10). The problem is then to adapt the DRV-72 driver to the use of those two sets of handshake lines.

A more interesting approach from the computer system point of view, is a GPIB (IEEE 488) interface bus. From the hardware point of view, this is a more complex task, but this problem will be studied as new VLSI chips ease this task.

3.5. Digital signal processing modules.

In section 2, the measurement time was studied. An important factor was the recovery time before another measurement could be started.

In random excitation measurements, this time is spent mostly on the calculation of the FFT and the correlation functions of the data. When performing a ZOOM transform, the frequency translation and the digital filtering also take a lot of time. This time is of course proportional to the number of channels and it might become a limiting factor for multichannel measurements, unless a very fast (one for the whole system) or a very cheap (one for each channel) processing unit is designed. So far, all commercial products have one central FFT processor.

There are different approaches to perform FFT's.

3.5.1. A software FFT.

In the classical systems (HP.5451C...), the FFT is microprogrammed and takes 50...80 milliseconds for an 1024 point transform. When using a HP.1000F computer, even an optimised program (Radix 8-4-2), written in Fortran (6), takes 400 ms. Microprogramming the HP.1000 can reduce this time to 80 ms, but this is a time consuming (or expensive) task. When using a desk-top computer, a 1024 point FFT takes seconds or even minutes.

The fastest way at this moment is to use an array procesor, which takes only 4 millisec's (7), but this solution is rather expensive as most modern array processors are in fact too powerful. Smaller, custom designed array processors may be the solution.

3.5.2. A dedicated FFT processor.

3.5.2.1. Design criteria.

When considering to develop your own FFT processor, the execution time remains the primary design goal. But, as such a processor would most probably be a fixed point (or block floating point) calculator, the calculation word length must be chosen corresponding to the accuracy demands.

In (8), a theoretical upper bound for the roundoff-error, expressed as RMS(error)/RMS(signal) is given. This error decreases by a factor two for each additional bit, and is proportional to the square of the block size (if the data are scaled after each FFT-step).
For a frequency domain S/N of 60dB, 12 bits are suited up to 128 points, 16 bits up to 2048 points. Experimental results gave better results, as the error remains well below the theoretical upper bound, by an amount depending on the signal type.
Another error arises from the coefficient word lenght. Contrary to the round-off noise, this error is biased. A good choice is to take the same resolution for data and coefficients.

3.5.2.2. FFT processors.

A design of a discrete hardware FFT processor is rather cumbersome

but the arrival of new VLSI products (4) for digital signal processing purposes may make such design feasible. A signal processing unit based upon such chips consists of a small number of powerfull components. There already exists some complete all-in-one processors. Those DSP-processors have a multiplier, data and coefficient memory and a ALU on chip. They may be programmed for FFT purposes. Unfortunately, only very few of those IC's are available as pre-programmed FFT-processors. Their price is still high, but will decrease considerabely in the future.

Another alternative is the use of microprocessors. The price of 16-bit microprocessors is steadily going down and their performances increase. Each channel should have his own microprocessor in order to realise a sufficiently high calculation speed. A new evolution in this area is the integration of a hardware multiplier on the microprocessor chip, so that multiplication times of 2 microseconds can be obtained. At this moment, this is still a software, but internally programmed, operation. As this function is a single instruction operation, the only difference for the user is the multiplication time, which is about 7 microsec. for a 16*16 MUL. This solution is very interesting as such microprocessors could still be programmed with the usual development systems.

3.5.3. Other DSP applications.

The same considerations are valid for the ZOOM transform as well. As for stepped-sine measurements, the calculation time becomes less important due to the long system stabilisation time, which can be used in an efficient way for this purpose. Nevertheless, it will be studied if it is feasible to perform this calculation in a hardware module.

4. APPLICATIONS.

At this moment, the acquisition, generator and control modules are operational. The digital signal processing is still performed by a computer, but an extension with a dedicated FFT processor is under study.

4.1. Stepped sine measurements.

So far, the system has mainly been used in stepped-sine measurements in order to analyse the feasibility and the characteristics of this technique (3). In this study, the accuracy of this method, the influence of measurement parameters (number of points/period...) and the effect of the transient system response after a frequency change were analysed. As the long measurement time is one of the main drawbacks of this method, an attempt was made to optimize this time by doing multichannel acquisition, with the corresponding signal processing being done during the system stabilisation time.

Because of the system's flexibility, completely automated measurements were possible. This has been applied to analyse the influence of test conditions on the mechanical characteristics of rubber elements. The feasability to use this system for the study of system non-linearities will also be investigated.

4.2. Modal analysis system.

The final design goal however, was to develop a multichannel measurement system for modal analysis purposes. Since such a system would consist of an analog front end, connected to a general purpose computer (mini or micro), which can easily be programmed, the flexibility is high. At this moment, an 8 channel system is completed. In order to use it for modal analysis, measurement software for the system control, data acquisition and signal processing has to be written. In commercial Fourier Analysers, these tasks are performed by firmware.

The direct application of this system will be to analyse the characteristics of multiple excitation measurements, which appear to be promising (2), when applied to complex structures (cars, planes...) (9).

Another topic, which is investigated, is the feasability of using modal analysis for quality control purposes. As the minimisation of the measurement time is essential for this goal, a multichannel system will be a necessity.

Another application of the Digital Data Harvester is to develop a low-cost impulse excitation measurement system, based on a desk computer.

4.3. Data acquisition applications.

Besides of these concrete research topics, this system can be used in any modal analysis or in any signal processing application in the same frequency range (to10 kHz.). Current applications in our lab are the acquisition of geometry accuracy measurement data and the analysis of the static characteristics of air bearings. In this last application, the force-displacement relationship of the air bearing is measured. A slowly varying force is applied and measured by means of a strain gauge. The corresponding displacements at different points of the bearing are measured with inductive pick-up's.

Future applications will be the incorporation of this system in a rubber fatigue analysis equipment and the analysis of the dynamic properties of air-bearings.

5. SUMMARY.

To reduce the measurement time and to increase the consistency of the calculated system parameters, a new multichannel data-acquisition front-end (The Digital Data Harvester) is developed to be used with a general purpose mini- or microcomputer.

The basic principle in the design of such a system is the modularity of the different subsystems.
The basic subsystem modules are :

* A measurement channel in which the signal is amplified, filtered, sampled, digitised and buffered.

* A signal generator with a fully programmable sine-wave generator.

* A controller.

* An interface to the computer.

Because of its modular design, it soon became apparent that it was very easy to configure other systems, based on the same modules. Besides the classical Modal Analysis applications, these systems are also used in general dynamic analysis and digital signal processing problems.

6. REFERENCES

1. J.S. BENDAT and A.G. PIERSOL 1980 Engineering Applications of Correlation and Spectral Analysis. Wiley.

2. R.J. ALLEMANG 1980 Ph.D. Dissertation, Univ. of Cincinnati. Investigation of Some Multiple Input/Output Frequency Response Function Experimental Modal Analysis Techniques.

3. F. LEMBRECHTS and J. SMETS 1983 Mech. Eng. Thesis 83E15, K.U. Leuven, Dept. Werktuigkunde. Studie van Stepped-Sine Excitatie en Implementatie van een Algoritme voor Automatische Metingen.

4. J.V. GINDERDEUREN 1982 Report ESAT, Dept. Elektrotechniek, K.U. Leuven, presented at the KVIV-TI Studiedag: Recente IC's, 24-05-82. Geintegreerde Schakelingen voor Signaalverwerking.

5. B.V. UFFEL and L. VERPOOTEN 1982 El. Eng. Thesis, ESAT, Dept. Elektrotechniek, K.U. Leuven. Digitale Synthesiser.

6. G.D. BERGLAND 1969 IEEE Trans. on Audio and Electroacoustics, AU-17, 2, 138-144. A Radix 8 FFT Subroutine for Real Valued Series.

7. V. THIEBAUD 1981 Proc. Seminar on Modal Analysis, K.U. Leuven. 128-channel Acquisition System, Based on an Array Processor and a Large Disc, for Structural Vibration Analysis.

8. P.D. WELCH 1969 IEEE Trans. on Audio and Electroacoustics, AU-17, 2. A Fixed Point Fast Fourier Transform Error Analysis.

9. C. HUTIN and G. CATTEAU 1982 Proc. Seminar on Modal Analysis, K.U. Leuven. Presentation of a Modal Analysis System as Used in the Aeronautic Field.

10. L.W. JAMES 1982 Interface 1000, Publication of the HP-1000 User Group. Unique Interfaces Available for the M-E-F Series Computer.

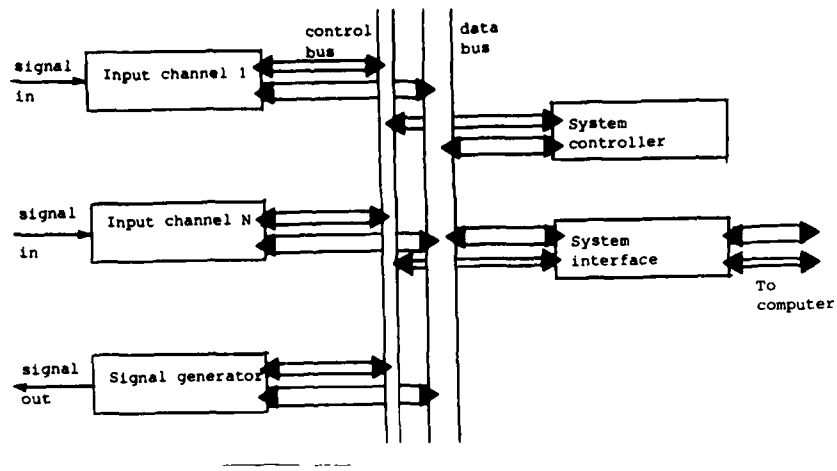

Fig.1 System modules

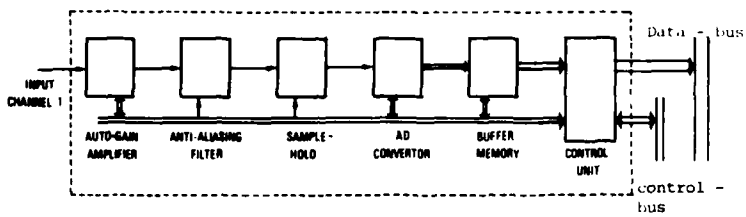

Fig.2 Data-acquisition channel

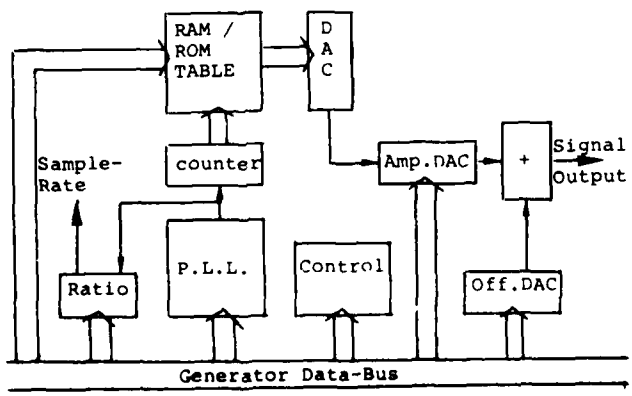

Fig.3 Signal generator

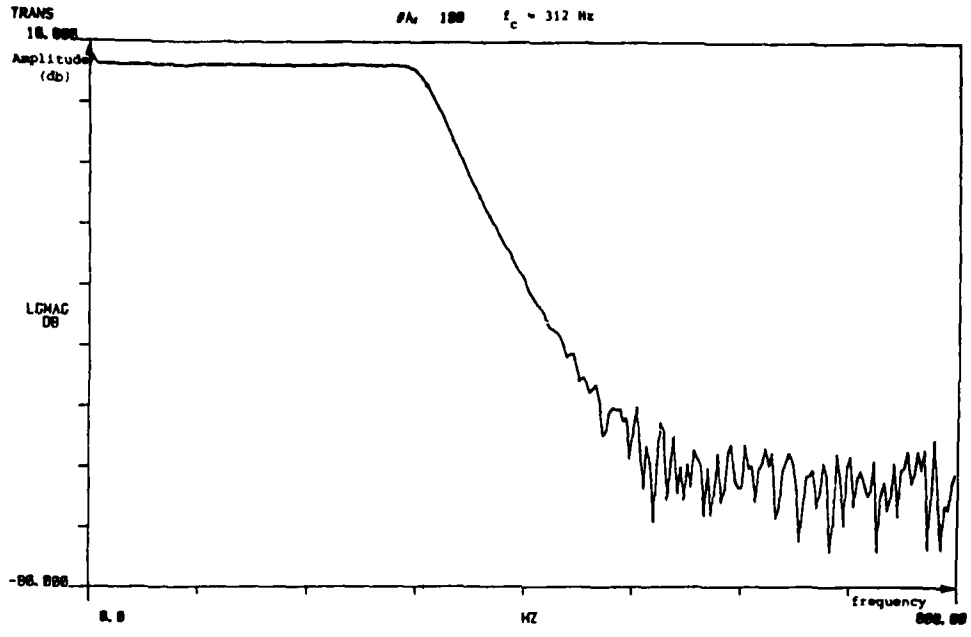

Fig.4a Filter Transfer Function (Amplitude)

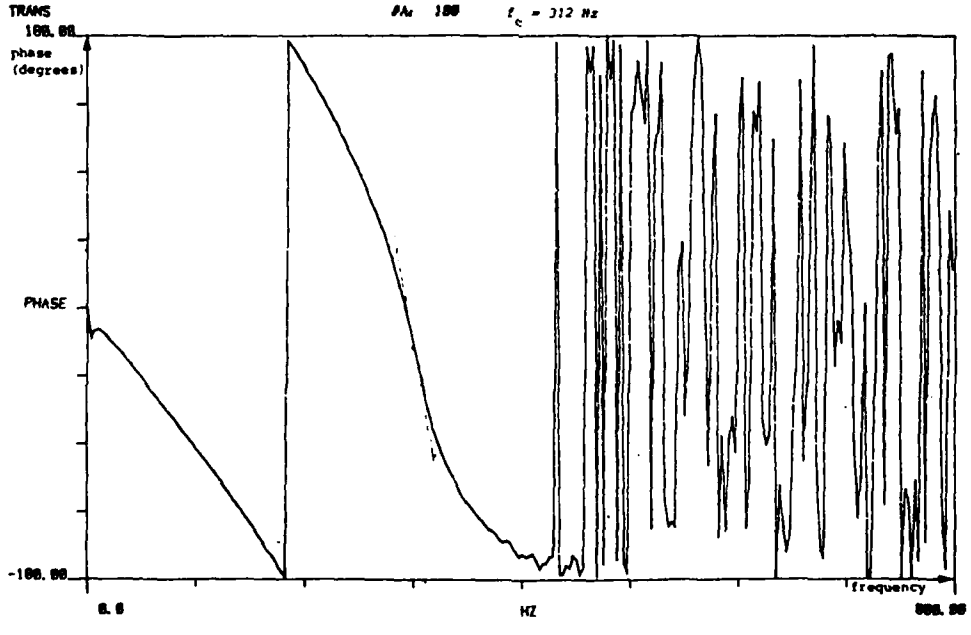

Fig.4b Filter Transfer Function (Phase)

LIMITATIONS ON THE IDENTIFICATION OF DISCRETE STRUCTURAL DYNAMIC MODELS

Alex Berman
Kaman Aerospace Corporation
Bloomfield, Connecticut USA

1. INTRODUCTION

Discrete linear analytical models of continuous structures play an important role in dynamic analysis. A good model will not only predict responses over the frequency range of interest, but will also be representative of the physical characteristics of the structure. Thus, it will have the capability to predict the effects of changes in physical parameters and it will correctly represent the structure when it is treated as a component of a larger system.

A model derived from the known physical parameters of the structure may not adequately predict measured dynamic characteristics. A model derived from dynamic testing may not be a good representation of the physical characteristics of the structure.

In recent years, a number of procedures have been suggested and applied which use measured dynamic data to identify an analytical model or to improve an existing model. Typical of these methods are: Rodden, 1967 [1], measured modes are used to identify static influence coefficients; Berman and Flannelly, 1971 [2], measured modes are used to improve a mass matrix and identify an "incomplete" stiffness matrix; Collins, et al, 1974 [3], a statistical iterative method is used to modify physical parameters; Baruch, et al, 1978 [4], measured modes and an analytical stiffness matrix are corrected; Chen and Garba, 1980 [5], and Grossman, 1982 [6], techniques for modifying physical parameters are improved; Berman, Wei, Nagy, 1980 [7], 1983 [8], mass and stiffness matrices are improved using modal data; Leuridan, et al, 1982 [9], mass damping, and stiffness matrices are estimated using response data.

Few of the methods published have been successfully applied to realistic structures. Rarely has there been any discussion of the physical relationships between an analytical model and test data which tend to limit the application of mathematically correct algebraic relationships. The purpose of this paper is to identify some of these limitations with the objective of directing research in this area in more productive directions.

2. PROBLEM DESCRIPTION

In the problem under discussion, it is assumed that there exists a linear undamped continuous structure which is available for dynamic testing. Measurements are made at a finite number of points on the structure at a continuous range of frequencies. Data is assumed to be available which can be in the form of mobility matrices (displacement per unit force) or which can be transformed into natural frequencies and modal displacements at the points of measurement. All the measured data has some error associated with it.

It is desired to formulate a discrete linear analytical model of this structure consisting of a mass and stiffness matrix where the degrees of freedom of the analytical model correspond to the points of measurement or a subset of them. The analytical model should be representative of the physical characteristics of the structure and should predict the dynamic response (mobility) and natural frequencies and modes of the structure.

There may exist an analytically derived approximation to the model. A limitation on the frequency range of applicability of the model would be acceptable.

The question to be considered is this: is it possible to use the test data to identify or improve an analytical model of the test structure, and if so, what limitations, if any, are there on this process?

3. PARAMETER TYPES

References [10], [11] briefly discuss the characteristics of two classes of parameters: those associated with a test ("measurable") and those associated with the derivation of an analytical model ("intuitive"). The measurables include mobility, normal modes, natural frequencies. The intuitive parameters include mass, stiffness, impedance. The problem discussed here is related to the use of measurable parameters to help to identify intuitive parameters. Recognition of the distinct characteristics of these parameter types is a first indication of possible difficulties.

The intuitive parameters are directly related to the geometry and the physical characteristics (e.g., mass, moduli of elasticity) of the structure. The value of each parameter of a discrete model is also completely dependent on the specific formulation of the model, that is, on the specific set of degrees of freedom selected by the modeler. These parameters are precise but not completely accurate. As will be shown below, intuitive parameters cannot be directly measured (for a realistic model of more than a trivial number of degrees of freedom.)

The measurable parameters are completely independent of any model formulation. That is, the response of a point on the structure depends only on the location of that point and the location of the excitation regardless of where the degrees of freedom of a model may have been placed. These parameters may be accurate but are not precise due to unavoidable equipment limitations.

The conversion of either parameter type to the other involves a matrix inversion or the equivalent (e.g., solution of a set of differential equations). Since derived intuitive parameters are numerically precise, the matrices may be inverted but the results may not be accurate. Since measurable parameters are not precise, meaningful inversions may not be possible. This is discussed further in a following section.

4. DIRECT MEASUREMENT

As an illustration of the statement made above that intuitive parameters cannot be directly measured, consider the stiffness matrix, K. K is a static matrix which relates deflection, x, to applied steady forces, f:

$$Kx = f \tag{1}$$

where K is an n x n (n = number of degrees of freedom) matrix and x, f are n element vectors. Given the physical characteristics of the structure and the degrees of freedom of the analytical model, the elements of K may be calculated theoretically.

Consider now the possibility of directly measuring the elements of K by a test procedure. From equation (1) it is seen that the i, jth element may be written:

$$K_{ij} = (\partial f_i / \partial x_j) \tag{2}$$

or, K_{ij} is the force at degree of freedom i required to produce a unit displacement at degree of freedom j, while all other degrees of freedom of the

model are constrained to be zero. For any realistically sized model this is obviously an impossible condition to implement in a test.

Note that a completely opposite conclusion results when one considers the inverse of K, the static influence matrix, C, which is a measurable quantity by the previous definition. C cannot be computed directly from the physical data, except by inverting a calculated K matrix or by solving differential equations. C is defined as:

$$Cf = x \tag{3}$$

and

$$C_{ij} = (\partial x_i / \partial f_j) \tag{4}$$

or, C_{ij} is the displacement at degree of freedom i due to a unit force at degree of freedom j, while all other forces are zero. These constraints are trivial and it is possible to measure this matrix.

Note also that the constraints on K_{ij} depend on the set of specific degrees of freedom of the model, while C_{ij} depends only on the location of degrees of freedom i and j and will not vary with the model formulation.

Since $K = C^{-1}$ and C is measurable, consider this as a possible means of identifying the stiffness matrix. For an n degree of freedom model of a structure, K and C may be expressed as follows (see Ref. [2]):

$$K = \sum_{i=1}^{n} \Omega_i^2 / m_i \; M \phi_i \phi_i^T M \tag{5}$$

$$C = \sum_{i=1}^{n} 1/(\Omega_i^2 m_i) \; \phi_i \phi_i^T \tag{6}$$

where Ω_i, m_i, ϕ_i are the natural frequency, generalized mass, and modal vector of the ith mode and M is the mass matrix (which is assumed to be known for the time being). Note that the dominant terms of K are the high frequency modes (Ω^2 is in the numerator) and the dominant terms of C are the low frequency modes.

K may be obtained from a measured C only if this matrix contains the necessary information regarding the high frequency modes. For a model of even modest size (say, 20 degrees of freedom), the measurement of C accurately enough to represent the effects of the high frequency modes (whose influence decreases by Ω_i^2) is virtually impossible. For larger models such accuracy is unachievable.

If the matrix C (of order n) does not contain information about all n modes it is singular. In practice, noise in the measurements will allow a numerical inversion; however, information which is not contained in the matrix cannot be extracted and no numerical procedure can meaningfully perform the operation, $K = C^{-1}$. The numerical inverse of a measured C matrix will have no physical meaning.

Another possibility is to measure the first n modes of the structure and form K as in equation (5). It will be shown below that this procedure will not identify a K matrix which represents the structural characteristics since the

higher modes used are those of the structure and not of the model. The modes in equation (5) are those of the model. The high modes of the structure ($i \approx n$) are not the same as those of a valid model.

5. RELATIONSHIPS BETWEEN THE STRUCTURE AND THE MODEL

The structure tested may be thought of as being represented by a large order unknown discrete model of order s where $s \to \infty$. The analytical model is of order n where $n \ll s$. The n degrees of freedom of the model may be considered to be a subset of the s degrees of freedom of the structure.

The complete model of a linear, undamped structure may be written in the frequency domain as:

$$(K_s - \omega^2 M_s)\, x_s = f_s \tag{7}$$

or

$$Z_s(\omega)\, x_s = f_s \tag{8}$$

where K_s and M_s are of order s, x_s and f_s represent the response and applied forces at the s degrees of freedom of the structure at a frequency of ω and $Z_s\ (\omega)$ is the corresponding impedance matrix.

Consider that the degrees of freedom are ordered so that the subset corresponding to the model are at the top of the vectors and then the upper left partitions of the matrices correspond to the model degrees of freedom.

$$Z_s\ (\omega) = \begin{bmatrix} Z_1 & Z_2 \\ Z_2^T & Z_4 \end{bmatrix} \tag{9}$$

The mobility, $Y_s\ (\omega) = Z_s^{-1}(\omega)$ may also be written

$$Y_s\ (\omega) = \begin{bmatrix} Y_1 & Y_2 \\ Y_2^T & Y_4 \end{bmatrix} \tag{10}$$

and the mobility of the model degrees of freedom is

$$Y_M(\omega) = Y_1 = (Z_1 - Z_2 Z_4^{-1} Z_2^T)^{-1} \tag{11}$$

Since Y is a measurable quantity and represents the actual response of the structure, the inverse of Y_M is the impedance of the model at the specified forcing frequency (see Ref. [12]) or

$$Z_M\ (\omega) = Z_1 - Z_2 Z_4^{-1} Z_2^T \tag{12}$$

Assuming a model of the form of equation (7) for the reduced degrees of freedom, equation (12) becomes

$$Z_M(\omega) = K_M - \omega^2 M_M$$

$$= (K_1 - \omega^2 M_1) - K_2 (K_4 - \omega^2 M_4)^{-1} K_2^T \qquad (13)$$

where it has been assumed, for simplicity, that $M_2 = 0$ (as in the case of a diagonal mass matrix), and the subscripts refer to partitions of the matrices as in equations (9) and (10).

The stiffness matrix of the reduced model may be obtained from equation (13) when $\omega = 0$

$$K_M = K_1 - K_2 K_4^{-1} K_2^T \qquad (14)$$

and then, from equation (13)

$$M_M = M_1 + K_2 K_4^{-1} M_4 (I - \omega^2 K_4^{-1} M_4)^{-1} K_4^{-1} K_2^T \qquad (15)$$

Equation (14) is that of Turner [13] and equation (15) reduces to that of Guyan [14] at $\omega = 0$.

Equations (14)-(15) represent an analytical model which would exactly predict the steady state response of the structure at all degrees of freedom of the analytical model at any frequency. Note that this model is nonlinear since the mass matrix is a function of the forcing frequency.

In the problem under consideration K_s and M_s are unknown; and it is desired to identify constant K_M, M_M. From equation (15) it is apparent that a constant coefficient model can only be an approximation with limits on the frequency range of applicability. In engineering practice, it is commonly accepted that for such a model with n degrees of freedom, the validity of the model will only cover a frequency range of up to approximately $\Omega_{n/2}$. The specific frequency range, of course, depends on the characteristics of the actual structure and the formulation of the model.

Note that equations (14) and (15) do not represent a means of obtaining M_M and K_M from test data since none of the matrices on the right hand sides of these equations are known. They are shown to illustrate the relationships between a desired model and the actual structure.

6. SYNTHESIS OF STIFFNESS MATRIX

Based on known physical characteristics of a linear structure it is possible to define a unique constant stiffness matrix (equation (14)) with physical meaning (equation (2)). Direct measurement of the stiffness matrix has been shown in Section 2 to be not possible.

The modal expansion of equation (5) suggests the possibility of measuring the first n modes and frequencies of the structure and synthesizing K (assuming M is known) by summing the modal contributions.

Equation (5) is a valid representation only for a linear model where the modes and frequencies are the eigensolutions of the model as distinguished from those of the structure (unless they are identical). There are two related inconsistencies in the above suggestion. First, from equation (15) it is seen that for a valid model that includes all n modes, the model is not linear.

Second, as also discussed in Section 5, the n modes of a linear model that includes a valid K matrix cannot be the same as the corresponding n modes of the structure.

It may be possible, given an appropriate constant mass matrix, to sum the measured modes as in equation (5). This will yield a linear model which will have the same modes and frequencies as the structure. There is no reason to expect, however, that such a model will have any physical reality (or that K matrix may be related to the physical characteristics of the structure) or that the model will have the capability to predict any dynamic characteristics other than those which were actually measured.

There is another difficulty associated with the use of n measured modes in an n degree of freedom model of a continuous structure. It is apparent that n points cannot describe the shape of the higher modes which may have approximately n nodes and n antinodes (e.g., for the simple case of a thin beam). In addition, it is unlikely that the mass matrix required to make these poorly described modes orthogonal will have any relation to physical reality.

In reference [2] an "incomplete" stiffness matrix is formed by summing the lower order terms of equation (5). It is recognized that this matrix does not represent the physical characteristics of the structure. While this model may have valid specialized capabilities, these must be demonstrated for any particular application.

7. EVALUATION OF APPROACHES

Methods which use test data alone to identify a linear M and K model of a continuous structure, where the identified parameters can be physically related to the static structural characteristics, appear to be unachievable. Variations in the mathematical formulations where, for example, K is expressed in terms of the inverse of a measured modal matrix or where mobility measurements are used directly are simply algebraic manipulations and the same conclusions must be drawn.

Other methods use an approximate M and K model based on analysis and attempt to adjust these to agree with test data over a limited frequency range. Such methods have a potential for success since a linear model may adequately represent the structure when the frequency range is limited. Since the model is of order n and the number of modes is less than n, there are an infinite number of models which will satisfy the eigensolution requirements and will approximate the physical characteristics.

Methods of this type fall in two classes: a limited number of physical parameters are varied to modify M and K or the actual elements of M and K are varied. Since there are an infinite number of solutions to the problem, there is no reason to assume that computed variations in a limited set of physical parameters has any necessary relationship to the "true" values of these quantities. Selection of different parameters may also result in a different but "good" solution.

Methods which modify all or a subset of the actual elements of the matrices result in models which may not represent physically realistic structures. Since there are an infinity of such models, any such valid procedure must select a solution which represents some minimum variation from the original analytical solution. If the changes are large enough to destroy the physical interpretability of the model, and since the changes are minimum, one must conclude that either the analysis or the test data or both are in error. The result of an analysis of this type can only be considered to be successful if the changes fall within the original expected uncertainties in the analytical model.

8. NUMERICAL ILLUSTRATION

As an illustration of the phenomena described in Section 5 a simple structure and a test are simulated. The structure consists of twenty lumped masses connected in series by springs with mass number 1 connected to ground. A test is simulated with modal measurements made at seven points. A seven degree of freedom model is desired to represent the twenty degree of freedom structure.

Table 1 contains the description of the mass and stiffness elements and the first seven exact modal displacements and natural frequencies. In the simulated test the natural frequencies and the modal displacements are available. A seven degree of freedom model, however, would only predict mode shapes at the seven test points.

Table 1 Description of simulated test specimen and modes and frequencies

Mass No.	Test Point	Mass kg	Spring n/m x10^{-6}	Mode= f(hz)=	1 9.5	2 31.0	3 48.0	4 70.0	5 81.2	6 104.2	7 119.2
1		0.8	0.6		.09	.39	.33	-.62	.79	-.22	.54
2		1.8	1.8		.12	.51	.42	-.78	.95	-.25	.59
3		1.2	1.4		.17	.65	.50	-.78	.85	-.15	.22
4	1	1.6	1.0		.22	.81	.55	-.60	.43	.06	-.44
4		1.2	0.8		.29	.95	.51	-.13	-.33	.28	-.77
6		1.0	1.8		.33	.99	.46	.09	-.60	.30	-.63
7		1.0	2.0		.35	1.00	.40	.28	-.77	.25	-.32
8	2	1.8	0.6		.43	.98	.12	.83	-.99	-.09	1.00
9		0.6	0.2		.67	.60	-.80	1.00	.72	-.76	-.10
10		1.8	0.8		.73	.49	-.97	.89	1.00	-.68	-.33
11	3	1.0	0.4		.84	.18	-.93	-.11	.37	.79	.04
12		1.0	1.2		.87	.07	-.85	-.43	.08	1.00	.14
13		1.8	2.0		.89	0	-.76	-.57	-.10	.91	.16
14	4	1.8	0.6		.94	-.22	-.25	-.73	-.64	-.56	-.04
15		2.0	1.6		.95	-.29	-.03	-.62	-.65	-.84	-.09
16	5	0.6	1.2		.97	-.37	.26	-.28	-.38	-.61	-.08
17		1.2	0.8		.99	-.48	.68	.28	.11	-.08	-.02
18	6	2.0	1.4		.99	-.53	.87	.55	.36	.26	.02
19		1.0	1.2		1.00	-.55	.95	.68	.50	.46	.05
20	7	0.2	0.4		1.00	-.56	1.00	.76	.57	.59	.06

Equations (14), (15) represent a reduced model which represents the static characteristics of the structure but is seen to be a function of frequency. Seven degree of freedom models were formulated at several specific frequencies and each was assumed to be constant and an eigenanalysis was performed. The results of these computations are shown in Figure 1.

Note that only when the model frequency equals an eigenvalue is the eigenvalue exactly representative of the actual structure. At any specific value of the model frequency, no more than three eigenvalue are good approximations in this case.

It has also been observed that the degrees of freedom of the model cannot properly describe the shapes of the actual modes of the structure. This is apparent from Table 1.

As an illustration of how the model modes vary with the model frequency, Table 2 gives the displacements of mode 3 for various model frequencies (48 hz represents the exact mode).

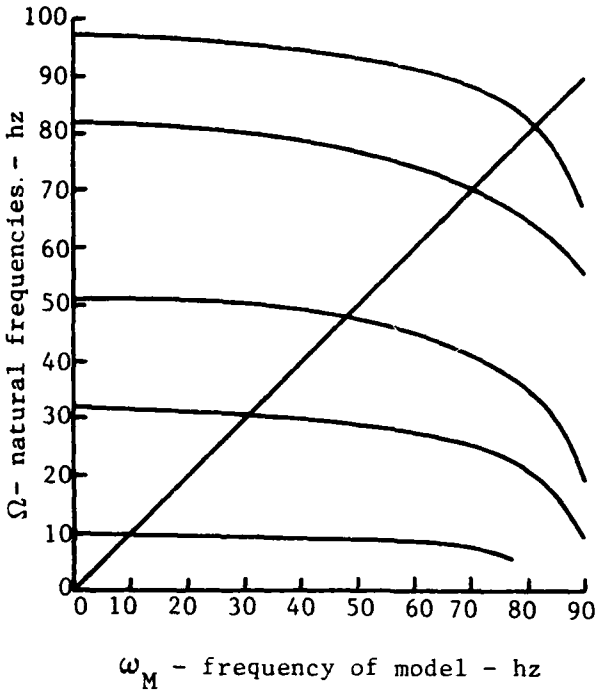

Figure 1 Effect of model frequency on natural frequencies

Table 2 Effect of model frequency on shape of mode 3

Test Point	Model frequency - hz. 0	40	48	60	70
1	.53	.54	.55	.58	.65
2	.15	.13	.12	.12	.17
3	-.95	-.95	-.93	-.89	-.78
4	-.38	-.28	-.25	-.16	-.01
5	.20	.23	.26	.32	.42
6	.86	.86	.87	.88	.90
7	1.00	1.00	1.00	1.00	1.00

9. CONCLUDING REMARKS

The purpose of this paper has been to open the technical consideration of what is and what is not possible in the field of the identification of structural dynamics models. First indications suggest that rather severe limitations exist on the use of test data alone and that the most promising procedures include a combination of test and analysis.

In the last mentioned class of procedures, the number of unknowns (elements of matrices) should be very much greater than the conditions to be met (modes and frequencies), thus small changes in the elements can be expected if the analysis and the data are good. However, since the solution is only one of an infinity of solutions, no physical interpretation should be made of the numerical results. The best one can say is that the model is a reasonable physical representation and it predicts the measured dynamic behavior of the structure. One may presume that such a model may be used for other analyses of the structure with greater confidence than the original analytical model.

REFERENCES

1. W.P. RODDEN 1967 AIAA Journal 5, 991-1000. A method for deriving structural influence coefficients from ground vibration tests.

2. A. BERMAN and W.G. FLANNELLY 1971 AIAA Journal 9, 1481-1487. Theory of incomplete models of dynamic structures.

3. J.D. COLLINS, G.C. HART, T.K. HASSLEMAN, and B. KENNEDY 1974 AIAA Journal 12, 185-190. Statistical identification of structures.

4. M. BARUCH and I.Y. BAR ITZHACK 1978 AIAA Journal 16, 346-351. Optimal weighted orthogonalization of measured modes.

5. J.C. CHEN and J.A. GARBA 1980 AIAA Journal 18, 684-690. Analytical model improvement using modal test results.

6. D.T. GROSSMAN 1982 AIAA paper 82-0640. An automated technique for improving modal test/analysis correlation.

7. A. BERMAN, F.S. WEI, and K.V. RAO 1980 AIAA paper 80-0800. Improvement of analytical dynamic models using modal test data.

8. A. BERMAN and E.J. NAGY 1983 AIAA Journal 21, 1168-1173. Improvement of a large analytical model using test data.

9. J.M. LEURIDAN, D.L. BROWN, and R.J. ALLEMANG 1982 AIAA paper 82-0767. Direct system parameter identification of mechanical structures with application to modal analysis.

10. W.G. FLANNELLY and A. BERMAN 1972 System Identification of Vibrating Structures, ASME. State-of-the-art of system identification of aerospace structures.

11. A. BERMAN 1975 Shock and Vibration Digest, Vol. 7, No. 1. Determining structural parameters from dynamic testing.

12. A. BERMAN 1973 Shock and Vibration Bulletin, No. 43, Part 2. Vibration Analysis of structural systems using virtual substructures.

13. M.J. TURNER, R.W. CLOUGH, H.C. MARTIN, and L.J. TOPP 1956 Journal of the Aeronautical Sciences 23 805-823. Stiffness and deflection analysis of complex structures.

14. R.J. GUYAN 1965 AIAA Journal 3, 380. Reduction of stiffness and mass matrices.

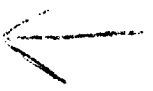

FOOLPROOF METHODS FOR FREQUENCY RESPONSE MEASUREMENTS

H.G.D. Goyder

U.K.A.E.A. Harwell

1. INTRODUCTION

The theoretical analyses of a structure is always approximate because of the impossibility of accurately modelling every feature. Thus when a structure has many important resonances or complicated damping mechanisms, measurement methods are the only means of determining dynamic behaviour. In addition, measurements can be used to determine the characteristics of non-linear structures which are frequently too complicated to be analysed theoretically. Consequently measurement methods form an important part of vibration analysis.

High quality measurements are often difficult to achieve and it is the objective of this paper to present three techniques which greatly enhance the accuracy and precision of structural vibration measurements. The measurement techniques considered below all relate to the frequency response function or transfer function which expresses the steady state response of a structure to a harmonic excitation. Thus the frequency response function can be defined as:-

$$H(i\omega) = \frac{Q}{P} \qquad (1)$$

where

$$q(t) = Q e^{i\omega t}$$

$$p(t) = P e^{i\omega t}$$

The real part of q and p are the response (displacement, velocity or acceleration) and the force respectively. Q and P may be complex in order to express a phase angle. Although defined using harmonic excitation the frequency response function may also be defined using transient or random excitation [1]. For a linear structure the frequency response function completely defines the relationship between any force and the response of the structure. For a non-linear structure a single frequency response function is not sufficient to completely describe the response and several special frequency response functions must be used. This is described below.

Three problems which cause significant errors in the measurement of frequency response functions are:-

1. Nonlinearities and Noise
2. Errors due to electrodynamic shakers
3. Interpretation and model fitting of frequency response functions.

Techniques for overcoming these problems are presented below.

2. NONLINEARITIES AND NOISE

Figure 1 shows the results of applying four conventional measurement methods to the same nonlinear structure. The modulus of a frequency response function is shown in each case. The structure consisted of a single degree of freedom system with a cubic stiffness nonlinearity. The equation for the structure was

$$\ddot{q} + 2\zeta\omega_0\dot{q} + \omega_0^2(1+\epsilon^2)q = \frac{1}{m}p \qquad (2)$$

where for the cases shown in figure 1

$\zeta = 0.03$
$\omega_0 = 2\pi\ s^{-1}$
$\epsilon^2 = 0.4$
$m = 1.0\ kg$

The continuous equation was represented by a finite difference equation and the measurement methods simulated digitally. By using a small time step for calculating the response the finite difference equation was found to represent the continuous equation with an accuracy of better than 1%. The actual number of points used to simulate the measurement methods was less than that calculated so that realistic sampling rates could be used.

2.1 Figure 1(A)

This frequency response function was obtained using steady state harmonic excitation. For each frequency a force was applied which consisted of a constant amplitude sinewave, The response was allowed to reach steady state conditions and was then found to consist of a number of frequencies. The amplitude and phase of the harmonic in the response at the same frequency as the excitation was determined. The ratio of the amplitude of this harmonic to the amplitude of the force constitutes the frequency response function shown in the figure. The same amplitude of force was chosen for each frequency and this amplitude was selected so that the displacement of the system would be equal to 1.0m at resonance if $\epsilon = 0$. This type of frequency response function is sometimes known as a describing function.

2.2 Figure 1(B)

This frequency response function was determined by applying the force as a very short pulse shape to the structure. Pulses of the type chosen are often obtained by using a hammer to excite the structure. The frequency response function was then obtained by dividing the Fourier transform of the response by the Fourier transform of the force. The pulse was selected so that the maximum value of the response in the time domain was 1.0m with $\epsilon = 0$. The modulus of the frequency response function is shown in the figure.

2.3 Figure 1(C)

This frequency response function was obtained in a similar manner to the previous case. However instead of a pulse the force consisted of a rapid frequency sweep between 0 Hz and 2 Hz in 50 sec. (This sweep is rapid compared with the reverberation time of the structure.) The frequency response function was once again determined from the ratio of Fourier transforms. The pulse was selected so that the maximum displacement in the time domain would be equal to 1.0 m if $\epsilon = 0$.

2.4 Figure 1(D)

This frequency response function was obtained by using a Gaussian random force and determining spectral density functions associated with the force and response. The equation used was

$$H(i\omega) = \frac{S_{xp}}{S_{pp}} \qquad (3)$$

where S_{yp} is the cross spectral density function between the response and force and S_{pp} is the autospectral density (power spectral density) of the force. The force was chosen such that the r.m.s. value of the response would be 0.5m if $\epsilon = 0$.

It can be seen that the force has been chosen in each case to give a comparable response displacement. Thus the nonlinear effects will act to approximately the same degree to produce comparable deviations from linear behaviour. It can be seen that figure 1(d) shows a remarkable similarity to the response of a linear structure. This is no coincidence and will be examined further in the following sections. The frequency response functions (a), (b) and (c) show considerable distortion from the response expected for a linear structure. This distortion makes these frequency response functions difficult to interpret. For example no method has yet been devised for estimating parameters such as natural frequency or damping from these response functions. Consequently the use of sinusoidal, pulse or sweep excitation does not seem appropriate for the measurement of frequency response functions which contain nonlinearities. This is particularly disappointing when considering sinusoidal steady state testing which is generally an easy to use and robust technique.

The effect of noise on the above measurement techniques can cause additional errors. Noise can generally be removed by averaging the results of repeated tests. In the case of random excitation this is automatic but special care must be used with the other techniques especially if the noise is harmonic. For examples of averaging see [2].

3. RANDOM EXCITATION

The use of random excitation in the above examples produced a frequency response function that looked as if it could have been produced by a linear structure. It is a property of random excitation that the frequency response function constructed will always be that of a linear structure. This linear frequency response function which respresents a nonlinear structure has very favourable properties. For example the frequency response function is an optimum model of the nonlinear structure. Also the energy dissipated within the nonlinear structure is correctly modelled by the linear frequency response function.

These properties can be appreciated from figure 2. In figure 2(a) a nonlinear system is shown with force p and response q. A linear model of this nonlinear system is shown in figure 2(b). Here the force is the same but the response has the term q_e added to it to make it up to the output q. Figure 2(b) is similar to the problem of a linear system with noise added to the response. It was for this latter problem that the application of equation 3 was devised [1]. However conceptually there is very little difference between noise and nonlinearities in as much that both constitute an addition to the response that has no linear relationship with the force. Thus the method of testing using random excitation and using equation 3 provides a means of obtaining a best model of a nonlinear structure.

Although the best linear model is obtained, this model is only appropriate for the particular force spectral density used. For example if a force with a larger or smaller r.m.s. value was used then different linear frequency response functions would provide the best model of the nonlinear structure. One approach for modelling a nonlinear system is thus to measure a number of different linear frequency response functions corresponding to different levels of force. Alternatively a more complete analysis may be performed by measuring multi-dimensional frequency response functions [3]. These are defined by

$$H_n(\omega_1, \omega_2 \cdots \omega_n) = \frac{S_{qPP\ldots P}(\omega_1, \omega_2, \cdots \omega_n)}{n!\, S_{PP}\, S_{PP} \quad S_{PP}} \qquad (4)$$

These multidimensional frequency response functions relate the nonlinear part of the response q_e to the force p. In principle measurement of all the multi-dimensional frequency response functions for a structure would provide a complete model for the structure so that the response to any force could be predicted. This area is the subject of continuing research.

Thus a technique has been presented which permits the measurement of a linear frequency response function of a nonlinear structure.

4. ELECTRODYNAMIC SHAKERS

Electrodynamic shakers used to apply a force to a structure generally interact with the nonlinearities and noise to produce significant errors. Figure 3 shows the general configuration when testing a structure. It can be seen that there is a feedback path which results in the force containing information about the noise and nonlinearities represented by q_e. This feedback path results from the properties of the shaker [4]. The force output by the shaker is dependent on the amplitude of the displacement of the shaker coil and on the mass damping and stiffness of the coil and its suspension. Electro-magnetic effects also cause a feedback between the response and the force [5]. The effect of the feedback path is to correlate the force and the nonlinear and noise source via the feedback path. Thus if the technique of the previous section is applied directly the linear frequency response function will be corrupted by additional correlations between between the force and q_e. However an alternative for equation 3 may be used which overcomes this problem. The equation is

$$H(i\omega) = \frac{S_{qz}}{S_{pz}} \qquad (5)$$

where S_{qz} and S_{pz} are cross-spectral density functions between q and z and p and z where z is the input to the shaker. The input z is derived from the random generator used to drive the shaker and is thus independent of the noise and nonlinearities in the shaker and structure. The theory for this technique is given in [4] and is easily demonstrated.

Figure 4 shows the frequency response function measured for one resonance of a nonlinear system. The use of both equation 3 and 5 are shown. It can be seen that there are significant differences. These differences are due to shaker interactions which are eliminated by the use of equation 5. The non-linear system for this experiment consisted of a 2m steel tube with a loose support at its centre. The tube had a first resonance frequency at 74 Hz and was excited by a Ling 407 shaker.

5. INTERPRETATION OF RESPONSE FUNCTIONS

After a linear frequency response function has been measured it is necessary to interpret it. This is often achieved by determining a parametric model for the frequency response function in terms of resonance frequencies and damping ratios. Below is presented a novel form for plotting frequency response functions which considerably aids interpretation.

The frequency response function for a linear single degree of freedom oscillator has the form

$$H(i\omega) = \frac{1}{m(\omega_o^2 - \omega^2 + 2i\zeta\omega\omega_o)} \qquad (6)$$

where ω_o is the resonance frequency and ζ the damping ratio. Figure 5(a) and (b) shows the real and imaginary parts of this function plotted against frequency. Figure 5(c) shows the frequency response function plotted on the Argand diagram. Figure 5(c) is often regarded as the most useful for showing up detail in the frequency response function. This type of plot was first proposed by Kennedy and Pancu [6].

An alternative method for examining the frequency response function is to plot the reciprocal of the frequency response function. It can be seen from equation 6 that for an oscillator this gives

$$\frac{1}{H(i\omega)} = m(\omega_o^2 - \omega^2) + 2i m\zeta\omega\omega_o \qquad (7)$$

Figure 6(a) and (b) shows the real and imaginary parts of this function and figure 6(c) shows the function plotted on the Argand diagram. It can be seen that Figure 6 is simpler than the more usual method of plotting given in figure 5. There are several advantages associated with this method of plotting. The method separates the damping and mass-stiffness part of the frequency response function. This may be made even more simple if the reciprocal of the velocity frequency response function is plotted. In this case the real part is a constant proportional to damping.

The determination of the natural frequency and damping from the reciprocal frequency response function is simple. This may be done graphically or by simple linear curve fitting procedures. Curve fitting is particularly straightforward because the noise structure is often simpler on the reciprocal frequency response function compared to the usual frequency response function.

The manner in which this form of plotting shows up details of the frequency response function can be seen from figures 7 and 8. Figure 7 shows a plot on the Argand diagram of the linear frequency response function obtained for the nonlinear system described in section 2. This plot has been obtained using random excitation and the modulus is shown in figure 1. For comparison the reciprocal frequency response function is shown in figure 8. It can be seen that figure 8 enhances details and that although the frequency response function is a linear model of the nonlinear system it is more complicated than that of a linear single degree of freedom oscillator.

The reciprocal frequency response function has also been found to be useful when considering systems with several resonances.

6. CONCLUSIONS

Three techniques have been presented which enable high quality frequency response functions to be measured. It has been shown that despite nonlinearities and noise the use of a random force to excite a structure will produce a linear frequency response function. Also by means of a special application of cross spectral density functions the effects of interactions between the shaker and a structure may be overcome. Finally by plotting the reciprocal of the frequency response function it has been shown that interpretation of the measured frequency response function is simplified.

7. ACKNOWLEDGEMENTS

The author wishes to thank Mr. D. Frankum for his help with the calculations in figure 1. He also acknowledges the financial support of the UKAEA.

REFERENCES

1. J.S. BENDAT and A.G. PIERSOL 1971 Random data: analysis and measurement procedures. New York: Wiley-Interscience.

2. M.F. WHITE and R.G. WHITE 1976 'Journal of Sound and Vibration' 48 543-557. Frequency response testing in a noisy environment or with a limited power supply.

3. H.G.D. GOYDER (To appear) 'Journal of Sound and Vibration' On the measurement of frequency response functions in the presence of non-linearities and noise.

4. H.G.D. GOYDER (To appear) 'Journal of Sound and Vibration' On the use of electrodynamic shakers for frequency response measurements.

5. G.R. TOMLINSON 1979 Journal of Sound and Vibration 63(3) 337-350. Force distortion in resonance testing of structures with electrodynamic vibration exciters.

6. C.C. KENNEDY and C.D.P. PANCU 1947 Journal of the aeronautical sciences. Use of vectors in vibration measurement and analysis

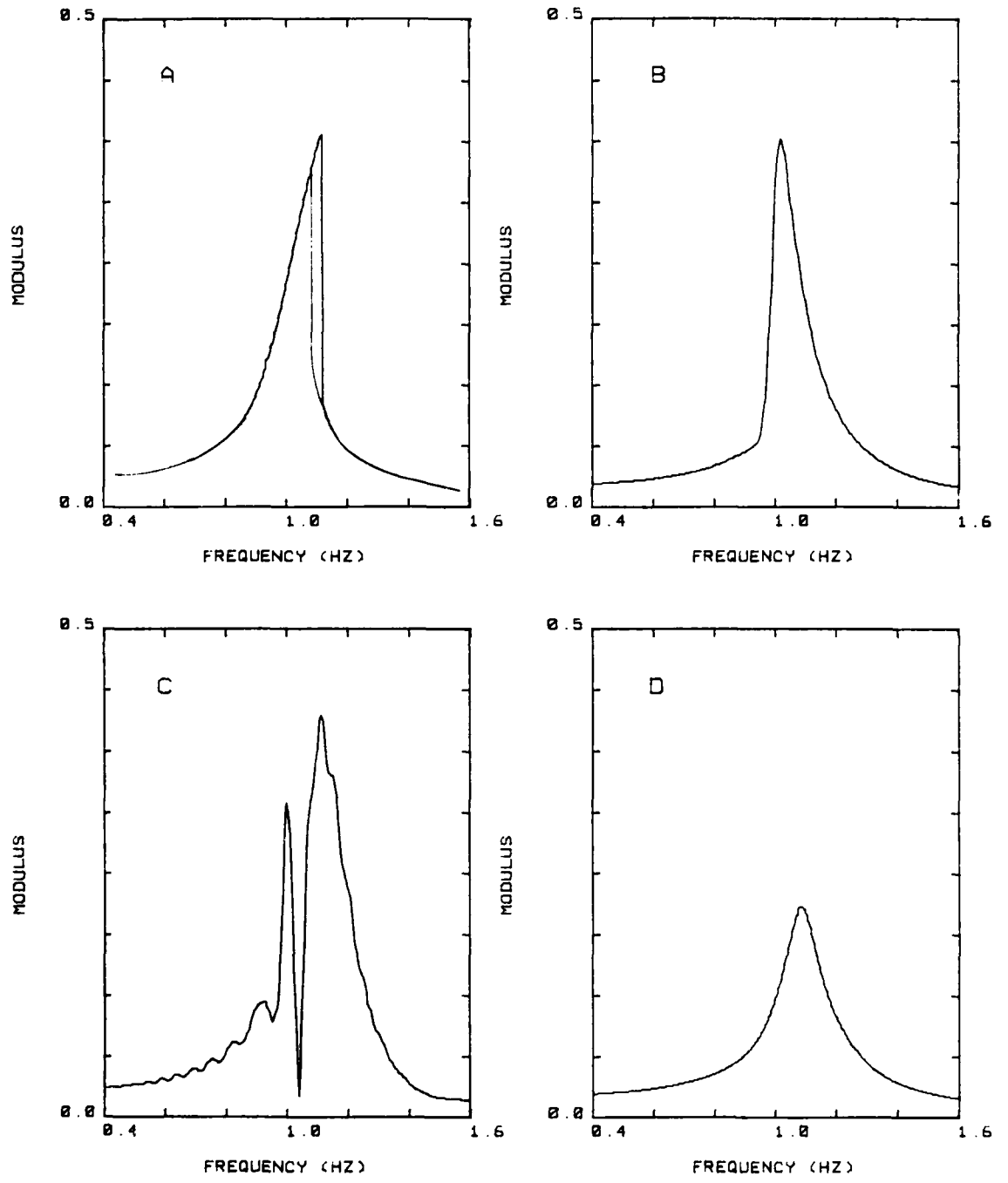

FIG. 1 MEASUREMENT OF A FREQUENCY RESPONSE FUNCTION.

A - SINUSOIDAL TESTING

B - PULSE TESTING

C - RAPID SWEEP TESTING

D - RANDOM TESTING

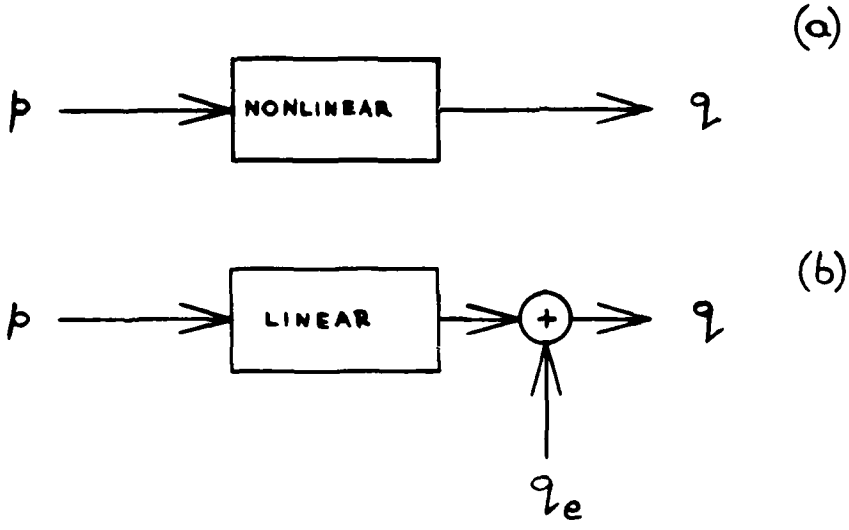

Fig 2: a) Nonlinear system b) Linear model of nonlinear system

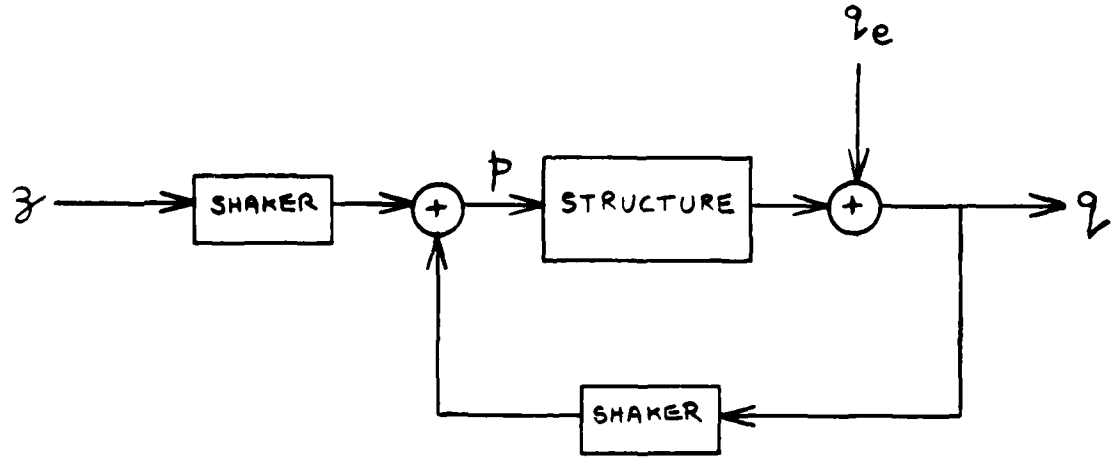

Fig 3: The interaction between the structure and shaker during a frequency response test

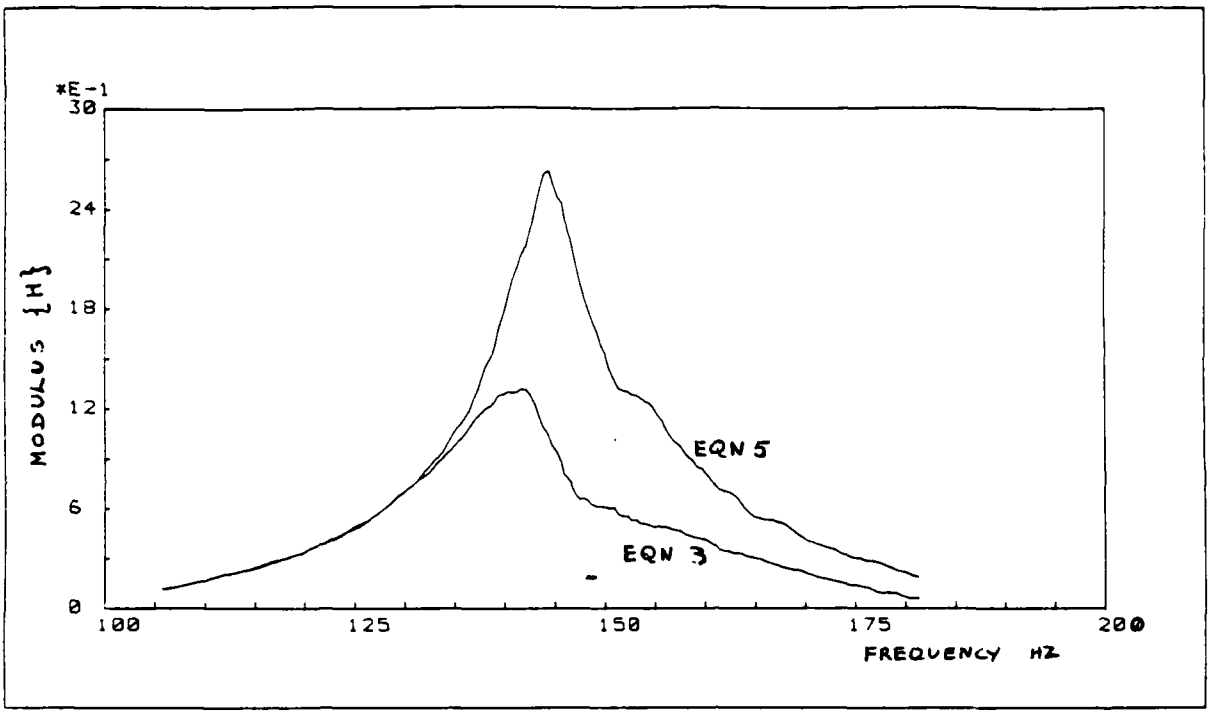

Fig 4: Frequency response functions determined from equations 3 and 5

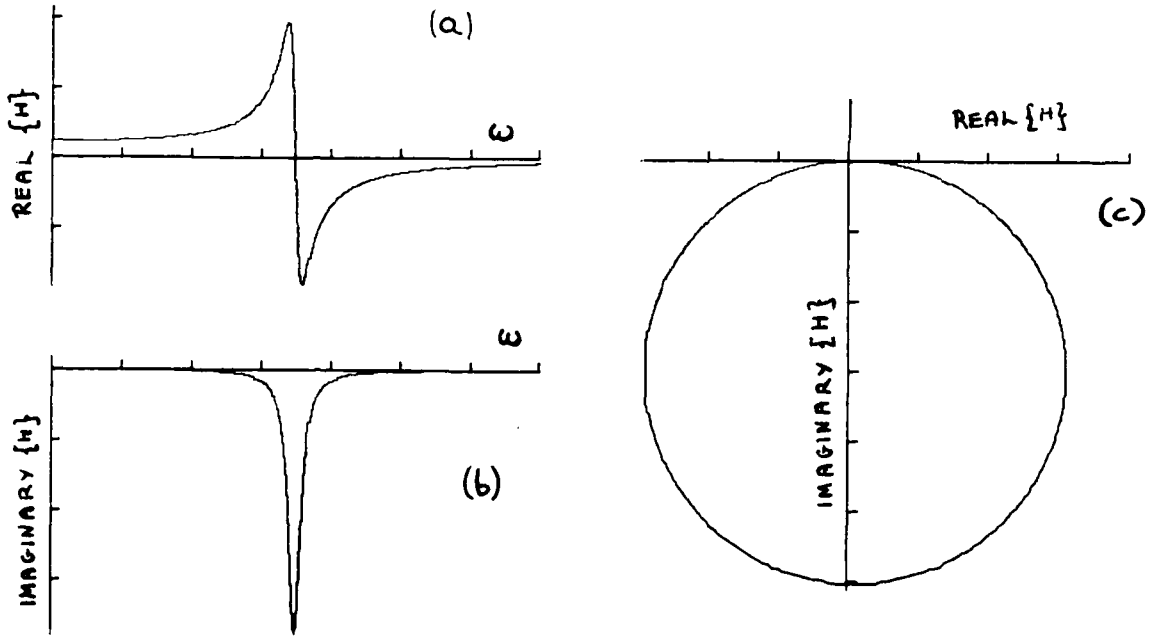

Fig 5: a) and b) Real and Imaginary parts of frequency response function
c) Function plotted on the Argand diagram

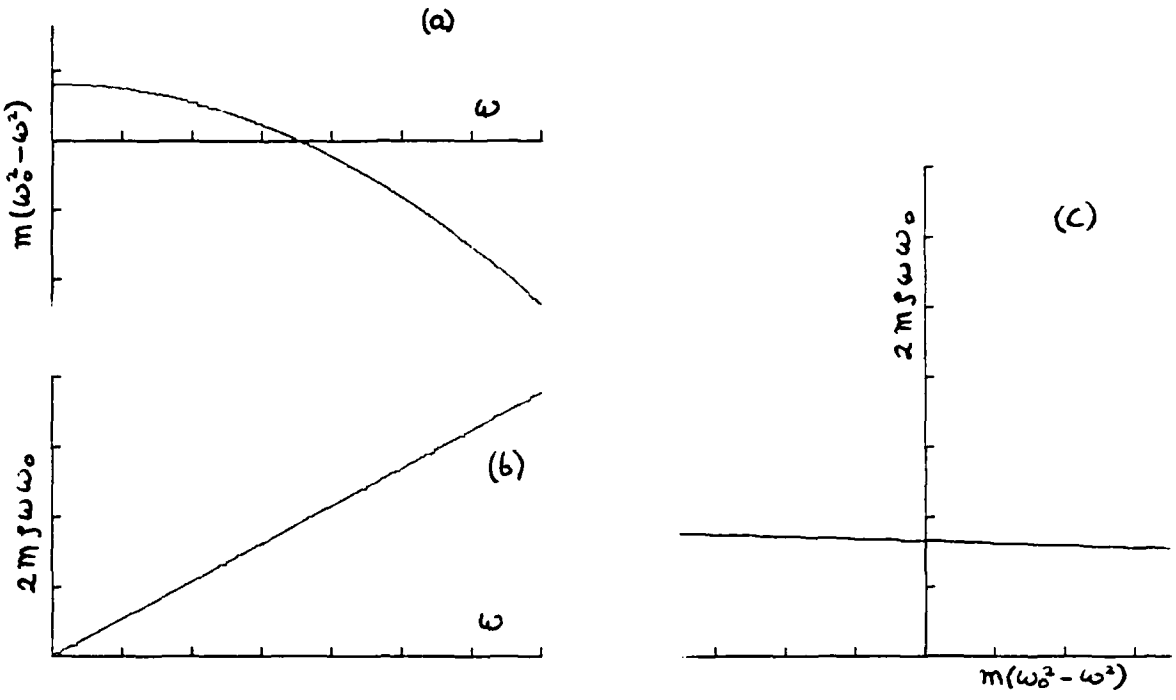

Fig 6: a) and b) Real and Imaginary parts of reciprocal frequency response function
c) Reciprocal function plotted on the Argand diagram

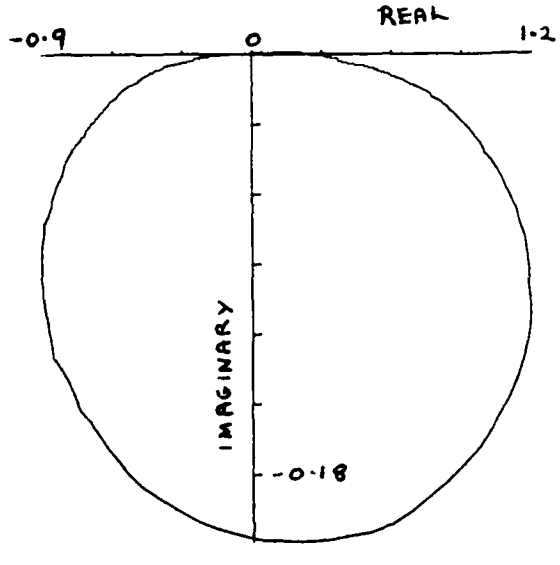

Fig 7: Response on Argand diagram

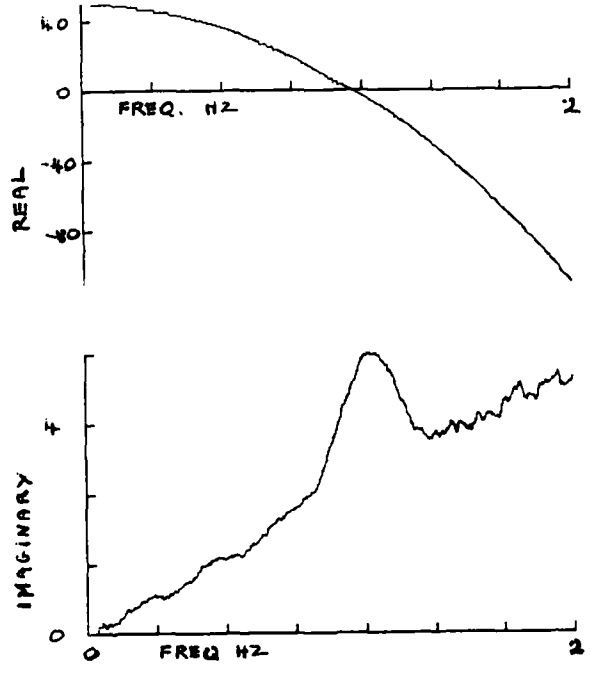

Fig 8: Real and Imaginary parts of reciprocal response function

AN INVESTIGATION OF THE BEHAVIOR OF THE SIMULTANEOUS THREE AXIS VIBRATION SYSTEM

G.K. Hobbs; Consultant

Robert Mercado; Santa Barbara Research Center

1. SUMMARY

Several high-rate production programs at Santa Barbara Research Center (SBRC) placed emphasis on finding economical and efficient screening systems. A quasi-random triaxial vibration system, including temperature cycling capability, was selected. Two Screening Systems, Inc., Multiaxial QRS-100s have been used at SBRC since June of 1980.

The systems have also been successfully used for locating defects. Some defects that have shown up during screening could not be found in the rework cycle under quiescent conditions nor could they be located using a single-axis vibration system in conjunction with thermal cycling.

To more thoroughly understand the behavior of the quasi-random multiaxis shaker, investigations of the motions in the time and frequency domains were undertaken, including the relationships between the three linear axes and between the three rotational axes. These investigations showed that the six axes of motion can be considered to be independent in terms of specimen response to the input motions.

2. THE SYSTEM INVESTIGATED

The QRS-100 is excited by pneumatically driven hammers which generate pulses. An ASD (or Fourier) analysis of these impacts shows a line spectrum with equally spaced lines. The fundamental frequency in the line spectra can be altered by changing the hammer velocity through varying the input air pressure. This is called smearing of the input. Each of the several (four are used as of this writing) hammers has a slightly different character and further smears the overall response of the QRS-100. The design of the structure between the hammers and the specimen to be screened further modifies the ASD as experienced by the specimen. The intervening structure is adjustable in several ways to allow variation in acceleration in the three axes and to control high-frequency rolloff. Substantial changes in the spectra can be attained by design changes in the structure between the hammers and the specimen.

Vibration is controlled by a microprocessor which controls the overall acceleration level. The air supply to the vibrators is modulated by a fast-acting digital flow valve which modulates the pressure in a quasi-random manner, resulting in spectral smearing of the input ASD. The overall grms input level is controlled using six multiplexed accelerometer feedback signals and maintaining an average as commanded by the program.

Temperature is controlled by an event programmer and a Research, Inc., temperature controller. The events programmer determines the rate of change of temperature, the temperature extremes and dwell times, and can also turn on the vibration controller and GN_2 purge (if desired) at specified times during the screen profile.

The mechanical shake table structure is mounted on air bags to allow motion of the entire system within the environmental chamber. The impacters are mounted to the outer ring on springs to provide adjustable high-frequency rolloff. The inner and outer rings are clamped together by an adjustable force elastomer interface to allow adjustment in distribution of energy between axes and also to

effect high-frequency rolloff. Finally, the tent-shaped fixture is bolted to the inner ring and there is a provision for mounting 12 specimens at a time. Figure 1 details a typical setup; further details of system configuration and performance are given [1, 2].

For the application at hand, the screen process was intended to expose part and workmanship defects. Note that there is no need to simulate actual field use conditions in a screen because once the flaws are removed under accelerated screening conditions, they will not fail under actual use conditions.

Figure 1. The QRS-100

3. EXPERIMENTS RUN, LINEAR MOTIONS

Reference 1 discussed screening results, fixture surveys, and the quasi-random response spectrum (QRRS). All of the results in Reference 1 were in terms of acceleration spectral density and were limited to linear motion only. Since knowledge of phase relationships between the axes was necessary to evaluate stresses due to multiaxial motion, including rotations, a more complete description of the motions was required.

The axes of motion are shown in Figure 2, which also shows the actuator arrangement. Note that the fixture is removed. Note also that the rear actuator is Screening Systems Model No. PV 1 5/8 - 1.6, whereas the other three are NAVCO MP 1-1 1/4.

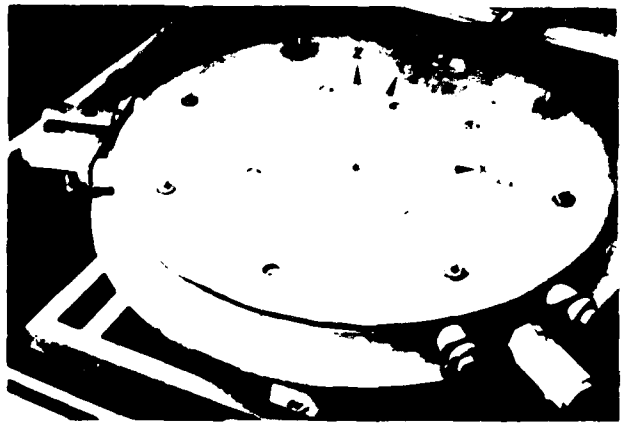

Figure 2. Axes and Actuator Arrangement

Each axis of motion of the QRS was examined to determine the statistical distribution of linear acceleration on the fixture. The probability and cumulative probability distributions were found to approximate the Gaussian distribution in both narrow- and broadband samples as previously reported [3].

For a sample of several locations on the fixture, auto- and cross-correlations were calculated. The autocorrelation functions implied a typical broadband random signal for all sample times and axes. The cross-correlations, however, were much more difficult to decipher as some samples appeared to be correlated and some did not. All showed evidence of the line spectra input from the actuators, and showed that the actuators had different repetition rates. The cross-correlation of different time samples taken at the same point always had varying character. Many cross-correlations were checked and none were the same, leading to the conclusion that the signals were nonstationary. These facts required the signals to be analyzed in the time domain.

In order to reduce the analysis problem as much as possible, only one actuator, the rear one in Figure 2, was utilized with the system run in the constant pressure (manual) mode. Only the motions of one location on the fixture were examined in detail and that was at one of the triaxial accelerometers used in the control system (Figure 3).

The signals from two accelerometers were fed into two charge amplifiers and tracking filters and were used to drive the vertical and horizontal axes of an oscilloscope. The bandpasses used in the investigations were 2 Hz, 10% of the center frequency, 100 Hz, and complete bandpass. Note that the two signals were not amplitude-controlled to be equal, so true Lissajous patterns were not formed. Since the only actuator used was mounted in the y direction, the y axis responses tended to exceed the x axis responses, which is not normally the case.

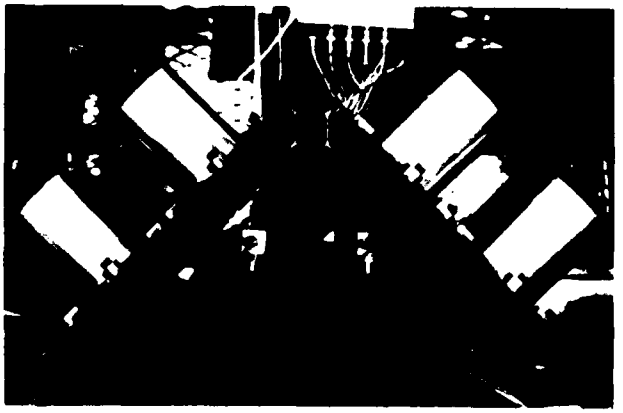

Figure 3. Control Accelerometer Arrangement

The tracking filters were first set to 2 Hz for a very close look at the behavior of the system. Note that the half-power bandwidth of a structure is generally much wider than this, so the specimen being screened responds to a much broader bandwidth (as discussed in [1]). For example, a structure with a natural frequency of 400 Hz, and with 4% of critical damping, has a half-power bandwidth of 32 Hz.

The actuator produces repeated impacts generating a line spectrum. The first line was at 68 Hz (for a given pressure) and the harmonics were found at exact integer multiples of 68 Hz. For the frequency range below 68 Hz and between the harmonics up to about 1000 Hz, there were essentially no signals when the analysis bandwidth was 2 Hz. At frequencies above 1000 Hz, system nonlinearities and slight changes in the actual repetition rate generated nearly continuous signals as the tracking filter was swept along. The ellipse drawn by the two

signals was found to be amplitude-modulated and to wobble at the lower frequencies (up to the fourth harmonic at 272 Hz). The amplitudes varied in time by factors of from 30% to 95%, and the angles of the principal axis varied about 5°. Above the fourth harmonic the ellipse was very unsteady and varied in amplitude and angle, with an ellipse principal axis varying 360°. (See Figures 4 and 5 for examples.)

Selection of a 10% bandwidth at center frequencies below the sixth harmonic (408 Hz) produced little change from the 2 Hz bandwidth, but above that frequency the difference was very great, as two or more lines of the spectra would pass through the filters. At these higher frequencies, the oscilloscope showed an elliptical outline with lines traced throughout the ellipse. The ellipse outline also changed with time to some extent. (See Figure 6.)

Examples of some of the phenomena are shown in Figures 4 through 9, all of which are annotated separately. Figure 4 illustrates a very narrow-band analysis at a harmonic of the repetition rate of the actuator, with the ellipse modulated and rotating; a double exposure of this type of figure is shown in Figure 5. Figures 6 and 7 illustrate the effect of a broader bandwidth than on Figure 4. Note that the gains used were always equal on the vertical and horizontal axes, but were changed as necessary to fill the frame. Figure 8 shows that using all four actuators rounds out the pattern. Figure 9 illustrates a bandwidth corresponding to 5% of critical damping.

The vector acceleration was studied mathematically in order to evaluate the probability distribution of the acceleration. A Monte Carlo model using three Gaussian distributions, each with 5.5 grms, was set up and run on an Apple II computer, and the resulting probability distribution is shown in Figure 10. Note that the distribution is similar to a lognormal distribution. The 1σ, 2σ, 3σ and 4σ points are shown on the figure. The "max acceleration" of 28.6g in the title block was used only for scaling the abscissa and was calculated as the 3σ

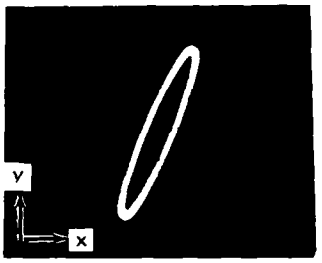

Figure 4. Experimental Results: Center Frequency, 409 Hz, Bandwidth 2 Hz, Modulated and Rotating, One Actuator

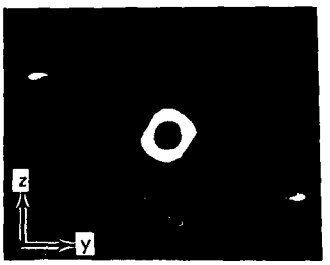

Figure 5. Experimental Results: Center Frequency, 346 Hz, Bandwidth 2 Hz, Four Actuators, Double Exposure

Figure 6. Experimental Results: Center Frequency, 409 Hz, Bandwidth 41 Hz, One Actuator

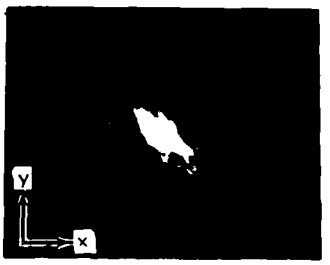

Figure 7. Experimental Results: Broadband, One Actuator

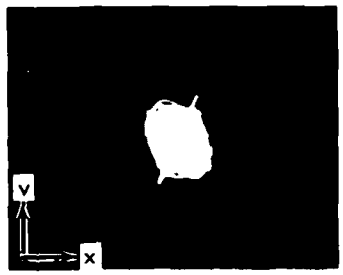

Figure 8. Experimental Results: Center Frequency, 433 Hz, Bandwidth 43 Hz, Four Actuators

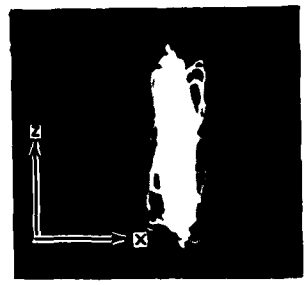

Figure 9. Experimental Results: Center Frequency, 433 Hz, Bandwidth 43 Hz, Four Actuators

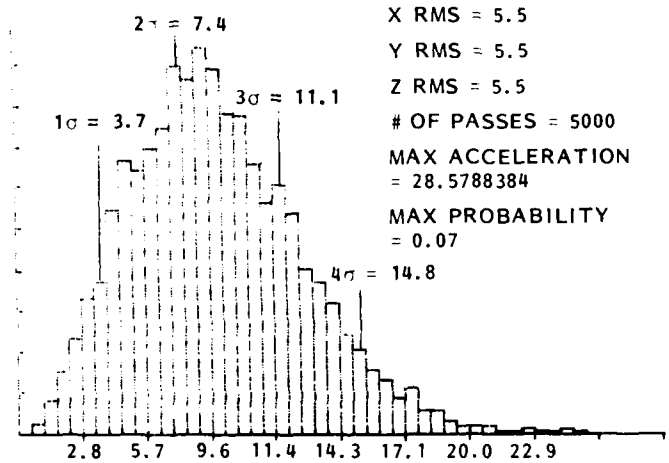

Figure 10. Vector Acceleration Probability Distribution

"vector" of the rms values for each axis as this was known to be an upper bound. Note that in 5000 samples the highest acceleration found was 25.7g.

The angular distribution of the acceleration vector was found to be uniform as the three distributions used had the same rms values. Other cases with non-equal rms values were run for completeness, but are not reported here.

4. CONCLUSION, LINEAR MOTIONS

Narrowband analysis of x and y, y and z, and x and z as pairs of signals shows that the signals are nonstationary and have no constant phase relationship even when only one actuator at a steady pressure is used. Analysis with a bandwidth of 10% of center frequency (about 5% of critical damping) with four actuators results in patterns where the vector acceleration occupies any part of an oblate spheroid in three space (recall that only one actuator in the y direction was used). This leads to the conclusion that the motions in the three axes are independent random variables. The dynamic response of a system exposed to the environment will accordingly be independently random in all three axes.

The oscilloscope patterns on a broadband basis show definitely preferred directions. However, any mode of a structure will respond principally to inputs within the half-power bandwidth of the mode and so broadband analysis is not really relevant for our purposes.

The vector acceleration was found to have an approximately lognormal distribution with the maximum value found in 5000 Monte Carlo trials being less than the 3σ "vector" sum of the rms values for each axis.

5. EXPERIMENTS RUN, ROTATIONAL MOTIONS

Preliminary studies had shown that substantial rotational accelerations existed. A more detailed study was undertaken in order to find the spatial and frequency relationships between the accelerations. The rotational accelerations were calculated from the linear accelerations as detailed in Figure 11.

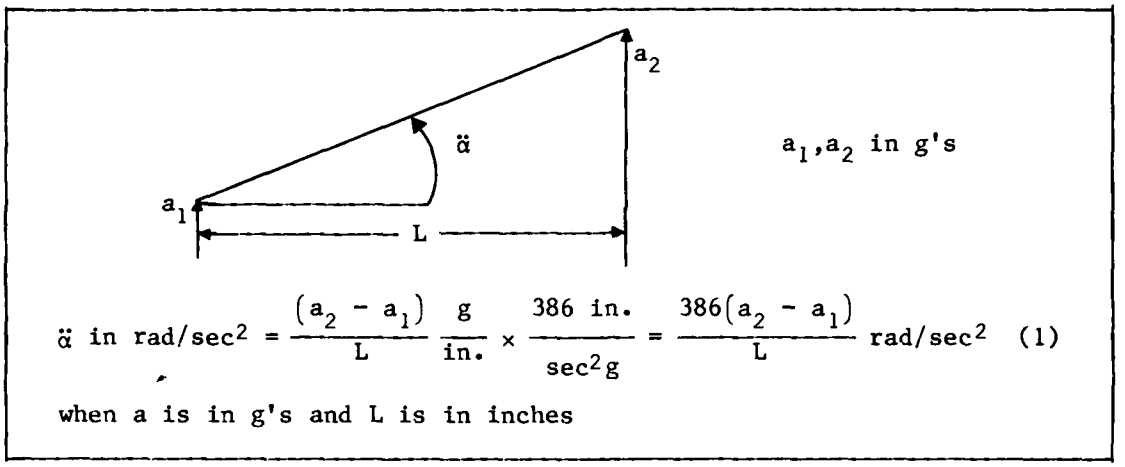

$$\ddot{\alpha} \text{ in rad/sec}^2 = \frac{(a_2 - a_1)}{L} \frac{g}{\text{in.}} \times \frac{386 \text{ in.}}{\text{sec}^2 g} = \frac{386(a_2 - a_1)}{L} \text{ rad/sec}^2 \quad (1)$$

when a is in g's and L is in inches

Figure 11. Rotational Acceleration Calculations

The angular acceleration spectral density (AASD) was calculated by spectral analysis of $\ddot{\alpha}$ rad/sec^2 and resulted in dimensional units of rad^2/sec^4-Hz. The dimension Hz results from division by the filter bandwidth. Two methods were used: digital real time analyzer (RTA), and narrowband analysis of each acceleration followed by summation (including phase angles) and then division by the filter bandwidth. Both techniques proved to be of value.

Prior to any data analysis all instrumentation was checked for proper level and phase relationships. All data was taken at the mounting interface of the unit being screened. All three rotational accelerations were stored on tape in raw linear acceleration form so that analysis in any form could be done later. All impacters were operational and both the constant pressure and automatic control modes were utilized.

When recording was complete, the next step was to make ASD plots using a real time analyzer and to make phase plots using a time series analyzer. Plots of ASD (linear) and phase angle between the two channels used for analysis were performed for many channels, two of which are shown in Figures 12 through 15. Note in Figures 12 and 13 that the ASD has a reasonably continuous distribution, in terms of the QRRS, considering that the analyzer utilized had a 13 Hz bandwidth. Note also that the two ASDs are somewhat different in terms of amplitude distribution. Similarly, each phase angle plot looked different except at a few frequencies as shown.

Further analysis of each acceleration was performed by use of a dual channel oscilloscope in two ways. A time domain photo of the filtered output from two in-line paired accelerometers 3.86 inches apart is shown in Figure 16. The center frequency is 735 Hz and the filter bandwidth is 15 Hz. Note that the phase angle between the signals is not constant.

Driving the oscilloscope with the filtered output on the vertical channels and with the sweep oscillator output on the horizontal channel resulted in Figure 17. The same type of pattern was evident at many other frequencies showing that the amplitude and phase angles were nonstationary.

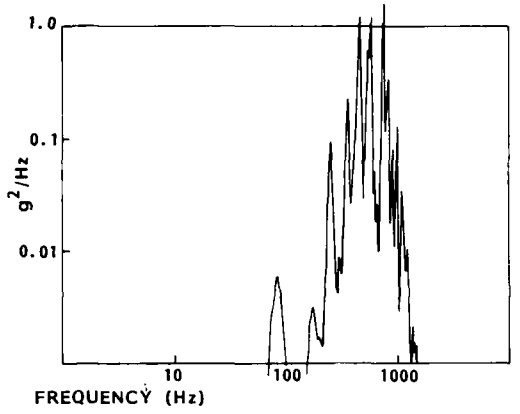

Figure 12. ASD Plot, Channel 2

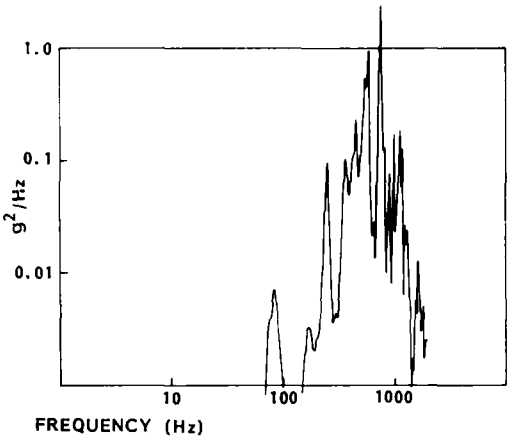

Figure 13. ASD Plot, Channel 4

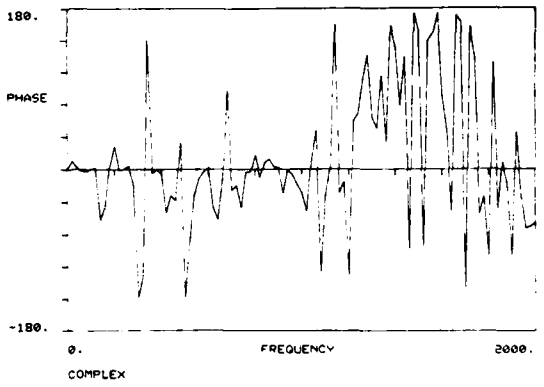

Figure 14. Phase Plot, Channels 2 and 4

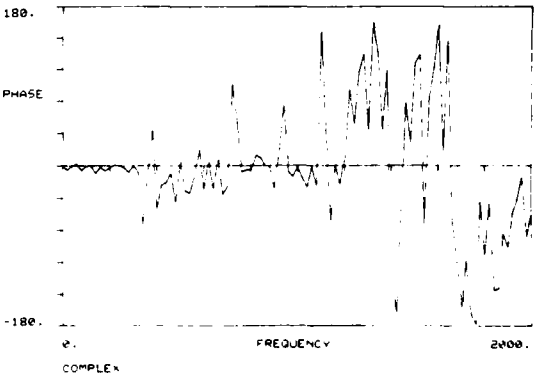

Figure 15. Phase Plot, Channels 2 and 4

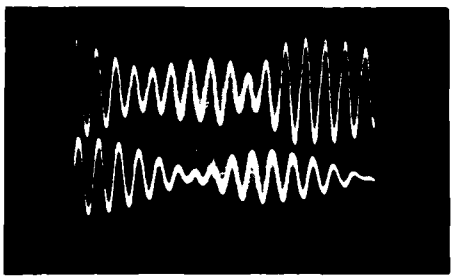

Figure 16. 735 Hz; 15 Hz Filter

Figure 17. 475 Hz; 15 Hz Filter

Another method of analysis was to set up the oscilloscope in the add mode (Figure 18) to obtain equation (1) (after inverting one signal from the tracking filter). Both narrowband signals could be observed on the oscilloscope and the resultant angular acceleration fed to the real time analyzer where the AASD can be observed and plotted if desired.

The AASD plot of the broadband output (i.e., without any filtering) is shown in Figure 19. The real time AASD was noted to vary by as much as 20 dB per second, again indicating nonstationary angular accelerations.

The final analysis of angular accelerations was done using the oscilloscope and driving the vertical and horizontal channels with two in-line accelerometers in order to see the relationships of linear and angular motion. A straight line

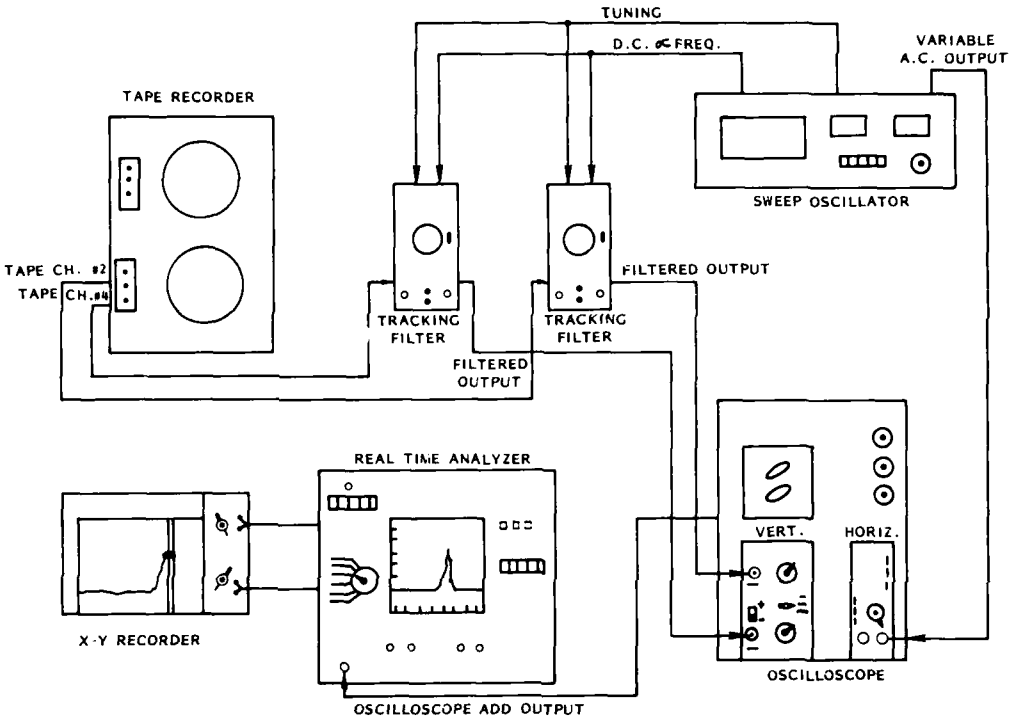

Figure 18. Add Mode Oscilloscope Setup (Rotational Analysis)

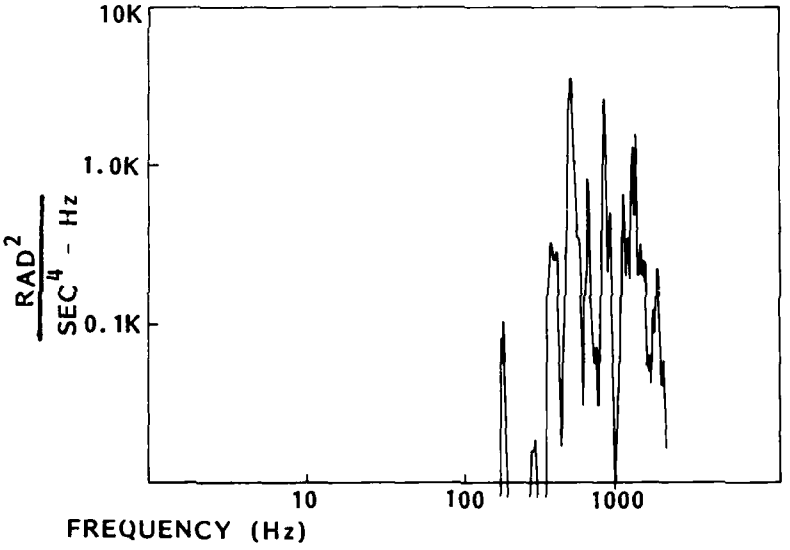

Figure 19. AASD Plot of Broadband Output

at 45° would indicate no rotation and purely in-phase motion. Other figures would indicate angular as well as linear motion. First, an electrodynamic shaker was analyzed with the accelerometers at the specimen mounting points and with a white noise input from 20 to 2000 Hz. The results are shown in Figures 20 through 22, which illustrate nearly perfect linear motion with very little rotation, which is supposed to be the case. A similar analysis was done on the QRS-100 run in the constant pressure mode and the results shown in Figures 23 through 25. The figures illustrate a large degree of out-of-phase motion at some times and in-phase at others, implying true six-degree of freedom motion.

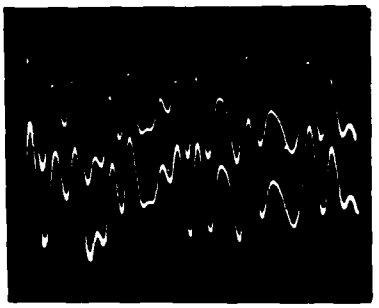

Figure 20. Two Broadband Waveforms on Electrodynamic Shaker

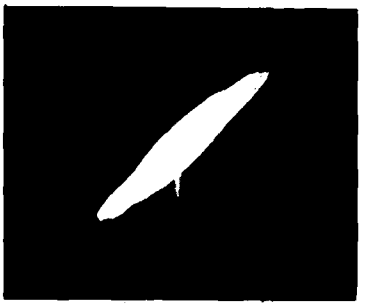

Figure 21. Narrowband (15 Hz) on Electrodynamic Shaker, Center Frequency 1000 Hz

Figure 22. 100 Hz Bandwidth on Electrodynamic Shaker, Center Frequency 1000 Hz

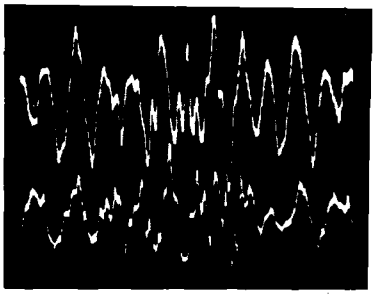

Figure 23. Two Broadband Waveforms on QRS-100 Systems

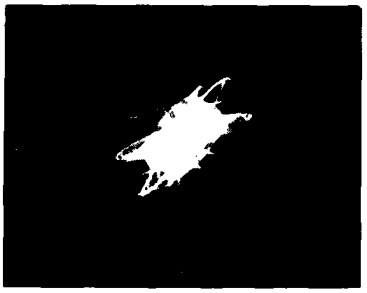

Figure 24. Narrowband (15 Hz) on QRS-100, Center Frequency 610 Hz

Figure 25. 100 Hz Bandwidth on QRS-100, Center Frequency 610 Hz

6. CONCLUSION, ANGULAR MOTION

The QRS-100 exhibits angular accelerations at nearly all frequencies when analyzed with a narrowband filter, and at all frequencies when analyzed with a filter corresponding to a typical structural half-power bandwidth.

7. SUMMARY AND AN EXAMPLE

The QRS-100 has accelerations in all six degrees of freedom as measured by a typical structural half-power bandwidth filter of 5% to 10% of the center frequency (2.5% to 5% critical damping). The motions are all nonstationary in time, have Gaussian distributions when measured independently, and are not correlated. The system therefore behaves as a six-axis shaker with all axes being independent.

This behavior explains the results of an investigation wherein a system which had failed screening on the QRS-100 with cracked solder joints would not exhibit anomalies when excited by a single-axis system. The specimen was excited in all principal axes on the single axis system at g levels from 1/2 grms to 15 grms at ambient, high and low temperatures, without intermittents being observed. Excitation by the QRS-100 at a 1 grms level at low temperature showed system intermittents about 92% of the time.

In this example, the six simultaneous axes of motion were just what was needed to cause the cracked solder joint to show an open condition. Many other examples of this type have occurred at SBRC. Further comparisons of single-axis shaker and QRS-100 shaker screening results are given in [1] and [2].

1. G.K. HOBBS, J.L. HOLMES, R. MERCADO 1982 SEECO 82, the Society of Environmental Engineers, London, England. Stress Screening Using Multiaxial Vibration.
2. G.K. HOBBS, R. MERCADO 1982 Reliability and Maintainability Symposium, Los Angeles, California. Quasi-Random Stress Screening Using the QRS-100.
3. A.J. CURTIS 1979 Hughes Aircraft Interdepartmental Correspondence. Analysis of Pneumatic Actuator (Baker Shaker) Vibration Signals.

RECENT EXPERIMENTAL DEVICES TO OBTAIN THE DYNAMIC PARAMETERS OF BRIDGES

William C. McCarthy and Kenneth R. White
New Mexico State University

Alberto G. Arroyo
University of Texas at San Antonio

1. INTRODUCTION

Full scale testing of structures continues to be the best means of obtaining the dynamic parameters necessary for design. For bridge structures, though, barriers exist that restrict field testing with difficulties that include possible structural damage, inadequate test control, cost, and limitations in accessibility. These difficulties contribute to a current lack of understanding of the dynamic behavior of bridges. To alleviate this problem, New Mexico State University (NMSU) has devised two test instruments, the tricoil sensor [1] and a portable vibration machine [2]. The tricoil sensor was designed to clearly measure movement in three orthogonal directions and succeeds in being superior to its counterpart, the accelerometer. The vibration machine complements the tricoil sensor with its operator control and operational flexibility. A thorough discussion of both instruments detail their composition, how they work, and their functional capacities.

A small bridge was constructed at NMSU to test the two instruments. Of particular concern was the vibration machines ability to produce a measurable response in a non-destructive manner. Three tests were initiated to define the fundamental frequencies and damping coefficients of the test bridge and to produce frequency response curves. An outline of the test procedures with corresponding results confirm the effectiveness of the two instruments.

2. TRICOIL SENSOR

The tricoil sensor of Figure 1 operates under the principle that current is generated when the coils move through a static magnetic field. The coils are ¼ in. (6.35 mm) in diameter by 7/8 in. (22.225 mm) long and are manufactured as miniature magnetic pickups by Power Instruments, Inc. Three coils, in an orthogonal orientation to monitor three dimensional vibrations, are rigidly attached to the inside of a 1 in. x 1 in. x 2 in. (25.4 mm x 25.4 x 50.8 mm) aluminum box which in turn is attached to a ¼ in. x 2 in. x 3 in. (6.35 mm x 50.8 mm x 76.2 mm) aluminum plate with a 6 lead electrical plug. The plate is bonded to the bridge commonly with the use of glue.

A signal is actuated by first placing a stationary electromagnet in close proximity to the tricoil sensor. Current is produced by inducing movement of the sensor in the magnetic field. The greater the movement the stronger the signal. The NMSU tests used on electromagnet with a field density of approximately 2500 gauss at the center of its core. A smaller permanent magnet may be used but an electromagnet tends to produce a clearer signal.

Two operational advantages plus its lower cost relative to an accelerometer makes the tricoil sensor a highly attractive vibration measuring device. Although some signal amplification is necessary, the tricoil does not require the amplification normally associated with an accelerometer. In addition, a lesser amount of filtering is needed to remove the noise from the tricoil signal. Figure 2 presents two steady state first bending mode responses from a similarly placed tricoil sensor and accelerometer. In this instance, the accelerometer used twice the amplification and one third again as much filtering to

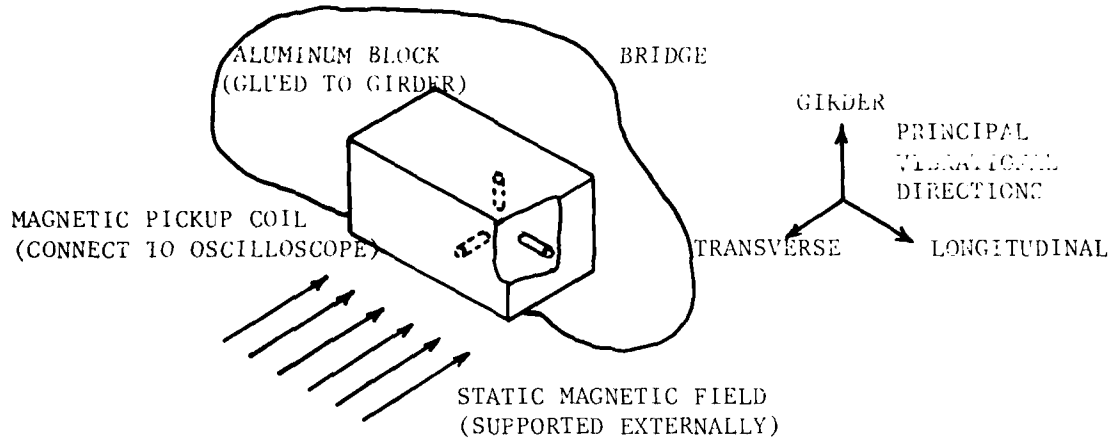

FIGURE 1. TRICOIL SENSOR PRINCIPLE

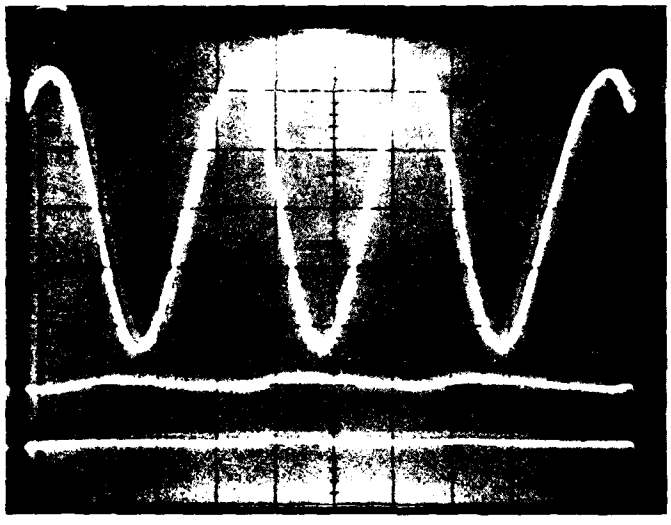

First Bending Mode Steady-State Response for Tricoil Sensor

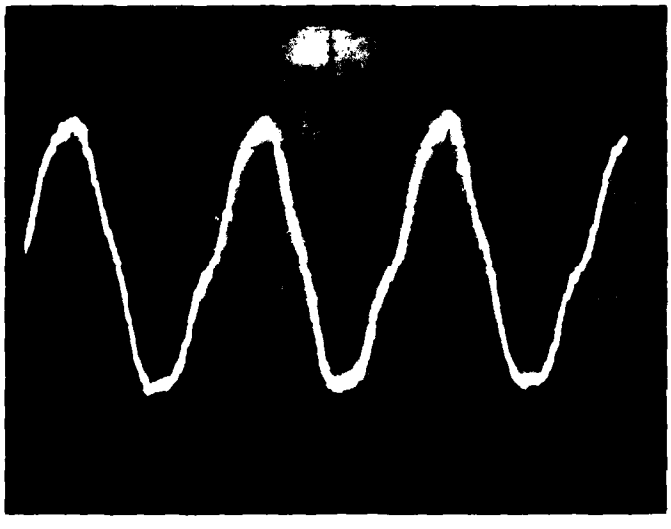

First Bending Mode Steady-State Response for Accelerometer

FIGURE 2. FREQUENCY-RESPONSE TEST FOR FIRST BENDING MODE

produce an acceptable but still inferior signal. Some degradation of the tri-coil signal is noted at higher frequencies but it is still insignificant in comparison to the accelerometers.

The main disadvantage of the tricoil sensor is that it produces amplitudes which are proportional to the mass velocity and, hence, the vibrations remain qualitative in nature. Thus, displacements and stresses may not be obtained without first calibrating the sensor, a lengthy process that has not as yet been accomplished.

3. VIBRATION MACHINE

The qualities desired of a field test vibration machine include frequency and force control, test flexibility, and compactness and so the NMSU vibrator was designed to have these features. The vibrator or shaker, illustrated in Figure 3, consists of two counter-rotating 18 in. (0.457 m) diameter spur gears operated by a 15 hp (11.186 kW) DC electric motor. A 36 in. (0.914 m) by 100 in. (2.54 m) channel frame supports the gear mechanism, motor, and counter-balancing weights. The frame is sufficiently strong to serve as a trailer body for transportation to the field.

Two masses are attached to the spur gears at an eccentricity of 6 in. so as to maintain synchronization of the gear mechanism. Thus, when the two masses are immediately adjacent, they generate a unidirectional force that is always perpendicular to the gear mechanism. This unidirectionality eliminates the interference effects that result when there are force created movements other than those under study. The force magnitude is controlled in two ways, the weight of the masses and the frequency at which they are rotated. Force levels, then, range as low as a few hundred to several thousands of pounds. Testing has indicated that a force magnitude as low as 400 lbs. (1.779 kN) acting on a field bridge produces an acceptable signal in the tricoil sensor. As a result, 1000 lbs. (4.448 kN) was used as a typical test force magnitude, thus, insuring the nondestructive goal of the research.

A belt drive with a 1 to 1 driving ratio turns the spur gears. This is sufficient to produce a 2 to 29 Hz frequency range which is thought to encompass the fundamental bending and torsional mode frequencies of most bridges. The force created by the rotating masses varies sinusoidally according to the equation

$$F = 2m\rho\omega^2 \sin \omega t \qquad (1)$$

where $2m$ = total eccentric mass

ρ = mass eccentricity

ω = angular velocity

with its maximum amplitude of $2m\rho\omega^2$. The dominate factor in the force magnitude is the angular velocity which is directly controlled by controlling the motor frequency. The motor and, through the belt drive transference, the vibration machine has an incremental tolerance of no more than 0.2 Hz. This sensitivity and force predictability insures that the testing remains under the contol of the operator. This assurance of operator control serves to establish confidence in the nondestructive capacity of the shaker.

Lubrication of the spur gear mechanism results in a very low friction coefficient. When power to the motor is terminated, the gears coast smoothly down through the various frequencies and corresponding decreasing force levels. However, the study of free vibration requires no external excitation force. For this reason, the shaker is equipped with a hydraulically operated braking system.

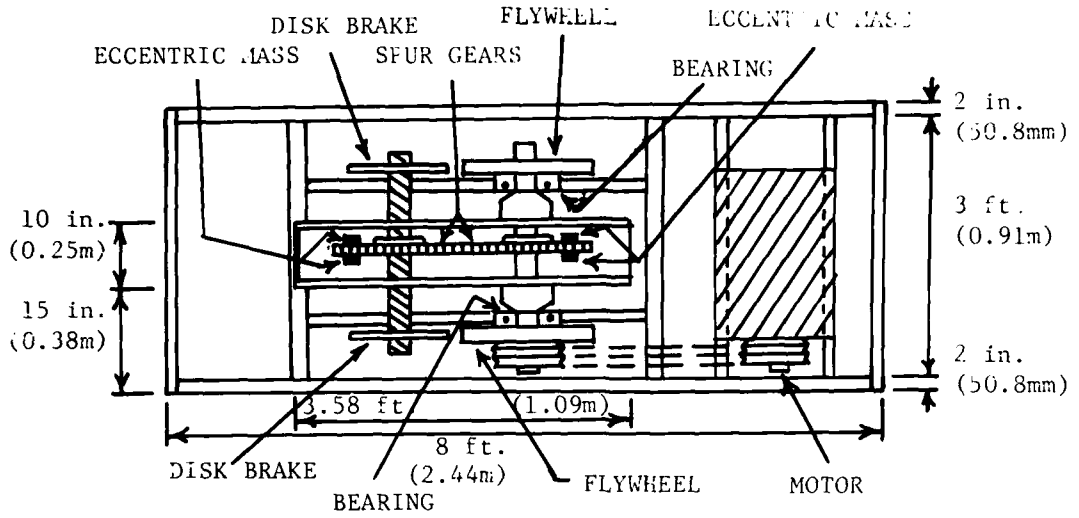

(a) BRIDGE DYNAMIC EXCITATION MACHINE-TOP VIEW

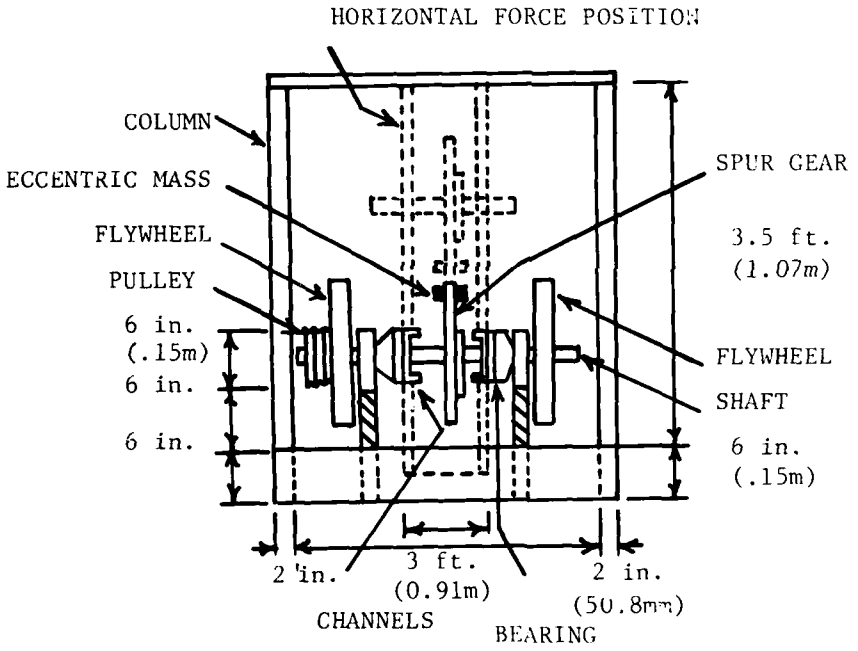

(b) BRIDGE DYNAMIC EXCITATION MACHINE-FRONT VIEW

FIGURE 3. BRIDGE DYNAMIC EXCITATION MACHINE

The braking is sufficiently fast and yet smooth to result in little disturbance of the signal from the tricoil sensor.

Perhaps the best feature of the vibration machine is its ability to quickly convert from a vertical force generator to a horizontal force generator shown in Figure 4. This is accomplished by a right angle rotation of the total gear mechanism which is then bolted in place, a process that takes but a few minutes. The shaker is designed so that no other changes are needed before testing commences. A horizontal force capacity permits the study of bridge supports under conditions that more accurately simulate earthquake behavior but to a much less degree. It also expands upon its potential use as a dynamic test instrument for structures other than bridges.

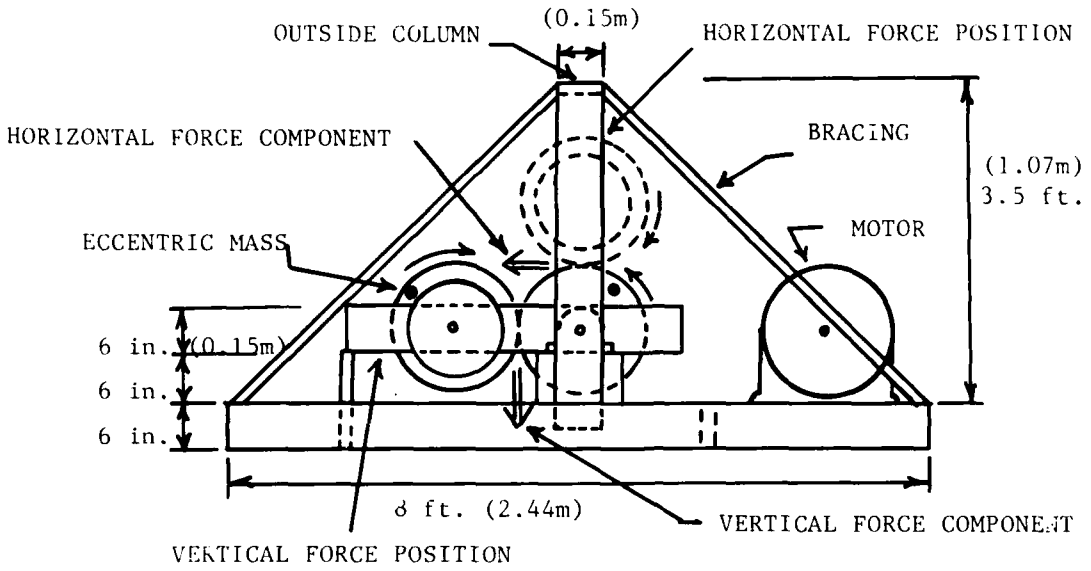

FIGURE 4. BRIDGE DYNAMIC EXCITATION MACHINE-DUAL POSITIONS

4. DYNAMIC TESTS

Three tests were devised to check the function of the bridge vibrator and tricoil sensor. The tests, summarized below as they apply to the simple supported NMSU test bridge, are representative of procedures required to obtain the dynamic parameters of field bridges.

4.1 Run Down Test

The shaker is positioned at the center of the bridge with a tricoil sensor attached beneath. The bridge is excited to a high frequency, approaching 29 Hz, at which time the power is turned off and the vibrator is allowed to coast down slowly through the frequency levels. When the frequency roughly corresponds to a resonant frequency of the structure, the signal from the tricoil sensor is greatly amplified as exhibited by the first bending mode response of Figure 5. The run down test, therefore, approximately identifies the lower natural periods of a bridge.

4.2 Frequency Response Curve Test

The tricoil sensors and shaker are selectively located on the bridge in positions indicative of the mode under study. The shaker and tricoil sensor, for example, remain at the center of the structure when studying the first bending mode response. The bridge is brought to steady state resonance with guidance from the run down test. Then, the frequency is varied through a range of ± 2 Hz at roughly 20 point intervals within this range while the response of the structure is recorded. The bridge is vibrated at each point for a sufficient time to insure steady state. A plot of the response amplitude versus exciting frequency for all points is the frequency response curve for that mode. In addition to giving an exact natural frequency, the frequency response curve may yield a damping ratio according to the formula

$$\xi = \frac{f_2 - f_1}{2f} \qquad (2)$$

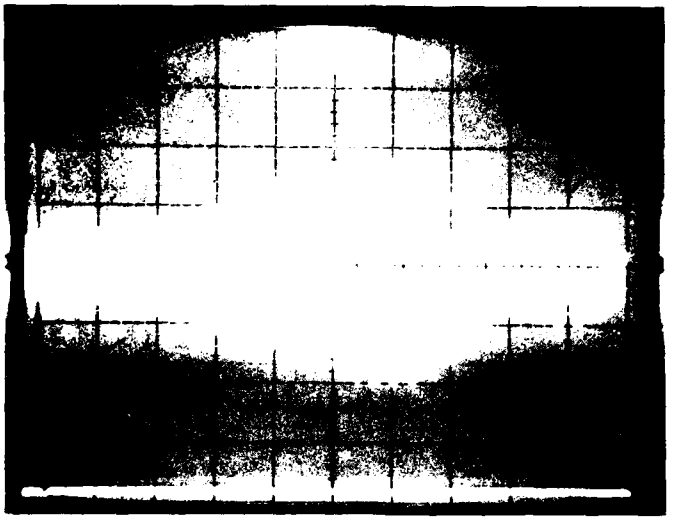

FIGURE 5. RUNDOWN TESTS FOR FIRST BENDING MODE

where: ξ = damping ratio

f_1 = first frequency on the curve with a response amplitude equal to $1/\sqrt{2}$ times the maximum amplitude

f_2 = second frequency on the curve with a response amplitude equal to $1/\sqrt{2}$ times the maximum amplitude

f = natural frequency of the bridge.

Equation 2 is called the bandwidth method by Paz [3] who outlined the procedure.

4.3 Transient Vibration Test

The shaker and sensors are positioned in exactly the same manner as for the frequency response curve test. The bridge is again excited to one of its natural frequencies and held for a brief period to assure steady state. Power to the vibrator is then terminated while the brake is immediately applied. This results in a transient or decay response of the structure now in free vibration. The first bending mode transient response is presented in Figure 6.

The transient response may be used to obtain a second damping ratio by the logarithmic decrement method [3] according to the formula

$$\ln \frac{y_{n+1}}{y_1} = -2\pi n\xi \qquad (3)$$

where: ξ = damping ratio

n = cycle number

y_1 = response amplitude at the first cycle

y_{n+1} = response amplitude at the n+1 cycle.

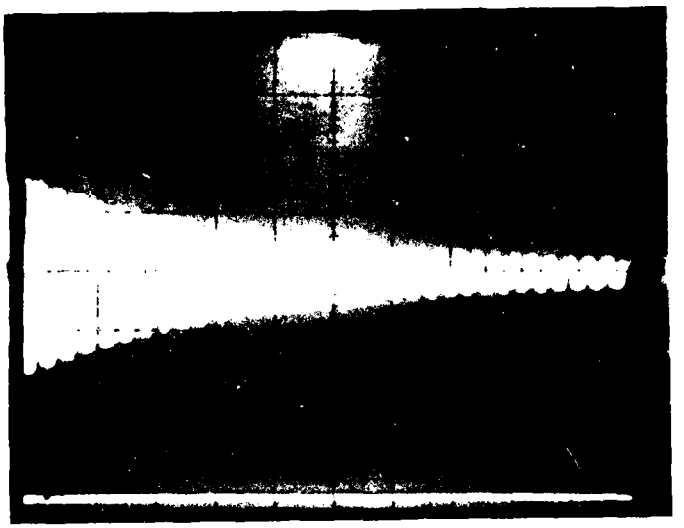

FIGURE 6. TRANSIENT RESPONSE TEST FOR FIRST BENDING MODE

5. EXPERIMENTAL RESULTS

Beyond establishing the worthiness of the vibration machine and tricoil sensor, the goal was to determine the first and second bending and the first torsional mode dynamic parameters of the NMSU test bridge. The run down test, however, quickly determined that the second bending mode frequency was higher than the 29 Hz capacity of the shaker. Thus, the goal was modified to the development of frequency response curves and the calculation of damping ratios for the first bending and torsional modes only.

The NMSU test bridge is a 7 ft. (2.134 m) wide, 44 ft. (13.411 m) long by 1.67 ft. (0.508 m) deep prestressed concrete double tee beam. The flange has an average depth of 2 in. (50.8 mm) and the web an average thickness of 5 in. (127 mm) placed 4 ft. (1.219 m) on-centers. The bridge has a simple span of 34 ft. (10.363 m) with 5 ft. (1.524 m) cantilevered ends.

Figure 7 is a plot of the first bending mode frequency response curve using a total spur gear eccentric weight of 4.84 lbs. (21.529 N). A number of dynamic factors may be deduced from the curve with the most obvious being a first bending mode resonant frequency at 6.4 Hz. The bandwidth method of equation 3 produced a damping ratio of 2.1%. The curve is observed to be slightly unsymmetrical which implies some slight non-linearity in the structure. To test this, a second series of tests were run using a total eccentric weight of 6.17 lbs. (27.445 N). The respective maximum response amplitudes were 4.9 and 5.86. The force ratio of 1.27 versus an amplitude ratio of 1.2 for the two weight categories is sufficiently close to indicate essentially linear behavior.

A frequency response curve was also developed for the first torsional mode. The result was an average resonant frequency of 21 Hz. Average is used since a definite non-linearity was revealed when the natural frequency varied by ± 10% depending upon the magnitude of the eccentric weight. The average bandwidth damping ratio was found to be 1%. It is thought that cracks in the beam contributed to the torsional non-linearity.

The first bending mode transient response of Figure 6 produced the amplitude values of Table 1. The damping ratio, ξ, varies between 1.47% and 1.01%

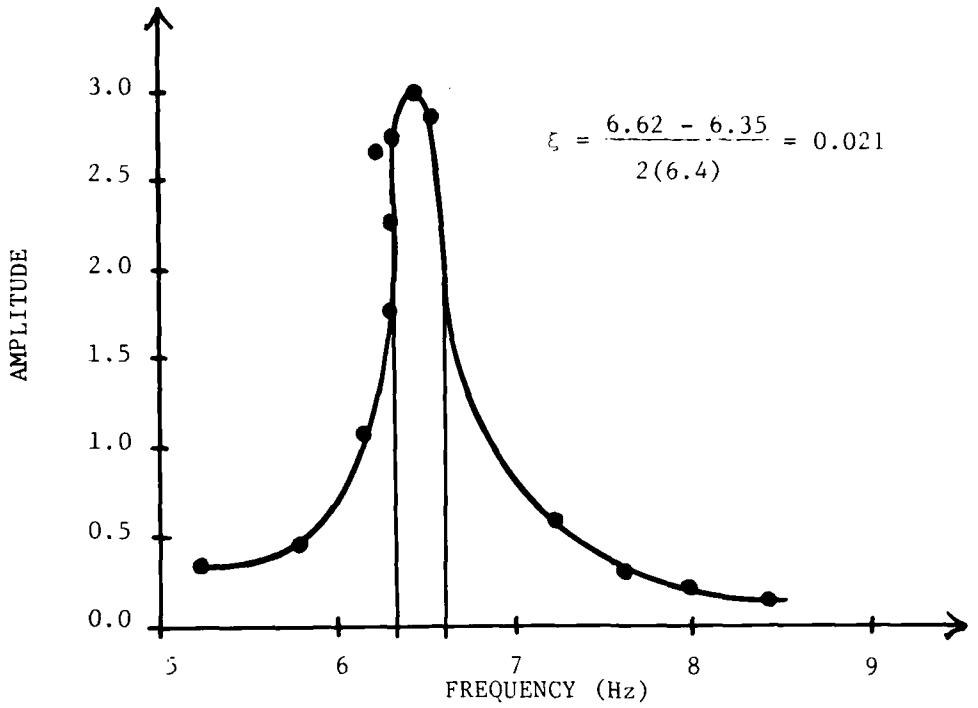

FIGURE 7. NORMALIZED FREQUENCY-RESPONSE CURVE FOR FIRST BENDING MODE TEST A AND SENSOR Z

depending upon the cycle used in the logarithmic decrement method of Equation 4. In any case, the bridge damping is very low. A difference in the ratios by the methods of Equation 3 and 4 is due to the theoretical assumptions of their derivation. The best that one can say then is that the damping falls between 1 and 2% of critical.

n	1	2	3	4	5	10	15	19
$\frac{y_1}{y_{n+1}}$	$\frac{1.7}{1.55}$	$\frac{1.7}{1.42}$	$\frac{1.7}{1.35}$	$\frac{1.7}{1.20}$	$\frac{1.7}{1.15}$	$\frac{1.7}{0.80}$	$\frac{1.7}{0.6}$	$\frac{1.7}{0.45}$
ξ	0.0147	0.0143	0.0122	0.0138	0.0124	0.0119	0.0110	0.0101

TABLE 1. LOGARITHMIC DECREMENT DAMPING RATIOS - FIRST BENDING MODE

6. DYNAMIC ANALYSIS

An attempt to analytically reproduce the natural frequencies was only partially successful. The ICES STRUDL II [4] plane grid modal analysis was used because of the economy of the computer program and its torsional mode capabilities. The bridge was subdivided into 157 longitudinal and transverse grid members interconnecting 92 nodes. Moment of inertia and area were calculated using standard formulas except that the transverse diaphragms were given near zero area to assure equivalent mass. Damping was not considered.

The STRUDL first bending, first torsional, and second bending mode frequencies were 6.41 Hz, 20.69 Hz, and 25.26 Hz, respectively. Both fundamental

modes were on target with only the second bending mode failing to compare. The run-down test did not reveal any resonant responses between 22 Hz and the 29 Hz upper limit. One explanation is that the structural model falls short of defining the true nature of the test bridge particularly the prestress aspect which was disregarded in the analysis.

7. CONCLUSIONS

Both field test instruments exceeded their expectations. In most aspects, the tricoil sensor out-performed the accelerometer. The clear tricoil signal eliminated the need for data refining techniques in the tests carried out on the NMSU test bridge. It is expected that this would remain true for most test situations.

Vertical force testing of the vibration machine was extensive and the operations proved effective and efficient. One unanticipated drawback was the added dead weight or other form of restraint required to prevent lateral movement of the shaker particularly during resonant vibrations. The weight would have to be added in the field and removed to reposition the machine, thereby, increasing the test time.

The shaker's horizontal force capacity has received only limited testing due in part to a lack of set-bridge test procedures in the horizontal mode. The vertical to horizontal changeover and vice versa proved convenient and quick. Horizontal operations were actually smoother than the vertical with no unwanted movements of the machine. As expected, however, a greater force was needed to elicit an observed response from the bridge.

Donated materials were primarily used in the construction of the vibration machine which prevented, for example, the use of high strength steel in the spur gears. Thus, the upper experimental boundaries of a portable vibration machine have yet to be realized in the existing shaker. An expanded capacity would be highly desirable for horizontal testing. Even so, the shaker, at its present level, is sufficient to carry out vertical force field testing for all but the largest of bridges.

8. REFERENCES

1. R.M. ZIMMERMAN and K.R. WHITE 1980 National Science Foundation, Earthquake Hazards Mitigation. Measurements of on-site dynamic parameters for seismic evaluations. Washington, D.C.

2. A.G. ARROYO 1982 Doctoral Dissertation, New Mexico State University. The dynamic characteristics of bridge through the design of a unique bridge vibration machine.

3. M. PAZ 1980 Structural Dynamics Theory and Computation. Van Nostrand Reinhold Company.

4. ICES STRUDL II 1971 The Structural Design Language. Department of Civil Engineering, Massachusetts Institute of Technology, Cambridge, Mass.

THE EXPERIMENTAL MEASUREMENT OF FLEXURAL WAVE POWER FLOW IN STRUCTURES

W. Redman-White
Institute of Sound and Vibration Research
University of Southampton

1. INTRODUCTION

When attempting to control vibration in structures, it is often desirable to be able to identify significant paths of vibration transmission from sources through the structure to some point of interest. In pursuance of this objective, consideration of vibration amplitudes at various points is of little help, since stationary waves may be present giving rise to large amplitudes whilst little power is being transmitted. The concept of wave intensity is therefore necessary, and is defined as the power flow per unit width of cross section area (in a uniform plate) and is measurable as a vector quantity at a given point. In beams, where wave propagation is in one dimension only, the power flowing through the total cross section is considered. If it is possible to obtain repeated measurements of intensity at many points on a structure, then a pattern of power flow may be identified.

Here, only power carried by flexural waves is considered; this is generally the most important, and is theoretically more difficult to measure than power due to other wave types. Many of the arguments to be developed here may be applied directly to other wave types.

2. FLEXURAL WAVE POWER

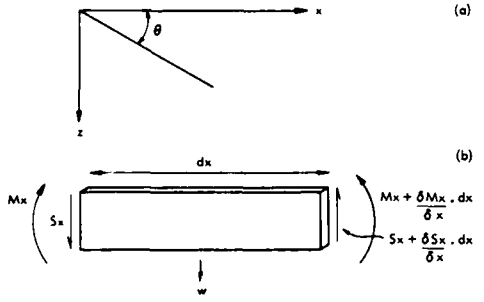

FIGURE 1: Moments and Forces on a Bending Beam

Figure 1 shows the moments and forces acting on an element of a uniform beam undergoing flexural wave motion, with the lateral deformation being denoted by w in the z direction. Power is transported by two components [1];

(i) The Shear Force component Ps, which is the product of the shear force and the transverse velocity:

$$Ps = EI \frac{\partial^3 w}{\partial x^3} \cdot \frac{\partial w}{\partial t} \qquad (1)$$

(ii) The Bending Moment component Pm, which is the product of the bending moment and the rotational velocity:

$$Pm = -EI \frac{\partial^2 w}{\partial x^2} \cdot \frac{\partial^2 w}{\partial x \partial t} \qquad (2)$$

where E is Young's modulus and I is the second moment of area of the beam. Far from discontinuities in the beam and the influence of decaying near field waves, the time averaged values of these two components are equal, providing the possibility of obtaining an estimate of the total power flow from a measurement of one component.

$$\langle P \rangle = 2 \langle Ps \rangle = 2 \langle Pm \rangle \qquad (3)$$

Figure 2 shows the moments and forces acting on an element of a uniform plate undergoing flexural wave motion. In this case, the intensity in a given direction (eg. the x direction in an arbitrary cartesian co-ordinate system) has three components:

(i) The Shear Force component J_{sx}, which is the product of the shear force in the x direction and the transverse velocity:

$$J_{sx}=D\left[\frac{\partial^3 w}{\partial x^3}+\frac{\partial^3 w}{\partial x \partial y^2}\right] \cdot \frac{\partial w}{\partial t} \qquad (4)$$

(ii) The Bending Moment component J_{mx}, which is the product of the bending moment in the x direction and the rotational velocity parallel to that direction:

$$J_{mx}=-D\,\frac{\partial^2 w}{\partial x^2}+\frac{\partial^2 w}{\partial y^2} \cdot \frac{\partial^2 w}{\partial x \partial t} \qquad (5)$$

(iii) The Twisting Moment component J_{tx}, which is the product of the twisting moment in the x direction and the rotational velocity about that direction:

$$J_{tx}= D(1-\nu)\,\frac{\partial^2 w}{\partial x \partial y} \cdot \frac{\partial^2 w}{\partial y \partial t} \qquad (6)$$

where D is the flexural stiffness of the plate, given by

$$D=\frac{Eh^3}{12(1-\nu^2)}$$

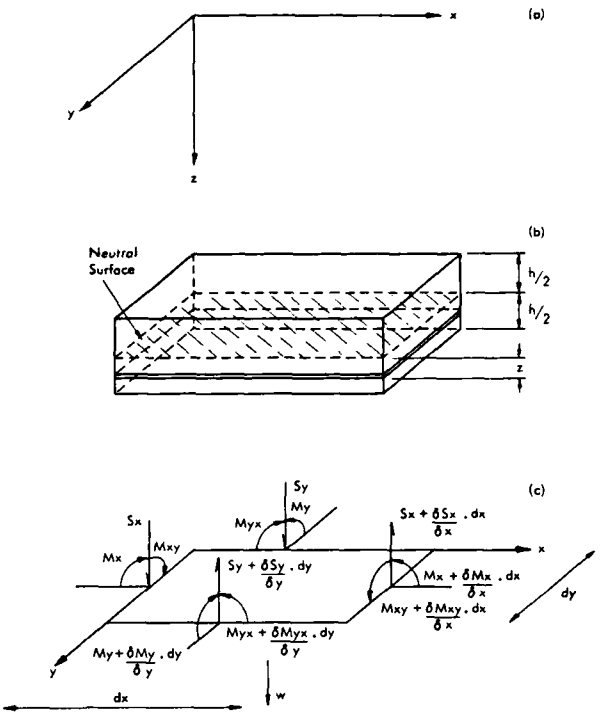

FIGURE 2: Moments and Forces on a Bending Plate

h is the thickness of the plate and ν is Poisson's ratio. It is easy to show that far from discontinuities and local sources and sinks, where the wavefield is composed of plane propagating waves, that

$$\langle J_x \rangle = 2\langle J_{sx} \rangle = 2\left[\langle J_{mx} \rangle + \langle J_{tx} \rangle\right] \qquad (7)$$

Hence in such circumstances, it is possible to estimate the total intensity at a point from a measurement of one component, specifically the shear force component.

3. REQUIREMENTS OF A POWER FLOW MEASUREMENT TECHNIQUE

Several measurement methods have been investigated [2] with the following requirements in mind:

(i) Simple time domain signal processing, to allow possible implementation as a portable real-time electronic instrument.

(ii) Ease of use. This is clearly important if many measurements are to be made on a structure to permit the identification of power flow patterns. Any transducer arrangement to be attached to the structure should be as simple as possible and easy to deploy and recover.

(iii) Immunity to instrumentation tolerances. The effect of basic experimental tolerances should not produce unacceptable errors in the measurement of a travelling wave or waves.

(iv) Good dynamic range performance. This is the ability of a measuring system to be able to give reliable results from a measurement of a travelling wave in the presence of a possibly much larger stationary (non-decaying) wave. This characteristic has been identified as probably the

most important [3] in any practical measuring system.

4. A ONE-DIMENSIONAL MEASURING TECHNIQUE USING TWO ACCELEROMETERS

This method is based on the relationship stated in Equation (3), i.e. that far from discontinuities and the influence of their decaying wavefields, the shear force and bending moment components are equal. Consider a travelling harmonic wave in a uniform beam with the displacement at a point described by:

$$w(x,t) = A\sin(\omega t - kx) \tag{8}$$

Substituting this into the expression for the shear force component of power flow, Equation (1), gives:

$$P_s = EI\omega k^3 A^2 \cos^2(\omega t - kx) \tag{9}$$

The output of a linear accelerometer attached to the surface of the beam will be:

$$\frac{\partial^2 w}{\partial t^2} = -\omega^2 A \sin(\omega t - kx) \tag{10}$$

and the output of a rotational accelerometer attached to the beam will be proportional to:

$$\frac{\partial^3 w}{\partial x \partial t^2} = k\omega^2 A \cos(\omega t - kx) \tag{11}$$

If a phase shift of $-\pi/2$ radians is applied to the signal from the linear accelerometer, it can be seen that the shear force component of power flow, and hence the total value, may be obtained using a two degree-of-freedom accelerometer [4,5]. In this context, a two degree-of-freedom accelerometer is an item which provides signals proportional to the transverse and rotational accelerations at the point of attachment. Hence,

$$Ps = \frac{EIk^2}{\omega^3} \cdot \frac{\partial^3 w}{\partial x \partial t^2} \cdot \frac{\partial^2 w}{\partial t^2}\,(q) \tag{12}$$

where (q) indicates "in quadrature". Since

$$k^4 = \frac{\omega^2 m_b}{EI}$$

where m_b is the mass per unit length of the beam, then the total time averaged power flow may be written:

$$\langle P \rangle = \frac{2\sqrt{m_b EI}}{\omega^2} \left\langle \frac{\partial^3 w}{\partial x \partial t} \cdot \frac{\partial^2 w}{\partial t^2}\,(q) \right\rangle \tag{13}$$

Although this expression has been developed for a single frequency, it may also be applied to a narrow band of frequencies.

There are disadvantages in the use of two degree-of-freedom accelerometers [2]; however, the required information may be obtained by the application of simple finite difference approximations [6] to the signals from two linear accelerometers attached to the beam some distance Δ apart, where Δ is small compared with the flexural wavelength λ:

$$\left.\frac{\partial^2 w}{\partial t^2}\right|_{x=0} \simeq \tfrac{1}{2}\left[\left.\frac{\partial^2 w}{\partial t^2}\right|_{x=+\frac{\Delta}{2}} + \left.\frac{\partial^2 w}{\partial t^2}\right|_{x=-\frac{\Delta}{2}}\right] \tag{14}$$

$$\left.\frac{\partial^3 w}{\partial x \partial t^2}\right|_{x=0} \simeq \frac{1}{\Delta}\left[\left.\frac{\partial^2 w}{\partial t^2}\right|_{x=+\frac{\Delta}{2}} - \left.\frac{\partial^2 w}{\partial t^2}\right|_{x=-\frac{\Delta}{2}}\right] \tag{15}$$

Letting a_1 denote the acceleration at $x=-\frac{\Delta}{2}$ and a_2 the acceleration at $x=+\frac{\Delta}{2}$; then the total time averaged power flow may be written:

$$\langle P \rangle \simeq \frac{\sqrt{m_b EI}}{\Delta\omega^2} \left\langle \left[(a_2 - a_1)(a_2(q) + a_1(q)) \right] \right\rangle \tag{16}$$

This expression may be further simplified:

$$\langle P \rangle \simeq \frac{2\sqrt{m_b EI}}{\Delta\omega^2} \left\langle \left[a_2 a_1(q) \right] \right\rangle \tag{17}$$

5. MEASUREMENT ERRORS DUE TO BASIC ASSUMPTIONS

5.1 Near Field Errors

The measurement method described is strictly only valid far from discontinuities where Equation (3) holds. Reference [5] analysed the error due to measuring only one power component close to a discontinuity; however, this analysis is not correct in the case of practical measurements implementing Equations (13) or (16). Analysis shows that in practice, provided that an error of ± 20% can be tolerated, measurements may be made as close as λ/10 from discontinuities. Figure 3 shows experimental results obtained using Equation (16) close to the force excitation of an "infinite beam" apparatus [2,7], with the predicted theoretical error curve for reference.

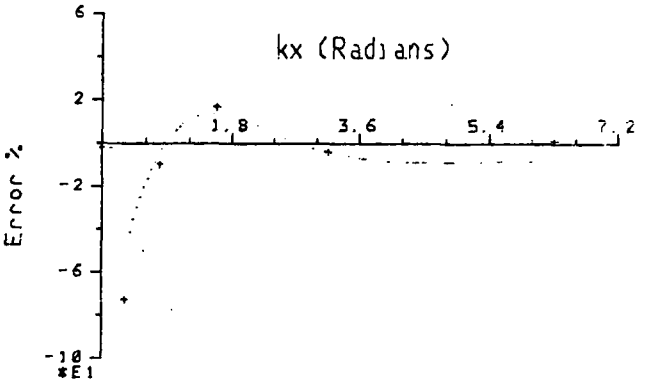

FIGURE 3: 2 accelerometer finite difference method experimental results in the near field of the force input to the infinite beam apparatus.

\+ Experimental results

---- Theoretical value of error

5.2 Finite Difference Errors

The power flow measurement expression, Equation (16) is not exact, but embodies an error due to the finite difference approximations. This leads to an underestimation of the true value, and the magnitude of the error increases with increasing accelerometer spacing Δ. As will be shown, there are good reasons for using relatively large values of Δ; however, it is possible to correct the results obtained exactly so that no penalty is incurred [2,6], thus:

$$P = \tilde{P} \cdot \frac{k\Delta}{\sin(k\Delta)} \tag{18}$$

where $\tilde{P}$ indicates that this is the measured value.

5.3 Bandwidth Limitations

The power flow measurement expression was derived in terms of single frequencies, and it is obvious that some error will result from the use of a finite measurement bandwidth [4]. Further, there is an additional error (but of

opposite sign) due to the variation of the value of $k\Delta$ with frequency, and hence the magnitude of the finite difference underestimation. The exact value of these errors will depend heavily on the power spectral density (P.S.D.) of the wave motion under consideration, but as an example, if the P.S.D. is constant, then a bandwidth ratio ($\delta f/f$) of 0.3 may be used with a measurement error of about 3%. In practice, it is advisable to use a much smaller measurement bandwidth than this [2].

6. SOURCES OF EXPERIMENTAL ERROR

6.1 Travelling Wave Results

This heading refers to the effects of measuring system tolerances on the results obtained from the measurement of a purely propagating wave motion. Inspection of Equations (16) and (17) shows that instrumentation channel gain tolerances only appear as a linear scaling of the result. Tolerances in the value of Δ do not appear as a linear scaling, but the sensitivity is not high.

There are two possible types of instrumentation phase tolerances, these being: relative phase tolerance between channels, manifesting itself in much the same way as accelerometer position tolerances; phase errors in the quadrature function have a simple cosine function. Note that if the simplified expression, Eqn (17), is implemented, both types of phase error are equivalent and the effects are the same as those due to relative phase differences between channels.

Figure 4 shows the effects of selected values of instrumentation tolerances on travelling wave measurements. No finite difference correction has been included. It can be seen that the general sensitivity is small.

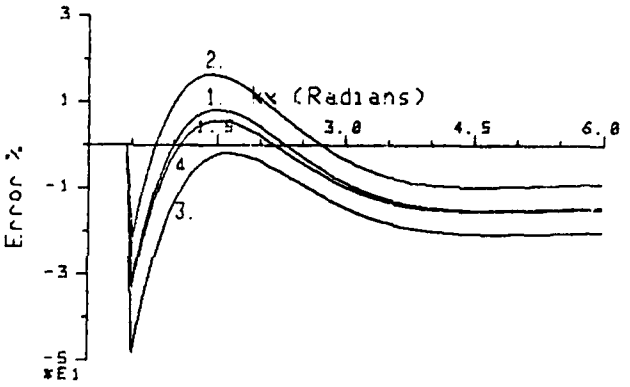

FIGURE 4: Two accelerometer finite difference method measurement error in the nearfield of a force input to an infinite beam $\Delta = 0.15\lambda$.
1. No instrumentation errors
2. Accelerometer 2 displaced by 0.015λ
3. $+5.0^{o}$ phase error in Ch.2
4. $+5.0^{o}$ phase error in quadrature function

6.2 Spurious Results due to Stationary Waves

This factor represents the main limitation of any intensity measurement system. It is simple to show that the system phase tolerances alone determine whether a measuring system produces a spurious response in a stationary (non-decaying) wavefield. Considering Equation (16), the system phase tolerances again divide into two types. If a phase error Θ is present in Channel 1, then if the displacement of the beam is described by:

$$w(x,t) = B\sin(\omega t)\,\sin(kx) \qquad (19)$$

Then the spurious result will be given by:

$$\langle \tilde{P}(x) \rangle = \frac{EIk^2\omega B^2}{2\Delta}\,\{\sin(\Theta)\left[\cos(k\Delta)-\cos(2kx-k\Delta)\right]\} \qquad (20)$$

Note that this function is spatially periodic with period $\lambda/2$, and the maximum value increases with Θ but decreases with increasing values of $k\Delta$. Hence to minimise this type of spurious response, as large a value of Δ as is practical should be used.

Now consider a phase error $\emptyset$ in the quadrature operation. If the displacement of the beam under consideration is again described by Equation (19) then

the spurious result will be given by:

$$\langle \tilde{P}(x) \rangle = \frac{EIk^2 \omega B^2}{2\Delta} \left[\sin(\emptyset)\sin(k\Delta)\sin(2kx+k\Delta) \right] \qquad (21)$$

Again, this function is spatially periodic, and its value increases with increasing $\emptyset$. However, as Δ is made larger, the spurious result increases. Numerical analysis shows that for most realistic values of phase tolerances the relative phase between channels will have by far the most dominant effect. If the simplified expression, Equation (17), is implemented, both types of phase tolerances will give rise to spurious responses equivalent to the relative channel phase tolerance described earlier, Equation (20), and therefore the effect of any error in the quadrature function will be much more significant. For this reason, the simplified implementation is not recommended. Figure 5 shows the variation in these two types of spurious result with Δ, where measurement is made in a wavefield consisting of a stationary wave and a travelling wave with relative amplitudes of 10 and 1 respectively.

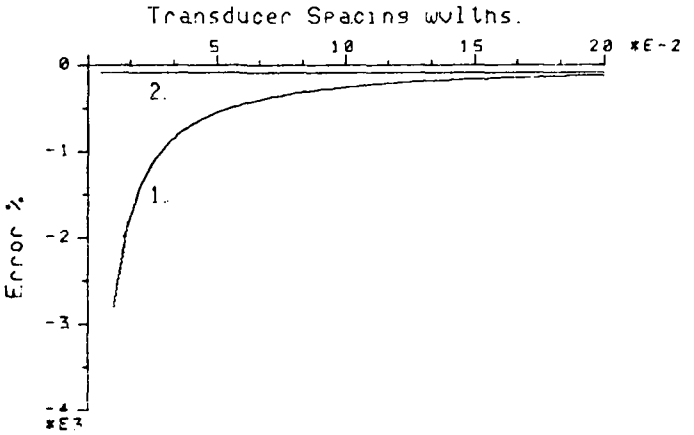

FIGURE 5: Two accelerometer finite difference method measurement errors in the presence of stationary waves. SWR=10:1, Maximum error shown as a function of accelerometer spacing Δ.
1. $+1.0^{o}$ phase error in Channel 2
2. -1.0^{o} phase error in quadrature function.

Experimental results bear these hypotheses out. Measurements were made on a beam excited at a heavily damped resonance, at positions corresponding to a node, antinode and midpoint of the stationary wave mode shape. Results, corrected for finite difference errors, were obtained using implementations of Equations (17) and (18) with a 5^{o} phase error introduced into the quadrature operation, and the results compared.

MEASUREMENT POSITION	NODE	ANTINODE	MIDPOINT
Standing Wave Ratio	2.10	1.86	2.07
Basic Measurement Error %	-16.3	-6.6	-9.5
Eqn (17), 5^{o} Quadrature Error %	-16.7	-11.3	-22.4
Predicted Measurement Error %	-0.4	-0.4	-19.0
Eqn (18), 5^{o} Quadrature Error %	-20.1	-55.2	-42.9
Predicted Measurement Error %	-14.4	-85.4	-57.8

Within experimental limits, the predicted trend has been followed.

7. TWO DIMENSIONAL MEASUREMENTS

Equation (7) may be invoked to allow this method to be extended to two dimensional measurements on uniform plates. Two obtain simultaneous measurements of the intensity components in two orthogonal directions, four accelerometers may be used disposed symmetrically at a distance of $\Delta/2$ from the nominal measurement position. An improvement in the signal-to-noise ratio may be obtained by the use of all four signals to provide the transverse acceleration information. Using the same notation as before:

$$\langle J_x \rangle \simeq \frac{\sqrt{m_p D}}{2\Delta\omega^2} \left\langle \left[(a_{x2}-a_{x1})(a_{x2}(q)+a_{x1}(q)+a_{y2}(q)+a_{y1}(q)) \right] \right\rangle \qquad (22)$$

where m_p is the mass per unit area of the plate. Similarly in the y direction.

Most of the preceding error analyses are directly applicable. However, there is an additional error due to the apparent value of Δ varying with the incident wave direction. This error is shown in a negative sense for clarity in Figure 6.

A simple finite difference correction is not therefore possible; nonetheless, as the angular variation is small, an approximate expression may be obtained [2].

$$J_x = \tilde{J}_x \cdot \frac{1}{\left[1 - \frac{(k\Delta)^2}{11}\right]} \qquad (23)$$

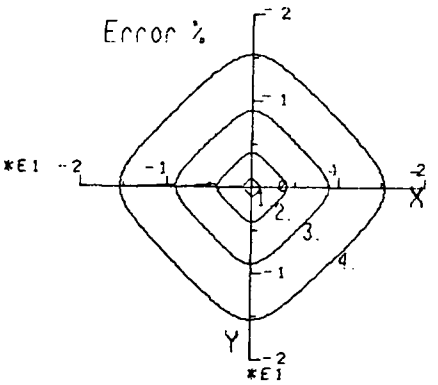

FIGURE 6: Four accelerometer 2-dimensional finite difference method measurement error as a function of incident wave direction

1. Δ=0.05 2. Δ=0.1λ
3. Δ=0.15 4. Δ=0.2λ

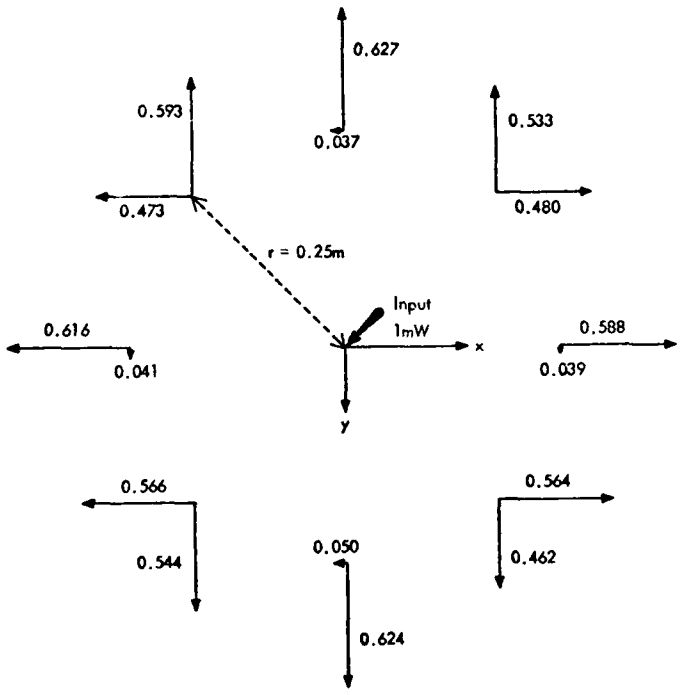

FIGURE 7

Figure 7 shows graphically experimental intensity results obtained at points on a circular contour around a force excitation on an "infinite plate" apparatus [2], normalised with reference to 1mW input power. Comparison of the "integrated" power crossing this contour with the input power from the excitation shows an error of only +6.7%.

8. CONCLUSIONS AND RECOMMENDATIONS

Reliable power flow measurements can be made in many situations, provided that adequate care is taken in the experimental technique. Certain guidelines can be offered to assist those interested in results rather than methodology.

(i) Implement Equation (16) or (for two dimensional measurements) Equation (22) directly without simplifications.

(ii) Avoid making measurements close to discontinuities in the structure (i.e. less than $\lambda/2$ away).

(iii) Use values of Δ in the region of $\Delta=0.15\lambda$ to 0.2λ. Mount the accelerometers first and then measure Δ accurately.

(iv) Correct the results using Equation (18) or Equation (23) as appropriate.

(v) Intensity patterns can change very rapidly with frequency; a narrow measurement bandwidth yields more information, and by excluding possible resonant responses at other frequencies, may improve dynamic range.

(vi) Take the utmost care in achieving the closest possible phase tolerances in the instrumentation and signal processing. The method of mounting the accelerometers on the structure can be quite significant in this respect. The signal processing system should have a phase tolerance of $\pm 0.3^{o}$ or better,

(vii) Bear in mind that dynamic range problems are the main source of error. If the standing wave ratio at a given frequency is greater than about 20:1, then it is probable that the results will be meaningless.

9. REFERENCES

1. CREMER L., HECKL M., UNGAR E.E., 1973. Structure Borne Sound. Springer-Verlag.

2. REDMAN-WHITE W. 1983. Ph.D. Thesis, University of Southampton. The measurement of Structural Wave Intensity.

3. REDMAN-WHITE W., WHITE R.G. To be published 1984. The Measurement of Structural Power Flow by Finite Difference Techniques and the Problem of Dynamic Range.

4. REDMAN-WHITE W., BROWN K.T., PINNINGTON R.J., 1981. Conference on Recent Developments in Acoustic Intensity Measurement, Senlis. Methods for Structural Power Transmission Measurement.

5. NOISEUX D.U., 1970. J.Acoust. Soc. Am. 47, 1, 238. Measurement of Power Flow in Uniform Beams and Plates.

6. PAVIC G. 1976. Ph.D. Thesis, University of Southampton. Techniques for the Determination of Vibration Transmission Mechanisms in Structures.

7. PINNINGTON R.J., 1982. Ph.D.Thesis, University of Southampton. Vibrational Power Transmission between Sources and Substructures.

8. MODAL AND DATA ANALYSIS OF NON LINEAR SYSTEMS

RECENT ADVANCES IN REDUCTION METHODS IN NON LINEAR STRUCTURAL DYNAMICS

Sergio R. Idelsohn* and Alberto Cardona**

Mechanics Laboratory of INTEC***
P.O. Box 91 - 3000 Santa Fe - ARGENTINA

1. INTRODUCTION

It is well recognized that the use of a large number of degrees of freedom in the discretization of complex structures is dictated by their topology rather than by the complexity of their behaviour. For a dynamic analysis, however, a limited number of suitably chosen generalized degrees of freedom (like for instance eigenmodes) is not only sufficient from the point of view of accuracy but also more cost effective. A certain number of techniques exist in the literature to reduce the number of degrees of freedom of finite element models in the case of dynamic analysis [1-4].

When dealing with non linear dynamic problems, some authors employ the so-called local mode superposition principle for the determination of the basis functions [2,4]. This principle states that small harmonic motions may be superimposed upon large static motion and that small forced motion may be represented in terms of the non linear (tangent stiffness) frequency spectrum. This procedure requires a continuous updating of the basis vectors (specially when dealing with geometrical non linearities) and so, it becomes expensive.

The present paper pursues the development of a new technique of reduction that applies specially in the case of non linear dynamics [5-6]. It consists in adding some derivatives of the displacements with respect to the modal amplitude parameters to the basis obtained by local mode superposition. The derivatives can be taken up to various orders. It is shown in the examples that this basis is adequate in order to approximate the system's behaviour with a very limited number of degrees of freedom and with a very limited number of updatings.

The resulting reduced system is integrated by using the Newmark's implicit algorithm. A control strategy to determine the correct moment in which the basis vectors should be updated is proposed. Only geometrical non linearities are treated in this paper but no difficulty exist to extend the concept to material non linearity.

2. STRUCTURAL EQUATIONS OF MOTION

The discretized structural dynamics equilibrium equations can be written as:

$$G(a) + M\,\ddot{a} = F \qquad (1)$$

(*) Scientific and Technological Research Staff Member of the National Council for Scientific and Technological Research of Argentina.

(**) Research Fellow of CONICET.

(***) Institute of Technological Development for the Chemical Industry, Universidad Nacional del Litoral (UNL) and CONICET.

where:

$G(a)$: internal forces vector (non linear function of the nodal parameters a).

M : mass matrix.

F : applied forces vector.

$a, \ddot{a}$: displacements and accelerations vectors.

A Rayleigh-Ritz technique is used to replace equation (1) by a reduced system of equations. This can be made by approximating the displacements increment Δa by the linear combination of R linearly independent vectors:

$$\Delta a = \Psi\, y \tag{2}$$

where Ψ is the matrix formed with R basis vectors and y is the vector of generalized displacements (dim R).

The system of differential equations to be solved now reads:

$$\overline{G}(a_o + \Psi\, y) + \overline{M}\, \ddot{y} = F \tag{3}$$

where:

$$\overline{G}(a_o + \Psi\, y) = \Psi^T\, G(a_o + \Psi\, y)$$

$$\overline{M} = \Psi^T\, M\, \Psi \tag{4}$$

$$\overline{F} = \Psi^T\, F$$

3. BASIS VECTORS COMPUTATION

According to the local mode superposition principle the R lower frequencies and their corresponding modes govern the response:

$$\Delta a = \sum_{r=1}^{R} \phi_r\, z_r \tag{5}$$

where ϕ_r are the instantaneous modes of free vibration obtained by solving:

$$\left(K\,(a_o) - \omega_r^2\, M\right) \phi_r = 0 \tag{6}$$

$K(a_o)$ denotes the tangent stiffness matrix computed at the position a_o .

If only these computed eigenmodes are used as a basis, the cost of the analysis will be too high because of the updating of the basis.

Noting that the instantaneous free vibration modes are a function of the displacements vector a , we can rewrite equation (5) as:

$$\Delta a = \sum_{r=1}^{R} \phi_r(a)\, z_r \tag{7}$$

AD-A143 301 PROCEEDINGS OF THE INTERNATIONAL CONFERENCE ON RECENT ADVANCES IN STRUCTU..(U) SOUTHAMPTON UNIV (ENGLAND) INST OF SOUND AND VIBRATION RESEAR.. M PETYT ET AL. 2/6

UNCLASSIFIED 1984 F/G 20/11 NL

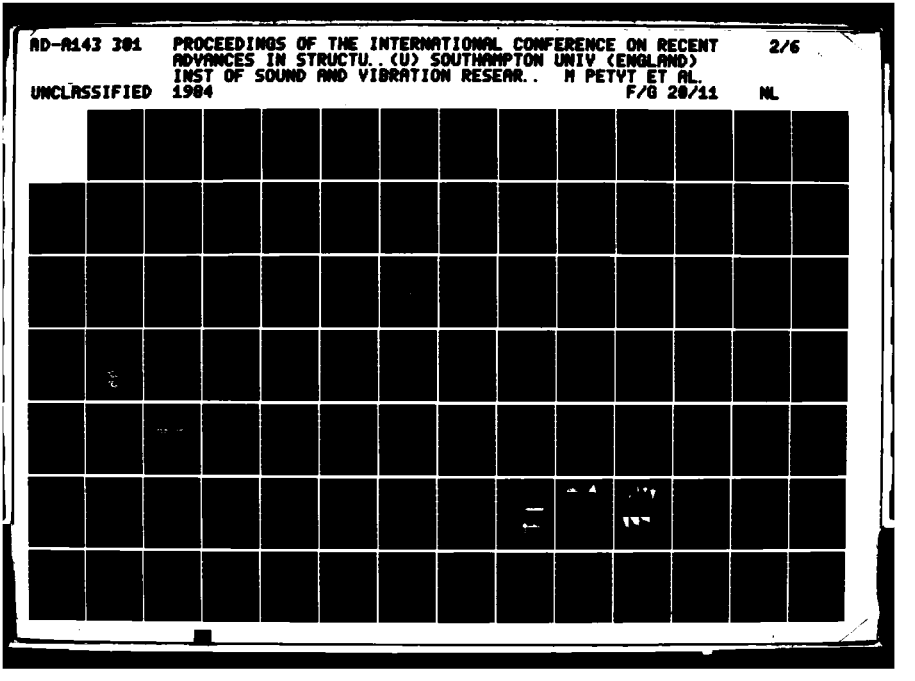

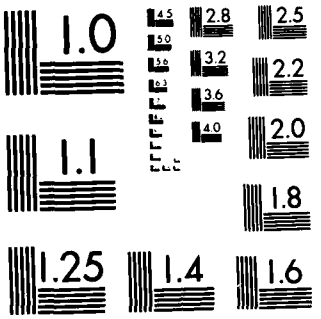

Assuming that the tangent eigenmodes can be developed into a Taylor series, we will be able to express the nodal increments as

$$\Delta a = \phi_r(a_o)\ z_r + \left(\frac{\partial \phi_r}{\partial z_s}\right)\ (a_o)\ \ z_s\ z_r + \ldots \tag{8}$$

where repeated indexes imply summation from 1 to R . The displacement increments are then written as a linear combination of the tangent eigenmodes and their derivatives evaluated at t_o .

$$\Delta a = L\left\{\ \phi_r(a_o)\ \ ,\ \left(\frac{\partial \phi_r}{\partial z_s}\right)\ (a_o)\ \ ,\ \ldots\ \right\} = \Psi\, y \tag{9}$$

In order to get the desired derivatives we differentiate the modal equations (6):

$$\frac{\partial}{\partial z_s}\left\{\left(K\ (a) - \omega_r^2\ M\right)\ \phi_r\right\} = 0 \tag{10}$$

This procedure leads to the following system of linear equations:

$$\left(K - \omega_r^2\ M\right)\ \frac{\partial \phi_r}{\partial z_s} = -\frac{\partial K}{\partial z_s}\ \phi_r + \frac{\partial \omega_r^2}{\partial z_s}\ M\ \phi_r \tag{11}$$

where all terms are evaluated at a_o .

The coefficients matrix is singular (see eq. 6). In order to solve this system, we express it in the basis given by:

$$\Psi_i \begin{cases} \phi_r & i = k \\ e_i & i \neq k \end{cases} \quad , \quad i = 1,\ n \tag{12}$$

where k is such selected that the k-th component of ϕ_r :

$$(\phi_r)_k \neq 0 \tag{13}$$

and e_i denotes the n-dimensional vector with a unit value in its i-th component. Due to the singularity, the k-th component of $\left(\partial \phi_r / \partial z_s\right)$ in this basis is not determined. We will assume for it a zero value.

The k-th equation of the system expressed in the basis (12) reads:

$$\frac{\partial \omega_r^2}{\partial z_s} = \phi_r^T \frac{\partial K}{\partial z_s}\ \phi_r \tag{14}$$

By replacing this expression into the remaining equations, we obtain the following linear system:

$$\left(K - \omega_r^2\ M\right)_*\ \ \left\{\frac{\partial \phi_r}{\partial z_s}\right\}_* = \left\{\left(M\ \phi_r\ \phi_r^T - I\right)\ \frac{\partial K}{\partial z_s}\ \phi_r\right\}_* \tag{15}$$

where $(\ )_*$ and $\{\ \}_*$ notes for the matrix and vector obtained by deleting its k-th row and column.

This procedure, although it gives the exact modal derivatives, is costly because we need to factorize an N-dimensional coefficients matrix to get the derivatives of a new eigenmode.

In order to avoid the refactorization, the following approximation is proposed. All the inertial terms are neglected in eq. (15), giving a sort of static determination of the modal derivatives as:

$$K \frac{\partial \phi_r}{\partial z_s} = - \frac{\partial K}{\partial z_s} \phi_r \tag{16}$$

In this case, the modal derivatives are computed by performing a single factorization of a coefficients matrix.

Although this approximation seems to be rather crude it will be shown in the examples that it gives practically the same results as when the exact tangent eigenmodes are employed.

4. EVALUATION OF THE STIFFNESS MATRIX DERIVATIVES

The computation of the modal derivatives requires to differentiate the stiffness matrix with respect to the generalized displacement amplitudes z_r . This differentation can be carried out either exactly or numerically.

In the former process, the finite element routines should be modified in order to compute the vector $\partial K/\partial z_s \, \phi_r$ as follows:

$$\frac{\partial K}{\partial z_s} \phi_r = \frac{\partial K}{\partial a} \frac{\partial a}{\partial z_s} \phi_r = \frac{\partial K}{\partial a} \phi_s \, \phi_r \tag{17}$$

This vector is computed at the element level and then assembled as an internal forces vector.

In order to avoid the need of modificate the finite element routines, the stiffness derivative can be evaluated numerically by using:

$$\frac{\partial K}{\partial z_s} (a_o) = \frac{K (a_o + \phi_s \, \delta z) - K (a_o)}{\delta z} \tag{18}$$

This process requires to reevaluate the stiffness matrix, giving an small increment $\phi_s \, \delta z$. The increment parameter δz should be small enough so that the differentation can be accurately accomplished, but also, it must be large enough to avoid any computer round-off error.

5. NUMERICAL TIME INTEGRATION OF THE REDUCED EQUATIONS OF MOTION

The reduced system of ordinary differential equations (3) is integrated by using a specially oriented version of the Newmark's time integration scheme. Complete details of it are given in ref. 6.

Due to the continuously changing characteristics of the non linear system, the basis needs to be periodically updated so that it can represent adequately the system's response.

An error measure that indicates the need of performing a basis updating is defined as:

$$\varepsilon = \frac{1}{N} \frac{||R||}{(||F|| + ||M\ddot{a}||)} \tag{19}$$

where.

$$R = F - G(a) - M\ddot{a}$$

N : number of degrees of freedom of the complete system.

Whenever this measure exceeds a predefined tolerance, a basis updating is performed. In order to avoid any progressive deterioration of the basis, the initially computed vectors are retained throughout the analysis as belonging to the basis. Then, at each updating only a given set of vectors is computed and added to the first basis, as indicated in fig. 1.

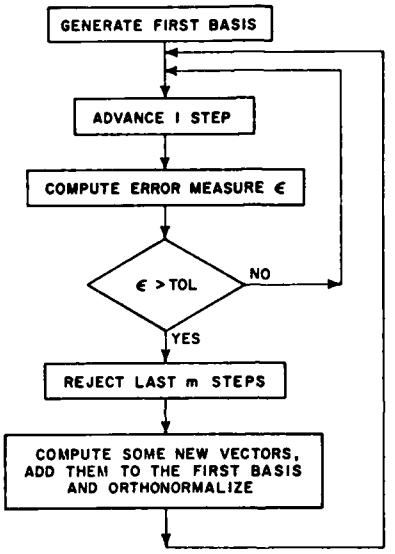

Fig. 1 - Strategy for the basis updating process

6. GEOMETRICALLY NON LINEAR EXAMPLES

The cantilever beam displayed in fig. 2 was discretized by using 5 elements numbering 28 degrees of freedom (DOF). The resultant system of ordinary differential equations was reduced to a 6 DOF's system by computing the three first tangent eigemodes and the three derivatives of the first two modes. Firstly, the modal derivatives were computed exactly (eq. 15). Secondly, they were calculated approximately by using eq. 16.

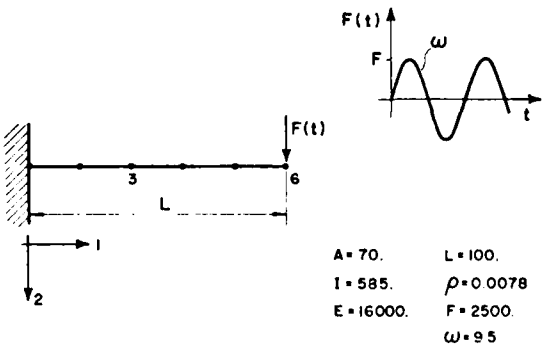

Fig. 2 - Cantilever beam. Problem description

The displacements in time of node 6 are shown in figs. 3 and 4 together with the exact solution obtained by integrating the complete system. We can see the complete agreement between both reduced system solutions and also, their accuracy when comparing with the complete system response.

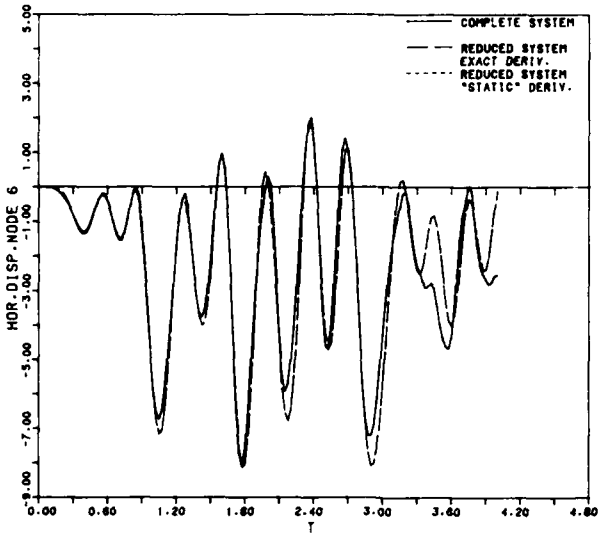

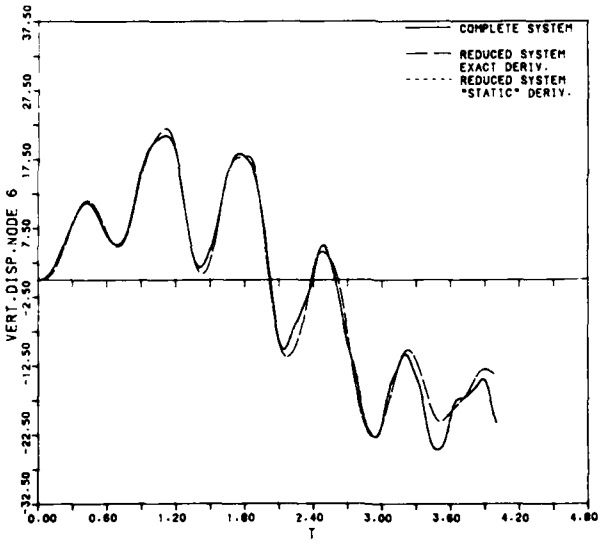

Figs. 3 & 4 - Response at node 6 of the beam

It should be noted that both reduced system solutions were obtained without any basis updating; that is to say, the same basis was employed during the whole analysis. The error measure attained maximum values of 0.0551 and 0.0565 for the exact and statically equivalent modal derivatives solution, respectively.

The clamped arch represented in fig. 5, submitted to an excentrical suddenly applied load, was also solved. The 78 DOF's system that results from the discretization was reduced to a 11 DOF's system. The three first tangent eigenmodes and the three derivatives of the first two modes were added (fig. 1). The error tolerance was set at 0.045 for both reduced system solutions: the first with exact modal derivatives and the second with statically equivalent ones.

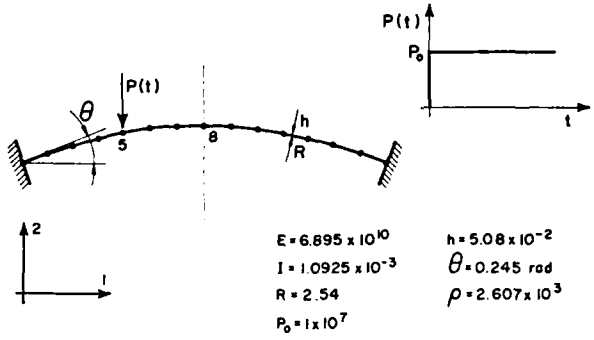

Fig. 5 - Clamped arch. Problem description

Figs. 6 and 7 show the response obtained at node 8. Two basis updatings were required in the exact derivatives solution, and only one updating was needed in the approximate derivates solution. We can see again the similar performance of both methods for giving the response.

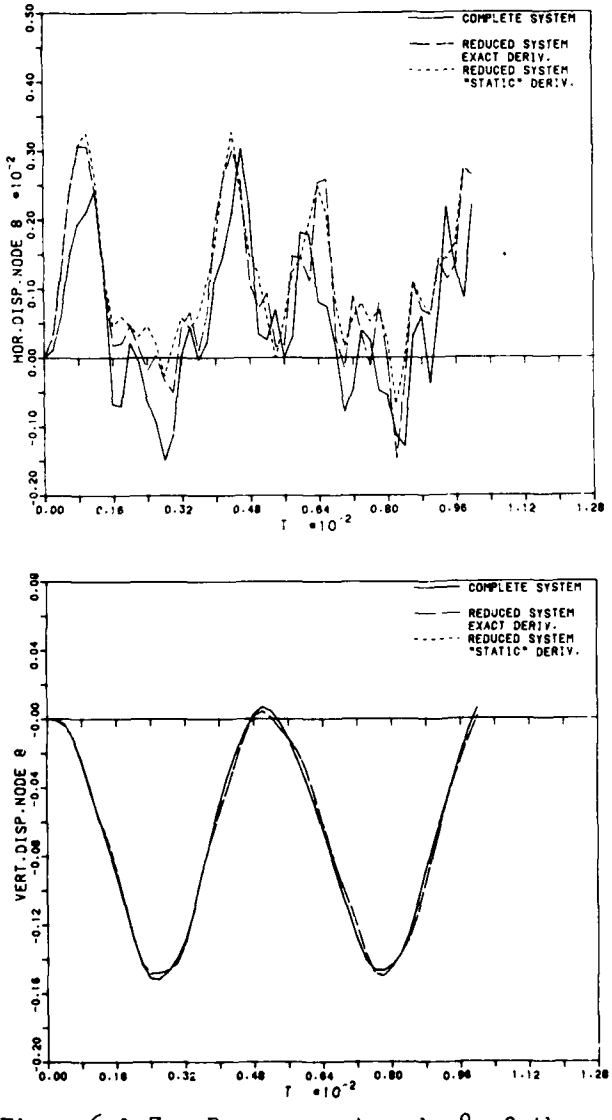

Figs. 6 & 7 - Response at node 8 of the arch

7. CONCLUDING REMARKS

A computational algorithm for predicting the dynamic non linear response of a structure by means of a reduction method is described. In it, the non linear system of ordinary differential equaticns obtained from the finite element discretization, is reduced by employing a Rayleigh-Ritz analysis.

The use of the tangent eigenmodes and their derivatives as basis vectors is suggested. An approximate computation of the modal derivatives is proposed, which is enough from the point of view of accuracy in the calculated response and also, is faster computed than the exact modal derivatives.

ACKNOWLEDGEMENTS

The authors acknowledge the support provided by the National Council for Scientific and Technological Research of Argentina (CONICET) and Universidad Nacional del Litoral, Santa Fe, Argentina (UNL).

REFERENCES

1. K.J. BATHE and S. GRACEWSKI 1981 Computers and Structures 13, 699-707. On non linear dynamic analysis using substructuring and mode superposition.

2. N.F. MORRIS 1977 Computers and Structures 7, 65-72. The use of modal superposition in non linear dynamics.

3. A.K. NOOR 1981 Computer and Structures 13, 31-44. Recent advances in reduction methods for non linear problems.

4. R.E. NICKELL 1976 Computer Methods in Applied Mechanics and Engineering 7, 107-129. Non linear dynamics by mode superposition.

5. S. IDELSOHN and A. CARDONA 1982 Cuaderno N° 16 ed. by Comite Argentino de Transferencia de Calor y Materia. Metodos de doble discretizacion aplicados al analisis dinamico de estructuras.

6. S. IDELSOHN and A. CARDONA 1983 Report GTM-23, INTEC, Santa Fe. A reduction method for non linear structural dynamic analysis.

FEASIBILITY OF USING MODAL ANALYSIS TECHNIQUES FOR NONLINEAR MULTIDEGREE OF FREEDOM SYSTEMS

Rajendra Singh, Chanyudh Nopporn and Henry Busby

Department of Mechanical Engineering
The Ohio State University
206 West 18th Avenue
Columbus, Ohio 43210 USA

1. INTRODUCTION

Experimental modal analysis systems are now widely available and used extensively for system identification, diagnostics and mathematical model development. A typical user treats the system as a "black box" and generally relies on the commercial software. Moreover, he may not be aware of the underlying assumptions and the limitations associated with modal extraction and synthesis. Thus there is a potential for misusing the technique which could lead to incorrect results and conclusions. This is especially true when the structure is inherently nonlinear or when vibratory amplitudes are no longer small. The focus of this paper is to examine the feasibility of using conventional modal analysis techniques for such cases.

The general theory of modal analysis is strictly valid for linear systems [1-3]. Typically, dynamic compliance transfer functions $H(\omega)$ or impulse responses $h(t)$ are measured at a number of locations, and then using the modal expansion theorem, as shown below, one can estimate natural frequencies ω_r, mode shapes ψ_r, damping ratios ζ_r, modal masses and modal stiffnesses over the frequency range of interest [2,3]; see the List of Symbols for identification.

$$H_{jk}(\omega) = \sum_{r=1}^{\infty} [A_{jkr}/(s - s_r)] + [A^*_{jkr}/(s - s^*_r)] \tag{1}$$

or,

$$h_{jk}(t) = \sum_{r=1}^{\infty} A_{jkr}\, e^{s_r t} + A^*_{jkr}\, e^{s^*_r t} \tag{2}$$

where

$$s_r = -\zeta_r \omega_r + i\, \omega_r \sqrt{1 - \zeta_r^2} \tag{3}$$

Modal analysis techniques have been applied to both symmetric and nonsymmetric systems, structures with repeated roots, etc. However, in each case the vibrating system is considered linear with small perturbations [1-3]. The only exception is the system with nonlinear damping, such as Coulomb or hysteretic damping, but the conventional techniques generally treat it as the linear equivalent - viscous damping case [4,5].

2. NONLINEAR SYSTEMS

Nonlinearities in a vibrating system could generally result due to the following: (a) nonlinear stiffness, (b) nonlinear damping, (c) finite amplitudes, and (d) physical gap (dead zone) between a mass and a spring; we could however combine case (d) with (a) [6]. Case (b) will not be considered here as the equivalent linear damping models are generally used; see References [4 and 5]. Thus our focus will be on non-linear springs and on large excitation levels which would drive the system to finite amplitudes.

An extensive amount of literature is available on the analytical or computational techniques applied to nonlinear systems; References [6-10] are typical. But the same cannot be said for the application of modern experimental techniques to nonlinear vibratory systems. In fact, only two studies have been published recently, and both have been applied to only a single degree of freedom system [11,12]. Ulm and Morse [11] have examined a vibratory system on an analog computer which is described by the Duffing's equation for different force levels and for varying degrees of stiffness nonlinearity; both swept sine and random inputs yielded sharp jumps in the amplitude and phase plots, shape distortion of the Nyquist plots, and poor coherence at the third harmonic of the system resonances. Moreover, higher excitation levels generally lead to more deviations in the transfer functions from the linear system response. Okubo [12] has also analyzed this system numerically with an impulse excitation somewhat similar to those applied in experimental testing. He has also reported distortions in transfer functions such as split and sharp peaks in the magnitude plots, real and imaginary parts in reverse, and additional small circles in the Nyquist plane. Both Ulm and Morse [8] and Okubo [9], however, claim that further research efforts are definitely required as their investigations have been preliminary and only the frequency response functions of a single degree of freedom system have been examined. Thus, no information on the mode shape distortion for the multidegree of freedom system is available.

3. SCOPE AND OBJECTIVES

An experimentor would obviously like to know if the system being tested is nonlinear in nature and the extent of nonlinearities associated with the modal analysis experiment. Moreover, the severity of assuming linear or approximately linear system for a nonlinear structure is also of interest. Through our study, we should be in a position to answer some of these questions.

Our example case is a three degree of freedom nonlinear mechanical system with finite amplitudes. For this system we are examining the following: (i) frequency response functions: magnitude $M(\omega)$ and phase $\phi(\omega)$ plots, real $Re(\omega)$ and imaginary $Im(\omega)$ plots, and Nyquist plots (Im vs. Re); (ii) coherence functions $\gamma^2(\omega)$; (iii) natural frequencies ω_r; and (iv) mode shapes ψ_r. Since for the nonlinear system ω_r and ψ_r are dependent on force and motion, we will be comparing normalized responses at a given resonant frequency. An attempt will be also made here to compare experimental results with analytical predictions wherever possible.

4. EXAMPLE CASE

Figure 1 shows the example case which allows a combination of translational (q_1, q_2) and rotational (q_3) motions, with three degrees of freedom. The dampers are assumed here to be linear given by the equivalent-viscous damping coefficient c. Translational springs are considered to be the hardening type such that the restoring force f_s is equal to $k\,\Delta q + \beta\,\Delta q^3$ (Duffing type) where k and β are spring constants and Δq is the relative displacement. The forcing functions are assumed to be sinusoidal forces and applied at the masses. Initial conditions are assumed to be zero. The equations of motion are as follows:

$$m_1\ddot{q}_1+c_1\dot{q}_1+c_2(\dot{q}_1-\dot{q}_2)+k_1q_1+\beta_1q_1^3+k_2(q_1-q_2)+\beta_2(q_1-q_2)^3=F_1e^{i(\omega t+\theta_1)} \tag{4}$$

$$(m_2+m_3)\ddot{q}_2+m_3l\ddot{q}_3\cos(q_3)-m_3l\dot{q}_3^2\sin(q_3)+c_2(\dot{q}_2-\dot{q}_1)+k_2(q_2-q_1)+\beta_2(q_2-q_1)^3$$
$$=F_2e^{i(\omega t+\theta_2)}+F_3e^{i(\omega t+\theta_3)} \tag{5}$$

$$m_3 l\ddot{q}_2\cos(q_3)+m_3 l^2\ddot{q}_3+c_3\dot{q}_3+m_3 gl\sin(q_3) = F_3 e^{i(\omega t+\theta_3)}l\cos(q_3) \qquad (6)$$

Many cases of this nonlinear system can be examined by varying spring constants (k and β) and force levels (F). This example case can also be reduced to the single and two degree of freedom systems. Of course, in each case we can also examine the linear system with small perturbations about the operating point i.e. $\beta = 0$, and q_1, q_2 and q_3 are small.

5. ANALYTICAL FREQUENCY RESPONSE FUNCTIONS

We consider only the steady state harmonic solution. Assuming response only at ω and ignoring higher harmonic terms, we obtain the frequency equations which are solved numerically using Newton-Raphson method. Frequency response functions of normalized response with dimensionless frequency are then generated over the frequency range of interest which covers essentially the first three modes of the linear system.

6. EXPERIMENTAL METHODOLOGY

Since it is difficult, if not impossible, to build a physical system with known and controlled nonlinearities for testing purposes, we have conducted a simulated experiment. The physical system is simulated by an analog computer circuit, as shown in Figure 2, and the computer outputs are considered as physical system outputs. The forcing function $f_k(t)$ is band-limited white noise which would excite the system over all frequencies of interest. This input along with an output q_i are acquired and processed by a two channel FFT analyzer, in a manner identical to that which we would employ for a real structure. Only transfer functions in various forms, are analyzed and plotted; standard modal extraction techniques [2,3] are not used here.

7. RESULTS AND DISCUSSION

7.1 Presentation of Results

In order to perform some parametric studies we now simplify the general system and assign numerical values to the system parameters and variables, as listed in Table 1. We also define several dimensionless quantities (given by an overbar) as the results are presented in the dimensionless form; see Table 1.

Table 1. Example Case Values and Dimensionless Quantities

$m_1 = m_2 = m_3 = m$; $k_1 = k_2 = k$; $c_1 = c_2 = c$; $c_3 = 0$; $\bar{c} = 0.05$; $\beta_1 = 0$, $\beta_2 = \beta$;

$\bar{\beta} = 0$, 0.3, 0.5, and 5.0; $F_2 = F_3 = 0$, $F_1 = F$; $\theta_1 = 0$.

$\bar{q} = q/\ell$, $\bar{F} = F/k\ell$, $\bar{\beta} = \beta\ell^2/k$, $\bar{c} = c/2\sqrt{mk}$, $\bar{\omega} = \omega\, m^2/k^2$, $\bar{\omega}_r = \omega_r\, m^2/k^2$,

$$\bar{H}_{jk}(\bar{\omega}) = \frac{\bar{q}_j}{\bar{F}_k}(\bar{\omega}) = M(\bar{\omega})\, e^{i\phi(\bar{\omega})} = Re(\bar{\omega}) + i\, Im(\bar{\omega}), \text{ where } j,k = 1,2,3$$

Let us now define the following modal parameters which could be used to indicate the extent of nonlinearity. 1) Modal response ratio, $\bar{R}_{jr} = \bar{H}_{jkr}/\bar{H}_{ikr}$, $j,k = 1,2,3$. Now for the forcing function case we obtain $\bar{R}_{1r} = \bar{q}_{1r}/\bar{q}_{1r} = 1.0$, $R_{2r} = q_{2r}/q_{1r}$ and $\bar{R}_{3r} = \bar{q}_{3r}/\bar{q}_{1r}$. For the linear case, $\psi_r^T = \{1, R_{2r}, R_{3r}\}$ where

ψ_r^T is the transpose of the rth mode, normalized by taking the modal response of m_1 equal to unity. 2) 'Backbone' natural frequency $(\bar{\omega}_r)_o$: we establish it as a reference frequency for the rth mode as this would be equal to the natural frequency $\bar{\omega}_r$ if the system were linear. All $\bar{R}_{jr}$ values are computed at frequency $(\bar{\omega}_r)_o$. 3) Modal frequency of highest magnitude $(\bar{\omega})_{max}$: at this frequency the normalized transfer function magnitude M has the maximum value for the rth mode. We also note for a nonlinear system $(\omega_r)_o$ may not be equal to $(\omega_r)_{max}$ which one would extract from the measured or computed $M(\omega)$ data. For a linear system, $(\omega_r)_o = (\omega_r)_{max}$.

7.2 Case I: Non-linear Spring (β_2)

We treat the second spring as the nonlinear spring with values of $\bar{\beta}_2 = 0$, 0.3, 0.5 and 5.0. For this case the response amplitudes are considered small especially for q_3, i.e. $\sin q_3$ and $\cos q_3 \simeq 1$. The dimensionless damping c is taken to be equal to 0.05. For $\bar{\beta}_2 = 0$ case, the system is of course reduced to the linear case.

Figures 3-7 present driving point compliance $\bar{H}_{11}(\bar{\omega})$ spectra in different forms for the linear ($\bar{\beta}_2 = 0$) and nonlinear ($\bar{\beta}_2 = 5$) cases; both experimental and analytical results are shown here. We note that the third mode is highly nonlinear and exhibits jump phenomenon strongly. Experimentally, we do not duplicate it. The measured coherence function $\gamma_{11}^2(\bar{\omega})$ is also shown here in Figure 8; γ_{11}^2 shape is considerably distorted for the nonlinear case which is in agreement with the results of Ulm and Morse [11] for the single degree of freedom.

Table 1 compares the analytical and experimental results for natural frequencies $\bar{\omega}_r$ and modal response ratio $\bar{R}_{jr}$. We note that $(\bar{\omega}_r)_o$ differs from the $(\bar{\omega}_r)_{max}$ only for the third mode and the deviation is directly related to the β_2 value. The modal response results show significant discrepancies between analysis and experiment. However, the relative phase information is still maintained, i.e. the experiment distorts the relative amplitudes more and relative phases less.

7.3 Case II: Finite Amplitudes ($\bar{q}_3$)

Now we consider the second spring as linear, i.e. $\beta_2 = 0$ and examine the finite amplitude motion of the pendulum (q_3). Although for the analytical part we retain $\sin \bar{q}_3$ and $\cos q_3$ in the equations of motion, we approximate experimentally these by taking the first two terms of the series, i.e. $\sin q_3 \simeq q_3 - q_3^3/6$ and $\cos q_3 = 1 - q_3^2/2$. This was necessitated by the fact that more function generators for the analog computer circuits were not available; this approximation is however valid as long as q_3 is less than or equal to approximately $\pi/4$. Figures 9-11 examine the driving point compliance spectrum $\bar{H}_{11}(\bar{\omega})$ in real, imaginary and Nyquist forms; we note that the finite amplitudes introduce the spring softening effect and thus the curves are shifted to the left and somewhat distorted. Thus in a real structural experiment, we can expect softening or hardening effects if the excitation force levels are high enough to produce large motions. We again note that the coherence function γ_{11}^2, as shown in Figure 12, is distorted for the finite amplitudes case.

8. CONCLUDING REMARKS

Space limitation prevents us from presenting further results and a more detailed discussion. However, based on the examples presented here and others worked out by us, including the single and two degree of freedom nonlinear system problems, we can draw the following conclusions; 1. Measured transfer function plot may not truly reflect the true behavior of a system as it does not show any jump phenomena, instability regions or shape distortions though can

alert us to the fact that the structure is nonlinear. 2. Modal response data base can still give us a rough idea about the natural frequencies and mode shape; this information could be sufficient for solving vibration and noise problems but certainly not suitable for mathematical model building. 3. Coherence function estimates can be used as the 'warning signals' for the nonlinearities or finite amplitude motions. Our results are of course more comprehensive than Ulm and Morse [11] and Okubo [12] results but they are all compatible with each other.

Overall, it seems that an experimenter has to be very careful and should use the experimental modal analysis techniques with some discretion. Also, excitation signals, especially those which contain spectral energy over a broad frequency range, along with levels should be chosen judiciously; the single frequency excitation or slow sinusoidal sweeps should be more suitable.

Further research work in this area is definitely required; it could focus on the following aspects: (i) feasibility study for higher degree of freedom and continuous nonlinear systems, (ii) time domain data processing and modal extraction techniques, suitable for nonlinear systems [13,14] and (iii) an examination of the role of nonlinear damping mechanisms.

REFERENCES

1. D. L. Brown, 1982, First International Modal Analysis Conference, Orlando, Florida, Proceedings, ix-xiii. "Modal Analysis - Past, Present and Future."

2. R. W. Potter, 1975, Shock and Vibration Digest, 7(11), 3-11. "A General Theory of Modal Analysis for Linear Systems."

3. D. L. Brown, R. J. Allemang, K. Zimmerman, and M. Mergeay, 1979, Society of Automotive Engineers, Paper No. 790221, "Parameter Estimation Techniques for Modal Analysis."

4. M. Richardson and R. Potter, 1975, 46th Shock and Vibration Symposium, San Diego, California. "Viscous vs Structural Damping in Modal Analysis."

5. J. P. Bandstra, 1983, Journal of Vibration, Acoustics, Stress and Reliability in Design, 105, 382-392. "Comparison of Equivalent Viscous Damping and Nonlinear Damping in Discrete and Continuous Vibrating Systems."

6. S. Levy and J. P. D. Wilkinson, 1976, The Component Element Method in Dynamics with Application to Earthquake and Vehicle Engineering, McGraw-Hill, Inc., New York.

7. C. H. Cooke and R. A. Struble, 1966, Quarterly of Applied Mathematics, XXIV (3), 177-193. "On the Existence of Periodic Solutions and Normal Mode Vibrations of Nonlinear Systems."

8. R. M. Evanowski, 1976, Elsevier. Resonance Oscillations in Mechanical Systems.

9. A. H. Nayfeh, 1973, Wiley-Interscience, New York. Perturbation Methods.

10. R. J. Cipra and J. J. Uicker, Jr., 1981, Journal of Mechanical Design, 103, 849-865. "On The Dynamic Simulation of Large Nonlinear Systems. Parts 1 and 2."

11. S. C. Ulm and I. E. Morse, 1982, American Society of Mechanical Engineers, Paper No. 82-DET-138. "Recognizing System Nonlinearities Using Modal Analysis Tests."

12. N. Okubo, November 1982, Sound and Vibration, 34-37. "The Effect of Nonlinearity on Transfer Function Measurement."

13. S. R. Ibrahim and R. S. Pappa, May 1981, Shock and Vibration Bullitin, U.S. Naval Res. Lab., 51 (3), 43-72. "A Parametric Study of the Ibrahim Time Domain Modal Identification Algorithm."

14. S. R. Ibrahim and R. S. Pappa, September-October 1982, Journal of Space Craft, 19 (5), 459-465. "Large Modal Survey Testing Using the Ibrahim Time Domain Identification Technique."

LIST OF SYMBOLS

A modal residue (complex valued)

c damping coefficient

f force

F force amplitude

g acceleration due to gravity

h impulse response

H dynamic compliance (complex valued)

i imaginary unit

Im imaginary part of $\bar{H}(\bar{\omega})$

k linear spring constant

ℓ pendulum length

m mass

M magnitude of $\bar{H}(\bar{\omega})$

q generalized displacement

R modal response ratio

Re real part of $\bar{H}(\bar{\omega})$

s Laplace variable

t time

β nonlinear spring constant

γ coherence function

ϕ phase of $\bar{H}(\bar{\omega})$

θ phase of force f

ω circular frequency

ζ damping ratio

ψ mode shape

ε error

Subscripts

j response location

k excitation point

r modal index

o backbone frequency

max modal frequency of highest magnitude

Superscripts

* complex conjugate

- dimensionless or normalized

$\dot{} \quad \frac{d}{dt}$

$\ddot{} \quad \frac{d^2}{dt^2}$

T transponse

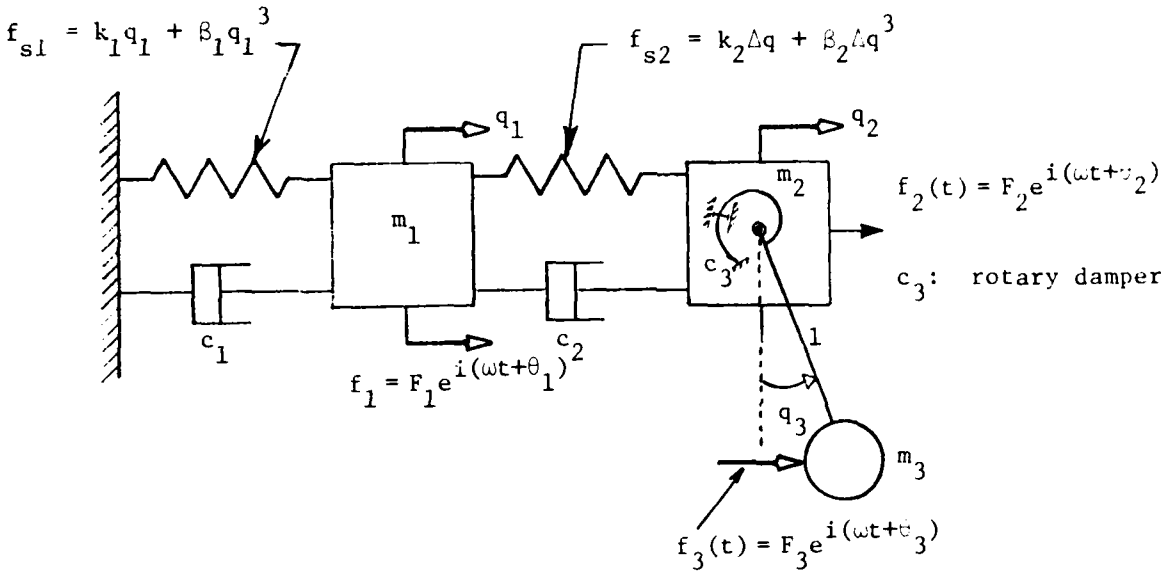

Figure 1. Example case

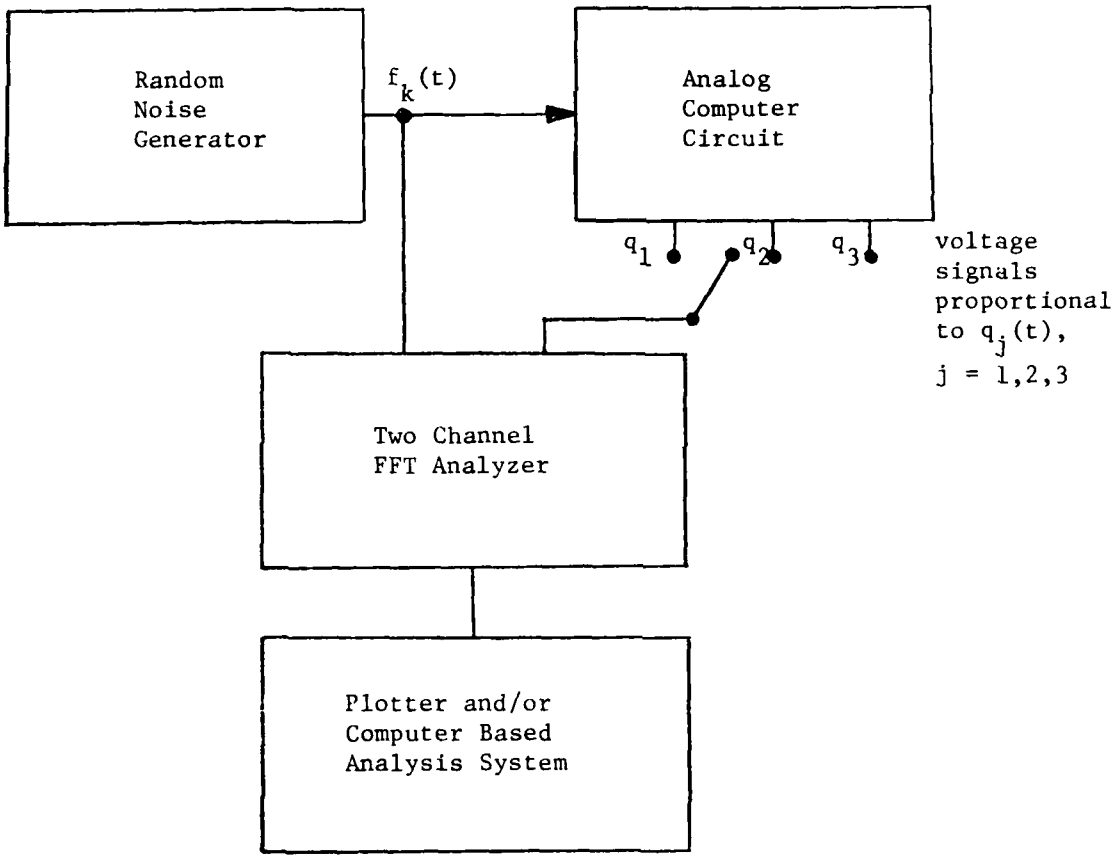

Figure 2. Experimental setup

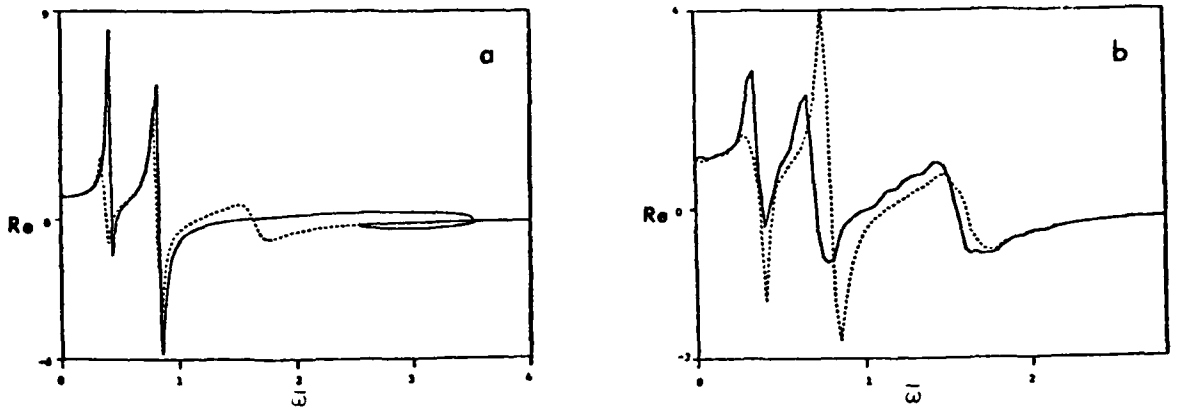

Fig. 3 Real part of the driving point compliance $\bar{H}_{11}(\bar{\omega}) = \frac{\bar{q}_1}{\bar{F}_1}(\bar{\omega})$ for Example Case I. a. Analytical. b. Experimental. —— $\bar{\beta}_2 = 5.0$, --- $\bar{\beta}_2 = 0$.

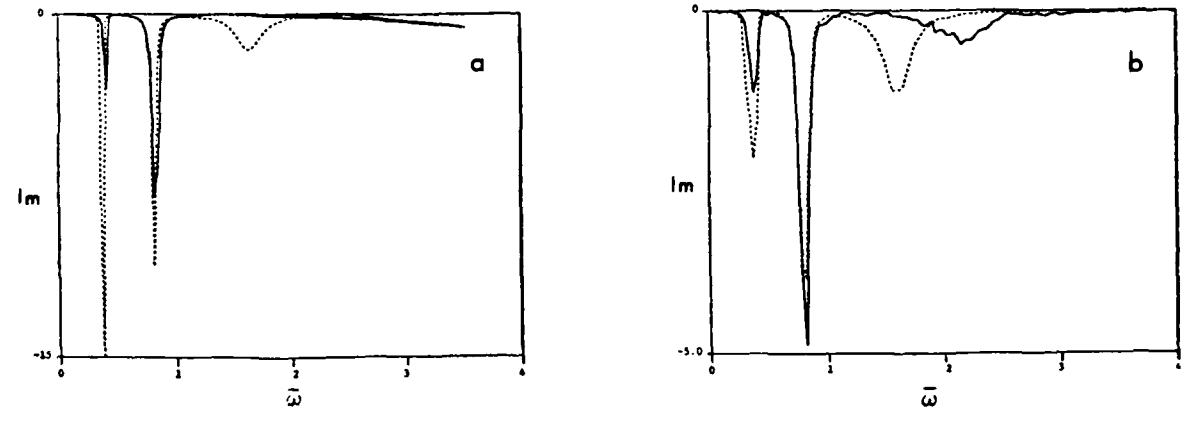

Fig. 4 Imaginary part of $\bar{H}_{11}(\bar{\omega})$. See Fig. 3 caption.

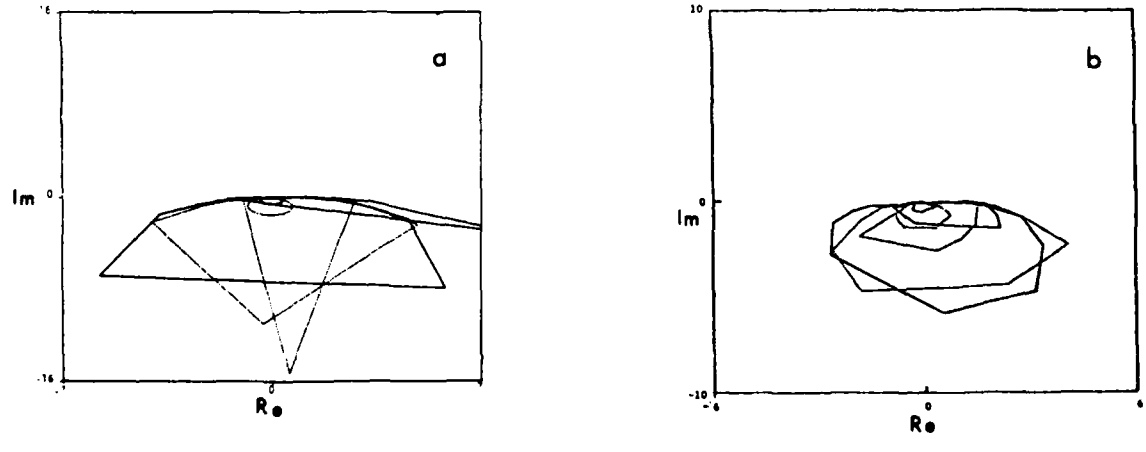

Fig. 5 Nyquist plot of $\bar{H}_{11}(\bar{\omega})$. See Fig. 3 caption.

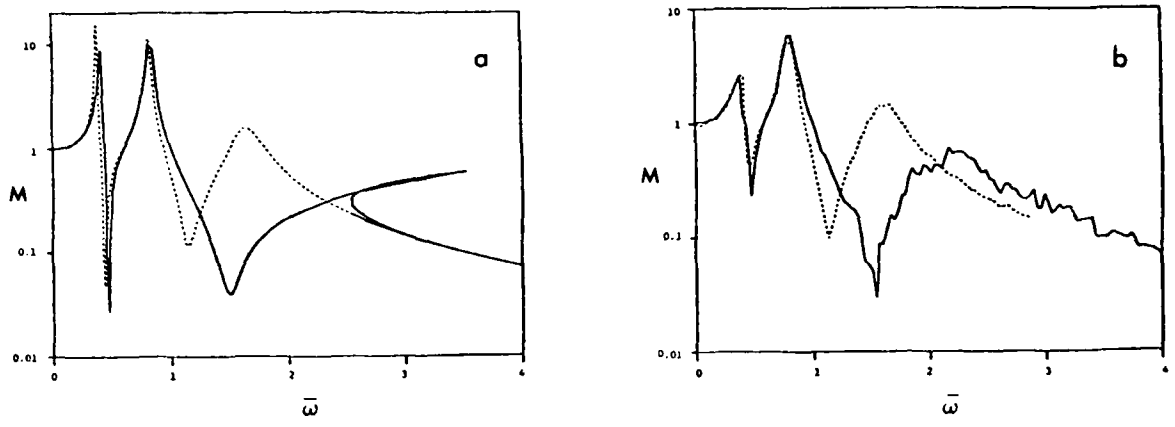

Fig. 6 Magnitude of $\bar{H}_{11}(\bar{\omega})$. See Fig. 3 caption.

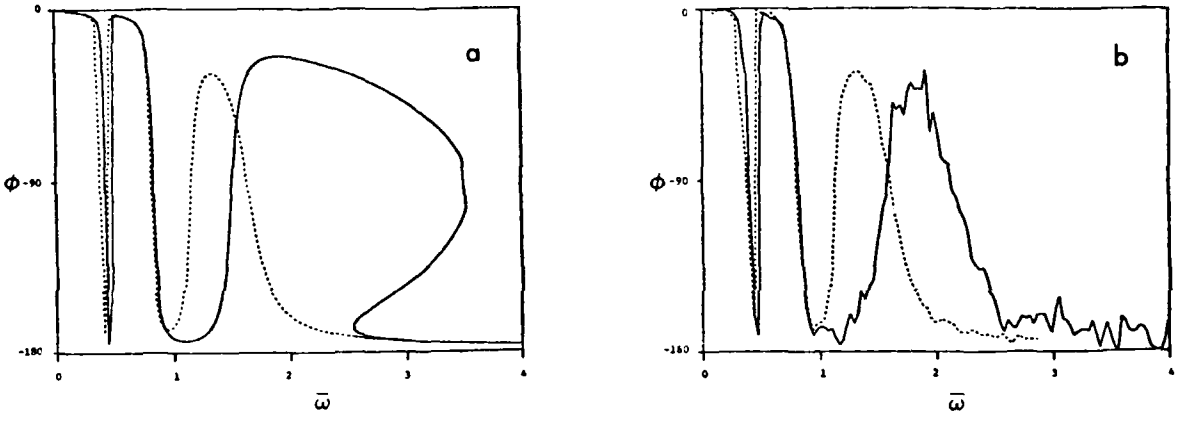

Fig. 7 Phase of $\bar{H}_{11}$. See Fig. 3 caption.

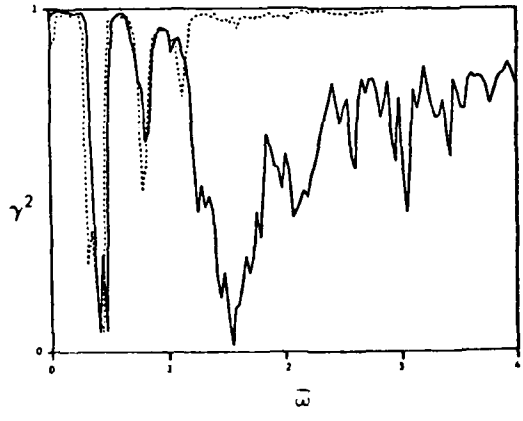

Fig. 8 Experimentally measured coherence function $\gamma_{11}^2(\bar{\omega})$ for the transfer function $\bar{H}_{11}(\bar{\omega})$. See Fig. 3 caption.

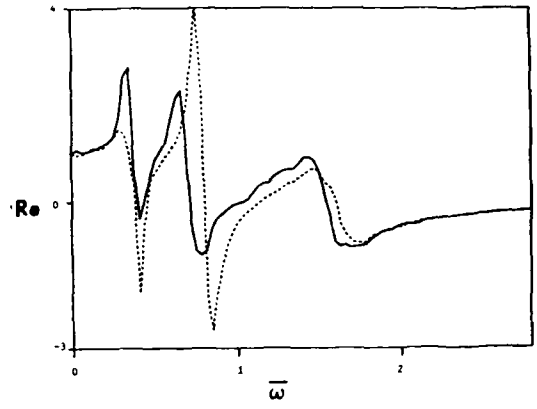

Fig. 9 Real part of the experimentally measured driving point compliance $\bar{H}_{11}(\bar{\omega}) = \frac{\bar{q}_1}{\bar{F}_1}(\bar{\omega})$ for the Example Case II. —— Finite amplitudes, --- small amplitudes.

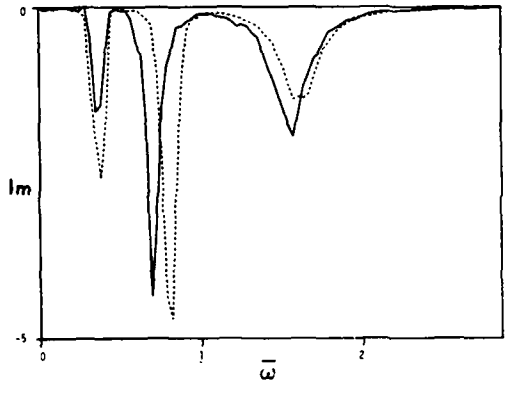

Fig. 10 Imaginary part of the measured $\bar{H}_{11}(\bar{\omega})$. See Fig. 9 caption.

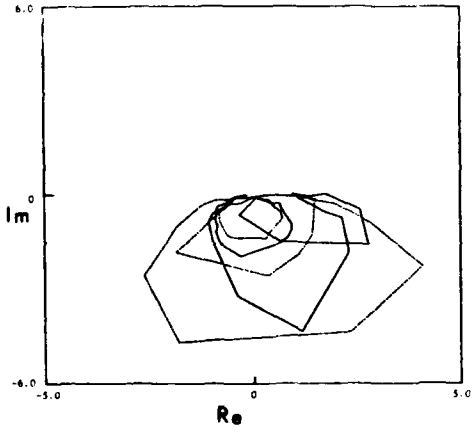

Fig. 11 Nyquist plot of the measured $\bar{H}_{11}(\bar{\omega})$. See Fig. 9 caption.

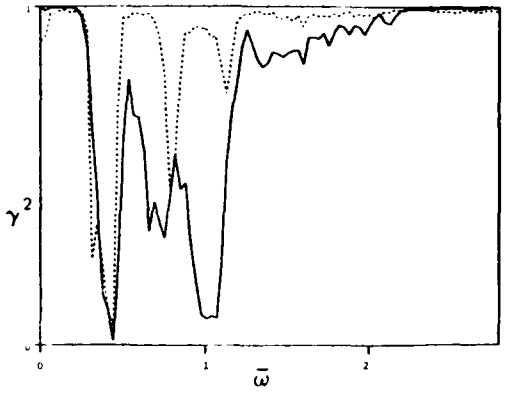

Fig. 12 Experimentally measured coherence function $\gamma_{11}^2(\omega)$ for $\bar{H}_{11}(\bar{\omega})$. See Fig. 9 caption.

Table 2. Natural Frequency and Modal Response Results for Case I.

		Natural Frequency $\bar{\omega}_r$					Modal Response Ratio $\bar{R}_{jr}$ at $(\bar{\omega}_r)_o$					
							$\bar{R}_{2r}$			$\bar{R}_{3r}$		
Nonlinear Spring Constant $\bar{\beta}_2$	Modal Index r	$(\bar{\omega}_r)_o$ Anal.	$(\bar{\omega}_r)_{max}$ Anal.	$(\bar{\omega}_r)_{max}$ Exper.	Comparison % $\frac{(\bar{\omega}_r)_o-(\bar{\omega}_r)_{max}}{(\bar{\omega}_r)_o}$ Exp	ϵ for* $(\bar{\omega}_r)_{max}$	Anal.	Exper.	ϵ*	Anal.	Exper.	ϵ*
0	1	0.377	0.377	0.377	0%	0%	1.854	2.09	12.73%	2.314	2.4	3.7%
	2	0.817	0.817	0.817	0%	0%	1.334	1.131	15.22%	-2.164	-2.3	6.3%
	3	1.634	1.634	1.634	0%	0%	-0.7262	-0.757	4.24%	0.803	0.826	2.86%
0.3	1	0.377	0.408	0.377	0%	7.6%	1.391	1.941	40.55%	1.724	2.35	36.31%
	2	0.817	0.817	0.817	0%	0%	1.121	1.355	20.87%	-1.819	-1.822	0.16%
	3	1.634	2.105	1.76	7.71%	16.39%	-1.46	-1.061	27.33%	1.612	1.15	28.66%
0.5	1	0.377	0.408	0.377	0%	7.6%	1.345	1.96	45.72%	1.679	2.514	49.73%
	2	0.817	0.817	0.817	0%	0%	1.109	1.603	44.54%	-1.798	-2.45	36.26%
	3	1.634	2.262	1.885	15.4%	16.67%	-1.675	-1.41	15.84%	1.853	1.48	20.13%
5.0	1	0.377	0.408	0.377	0%	7.6%	1.204	2.0	66.11%	1.5	1.81	20.67%
	2	0.817	0.817	0.817	0%	0%	1.061	1.08	1.791%	-1.722	-2.32	34.73%
	3	1.634	3.518	2.796	71.1%	20.5%	-6.764	-3.402	49.7%	7.481	4.32	42.25%

* ϵ = (analytical value - measured value) 100/(analytical value), %

MODAL ANALYSIS AND INDENTIFICATION OF STRUCTURAL NON-LINEARITY

G.R. Tomlinson and N.E. Kirk
Simon Engineering Laboratories
University of Manchester

1. INTRODUCTION

When it is suspected that a structure is non-linear, e.g. unfamiliar distortions of transfer functions, unacceptable deviations in curve fits or significant amplitude dependent behaviour is observed, there are few, if any, established methods for reliably identifying the nature or quantifying the importance of non-linearity. The reasons for wanting to pursue an analysis into the non-linear domain whereby a reliable identification method would be of value can be described in three general ways.

Firstly, an accurate linear model of the system is desired if possible. This may be the case where a comparison is to be drawn with the results from a linear finite element analysis. Secondly, the existence of non-linearity is to be established and the need is for an estimate of its effect on the structures response in service, i.e. the behaviour of the non-linear system is desired when the input is typical of operating conditions. Finally, it is required that the non-linearity be identified fully enough to enable an implicit mathematical model to be constructed, such as a set of non-linear differential equations. These may then be solved to predict the response of the structure to various input conditions whereby the dependence of the modal parameters on these can be established. In this case the non-linear coefficients of the structural system equations have to be determined.

Depending upon the aim of the investigation, consideration has to be given to the method of testing a structure since the method of testing can either be aimed at eliminating non-linear behaviour or at highlighting it for indentification purposes. For example, multi-point sinusoidal testing is advantageous for minimising non-linear effects(1) since the structure is forced into the shape of a normal mode of the equivalent linear system and, at the same time, this also allows for the amplitude force dependence of the modal parameters to be established.

If actual operating conditions are to be reproduced as closely as possible during testing, the input signals may well be random in nature. Studies of non-linear elements to random inputs have been carried out (2,3) but general difficulties in identifying the nature of the non-linearity have been encountered.

The testing method most commonly used in the identification of non-linear structures is the single frequency sinusoidal input. Most non-linearities will have a response to this excitation which is dominated by the fundamental frequency (particularly in the resonant regimes) and much work has been carried out using this test method for simple systems (4,5).

The principal limitation to date, regardless of the testing procedure employed, is that in order to analyse non-linear structures important assumptions have to be made. These refer to an assumed model, or models, of the non-linearity and to the degree of non-linearity present. A method recently developed which overcomes several of these shortcomings is presented. The method employs the Hilbert transform which provides a relationship between the real and imaginary parts of the measured complex frequency response functions.

This relationship is shown to be very useful in identifying and characterising non-linearities and examples of the application of the technique and the

possible advantages of employing time domain procedures are discussed.

2. APPLICATION OF THE HILBERT TRANSFORM IN MODAL TESTING

A detailed analytical description of the development of the Hilbert transform for application in the domain of modal analysis is presented in (6),(8). However, for completeness the major formulae necessary will be presented.

For any complex analytical function from which the real part can be derived from its imaginary part, or visa versa, this relationship is known as a Hilbert transform pair. In modal analysis we assume such a function exists, namely the relationship between the output response and the input excitation.

In terms of the commonly measured quantity Mobility, our complex analytic function is

$$G(\omega) = \frac{\dot{x}}{F} = \frac{\text{output velocity response}}{\text{input force}} = \sum_{r=1}^{m} \frac{i\omega (X_R + iX_I)}{\omega_r^2 (1 + i\delta_r) - \omega^2} \tag{1}$$

The Hilbert transform of $G(\omega)$ in the frequency domain will be defined as

$$H\left[G(\omega)\right] = H(\omega) = \text{Re } H(\omega) + i\,\text{Im}H(\omega) \tag{2}$$

Employing Cauchy's formula for the integral relation of a complex variable allows us to write

$$G(\omega') = \frac{-1}{2i\pi} \oint_C \frac{G(\omega)d\omega}{\omega - \omega'} \tag{3}$$

Choice of a suitable integration contour in the complex plane (6) results in equation (3) being expressed as

$$G(\omega_c) = -\frac{1}{\pi i} \text{ PV} \int_{-\infty}^{\infty} \frac{G(\omega)\, d\omega}{\omega - \omega_c} \tag{4}$$

where PV designates the Cauchy principal value of the integral.

Equation (4) can be expressed as real and imaginary functions,

$$\text{Re } G(\omega_c) = -\frac{2}{\pi} \text{ PV} \int_0^{\infty} \frac{\omega \text{Im}G(\omega)d\omega}{\omega^2 - \omega_c^2} \tag{5}$$

$$\text{Im } G(\omega_c) = \frac{2\omega_c}{\pi} \text{ PV} \int_0^{\infty} \frac{\text{Re } G(\omega)d\omega}{\omega^2 - \omega_c^2} \tag{6}$$

Equations (5) and (6) are the Hilbert transform pair which can be used to derive the real part of $G(\omega)$ from its imaginary part and visa versa.

2.1 The Hilbert transforms and non-linear systems

For a linear system which is governed by equation (1), the equality $H(\omega) = G(\omega)$ holds. That is, the Hilbert transform can be used to derive the real part of $G(\omega)$ from its imaginary part and visa versa using equations (5) and (6). In practice this means that when the mobility frequency response function (or functions) is obtained, using swept sine excitation, the procedure is to compute the imaginary part of the frequency response function by taking the Hilbert transform of the real part and to compare this with the actual (measured) imaginary response. This procedure is also applied to the real part.

If good correlation exists between the Hilbert transformed functions and the measured functions then the system is classified as linear. However, when the mobility data is polluted by non-linearity, then we have a criterion which is stated as, if $H(\omega) \neq G(\omega)$, the system is non-linear. Another way of examining this criterion is to say that if the equality conditions exist such that $H(\omega) = G(\omega)$, then from equations (2) and (4),

$$G(\omega) = ReG(\omega) + \frac{i}{\pi} \; PV \int_0^{\infty} \frac{Re\; G(\omega)\; d\omega}{\omega \; - \omega_c} \tag{7}$$

This can be written as a convolution (7) by noting that

$$H\left[f(x)\right] = \frac{-1}{\pi x} * f(x) \tag{8}$$

$$\therefore \quad G(\omega) = ReG(\omega) + \left(\frac{-1}{\pi_\omega}\right) * ReG(\omega) \tag{9}$$

If $G(\omega)$ is the Fourier transform of a real signal $g(t)$,

$$\text{i.e. } G(\omega) = \int_{-\infty}^{\infty} g(t)\; e^{-2\pi\, i\omega t} dt \tag{10}$$

then taking the inverse Fourier transform of equation (9) gives

$$F^{-1}\left[G(\omega)\right] = g(t) = E(t)\left[1 + sgnt\right] \tag{11}$$

where $sgnt = F^{-1}\left(\frac{i}{\pi\omega}\right) = +1$ for $t > 0$

$= -1$ for $t < 0$

and $E(t)$ is a real even function.

Hence equations (7) to (11) state that $g(t)$ is real and <u>causal</u> only if $H(\omega) = G(\omega)$. The corollary of this is that if $g(t)$ is real and non-causal then $H(\omega) \neq G(\omega)$ and the system is non-linear. This aspect re-emerges when the time domain concept of carrying out the Hilbert transform is examined in a later section.

It is worthwhile mentioning that the same conclusions regarding the real and causal properties have been derived using Parseval's theorem by Vinh(9).

3. IDENTIFYING NON-LINEARITIES IN MODAL TEST DATA

In order to apply the Hilbert transform method, discrete versions of equations (5) and (6) are necessary. These will merely be quoted and reference to (5) gives details of their derivation.

Discretising the mobility frequency response real and imaginary functions into n points gives

$$Re\; H(\omega_j) = \frac{-2}{\pi} \sum_{k=1}^{n} \frac{ImG(\omega_k) \cdot \omega_k \Delta\omega}{\omega_k^{\,2} - \omega_j^{\,2}} + E_R \tag{12}$$

$$Im\; H(\omega_j) = \frac{2}{\pi}\, \omega_j \sum_{k=1}^{n} \frac{Re\; G(\omega_k)\Delta}{\omega_k^{\,2} - \omega_j^{\,2}} + E_I \tag{13}$$

$$\text{with } \Delta\omega = \omega_{j+1} - \omega_j;\; k \neq j$$

The terms E_R and E_I represent the real and imaginary correction terms since the mobility function does not extend to infinity.

These terms (derived in (5)) are:

$$E_R = \frac{X_R}{\pi(\omega_c^2 - \omega_r^2)} \left\{ \omega_r \ln \frac{(\omega_n + \omega_r)(\omega_r - \omega_1)}{(\omega_n - \omega_r)(\omega_r + \omega_1)} + \omega_c \ln \frac{(\omega_c + \omega_1)(\omega_n - \omega_c)}{(\omega_c - \omega_1)(\omega_n + \omega_c)} \right\} \quad (14)$$

$$E_I = \frac{\omega_c X_I}{\pi(\omega_c^2 - \omega_r^2)} \left\{ \ln \frac{\omega_c^2 (\omega_r - \omega_1)(\omega_r + \omega_1)(\omega_n - \omega_c)(\omega_n + \omega_c)}{\omega_r^2 (\omega_c - \omega_1)(\omega_c + \omega_1)(\omega_n - \omega_r)(\omega_n + \omega_r)} \right\} \quad (15)$$

where X_R, X_I, ω_r are estimates of the real and imaginary modal constants and resonant frequency respectively.

An alternative to the above approach has been developed by Haoui (10) whereby a series expansion for the correction terms is employed. This has the advantage that no estimates of the modal parameters are required for the correction terms. However, this approach requires that a mobility function begins at zero frequency with zero magnitude.

In order to demonstrate how the method works, equations (12) to (13) have been applied to the mobility response data from the digital simulation of a single mode system with two types of structural non-linearity, Coulomb friction and a cubic non-linear stiffness. The results shown in Figures 1 and 2 for both low and high excitation levels clearly demonstrate the ability of the method to identify non-linear effects. It can be seen from Figure 1 that when the force excitation level is small, the Coulomb friction results in a large symmetrical discrepancy between the data and the Hilbert transforms whereas at the higher excitation level (where the friction is almost saturated) the data and the transforms almost overlay, indicating a linearised system.

Conversely, Figure 2 shows that for the non-linear stiffness the low excitation level results in good correlation between the data and the transforms. At the higher excitation level a divergence between the data and the transforms indicates a non-linearity.

In this case it is observed that with a stiffening non-linearity the symmetry between the data and the transforms is destroyed.

Figure 3 shows the results of the method applied to tests on an aircraft aileron. In 3(a) the real and imaginary parts of the mobility frequency response function and their transforms are displayed, these results being obtained at one intermediate force excitation level. The lack of correlation, together with the asymmetry characteristics indicate a softening spring characteristic in all three modes.

Figure 3(b) shows the results of tests carried out at the same excitation and response points for several force excitation levels. Confirmation of the existence and character of the non-linearity, as identified by the Hilbert transform, is readily seen. A further point of interest is that tests carried out at a low excitation level indicated good reciprocity, whereas reciprocity tests carried out at the intermediate force excitation level, where the Hilbert transform indicated non-linearity, gave poor correlation.

Application of the Hilbert transform to several types of non-linearity has been studied (8) and it has been shown that each non-linearity can be identified uniquely by the differences between the transformed and original data. In an attempt to quantify the level of non-linearity, transform describers have been employed. These are frequency moment integrals which are based on the principal of statistical moments.

3.1 Transform Describers

Utilising the fact that non-linearity creates symmetry/asymmetry characteristics between the original and transformed data, frequency moment integrals which are centred around the resonant frequency can be derived. The difference between the moments of the original and the transformed data is a measure of the level of the non-linearity.

In order to ensure generality, the moment integrals are based on the half-power points mode by mode.

The moment integrals employ the equation:

$$M^{(n)} = \int_{\omega_A}^{\omega_B} \omega^n \, S(\omega) \, d\omega \qquad (16)$$

where ω_A, ω_B, are the half-power points of the mode of interest, $S(\omega)$ is $G(\omega)$ for the actual data and $H(\omega)$ for the transformed data. The Hilbert transform describer is defined as

$$HTD = \frac{M_H^{(n)}}{M_G^{(n)}} = \frac{\text{moment integral of transformed data}}{\text{moment integral of actual data}} \qquad (17)$$

Tabulated values of these frequency moments for n = 1 to 3 have been presented in (8) and it was shown that these can be used to confirm the character of the non-linearity. These describers can be evaluated for both the real and imaginary sets of data.

Basically, the describers behave as indicated below:

For a linear system:

$$\frac{M_H^{(n)}}{M_G^{(n)}} = 1$$

For a non-linear system, $\frac{M_H^{(n)}}{M_G^{(n)}}$ will be dependent upon the nature of the non-linearity and upon the value of n in equation (16). However, they will be either greater or less than unity and their trends can uniquely identify the character of a single non-linear element in systems with well spaced modes.

In order to establish a relationship between the errors in the modal parameters derived using a frequency domain curve fitting algorithm employing a linear model governed by equation (1) and the transform describers, the responses from a series of digitally simulated single mode non-linear systems were analysed. The analysis consisted of curve fitting the linear model and extracting the modal parameters, natural frequency and modal damping. This was then repeated for the non-linear system at various excitation levels. The differences between the modal parameters was then expressed as a percentage error based upon the linear model. Transform describers were obtained in each case from the original and Hilbert transformed data and again expressed as a percentage change for increasing excitation force. Figures 4 and 5 show the trends obtained for systems with Coulomb damping and a hardening spring. Although the clear trend is one of increasing error in the modal parameter with transform describer, insufficient information is available to uniquely relate the error in the describer to the error in a modal parameter since the trends observed are dependent upon other system parameters, e.g. the magnitude of the linear damping.

Thus, the use of the transform describers is limited at the moment to identifying non-linearities; the ability to quantify the importance, i.e. a strong or weak non-linearity, still remains unanswered.

4. FREQUENCY DOMAIN AND TIME DOMAIN TRANSFORMS

The Hilbert transform in the fequency domain is a continuous transform over all frequencies. The use of a discrete transform, as defined by equations (12) to (15) introduces errors, particularly if the modal damping is small, since there is a loss of information in the resonant region.

The condition $\Delta\omega < \delta_r \omega_r/2$ (18)

for the r^{th} mode can result in the true peak amplitude being missed entirely and then the transform will not be identical to the original data even for a linear system. This effect is clearly seen in Figure 6(a) and (b) where simulated data for a lightly damped linear single-mode system has been transformed using a 40 point function in 6(a) and a 120 point function in 6(b).

Figure 7 shows the actual mobility data and the transforms of the mobility data obtained from tests carried out on a cantilever plate, using stepped sine excitation. The two lower modes, where the condition defined in equation (18) exists, display errors caused by lack of resolution. The transform of the higher modes is in close agreement with the original data and in these modes

$$\Delta\omega > \delta_r \omega_r/2$$

An additional disadvantage of the frequency domain approach is that of the speed limitation. The number of calculations required in a point by point frequency transformation is n^2, where n is the number of frequency points. However, if we consider the alternative, transforming in the time domain, then several advantages are obvious.

Considering the Hilbert transform of our mobility complex frequency response function expressed as a convolution in frequency, we have, from equation (9),

$$H(\omega) = \frac{-1}{\pi\omega} * G(\omega) \qquad (19)$$

This appears as a multiplication in the time domain

$$H(\omega) = F\left[\text{sgnt} \times F^{-1}(G(\omega))\right] \qquad (20)$$

If the Fourier transforms involved are evaluated by a FFT algorithm, a useful increase in speed is seen over the frequency domain approach.

Equation (20) has been applied to simulated data for a linear single mode system whereby the real and imaginary mobility data are inverse Fourier transformed, the time characteristic multiplied by sgnt and the result Fast Fourier transformed back to the frequency domain. Figure 8 shows the results of these operations and it can be seen that there is a small difference between the original and time domain transformed data which should not be present for a linear system. Figure 9 shows the results of applying this approach to non-linear data and the differences in the transformed and original data is much more significant due to the presence of the non-linearity. The discrepancies which arise in the linear case are due to the fact that the mobility functions do not extend to zero, thus "edge or leakage effects" are present which, in the frequency domain, required the correction terms, equations (14) and (15) being applied to the transforms. The "leakage effects" are seen in the time domain as a non-causal signal. It has already been shown that in order for the Hilbert transform, $H(\omega)$ to be equal to the mobility function $G(\omega)$ (equations (7) to (11)), the time signal $g(t)$ must be real and causal. Figure 10 shows the inverse Fourier transform of the mobility data presented in Figure 8, the real valued signal for $t < 0$ indicates non-causality. Thus, when the Hilbert transform of this total time signal is taken, errors

are introduced.

However, these effects are small and when one considers that the number of calculations involved using this approach is $2n\log_2(n)$, compared to $2n^2$, for the frequency domain approach, it is apparent that there is a considerable time saving.

CONCLUSIONS

The application of the Hilbert transform in modal analysis has shown that non-linearity can be detected and identified without any prior assumptions. The ability to uniquely identify a particular non-linearity is dependent upon the predominance of that characteristic in a particular mode. The use of frequency moments offers a numerical basis for identifying the nature of a non-linearity, but the quantification of non-linearity in relation to the errors expected using a linear model is yet to be achieved. However, it has been shown that there is a definite trend between the changes in the frequency moments and the magnitude of the errors in the modal parameters.

The Hilbert transform in the time domain offers a considerable saving in computation time and allows the benefits of FFT procedures to be employed. The creation of a non-causal signal in the inverse FFT, which results in non-ideal transforms, is a present a penalty of using this approach.

REFERENCES

1. R.FILLOD, 1980. BISM - Lab.Mechanique appliquee CNRS-Besançon. Identification des structures lineaires des responses harmoniques mesurees.

2. M.APETAER and F.OPICKA, 1979. Journal of Sound & Vibration, 62(1), pp 141-149. Output from a non-linear "friction" element with stochastic input.

3. S.H.CRANDALL, 1963. Journal of the Acoustical Society of America, 35(11), pp 1700-1705. Equivalent linearisation techniques:perturbation techniques for random vibrations of non-linear systems.

4. G.R.TOMLINSON and J.H.HIBBERT, 1979. Journal of Sound and Vibration 64(2), pp 233-234. Identification of the dynamic characteristics of a structure with Coulomb friction.

5. M.SIMON, 1983. Ph.D.thesis, University of Manchester. Developments in the modal analysis of linear and non-linear structures.

6. M.SIMON and G.R.TOMLINSON, 1983. Modal analysis of linear and non-linear structures employing the Hilbert transform. (To be published).

7. R.BRACEWELL, 1978. The Fourier integral and its application. McGraw-Hill.

8. G.R.TOMLINSON and N.E.KIRK, 1983. Proceedings of the 8th International Seminar on modal analysis, K.U.Leuven. On the identification of non-linearities in modal testing employing the Hilbert transform.

9. T.VINH, A.HAOUI and Y.CHEVALIER, 1983. Euromech 168, "Modal analysis of structures with applications to the mechanics of materials". University of Manchester. Applications of the Hilbert transform in the analysis of non-linear structures.

10. A.HAOUI, 1983. Memoire pour Diplome d'Ingenieur, ISMCM,St.Ouen,Paris. Analyse modal de systemes mechanique non-linearities extension de techniques existants identification.

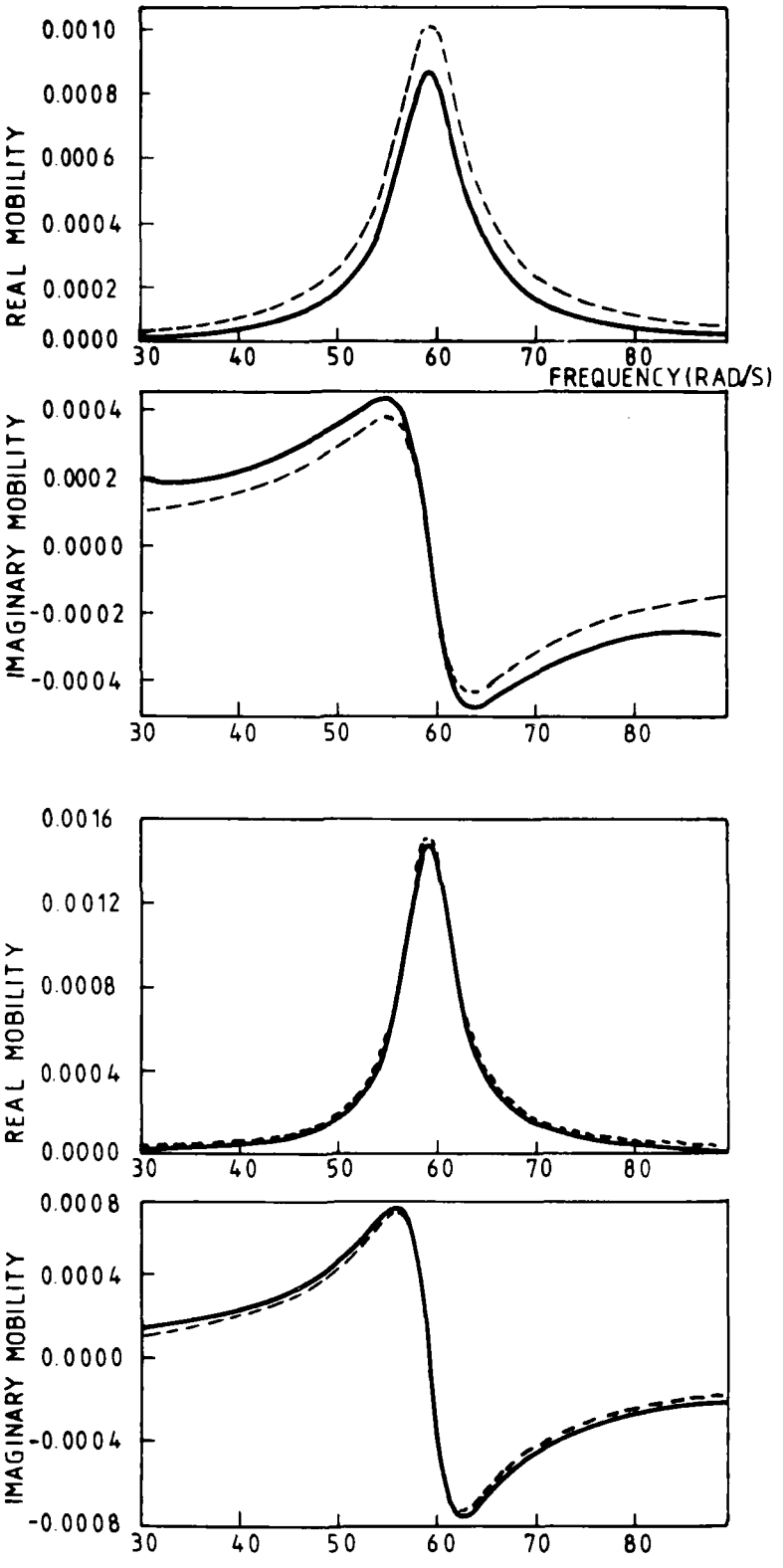

FIGURE 1

S.D.O.F. SIMULATION WITH COULOMB FRICTION NON-LINEARITY

a) low force excitation level

b) high force excitation level

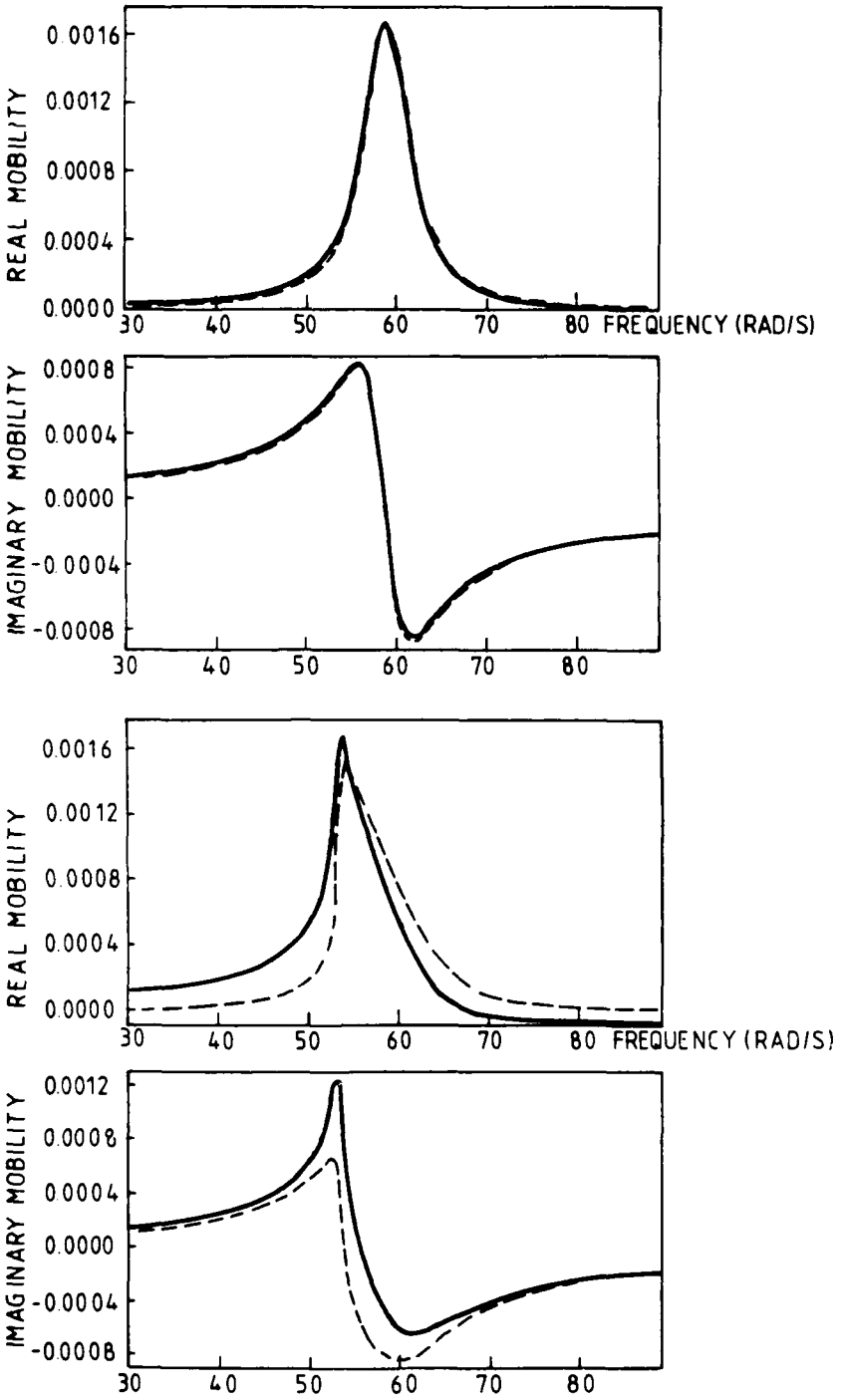

FIGURE 2.

S D O F SIMULATION WITH SOFTENING CUBIC STIFFNESS NON-LINEARITY.

a) low force excitation level

b) high force excitation level

Governing equation $mx + k(1+i\delta)x + f(x, \dot{x}) = Fe^{jwt}$

with $m = 100$ kg
$k = 35 \times 10^4$ Nm^{-1}
$\delta = 0.1$

} For all analyses; $f(x, \dot{x})$ = non linear function

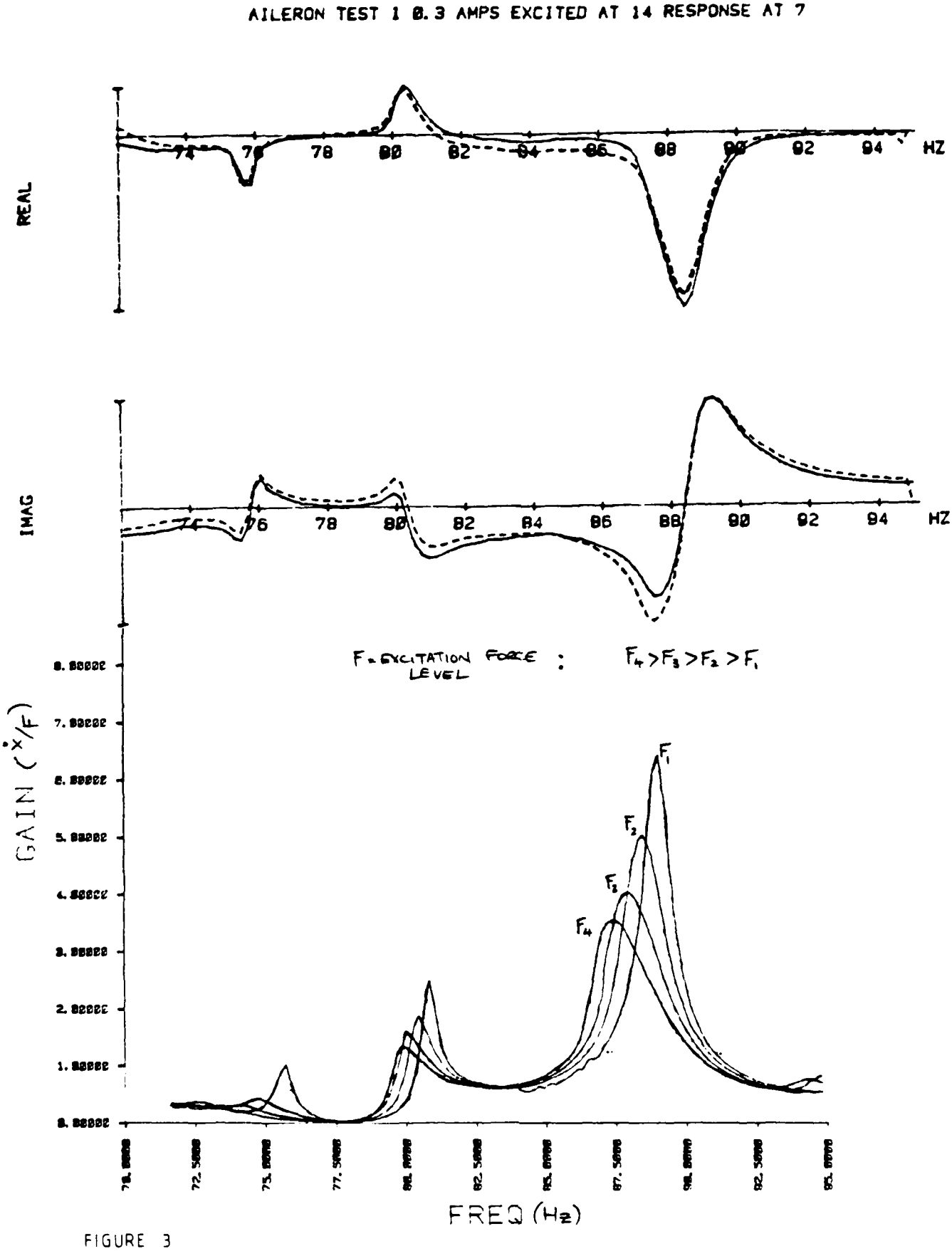

FIGURE 3

Results from an aircraft aileron test :

a) Hilbert transform at an intermediate excitation level.

b) Frequency response functions at several excitation levels confirming Hilbert transform prediction.

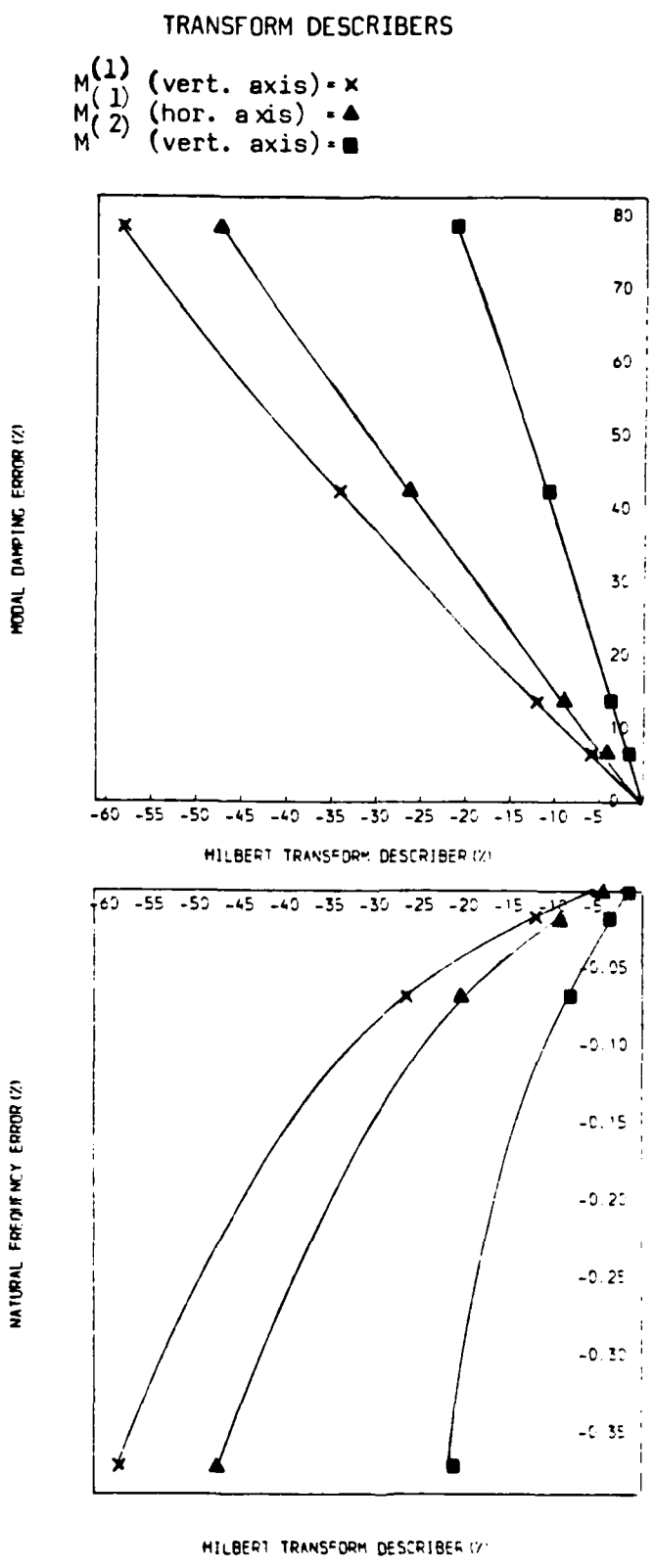

FIGURE 4

Error in modal damping and natural frequency as a function of Hilbert transform describer for a S.D.O.F. system with a friction non-linearity.

TRANSFORM DESCRIBERS

$M^{(1)}_{(1)}$ (vert. axis) = ×
$M^{(1)}_{(2)}$ (hor. axis) = ▲
$M^{(2)}$ (vert. axis) = ■

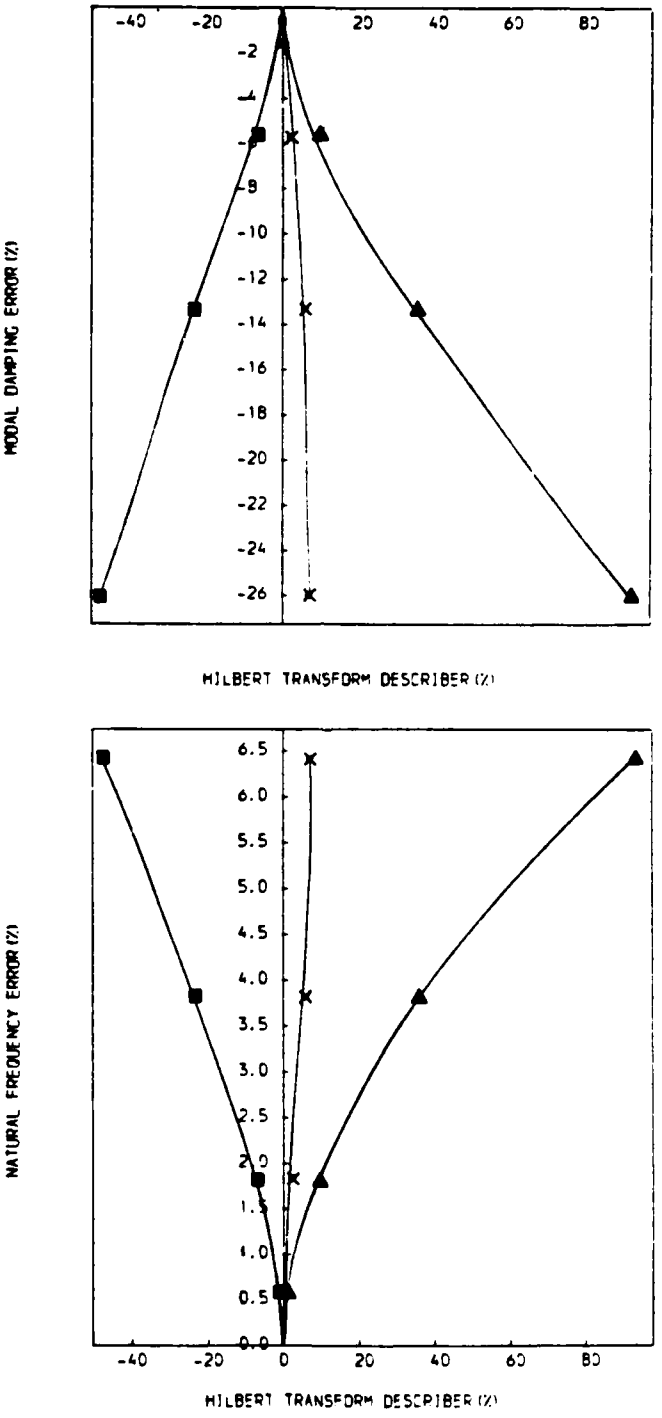

FIGURE 5

Error in modal damping and natural frequency as a function of Hilbert transform describer for a S.D.O.F. system with a hardening cubic stiffness non-linearity.

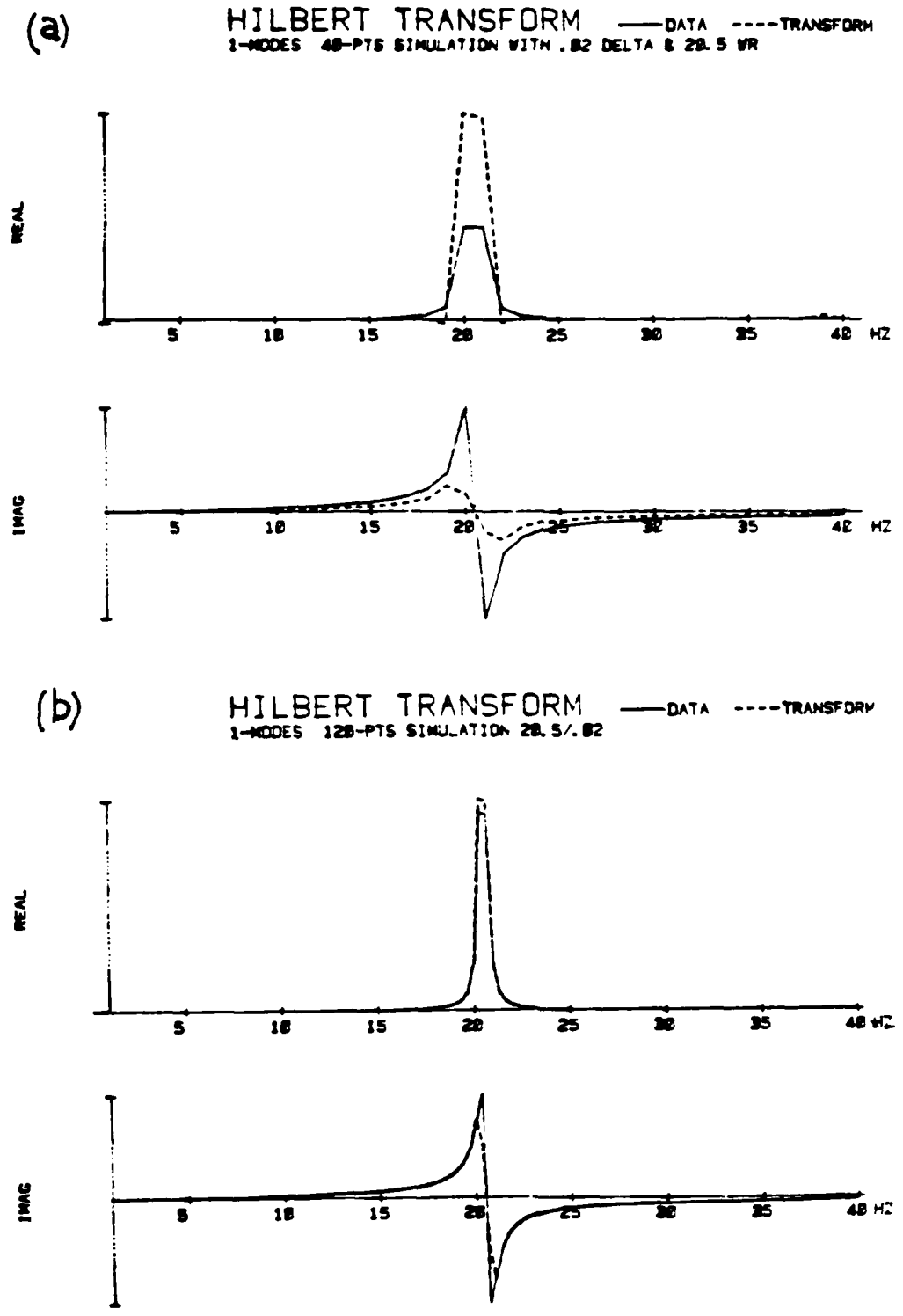

Figure 6 (a) Hilbert transform of theoretical mobility transfer function of 40 points; (b) the same transfer function represented by 120 points. The errors caused by lack of frequency resolution can be seen.

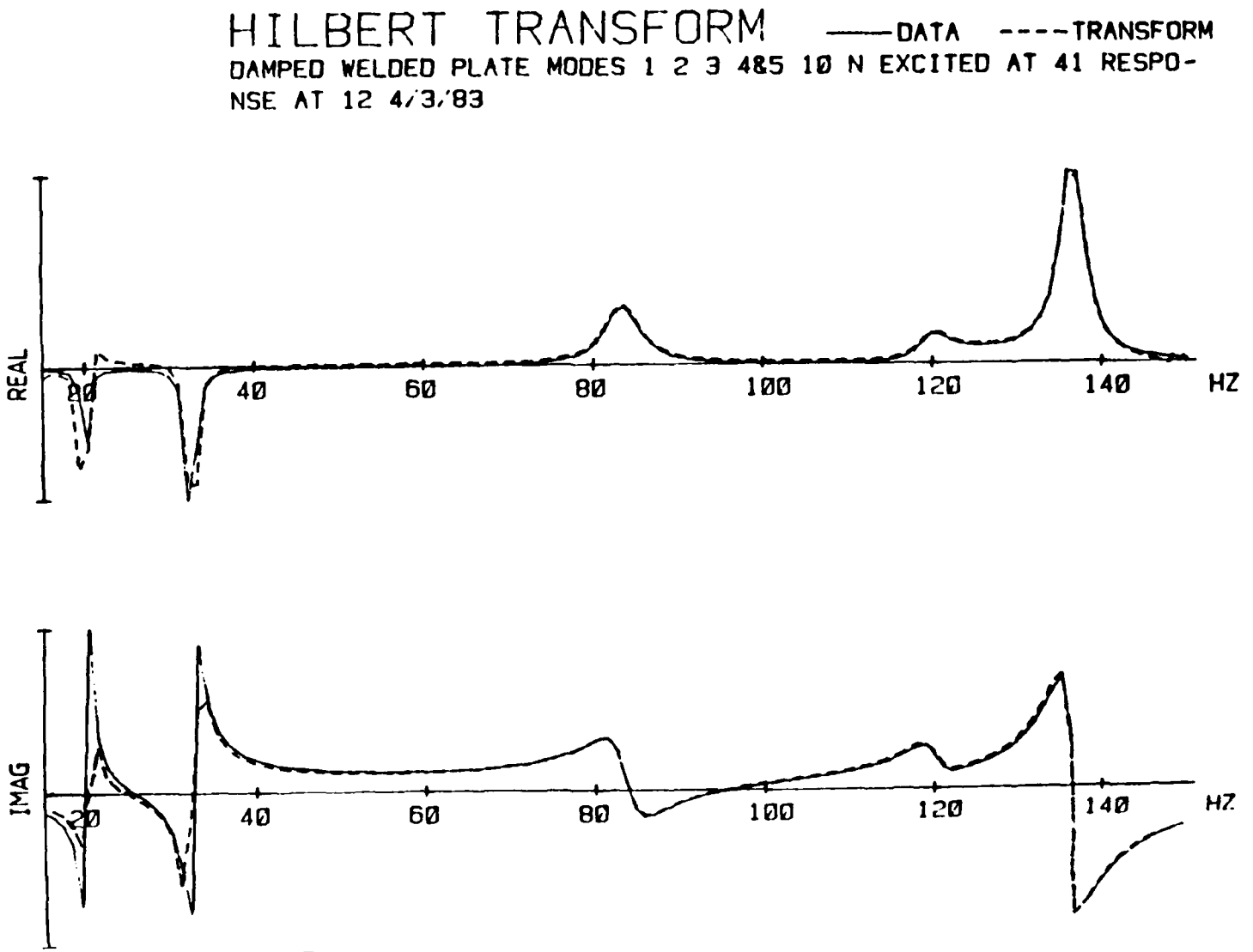

FIGURE 7
The effects of resolution of the Hilbert transform of a linear frequency response function.

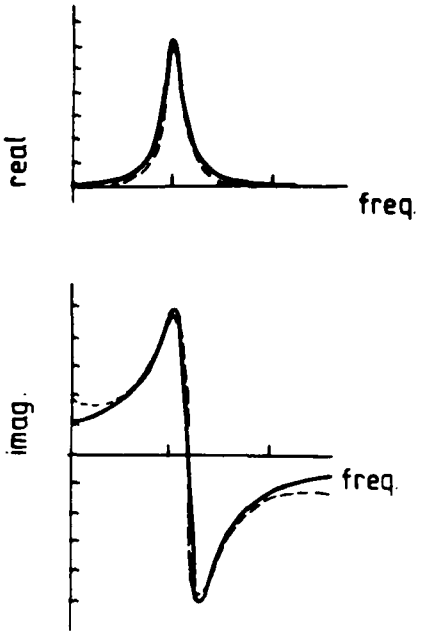

FIGURE 8

The time domain Hilbert transform of a linear mobility

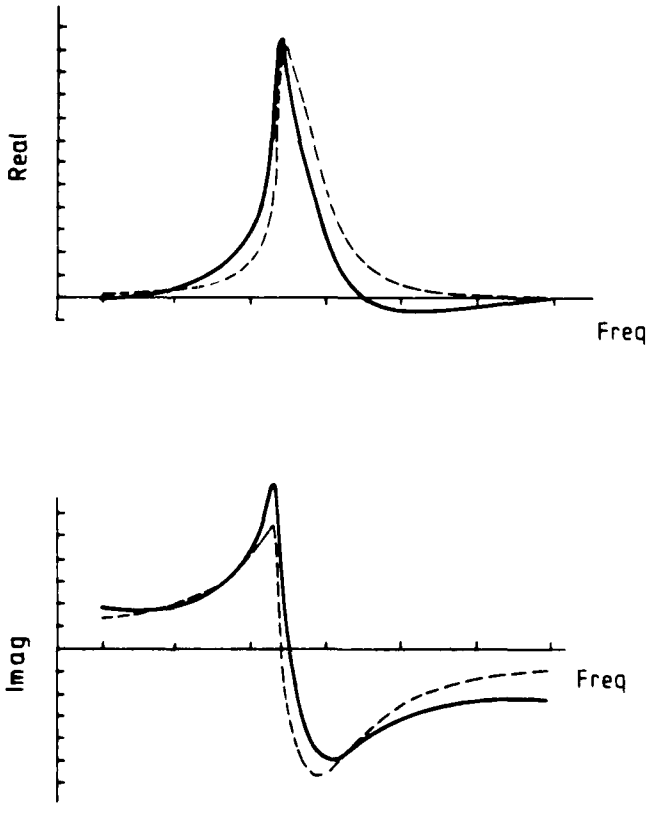

FIGURE 9

The time domain Hilbert transform of a non-linear mobility

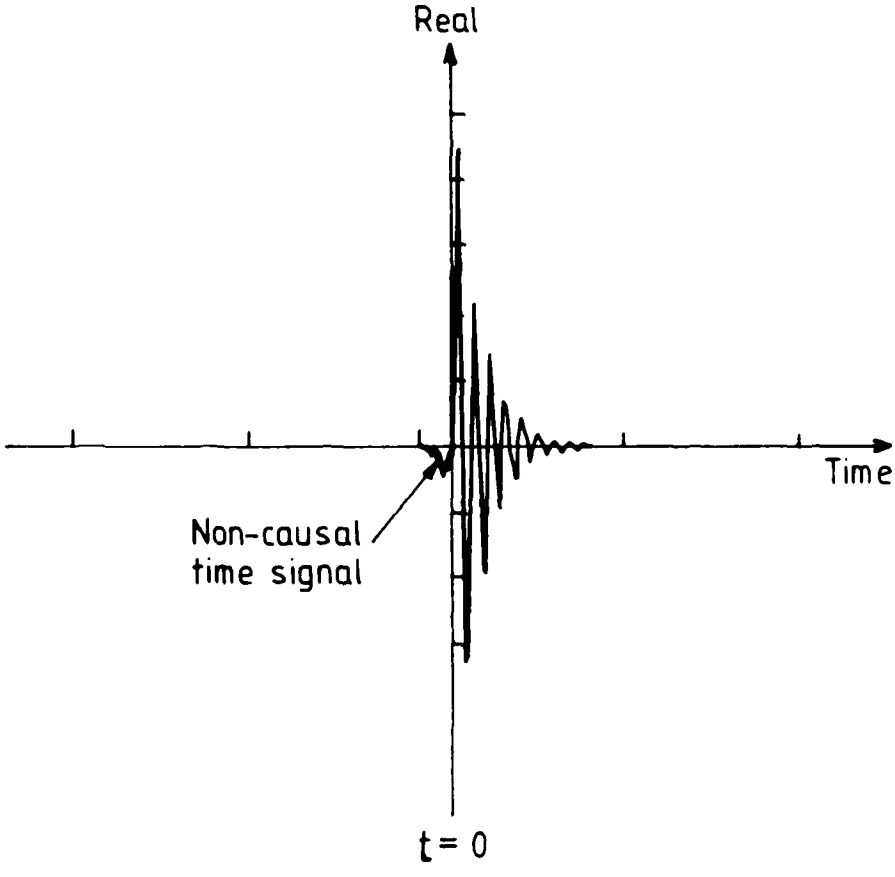

FIGURE 10

The time response of the data in Figure 8.
Note non-causal nature (i.e. negative time component)

TIME DOMAIN ANALYSIS OF NONLINEAR VIBRATION DATA

S. F. Masri R. K. Miller H. Sassi

Civil Engineering Department
University of Southern California

T. K. Caughey

Division of Engineering
California Institute of Technology

1. INTRODUCTION

The identification and modeling of nonlinear multidegree-of-freedom (MDOF) dynamic systems through the use of experimental data is a problem of considerable importance in the structural dynamics area. Since the model structure in many practical dynamic problems is by no means clear, an increasing amount of attention has recently been devoted to nonparametric identification methods.

However, the traditional nonparametric identification techniques have their own problems, including restrictions on the nature of dynamic systems to be identified (nonhysteretic, stationary) and on the input signal that can be used (white noise). Furthermore, when dealing with systems incorporating commonly encountered nonlinearities (e.g., polynomial ones), the computational effort required to evaluate higher-order terms is prohibitive, coupled with very demanding (and usually unrealistic) storage requirements.

This paper presents an approximate method for the time-domain analysis of vibration data obtained from the response of MDOF dynamic systems that are undergoing nonlinear deformations. In addition to providing a convenient procedure for the nonparametric identification of arbitrarily nonlinear structural systems, the proposed data-processing method furnishes a rational approach for a systematic procedure of model-order reduction in nonlinear systems.

2. FORMULATION

2.1 Introduction

Consider a discrete nonlinear dynamic system whose motion is governed by

$$M\ddot{\underset{\sim}{x}} + \underset{\sim}{f}(\underset{\sim}{x},\dot{\underset{\sim}{x}}) = \underset{\sim}{p}(t) \ , \qquad (1)$$

where M = diagonal mass matrix of order n, $\underset{\sim}{x}(t)$ = displacement vector = $\{x_1,x_2,\ldots,x_n\}^T$, $\underset{\sim}{f}$ = function that represents nonconservative nonlinear forces, and $\underset{\sim}{p}(t)$ = excitation vector.

Assume that "equivalent" stiffness matrix K corresponding to the range of motion of interest can be determined. This step could be accomplished, for example, by using modal identification techniques to process experimental measurements from the response of the physical systems. Alternatively, in the case of large nonlinear finite element models, where the time history response is obtained by treating the system as a piece-wise linear model, matrix K is directly available since it is repeatedly reconstructed to reflect changing response levels.

2.2 Restoring Force Estimation

Now solving the eigenvalue problem associated with the linearized version of Eq. (1) results in the transformation

$$\underset{\sim}{x} = \phi \, \underset{\sim}{u} \tag{2}$$

where ϕ is the eigenvector matrix and $\underset{\sim}{u}$ is the vector of generalized coordinates.

Making use of Eq. (2), the system equation of motion Eq. (1) can be converted to the form

$$\mathcal{M} \, \ddot{\underset{\sim}{u}} + \underset{\sim}{h}(\underset{\sim}{u},\dot{\underset{\sim}{u}}) = \underset{\sim}{q}(t) \tag{3}$$

where $\mathcal{M}$ is a diagonal mass matrix given by

$$\mathcal{M} = \phi^T \, M \, \phi \, , \tag{4}$$

$\underset{\sim}{h}$ is a vector corresponding to the transformed nonlinear forces acting on the system,

$$\underset{\sim}{h}(\underset{\sim}{u},\dot{\underset{\sim}{u}}) = \phi^T \, \underset{\sim}{f}(\underset{\sim}{x},\dot{\underset{\sim}{x}}) \, , \tag{5}$$

and $\underset{\sim}{q}(t)$ is a vector corresponding to the generalized excitation forces,

$$\underset{\sim}{q}(t) = \phi^T \, \underset{\sim}{p}(t) \, . \tag{6}$$

An alternative form of Eq. (3) is

$$\underset{\sim}{h}(\underset{\sim}{u},\dot{\underset{\sim}{u}}) = \phi^T (\underset{\sim}{p}(t) - M \, \ddot{\underset{\sim}{x}}) \, . \tag{7}$$

Note from Eq. (7) that if the terms appearing on the right-hand-side (RHS) are known, the time history of each component of vector $\underset{\sim}{h}$ can be determined.

Note also that in the case of a linear system, due to the orthogonality condition associated with ϕ, the set of equations represented by Eq. (7) are decoupled; i.e., each component h_i of $\underset{\sim}{h}$ depends only on the i^{th} generalized coordinate u_i rather than on all components of u.

Guided by the preceding observation, the central idea of the present method is that in the case of nonlinear dynamic systems commonly encountered in the applied mechanics field, a judicious assumption is that each component of $\underset{\sim}{h}$ can be expressed in terms of a series of the form:

$$h_i(\underset{\sim}{u},\dot{\underset{\sim}{u}}) \approx \hat{h}_i(\underset{\sim}{u},\dot{\underset{\sim}{u}}) \, , \tag{8}$$

where

$$\hat{h}_i(\underset{\sim}{u},\dot{\underset{\sim}{u}}) = \sum_{j=1}^{J_{max_i}} h_i^{(j)} \, (v_{1_i}^{(j)}, v_{2_i}^{(j)}) \, . \tag{9}$$

The approximation indicated in Eq. (9) is that each component h_i of the nonlinear generalized restoring force h can be adequately estimated by a collection of terms $h_i^{(j)}$ each one of which involves a pair of generalized coordinates (displacements and/or velocities). The particular choice of combinations and permutations of u_k and $\dot{u}_\ell$ and the number of terms J_{max_i} needed for a given h_i depends on the nature and extent of the nonlinearity of the system and its

effects on the specific "mode" i. Note that the formulation in Eq. (9) allows for "modal" interaction between all modal displacements and velocities, taken two at a time.

2.3 Series Expansion

The individual terms appearing in the series expansion of Eq. (9) may be evaluated by using the least-squares approach to determine the optimum fit for the time history of each h_i. Thus, $h_i(1)$ may be expressed as a double series involving a suitable choice of basis functions,

$$h_i(\underset{\sim}{u},\dot{\underset{\sim}{u}}) \approx \hat{h}_i^{(1)}(v_{1_i}^{(1)}, v_{2_i}^{(1)}) \ , \tag{10}$$

where

$$\hat{h}_i^{(1)} = \sum_k \sum_\ell {}^{(1)}C_{k\ell}^{(i)} T_k(v_{1_i}^{(1)}) \ T_\ell(v_{2_i}^{(1)}) \ . \tag{11}$$

By extending this procedure to the residual error to account for all "modes" that have significant interaction with "mode" i, Eq. (9) is obtained.

2.4 Least-Squares Fit

Using two-dimensional orthogonal polynomials to estimate each $h_i(\underset{\sim}{u},\dot{\underset{\sim}{u}})$ by a series of approximating functions $\hat{h}_i^{(j)}$ of the form indicated in Eq. (11), then the numerical value of the $C_{k\ell}$ coefficients can be determined by invoking the applicable orthogonality conditions for the chosen polynomials. While there is a wide choice of suitable basis functions for least-squares application, the orthogonal nature of the Chebyshev polynomials and their "equal ripple" characteristics make them convenient to use in the present work.

2.5 Response Prediction

Once the coefficients ${}^{(j)}C_{k\ell}^{(i)}$ have been extracted from the nonlinear system response in the manner outlined above, they constitute a reduced-order nonparametric model of the system. When used with the same excitation employed for identification they can reconstruct the (approximate) response of the higher-order model. Even more important is the ability to use these same coefficients to predict the estimated response time history of the nonlinear system when subjected to an excitation signal that is different from that used for identification purposes.

The procedure for the approximate model response predictions is based on the (numerical) solution of the reduced-order system equations of motion expressed in the form:

$$\mathcal{M}_{ii}\ddot{u}_i(t) + h_i(t) = q_i(t) \ , \qquad i = 1,2,\ldots,r \leq n \ . \tag{12}$$

Given $\underset{\sim}{p}(t)$ and initial conditions $\underset{\sim}{x}(t_0)$, $\dot{\underset{\sim}{x}}(t_0)$, once $h_i(t)$ is determined from Eq. (9), and making use of Eq. (6) to determine $q_i(t)$, the governing equations of motion (12) can be incrementally (numerically) solved to compute the response u_i at the next time increment $(t + \Delta t)$. The approximate response time histories of all of the system's n degrees of freedom may then be found from

$$\underset{\sim}{x}(t) = \Phi \ \underset{\sim}{u}(t) \ , \tag{13}$$

and the nonlinear restoring forces acting on the system will be found from

$$\underset{\sim}{f}(\underset{\sim}{x},\dot{\underset{\sim}{x}}) = \underset{\sim}{p}(t) - M\,\phi\,\ddot{\underset{\sim}{u}}(t) \quad . \tag{14}$$

3. APPLICATIONS

3.1 Example Limited-Slip/Hysteretic Model Characteristics

To illustrate the application of the method under discussion, consider the hypothetical finite element model shown in Fig. 1. This three-dimensional structure consists of three equal masses m_i that are interconnected by means of 12 truss elements anchored to an interface at three locations thus resulting in a redundant system with 9 degrees of freedom.

The arbitrary nonlinear elements, denoted by g_i, that are interposed between the masses and between the support points are dependent on the relative displacement z and velocity $\dot{z}$ across the terminals of each element.

To illustrate the range of validity of the present method, nonlinear elements possessing limited-slip as well as hysteretic-type force-deformation characteristics will be considered. Such nonlinearities not only involve cross-product terms of displacement and velocity, but are of course not even expressible in polynomial form. Hysteretic systems, widely encountered in all areas of applied mechanics, are among the more difficult types of nonlinear properties to investigate and identify [1-6]. Also, many aerospace engineering structures, particularly deployable structures containing collapsible or retractable elements, allow a limited amount of slip to take place between members. Such a structural behavior simultaneously involves Coulomb friction forces, deadspace-nonlinearities, as well as hysteretic characteristics [6].

In the example structure under discussion, 6 elements ($g_1, g_2, g_4, g_6, g_9, g_{10}$) have limited-slip properties, and the remaining 6 elements ($g_3, g_5, g_7, g_8, g_{11}, g_{12}$) have bilinear-hysteretic characteristics of the type shown in Fig. 2.

The geometrical configuration as well as the material properties of the elements of the nonlinear model are given in Fig. 1 together with the indices that relate the structure 9 degrees of freedom to the global (X,Y,Z) axes.

3.2 Test Excitation and Response Measurement

Subjecting the nonlinear system to the wideband stationary random excitation applied uniformly to each of the 3 masses in the global X direction for a length of time much longer than the longest system period of interest, results in the response time history depicted in Fig. 3. This can be thought of as an equivalent test in which the structure is mounted on a vibration generator. For ease in visualizing the qualitative behavior of the system, the same scale is used for plotting the displacement time histories of all 9 DOF.

The variation of each member internal force $g_i(t)$ with the corresponding member deformation $z_i(t)$ is shown in Fig. 4. For ease of comparison, the 12 plots in Fig. 4 use identical scales.

3.3 Identification

Following the procedure given in Section 2.1, an equivalent stiffness matrix K of order 9 x 9 corresponding to the small oscillations (linearized) range of motion is determined. The mass matrix M is diagonal and equal to $M = m_o I$, where m_o is a constant equal to 1.0 and I is the identity matrix of order (9 x 9). The linearized frequencies are fairly clustered and they span a range $\omega_9:\omega_1$ of $\approx$ 5:1.

Plots of the time histories of the dominant components of the generalized restoring force $\underset{\sim}{h}$ are shown in Fig. 5(a) and (b), and the variation of each $h_i(t)$ with its corresponding state variable $u_i(t)$ are presented in Figs. 5(c) and (d). It is clear from Fig. 5(d) that h_3, the generalized restoring force associated with the third mode, exhibits pronounced hysteretic characteristics.

Performing the identification procedure in the manner indicated in Section 2, the approximate nature of each $h_i(t)$ is determined in accordance with the steps given by Eqs. (8)-(11). A summary of the pertinent information for each of the identified h_i is given in Fig. 6. Note that, for the present example, sufficient accuracy in estimating the h_i's is achieved without involving terms that depend on modal interaction.

Each of the identified functions $\hat{h}^{(j)}(v_1,v_2)$ when expressed in terms of its corresponding state variables defines a surface covering the v_1-v_2 plane. The approximate surface, as defined by Eq. (9), for each of the identified h's is plotted in a three-dimensional form in Fig. 7, which also shows the 3-D representation of the "exact" value of h plotted as a function of θ_1 and θ_2 where $\theta_i = \cos^{-1} v_i$. The values of the equivalent linear stiffness and equivalent viscous damping associated with each of the generalized coordinates u_i can be readily ascertained from the 3-D plots of Figs. 7(b) and (d).

A comparison of the time history of the exact and approximate modal h is shown in Fig. 5(a) and (b).

3.4 Validation of Identified Model

In order to demonstrate the validity of the present identification approach, the model representation expressed by the $C_{k\ell}$ coefficients shown in Fig. 6, which were extracted from the original ("exact") model response under a probing signal consisting of stationary broad-band excitation, will now be used to predict the response of the original model when subjected to nonstationary random excitation consisting of modulated white noise of the form

$$p_o(t) = e(t)\, n(t) \tag{15}$$

where e(t) is a deterministic envelope function

$$e(t) = a_1 \exp(a_2 t) + a_3 \exp(a_4 t) \tag{16}$$

with the a's being arbitrary constants, and n(t) is the output of a Gaussian white noise process.

Using the identification results for prediction purposes, by following the steps indicated in Eqs. (12)-(14), results in the response time history shown in Figs. 8 and 9. It is seen that satisfactory agreement is obtained between the measured and predicted response both in amplitude as well as frequency content. As one would expect the results shown in Fig. 8 indicate that the least deviation error is achieved in the primary degrees of freedom (x_1,x_4,x_7) which dominate the displacement response. Similar comments apply to the higher-derivative response measures of velocity and acceleration.

Due to the nature of the identification method under discussion, in which the generalized nonlinear system restoring forces are matched by an approximating analytical expression, good agreement is obtained between the measured and predicted system acceleration, particularly for the primary degrees of freedom. In fact, due to the excellent agreement between the two acceleration curves shown in each of the Figs. 9(a), (d) and (g), one would need to examine

carefully a much more expanded time scale before any detectable variation between the two curves is discernible. Further details regarding this study are available in Ref. [7].

4. SUMMARY AND CONCLUSIONS

An approximate method is presented for identifying and reducing the order of discrete multidegree-of-freedom dynamic systems that possess arbitrary nonlinear characteristics. The utility of the proposed method is demonstrated by considering a redundant three-dimensional finite element model consisting of 12 nonlinear truss elements half of which incorporate hysteretic characteristics, and the remaining half having limited-slip properties. This structure, which has 9 DOF, is subjected to stationary wideband random excitation and subsequently a nonlinear reduced-order model of 2 DOF is developed. The original structure is then subjected to a new nonstationary random excitation and its measured response is compared to the predictions obtained by subjecting the reduced-order model to this new excitation. In spite of the reduction of the nonlinear model-order by a factor of 4.5, satisfactory agreement is obtained in regard to the deviation error between the predicted and measured response time history of all degrees of freedom of the original model. This deviation error is least in the case of the primary (dominant) DOF. Furthermore, the accuracy of the predicted accelerations are as good, if not better, than the lower-derivative response measures.

ACKNOWLEDGMENTS

This study was supported in part by a grant from the National Science Foundation.

REFERENCES

1. Caughey, T. K., "Random Excitation of a System with Bilinear Hysteresis," Journal of Applied Mechanics, Vol. 27, No. 4, December 1960, pp. 649-652.

2. Iwan, W. D., "The Steady-State Response of the Double Bilinear Hysteretic System," Journal of Applied Mechanics, Vol. 32, No. 4, Dec. 1965, pp. 921-925.

3. Caughey, T. K., "Nonlinear Analysis, Synthesis and Identification Theory," Proc. Symposium on Testing and Identification of Nonlinear Systems, California Institute of Technology, March 1975, pp. 1-14.

4. Ibanez, P., "Review of Analytical and Experimental Techniques for Improving Structurel Dynamic Models," Welding Research Council Bulletin, No. 249, June 1979.

5. Andronikou, A. M., and Bekey, G. A., "Identification of Hysteretic Systems," Proc. of the 18th IEEE Conf. on Decision and Control, Dec. 1979, pp. 1072-1073.

6. Iwan, W. D., "Steady-State Dynamic Response of a Limited Slip System," Journal of Applied Mechanics, Vol. 35, June 1968, pp. 322-326.

7. Masri, S. F., Miller, R. K., Sassi, H, and Caughey, T. K., "Time Domain Analysis of a Nonlinear System with Limited Slip," University of Southern California Report USC-CE-8300, Dec. 1983.

NODE i	x_i	y_i	z_i
1	-5	0	0
2	0	4	0
3	3	0	0
4	-5	3	-10
5	5	3	-10
6	0	-2	-10

(a) Structure Geometry

DOF	STRUCTURE COORDINATE	NODE
1	x_1	1
2	y_1	
3	z_1	
4	x_2	2
5	y_2	
6	z_2	
7	x_3	3
8	y_3	
9	z_3	

(c) Degree-of-freedom Indices

ELEMENTS CONNECTIVITIES AND PROPERTIES

ELEMENT NUMBER i	NODE II(i)	NODE JJ(i)	TYPE	$\alpha_1^{(i)}$	$\alpha_2^{(i)}$	$\alpha_3^{(i)}$	$\alpha_4^{(i)}$	$\alpha_5^{(i)}$
1	1	2	SLIP	200	0	0.1	0.2	
2	1	3	SLIP	200	0	0.1	0.2	
3	1	4	HYSTERETIC	200	1	83	0	0.2
4	1	5	SLIP	200	0	0.1	0.2	
5	1	6	HYSTERETIC	200	1	83	0	0.2
6	2	3	SLIP	200	0	0.1	0.2	
7	2	4	HYSTERETIC	200	1	83	0	0.2
8	2	5	HYSTERETIC	200	1	83	0	0.2
9	2	6	SLIP	200	0	0.1	0.2	
10	3	4	SLIP	200	0	0.1	0.2	
11	3	5	HYSTERETIC	200	1	83	0	0.2
12	3	6	HYSTERETIC	200	1	83	0	0.2

(b) Elements Connectivities and Properties

NOTATION

i - nodes ; i = 1, 2, . . . , 6

[j] - elements ; j = 1, 2, . . . , 12

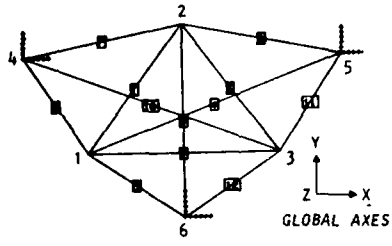

(d) Top View

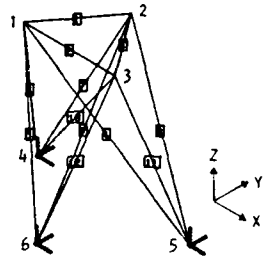

(e) Side View

Fig. 1. Example of nonlinear 9 DOF finite element model characteristics.

Bilinear Hysteretic

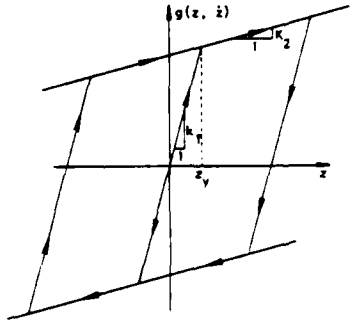

$\alpha_1^{(i)} = k_1$ = stiffness in elastic range

$\alpha_2^{(i)}$ = viscous damping term in linear range

$\alpha_3^{(i)} = k_2$ = stiffness in nonlinear range

$\alpha_4^{(i)}$ = viscous damping term in non-linear range

$\alpha_5^{(i)} = z_y$ = yield displacement level.

Physical Model of Limited Slip System [6]

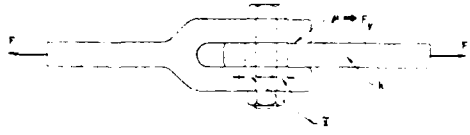

Limited Slip

$\alpha_1^{(i)} = k$ = stiffness in linear range

$\alpha_2^{(i)} = c$ = viscous damping term

$\alpha_3^{(i)} = z_y$ = yield displacement = F_y/k

$\alpha_4^{(i)} = z_g$ = gap size

Fig. 2. Nonlinear restoring force characteristics.

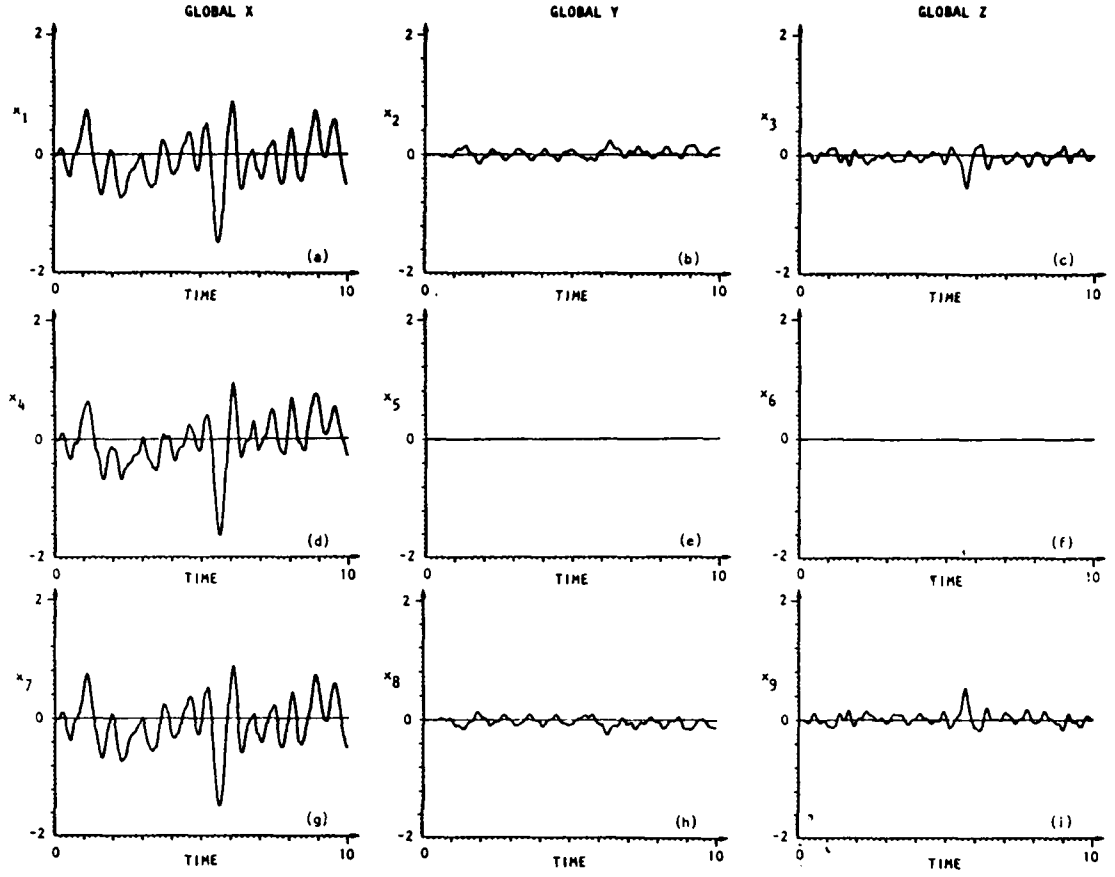

Fig. 3. Displacement time history of $x_i(t)$ of the nonlinear system under random excitation.

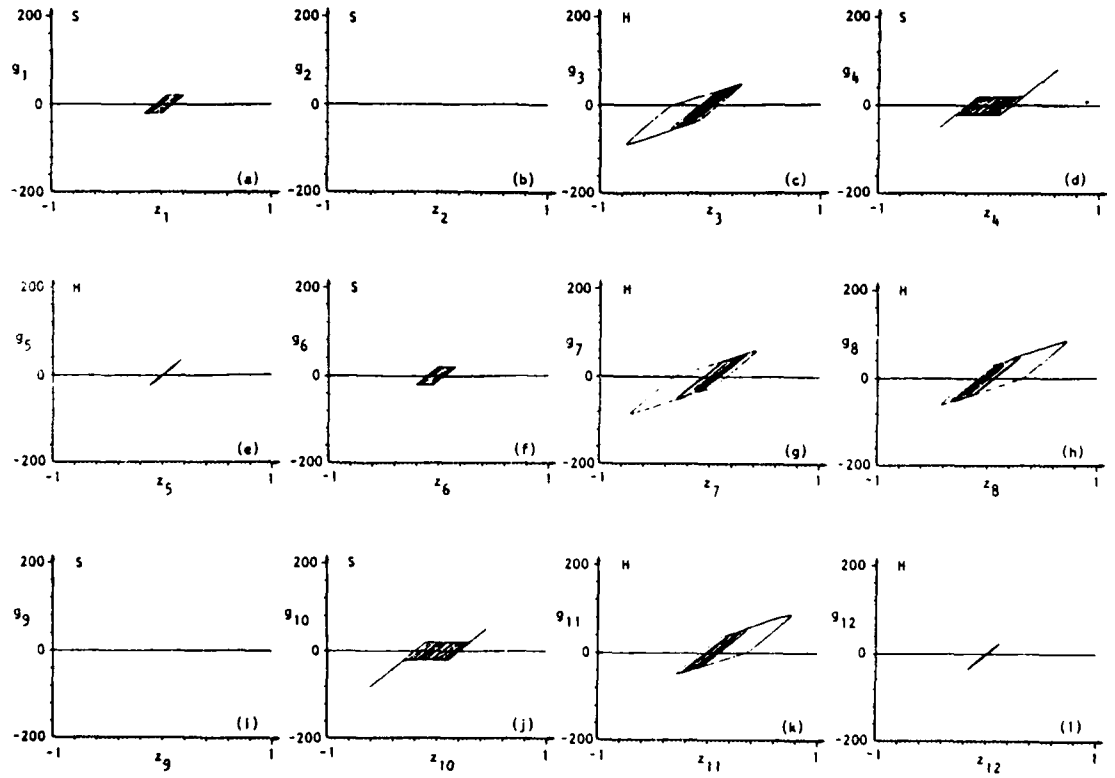

Fig. 4. Variation of element internal force $g_i(t)$ with the corresponding element deformation $z_i(t)$.

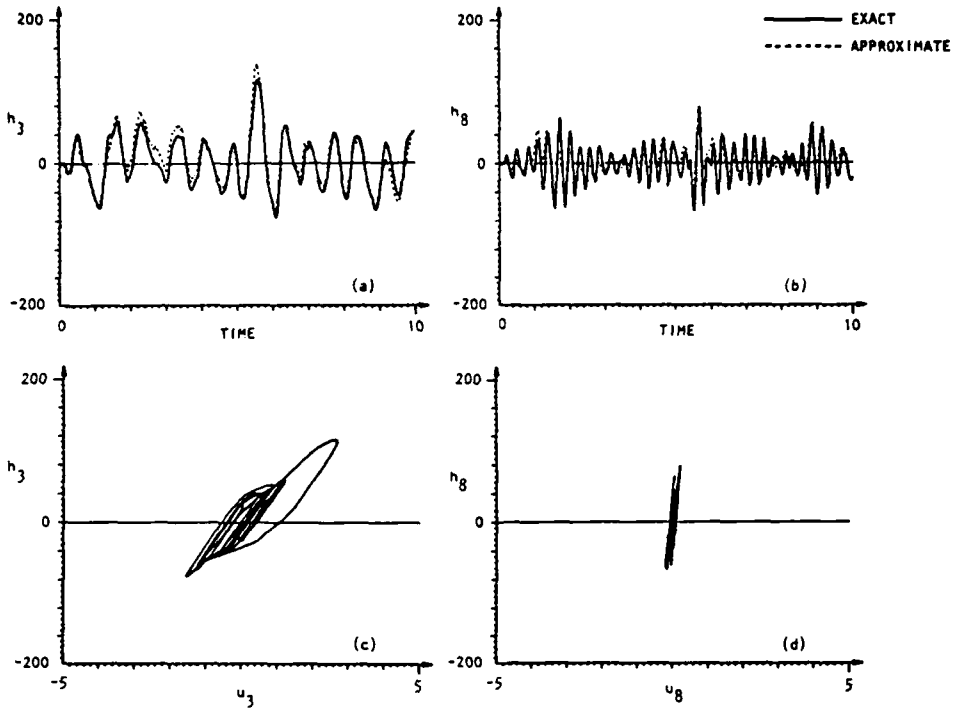

Fig. 5. Dominant generalized restoring forces $\underset{\sim}{h}(t)$ of reduced-order model.

$\hat{h}_3^{(1)}(v_1,v_2)$; $v_1 = u_3$; $v_2 = \dot{u}_3$

k \ ℓ	$T_0(v_2)$	$T_1(v_2)$	$T_2(v_2)$	$T_3(v_2)$
$T_0(v_1)$	32.1	36.5	4.42	2.64
$T_1(v_1)$	97.4	2.13	-2.19	0.83
$T_2(v_1)$	4.36	3.47	6.06	2.12
$T_3(v_1)$	-3.60	-3.55	5.78	0.67

$\hat{h}_8^{(1)}(v_1,v_2)$; $v_1 = u_8$; $v_2 = \dot{u}_8$

k \ ℓ	$T_0(v_2)$	$T_1(v_2)$	$T_2(v_2)$	$T_3(v_2)$
$T_0(v_1)$	13.7	9.0	6.5	-2.4
$T_1(v_1)$	49.4	-0.5	-5.3	1.8
$T_2(v_1)$	7.5	-0.6	2.3	1.4
$T_3(v_1)$	2.2	-1.0	-3.5	-0.2

Fig. 6. Coefficients $^{(j)}C_{k\ell}^{(i)}$ of two-dimensional Chebyshev series for the identification of modal restoring functions for the reduced-order nonlinear model.

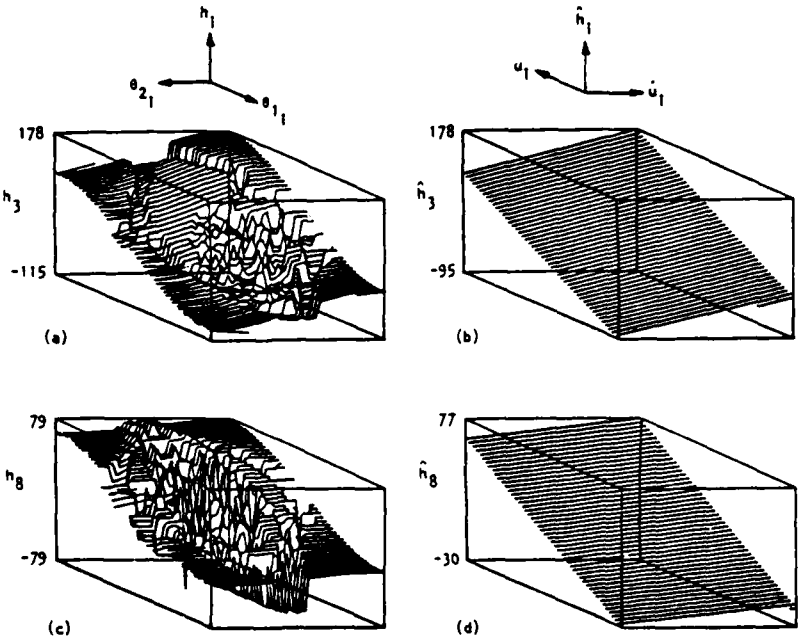

Fig. 7. Three-dimensional plots of the exact h_i and approximate $\hat{h}_i$.

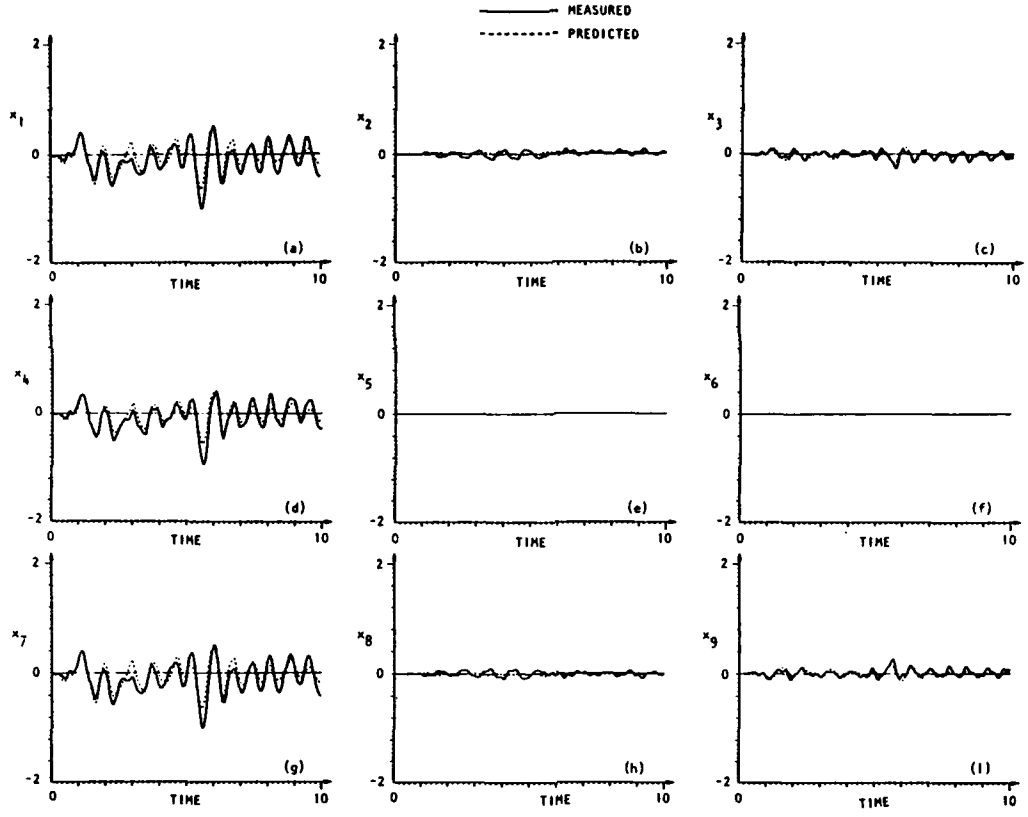

Fig. 8. Comparison between the measured and predicted displacement of the hysteretic system under nonstationary excitation by using a reduced-order model identified with a different stationary random excitation.

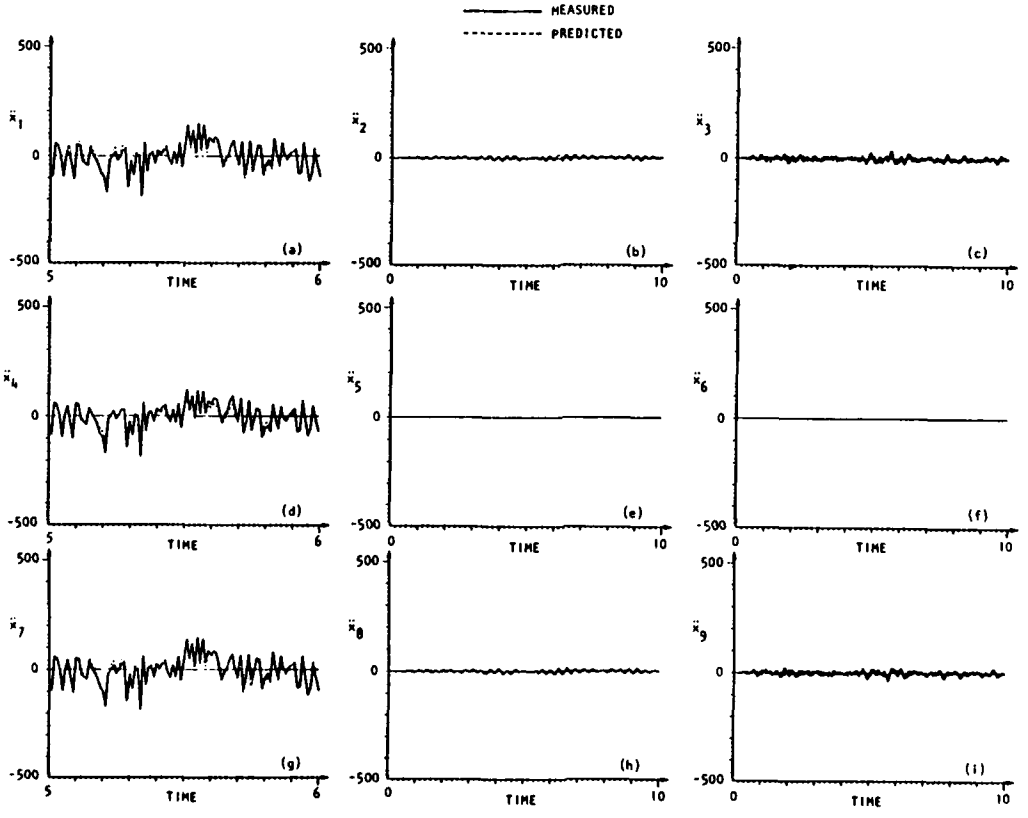

Fig. 9. Comparison between the measured and predicted acceleration of the hysteretic system under nonstationary excitation by using a reduced-order model identified with a different stationary random excitation.

EXTENDED DAMPING MODELS FOR VIBRATION DATA ANALYSIS

J. A. Fabunmi

Center for Rotorcraft Education and Research
Aerospace Engineering Department
University of Maryland

1. INTRODUCTION

Steady state vibratory response of structures to dynamic excitations is possible because of the mechanisms present in those structures which dissipate the energy that would otherwise cause the responses to grow without bounds. The theories that are used to analyze the vibration of structures, or interpret measured vibration data are only as good as the model adopted for characterizing the damping in the structure. An instructive discussion of the role of damping in vibration theory has been given by Crandall [1].

Nowadays, it has become accepted to use various techniques of Modal Analysis to study the vibration characteristics of a wide variety of structures, ranging from simple beams to complex Aerospace Structures [2]. These techniques have proven sufficiently powerful to the extent of identifying the resonant frequencies and "mode shapes" of most practical structures. However, only limited success has been achieved in predicting unmeasured mobilities or vibration levels. In applications such as Analytical Testing [3], Systems Identification [4] or Force Determination [5], to name a few, where these mobilities are the starting point for further analyses, there arises a need for more accurate damping models.

In current modal testing and analysis practice, two types of damping models are popular, based on viscous or hysteretic damping assumptions. They both lead to systems of constant coefficient linear differential equations of motion, from which the derivation of the mobility functions are straightforward [6]. In the quest for more comprehensive damping models, this paper reexamines the way in which damping considerations enter the equations of motion for steady vibrations. For single degree of freedom systems, Jacobsen [7] approximated a general velocity power damping law by a coefficient multiplying the first power of velocity, with the appropriate sign to assure energy dissipation. This coefficient turned out to depend on both frequency and response level, and was determined by matching the work dissipated per cycle of oscillation at any given frequency of excitation. The effectiveness of this approximation has since been established by exact analysis and experiment for zeroth and first power velocity damping laws [8].

An extension of this idea to a simple 3-degree of freedom system results in a frequency domain system of equations, with a damping matrix which depends on both frequency and response levels. These equations are investigated numerically to study how the departures from linear damping models affect the shape of the mobility functions, calculated as the ratio of response to excitation over a selected frequency band.

In mobility testing practice, a structure is said to behave "linearly" when the measured mobilities are independent of the excitation level. For such structures, it is possible to leave out the dependence of the damping matrix on the response levels. In the resulting equations, the damping matrix can have a general functional dependence on frequency, usually consisting of linear combinations of various frequency

powers. By suitably defining a set of complex valued vectors, termed "damped modes", it is shown that the mobility function can be expressed in the usual modal series form, suitable for modal analysis. The difference now is that the modal functions now have a more general dependence on frequency than the usual formulations. This permits the "tailoring" of the assumed damping laws to the actual behavior of a particular structure or class of structures. It then becomes possible to identify modal parameters which are most consistent with the measured data.

2. SPRING-MASS SYSTEM WITH GENERAL DAMPING

The extension of Jacobsen's approximation to multiple degree of freedom systems is developed by considering a simple arrangement of masses, springs and dampers shown in figure 1. Three lumped masses M_1, M_2 and M_3 are connected by linear springs K_1, K_2, K_3 and nonlinear dampers (C_1, n_1), (C_2, n_2) and (C_1, n_3); where the damping force of the jth damper is:

$$f_j = -C_j \left| \frac{dx}{dt} \right|^{n_j} \mathrm{SGN}\left(\frac{dx}{dt}\right) \qquad (1)$$

where $\left|\frac{dx}{dt}\right|$ is the magnitude of the relative velocity between the ports of damper and $\mathrm{SGN}\left(\frac{dx}{dt}\right)$ is its sign. The approximation consists of replacing equation (1) by:

$$f_j \simeq -C_j' \cdot \frac{dx}{dt} \qquad (2)$$

for harmonic motions. In appendix I, it is shown that during such motions; i.e.

$$x(t) = X \sin \omega t,$$

the damping force in equation (2) will dissipate the same amount of energy per cycle of oscillation if:

$$C_j' = \frac{2C_j}{\sqrt{\pi}} \frac{\Gamma\left(\frac{n_j+2}{2}\right)}{\Gamma\left(\frac{n_j+3}{2}\right)} X^{n_j-1} \omega^{n_j-1} \qquad (3)$$

where $\Gamma(\ )$ is the gamma function of the argument and ω is the frequency. Steady state forced response of the system in figure 1 is then determined by the following system of equations in the frequency domain:

$$(-\omega^2 [M] + [K] + i [D(\omega)])\{\bar{y}\} = \{\bar{N}\} \qquad (4)$$

where $\{N\} = \{\bar{N}\}e^{i\omega t}$ is the harmonic forcing vector, $\{y\} = \{\bar{y}\}e^{i\omega t}$ is the vector of displacements of the lumped masses from equilibrium and $\{\bar{y}\}$, $\{\bar{N}\}$ are complex valued vectors of the amplitudes of response and excitation respectively. The matrices in (4) are defined as follows:

$$[M] \equiv \begin{bmatrix} M_1 & 0 & 0 \\ 0 & M_2 & 0 \\ 0 & 0 & M_3 \end{bmatrix}$$

$$[K] \equiv \begin{bmatrix} K_1 + K_2 & -K_2 & 0 \\ -K_2 & K_2 + K_3 & -K_3 \\ 0 & -K_3 & K_3 \end{bmatrix}$$

$$[D(\omega)] \equiv \begin{bmatrix} D_1(\omega) + D_2(\omega) & -D_2(\omega) & 0 \\ -D_2(\omega) & D_2(\omega) + D_3(\omega) & -D_3(\omega) \\ 0 & -D_3(\omega) & D_3(\omega) \end{bmatrix}$$

where

$$D_1(\omega) \equiv \omega C_1'' \, |\bar{y}_1|^{n_1 - 1}$$

$$D_2(\omega) \equiv \omega C_2'' \, |\bar{y}_2 - \bar{y}_1|^{n_2 - 1}$$

$$D_3(\omega) \equiv \omega C_3'' \, |\bar{y}_3 - \bar{y}_2|^{n_3 - 1}$$

and

$$C_j'' \equiv \frac{2C_j}{\sqrt{\pi}} \frac{\Gamma\left(\frac{n_j + 2}{2}\right)}{\Gamma\left(\frac{n_j + 3}{2}\right)} \omega^{n_j - 1}$$

The notation $|( )|$ denotes the magnitude of the complex quantity ( ).

If the dampers obey a first power velocity law, equation (4) reduces to the familiar set of equations governing a viscously damped system. Relative to the [M] and [K] matrices, the elements of the $[D(\omega)]$ matrix are small, at most frequencies. However, in the neighborhood of an undamped natural frequency, when the $\omega^2[M]$ and [K] matrices neutralize each other, the role of $[D(\omega)]$ becomes pronounced. For lightly damped systems, this region is narrow, and the damping matrix can be replaced by the constant values assumed at that frequency. The resulting equations now resemble the hysteretic damping form. Although the physical arguments may be slightly different, the measured behavior of the structure agrees with these equations. In the study of structures with moderate levels of damping, both viscous and hysteretic damping models have been used with comparable success [6, 2].

2.1 Numerical Study

The system considered for numerical investigation of equations (4) consists of three uniform masses M, springs K and dampers (C, n). Let,

$$\omega_o^2 \equiv \frac{K}{M} \qquad \frac{\omega}{\omega_o} \equiv \tilde{\omega}, \qquad \{\bar{\mu}\} \equiv \frac{1}{M\omega_o^2} \{\bar{N}\}$$

$$\eta \equiv \frac{1}{\sqrt{\pi}} \frac{\Gamma\left(\frac{n + 2}{2}\right)}{\Gamma\left(\frac{n + 3}{2}\right)} \cdot \frac{C\omega_o^{n-2}}{M},$$

$$\begin{Bmatrix} \tilde{\bar{D}}_1(\omega) \\ \tilde{\bar{D}}_2(\omega) \\ \tilde{\bar{D}}_3(\omega) \end{Bmatrix} \equiv 2\eta\tilde{\omega}^{n} \begin{Bmatrix} |\bar{y}_1|^{n-1} \\ |\bar{y}_2 - \bar{y}_1|^{n-1} \\ |\bar{y}_3 - \bar{y}_2|^{n-1} \end{Bmatrix}$$

and
$$[D(\omega)] \equiv \begin{bmatrix} \tilde{\bar{D}}_1(\omega) + \tilde{\bar{D}}_2(\omega) & -\tilde{\bar{D}}_2(\omega) & 0 \\ \tilde{\bar{D}}_2(\omega) & \tilde{\bar{D}}_2(\omega) + \tilde{\bar{D}}_3(\omega) & -\tilde{\bar{D}}_3(\omega) \\ 0 & -\tilde{\bar{D}}_3(\omega) & \tilde{\bar{D}}_3(\omega) \end{bmatrix} ;$$

then for this uniform system, equation (4) can be written as:

$$\left[\begin{bmatrix} 2-\tilde{\omega}^2 & -1 & 0 \\ -1 & 2-\tilde{\omega}^2 & -1 \\ 0 & -1 & 1-\tilde{\omega}^2 \end{bmatrix} + i[\bar{D}(\tilde{\omega})] \right] \{\bar{y}\} = \{\bar{\mu}\} \qquad (5)$$

Equation (5) is solved numerically by a method outlined in appendix II, for selected ranges of $\tilde{\omega}$ between 0 and 2. This range of values can be shown to cover all the three possible resonances of the system. In order to simulate single point mobility testing, only one element of $\{\bar{\mu}\}$ is non zero. The value assigned to this element is used to specify the excitation level. The responses computed for each node are then ratioed to this number in order to obtain the displacement mobilities. The parameters varied in this study are:

μ_3: a measure of the excitation level at node 3
η: a measure of the damping ratio. (Note that when the damping exponent is unity, this quantity is exactly the ratio of viscous damping coefficient to the critical damping coefficient).
and n : the exponent in the assumed damping law.

3. MODAL ANALYSIS

Let a set of 'damped' modes of the system be defined by the following characteristic equation

$$([K] + i[D(\omega)])\{\phi\} = \lambda(\omega)[M]\{\phi\} \qquad (6)$$

$\{\phi\} = \{\phi^R\} + i\{\phi^I\}$ is the complex characteristic vector, which are here termed 'damped modes' in analogy to 'flutter modes' in aeroelasticity where similar equations are encountered (see, for example [9]). For combinations of $(\lambda_j(\omega), \{\phi\}_j)$ and $(\lambda_\kappa(\omega), \{\phi\}_\kappa)$ which satisfy equation (6), it follows that:

$$\{\phi\}_\kappa^T([K] + i[D(\omega)])\{\phi\}_j = \lambda_j(\omega)\{\phi\}_\kappa^T[M]\{\phi\}_j$$

and $$\{\phi\}_j^T([K] + i[D(\omega)])\{\phi\}_k = \lambda_k(\omega)\{\phi\}_j^T[M]\{\phi\}_\kappa \qquad (7)$$

where $\{\phi\}^T$ denotes the transpose of $\{\phi\}$. By virtue of the symmetry of the [K], [M] and [D(ω)] matrices, equation (7) leads to the following orthogonality relationships:

$$\{\phi\}_j^T[M]\{\phi\}_\kappa = m_j\delta_{jk}$$

and $$\{\phi\}_j^T([K] + i\,[D(\omega)])\{\phi\}_\kappa = (k_j + id_j(\omega))\delta_{jk} \qquad (8)$$

where $$m_j \equiv \{\phi\}_j^T\,[M]\{\phi\}_j$$

$$k_j \equiv \{\phi\}_j^T[K]\{\phi\}_j$$

$$d_j(\omega) \equiv \{\phi\}_j^T[D(\omega)]\{\phi\}_j$$

and $$\delta_{jk} = \begin{cases} 0 & j \neq k \\ 1 & j = k \end{cases}$$

From equations (6) and (8), it follows that

$$\{\phi\}_j^T\,([K] - \omega^2[M] + i[D(\omega)])\{\phi\}_k = (k_j - \omega^2 m_j + id_j(\omega))\delta_{jk} \qquad (9)$$

$$= (\lambda_j(\omega) - \omega^2)m_j\delta_{jk}$$

It has been shown in [3] that the frequency dependent characteristic numbers are of the form:

$$\lambda_j(\omega) = \Omega_j^2(1 + ig_j(\omega)) \qquad (10)$$

where Ω_j^2 is a nonnegative real number associated with the jth mode, and by considering the form of the [D(ω)] matrix, the function $g_j(\omega)$ can be expressed as:

$$g_j(\omega) = \alpha_{oj} + \sum_{k=1}^{N_d} \alpha_{kj}\omega^{n_k} \qquad (11)$$

Where, in general there may be N_d different damping exponents in the system, and α_{oj}, α_{kj}; $k = 1,2,\ldots N_d$ are damping coefficients associated with each damping power law.

If [φ] denotes a complex valued modal matrix, such that its jth column is the jth damped mode, equation (4) can be rewritten as:

$$\{\bar{y}\} = [\phi]([\phi]^T([K] - \omega^2[M] + i[D(\omega)])[\phi])^{-1} [\phi]^T\{\bar{N}\} \qquad (12)$$

Equations (9) and (10) can then be substituted into (12) to yield

$$\{\bar{y}\} = [\phi]\left[\frac{1}{m_j\Omega_j^2(1 - \frac{\omega^2}{\Omega_j^2} + ig_j(\omega))}\right] [\phi]^T\{N\} \qquad (13)$$

The matrix of displacement mobilities $[Y(\omega)]$ is defined by the following relationship:

$$\{\bar{y}\} = [Y(\omega)]\{\bar{N}\} \qquad (14)$$

Therefore, by comparison of equations (13) and (14)

$$[Y(\omega)] = \sum_{n=1}^{N\to\infty}\left[\frac{\{\phi\}_n\{\phi\}_n^T}{m_n}\right] \frac{1}{\Omega_n^2(1 - \frac{\omega^2}{\Omega_n^2} + ig_n(\omega))} \qquad (15)$$

Equation (15) expresses the mobility functions in form of a series of modal functions, summed over all the important modes in a given frequency band. The difference between this equation and existing modal series formulations is that the function $g_n(\omega)$ admits more general damping assumptions than just viscous or hysteretic damping.

4. DISCUSSION OF NUMERICAL RESULTS

The numerical results presented here were obtained by using equation (5) to simulate the process of single point mobility testing of the structure depicted in figure 1. Steady state excitation at coordinate #3 was simulated over selected frequency bands, and although the responses at all other coordinates were computed, in each case, only typical mobility plots for one coordinate is presented for the purposes of the present discussion.

Figure 2a shows the plot of Y_{31} displacement mobility over the range of $\tilde{\omega}$ between 0. and 2.0, with 60 computation points, for different damping ratios η= 0.02, 0.1 and 0.5, with constant forcing level $\mu_3 = 0.1$, and damping exponent $n = 1.2$. Y_{31} displacement mobility means the displacement response of coordinate #1 per unit forcing at coordinate #3. Due to the symmetry of the mass, stiffness and damping matrices, both Y_{31} and Y_{13} will yield the same results. As expected, increasing the damping ratio reduces the peak responses at resonance and broadens the band of influence of a given mode. A better definition of the behavior of the response around a given mode is achieved by increasing the number of computation points per frequency spacing. Thus, in figure 2b is a

narrower range of ω between 0.82 and 1.49 centered near the second resonant mode with 100 computation points, for the same Y_{31} mobility. Here, it is seen that the damping ratio, for the exponent of the damping law being considered, affects not only the level of response at resonance, but also the shape of the modal loop.

In fugres 3a and 3b, the effect of different forcing levels are shown: μ_3 = 0.1, 0.5, 1.0, 2.0 and 10.0, while the damping ratio μ = 0.1 and damping exponent n = 1.2 were held fixed. On the broad band plot, slight decreases in the peak mobility values with increasing force level are observed in regions close to the resonant modes. In mobility testing practice, considerable judgement about the linearity of the structure is based on comparisons of the measured mobilities at different force levels. If this is done using broad band data, many structures "pass" this linearity check. However, figure 3b shows that a narrow band plot, around a selected mode (here, mode #2), reveals that the forcing level affects not only the response level, but also the shapes of the curves at resonance. It is interesting to note that the decreasing mobility peaks with increasing force level has been reported during actual testing of helicopter-like structures [10]. When these calculations were repeated with an exponent of unity in the damping law, no difference in mobilities were observed at different force levels.

In figures 4a, 4b and 4c, the effect of different damping exponents on the displacement mobility Y_{33} are presented. The exponents considered were n = 1.2, 1.5, 2.0, and 3.0, while the damping raio η = 0.1 and force level μ_3 = 0.5 were kept the same. Again, it is seen that the broad band plot does not reveal much about the differences in the mobilities. Figures 4b and 4c, however, show that the different exponents result in different shapes of the mobility functions around the resonant modes. (The dotted lines in all of these plots are used to indicate areas where the convergence of the solution scheme was slow, and the computation was programmed to exit, in order to avoid run-away iterations). The modal loop departs from its circular form as the damping exponent is increased. In fact, the "flattening" of the circle, resembles a behavior that has often been blamed on signal processing errors. Although there is no doublt that signal processing errors can be very significant, it is nevertheless important to recognize that in some cases, the structure can be revealing more of its own nature than the model being used to analyse its responses.

It seems apparent from the foregoing discussions that departures of the modal loops from pure circles, may be indicative of damping mechanisms that are more general than viscous or hysteretic damping. Current efforts are being exerted on the methods for fitting equation (15) to these mobility functions, with the aim of establishing new techniques for identifying the modal parameters that are more consistent with damping mechanisms exhibited by a given structure. The results of these studies will be published at a later date.

5. CONCLUSIONS

A simple 3 degree of freedom spring-mass-damper system has been used to investigate the response of structural systems when the damping mechanisms are more general than viscous or hysteretic damping. A formulation of the modal series expression for the mobilities for such generally damped structures was also presented. This formulation allows the modelling of general damping behavior by means of a frequency dependent function, the form of which is indicative of the velocity power laws prevailing in the damping mechanism.

A numerical simulation of mobility testing of this simple structural model revealed trends in the mobility functions which are similar to those reported in the testing practice of damped complicated structures such as helicopters and the like. It was found that departures of the modal loops from pure circles may be due to the existence of non-linear damping mechanisms within the system. Linearity checks of broad band mobility data may not be sufficient to establish the degree to which a structure is exhibiting non-linear damping behavior. When the exponent of the velocity power law, prevailing in the damping behavior of a structure is larger than unity, it was found that the peak mobilities at resonance decrease with increasing excitation level.

Further research is needed to validate new modal analysis techniques for handling structures with damping behavior which departs significantly from viscous or hysteretic damping models.

ACKNOWLEDGEMENTS

This work is part of ongoing research funded by the United States Army Research Office, through the Center for Rotorcraft Education and Research at the University of Maryland, headed by Prof. Al Gessow. The author also wishes to acknowledge the computational facilities provided by the Computer Science Center of the same University.

REFERENCES

1. S.H. CRANDALL 1970 Journal of Sound and Vibration Vol. 11, No. 1. The role of damping in vibration theory.

2. VARIOUS AUTHORS 1982 Proceedings of the First International Modal Analysis Conference. Orlando, Florida.

3. W.G. FLANNELLY, J.A. FABUNMI and E.J. NAGY 1981 NASA CR 3429. Analytical Testing.

4. N. GIANSANTE, A. BERMAN, W.G. FLANNELLY, E.J. NAGY and J.A. FABUNMI 1981 Kaman Aerospace Corporation Report No. R-1631. Structural Systems Identification technology verification.

5. R. JONES, W.G. FLANNELLY, E.J. NAGY and J.A. FABUNMI 1981 Kaman Aerospace Corporation Report No. R-1625. Experimental Verification of Force Determination and Ground Flying on a full scale helicopter.

6. D.J. EWINS 1979 SEE Journal. Whys and Wherefores of Modal Testing.

7. L.S. JACOBSEN 1930 Trans. ASME Vol. 52, No. 15, APM 169-181. Steady forced vibration as influenced by damping.

8. J.P. DEN HARTOG 1931 Trans. ASME Vol. 53, No. 9, APM 107-115. Forced vibrations with combined coulomb and viscous friction.

9. A.V. SRINIVASAN and J.A. FABUNMI 1983 ASME Paper No. 83-GT-129. Cascade Flutter analysis of cantilevered blades.

10. D.J. EWINS 1983 Vertica. Vol. 7, No. 1. The effects of slight nonlinearities on of modal testing of helicopter-like structures.

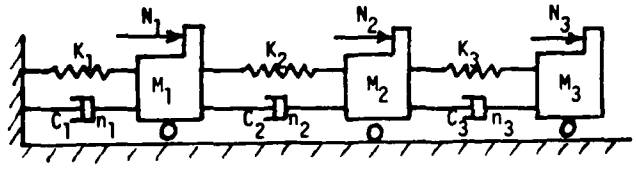

Note: Damping law of i^{th} damper is $f_d = \mp C_i \left(\frac{dx}{dt}\right)^{n_i}$

Figure 1. 3 DOF mass-spring-damper system with non-linear damping.

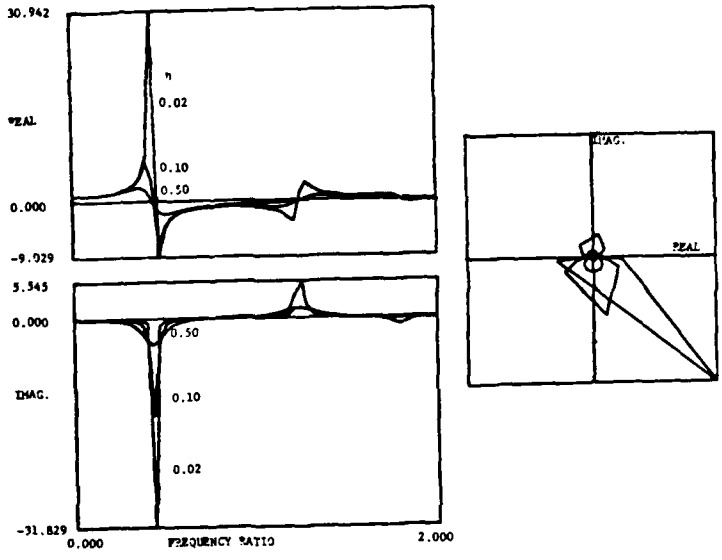

Figure 2a. Broad band plot of Y_{31} mobility, for different damping ratios. (n=1; μ_3=0.100)

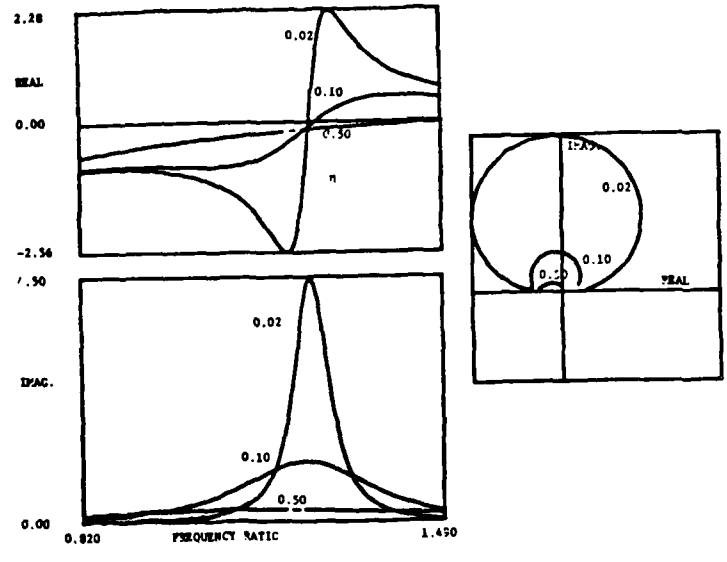

Figure 2b. Narrow band plot of Y_{31} mobility near the second mode, for different damping ratios. (n=1.2; μ_3=0.100)

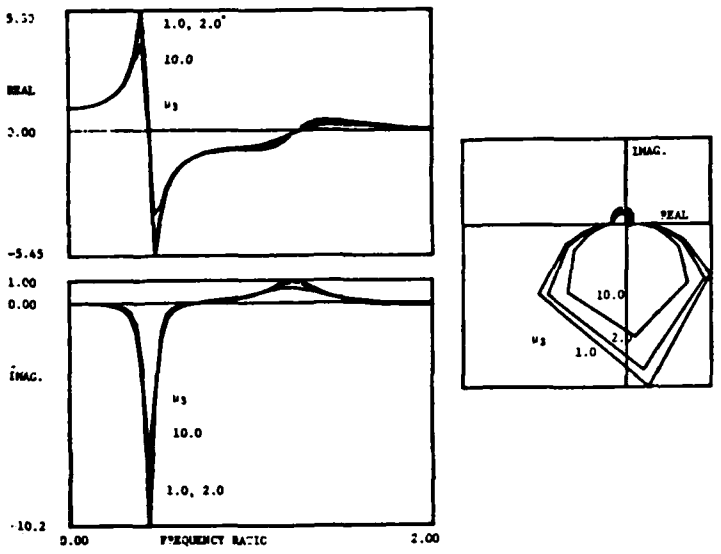

Figure 3a. Broad band plot of Y_{31} mobility, for different force levels. (n=1.2; η=0.10)

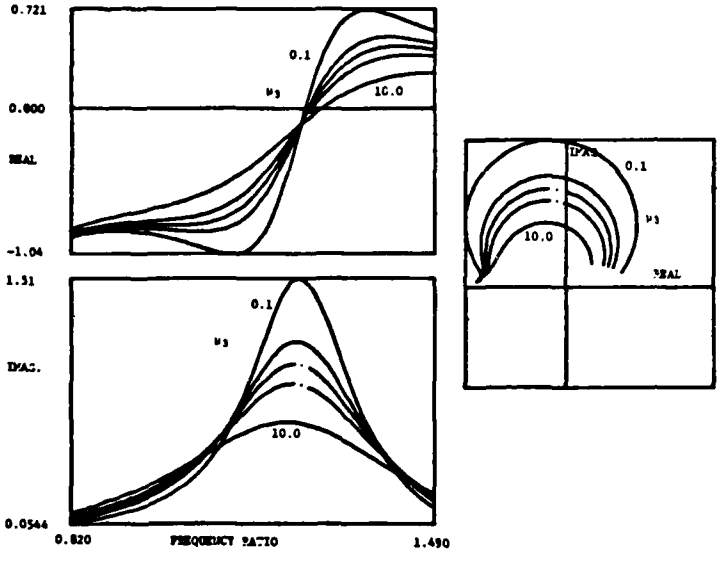

Figure 3b. Narrow band plot of Y_{31} mobility near the second mode, for different force levels. (n=1.2; η=0.10)

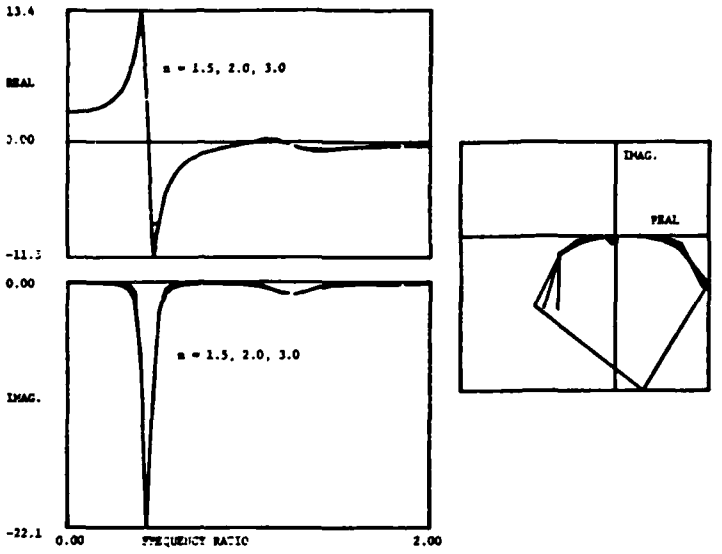

Figure 4a.
Broad band plot of Y_{33} mobility for different damping exponents. (η=0.10; μ_3=0.50)

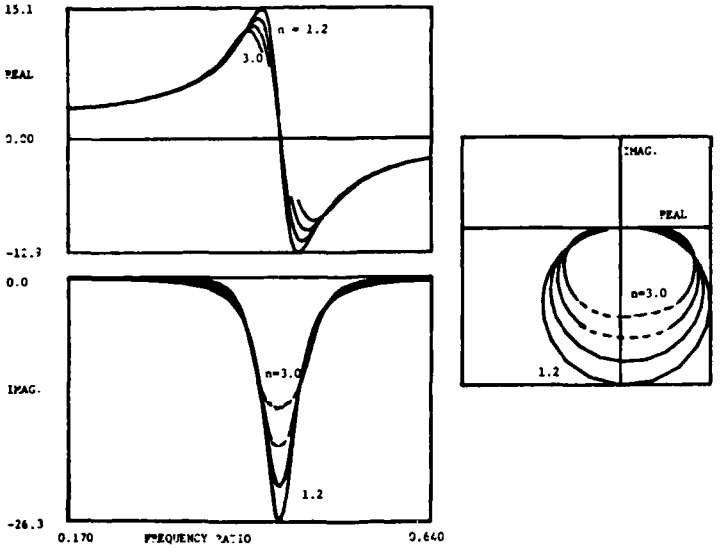

Figure 4b.
Narrow band plot of Y_{33} mobility near the first mode, for different damping exponents. (η=0.10; μ_3=0.50)

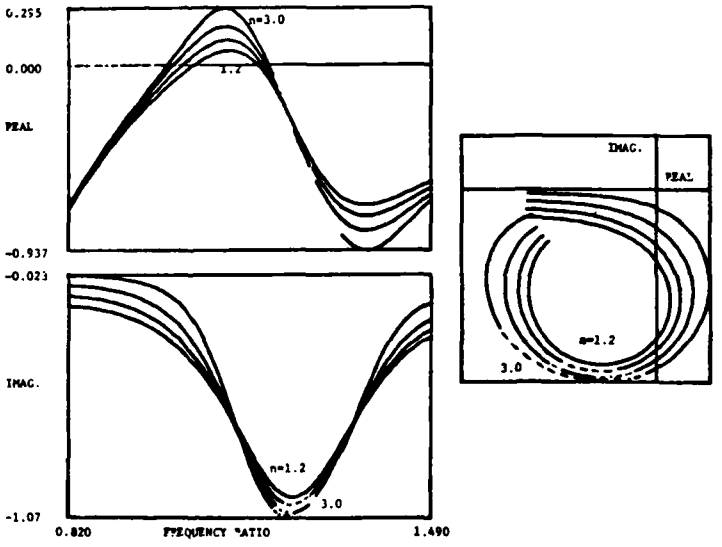

Figure 4c.
Narrow band plot of Y_{33} mobility near the second mode, for different damping exponents. (η=0.10; μ_3=0.50)

APPENDIX I

The energy dissipated per cycle of oscillation by the damping force given in equation (1) is:

$$W_n = C_n \int_0^{2\pi/\omega} \left(\frac{dx}{dt}\right)^{n+1} . dt \qquad \text{(I-1)}$$

For harmonic motions given by $x = X\sin(\omega t)$;

$$W_n = 4C_n X^{n+1} \omega^{n+1} \int_0^{\pi/2\omega} [\cos(\omega t)]^{n+1} \, dt \qquad \text{(I-2)}$$

It can be shown that:

$$\int_0^{\pi/2} [\cos(\theta)]^{2m+1} \, d\theta = \frac{\sqrt{\pi}}{2} \frac{\Gamma(m+1)}{\Gamma(m+3/2)} \qquad \text{(I-3)}$$

Hence, for $n = 2m$,

$$W_n = 4C_n X^{n+1} \omega^n \frac{\sqrt{\pi}}{2} \frac{\Gamma(\frac{n+2}{2})}{\Gamma(\frac{n+3}{2})} \qquad \text{(I-4)}$$

When $n = 1$, $W_1 = \pi C_1 X^2 \omega$. Therefore, the required coefficient of a first power velocity damping law that will make the dissipated energy equal that of a general power velocity damping law is:

$$C'_j = \frac{2}{\sqrt{\pi}} C_j \frac{\Gamma(\frac{n_j+2}{2})}{\Gamma(\frac{n_j+3}{2})} X^{n_j-1} \omega^{n_j-1} \qquad \text{(I-5)}$$

APPENDIX II

Let the response of node j at a selected frequency ratio be $y_j = y_j^R + iy_j^I$, and the j^{th} element of the forcing vector be $\mu_j = \mu_j^R + i\mu_j^I$. The solution to equation (5) can be sought as roots of the following non-linear system of equations:

$$\tilde{z}(x,\omega) = \begin{bmatrix} \tilde{[E(\omega)]} & -\tilde{[D(\omega,x)]} \\ \tilde{[D(\omega,\bar{x})]} & \tilde{[E(\omega)]} \end{bmatrix} \cdot \{\bar{x}\} - \{\mu'\} = 0 \qquad \text{(II-1)}$$

where, $\{x\}^T \equiv [y_1^R, y_2^R, y_3^R, y_1^I, y_2^I, y_3^I]$;

$\{u'\}^T \equiv [\mu_1^R, \mu_2^R, \mu_3^R, \mu_1^I, \mu_2^I, \mu_3^I]$;

$$[\tilde{E}(\tilde{\omega})] \equiv \begin{bmatrix} 2 - \tilde{\omega}^2 & -1 & 0 \\ -1 & 2 - \tilde{\omega}^2 & -1 \\ 0 & -1 & 1 - \tilde{\omega}^2 \end{bmatrix}$$

and $[D(\tilde{\omega},\bar{x})]$ is the same as $[\bar{D}(\tilde{\omega})]$ defined earlier, with the elements of the $\{\bar{x}\}$ vector placed appropriately.

Let a perturbed function be defined as:

$$\{z(J,\bar{x},\tilde{\omega})\} \equiv \{z(0,\bar{x},\tilde{\omega})\} + (\{z(\bar{x},\tilde{\omega})\} - \{z(0,\bar{x},\tilde{\omega})\})\frac{J}{N} \qquad \text{(II-2)}$$

where,
$$\{z(0,\bar{x},\tilde{\omega})\} = \begin{bmatrix} [E(\tilde{\omega})] & -[D(\tilde{\omega})] \\ 0 & \\ [D_0(\tilde{\omega})] & [E(\tilde{\omega})] \end{bmatrix} \{\bar{x}\} - \{\bar{u}'\} \qquad \text{(II-3)}$$

with

$$[D_0(\tilde{\omega})] \equiv 2\eta\tilde{\omega}^n \begin{bmatrix} 2 & -1 & 0 \\ -1 & 2 & -1 \\ 0 & -1 & 1 \end{bmatrix}$$

N is some selected integer, and J is also an integer which varies from 1 to N. It is apparent that $\{z(N,\bar{x},\tilde{\omega})\} = \{z(\bar{x},\tilde{\omega})\}$. The root of $\{z(J-1,\bar{x},\tilde{\omega})\} = 0, \{\bar{x}\}_{J-1}$ is a suitable starting vector for seeking the root of $\{z(J,x,\omega)\} = 0$, using the well known second order convergent Newton-Raphson scheme, whereby:

$$\{\bar{x}^{k+1}\}_J = \{\bar{x}^k\}_J - \left[\frac{\partial\{z\}^k}{\partial\{x\}}\right]^{-1}_J \{z(J,\bar{x}^k,\tilde{\omega})\} \qquad \text{(II-4)}$$

The matrix $\left[\frac{\partial\{z\}^k}{\partial\{x\}}\right]$ is the Jacobian of the $\{z\}$ vector with respect to the $\{x\}$ vector, evaluated with the $\{\bar{x}^k\}_J$ values.

With $\{\bar{x}^0\}_J = \{\bar{x}\}_{J-1}$, equation (II-4) is iterated until suitable convergence is achieved. The final solution for J = N, is the desired root of quation (II-1).

9. NON LINEAR DYNAMICS OF PLATES

NON-STATIONARY RESPONSES OF NON-LINEAR RECTANGULAR PLATES DURING TRANSITION THROUGH PARAMETRIC RESONANCES, PART 1: THEORY

G.L. Ostiguy
Ecole Polytechnique
Montréal, Canada

and

R.M. Evan-Iwanowski
Syracuse University
Syracuse, N.Y.

1. INTRODUCTION

When a rectangular plate sustains an in-plane load of the form $N_y(t) = N_{yo} + N_{yt} \cos \eta t$, where $\cos \eta t$ is a harmonic function of time, parametric resonances may occur for some combinations of the natural frequencies of the plate, Ω_i, and the excitation parameters N_{yo}, N_{yt}, and η. In general, these parameters are considered to be constant and the resulting oscillatory motion is referred to as stationary.

When the external excitation parameters, N_{yt} or η, vary with time, we encounter the case of non-stationary response. The non-stationary characteristics of the excitation are commonly encountered in practice and the study of non-stationary response is very important in properly evaluating the transition through resonance and for predicting the response when, in a dynamic system, parameters are changing with time.

Parametric vibration of columns, plates and shells loaded by axial periodic forces has received considerable attention in the literature. Most authors have treated the instability or steady-state response aspects of the problem, whereas little attention has been given to the transient or non-stationary response of the stable problem. Stationary responses of non-linear rectangular plates were studied by Ostiguy and Evan-Iwanowski [1,2].

Broadly speaking, non-stationary mechanical systems are those systems whose parameters, such as mass, stiffness, material properties, frequency or amplitude of external perturbation, are time dependent. Apparently, Lewis [3] was the first to present a solution for the response of a non-stationary, linear, single-degree-of-freedom system whose frequency is a linear function of time. An outstanding contribution in this field of mechanics was made by the Russian school. An extensive treatment of non-stationary responses of mechanical systems is presented in an excellent monograph by Mitropolskii [4]. More recently, Evan-Iwanowski [5] has provided a comprehensive treatment of non-stationary and non-linear vibrations in multiple-degree-of-freedom systems.

Previous investigations of non-stationary response of continuous mechanical systems (structures) have been concentrated on several problems including transverse-torsional vibrations of beams, rotating shafts and blades, behaviour of gyroscopic systems, and parametrically-excited columns and cylindrical shells. The only known work on the non-stationary parametric response of rectangular plates is analytical in nature and is due to Panton [6].

The present work deals with the problem of the non-stationary parametric response of non-linear rectangular plates simply supported along its edges and subjected to the action of periodic in-plane forces uniformly distributed along two opposite edges. The non-stationary response of the plate during a logarithmic sweep of the excitation frequency through a system resonance is evaluated for a wide variety of cases. The validity of these results is ascertained experimentally [7].

2. FORMULATION OF THE PROBLEM

2.1 Analytical Model

The mechanical system under investigation is a rectangular plate simply supported along its edges and acted upon by periodic in-plane forces, as shown in Figure 1. The xy plane is selected in the middle plane of the plate and the origin at its center. In-plane loading, uniformly distributed along two opposite edges, is of the following form:

$$N_y(t) = N_{yo} + N_{yt} \cos \theta(t) \tag{1}$$

where $\dot{\theta}(t) = d\theta/dt = \eta(t)$ is the instantaneous frequency of excitation.

The plate is initially flat, of uniform thickness, elastic, homogeneous and isotropic. It is also assumed that the plate thickness h and the resulting displacements are small compared with the wavelength of lateral vibrations. This assumption allows us the use of thin plate theory. Consequently, we can assume that the loading frequencies over which parametric (lateral) vibrations occur are considerably below the natural frequencies of longitudinal (in-plane) vibrations, and in-plane inertia forces can be neglected.

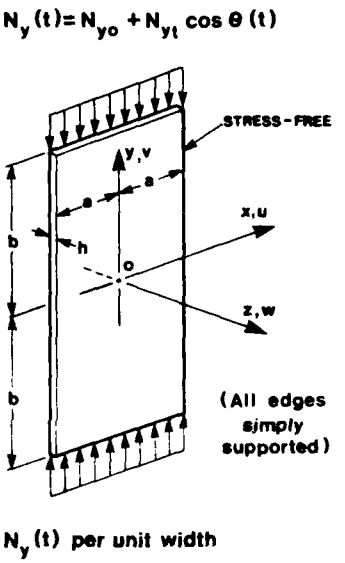

Figure 1. Plate and load configuration

2.2 Basic Equations

The plate theory used in this analysis may be described as the dynamic analogue of the von Karman large-deflection theory and is derived in terms of the stress function F and the lateral displacement w. When in-plane inertia is neglected, the basic equations governing the non-linear vibrations of rectangular plates are reduced to the following set of equations:

$$\nabla^4 F = E \left[w,_{xy}^2 - w,_{xx} w,_{yy} \right] \tag{2a}$$

$$\nabla^4 w = \frac{h}{D} \left[F,_{yy} w,_{xx} + F,_{xx} w,_{yy} - 2F,_{xy} w,_{xy} - \rho w,_{tt} \right] \tag{2b}$$

where the Airy stress function is defined by

$$F,_{yy} = \sigma_x, \quad F,_{xx} = \sigma_y, \quad -F,_{xy} = \tau_{xy}. \tag{3}$$

In these equations, σ_x, σ_y and τ_{xy} are membrane stresses, ρ is the density, $D = Eh^3/(1 - \nu^2)$ is the flexural rigidity of the plate, E and ν are Young's modulus and Poisson's ratio, respectively. Subscripts following a comma stand for partial differentiation and the operator $\nabla^4 = \partial^4/\partial x^4 + 2\partial^4/\partial x^2 \partial y^2 + \partial^4/\partial y^4$.

The in-plane loading, $N_y(t)$, combined with the stretching of the middle surface owing to large deflections of the plate give rise to in-plane or membrane forces per unit length N_x, N_y and N_{xy}. These forces are related to the membrane streses by

$$N_x = h\sigma_x, \quad N_y = h\sigma_y, \quad N_{xy} = h\tau_{xy}. \tag{4}$$

The in-plane loading, acting on the boundary, is taken into account in the boundary conditions.

2.3 Boundary Conditions

Rectangular plates considered in this study are simply supported on all four edges and, consequently, the lateral deflections and the moments at the four edges of the plate are zero. This can be expressed in terms of w as follows:

$$w = w_{,xx} + \nu\, w_{,yy} = 0 \qquad \text{along } x = \pm a, \tag{5a}$$

$$w = w_{,yy} + \nu\, w_{,xx} = 0 \qquad \text{along } y = \pm b. \tag{5b}$$

The external in-plane forces acting on the plate are uniformly distributed along two opposite edges ($y = \pm b$), as shown in Figure 1. The two vertical supported edges ($x = \pm a$) are stress-free. These stress conditions may be expressed in terms of the stress function F as follows:

$$F_{,yy} = 0, \qquad F_{,xy} = 0 \qquad \text{along } x = \pm a, \tag{6a}$$

$$F_{,xx} = -N_y(t)/h, \qquad F_{,xy} = 0 \qquad \text{along } y = \pm b. \tag{6b}$$

The problem consists in determining functions F and w which satisfy the governing equations, together with the boundary conditions.

2.4 DERIVATION OF TEMPORAL EQUATIONS OF MOTION

In general, a rectangular plate subjected to parametric excitation may exhibit lateral vibrations in several spatial modes; each spatial mode is associated with an infinite number of temporal modes. In the present analysis we establish the boundaries of the principal instability region and determine the amplitude of motion in a resonant regime for each spatial mode.

An approximate solution of the governing equations (2a) and (2b) is obtained, in the case of standing flexural waves, by assuming:

$$F(x,y,t) = \sum_m \sum_n f_{mn}(t)\, X_m(x)\, Y_n(y) - x^2 N_y(t)/2h \tag{7a}$$

$$w(x,y,t) = w_{pq}(t)\, \Phi_p(x)\, \Psi_q(y) \tag{7b}$$

where $f_{mn}(t)$ are the time-dependent load factors and $w_{pq}(t)$ are the time-dependent generalized coordinates of the system. The indices p and q correspond to the number of half-waves in the direction of axes Ox and Oy, respectively. The spatial functions $X_m(x)$, $\Phi_p(x)$, $Y_n(y)$ and $\Psi_q(y)$ are assumed to be orthogonal in their respective intervals and to satisfy the relevant boundary conditions.

Because the theory of dynamic stability comprises both the static stability and vibration theories, it is customary to use either the eigenfunctions of free vibration or static stability as coordinate functions for approximate representation of solutions. When a flat rectangular plate is compressed in its middle plane by forces uniformly distributed along two opposite edges, the eigenfunctions for free vibration and static stability are identical. Furthermore, the plane buckles in such a way that there can be several half-waves in the direction of compression but only one half-wave in the perpendicular direction.

Previous considerations, experimental evidence, and boundary conditions requirements led to the selection of the following spatial forms for use in this study:

$$X_m = \cosh \alpha_m x/\cosh \alpha_m a - \cos \alpha_m x/\cos \alpha_m a, \qquad m = 1,2,\ldots$$
$$Y_n = \cosh \beta_n y/\cosh \beta_n b - \cos \beta_n y/\cos \beta_n b, \qquad n = 1,2,\ldots \tag{8a}$$

and $\Phi_p = \cos p\pi x/2a, \qquad p = 1; \qquad \Psi_q = \begin{cases} \cos q\pi y/2b, & q = 1,3,\ldots \\ \sin q\pi y/2b, & q = 2,4,\ldots \end{cases}$ (8b)

where α_m and β_n are obtained from the transcendental equations

$$\text{(i)} \quad \tanh \alpha_m a + \tan \alpha_m a = 0, \qquad \text{(ii)} \quad \tanh \beta_n b + \tan \beta_n b = 0. \tag{9}$$

Substituting expressions (7) into governing equations (2) and using the orthogonality properties of the assumed functions, equations (2a) and (2b) can be reduced to:

$$\text{(a)} \ \sum\sum A_{mn}X_mY_n = \sum\sum B_{mn}X_mY_n; \qquad \text{(b)} \ C_{pq}\Phi_p\Psi_q = D_{pq}\Phi_p\Psi_q, \tag{10}$$

Equating coefficients of like spatial forms, one obtains

$$\text{(a)} \ A_{mn} = B_{mn}; \qquad \text{(b)} \ C_{pq} = D_{pq}, \tag{11}$$

where A_{mn} include f-coefficients, B_{mn} and C_{pq} include w-coefficient and D_{pq} include f and w-coefficients and terms corresponding to the in-plane loading and the lateral inertia of the plate.

Equations (11a) relate the f-coefficients to the w-coefficient. The solution of (11a) can be represented in the form

$$f_{mn} = F_{mn}\, E\, w_{pq}^2 \tag{12}$$

where coefficients F_{mn} depend on the plate aspect ratio and on the spatial mode of vibration being studied. The substitution of expressions (12) into equation (11b) along with the introduction of a convenient set of parameters result in the following second-order non-linear differential equation with periodic coefficients for the large amplitude parametric vibrations of rectangular plates in any spatial mode (p,q)

$$\ddot{w}_{pq} + \Omega_{pq}^2 \left[1 - 2\mu_{pq} \cos \theta(t)\right] w_{pq} + \gamma_{pq} w_{pq}^3 = 0, \tag{13}$$

where the dots denote differentiation with respect to time, and

$$\text{(a)} \ \omega_{pq} = \left[\pi^2/4a^2 r\right]\left[rp^2 + q^2/r\right]\sqrt{D/\rho h}$$

$$\text{(b)} \ N_{pq} = \left[\pi^2 D/4a^2q^2\right]\left[r^2p^4 + 2p^2q^2 + q^4/r^2\right]$$

$$\text{(c)} \ \Omega_{pq} = \omega_{pq}\sqrt{1 - N_{yo}/N_{pq}} \qquad \text{(d)} \ \mu_{pq} = N_{yt}/2\left[N_{pq} - N_{yo}\right] \tag{14}$$

and $r = b/a$ is the plate aspect ratio.

In the foregoing, ω_{pq} is the free vibration frequency of the unloaded plate, N_{pq} represents the static critical load according to linear theory and Ω_{pq} is the natural frequency of lateral vibration of a plate loaded by a constant component of axial force. The quantity μ_{pq} is called the excitation (or load) parameter, and γ_{pq} is the coefficient of non-linear elasticity. For further details, see [1,8].

Introducing viscous damping, the differential equation for the damped vibrations of the plate in any spatial mode (p,q) is written as

$$\ddot{w}_{pq} + 2C_{pq}\dot{w}_{pq} + \Omega_{pq}^2 \left[1 - 2\mu_{pq} \cos \theta(t)\right] w_{pq} + \gamma_{pq} w_{pq}^3 = 0, \qquad (p = 1,\ q = 1,2,3,\ldots). \tag{15}$$

Since equation (15) has the same general form for all spatial modes of vibration, the subscripts p and q may be omitted for simplification and we obtain

$$\ddot{w} + 2C\dot{w} + \Omega^2 \left[1 - 2\mu \cos \theta(t)\right] w + \gamma w^3 = 0. \tag{16}$$

Equation (16) constitutes the final form assumed by the equation of motion, which may be considered as an extension of the standard Mathieu-Hill equation.

3. SOLUTION OF THE TEMPORAL EQUATION OF MOTION

3.1 First-Order Asymptotic Approximation

In non-stationary problems the coefficients in the equations of motion are time-dependent. Mathematical techniques available for explicit solutions of such problems are relatively limited, and approximate techniques are used. The methods of asymptotic expansions in powers of a small parameter ε, developed by Mitropolskii [4] and generalized by Agrawal and Evan-Iwanowski [9], are a most effective tool for studying non-linear vibrating systems with slowly varying parameters.

Assuming that the damping, the excitation and the non-linearity are small and that the instantaneous frequency of excitation and the excitation parameter vary slowly with time, the temporal equation of motion (16) can be written in the following asymptotic form:

$$\ddot{w} + \Omega^2 w = \varepsilon\left[2\mu(\tau) \cos \theta(t)\, w - \gamma w^3 - 2C\dot{w}\right] \tag{17}$$

where $\tau = \varepsilon t$ represents the slowing time.

Confining our attention to the investigation of principal parametric resonance $\eta \simeq 2\Omega$, we seek a first-order asymptotic solution of equation (17) in the following form:

$$w = W \cos\left(\tfrac{1}{2}\theta + \psi\right) \tag{18}$$

where W and ψ are functions of time defined by the system of differential equations

$$\begin{aligned} \frac{dW}{dt} &= \varepsilon\, A_1(\tau, W, \psi) \\ \frac{d\psi}{dt} &= \Omega - \tfrac{1}{2}\eta(\tau) + \varepsilon B_1(\tau, W, \psi). \end{aligned} \tag{19}$$

Functions $A_1(\tau, W, \psi)$ and $B_1(\tau, W, \psi)$ are selected in such a way that equation (18) would, after replacing W and ψ by the functions defined in equation (19), represent a solution of equation (17).

Following the general scheme of constructing asymptotic solutions for vibrating systems, we arrive at the following coupled first-order differential equations for the unknown quantities A_1 and B_1:

$$\begin{aligned} \left[\Omega - \tfrac{1}{2}\eta\right] \partial A_1/\partial\psi - 2W\Omega B_1 &= W\Omega^2\mu \cos 2\psi - \tfrac{3}{4} W^3\gamma, \\ \left[\Omega - \tfrac{1}{2}\eta\right] W\, \partial B_1/\partial\psi + 2\Omega A_1 &= -W\Omega^2\mu \sin 2\psi - 2W\Omega C. \end{aligned} \tag{20}$$

By inspection, the solution of these two equations that characterize the response of our system is observed to be

$$\begin{aligned} A_1 &= -\left[W\Omega^2\mu(\tau)/\eta(\tau)\right] \sin 2\psi - WC \\ B_1 &= -\left[\Omega^2\mu(\tau)/\eta(\tau)\right] \cos 2\psi + \left[3\gamma/8\Omega\right] W^2. \end{aligned} \tag{21}$$

Using these values and transforming all system parameters back to their real time values, the expressions for $\dot{W}$ and $\dot{\psi}$ become

$$\dot{W} = - \left[\Omega^2 \mu(\tau)/\eta(\tau)\right] W \sin 2\psi - WC ,$$
$$\dot{\psi} = \Omega - \tfrac{1}{2}\eta(\tau) - \left[\Omega^2 \mu(\tau)/\eta(\tau)\right] \cos 2\psi + \left[3\gamma/8\Omega\right] W^2 . \qquad (22)$$

These relationships define the rate of change of amplitude and phase angle as functions of the slowly varying frequency of external periodic excitation $\eta(\tau)$, slowly varying excitation parameter $\mu(\tau)$, $W(t)$ and $\psi(t)$. By integrating this system of equations, the amplitude $W = W(t)$ and the phase angle $\psi = \psi(t)$ can be obtained as functions of time. The lateral displacement $w = w(t)$, which completely describes the non-stationary vibrational process, can then be found from equation (18) in the first approximation.

3.2 Stationary Response

The stationary response and the boundaries of the principal region of parametric instability associated with each spatial form of vibration may be calculated as a special case of the non-stationary motion in the resonant regime described by equations (18) and (22).

For obtaining stationary values of the amplitude W and phase ψ, we equate to zero the right-hand sides of equations (22). Eliminating ψ and solving for W as a function of the excitation frequency η, we obtain

$$W = \sqrt{[8\Omega/3\gamma]\left[- (\Omega - \tfrac{1}{2}\eta) \pm \sqrt{(\mu^2\Omega^4/\eta^2) - C^2}\right]} , \qquad (23)$$

where we admit only positive real values for the amplitude. The $\pm$ sign upon the inner radical indicates the possibility of two solutions. These solutions are represented in Figure 2. A stability analysis [8] has shown that one solution (upper branch) is stable and attainable by the system while the other solution (lower branch) is unstable and not physically realizable.

The stationary phase angle ψ may be determined from the first of equations (22). This gives

$$\psi = \tfrac{1}{2} \sin^{-1} (-C\eta/\mu\Omega^2) \qquad (24)$$

where $0 \geq \psi > - \pi/4$ for positive damping ($C > 0$).

Equation (23) shows that the amplitude of the stationary response depends basically on two factors at any frequency η. First, it depends on the magnitude of the non-linear term of the system, which in this case is the elasticity parameter γ. Second, it depends on the magnitudes of the loading and damping parameters, μ and C, respectively. The non-linear term controls the so-called backbone curve. The backbone of the stationary response is that curve lying halfway between stable and unstable branches. For the system under consideration, γ is strictly positive and the backbone has a right-hand overhang, indicating a hard spring system response.

In equation (23) the inner radical has to be real in order that the physical amplitude of the response W be real. This results in the following condition :

$$C \leq (\mu\Omega/2)(2\Omega/\eta) \qquad (25)$$

which states that the loading parameter μ must be sufficiently large to overcome the effect of the damping forces acting on the plate. Otherwise, no physically realizable solution exists.

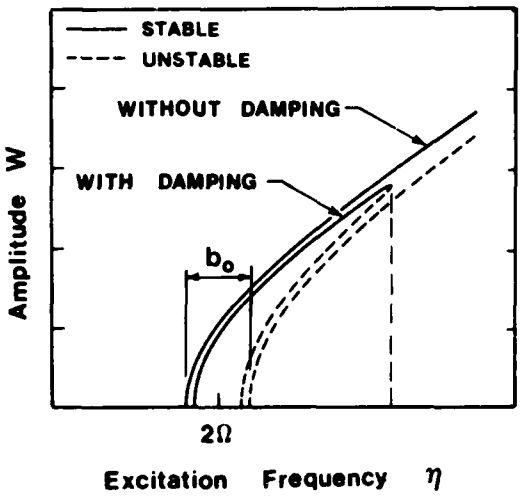

Figure 2. Stationary response curves

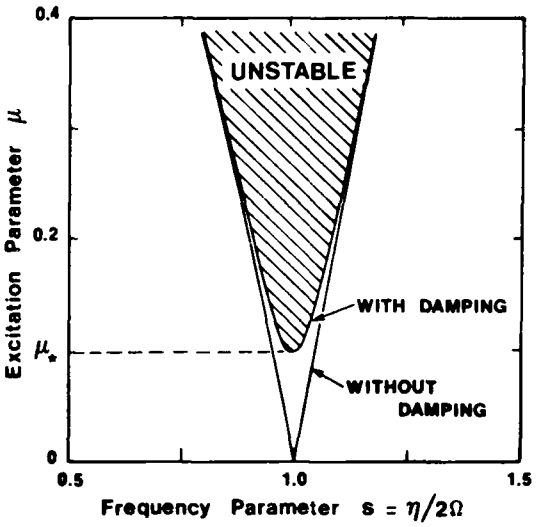

Figure 3. Principal region of parametric instability

The base width of the stationary response is the only region in which vibrations may normally initiate. By setting $W = 0$, we obtain

$$\eta^4 - 4\Omega\eta^3 + 4\,(\Omega^2 + C^2)\,\eta^2 - 4\mu^2\Omega^4 = 0. \tag{26}$$

Intoducing the frequency parameter s and decrement of damping Δ defined by

$$\text{(a)}\quad s = \eta/2\Omega\ , \qquad \text{(b)}\quad \Delta = 2\pi C/\Omega\ , \tag{27}$$

equation (26) can be written as

$$s^4 - 2s^3 + \left[1 + \Delta^2/4\pi^2\right] s^2 + \mu^2/4 = 0. \tag{28}$$

Equation (28) makes it possible to calculate the boundaries of the principal region of instability (Figure 3). If damping is negligible ($\Delta = 0$), the roots of this equation can be found explicitly. By performing elementary operations, we obtain

$$s = \tfrac{1}{2}\left[1 + \sqrt{1 \pm 2\mu}\right] \quad \text{or} \quad \eta_* = \Omega + \Omega\sqrt{1 \pm 2\mu}. \tag{29}$$

Thus, the maximum base width b_o of the stationary reponse is

$$b_o = \Omega\left[\sqrt{1 + 2\mu} - \sqrt{1 - 2\mu}\right]. \tag{30}$$

3.3 Non-stationary Motion During Transition Through Resonance

The main objective in the studies of non-stationary systems is the determination of deviations of non-stationary responses from corresponding responses of equivalent stationary systems, i.e. systems whose parameters are constant. It is expected that the most pronounced differences in the responses of stationary and non-stationary systems will occur near the resonances or near the resonance zones of these systems.

The non-stationary response is obtained by numerically integrating equations (22) governing W and ψ. It may be pointed out that numerical integration of first-order equations governing amplitude and phase is a much simpler process than integration of the original second-order equation of motion since we have to evaluate the envelope of an oscillatory function and not the function itself.

In the present non-stationary analysis, the sweep of the excitation frequency is taken to be logarithmic as given by

$$\eta(t) = \eta_o[2^{mt}]$$

where η_o is the initial frequency (at $t = 0$), m is the rate of sweep (in octaves per unit of time) and t is the time. The rate of sweep m may be positive or negative; in the former case, the sweep is in the direction of increasing frequencies.

The system of differential equations (22) is integrated numerically using a fourth-order Runge-Kutta algorithm due to Gill (Subroutine DRKGS from IBM). The initial values of the variables W, ψ and η are chosen as those corresponding to a stationary case.

4. NUMERICAL RESULTS AND DISCUSSION

The non-stationary response of the plate during a logarithmic sweep of the excitation frequency $\eta(t)$ through a principal parametric resonance was studied for a wide variety of cases and the results shown in Figures 4-7 are typical of those obtained. To show the non-stationary deviations from stationary results, the latter are plotted along with the non-stationary results. The specified values of the plate parameters and material constants used for the numerical calculations are given in Table 1, and correspond to those of a particular test plate used during the experimental investigation [7].

TABLE 1. Specifications of Plate Parameters

Test Plate	Material	E (GPa)	ν	ρ (kg/m^3)	Dimensions (mm)	Aspect ratio r
E.1	Acrylic*	4.41	0.38	1188	292 x 406 x 1.60	1.39

*Polymethyl Methacrylate

The main parameters responsible for the modification of the parametric responses in non-stationary regimes are the conditions of in-plane loading, the amount of damping, the initial stationary amplitude, and the rate as well as direction of the sweep. It is obvious from the results shown in Figures 4-7 that the rate of sweep of the excitation frequency η in the direction of the overhang may play a significant role in the modification of the non-stationary response. When the frequency sweep is relatively slow, the non-stationary response simply follows the stable branch of the stationary response. As the sweep rate is increased the lag in amplitude build-up at the start increases but the response eventually catches up with the stationary curve. For rapid increasing transitions, the non-stationary response increases somewhat inside the resonance zone but returns rapidly to the zero-amplitude stable position afterwards. When the sweep is in the opposite direction to the overhang, the influence of the sweep rate is much less pronounced.

The results exhibited in Figures 4 and 5 show that, in the absence of damping, the amplitude and the phase display significant "beating" effects. These rapid changes overshoot the curves of the stationary case. When a small amount of damping is present, damped "beats" of smaller amplitude about the stationary curve are experienced after the first maxima, eventually becoming asymptotic to the stationary curve as the transition continues. If damping is sufficiently large, the "beat" phenomenon is almost completely eliminated.

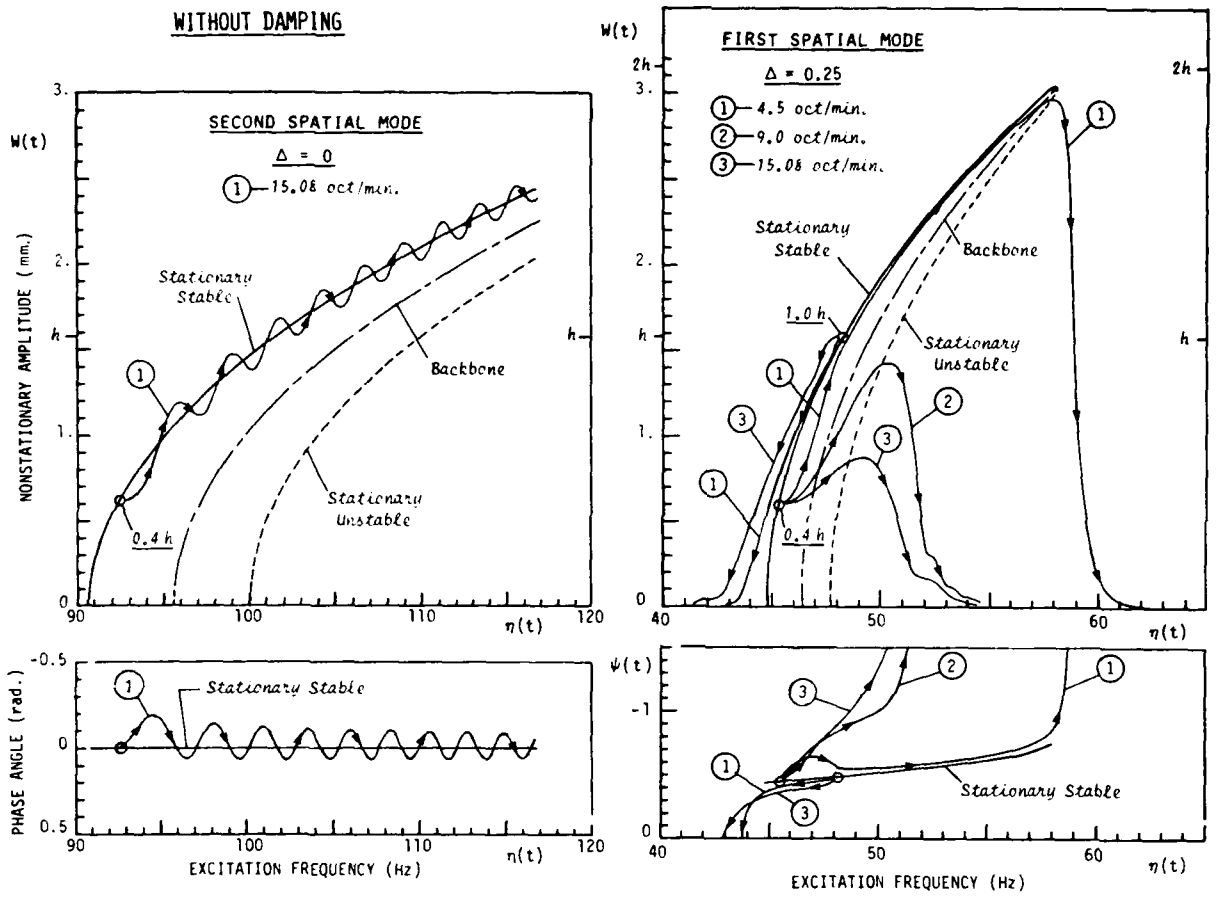

Figure 4. Non-stationary parametric response of a rectangular plate.

The results presented in Figures 6 and 7 indicate that an increase in the initial amplitude of vibration or the in-plane loading has a significant destabilizing influence on the system when the sweep is into the instability zone (increasing frequency). It was observed, however, that the value of the initial amplitude or the in-plane loading, has a negligible effect on the non-stationary response when the sweep is away from the instability region [8].

5. CONCLUSIONS

Based on the results of this investigation, the following conclusions can be drawn :

1) The theory developed correctly predicts the stationary and the non-stationary response of rectangular plates within a principal region of instability.

2) Stationary parametric responses exhibit the typical hard spring effect with the upper curve being stable.

3) The non-stationary response to a logarithmic sweep of the excitation frequency through a resonance displays a "beat" effect; however, if damping is sufficiently large, the "beat" phenomenon is almost completely eliminated.

4) The main parameters responsible for the modification of the parametric response in non-stationary regimes are the conditions of in-plane loading, the amount of damping, the initial stationary amplitude, and the rate as well as the direction of the sweep.

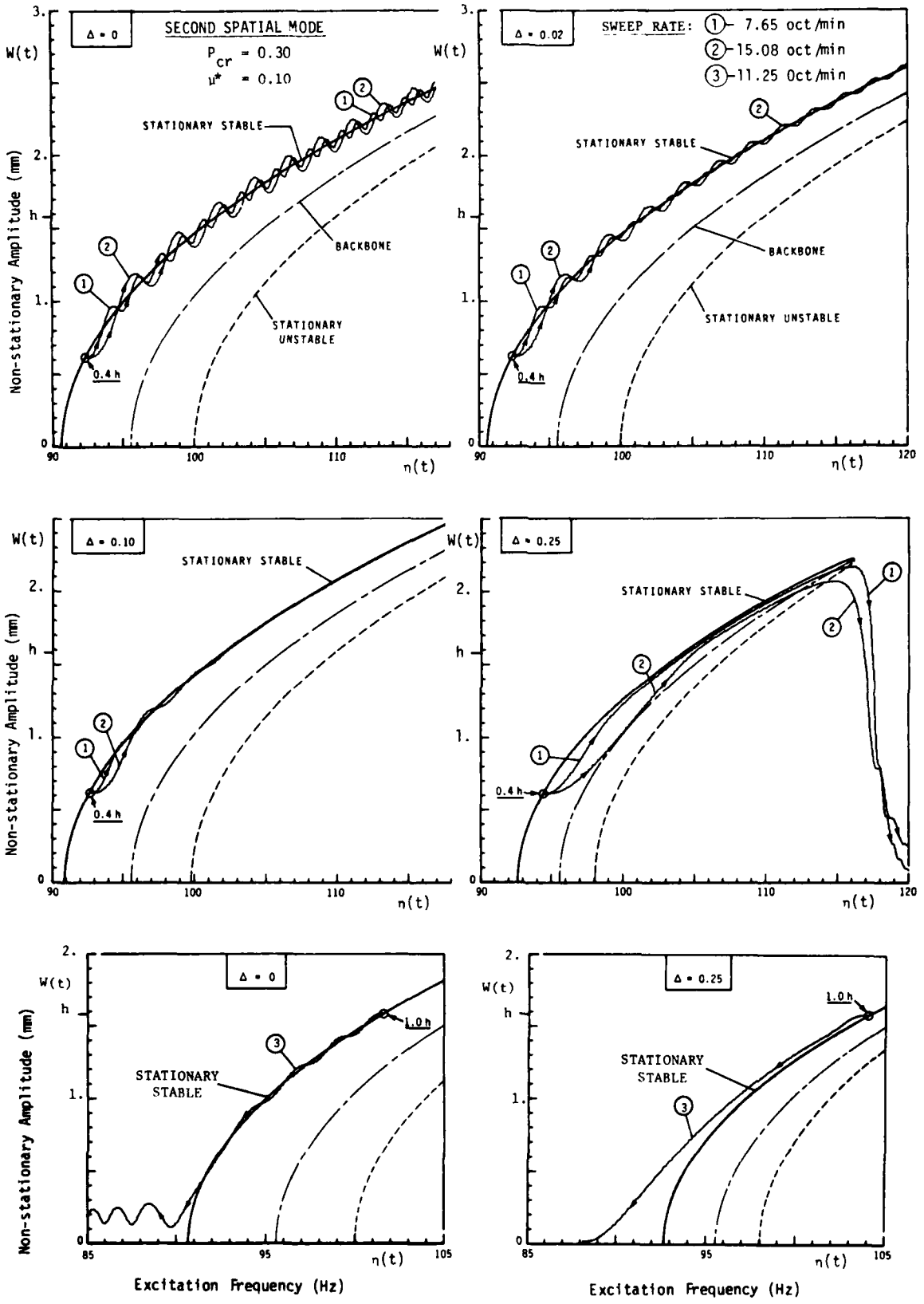

Figure 5. Influence of linear damping on the non-stationary parametric response of a rectangular plate.

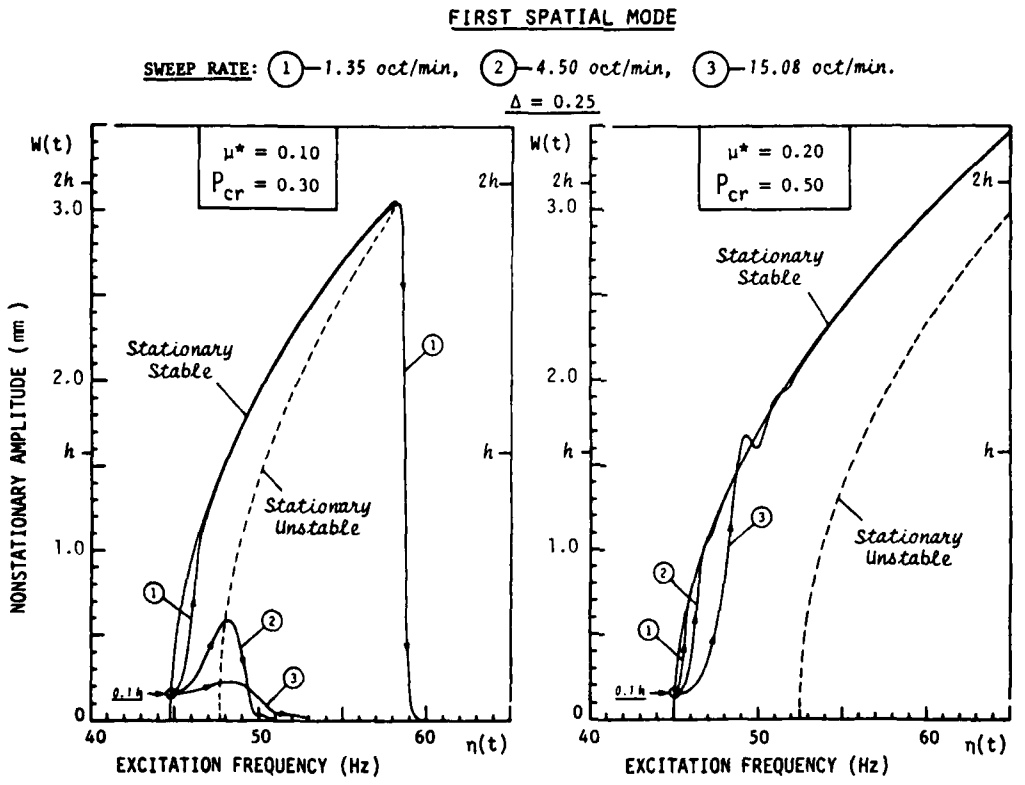

Figure 6. Effect of varying load parameter μ* on the non-stationary parametric response of a rectangular plate.

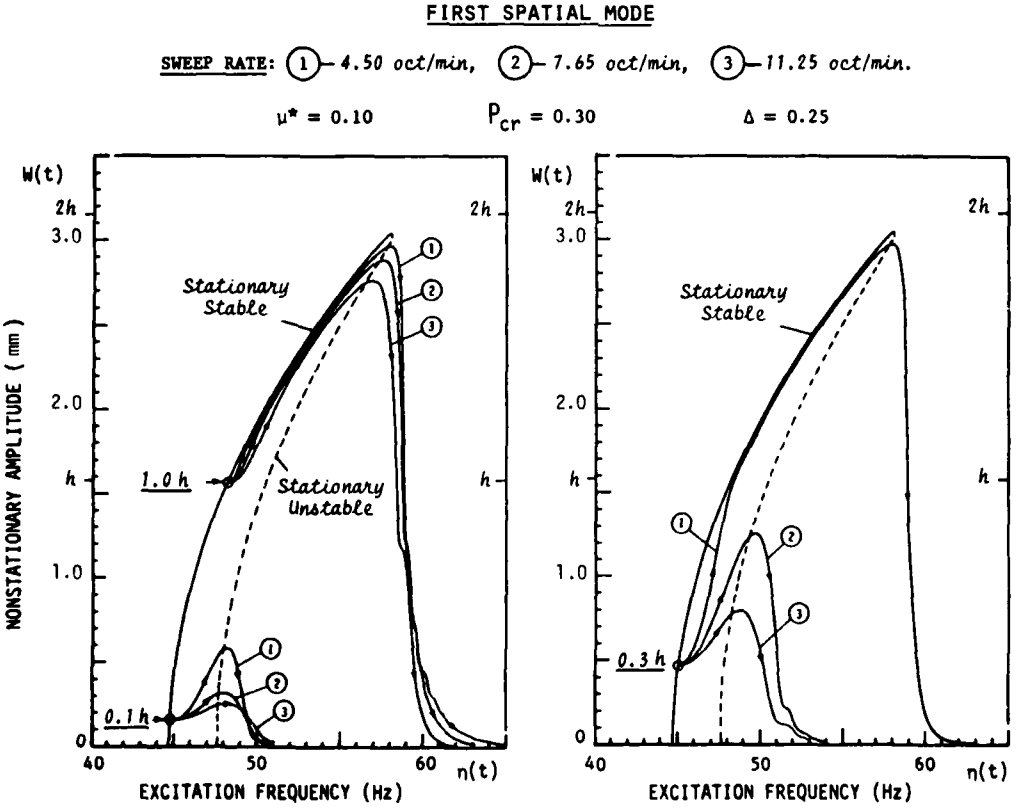

Figure 7. Effect of varying initial (stationary) amplitude on the non-stationary parametric response of a rectangular plate.

ACKNOWLEDGMENT

This study was sponsored in part by the Natural Sciences and Engineering Research Council of Canada (Grants A-4207 and RD-826), for which the authors express gratitude.

REFERENCES

1. G.L. OSTIGUY and R,M. EVAN-IWANOWSKI 1982 ASME Journal of Mechanical Design 104, 417-425. Influence of the Aspect Ratio on the Dynamic Stability and Non-linear Response of Rectangular Plates.

2. G.L. OSTIGUY and R.M. EVAN-IWANOWSKI 1982 Mécanique Matériaux Electricité (G.A.M.I.) 394-395, 472-478. Etude expérimentale sur la stabilité dynamique et la réponse des plaques rectangulaires.

3. F.M. LEWIS 1932 Transactions of the ASME 54 (23), 253-261. Vibrations During Acceleration Through a Critical Speed.

4. Yu A MITROPOLSKII 1964 Problems of the Asymptotic Theory of Non-stationary Vibrations. Moscow: Izdatel'stvo Nauka; 1965 (English translation) New York: D. Davey & Co., Inc.

5. R.M. EVAN-IWANOWSKI 1976 Resonance Oscillations in Mechanical Systems. New York: Elsevier/North-Holland Inc.

6. L.E. PANTON 1970 M.S. Thesis, Syracuse University. Non-stationary Resonance of a Non-linear Orthotropic Plate.

7. G.L. OSTIGUY and R.M. EVAN-IWANOWSKI 1984 Proceedings of the Second International Conference on Recent Advances in Structural Dynamics, University of Southampton. Non-stationary Responses of Non-linear Rectangular Plates During Transition Through Parametric Resonances, Part 2: Experiment.

8. G.L. OSTIGUY 1976 Ph.D. Dissertation, Syracuse University, N.Y. Effects of Aspect Ratio on Parametric Response of Non-linear Rectangular Plates - Analysis and Experiment.

9. B.N. AGRAWAL and R.M. EVAN-IWANOWSKI 1973 Journal of the American Institute of Aeronautics and Astronautics (AIAA Journal) 11, (7), 907-912. Resonances in Non-stationary, Non-linear, Multidegree-of-freedon Systems.

DEFINITION OF SYMBOLS

N^* : lowest critical load

$P_{cr} = N_{yo}/N^*$: ratio of critical loading

$r = b/a$: plate aspect ratio

μ^* : normalized excitation parameter.

NON-STATIONARY RESPONSES OF NON-LINEAR RECTANGULAR PLATES DURING TRANSITION THROUGH PARAMETRIC RESONANCES, PART 2: EXPERIMENT

G.L. Ostiguy
Ecole Polytechnique
Montréal, Canada

and

R.M. Evan-Iwanowski
Syracuse University
Syracuse, N.Y.

1. INTRODUCTION

A typical example in regard to parametric instability of structures is the case of a simply-supported rectangular plate acted upon by a periodic in-plane load. When a plate sustains an in-plane load of the form $P(t) = P_o + P_t \cos \eta t$, where $\cos \eta t$ is a harmonic function of period T, the plate becomes laterally unstable over certain regions of the (P_o, P_t, T) parameter space. Principal parametric resonances occur when the excitation frequency η and the modal frequency Ω_i satisfy approximately the relationship $\eta = 2\Omega_i$. If the system parameters are kept constant the resulting oscillatory motion is referred to as stationary. Stationary responses of non-linear rectangular plates were studied analytically and experimentally by Ostiguy and Evan-Iwanowski [1,2].

When the excitation parameters, P_o, P_t or η, vary with time, we encounter the case of non-stationary response. The main objective in the study of non-stationary systems is the determination of deviations of non-stationary responses from corresponding responses of equivalent stationary systems, i.e. systems whose components are constant. It is expected that the most pronounced differences in the responses of stationary and non-stationary systems will occur near the resonances or near the resonance zones of these systems. In the case when the frequency of external excitation is time-variant, the problem of modification of stationary responses near a resonance is referred to as a passage (or transition) through a resonance or resonance zone.

Although several theoretical investigations have been carried out on the non-stationary parametric response of structures, experimental evidence is far from adequate in many cases and is even non-existent in some cases. In this context, an experimental study of the non-stationary parametric response of simply-supported non-linear rectangular plates was performed. Special attention was paid to satisfy the boundary conditions assumed in the analytical model [3] so as to draw conclusions with sufficient degree of confidence. Experimental data have been compared with analytical predictions to form a qualitative and quantitative verification of the solution.

2. SUMMARY OF ANALYSIS

The specific conceptual model under investigation is a rectangular plate initially flat, of uniform thickness (thin), elastic, isotropic, simply supported along its edges and subjected to the action of periodic in-plane forces uniformly distributed along two opposite edges, as shown in Figure 1.

The plate theory used in the analysis [3,4] may be described as the dynamic analogue of the von Karman large-deflection theory and is derived in terms of the stress function F and lateral displacement w. The governing equations are :

$$\nabla^4 F = E \left[w,^2_{xy} - w,_{xx} w,_{yy} \right]$$

$$\nabla^4 w = \frac{h}{D} \left[F,_{yy} w,_{xx} + F,_{xx} w,_{yy} - 2F,_{xy} w,_{xy} - \rho w,_{tt} \right]$$

The boundary conditions are related to both the lateral displacement w and the stress function F. Since the plate is simply supported on all four edges, the supporting conditions are :

$$w = w_{,xx} + \nu\, w_{,yy} = 0 \qquad \text{along } x = \pm a,$$
$$w = w_{,yy} + \nu\, w_{,xx} = 0 \qquad \text{along } y = \pm b.$$

The loading conditions assumed in the analytical model (Figure 1) result in the following stress conditions:

$$F_{,yy} = 0, \quad F_{,xy} = 0 \qquad \text{along } x = \pm a,$$
$$F_{,xx} = -N_y(t)/h, \quad F_{,xy} = 0 \qquad \text{along } y = \pm b,$$

where $N_y(t) = P(t)/2a$.

The problem consists in determining functions F and w which satisfy the governing equations, together with the boundary conditions. The solution for the Airy stress function is represented by a double series consisting of the appropriate Beam Functions which satisfy the boundary conditions:

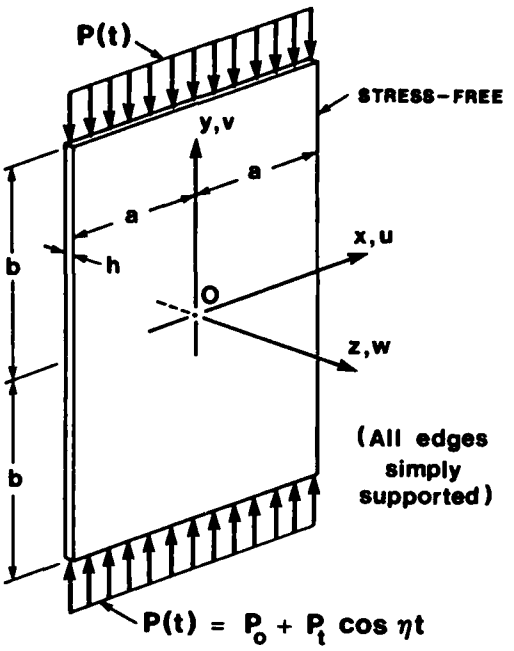

Figure 1. Plate and load configuration.

$$F(x,y,t) = \sum_m \sum_n f_{mn}(t)\, X_m(x)\, Y_n(y) - x^2 N_y(t)/2h$$

The continuous system is spatially discretized by means of a single-term modal approximation for the lateral displacement

$$w(x,y,t) = w_{pq}(t)\, \Phi_p(x)\, \Psi_q(y)$$

where $\Phi_p(x)$ and $\psi_q(y)$ are the eigenfunctions of free vibration for the linearized system.

Using the orthogonality properties of the assumed functions, introducing viscous damping and omitting the subscripts p and q for simplification, the governing equations are reduced to the following differential equation for the damped vibrations in any spatial mode:

$$\ddot{w} + 2C\dot{w} + \Omega^2 \left[1 - 2\mu \cos \theta(t)\right] w + \gamma\, w^3 = 0$$

where μ is the excitation parameter, γ is the coefficient of non-linear elasticity and C is the coefficient of linear damping. This temporal equation may be considered as an extension of the standard Mathieu-Hill equation.

A first-order asymptotic solution for principal parametric resonance is obtained in the following form:

$$w = W \cos\left(\tfrac{1}{2}\theta + \psi\right) \tag{1}$$

where W and ψ are defined by the system of differential equations

$$\dot{W} = -\left[\Omega^2 \mu(\tau)/\eta(\tau)\right] W \sin 2\psi - WC\,,$$

$$\dot{\psi} = \Omega - \tfrac{1}{2}\eta(\tau) - \left[\Omega^2 \mu(\tau)/\eta(\tau)\right] \cos 2\psi + \left[3\gamma/8\Omega\right] W^2. \tag{2}$$

By integrating this system of equations, the amplitude W and the phase ψ of the non-stationary response can be obtained as functions of time.

For obtaining stationary values of the amplitude W and phase ψ, we set in equation (2) $\dot{W} = \dot{\psi} = 0$. Eliminating ψ from the ensuing equations, we obtain the amplitude-frequency relation:

$$W = \sqrt{[8\Omega/3\gamma]\left[-(\Omega - \tfrac{1}{2}\eta) \pm \sqrt{(\mu^2\Omega^4/\eta^2) - C^2}\right]},$$

where the ± sign indicates the possibility of two solutions; one is table, the other one is unstable. These solutions are represented in Figure 2. The stationary phase angle ψ is found to be

$$\psi = \tfrac{1}{2} \sin^{-1} (-C\eta/\mu\Omega^2)$$

where $0 > \psi > -\pi/4$.

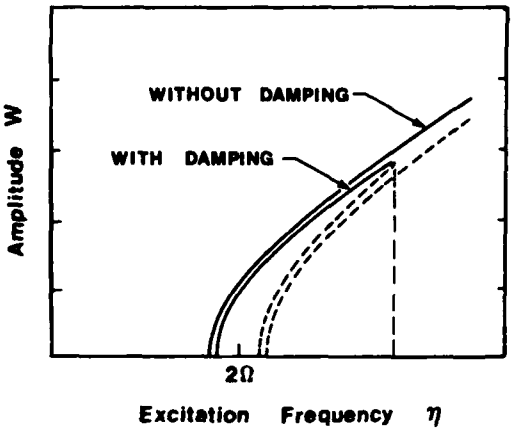

Figure 2. Stationary response curves.

3. EXPERIMENTAL INVESTIGATION

3.1 Laboratory Apparatus

The experimental setup permits an experimental investigation of the dynamic stability and non-stationary parametric response of simply-supported rectangular plates subjected to an in-plane load of the form $P(t) = P_o + P_t \cos \eta t$ which is uniformly distributed along two opposite edges. The apparatus admits the load parameters P_o, P_t and η as independent variables. The amplitude of the plate vibrations, the load parameters, the frequency spectrum and mode shapes of the lateral response, and the time-dependent excitation and response characteristics are measured directly. The block diagram shown in Figure 3 indicates the general functioning of various components used in measuring and recording the response.

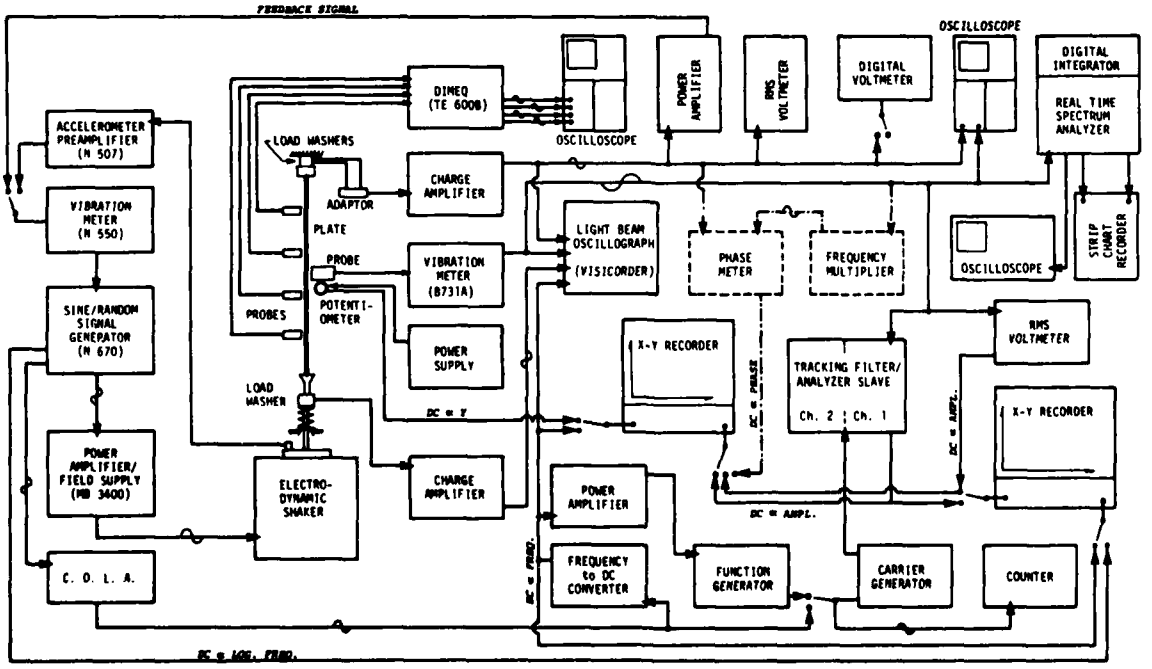

Figure 3. Block diagram of experimental apparatus.

3.2 Excitation System

An electrodynamic shaker is used to impart a dynamic force at the base of the plate. The shaker is driven by a sinusoidal signal of variable frequency and amplitude originating from a sine-random generator. The frequency of the excitation signal can be held stationary or swept automatically at various logarithmic sweep rates either up or down. The output signal level from the sine-random generator is automatically regulated by means of a compressor to control the amplitude P_t of the harmonic in-plane load applied on the plate by the shaker. The necessary feedback for system control is produced by a load transducer. An accelerometer mounted onto the vibrating head of the shaker table could be used to monitor the motion of the shaker table.

3.3 Loading Apparatus

The experimental apparatus depicted in Figure 4 was designed to accommodate rectangular plates of various aspect ratios and to match the theoretical assumptions as closely as possible.

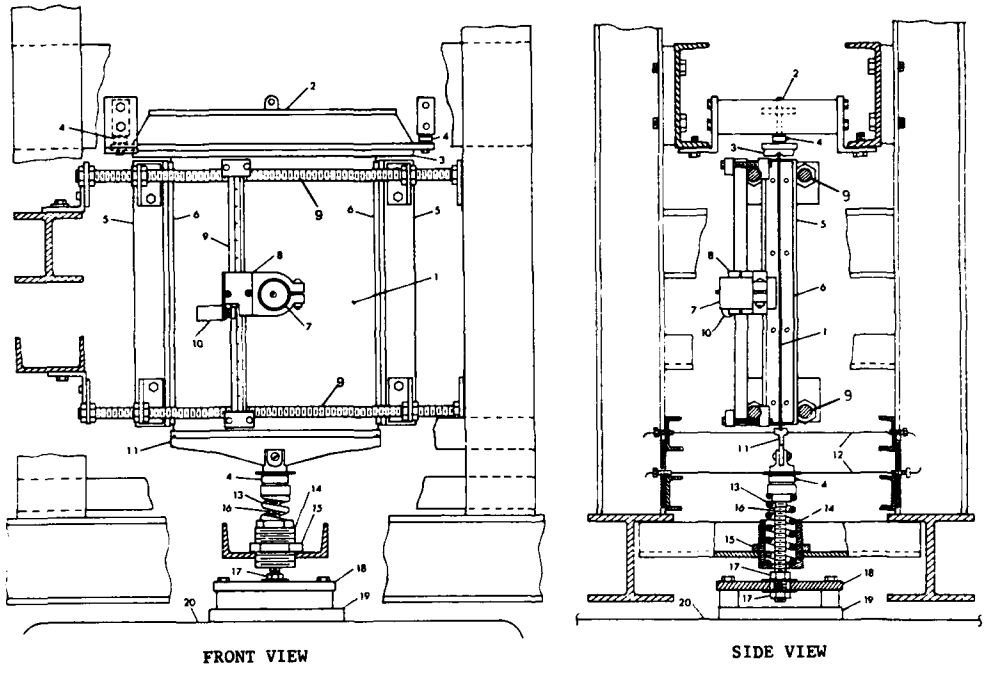

Figure 4. Schematic diagram of plate supports and loading system.

The loading apparatus consists of a linear spring (13), an adjustable head (14) and a lock nut (15), a threaded stud (16), a quartz load washer (4), and a loading beam (11) constrained by a wire suspension (12) to move in a vertical plane. The initial static preload P_o is transmitted to the loading beam by the spring and the adjustable head secured to the frame. The dynamic portion P_t of the in-plane loading is provided by the shaker table which is attached to the loading beam by means of the threaded stud. The beveled upper and lower edges of the plate specimen (1) are placed in V-grooves to simulate simply-supported boundary conditions.

The support at the upper edge is provided by a load transducer consisting of a loading bar (3), a rigid support (2) and two load washers (4). The edge restraints along the vertical edges of the plate are supplied by adjustable knife edges (6) fastened to vertical side fixtures (5). In order to accommodate rectangular plates of various aspect ratios, these side fixtures are mounted on horizontal screws secured to the frame thus permitting continuous width adjustment.

In order to realize a uniform load distribution, a special loading apparatus was contrived. As shown in Figure 5, a deep groove was machined in loading beams then filled with silicone rubber molded in place. Since the resulting in-plane rigidity of the V-groove is very small compared to the in-plane rigidity of the plate itself, the load distribution achieved by this experimental arrangement agrees very closely with the theoretical conditions.

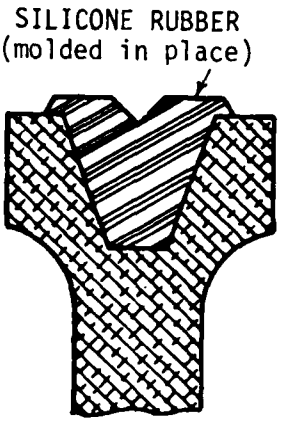

Figure 5. Cross-section of the loading beam.

3.4 Measurement System

Parameters P_o and P_t of the in-plane load at the upper edge of the plate are measured by the load transducer described previously. Signals from the two load washers are combined and suitably scaled for direct measurement and display on calibrated readout equipment.

The lateral vibration and the shape of the deflected plate, $w(x,y,t)$, is measured by a capacitive sensor (7) placed in proximity to the plate surface. The non-metallic plate is sprayed with a conductive paint, causing the surface of the specimen to be electrically conducting. The signal from the associated vibration meter serves as an input to a true RMS voltmeter which provides an analog DC output for recording purposes. A ten-turn linear potentiometer, attached to the front probe holder, provides a DC signal proportional to the position of the probe along the vertical centerline of the plate.

The frequency spectrum of the lateral response is determined by a real-time spectrum analyzer and is continuously monitored on the screen of an oscilloscope. When the temporal response of the plate is not purely harmonic, the signal may be processed by a tracking filter/analyzer to determine the amplitude of vibration and the mode shape associated with each frequency component.

A frequency counter is used to measure the frequency of the various sinusoidal signals. An accurate linear potentiometer, driven by frequency scale pointer shaft of the generator, supplies a DC voltage proportional to the Log of frequency, thus providing a frequency drive for X-Y plotters. Time-dependent excitation and response characteristics are recorded on an oscillograph. X-Y plotters are used primarily to record mode shapes and response levels as a function of frequency.

3.5 Plate Specimens

In order to verify the theoretical results and to highlight the influences of the damping and the aspect ratio on the non-stationary parametric response of rectangular plates, three different specimens have been used. All test plates were cut from commercially available plastic sheets. The dynamic mechanical properties of the materials were determined experimentally [4]. A summary of the test plate characteristics is given in Table 1.

3.6 Laboratory Techniques

Prior to any experiment, several precautions were necessary to insure that each instrument was properly calibrated and the mechanical system properly aligned. Standard operator procedures were used to calibrate the instruments to manufacturer's specifications where applicable.

TABLE 1. Specifications of Plate Parameters

Test Plate	Material	E (GPa)	ν	ρ (kg/m^3)	Dimensions (mm)	Aspect ratio r
E.1	Acrylic*	4.41	0.38	1188	292 x 406 x 1.60	1.39
E.2	Acrylic	4.41	0.38	1188	209 x 406 x 0.99	1.94
E.4	Polyvinyl chloride	3.30	0.388	1365	292 x 406 x 1.42	1.39

*Polymethyl Methacrylate

3.6.1 Preliminary Procedure

The initial static preload P_o is applied at the base of the plate assembly by tightening the adjustable head and locknut to compress the spring (13). The preload is measured from the load transducer output.

The dynamic portion of the in-plane loading is provided by the shaker. After the sine-random generator is set at some frequency located outside a parametric instability zone, the shaker signal is gradually increased until the desired amplitude P_t of the dynamic load is obtained. The compressor circuit then maintains that load level for all subsequent frequency changes of plate response levels.

The characteristic frequencies η_1 and η_2 corresponding to the onset of parametric resonance and the stationary amplitude response curve could then be determined experimentally following the procedure depicted in Figure 6. Details of the procedure can be found in Reference [4].

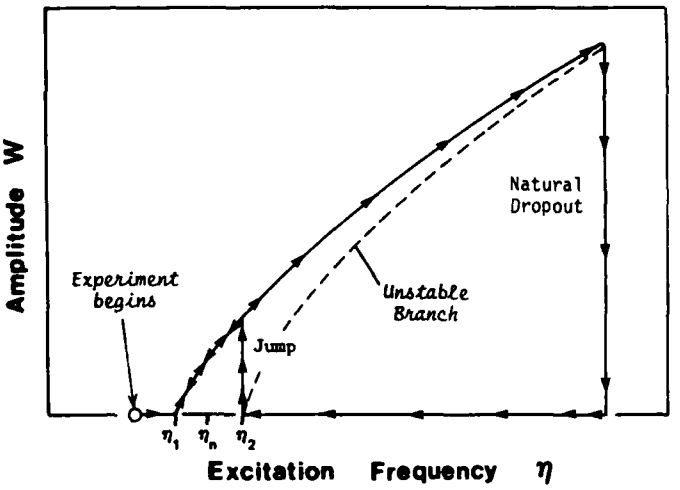

Figure 6. Experimental determination of the stationary parametric response.

3.6.2 Non-stationary Response

The non-stationary motion during a passage through a resonance zone depends strongly upon the initial conditions at the start of the frequency sweep. Two types of transition were considered experimentally:

1. Transition through the resonance zone, where the initial frequency is inside the resonance zone and the initial conditions correspond to some non-zero stationary values;

2. Complete passage through the resonance zone, where the initial frequency is outside the resonance zone and the initial conditions correspond to the trivial stable case ($W \approx 0$).

The experimental determination of the non-stationary parametric response of the plate is straightforward. A typical experiment of type 1 proceeds as follows. After completion of the preliminary procedure, the load frequency is set at some value inside the resonance zone and the system is allowed to vibrate

laterally in a stationary regime before the sweep generator is actuated. The trace and the amplitude of the non-stationary response are then recorded while the excitation frequency η is swept logarithmically through the resonance zone at a preselected rate. In type 2 experiments, the initial load frequency is set at a value slightly lower than η_1 (for an increasing frequency sweep) or slightly greater than η_2 (for a decreasing sweep), and the automatic frequency scanning device is actuated.

3.7 Experimental Results and Conclusions

The non-stationary motion during a transition through a resonance zone was determined experimentally for a wide variety of cases. Figures 7 through 10 represent typical traces of non-stationary responses that were obtained by starting with some initial stationary values and logarithmically varying the load frequency either up or down. The results are qualitatively the same as those predicted by theory (see Figure 10) and agree reasonably well quantitatively with the theoretical predictions [3]. A few observations are to be noted. At the start of the non-stationary response, a plateau of varying width is present in all cases. This is partly due to the inherent time lag involved in the voltmeter analog response to rapidly varying amplitudes. A similar but smaller plateau is present in analytic results. The observable larger shifts of the non-stationary curves from the steady-state responses (see Figure 10) can also be attributed to the time lag in instrumentation. It may also be seen that the amplitudes measured experimentally are slightly larger than those predicted by theory, at very high amplitudes of vibration. This is partly due to a small relaxation of the constraints at the boundaries and partly due to the fact that the first-order asymptotic approximation tends to exagerate the effect of non-linearity [5].

Typical records of the non-stationary motion and of the dynamic in-plane loading are shown in Figure 7. It may be observed that the period of vibration of the rectangular plate within a principal region of instability is twice that of the periodic in-plane load.

The influence of the sweep rate on the stability and non-stationary response of the system during a transition of the excitation frequency through resonance regions is highlighted in Figure 8. One can observe that for rapid increasing transitions, the non-stationary response increases somewhat inside the resonance zone but returns to the zero-amplitude solution afterwards. The stabilizing influence of damping is illustrated in Figure 9 by the fact that greater loading conditions are required on specimen E.1 to produce similar responses. The results also indicate that the amplitude decay during dropout is much slower for specimen E.4.

The non-stationary motion during a complete passage through a resonance zone was also investigated experimentally. For increasing transition into the resonance zone (Figure 11), the plate does not respond until the frequency has penetrated the instability zone for some finite distance, thus giving rise to a rapid jump to the stable branch. The penetration effect increases with increasing sweep rates; for sufficiently large sweep speeds, the jump phenomenon is not manifest and no parametric vibrations are apparent at all. Similar behaviour is also observed for decreasing transition (Figure 12). This means that the sweep rate may have a pronounced effect on the lateral stability of the plate. The results also indicate that the sweep rate necessary to preclude a parametric oscillation increases as the parameter μ is increased.

ACKNOWLEDGMENT

This study was sponsored in part by the National Sciences and Engineering Research Council of Canada (Grants A-4207 and RD-826), for which the authors express gratitude.

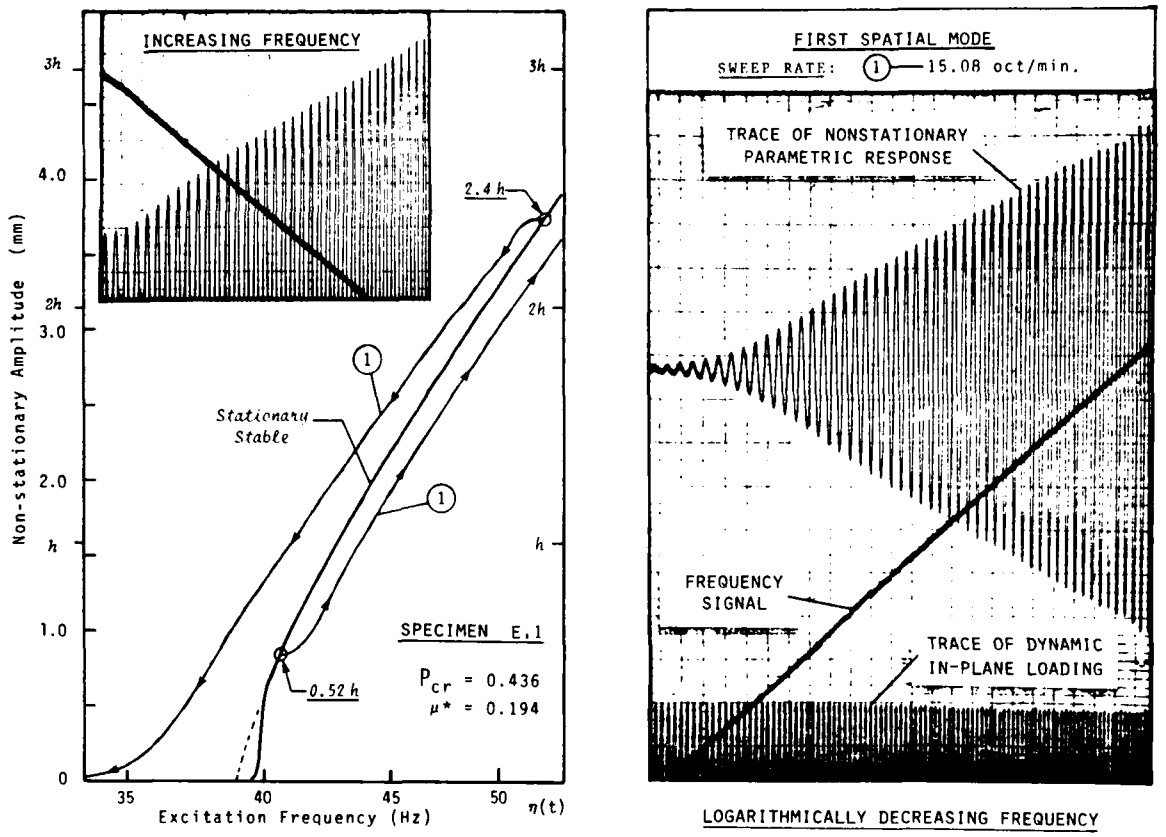

FIGURE 7 TYPICAL RECORDS OF THE NONSTATIONARY PARAMETRIC RESPONSE OF A RECTANGULAR PLATE.

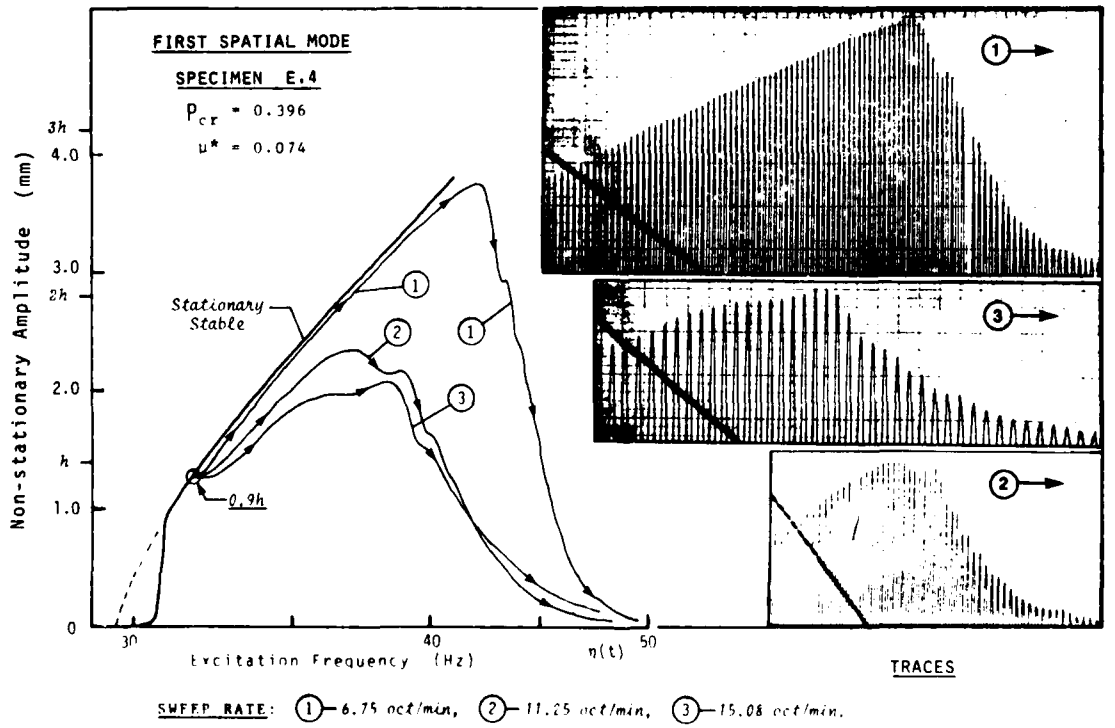

FIGURE 8 EXPERIMENTAL NONSTATIONARY PARAMETRIC RESPONSE IN FIRST MODE SHAPE

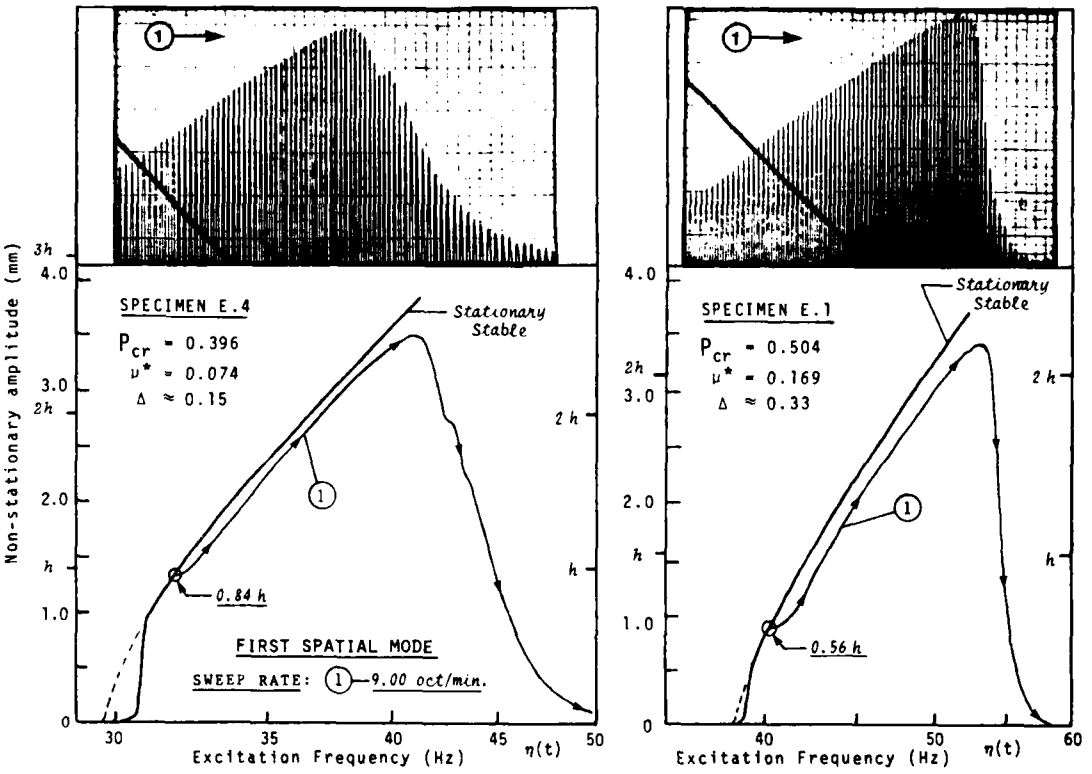

FIGURE 9 INFLUENCE OF INTERNAL DAMPING ON THE NONSTATIONARY PARAMETRIC RESPONSE OF RECTANGULAR PLATES (EXPERIMENTAL RESULTS)

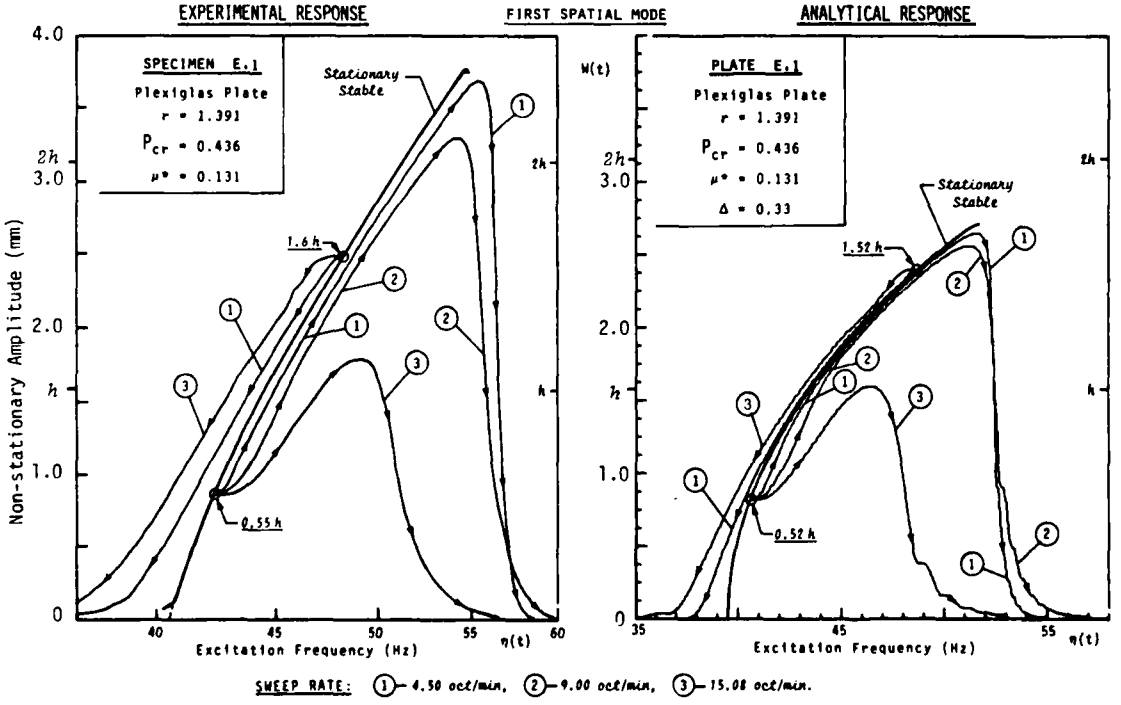

FIGURE 10 COMPARISON OF EXPERIMENTAL NON-STATIONARY PARAMETRIC RESPONSE WITH THEORY.

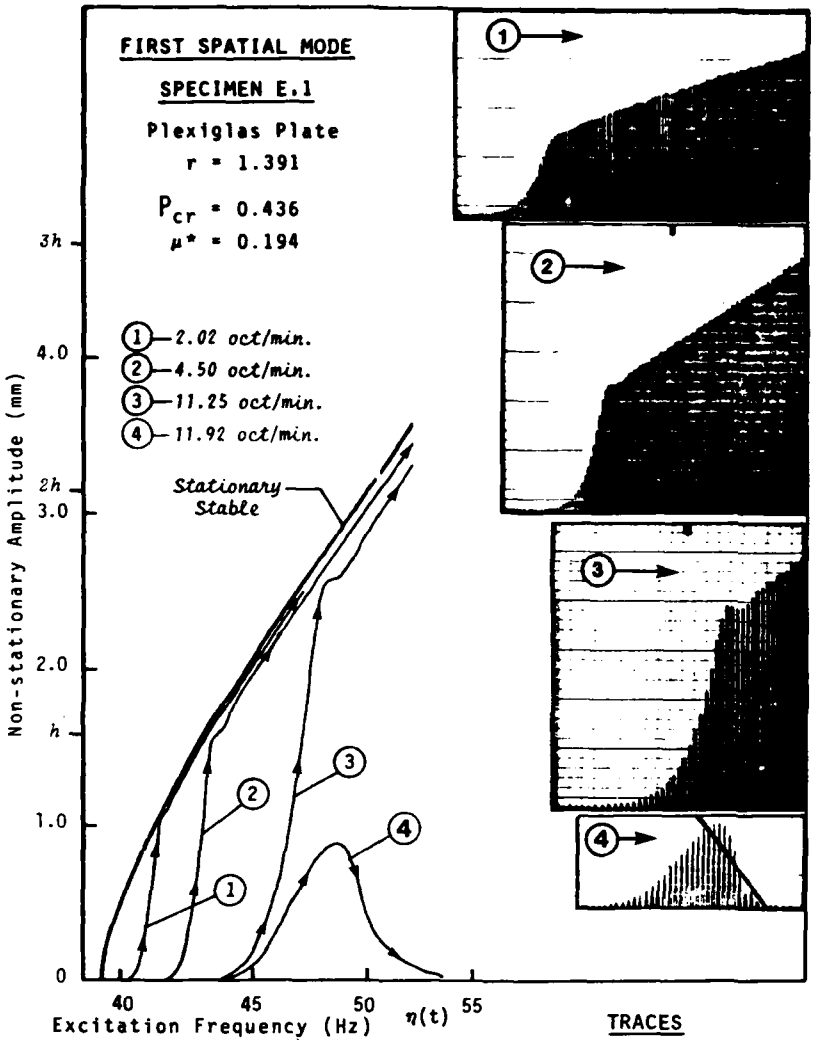

FIGURE 11 EXPERIMENTAL NON-STATIONARY PARAMETRIC RESPONSE DURING A PASSAGE THROUGH A RESONANCE ZONE (INCREASING FREQUENCY).

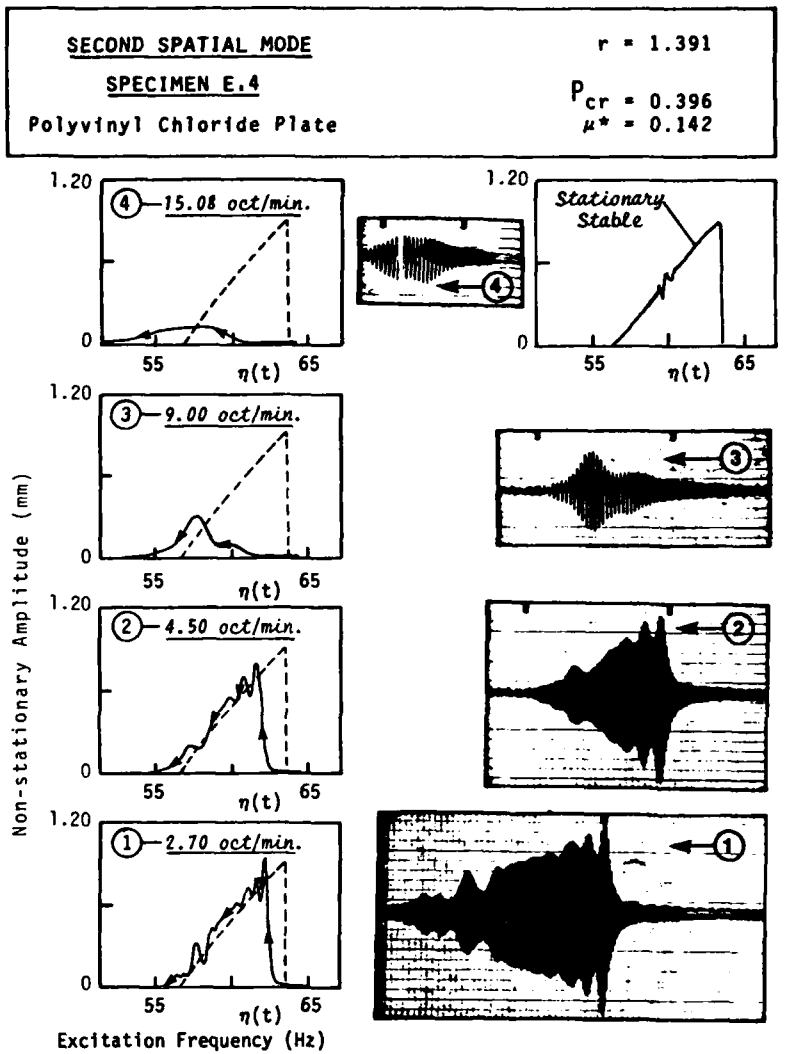

FIGURE 12 EXPERIMENTAL NON-STATIONARY PARAMETRIC RESPONSE DURING A PASSAGE THROUGH A RESONANCE ZONE (DECREASING FREQUENCY)

REFERENCES

1. G.L. OSTIGUY and R.M. EVAN-IWANOWSKI 1982 ASME Journal of Mechanical Design 104, 417-425. Influence of the Aspect Ratio on the Dynamic Stability and Non-linear Response of Rectangular Plates.

2. G.L. OSTIGUY and R.M. EVAN-IWANOWSKI 1982 Mécanique Matériaux Electricité (G.A.M.I.) 394-395, 472-478. Etude expérimentale sur la stabilité dynamique et la réponse des plaques rectangulaires.

3. G.L. OSTIGUY and R.M. EVAN-IWANOWSKI 1984 Proceedings of the Second International Conference on Recent Advances in Structural Dynamics, University of Southampton. Non-stationary Responses of Non-linear Rectangular Plates During Transition Through Parametric Resonances, Part I: Theory.

4. G.L. OSTIGUY 1976 Ph.D. Dissertation, Syracuyse University, N.Y. Effects of Aspect Ratio on Parametric Response of Non-linear Rectangular Plates - Analysis and Experiment.

5. R. KUI SIN LYAU 1969 M.S. Thesis, Syracuse University, N.Y. Passage Through Resonance of Non-linear Systems.

DEFINITION OF SYMBOLS

$D = Eh^3/12(1 - \nu^2)$: flexural rigidity of the plate

$\Delta^4 = \partial^4/\partial x^4 + 2\,\partial^4/\partial x^2\partial y^2 + \partial^4/\partial y^4$: operator

N_x, N_y, N_{xy} : membrane forces per unit width

P_E = critical load corresponding to a given buckling mode

P^* = lowest critical load

$P_{cr} = P_o/P^*$: ratio of critical loading

$r = b/a$: plate aspect ratio

$Y_n = \dfrac{\cosh \beta_n y}{\cosh \beta_n b} - \dfrac{\cos \beta_n y}{\cos \beta_n b}$, $n = 1,2,\ldots$: Beam Functions for F

$\Psi_q = \cos q\pi y/2b, \quad q = 1,3,\ldots$

$\Psi_q = \sin q\pi y/2b, \quad q = 2,4,\ldots;$ } eigenfunctions for w

$\mu = P_t/2(P_E - P_o)$: excitation parameter

μ^* = normalized excitation parameter

Ω = modal frequency of plate loaded by P_o.

NONLINEAR DYNAMIC ANALYSIS OF ANISOTROPIC RECTANGULAR PLATES BY A NEW METHOD

M. Sathyamoorthy

Department of Mechanical and Industrial Engineering
Clarkson College of Technology
Potsdam, New York 13676, U.S.A.

1. INTRODUCTION

Geometrically nonlinear static and dynamic analysis of anisotropic plates has received considerable attention in the literature in recent years [1,2]. This is mainly due to increasing use of composites in the design of structures where lightness and economy are important considerations. Several linear analyses have been carried out so far to determine the natural frequencies of anisotropic plates of various shapes [3-7] and different boundary conditions including those with elastically restrained edges [8]. However, nonlinear vibration studies of anisotropic plates of various geometries are limited [9,10] and a few approximate solutions that are available are based on mode shapes which are mainly in terms of trigonometric functions. In many cases the solutions are based on a single-mode approximation and the accuracy of the results depends upon the choice of the appropriate shape functions. Since closed-form solutions do not exist for many of these nonlinear problems, it is very difficult to evaluate the accuracy of these approximate solutions. The purpose of this paper, therefore, is to examine a new method of analysis which has been successfully used in the nonlinear dynamic analysis of beams [11].

This paper is concerned with the nonlinear static as well as dynamic analysis of anisotropic plates of rectangular and square geometries. A review of literature indicates [1,2,3] that these geometries are the ones most commonly dealt with in the past. The present approach, however, could be extended to the analysis of plates of some other geometries as well. The nonlinearities investigated here arise due to large deformation or large amplitude vibration and are included in the nonlinear strain-displacement relations. The stress-strain relationship is linear, however, and the material constants of the plate are with reference to an orthogonal system of axes. New type of functions called Self-Generating Functions are used to obtain the linear and nonlinear frequencies in dynamic problems and load-deflection behavior in static problems. Self-Generating Functions of zero-order are polynomials of eighth degree for any given boundary conditions of the plate. First-order polynomials are of sixteenth degree and can be easily generated from the zero-order polynomials. Further higher order polynomials can be readily obtained from polynomials of the previous order. These Self-Generating Functions have been successfully used by the author [11] in the investigations of the nonlinear dynamic behavior of beams with various boundary conditions.

The analysis here is carried out with the aid of nonlinear governing equations obtained by the use of the Berger-type approximation. Numerical results for linear and nonlinear frequencies are presented for rectangular and square anisotropic plates using the zero, first and second-order Self-Generating Functions. For nonlinear static problems, the corresponding nonlinear algebraic equations derived from the modal equations of the dynamic case are solved to obtain the load-deflection relations. Effects of amplitude, geometry and material constants on the static and dynamic behaviors are discussed along with comparisons wherever possible. Results corresponding to the three different Self-Generating Functions are tabulated to show the convergence. The Self-Generating nature of these polynomial functions enable one to improve the results by considering higher order functions and therefore obtain results which are more

reliable. Present results for all special cases are in excellent agreement with existing solutions for both nonlinear vibration and bending problems.

2. ANALYSIS

A plate of dimensions a and b and of constant thickness h composed of homogeneous anisotropic material is considered. The origin of the coordinate system is located at the left corner of the midplane of the undeformed plate. The principal elastic axes L and T are inclined at an angle ϕ to the x,y coordinate system which are parallel to the plate edges. The elastic stiffnesses a_{ij} are given by

$$\begin{Bmatrix} a_{11} \\ a_{12} \\ a_{22} \\ a_{16} \\ a_{26} \\ a_{66} \end{Bmatrix} = \frac{1}{\mu} \begin{bmatrix} m^4 & 2\mu_o & n^4 & 4\mu_o \\ \mu_o & \mu_1 & \mu_o & -4\mu_o \\ n^4 & 2\mu_o & m^4 & 4\mu_o \\ nm^3 & \mu_2 & -mn^3 & 2\mu_2 \\ mn^3 & \mu_3 & -nm^3 & 2\mu_3 \\ \mu_o & -2\mu_o & \mu_o & \mu_1-2\mu_o \end{bmatrix} \begin{Bmatrix} E_L \\ \nu_{LT}E_T \\ E_T \\ \mu G_{LT} \end{Bmatrix} \tag{1}$$

where E_L and E_T are the major and minor Young's moduli, ν_{LT} and ν_{TL} are the Poisson's ratios and G_{LT} is the shear modulus and

$$\begin{aligned} m &= \cos\phi & n &= \sin\phi \\ \mu &= 1-\nu_{LT}\nu_{TL} & \mu_o &= m^2n^2 \\ \mu_1 &= m^4+n^4 & \mu_2 &= mn(n^2-m^2) \\ \mu_3 &= mn(m^2-n^2) & \nu_{TL}E_L &= \nu_{LT}E_T \end{aligned} \tag{2}$$

The governing nonlinear dynamic equations which are based on the extended Berger-type theory can be written in terms of a_{ij} as below.

$$\varepsilon_1+\lambda_1\varepsilon_2+(\lambda_2+\lambda_3)\gamma = e = \frac{\delta^2h^2}{12} \tag{3}$$

$$C_1e\{w,_{xx}+\lambda_1 w,_{yy}+2(\lambda_2+\lambda_3)w,_{xy}\}$$

$$+ q(x,y)-\rho h\, w,_{tt} = \frac{h^3}{12} L(w) \tag{4}$$

where,

$$L(w) = a_{11}\, w,_{xxxx} + 4a_{16}\, w,_{xxxy} + 2(a_{12}+2a_{66})\, w,_{xxyy} + 4a_{26}\, w,_{xyyy} + a_{22}\, w,_{yyyy}$$

$$\lambda_1 = (a_{22}/a_{11})^{1/2} \quad ; \quad \lambda_2 = (-2a_{16}/a_{11})^{1/2}$$

$$\lambda_3 = (-2a_{26}/a_{11})^{1/2} \quad ; \quad C_1 = a_{11}h \quad ; \tag{5}$$

ε_1, ε_2 and γ are the median surface strains defined in terms of displacement components u^o, v^o and w as

$$\varepsilon_1 = u^o,_x + \frac{1}{2}\, w,_x{}^2$$

$$\varepsilon_2 = v^o,_y + \frac{1}{2}\, w,_y{}^2$$

$$\gamma = u^o,_y + v^o,_x + w,_x\, w,_y \tag{6}$$

$q(x,y)$ is the applied load per unit area of the plate, ρ is the mass density and h is the uniform plate thickness. In equations (4) and (5) a comma denotes partial differentiation with respect to the given coordinate.

Equations (3) and (4) constitute a system of two nonlinear equations governing the large amplitude flexural vibrations of anisotropic plates. Solutions to these equations are obtained with the help of the following Self-Generating Functions of zero, first and second orders. The subscripts ss and cc stand for the simply supported and clamped boundaries respectively.

zero-order:

$$w(x,y,t) = (w_o)_{ss}(x^4-2ax^3+a^3x)(y^4-2by^3+b^3y)$$

$$w(x,y,t) = (w_o)_{cc}(x^4-2ax^3+a^2x^2)(y^4-2by^3+b^2y^2) \tag{7}$$

first-order:

$$w(x,y,t) = (w_1)_{ss}(x^8-4ax^7+14a^3x^5-28a^5x^3+17a^7x)$$
$$(y^8-4by^7+14b^3y^5-28b^5y^3+17b^7y)$$

$$w(x,y,t) = (w_1)_{cc}(3x^8-12ax^7+14a^2x^6-14a^5x^3+9a^6x^2)$$
$$(3y^8-12by^7+14b^2y^6-14b^5y^3+9b^6y^2) \tag{8}$$

second order:

$$w(x,y,t) = (w_2)_{ss}(x^{12}-6ax^{11}+55a^3x^9-396a^5x^7 +1683a^7x^5-3410a^9x^3+2073a^{11}x)(y^{12}-6by^{11} +55b^3y^9-396b^5y^7+1683b^7y^5-3410b^9y^3+2073b^{11}y)$$

$$w(x,y,t) = (w_2)_{cc}(3x^{12}-18ax^{11}+33a^2x^{10}-198a^5x^7+297a^6x^6-330a^9x^3 +213a^{10}x^2)(3y^{12}-18by^{11}+33b^2y^{10}-198b^5y^7+297b^6y^6 -330b^9y^3+213b^{10}y^2) \quad (9)$$

For any given boundary condition, the zero-order function is first derived by solving a beam problem subjected to a uniformly distributed load. Since the deflection shape is now known, the corresponding inertia load is again applied on the beam to generate the first order function. This procedure is repeated for successive higher order functions. In the case of plates identical functions are used for both the x as well as y coordinate directions as shown in equations (7) to (9).

Assuming that the in-plane movements at the boundaries of the plate are fully prevented [12] equations (7), (8) and (9) are substituted in equation (3) and an integration procedure is followed to obtain e. The value of e thus obtained in each case is substituted again in equation (4) along with equations (7), (8) and (9) and Galerkin's method is used by integrating the resulting equation over the area of the plate. Such a procedure results in the following system of time-differential equations in the case of simply supported and clamped plates.

$$\bar{w}_{,\tau\tau}+A_{ss}\bar{w}+B_{ss}(\bar{w})^3 = C_{ss}q^*_o \quad (10)$$

$$\tilde{w}_{,\tau\tau}+A_{cc}\tilde{w}+B_{cc}(\tilde{w})^3 = C_{cc}q^*_o \quad (11)$$

$\bar{w}$ and $\tilde{w}$ in equations (10) and (11) are the nondimensional amplitudes. For each of the Self-Generating Functions in equations (7), (8) and (9) these amplitudes are obtained by nondimensionalizing the maximum values of w_o, w_1 and w_2 with respect to the thickness of the plate. q^*_o is the nondimensional applied uniformly distributed load given by $(q_o a^4/E_L h^4)$ and τ is the nondimensional time defined in terms of t as $\tau^2=t^2D_1/a^4\rho h$. D_1 is the flexural rigidity of the plate in the L direction given by $E_L h^3/12\mu$. In the absence of any externally applied load q^*_o, equations (10) and (11) can be solved in closed-form and the solutions will be in terms of variations of amplitude with frequency of vibration. In the case of nonlinear static problems, $\bar{w}$ and $\tilde{w}$ are independent of τ and therefore the time-dependent terms in equations (10) and (11) vanish resulting in a set of nonlinear algebraic equations. These equations are further used in order to obtain the nonlinear load-deflection relationships. The numerical results in both static and dynamic nonlinear cases are dependent upon the coefficients A, B, and C, which are obtained by performing all the integrations by hand.

3. NUMERICAL RESULTS

Numerical results are presented in Tables 1-6 for anisotropic rectangular and square plates. The plate material is treated to be homogeneous and its principal axes of elasticity are inclined arbitrarily with respect to the rectangular x and y coordinates. The elastic constants referred to the principal directions (L,T) are $(E_L/E_T)=3,10$; $\nu_{LT}=0.25,0.22$ and $(G_{LT}/E_L)=0.2,0.033$, for glass-epoxy and boron-epoxy materials, respectively. The ratio of the nonlinear frequency ω to

the corresponding linear frequency ω_o of the classical thin plate was computed for anisotropic plates of various aspect ratios and orientation angles at different nondimensional amplitudes. Self-Generating Functions of zero-order, first-order and second-order applicable for simply supported and clamped plates have been used to obtain the numerical results. Since higher order functions become more and more complex, the analytical effort required to solve the problem increases considerably. The results presented here are based on an extended Berger-type theory for which an assumption of an appropriate shape function for w alone is sufficient. The corresponding von Karman-type theory will, however, require not only a good choice of function for w but also for stress function F. An appropriate choice of F compatible with the corresponding w is often very difficult. Moreover, numerical results reported elsewhere [13] show very close agreements between these two nonlinear theories for orthotropic plates of various aspect ratios. The values of nondimensional fundamental frequency $\lambda[=(\omega a^2/h)(12\rho/E_1)^{1/2}]$ are given in Table 1 for clamped plates of various aspect ratios. Present results are extremely close to the exact solutions reported in [3]. Similar results for simply supported boundary conditions show close agreements with the results in the literature but the details are not presented here. Numerical values for the modal equation coefficients A, B and C are tabulated in Tables 2 to 4. For each of the cases considered here, these coefficients show a remarkable convergence. These coefficients have been compared with those from References [12,16] for ϕ=o. In the case of simply supported plates the agreement is exact whereas in the case of clamped plates the present values are better than those found in the literature. It is clear from the numerical values that each coefficient converges to a steady value fairly quickly. Finally, numerical results are presented in Tables (5) and (6) to show the variation of load with the deflection in the case of nonlinear static problems and the variation of frequency ratio with the amplitude in the large amplitude vibration cases. It is clear that the nonlinearity is of the hard-spring type for both static as well as dynamic problems.

4. REFERENCES

1. C.Y. CHIA 1980 Nonlinear Analysis of Plates. New York: McGraw-Hill.

2. M. SATHYAMOORTHY 1983 The Shock and Vibration Digest 15, 3-16. Nonlinear vibrations of plates - a review.

3. A.W. LEISSA 1969 NASA SP-160. Vibration of Plates.

4. D. MOHAN and H.B. KINGSBURY 1971 The Journal of the Acoustical Society of America 50, 266-269. Free vibrations of generally orthotropic plates.

5. M. J. MAURIZI and P.A. LAURA 1973 Journal of Sound and Vibration 26, 299-305. Vibration analysis of clamped, rectangular plates of generalized orthotropy.

6. R.S. SRINIVASAN and S.V. RAMACHANDRAN 1975 Journal of the Acoustical Society of America 57, 1113-1118. Vibration of generally orthotropic skew plates.

7. C.W. BERT 1977 The Shock and Vibration Bulletin 47, 89-94. Fundamental frequencies of orthotropic plates with various planforms and edge conditions.

8. A.A. LAURA and R.O. GROSSI 1979 Journal of Sound and Vibration 64, 257-267. Transverse vibrations of rectangular anisotropic plates with edges elastically restrained against rotation.

9. G. PRATHAP and T.K. VARADAN 1979 Journal of Sound and Vibration 63, 315-323. Nonlinear flexural vibration of anisotropic skew plates.

10. C.Y. CHIA and M. SATHYAMOORTHY 1980 Fibre Science and Technology 13, 81-95. Nonlinear vibration of anisotropic skew plates.

11. M. SATHYAMOORTHY 1982 Proceedings of the International Modal Analysis Conference, Orlando, Florida, 136-140. Large amplitude vibrations of moderately thick beams.

12. M. SATHYAMOORTHY and K.A.V. PANDALAI 1973 Journal of the Franklin Institute 296, 359-369. Nonlinear vibration of elastic skew plates exhibiting rectilinear orthotropy.

13. M. SATHYAMOORTHY 1983 (to appear) Proceedings of the Second International Conference on Composite Structures, Scotland. A new approach to the nonlinear dynamic analysis of composite plates.

14. R.F.S. HEARMON 1959 ASME Journal of Applied Mechanics 26, 537-540. The frequency of flexural vibration of rectangular orthotropic plates with clamped or supported edges.

15. R.F.S. HEARMON 1946 Proceedings of The Physical Society (London) 58, 78-92. The fundamental frequency of vibration of rectangular wood and plywood plates.

16. M. SATHYAMOORTHY and K.A.V. PANDALAI 1973 AIAA Journal 11, 1279-1282. Large amplitude flexural vibration of simply supported skew plates.

TABLE 1. Comparison of fundamental frequency results for clamped plates.

r	Isotropic		Boron-epoxy	
	Present	References	Present	References
0.5	24.6475(0)	25.6988*	23.4243(0)	24.8244*
	24.6456(1)	25.6495†	23.3855(1)	24.7932†
	24.6486(2)	26.4388@	23.3870(2)	25.5084@
		24.5800@		
1.0	36.0000(0)	38.9292*	28.4394(0)	32.9923*
	36.1018(1)	38.6986†	28.4776(1)	32.7535†
	36.1102(2)	40.3416@	28.4826(2)	34.2695@
		35.9860@		
1.5	60.8564(0)	64.7451*	40.7713(0)	47.8812*
	60.9481(1)	64.4753†	40.8444(1)	47.4995†
	60.9591(2)	66.8824@	40.8522(2)	49.7996@
		60.7500@		

(*,†,@) Calculated from References [14,15,3]
(0,1,2) Zero to Second-Order Self-Generating Functions.

TABLE 2. Values of A,B,C in Equations (10) and (11) for Anisotropic Rectangular Plates (r=0.5, ϕ=0).

A,B,C	Glass-epoxy			Boron-epoxy		
	(0)	(1)	(2)	(0)	(1)	(2)
A_{ss}	122.72	122.57	122.57	102.43	102.29	102.29
B_{ss}	194.37	191.38	191.33	172.82	170.16	170.13
C_{ss}	18.96	19.05	19.05	19.27	19.36	19.36
A_{cc}	548.70	546.88	546.95	513.46	510.32	510.33
B_{cc}	186.82	186.96	187.00	166.11	166.24	166.27
C_{cc}	20.24	20.45	20.46	20.57	20.78	20.79

TABLE 3. Values of A,B,C in Equations (10) and (11) for Anisotropic Square Plates (r=1, ϕ=30°).

A,B,C	Glass-epoxy			Boron-epoxy		
	(0)	(1)	(2)	(0)	(1)	(2)
A_{ss}	250.63	250.42	250.42	191.92	191.78	191.78
B_{ss}	346.06	340.73	340.66	201.46	198.36	198.32
C_{ss}	18.96	19.05	19.05	19.27	19.36	19.36
A_{cc}	798.45	804.18	804.59	554.69	560.74	561.10
B_{cc}	332.62	332.88	332.94	193.64	193.79	193.83
C_{cc}	20.24	20.45	20.46	20.57	20.78	20.79

TABLE 4. Values of A,B,C in Equations (10) and (11) for Anisotropic Rectangular Plates (r=1.5, ϕ=60°).

A,B,C	Glass-epoxy			Boron-epoxy		
	(0)	(1)	(2)	(0)	(1)	(2)
A_{ss}	720.61	719.93	719.93	578.39	577.87	577.87
B_{ss}	1017.07	1001.42	1001.23	676.31	665.91	665.78
C_{ss}	18.96	19.05	19.05	19.27	19.36	19.36
A_{cc}	2606.16	2613.54	2614.47	2005.32	2013.79	2014.60
B_{cc}	977.58	978.33	978.53	650.05	650.55	650.68
C_{cc}	20.24	20.45	20.46	20.57	20.78	20.79

TABLE 5. Values of Nondimensional Load q^*_o for Anisotropic Clamped Plates (r=1, ϕ=30°).

$\tilde{w}$	Glass-epoxy	Boron-epoxy
0.0	0.0	0.0
0.5	21.697	14.660
1.0	55.598	36.312
1.5	113.908	71.949

TABLE 6. Values of Nondimensional Frequency Ratio (ω/ω_o) for Anisotropic Clamped Plates (r=1.5, ϕ=60°).

$\tilde{w}$	Glass-epoxy	Boron-epoxy
0.0	1.0000	1.0000
0.5	1.0346	1.0299
1.0	1.1327	1.1153
1.5	1.2790	1.2448

LARGE AMPLITUDE VIBRATIONS OF INITIALLY STRESSED BIMODULUS THICK PLATES

Lien-Wen Chen and C. J. Lin

Department of Mechanical Engineering
National Cheng Kung University
Tainan, Taiwan, R.O.C.

ABSTRACT

The nonlinear governing differential equations of an initially stressed bimodulus thick plates are presented. The Galerkin approximate method is used to solve the large amplitude vibration problems of a simply supported rectangular bimodulus thick plate subjected to a combination of a pure bending stress and extensional stress in the plane of the plate. The Runge-Kutta method is employed to solve the nonlinear equations. The present results are compared with the previous results in the literature for ordinary thick plates and with the results of bimodulus plates in small amplitude region. Effects of various parameters on the large amplitude vibrations of bimodulus thick plates are studied.

1. INTRODUCTION

Recent investigations have shown that some composite materials behave differently in simple tension and compression (1). The tensile response of some polycrystalline graphites and high-polymers also behave differently in tension and compression (2) . This characteristic behavior is actually curvilinear, it is often approximated by two straight lines with a slope discontinuity at the origin. Thus, they are called bimodulus material (see Fig. 1).

The analysis, and hence the design, of structures fabricated from bimodulus materials is more difficult to accomplish than it is with conventional materials. The reason for the increased analytical difficulties is that it is not usually known a priori which parts of the structure are in tension and which are in compression. Kamiya studied large deflections of a circular plate by finite difference method (3). He also applied the energy method to large deflection problems of a rectangular plate (4). The effects of transverse shear had been studied by Kamiya in (5). Jones studied the buckling of bimodulus circular cylindrical shells (6) and the buckling of stiffened multi-layered bimodulus circular cylindrical shells (7).

The vibration problems of thick rectangular bimodulus composite plates are first studied by Bert and his associates (8). Bert and Kumar have also investigated the vibration of cylindrical shells (9). Recently, Chen and Doong studied the linear vibrations of initially stressed bimodulus thick plates (10).

The large amplitude vibration of initially stressed thick plates has not been reported in the literatures. In the present study, the nonlinear equations of a bimodulus thick plate in a general state of nonuniform initial stress are derived by using the average stress method of Brunelle and Robertson (11). The large amplitude vibrations of a simply supported rectangular plate in a state of initial stress are studied.

2. FORMULATION

The different properties in tension and compression of bimodulus materials can cause a shift in the neutral surface away from the geometric midplane, hence

symmetry about the midplane no longer holds. The result of this is that bending-stretching coupling of orthotropic type are exhibited, i.e. analogous to a two-layer cross-ply plate (one layer at 0^o and the other at 90^o) of ordinary orthotropic material. The governing equations of composite materials could be used for bimodulus materials except that the stress-strain relations must be of the bimodular form as in Ref. (8).

Chen and Doong derived the nonlinear governing equations for ordinary plates by average stress method (12, 13). In the present study, we used the same procedures combined with the convention expressions of the composite materials to derived the nonlinear governing equations of the initially stressed bimodulus thick plates.

We consider a simply supported rectangular plate in a state of initial stress. The state of initial stress is.

$$\sigma_{11} = \sigma_N + 2x_3\sigma_M / h \tag{1}$$

where σ_M and σ_N are taken to be constants. It is comprised of tensile and bending stresses (Fig. 2). The only non-zero stress and moment resultants are

$$N_{x_1} = \int_{-\frac{h}{2}}^{\frac{h}{2}} \sigma_{11}\, dx_3 = h\sigma_N \qquad N_{x_1} = \int_{-\frac{h}{2}}^{\frac{h}{2}} \sigma_{11}\, x_3 dx_3 = h^2\sigma_M / 6$$

$$M_{x_1}^* = \int_{-\frac{h}{2}}^{\frac{h}{2}} \sigma_{11}\, x_3^2 dx_3 = h^3\sigma_N / 12 \tag{2}$$

Lateral loads and body forces are taken to be zero. For a cross-ply composite plate, the laminate stiffnesses consist solely of A_{11}, A_{12}, A_{22}, A_{66}, B_{11}, B_{12}, B_{22}, B_{66}, D_{11}, D_{12}, D_{22}, D_{66}, S_{44} and S_{55}. The governing equations (3-7) and boundary conditions (8-9) are as follows:

$$\begin{aligned}
&\left(A_{11}\left(u_{1,1} + \tfrac{1}{2}w_{,1}^2\right) + A_{12}\left(u_{2,2} + \tfrac{1}{2}w_{,2}^2\right) + B_{11}\psi_{2,2} + B_{12}\psi_{2,2}\right)_{,1} \\
&+ \left(A_{66}\left(u_{1,2} + u_{2,1} + w_{,2}w_{,2}\right) + B_{66}\left(\psi_{1,2} + \psi_{2,1}\right)\right)_{,2} \\
&+ \left(N_{x_1}u_{1,1} + M_{x_1}\psi_{1,1}\right)_{,1} = \rho h\ddot{u}_1
\end{aligned} \tag{3}$$

$$\begin{aligned}
&\left(A_{12}\left(u_{1,1} + \tfrac{1}{2}w_{,1}^2\right) + A_{22}\left(u_{2,2} + \tfrac{1}{2}w_{,2}^2\right) + B_{12}\psi_{1,1} + B_{22}\psi_{2,2}\right)_{,2} \\
&+ \left(A_{66}\left(u_{1,2} + u_{2,1} + w_{,1}w_{,2}\right) + B_{66}\left(\psi_{1,2} + \psi_{2,1}\right)\right)_{,1} \\
&+ \left(N_x u_{2,1} + M_x \psi_{2,1}\right)_{,1} = \rho h\ddot{u}_2
\end{aligned} \tag{4}$$

$$\begin{aligned}
&\left\{\left(A_{11}\left(u_{1,1} + \tfrac{1}{2}w_{,1}^2\right) + B_{11}\psi_{1,1} + A_{12}\left(u_{2,2} + \tfrac{1}{2}w_{,2}^2\right) + B_{12}\psi_{2,2}\right)w_{,1}\right\}_{,1} \\
&+ \left\{\left(A_{66}\left(u_{2,1} + u_{1,2} + w_{,1}w_{,2}\right) + B_{66}\left(\psi_{1,2} + \psi_{2,1}\right)\right)w_{,1}\right\}_{,2} \\
&+ \left\{\left(A_{66}\left(u_{2,1} + u_{1,2} + w_{,1}w_{,2}\right) + B_{66}\left(\psi_{1,2} + \psi_{2,1}\right)\right)w_{,2}\right\}_{,1} \\
&+ \left\{\left(A_{12}\left(u_{1,1} + \tfrac{1}{2}w_{,1}^2\right) + B_{12}\psi_{1,1} + A_{22}\left(u_{2,2} + \tfrac{1}{2}w_{,2}^2\right)\right.\right.
\end{aligned}$$

$$+ B_{22}\psi_{2,2})w_{,2}\}_{,2} + (\kappa^2 S_{44}(\psi_1 + w_{,1}))_{,1} + (\kappa^2 S_{55}(\psi_2 + w_{,2}))_{,2}$$

$$+ (N_{x1}w_{,1})_{,1} = \rho h\ddot{w} \tag{5}$$

$$(B_{11}(u_{1,1} + \frac{1}{2}w_{,1}^2) + B_{12}(u_{2,2} + \frac{1}{2}w_{,2}^2) + D_{11}\psi_{1,1} + D_{12}\psi_{2,2})_{,1}$$

$$+ (B_{66}(u_{1,2} + u_{2,1} + w_{,1}w_{,2}) + D_{66}(\psi_{1,2} + \psi_{2,1}))_{,2}$$

$$+ (M_{x1}u_{1,1} + M_{x1}^*\psi_{1,1})_{,1} - \kappa^2(\psi_1 + w_{,1}) = \frac{\rho h^3}{12}\ddot{\psi}_1 \tag{6}$$

$$(B_{66}(u_{1,2} + u_{2,1} + w_{,1}w_{,2}) + D_{66}(\psi_{1,2} + \psi_{2,1}))_{,1}$$

$$+ (B_{12}(u_{1,1} + \frac{1}{2}w_{,1}^2) + B_{22}(u_{2,2} + \frac{1}{2}w_{,2}^2) + D_{12}\psi_{1,1}$$

$$+ D_{22}\psi_{2,2})_{,1} - \kappa^2 S_{55}(\psi_2 + w_{,2}) = \frac{\rho h^3}{12}\ddot{\psi}_2 \tag{7}$$

where the parameters and coefficients are defined in the Nomenclature section at the end of the paper.

The boundary conditions, for the simply supported plate, are on the x_1 = constant edges

$$w = 0$$
$$\psi_2 = 0$$
$$u_2 = 0 \tag{8}$$

$$\bar{F}_{11} + \Delta F_{11} = N_{x1}u_{1,1} + M_{x1}\psi_{1,1} + A_{11}(u_{1,1} + \frac{1}{2}w_{,1}^2) + B_{11}\psi_{1,1}$$
$$+ A_{12}(u_{2,2} + \frac{1}{2}w_{,2}^2) + B_{12}\psi_{2,2} = 0$$

$$\bar{M}_{11} + \Delta M_{11} = M_{x1}u_{1,1} + M_{x1}^*\psi_{1,1} + B_{11}(u_{1,1} + \frac{1}{2}w_{,1}^2) + D_{11}\psi_{1,1}$$
$$+ B_{12}(u_{2,2} + \frac{1}{2}w_{,2}^2) + D_{12}\psi_{2,2} = 0$$

on the x_2 = constant edges

$$w = 0$$
$$\psi_1 = 0$$
$$u_1 = 0 \tag{9}$$

$$\bar{F}_{22} + \Delta F_{22} = N_{x2}u_{2,2} + M_{x2}\psi_{2,2} + A_{22}(u_{2,2} + \frac{1}{2}w_{,2}^2) + B_{22}\psi_{2,2}$$
$$+ A_{21}(u_{1,1} + \frac{1}{2}w_{,1}^2) + B_{12}\psi_{1,1} = 0$$

$$\bar{M}_{22} + \Delta M_{22} = M_{x2}u_{2,2} + M_{x2}^*\psi_{2,2} + B_{22}(u_{2,2} + \frac{1}{2}w_{,2}^2) + D_{22}\psi_{2,2}$$
$$+ B_{21}(u_{1,1} + \frac{1}{2}w_{,1}^2) + D_{21}\psi_{1,1} = 0$$

3. Results and Discussions

The one term Galerkin approximate method is used to solve the nonlinear differential equations (3-7) for a simply supported rectangular plate. The displacement fields are assumed to be

$$
\begin{aligned}
w &= h\, w(t) \sin\frac{\pi x_1}{a} \sin\frac{\pi x_2}{b} \\
\psi_1 &= \psi_1(t) \cos\frac{\pi x_1}{a} \sin\frac{\pi x_2}{b} \\
\psi_2 &= \psi_2(t) \sin\frac{\pi x_1}{a} \cos\frac{\pi x_2}{b} \\
u_1 &= h u_1(t) \cos\frac{\pi x_1}{a} \sin\frac{\pi x_2}{b} \\
u_2 &= h u_2(t) \sin\frac{\pi x_1}{a} \cos\frac{\pi x_2}{b}
\end{aligned}
\tag{10}
$$

Substitute expression (10) into the governing equation (3-7) and use the Galerkin procedure. Then the following five nonlinear equations are obtained.

$$C_1 u_1 + C_2 \psi_1 + C_3 u_2 + C_4 w^2 + C_5 \psi_2 = \ddot{u}_1 \tag{11}$$

$$C_6 \psi_2 + C_7 u_1 + C_8 u_2 + C_9 w^2 + C_{32} \psi_1 = \ddot{u}_2 \tag{12}$$

$$C_{10} u_1 w + C_{11} u_2 w + C_{12} w^3 + C_{13} w + C_{14} \psi_1 w + C_{15} \psi_2 w + C_{16} \psi_1 + C_{17} \psi_2 = \ddot{w} \tag{13}$$

$$C_{18} u_1 + C_{19} u_2 + C_{20} w^2 + C_{21} \psi_1 + C_{22} \psi_2 + C_{23} w = C_{24} \ddot{\psi}_1 \tag{14}$$

$$C_{25} u_1 + C_{26} u_2 + C_{27} w^2 + C_{28} \psi_1 + C_{29} \psi_2 + C_{30} w = C_{31} \ddot{\psi}_2 \tag{15}$$

$$C_1 = -12\bar{A}_{11} - 12r_1^2 \bar{A}_{66} - \frac{12K_1 \cdot r_1^2}{K}$$

$$C_2 = -12\bar{B}_{11} - 12r_1^2 \bar{B}_{66} - \frac{2K_1}{K} \beta\, r_1^2$$

$$C_3 = -12r_1\bar{A}_{12} - 12r_1\bar{A}_{66}$$

$$C_4 = -\frac{128}{\pi^2} (3K)^{-\frac{1}{2}} (2\bar{A}_{11} - r_1^2 \bar{A}_{12} + r_1^2 \bar{A}_{66})$$

$$C_5 = -12r_1 (\bar{B}_{66} + \bar{D}_{12})$$

$$C_6 = -12\bar{B}_{66} - 12r_1^2 \bar{B}_{22} - \frac{2K_1 \beta r_1^2}{K}$$

$$C_7 = 12r_1 (-\bar{A}_{12} - \bar{A}_{66})$$

$$C_8 = -12 (\bar{A}_{66} + r_1^2 \bar{A}_{22} + \frac{K_1 r_1^2}{K})$$

$$C_9 = -\frac{128}{\pi^2} (3K)^{-\frac{1}{2}} r_1 (\bar{A}_{66} + 2r_1^2 \bar{A}_{22} - \bar{A}_{12})$$

$$C_{10} = -\frac{128}{\pi^2} (3K)^{-\frac{1}{2}} (-2\bar{A}_{11} + 2r_1^2 \bar{A}_{66} - r_1^2 \bar{A}_{12})$$

$$C_{11} = -\frac{256}{\pi^2} r_1 (3K)^{-\frac{1}{2}} (\bar{A}_{66} - \bar{A}_{12} - r_1^2 \bar{A}_{22})$$

$$C_{12} = -\frac{9}{K} (\frac{9}{2} \bar{A}_{11} + r_1^2 \bar{A}_{12} + \frac{9}{2} r_1^4 \bar{A}_{22} + 2r_1^2 \bar{A}_{66})$$

$$C_{13} = -\pi^2 (\bar{S}_{44} + r_1^2 \bar{S}_{55}) - 12 \frac{K_1}{K} r_1^2$$

$$C_{14} = -\frac{256}{\pi^2} (3K)^{-\frac{1}{2}} (\bar{B}_{11} + r_1^2 \bar{B}_{66} - r_1^2 \bar{B}_{12})$$

$$C_{15} = \frac{256r}{\pi^2} (3K)^{-\frac{1}{2}} (-\bar{B}_{66} + \bar{B}_{12} + r_1^2 \bar{B}_{22})$$

$$C_{16} = -\pi \left(\frac{\pi^2}{12} K\right)^{\frac{1}{2}} \bar{S}_{44}$$

$$C_{17} = -\pi r_1 \left(\frac{\pi^2}{12} K\right)^{\frac{1}{2}} \bar{S}_{55}$$

$$C_{18} = -\left(12\bar{B}_{11} + 12r_1^2 \bar{B}_{66} + \frac{2K_1 \beta r_1^2}{K}\right)$$

$$C_{19} = -12r_1 \left(\bar{B}_{12} + \bar{B}_{66}\right)$$

$$C_{20} = -\frac{128}{\pi^2} (3K)^{-\frac{1}{2}} \left(2\bar{B}_{11} - r_1^2 \bar{B}_{12} + r_1^2 \bar{B}_{66}\right)$$

$$C_{21} = -12 \left(\bar{D}_{11} + r_1^2 \bar{D}_{66}\right) - \frac{K_1 r_1^2}{K} - \frac{K\pi^2}{12} \bar{S}_{44}$$

$$C_{22} = -12r_1 \left(\bar{D}_{66} + \bar{D}_{12}\right)$$

$$C_{23} = -\pi \left(\frac{\pi^2}{12} K\right)^{\frac{1}{2}} \bar{S}_{44}$$

$$C_{25} = -12r_1 \left(\bar{B}_{66} + \bar{B}_{12}\right) \qquad C_{26} = -12 \left(\bar{B}_{66} + r_1^2 \bar{B}_{22}\right) - \frac{2K_1 \beta r_1^2}{K}$$

$$C_{27} = -\frac{128}{\pi^2} r_1 (3K)^{-\frac{1}{2}} \left(\bar{B}_{66} + 2r_1^2 \bar{B}_{22} - \bar{B}_{12}\right)$$

$$C_{28} = -12r_1 \left(\bar{D}_{66} + \bar{D}_{12}\right)$$

$$C_{29} = -12 \left(\bar{D}_{66} + r_1^2 \bar{D}_{22} + r_1 \bar{D}_{12}\right) - K \frac{\pi^2}{12} \bar{S}_{55}$$

$$C_{30} = -\pi r_1^2 \left(\frac{\pi^2}{12} K\right)^{\frac{1}{2}} \bar{S}_{55}$$

$$C_{24} = C_{31} = \frac{1}{12}$$

$$C_{32} = -12r_1 \left(\bar{B}_{66} + \bar{B}_{12}\right)$$

The fourth order Runge-Kutta method is used to integrate the nonlinear equation (11-15). The neutral surface positions although are functions of x_1 and x_2 for the large deflection of the plate, we neglect the influence of it and take the neutral surface positions to be a constant. The neutral surface positions are obtained from the static solutions which are the same procedure as in the references (8, 10). The time increment is $\Delta\tau = 0.0005$. The initial conditions are zero except $w(0) = w_{max}$. The value of w_{max} may vary from 0.2 to 1.0. We first use the present method to obtain the period of small amplitude vibration. The present results are compared with reference (10) as in Table 1. It can be seen that the solution method is satisfactorily accurate.

The maximum amplitude w_{max}, vs. frequency ratios Ω/Ω^* are plotted in Fig. 3, Ω^* is the nondimensional natural frequency of a bimodulus plate in large amplidue and Ω is the nondimensional frequency of small amplitude vibration of a bimodulus plate. It shows that the frequency ratio decreases when the maximum amplitude w_{max} increases. It means that the nonlinear frequency will increase as the amplitude becomes large. The effects of initial stress also are shown in Fig. 3. The tensile stresses increase the frequency ratio and compressive stresses decrease the frequency ratio. The compressive stresses have more significant effect especially when it approach the buckling load. Fig. 4 shows the effect of tensile to compressive modulus ratio E^t/E^c. $E^t/E^c = 1.5$ means the tensile strength is stronger than compressive strength, so will have higher frequency ratio than $E^t/E^c = 0.5$. The most interesting effect is shown in Fig. 5.

When the ratio β of bending to normal stress increases, the frequency ratio Ω/Ω^* decreases with $E^t/E^c = 0.5$. The reverse effect is seen for the $E^t/E^c = 1.5$ curve. The reason is that the neutral surfaces have different positions for different E^t/E^c.

Plots are made of period coefficient T* vs. thickness parameter a/h in Fig. 6. We can see that the period T* is small when the thickness of the plate is large. It means that the nonlinear frequency will increase with the thickness. The effects of $S = \frac{E}{G^*}$ on the period T* are shown in Fig. 7. G* is the transverse shear modulus. The shear resistance becomes large when G* is large. We can see that the large S will have large period T*. Large S means that it easily deforms in transverse direction, so that it will have lower frequency Ω^*.

4. CONCLUSIONS

The numerical studies of large amplitude vibrations of the simply supported rectangular bimodulus thick plates have been carried out. From the numerical results, the following conclusions are reached

(1) The nonlinear frequency will increase with the amplitude of vibration.

(2) The compressive stresses will reduce the frequency ratio Ω/Ω^* and the tensile stresses have reverse effect.

(3) The frequency ratio decreases as the bending to normal stress ratio increases when the tensile modulus E^t is smaller than the compressive modulus E^c. The reverse phenomena will appear when the E^t is larger than E^c.

(4) The thicker the plate is, the larger the nonlinear frequency is.

(5) When the plate is transverse isotropy, the weak deformation resistance in the transverse direction will reduce the nonlinear frequency Ω^*.

The large amplitude plate vibration of two or more layer of composite materials and the large amplitude of bimodulus circular plate will be studied. These studies are believed to be helpful to understand the vibration phenomena of thick bimodulus plates.

REFERENCES

1. Clark, S. K. Textile Research Journal, Vol. 33, No. 4, Apr. 1963, pp. 295-313. "The Plane Elastic Characteristics of Cord-Rubber Laminates".

2. Seldin, E. J., Carbon, 4, 1966, pp. 177-191. "Stress-Strain Properties of Polycrystalline Graphites in Tension and Compression at Room Temperature".

3. Kamiya, N., Journal of Engineering Materials and Technology, Trans., ASME, Vol. 97H, No. 1, Jan. 1975, pp. 52-56. "Large Deflection of a Different Modulus Circular Plate".

4. Kamiya, N., Journal of Structural Machanics, Vol. 3, No. 3, 1975, pp. 317-329. "An Energy Method Applied to Large Elastic Deflection of a Thin Plate of Bimodulus Material".

5. Kamiya, N., Nuclear Engineering and Design, Vol. 32, 1975, pp. 351-357. "Transverse Shear Effect in a Bimodulus Plate".

6. Jones, R. M., AIAA Journal, Vol. 9, No. 1, Jan. 1971, pp. 53-61. "Buckling of Circular Cylindrical Shells with Different Moduli in Tension and Compression".

7. Jones, R. M., AIAA Journal, Vol. 9, No. 5, May 1971, pp. 917-923. "Buckling of Stiffened Multilayered Circular Cylindrical Shells with Different Orthotropic Moduli in Tension and Compression".

8. Bert, C. W., Reddy, J. N., Chao, W. C., and Reddy, V. S., Journal of Applied Mechanics, Vol. 48, June, 1981, pp. 371-376. "Vibration of Thick Rectangular Plates of Bimodulus Composite Material".

9. Bert, C. W., and Kumar M., Journal of Sound and Vibration, Vol. 81, 1982, pp. 107-121. "Vibration of Cylindrical Shells of Bimodulus Composite Materials".

10. Doong, J. L. and Chen, L. W., ASME paper, 83-DET-29, also to appear in Journal of Vibration, Stress Analysis, Acoustics and Reliability. "Vibration of a Bimodulus Thick Plate".

11. Brunelle, E. J. and Robertson, S. R., AIAA Journal, Vol. 12, NM. 8, Aug. 1974, pp. 1036-1044. "Initially Stressed Mindlin Plates".

12. Chen, L. W. and Doong J. L., AIAA Journal Aug. 1983. "Post-Buckling Behavior of a Thick Plate".

13. Chen, L. W. and Doong J. L., Journal of Sound and Vibration, Aug. 22, 1983. "Large Amplitude Vibrations of an Initially Stressed Thick Plates".

NOMENCLATURE

a, b	side length of plate in x_1 and x_2 directions
A_{ij}	stretching stiffness
B_{ij}	bending-stretching coupling stiffness
D_{ij}	bending stiffnesses
D	$D = E_{11}{}^t h / (1-\nu_{11}{}^{t2})$
$\bar{A}_{ij}$	dimensionless in-plane stiffness $\bar{A}_{ij} = A_{ij} / hD$
$\bar{B}_{ij}$	dimensionless bending-stretching coupling stiffness $\bar{B}_{ij} = B_{ij} / h^2 D$
$\bar{D}_{ij}$	dimensionless bending stiffness $\bar{D}_{ij} = D_{ij} / h^3 D$
E^t, E^c	respective compressive and tensile Young's moduli
G^t, G^c	respective compressive and tensile shear moduli
G^{t*}, G^{c*}	respective cokpressive and tensile transverse shear moduli
h	plate thickness
K_1	initial stress coefficient $K_1 = 12bN_x / \pi^2 h^2 D$
N_{x1}, M_{xj}	stress and moment resultants
Q_{ijk}	plane-stress reduced stiffness coefficients
S	transversely isotropic parameter, $S = E_{11}{}^t / G^*$
S_{ii}	thickness-shear stiffnesses
u_1, u_2	in-plane displacement
w	transverse displacement
Z_n	neutral surface positions for $u_{1,1} + Z_n \psi_{1,1} = 0$
β	ratio of bending stress to normal stress, $\beta = \sigma_M / \sigma_N$
ρ	density
ψ_1, ψ_2	angular changes of lines initially normal to the middle surface
ν^t, ν^c	respective compressive and tensile Poisson's ratios
κ_4^2, κ_5^2	thickness-shear correction factors = $\pi^2/12$
$(\ )_{,12}$	$\partial^2 (\ ) / \partial x_1 \partial x_2$
K	$K = a^2 / h^2 K^2$
r_1	aspect ratio, $r_1 = a/b$
τ	time parameter, $\tau = t\sqrt{D/12\pi^2 \rho h a^2}$
T^*	period coefficient of bimodulus plate in large amplitude, having dimension τ
Ω^*	frequency of bimodulus plate in large amplitude vibration, $\Omega^* = 1/T^*$

Ω frequency of bimodulus plate in small amplitude vibration

K_1	-2	-1	0	1	2	3
A	6.8199	4.65	3.7605	3.2335	2.882	2.6271
B	6.834	4.6582	3.7593	3.2371	2.8854	2.6281

Table 1 Comparison of the present results of period with the results of linear theory.

A: Present results. B: results of linear theory

$a/h=10$, $a/b=1$, $S=4.55$, $E^t/E^C=1.5$, $\beta=0$

T=period.

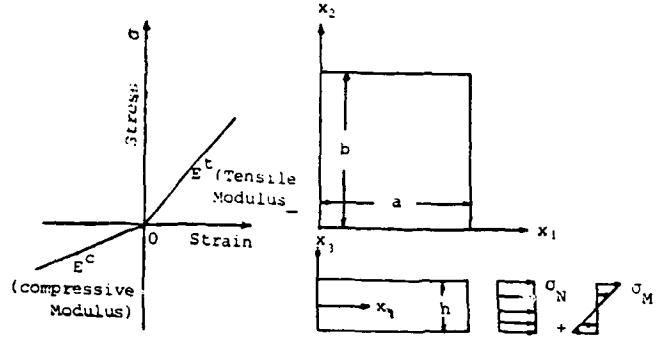

Fig. 1 Stress-strain relation of linearlized different modulus materials.

Fig. 2 The rectangular plate and the applied stress field.

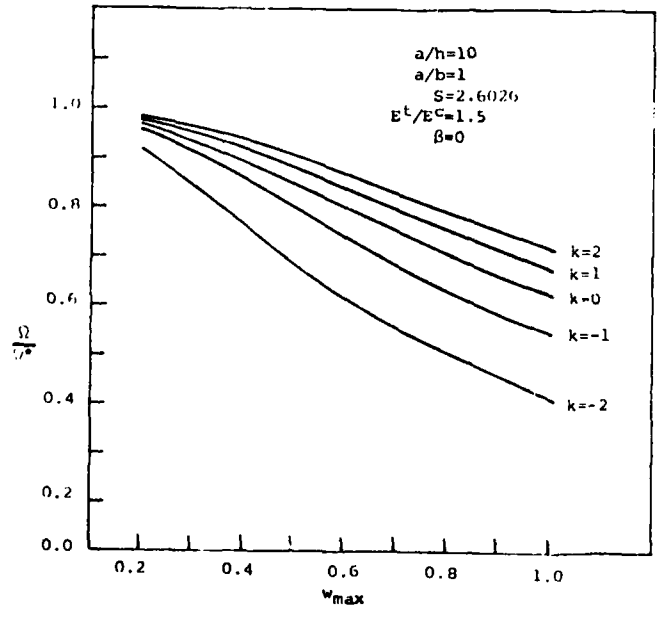

Fig. 3 Frequency ratio $\frac{\Omega}{\Omega^*}$ vs. w_{max} with various initial stresses K_1.

AD-A143 301 PROCEEDINGS OF THE INTERNATIONAL CONFERENCE ON RECENT ADVANCES IN STRUCTU..(U) SOUTHAMPTON UNIV (ENGLAND) INST OF SOUND AND VIBRATION RESEAR.. M PETYT ET AL. 3/6

UNCLASSIFIED 1984 F/G 20/11 NL

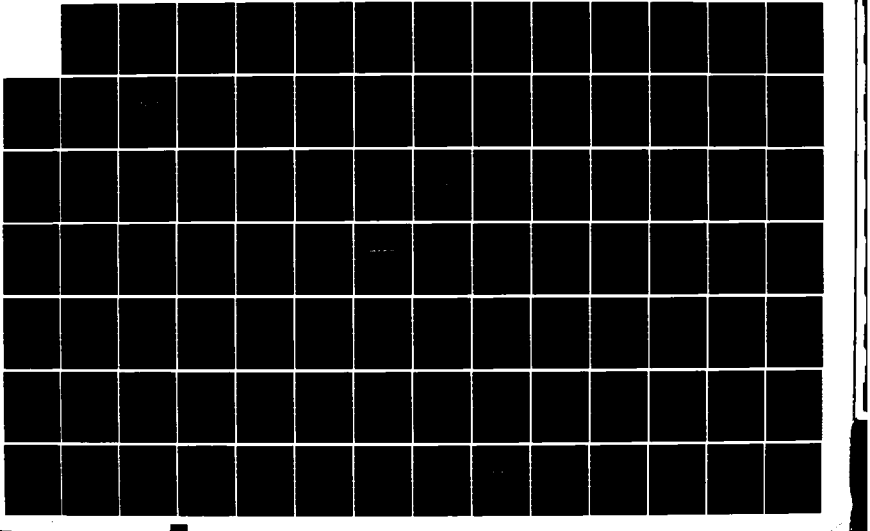

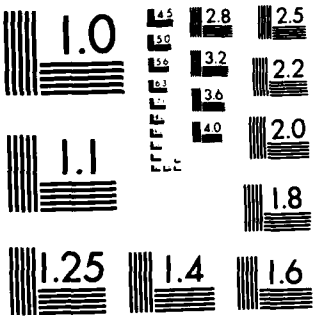

MICROCOPY RESOLUTION TEST CHART
NATIONAL BUREAU OF STANDARDS-1963-A

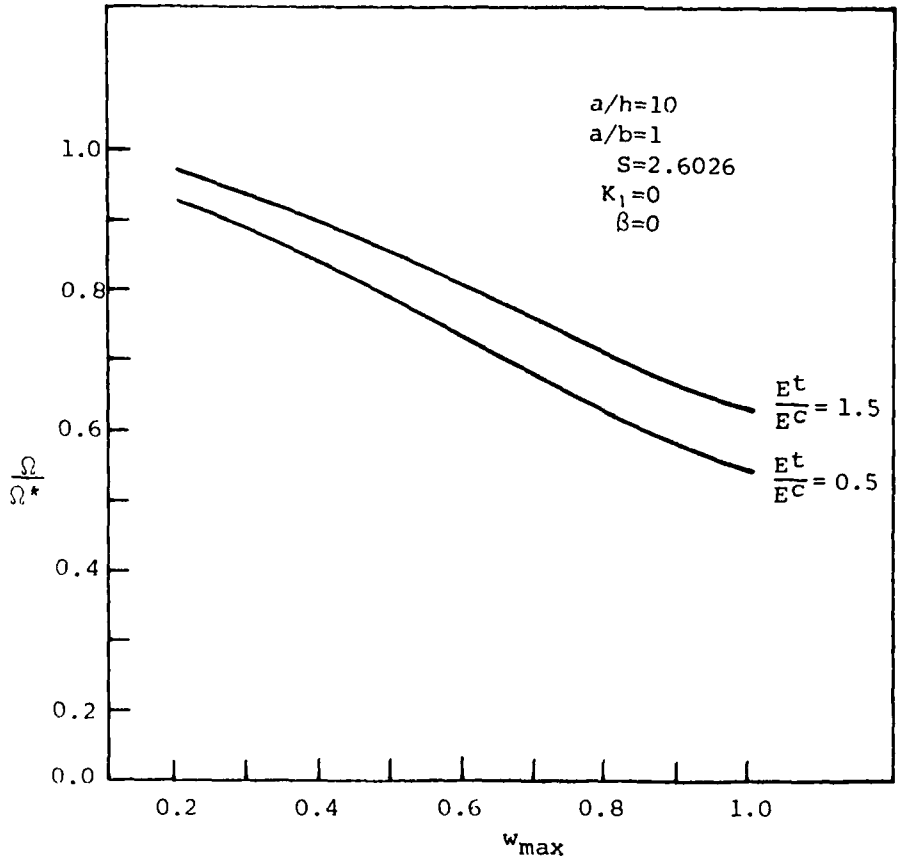

Fig. 4 Frequency ratio $\frac{\Omega}{\Omega^*}$ vs. w_{max}. E^t/E^c are equal to 1.5 and 0.5 in two curves, respectively.

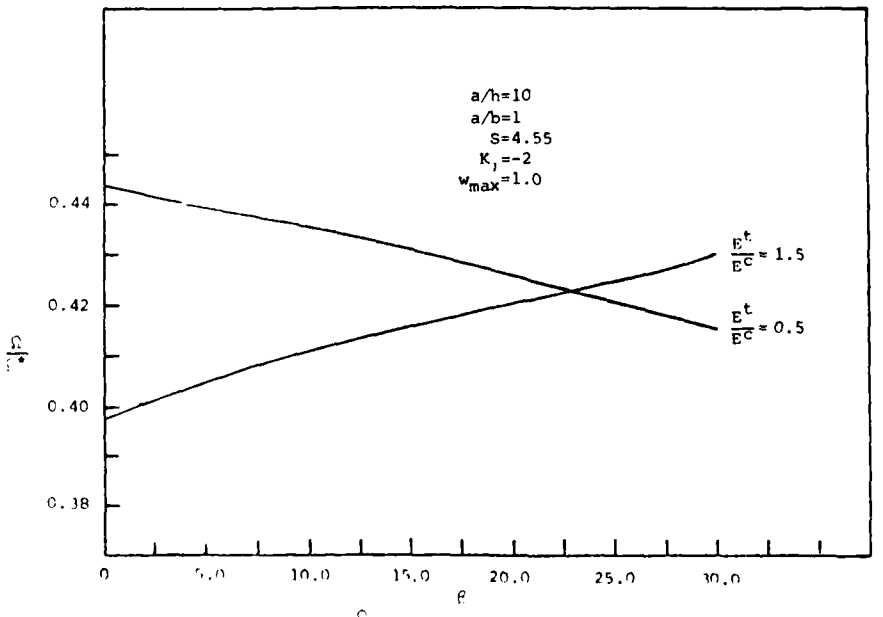

Fig. 5 Frequency ratio $\frac{\Omega}{\Omega^*}$ vs. bending to normal stress ratio ß.

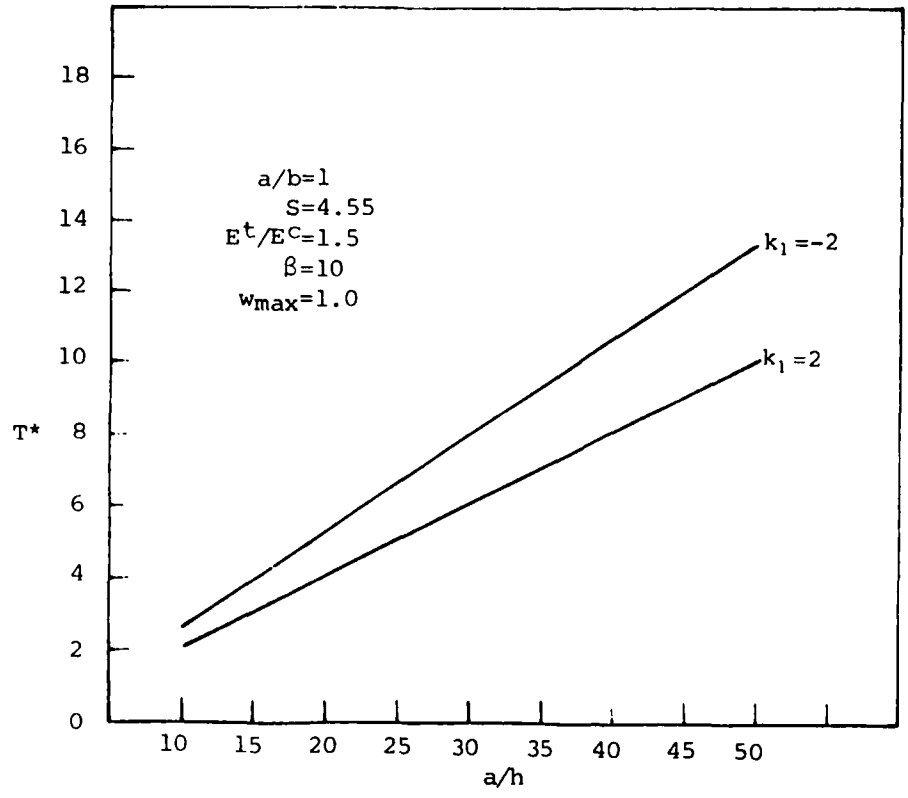

Fig. 6 Period coefficient T* vs. thickness parameter a/h.

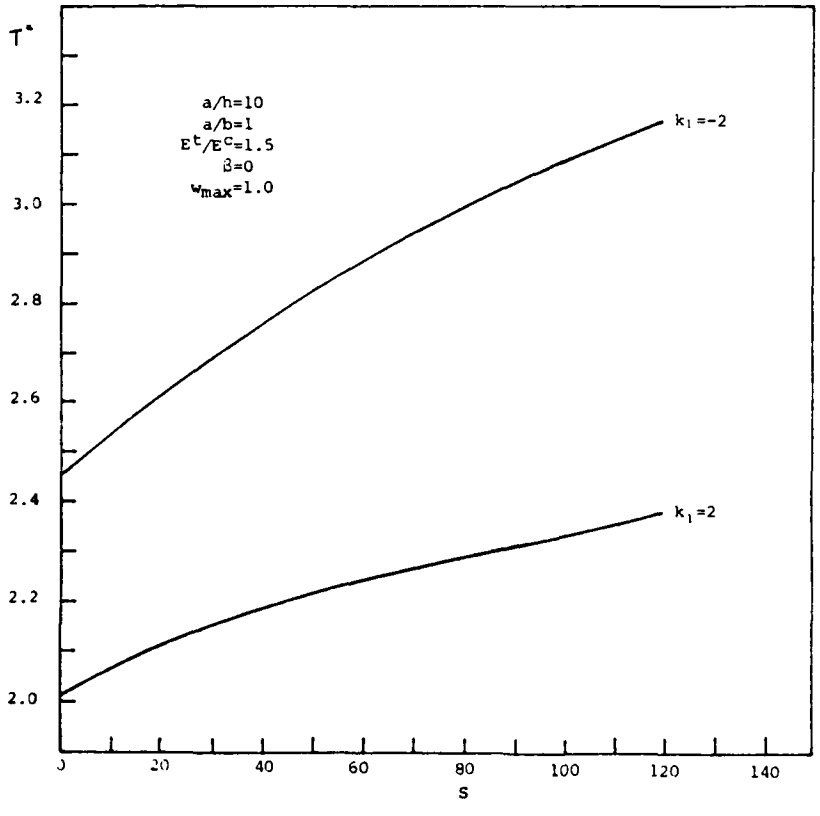

Fig. 7 Period coefficient T* vs. transverse isotropic parameter S.

NON-LINEAR MULTIMODE RESPONSE OF CLAMPED RECTANGULAR PLATES TO ACOUSTIC LOADING

Chuh Mei
Old Dominion University

and

Donald B. Paul
Air Force Wright Aeronautical Laboratories

1. INTRODUCTION

Acoustically induced fatigue failures in aircraft structural components have resulted in unacceptable maintenance and inspection burdens. In some cases, sonic fatigue failures have resulted in major structural redesigns. Therefore, accurate prediction methods are needed to determine the sonic fatigue life of structures.

Many analytical and experimental programs to develop sonic fatigue design criteria, however, have repeatedly shown a poor comparison between analytical and measured maximum root-mean-square (RMS) strain at high sound pressure levels. [1,2]. Deviations in excess of 100 percent are common. Neglecting large-deflections in the analysis has been identified as a major reason for the enormous discrepancy [2]. Recently, analytical efforts [3,4] with a single-mode approach, and a test program [5] have demonstrated that the prediction of panel random response is greatly improved by including the large-amplitude effect in the formulation. Test results [5] also show that there is more than one mode responding. Multiple modes were also observed by White [6] in experimental studies on aluminum and carbon fiber-reinforced plates under acoustic loading. White also showed that the fundamental mode responded significantly and contributed more than one-half of the total mean-square strain response. Therefore, in order to have an accurate determination of the random response of a structure, multiple modes should be used in the analysis. This paper presents an analytical solution technique for the large-amplitude random response of clamped rectangular plates considering multiple modes in the analysis. The von Kármán large-deflection plate equations are solved by a technique which reduces the fourth order nonlinear partial differential equations to a set of second order nonlinear differential equations with time as the independent variable. A Fourier-type series representation of the out-of-plane deflection and stress function is assumed. The compatibility equation is solved by direct substitution, and the equilibrium equation is solved through the use of Bubnov-Galerkin approach. The acoustic excitation is assumed to be Gaussian. The Krylov-Bogoliubov-Caughey equivalent linearization method [7,9] is then used so that the derived set of second order nonlinear differential equations are linearized to an equivalent set of second order linear differential equations. Transformation of coordinates from the generalized displacements to the normal-mode coordinates, and an iterative scheme are employed to obtain RMS maximum panel deflection, RMS maximum strain, and equivalent linear (or nonlinear) frequencies for rectangular plates at various excitation pressure spectral densities. Convergence of the results is demonstrated by using 4, 6, 10, and 15 terms in the transverse deflection function.

2. MATHEMATICAL FORMULATION AND SOLUTION PROCEDURE

Assuming that the effects of both inplane and rotatory inertia forces can be neglected, the dynamic von Kármán equations of a rectangular isotropic

plate are

$$L(w,F) = D\nabla^4 w + \rho h w_{,tt} + g w_{,t} - p(t)$$
$$- h(F_{,yy}w_{,xx} + F_{,xx}w_{,yy} - 2F_{,xy}w_{,xy}) = 0 \quad (1)$$

$$\nabla^4 F = E(w^2_{,xy} - w_{,xx}w_{,yy}) \quad (2)$$

The transverse deflection which satisfies the clamped boundary conditions

$$w = w_{,x} = 0 \quad \text{on } x = 0 \text{ and } a \quad (3a)$$

$$w = w_{,y} = 0 \quad \text{on } y = 0 \text{ and } b \quad (3b)$$

is assumed as

$$w(y,t) = h \sum_m \sum_n W_{mn}(t) f_m(x) g_n(y) \qquad m,n = 1,2,3,\ldots \quad (4)$$

where

$$f_m(x) = \cos\frac{(m-1)\pi x}{a} - \cos\frac{(m+1)\pi x}{a} \quad (5)$$

$$g_n(y) = \cos\frac{(n-1)\pi y}{b} - \cos\frac{(n+1)\pi y}{b} \quad (6)$$

Upon examination of the foregoing expression for the transverse deflection, it is found that the compatibility equation (2) can be identically satisfied if the stress function F is taken in the following form:

$$F = -P_x\frac{y}{2}^2 - P_y\frac{x}{2}^2 + Eh^2\sum_p\sum_q F_{pq}\cos\frac{p\pi x}{a}\cos\frac{q\pi y}{b} \qquad p,q = 0,1,2,\ldots \quad (7)$$

Direct substitution of Eqs. (4) and (7) into Eq. (2), performing the required differentiations, multiplications, and a Fourier analysis of the resulting terms yields a quadratic relationship between F_{pq} and W_{mn}

$$F_{pq} = \frac{1}{(p^2/\alpha + q^2\alpha)^2}\sum_m\sum_n\sum_k\sum_\ell B_{pqmnk\ell} W_{mn} W_{k\ell} \quad (8)$$

in which B_{pqmnkl} are integers (tabulated in Reference 10) and α=a/b. A complete description of the solution technique used to solve equation (2) is given in Reference [10].

The average edge loads P_x and P_y in Eq. (7) are determined from inplane boundary conditions. The particular inplane boundary condition of most interest in the study of sonic fatigue of structural panels is the one in which the edges are restrained from movement, that is

$$u=0 \qquad \text{on } x=0 \text{ and } a \tag{9a}$$

$$v=0 \qquad \text{on } y=0 \text{ and } b \tag{9b}$$

or

$$\int_0^a \frac{\partial u}{\partial x}\,dx = \int_0^a \left[\frac{1}{E}(F_{,yy} - \nu F_{,xx}) - \frac{1}{2} w_{,x}^2\right]dx = 0 \tag{10a}$$

$$\int_0^b \frac{\partial v}{\partial y}\,dy = \int_0^b \left[\frac{1}{E}(F_{,xx} - \nu F_{,yy}) - \frac{1}{2} w_{,y}^2\right]dy = 0 \tag{10b}$$

Performing the differentiation and integration as indicated in Eq. (10) yields relationships for P_x and P_y in terms of the deflection coefficients W_{mn}. These relations are too lengthy to reproduce here, but may be found in References [10] and [11].

With the assumed deflection w given by Eq. (4) and the stress function F given by Eq. (7), Eq. (1) is then satisfied by applying Bubnov-Galerkin method:

$$\iint L(w,F) f_r g_s\,dxdy = 0 \qquad r,s = 1,2,3,\ldots \tag{11}$$

The integration of each of the terms in Eq. (11) can be found in Ref. [10]. A set of nonlinear time-differential equations is obtained after performing the integration over the total area of the panel, and it can be written in matrix notation as

$$[M]\{\ddot{W}\} + [C]\{\dot{W}\} + [K]_L\{W\} + \{\beta(W)\} = \{p(t)\} \tag{12}$$

where [M], [C], and $[K]_L$ are the generalized mass, damping, and linear stiffness matrices, respectively, and $\{\beta\}$ is a vector function which is cubic in the generalized displacements $\{W\}$.

If the acoustic pressure excitation p(t) is stationary Gaussian, ergodic, and has a zero mean, then application of the Krylov-Bogoliubov-Caughey equivalent linearization technique [3,4,7-9] yields an equivalent set of linear equations as

$$[M]\{\ddot{W}\} + [C]\{\dot{W}\} + ([K]_L + [K]_{EL})\{W\} = \{p(t)\} \tag{13a}$$

or

$$[M]\{\ddot{W}\} + [C]\{\dot{W}\} + [K]\{W\} = \{p(t)\} \tag{13b}$$

The elements of the generalized equivalent linear or nonlinear stiffness matrix $[K]_{EL}$ can be derived from the expression [8]

$$(K_{EL})_{rsij} = \mathcal{E}\left[\frac{\partial \beta_{rs}}{\partial W_{ij}}\right] \tag{14}$$

where $\xi\{\}$ is an expected value operator. The elements $(K_{EL})_{rsij}$ are too lengthy to reproduce here, but may be found in Reference [11]. The approximate generalized displacements $\{W\}$, computed from the linearized Eq. (13), are also Gaussian and approach stationary because the panel motion is stable.

To determine the mean-square generalized displacements $\overline{w^2}_{mn}$ an iterative process is introduced. The undamped linear equation of Eq. (13a) is solved first, which required simply the determination of the eigenvalues and eigenvectors of the undamped linear equation

$$\omega_j^2 [M]\{\phi\}_j = [K]_L \{\phi\}_j \tag{15}$$

where ω_j is the linear frequency of vibration, and $\{\phi\}_j$ is the normal mode shape.

Apply a coordinate transformation, from the generalized displacements to the normal coordinates (this analysis will use the first 4 modes), by

$$\underset{mx1}{\{W\}} = \underset{mx4}{[\phi]} \underset{4x1}{\{q\}} \qquad 4<m \tag{16}$$

where each column of $[\phi]$ is a normal mode $\{\phi\}_j$. The damped linear equation of Eq. (13a) becomes

$$[M]\{\ddot{q}\} + [C]\{\dot{q}\} + [K]_L\{q\} = \{P(t)\} \tag{17}$$

where

$$[M] = [\phi]^T[M][\phi] \tag{18a}$$

$$[C] = [\phi]^T[C][\phi] = 2[\zeta\omega][M] \tag{18b}$$

$$[K]_L = [\phi]^T[K]_L[\phi] = [\omega^2][M] \tag{18c}$$

$$\{P\} = [\phi]^T\{p\} \tag{18d}$$

The jth row of Eq. (17) is

$$\ddot{q}_j + 2\zeta_j\omega_j\dot{q}_j + \omega_j^2 q_j = \frac{P_j}{M_j} \tag{19}$$

The mean-square normal coordinate is simply

$$\overline{q_j^2} \cong \frac{\pi S_p(\omega_j)}{4M_j^2\zeta_j\omega_j^3} \tag{20}$$

where $S_p(\omega)$ is the spectral density function of the excitation $P_j(t)$. The convariance matrix of the linear generalized displacements is

$$\overline{[W_{mn}W_{kl}]_L} = \frac{\pi}{4}\sum_j \{\phi\}_j \frac{S_p(\omega_j)}{M_j^2 \zeta_j \omega_j^3}\{\phi\}_j^T \tag{21}$$

This initial estimate of expected value on generalized displacements can now be used to compute the generalized linear stiffness matrix $[K]_{EL}$ through Eq. (14). The undamped linearized equation of Eq. (13) is solved again

$$\Omega_j^2[M]\{\phi\}_j = ([K]_L + [K]_{EL})\{\phi\}_j \tag{22}$$

where Ω_j is the equivalent linear or nonlinear frequency of vibration, and $\{\phi_j\}$ is the associated equivalent linear normal mode shape. Then Eq. (13) is transformed again and has the form as

$$[M]\{\ddot{q}\} + [C]\{\dot{q}\} + [K]\{q\} = \{P(t)\} \tag{23}$$

in which

$$[K] = [\phi]^T([K]_L + [K]_{EL})[\phi] = [\Omega^2][M] \tag{24}$$

the jth row of Eq. (23) is

$$\ddot{q}_j + 2\zeta_j\omega_j\dot{q}_j + \Omega_j^2 q_j = \frac{P_j}{M_j} \tag{25}$$

and the displacement convariance matrix is

$$\overline{[W_{mn}W_{kl}]} = \frac{\pi}{4}\sum_j \{\phi\}_j \frac{S_p(\Omega_j)}{M_j^2 \zeta_j \omega_j \Omega_j^2}\{\phi\}_j^T \tag{26}$$

The diagonal terms of $\overline{[W_{mn}W_{kl}]}$ are the mean-square generalized displacements $\overline{W^2}_{mn}$. As the iterative process converges on the iter-th cycle, the relations

$$(\overline{q_j^2})_{iter} \cong (\overline{q_j^2})_{iter-1} \tag{27a}$$

$$(\Omega_j^2)_{iter} \cong (\Omega_j^2)_{iter-1} \tag{27b}$$

$$(\overline{W_{mn}^2})_{iter} \cong (\overline{W_{mn}^2})_{iter-1} \tag{27c}$$

become satisfied. Convergence is considered achieved when the difference of the RMS displacements satisfies the requirement

$$\left|\frac{(\text{RMS } W_{mn})_{iter} - (\text{RMS } W_{mn})_{iter-1}}{(\text{RMS } W_{mn})_{iter}}\right| < 10^{-3} \text{ for all } m, n \tag{28}$$

Once the RMS generalized displacements are determined, the RMS deflection and the maximum RMS strain can be determined from Eqs. (4), (7) and the strain-displacement relations as follows.

For a rectangular plate ($a \geq b$) with clamped support along all four edges, the maximum bending strain occurs at the extreme-fiber perpendicular to its long edge at the midpoint.

$$(\varepsilon_y)_b = \pm \frac{h}{2} \frac{\partial^2 w}{\partial y^2} \tag{29a}$$

or

$$\left(\frac{\varepsilon_y b^2}{h^2}\right)_b = \pm \frac{\pi^2}{2} \sum_{mn} \sum f_m(x) \left[(n-1)^2 \cos\frac{(n-1)\pi y}{b} - (n+1)^2 \cos\frac{(n+1)\pi y}{b}\right] W_{mn} \tag{29b}$$

The membrane strain is given by

$$(\varepsilon_y)_m = \frac{1}{E} (F_{,xx} - \nu F_{,yy}) \tag{30a}$$

or

$$\left(\frac{\varepsilon_y b^2}{h^2}\right)_m = \frac{\pi^2}{8} \sum_{mn} \sum W_{mn} Z_y(W_{mn}) + \sum_{mnkl} \sum_{pq} \sum \sum \sum \sum \sum C_{pq} B_{pqmnkl} W_{mn} W_{kl} \tag{30b}$$

in which

$$C_{pq} = \frac{\pi^2 (\nu q^2 - p^2/\alpha^2)}{(p^2/\alpha + q^2\alpha)^2} \cos\frac{p\pi x}{a} \cos\frac{q\pi y}{b} \tag{31}$$

From

$$\varepsilon_y = (\varepsilon_y)_b + (\varepsilon_y)_m \tag{32}$$

the maximum mean-square strain becomes

$$\overline{\left(\frac{\varepsilon_y b^2}{h^2}\right)^2} = \overline{\left(\frac{\varepsilon_y b^2}{h^2}\right)_b^2} + 2\xi\left[\left(\frac{\varepsilon_y b^2}{h^2}\right)_b \left(\frac{\varepsilon_y b^2}{h^2}\right)_m\right] + \overline{\left(\frac{\varepsilon_y b^2}{h^2}\right)_m^2} \tag{33}$$

For Gaussian random processes with zero-mean we have

$$\xi(W_{ij} W_{kl} W_{mn}) = 0 \tag{34}$$

$$\xi(W_{ij} W_{kl} W_{mn} W_{rs}) = \xi(W_{ij} W_{kl})\, \xi(W_{mn} W_{rs}) + \xi(W_{ij} W_{mn})\, \xi(W_{kl} W_{rs}) + \xi(W_{ij} W_{rs})\, \xi(W_{kl} W_{mn}) \tag{35}$$

and the maximum RMS strain can be determined from Eq. (33).

3. RESULTS AND DISCUSSION

Using the present formulation, the nonlinear response of square and rectangular ($\alpha = 2$) plates with all edges clamped and subjected to broadband random excitation are studied. In the results presented, the white noise excitation is band-limited with a frequency bandwidth of 25 Hz to 6000 Hz, the damping ratio is assumed to be constant for all four normal modes and Poisson's ratio is equal to 0.3. Mean-square center deflection and maximum mean-square strain are presented in a nondimensional form. The nondimensional forcing spectral density parameter is defined as

$$S_f = \frac{2\pi \quad S_p \quad (\omega)}{\rho^2 h^4 \left(\frac{D}{\rho h b^4}\right)^{3/2}} \tag{36}$$

Also, since the loading is symmetric, only symmetric generalized displacements W_{mn} are retained in the transverse deflection function.

The convergence of the solution technique was examined in order to determine the degree of accuracy possible with a highly truncated transverse deflection function series. The mean-square center deflection versus the non-dimensional spectral density parameter using 4, 6, 10, and 15 terms in the deflection function for a square plate is shown in Figure 1. The particular generalized displacements that make up the various orders of the deflection function are shown in Table 1. Figure 1 clearly indicates that a 6-term solution gives accurate results for the nonlinear maximum defection while a 4-term solution will provide accurate linear results. The maximum strain occurs at the extreme fiber of the panel and at the midpoint of the long edge. The direction is perpendicular to the edge. Figure 2 shows the maximum mean-square strain versus S_f for the square plate using 4, 6, 10 and 15 terms in the deflection function. The convergence of the mean-square strain is much slower as compared with that of the mean-square deflection.

TABLE I
Generalized Displacements Used in Convergence Studies

Number of terms	Generalized Displacements														
	W_{11}	W_{13}	W_{31}	W_{33}	W_{15}	W_{51}	W_{35}	W_{53}	W_{17}	W_{71}	W_{55}	W_{37}	W_{73}	W_{19}	W_{91}
4	X	X	X	X											
6	X	X	X	X	X	X									
10	X	X	X	X	X	X	X	X	X	X					
15	X	X	X	X	X	X	X	X	X	X	X	X	X	X	X

Figures 3 and 4 show the maximum mean-square nondimensional deflection versus the nondimensional spectral density of acoustic pressure excitation for rectangular panels of aspect ratios of 1 and 2 with the damping ratio equal to 0.009, 0.018 and 0.027. Figures 5 and 6 show the maximum nondimensional mean-square strain versus the nondimensional spectral density for rectangular panels of aspect ratios of 1 and 2 with the damping ratio

equal to 0.009, 0.018 and 0.027. Ten terms were included in the deflection function, to generate the results shown in Figures 3 through 6.

4. CONCLUDING REMARKS

An analytical solution technique is presented for determining the large-amplitude random response of clamped rectangular panels while including multiple modes in the analysis. Accurate mean-square deflections can be obtained with the use of 6 terms in the deflection function, while it is necessary to consider as many as 10 or more terms for the accurate determination of the strains. In the numerical examples presented , a constant damping ratio for all four modes has been used. However, nonlinear damping phenomena have been observed in experiments [5,6]. Therefore, further effort, is needed to better understand the effects of nonlinear damping on panel response.

5. REFERENCES

1. I. HOLEHOUSE 1980 Sonic Fatigue Design Techniques for Advanced Composite Aircraft Structures, "AFWAL-TR-79-3028, AF Flight Dynamics Laboratory, WPAFB, OH.

2. C. MEI 1979 Large Amplitude Response of Complex Structures due to High Intensity Noise, AFFDL-TR-79-3028, AF Flight Dynamics Laboratory, WPAFB,OH.

3. C. MEI 1980 Response of Nonlinear Structural Panels Subjected to High Intensity Noise, AFWAL-TR-80-3018, AF Wright Aeronautical Laboratories, WPAFB, OH.

4. C. MEI, D. B. PAUL and K. R. WENTZ 1982 Large Amplitude Random Response of Symmetric Laminated Composite Plates. Shock and Vibration Bulletin, Bulletin 52, pp. 99-111.

5. C. MEI and K. R. WENTZ 1982 Analytical and Experimental Nonlinear Response of Rectangular Panels to Acoustic Excitation. 23rd Structures, Structural Dynamics and Materials Conference. New Orleans, LA. pp. 514-520.

6. R. G. WHITE 1978 Comparison of the Statistical Properties of the Aluminum Alloy and CFRP Plates to Acoustic Excitation. J. Composites. pp. 251-258.

7. W. D. IWAN and P. T. D. SPANOS 1978 On the Existence and Uniqueness of Solutions Generated by Equivalent Linearization. Int. J. Nonlinear Mech., Vol. 13. pp. 71-78.

8. T. S. ATALIK and S. UTKU 1976 Stochastic Linearization of Multi-Degree-of-Freedom Nonlinear Systems. Earthquake Eng. Struct. Dyn. Volume 4. pp. 411-420.

9. T. K. CAUGHEY 1971 Nonlinear Theory of Random Vibrations in Advances in Applied Mechanics, Edited by C. S. Yih, Vol. 11, Academic Press. pp. 209-253.

10. D. B. PAUL 1980 Ph.D Thesis, The Ohio State University. Large Deflections of Clamped Rectangular Plates with Arbitrary Temperature Distributions.

11. C. MEI 1983 AF Wright Aeronautical Laboratories, AFWAL-TR-83-3121. Large Deflection Multimode Reponse of Clamped Rectangular Panels to Acoustic Excitation.

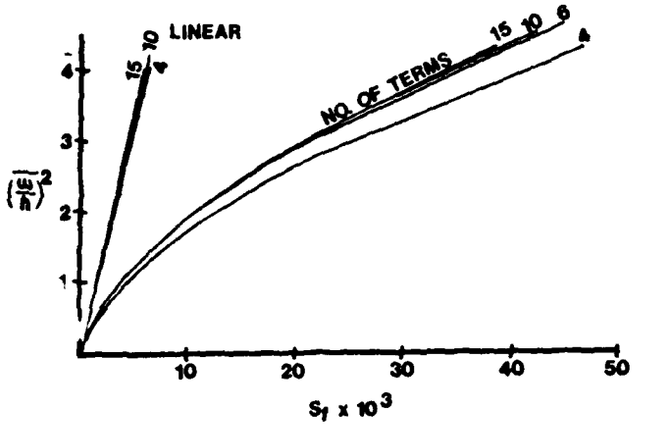

Figure 1. Convergence of the Mean-Square Center Deflection for the Square Plate ($\xi = 0.009$)

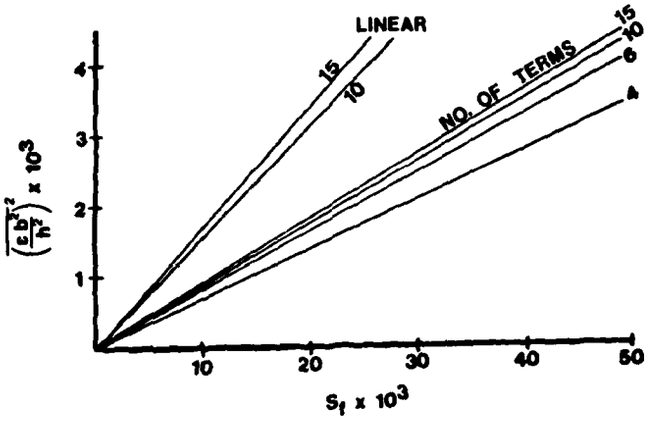

Figure 2. Convergence of the Maximum Mean-Square Strain for the Square Plate ($\xi = 0.009$)

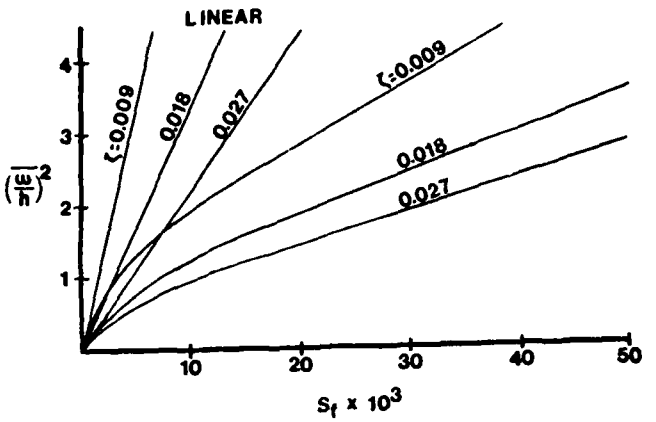

Figure 3. Mean-Square Center Deflection vs Pressure Spectral Density for a Clamped Square Plate

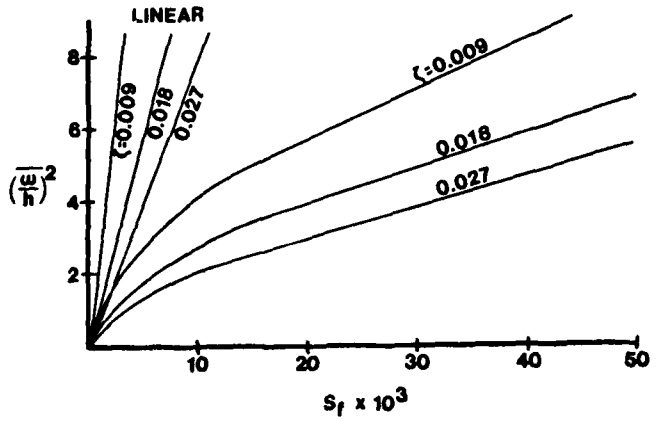

Figure 4. Mean-Square Center Deflection vs Pressure Spectral Density for a Clamped Rectangular ($\alpha = 2$) Plate

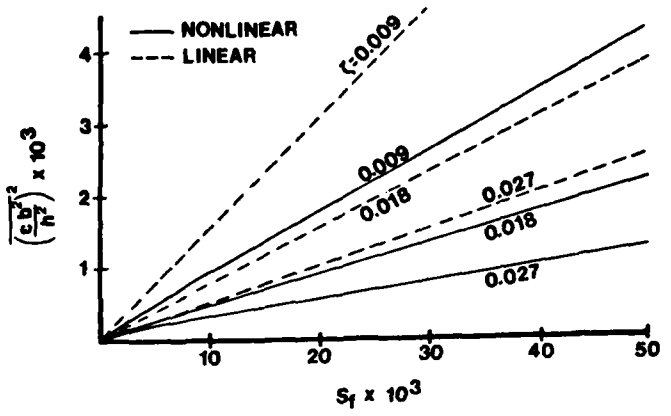

Figure 5. Maximum Mean-Square Strain vs Pressure Spectral Density for a Clamped Square Plate

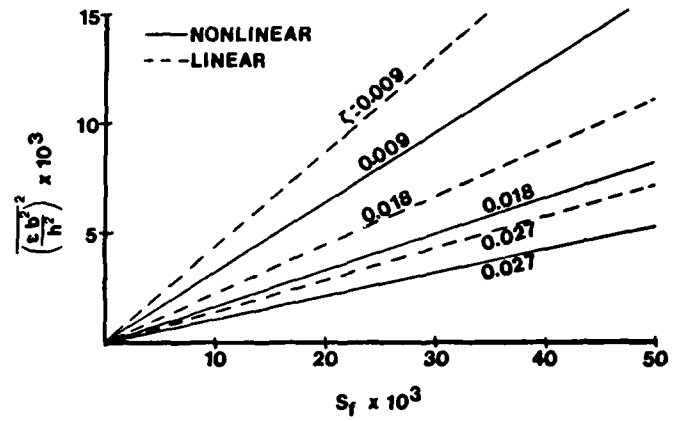

Figure 6. Maximum Mean-Square Strain vs Pressure Spectral Density for a Clamped Rectangular ($\alpha = 2$) Plate

10. RESPONSE TO SEISMIC EXCITATION

STEEL FIBROUS CONCRETE UNDER SEISMIC LOADING[a]

Levon Minnetyan[1], and Gordon B. Batson[2]

Department of Civil and Environmental Engineering
Clarkson College of Technology
Potsdam, New York 13676
USA

1. INTRODUCTION

Steel fibrous reinforced concrete is a structural material that has been under development in the last two decades [1,2]. Investigations into the effects on the strength, stiffness, and ductility properties of steel fiber concrete have included static loading, static cyclic loading, impact loading and low amplitude dynamic fatigue loading experiments [3,4,5,6]. Results from these investigations have shown that the addition of fibers to concrete mixes can significantly improve the performance of this material. The improvements on ductility are especially significant under dynamic loads. One area where the potential advantage of steel fiber reinforced concrete is foreseen is that of earthquake resistant design. Conventional reinforced concrete is often unable to maintain its stiffness under dynamic loads imposed by seismic conditions. Steel fibers have been shown to improve ductility and toughness properties of concrete mixes, provide higher first crack tensile strength and help to retard spalling under impulsive loading conditions. These characteristics can lead to better earthquake resistant designs. Steel fiber concrete can be used to reduce the required amounts of steel bar reinforcement at critical regions of the structure. Congestion with conventional bar reinforcements is known to be one of the major causes of bond deterioration at a critical region. In order that steel fiber concrete be considered an appropriate alternative for seismic design its nonlinear constitutive properties under seismic loading conditions must be known. To determine these characteristics a study of the behavior of steel fiber reinforced concrete when subjected to high intensity dynamic loadings at typical seismic conditions has been undertaken. This study addresses the question of determining the contribution of steel fibers to the dynamic stiffness and strength of reinforced concrete members; including the effects of loading history and cracking. An experimental research program is currently in progress with the objective of the identification of an appropriate mathematical model that can be used in earthquake resistant design.

2. INELASTIC RESPONSE UNDER SEISMIC LOADING

All reinforced concrete structures will crack at some intensity of static and/or dynamic loading. Serviceability of a structure should be maintained under static design loads and moderate seismic loads. It is not economically feasible to design a structure to remain serviceable under very intense seismic forces. However, safety against collapse of a structure should still be maintained under most intense seismic loads. To predict the performance of structures under seismic conditions we need, among other information, the stiffness, damping, and strength properties of structural members. The determination of dynamic resistance characteristics of cracked sections is essential for the assessment of the effectiveness of steel fibrous concrete for aseismic design of

[a]This material is based upon work supported by the National Science Foundation under Grant No. CEE-81-17904

[1]Assistant Professor

[2]Professor

structures.

The causes of cracking and the resulting inelastic effects on the constitutive relations of reinforced concrete have been investigated both experimentally and analytically [7]. It has been demonstrated that much of the inelastic action of a structure subjected to seismic loading occurs in the joint regions where large moment reversals take place and bond slip occurs [8]. Parallel to dynamic experimentation, pseudo-dynamic cyclic tests on beam-column joints reveal that after the establishment of a plastic hinge, flexural strength is mostly conserved by numerous hysteretic load cycles although the dynamic stiffness rapidly deteriorates [9].

The nonlinear inelastic seismic analysis of a reinforced concrete structure is usually based on a bilinear yield mechanism mode. This model assumes that a bilinear hinge will develop at the end of a frame member when the moment at that point exceeds the yield moment of the section. This bilinear behavior mechanism usually allows for about 90% to 95% reduction in stiffness of the section during yielding and provides a hysteretic energy loss mechanism in the joint. When used with provisions for global stiffness degradation after yielding at joints, the bilinear yield mechanism model has rendered a fairly close description of the actual structural response for typical test cases [10]. However, general stiffness properties of a structure change in a very complex fashion during the dynamic response and it is difficult to establish a truly general stiffness degradation model which will be applicable to all dynamic loading situations.

Further experimental and analytical research is needed to study the behavior of reinforced concrete sections under high intensity dynamic loads to assess the feasibility of alternative forms of reinforced concrete such as steel fiber concrete in aseismic design. The flexural behavior of a cracked section during the development of a plastic hinge is of primary interest.

In the past, the free vibration response of a cracked, reinforced concrete beam has been investigated analytically assuming a reduced flexural rigidity for the cracked part [11]. It is noted that this reduced flexural stiffness depends upon the beam cross-section, number and size of cracks, percentage and placement of reinforcement and other factors. Furthermore the dynamic flexural stiffness of the cracked portion is a function of both time and position of the beam. The theoretical results indicate the response of the system to be a nonlinear type with a soft characteristic. However, the basic assumptions for the formulation of the flexural stiffness are not explained. Neither is the stiffness reduction given explicitly for individual cases nor is there an indication how it can be determined for a specific cracked beam.

Theoretical and experimental investigations of dynamic properties of uncracked reinforced concrete beams are discussed in reference [12]. The authors of reference [12] acknowledge to have also conducted dynamic experiments with cracked beams but that they could find "no definite correlation" between the dynamic responses of cracked and uncracked beams.

Fatigue experiments with steel fibrous reinforced concrete beams have assessed the relative effects of fiber concentration, fiber shape, load intensity, forcing frequency and load reversal on the fatigue life of beams [6, 13]. However, these dynamic experiments have not included the hign intensity loads that would represent seismic effects.

Dynamic characteristics of reinforced concrete beam-column specimens were measured for various levels of cracking in reference [14]. This reference concludes that natural frequencies will be lower after cracking. This observation is generally correct but incomplete. The natural frequency of a cracked

structure will depend on the vibration amplitude as well as the amount of cracking and crack patterns.

3. CRACKED BEAM - A CONSERVATIVE TREATMENT

Let us consider the free vibration response of the first mode of a simply supported homogeneous conservative beam of density ρ, elastic modulus E, with a vertical crack of length d_c at its midspan as shown in Fig. 1-a. For dimensional simplicity the beam is assumed to have a rectangular cross-section of unit width. The crack will be open or closed during different stages of a vibration period depending upon the deflected position of the beam (Figures 1-b, 1-c).

If the free vibration amplitude α is smaller than the static deflection δ of the cracked beam under its self weight, the crack will always stay open and there will be a constant natural frequency lower than that of the uncracked beam but still independent of the vibration amplitude. The energy or the integral curve [15] in the displacement-velocity plane will be a complete ellipse as S_1 in Fig. 2, with gravitational datum corresponding to the static deflection δ of the cracked beam. On the other hand, if α is greater than δ the energy curve will follow S_2 for portion of the vibration period while the crack is open; however, a transition will occur at $y = -\delta$ when the crack will close and the energy curve will follow the ellipse S_2^* beginning at point A until the crack opens again at point B. The energy curve S_2^* has a higher gravitational datum corresponding to the static deflection of the uncracked beam, but it has an equally lower elastic potential datum such that conservation of energy is satisfied. The time contribution of the followed path A-B of S_2^* is less than the time subtracted by deleting corresponding part of S_2. The result is a decrease in the free vibration period T or increase in the free fibration frequency ω of the cracked beam; indicating a hard characteristic for this conservative dynamic system. Numerical results of amplitude versus natural frequency computed by the methods described in reference [16] are plotted for three different crack depths in Fig. 3. For actual cracked reinforced concrete beams, nonlinear material behavior will soften the vibration characteristics such that a frequency-amplitude relationship may look as shown in Fig. 4; still partially contradicting the soft nonlinear characteristic assumptions of references [11] and [14].

The phenomenon described above is very common during actual seismic loading of structures. In some publications it is referred to as "a greater elastic response due to a lengthening period" [17]. This observation seems to agree with our hypothetical amplitude frequency relationship depicted in Fig. 4. If Fig. 4 were to be obtained from actual experiments it could be interpreted as a close-to-linear behavior with possible scattering of data. However, linear superposition methods are not valid in this case since apparent linear behavior for a specific cracked inelastic beam will be due to the contribution of opposing nonlinear effects. Consequently, the influence of opening and closing of cracks and the effect of material nonlinearities due to high stresses at cracked regions must be taken into account simultaneously to interpret the true implications of experiments. The closing of cracks during a seismic acceleration period of long duration will generate an impulsive load on the structure and actually determine the failure direction of the entire frame. This behavior has been observed in most earthquakes and described as "pumping" by Newmark [18]. Pumping is due to a partial ultraharmonic excitation of a structural system with asymmetrical nonlinear vibration characteristics. Pumping will influence the sense for the P-Δ effect which will eventually impose the collapse mechanism on the structure [19].

4. CURRENT EXPERIMENTAL SCOPE

Within the experimental portion of the present investigation, beam

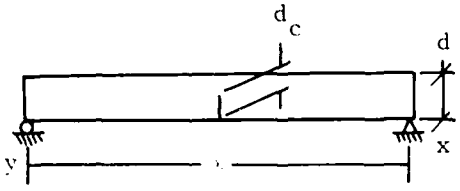

Fig. 1-a. Beam with Vertical Crack at Midspan

Fig. 1-b. Downward Deflection - Crack is Open

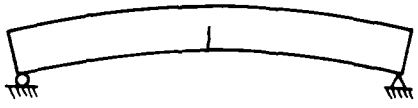

Fig. 1-c. Upward Deflection - Crack is Closed

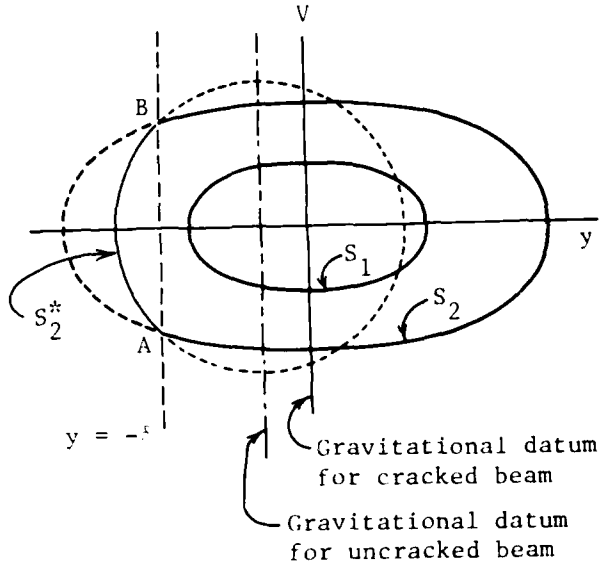

Fig. 2. Energy Curves for Conservative Cracked Beam

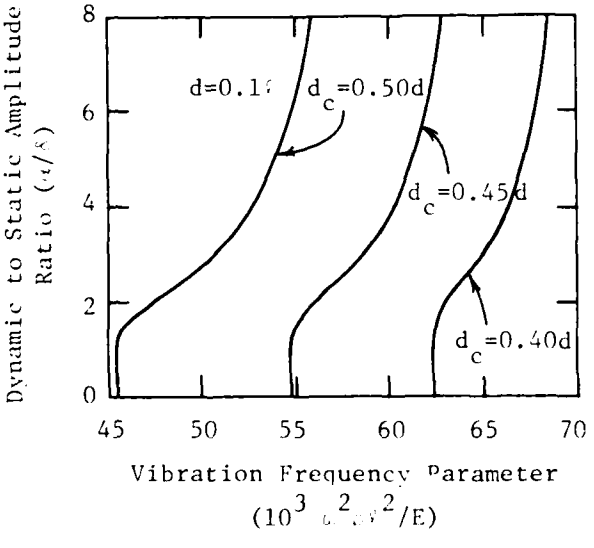

Fig. 3. Amplitude-Frequency Relationships for Conservative Cracked Beam

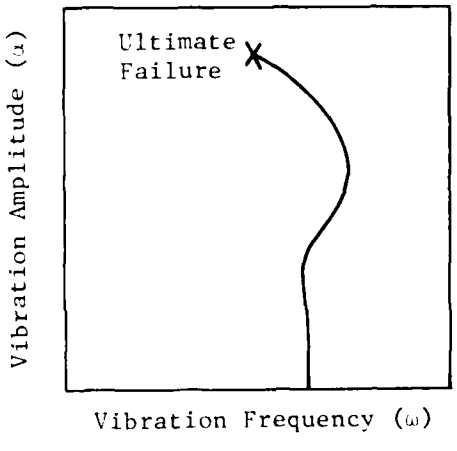

Fig. 4. Amplitude-Frequency Relationship for a Cracked Beam with Material Nonlinearities

specimens of two different lengths with three types of reinforcement for each length are fabricated and subjected to dynamic loads. To keep the material and equipment cost down relatively small beam cross-sections are used for the experiments. A typical beam cross-section measures six inches deep and four inches wide (152 mm x 102 mm). It has been shown that flexural tensile strength is not significantly altered by size effects when specimen depth is six inches or greater [20]. However, shear strength may be altered by size of beam as shown by prototype beam tests by G. Williamson at CERL [21]. The difference in failure mode of prototype used by Williamson and small size beams tested by Batson et al. [6] is an important point under investigation in the current project.

The steel fibers used are all of the same type with hooked or bent ends and are supplied in water soluble glued bundles. The amount of steel fibers is constant at 3/4 percent by volume for all steel fibrous concrete mixes. The maximum aggregate size is limited to 3/8 in. (9.5 mm) peastone regardless of beam size. This is to assure effective crack arrest by the close spacing of the steel fibers.

To date thirty-three long span beams and thirty-three short span beams have been tested. The long span beams measure 6 in. x 4 in. x 8 ft. (152 mm x 102 mm x 2.4 m) and include three reinforcement types shown in Fig. 5.

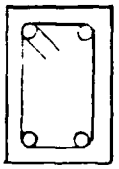

2#4 T&B standard shear reinforcement without fiber

Type L1

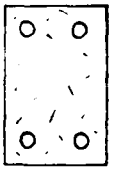

2#4 T&B without shear reinforcement with fiber (∿ 3/4% by Vol.)

L2

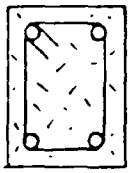

2#4 T&B with shear reinforcement and with fiber (∿ 3/4% by Vol.)

L3

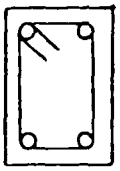

2#3 T&B standard shear reinforcement without fiber

Type S1

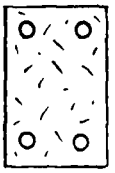

2#3 T&B without shear reinforcement with fiber (∿ 3/4% by Vol.)

S2

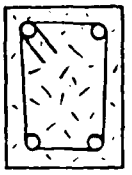

2#3 T&B with shear reinforcement and with fiber (∿ 3/4% by Vol.)

S3

Fig. 5. Types of Reinforcement

These reinforcement types include longitudinal steel with standard shear reinforcement, longitudinal steel with fibers but without standard shear reinforcement, and longitudinal steel with both fibers and standard shear reinforcement. Building codes do not at this time recognize fiber reinforcement for resisting shear. However, the steel fibrous types without standard shear reinforcement are also included to assess the trade-off between stirrups and fibers in effectiveness to resist shear. The short span beams have the same cross-sections but are fabricated merely 4 ft. (1.22 m) long. Eleven specimens of each reinforcement type have been tested. From each type three beams are tested under full dynamic cyclic loading at 1.0 H_z loading frequency. Three other specimens are tested under the same loading magnitude but at a reduced rate of 0.2 H_z. The remaining beams are tested under partial moment reversal, similarly at 1.0 H_z and 0.2 H_z frequencies. An electrohydraulic ram capable of sustaining a sinusoidal varying force is used to excite the beam specimens which are dynamically simply supported and loaded at midspan. Beam deflections are measured by the use of Linear Variable Displacement Transducers (LVDT's), placed along the beam. A microcomputer is used to control the testing and to accumulate the experimental data in digital format [22].

5. RESULTS

At present, the outcome of sixty-six dynamic experiments can be best summarized in terms of the average relative performance of the different reinforcement types. In the case of long span beams the flexural tensile stresses were more significant compared to shear effects. All long span beams failed gradually as the dynamic stiffness was lost over many cycles of loading. The relative performance of these beams is summarized in Table 1. The three

Table 1 Long Beams

Type of Shear Reinforcement	Average Relative Initial Stiffness	Average Relative Dynamic Ductility	
		0.2 H_z	1.0 H_z
Conventional Stirrups	1.00	1.0	8.8
Fibers	1.00	1.1	81
Stirrups and Fibers	1.04	3.2	36

different types of long beams are loaded under the same dynamic loadings. Loading is sufficiently intense to start cracks in the specimens with the first cycle of loading. Initial stiffness is defined as the ratio of force to displacement at the first load peak. Relative initial stiffness is the initial stiffness normalized with respect to that of a conventionally reinforced beam. It is observed, from Table 1, that the average relative initial stiffness is about the same for all three types of long beams. Dynamic ductility is defined as the number of cycles before a "failed" deformation state is reached. At the slow loading rate of 0.2 H_z the improvement in dynamic ductility with the addition of fibers is very small. However, at the faster loading rate of 1.0 H_z the fibers have a more significant influence. The most interesting result is that fibers by themselves are more effective than having both the same amount of fibers and stirrups when the loading is applied at 1.0 H_z. It is also noteworthy to observe the very significant dependence of dynamic ductility on the loading rate for all types of reinforcement.

Table 2 summarizes the relative performance of different reinforcement

types for the short span beams. For these short beams the shear effects control

Table 2 Short Beams

Type of Shear Reinforcement	Average Relative Initial Stiffness	Average Relative Dynamic Ductility	
		0.2 H_z	1.0 H_z
Conventional Stirrups	1.00	1.0	5.0
Fibers	1.26	27	45
Stirrups and Fibers	1.19	8.5	11

the deformations, cracking, and the failure mode of the beams. Unlike the long beams, the short beams usually fail in a sudden "catastrophic" manner without much warning. Table 2 indicates that fibers are relatively more effective as shear reinforcement for the shorter beams under significant shear loading. It is also observed that the loading rate effects are not as dramatic when the fibers are used as shear reinforcement in short beams. Another difference from the long beams is that in the case of short beams, the shear reinforcement type affects the initial stiffness. Also, experimental data indicates that the short beams with only conventional stirrup type shear reinforcement deteriorate significantly during the first three cycles of loading, whereas the steel fibrous short beams retain the dynamic stiffness over a much larger number of loading cycles.

6. CONCLUSIONS

In summary, from the current experimental results, it may be deduced that replacing the conventional shear reinforcement with steel fibers at high shear regions will improve the dynamic stiffness by 26 percent and the dynamic ductility is increased nine fold at 0.2 H_z frequency of dynamic loading. However, if the fibers are added to conventional stirrups, then the dynamic stiffness increases only 19 percent and the dynamic ductility merely doubles. At first glance these results would indicate that stirrups should be excluded from steel fibrous concrete reinforcement. However, it should be noted that no axial forces are considered in the present investigation. It is believed that stirrups will still be necessary to provide the confining reinforcement when axial compression forces are added to shear and bending effects. Another reason to include stirrups with steel fibrous concrete members is to soften the final failure behavior of these structural members. Experimental beams with only steel fibers had the best stiffness characteristics and lasted through the largest number of dynamic loading cycles. However, their failure was precipitated very suddenly and without much advance warning during loading of short beams. Including also the conventional stirrups in addition to steel fibers softens the failure pattern at a reasonable cost of somewhat reduced dynamic stiffness and ductility.

Finally, it is relevant to note that the present experimental investigation is scheduled to continue with additional types of reinforcement and prototype sizes of beams. In addition, a system identification program is currently in progress to identify a practical mathematical model for the behavior of steel fibrous reinforced concrete beams to be used as a tool in earthquake resistant design with this material.

6. REFERENCES

1. Romualdi, J.P. and Batson, G.B., "Behavior of Reinforced Concrete Beam with Closely Spaced Reinforcement," ACI Journal, Proceedings V. 60, No. 6, June 1963, pp. 775-790.

2. Romualdi, J.P. and Mandel, J.A., "Tensile Strength of Concrete Affected by Uniformly Distributed Closely Spaced Short Lengths of Wire Reinforcement," ACI Journal, Proceedings Vol. 61, No. 6, June 1964, pp. 657-671.

3. Batson, G.B., Jenkins, E., and Spatney, R., "Steel Fibers as Shear Reinforcement in Beams," ACI Journal, Vol. 69, No. 10, October 1972, pp. 640-644.

4. Henager, C.H., "A Steel Fibrous, Ductile Concrete Joint for Seismic-Resistant Structures," ACI Spring Conference, San Francisco, Calif., 1974. Also published in SP-53, ACI, Detroit, 1977.

5. Romuladi, J.P. and Ramey, M.R., "Effects of Impulsive Loads on Fiber-Reinforced Concrete Beams," Contract No. OCD-PS-64-21, Carnegie Institute of Technology, Pittsburgh, for Office of Civil Defense, Secretary of the Army, Department of Defense, Oct. 1965, 77 p.

6. Batson, G., Ball, C., Bailey, L., Landers, E. and Hooks, J., "Flexural Fatigue Strength of Steel Fiber Reinforced Concrete Beams," ACI Journal, Proceedings Vol. 69, No. 11, Nov. 1972, pp. 673-677.

7. American Concrete Institute, Causes, Mechanism, and Control of Cracking in Concrete, SP-20, ACI, 1968.

8. Blume, J.A., Newmark, N.M., and Corning, L.H., "Design of Multistory Reinforced Concrete Buildings for Earthquake Motions," Portland Cement Association, Skokie, Illinois, 1961.

9. Bertero, V.V., and Popov, E.P., "Seismic Behavior of Ductile Moment-Resisting Reinforced Concrete Frames," Reinforced Concrete Structures in Seismic Zones, SP-53, ACI, Detroit 1977, pp. 247-291.

10. Clough, R.W., "Predicting the Earthquake Response of Reinforced Concrete Structures," Reinforced Concrete Structures in Seismic Zones, SP-53, ACI, Detroit 1977, pp. 59-79.

11. Tsalik, A.M., "Free Vibrations of Reinforced Concrete Bars with Cracks in Flexure," Prikladnaya Mekhanica, Vol. 3, No. 12, December 1967, pp. 104-108.

12. James, M.L., Lutes, L.D., and Smith, G.M., "Dynamic Properties of Reinforced and Prestressed Concrete Structural Components," ACI Journal, Vol. 61, No. 11, November 1964, pp. 1359-1379.

13. Kormeling, H.A., Rinhardt, H.W., and Shah, S.P., "Static and Fatigue Properties of Concrete Beams Reinforced with Continuous Bars and with Fibers," ACI Journal, January-February 1980, No. 1, Vol. 77, pp. 36-43.

14. McCafferty, R.M., and Moody, M.L., "Dynamic Characteristics of Reinforced Concrete Beam-Column Specimens for Various Levels of Cracking," Preprints, Fifth World Conference on Earthquake Engineering, Rome, June 25-29, 1973.

15. Stoker, J.J., Nonlinear Vibrations, Interscience Publishers, 1950.

16. Timoshenko, S., Vibration Problems in Engineering, D. Van Nostrand Co. Inc., 3rd Ed., 1955.

17. Biggs, J.M., Hansen, R.J., and Holley, M.J., Jr., "On Methods of Structural Analysis and Design for Earthquake," Structural and Geotechnical Mechanics, W.J. Hall, Ed., Prentice Hall, 1977, pp. 91-101.

18. Newmark, N.M., "Current Trends in the Seismic Analysis and Design of High-Rise Structures," Earthquake Engineering, R.L. Wiegel, Editor, Prentice Hall, Inc., Englewood Cliffs, N.J., 1970, pp. 403-424.

19. Popov, E.P. and Bertero, V.V., "On Seismic Behavior of Two R/C Structural Systems for Tall Buildings," Structural and Geotechnical Mechanics, W.J. Hall, Ed., Prentice Hall, 1977, pp. 117-140.

20. Sabnis, G.M., and Mirza, S.M., "Size Effects in Model Concretes?," Journal of the Structural Division, ASCE, Vol. 105, No. ST6, June 1979, pp. 1007-1020.

21. Williamson, G.R. and Knab, L.I., "Full-Scale Fibre Concrete Beam Tests," Proceedings, RILEM Symposium, Fibre-Reinforced Cement and Concrete, Construction Press, Lancaster, England, Sept. 1975, pp. 209-214.

22. Glebas, T., Minnetyan, L., and Batson, G.B., "Computer Based Testing of Dynamic Response," ASCE-EMD Specialty Conference Proceedings, Recent Advances in Engineering Mechanics and Their Impact on Civil Engineering Practice, Vol. I, Purdue University, West Lafayette, Indiana, May 23-25, 1983, pp. 589-592.

INELASTIC ANALYSIS OF SHORT HIGHWAY BRIDGES SUBJECTED TO STRONG GROUND MOTIONS

Mehdi Saiidi, James D. Hart, and Bruce M. Douglas
Civil Engineering Department, University of Nevada, Reno

1. ABSTRACT

Static and dynamic nonlinear modeling of short highway bridges subjected to lateral loads are discussed. The behavior of inelastic bridge components, namely, foundation elements, elastomeric bearing pads, and pier elements is reviewed in view of the available experimental data. Two hysteresis models were used in the model: the Ramberg-Osgood and the Trilinear Q-hyst model. The calculated and measured static and free-vibration response of a five-span bridge (The Rose Creek Interchange) which was tested as part of the project are presented. It is pointed out that no universally accepted method to determine the basic nonlinear properties of pile foundations and elastomeric bearing pads are available. This leads to a drawback in any realistic nonlinear analysis of bridges for which the response is usually greatly affected by these components. For the Rose Creek Bridge, however, it was possible to obtain a somewhat reasonable estimate of the response utilizing the results from an ambient vibration testing of the bridge and a detailed geotechnical analysis of the foundations.

2. INTRODUCTION

One of the design philosophies common to many seismic codes is that a structure must not collapse, though may be severely damaged, in the event of the maximum credible earthquake. Allowance for considerable damage is necessary to keep the design economical. In ductile structures, damage under strong earthquakes is associated with significant nonlinear effects. Even moderate earthquakes can cause pronounced nonlinear action in some parts of the structure. Any analysis of structures for moderate to severe ground motions, therefore, should account for inelastic behavior of structural components and the structural unit.

The 1971 San Fernando earthquake in California revealed that highway bridges could be affected severely by strong earthquakes. Many bridges collapsed as a result of the earthquake and several others suffered substantial damage. To predict the response of bridges to strong ground motions, analytical models are needed to assist the engineer in the design of earthquake-proof bridges. Chen and Penzien [1] developed a nonlinear analytical model assuming an elasto-plastic hysteresis model for inelastic components. In a study by Gillies and Shepherd [2] a highway bridge was analyzed assuming elastic behavior at the elastomeric bearing pads and assuming that the foundations were fixed, restricting the nonlinear effects to the sub- and super-structure.

This paper describes an analytical model which takes into account the inelastic behavior of all nonlinear components to predict the lateral response of short bridge systems. The model was developed in conjunction with experimental tests of a five-span reinforced concrete bridge near Winnemucca, Nevada [3].

3. INELASTIC MODELING

A computer program was developed for the analysis of short to intermediate bridges with single-column piers. A schematic view of the bridge model is shown in Fig. 1. At the abutments, three springs, one translational and the other two rotational, were assumed. The springs in translation and rotation with respect to the vertical axis were assumed to be nonlinear, while the

other spring was treated as a linear system because of its relatively small contribution to the response of the bridge. Other possible degrees of freedom were restrained because they were not expected to be significant. Deck and pier elements were idealized as line members with nonlinearity allowed only at the base of pier elements. The pier foundation effect was represented by two nonlinear springs at the base of each pier. Only translation in the transverse direction and rotation with respect to an axis parallel to the longitudinal axis of the bridge were accounted for. Other possible degrees of freedom were fixed because, under lateral loads, their effect was believed to be negligible.

3.1 Structural Component

Idealization of different components of the bridge was based on the available experimental data and judgement. In developing a particular hysteresis model, no attempt was made to "curve-fit" any specific test data. Rather models were chosen to represent the general characteristics of the measured response.

3.1.1 Piers

In bridges with single-column piers the maximum moment usually occurs at the bottom of the pier. In many bridges the pier section near the base is smaller than other parts to avoid the transfer of a large moment in the longitudinal direction of the bridge. The pier section near the base in the Rose Creek Bridge, for example, had a yield moment which was approximately one-third of the yield moment for other sections. The nonlinear behavior, therefore, was assumed to be concentrated at the base of the pier over the height where the section is "weak". The shear resistance was assumed to be sufficiently large to prevent shear failure.

The moment-curvature relationship for reinforced concrete elements consists of three distinct parts: precracked, cracked, and yielded parts, with each part having a smaller slope than the previous part (primary curve in Fig. 2). To determine stiffness variations upon unloading and reloading after load reversal, a hysteresis model was developed which is a modified version of the Q-hyst model [4], in that the primary curve consists of three linear segments as opposed to a bilinear primary curve used in the original model. The new version was called "TQ-hyst".

The primary curve is assumed to be symmetric with respect to the origin. The rules for unloading and load reversal are similar to those used in the Q-hyst model. The unloading branch in the cracked stage is obtained by connecting the unloading point to the cracking point on the other side. For the post-yielding stage, the slope of unloading branch is determined by first finding the slope of a line connecting the yield point on one side to the cracking point on the other side of displacement/rotation axis, and then multiplying this slope by the square root of the ratio of the maximum displacement/rotation to the yield value. This formula is an empirical relationship developed based on experimental testing of reinforced concrete joints [5].

The load reversal branch after yielding occurs in at least one direction is determined by connecting the intersection of the last unloading branch and the horizontal axis to a point on the primary curve on the other side, with abscissa being equal to the largest deformation ever reached. Should an unloading take place before the primary curve is reached, the slope will be the same as the slope of the latest unloading branch.

3.1.2 Foundation

It is known that most soil types exhibit inelastic behavior even at very small strains. In lateral loading of soil samples, typically a curved relationship with gradual but significant decrease in stiffness is obtained. Due to the large variability in soil properties, construction of this curve without testing of the soil, at best, represents an approximation. Added to this is the effect of foundation structure. The Rose Creek Bridge is supported on pile foundations. In testing of the bridge, it was found that the foundation system displaced and rotated when the bridge was subjected to lateral loads, indicating that rotation of the pile cap had a significant contribution to the lateral deformations. Studies on the cyclic behavior of foundations have generally revealed that the hysteresis relationships include substantial deterioration of strength and stiffness with a trend similar to what is assumed in the TQ-hyst model. An exception to this is densification and therefore stiffening of dense sand [6]. In the absence of extensive experimental data for lateral and rotational behavior of foundation systems, the TQ-hyst model was assumed to represent the behavior of the foundation at pier bases.

3.1.3 Bearing Pads

Cyclic testings of neoprene bearing pads in shear have shown that a nonlinear effect is present even at small load amplitudes [7]. As loading continues a reduction in stiffness is observed until slippage occurs. Upon unloading and reversing the loads, stiffness changes. Cyclic loadings of pads for vertical loads, on the other hand, have shown some stiffening effects as loading progresses. This is, of course, due to compaction of neoprene layers as compressive load is applied. In seismic modeling of bridges for lateral loads, the vertical response of bearing pads enters the analysis in considering rotation at the abutments about the longitudinal axis of the bridge. Due to the relatively large vertical gravity forces acting on the pads, variations in the vertical force due to the rotation are not expected to lead to any significant nonlinear effects. As a result, the vertical behavior of the pads was assumed to be linear.

For the lateral behavior of the pads, however, the Ramberg-Osgood model [8] was adopted to represent the cyclic response (Fig. 3). This was decided after a qualitative study of the available experimental data. Two equations are used to determine deformations as a function of force at different stages. The shape and the degree of curvature are controlled by one parameter, G. For loading on the primary curve, Eq. (1) is used.

$$D = F\,(D_y/F_y)\,(1+|F/F_y|^{G-1}) \qquad (1)$$

in which D and F are deformation and force at any arbitrary point, and D_y and F_y are deformation and force at point A (Fig. 3). The second equation is used to define the curve at unloading and load-reversal stages.

$$D = (F-F_o)\,(D_y/F_y)\,(1+|(F-F_o)/2F_y|^{G-1})+D_o \qquad (2)$$

in which D_o and F_o are deformation and force at the largest excursion point.

To determine the force for a given deformation, the Newton-Raphson iterative method is used in Eqs. (1) and (2).

The Ramberg-Osgood model was used in both translation, and rotation about the longitudinal axis of the bridge at the abutments.

3.1.4 Deck Element

The design of bridge decks is usually controlled by the vertical loads. The relatively large width of bridge deck results in large stiffness and large cracking moment and shear resistance unlikely to be exceeded as a consequence of lateral loading. The deck element, therefore, was assumed to remain elastic.

3.2 Total Bridge Structure

Based on the idealizations described in Sec. 3.1 a computer model was developed for static and free-vibration analysis of highway bridges subjected to lateral loads. The "P-Delta" effects were accounted for in the modeling. Structural nodes were assumed at the abutments, pier caps, and at the pier bases. Masses were assumed to be lumped at the nodes. Full advantage was taken of symmetry of element stiffness matrices in storing the stiffnesses. Nodes and degrees-of-freedom were numbered in such a way to minimize the bandwidth of structural stiffness matrices. Stiffness submatrices corresponding to lateral and rotational degree-of-freedom were partitioned and static condensation was used to minimize the size of matrices to be inverted.

In the static analysis part of the model, horizontal forces are applied at pier-deck intersections, abutments, and pier bases. For each load increment the status of the nonlinear elements is checked and their stiffnesses are updated as necessary. To allow for close monitoring of force-deformation variations, the loads should be applied in small increments. For each load increment, lateral displacements, rotation, and all the internal forces are computed.

The dynamic analysis portion of the computer model determines the free-vibration response of the bridge with initial displacements being those caused by the static forces. The initial stiffness and the status of hysteresis curves for different components used at the start of the free-vibration analysis are those determined at the end of last static load increment. The differential equation of motion is formulated in an incremental form and integrated using small time intervals, following Newmark's β method [9]. A β value of 0.25 was used in the analysis which corresponds to constant acceleration over each time interval. This procedure results in an unconditionally stable response for elastic structures. The acceleration and lateral displacement are calculated for each time interval and stored for plotting the response histories.

4. THE ROSE CREEK BRIDGE

The Rose Creek bridge is a five-span reinforced concrete multi-cell box girder bridge with a total length of 120m, located on highway I-80 near Winnemucca, Nevada (Fig. 4). The substructure consists of four single piers (Fig. 5) and the abutments, all of which are supported by pile foundations. The deck is continuous with no intermediate expansion joints, and is supported by five elastomeric bearing pads at each abutment. The bridge was designed based on the 1965 AASHTO document, Standard Specifications for Highway Bridges, the Interim Specifications through 1967, and the 1966 BPR Ultimate Strength Design Criteria.

The reinforcement distribution in the piers is shown in Fig. 6. The connection to the footing is a hinged connection in the longitudinal direction of the bridge, but is rigid in the transverse direction through the dowels. The dowels are made from #11 bars in all the piers. Because no yielding of the reinforcement in the deck was expected, the deck steel did not enter the analysis and is not shown.

5. EXPERIMENTAL STUDIES

The Rose Creek bridge was subjected to static and dynamic loads. The static loads were applied in the transverse direction of the bridge at the intersection of the piers and the deck by four hydraulic rams acting at an angle of 45^{o}. The rams were loaded manually at low rate. Temporary reaction foundations were built to support the rams. The bridge was loaded to several amplitudes and the ram loads were simultaneously released to allow for free-vibration testing of the bridge.

The static data collected included the lateral deflection of the deck at ends, pier caps, and the center of the middle span. The footings were excavated to allow for close inspection of pier to pile cap connections. Because the shear keys (Fig. 3) were the weakest part of the piers while they carried the maximum moment, they were examined very carefully to monitor any crack formation or propagation. For each free-vibration test, the acceleration response histories were measured and recorded on FM tapes.

6. ANALYTICAL AND EXPERIMENTAL RESULTS

The Rose Creek Bridge was analyzed using the analytical model described in Sec. 3. The basic properties of pier and deck elements were determined based on geometry and reinforcement distribution using the average of measured strength for 28-day concrete samples and the specified yield strength of steel. The effect of gravity loads on moment-curvature relationship for piers was taken into account, but the uplift component of ram loads was neglected.

To determine the basic backbone curve for the neoprene elastomeric abutment springs the available guidelines prepared by the manufacturer were initially used, but the results appeared to lead to unreasonably "soft" abutments. Douglas and Richardson [10] have attributed the stiffening of the elastomeric bearing pads to aging effect. Estimates of initial stiffness of the pads for ambient level of vibration were available in a report by Gates and Smith [11]. These values were used as the slope of tangent to the back-bone curves. A brief parameter study showed that amplitudes were insensitive to the value of "G" used in the Ramberg-Osgood equations, but the effective period was affected by G. A good correlation was observed with G = 9.

Attempts were made to determine the primary curves for pier foundation springs based on the soil profile and properties of the piles and the pile caps. Information was needed on the lateral and the rotational behavior of pile groups. No procedure for finding these properties could be found in the available literature. The only information was the lateral stiffness of the pile groups used in the Rose Creek Bridge, with cyclic effects included [12]. The values were modified by excluding the cyclic effects and used for the translational springs. The rotational springs were assumed to be fixed due to the fact that no procedure for calculating pile group rotations could be found.

The lateral displacement of the deck center of the bridge subjected to lateral loads is shown in Fig. 7. It can be seen that the experimental data exhibited a slight degree of nonlinearity. No visible nonlinear behavior could be observed in the analytical result. This is, in part, due to the fact that for small loads, the only source of nonlinearity in the model is the elastomeric bearing system, which does not affect the response at the center of the deck to any great extent. The response at the bearing pads, on the other hand, showed a slight but visible nonlinear effect (Fig. 8). The plan view of the deflected shape of the bridge is shown in Fig. 9. The kink in the measured shape is perhaps due to an error in the measurements. It can be seen in Figs. 7 through 9 that the analytical results were less than the measured

values. This is attributed to the fact that the pier foundations were assumed to be fixed against rotation for this paper. A parallel study is being conducted to characterize the rotational stiffness of the pile group foundations, and its preliminary results have confirmed this observation.

The measured and calculated free-vibration acceleration histories for three locations of the deck are shown in Fig. 10. The initial displacements used in this analysis were those calculated in the static analysis, and, as it was pointed out earlier, were smaller than the measured values. Reasonably good correlation was observed during the first four seconds in the response for piers 1 and 2. The correlation in the rest of the response and for the north abutment was not close, with calculated peaks being generally larger than the measured ones at pier 1 and 2 but smaller than the measured peaks at the north abutment. The modeling of the nonlinear behavior cannot be evaluated in detail based on these response histories because of the fact that only a limited degree of nonlinearity was present in both the calculated and measured response and that the basic properties of the elastomeric bearing pads and foundation springs were approximate. Nevertheless, the relatively good agreement observed in the large-amplitude part of the responses can be an indication that the assumptions and idealizations made in developing the analytical model are somewhat realistic.

7. CONCLUSIONS

The study presented in this paper showed that the nonlinear effects should be taken into account if a reasonable estimate of seismic response is to be obtained. Unlike building structures, where the response is usually dominated by the superstructure, bridge response is significantly affected by the foundation and abutments. It was found that for the Rose Creek Bridge the lateral displacement was underestimated at the 'eck center by more than 30 percent as a result of restraining the pier found tions against rotation. The currently available literature dealing with the seismic aspects of geotechnical engineering do not provide adequate guidelines to determine basic nonlinear force-deformation properties of pile groups for translation and rotation. Another parameter for which information is inadequate is the nonlinear force-deformation characteristics of elasto-meric bearing pads, and their cyclic behavior. This information is needed for a realistic modeling of the nonlinear response of bridges. Nonetheless, based on the limited experimental data on the behavior of foundation and bearing pads, and their qualitative incorporation in the study presented in this paper, it can be concluded that the proposed model is a reasonably good start for nonlinear modeling of dynamic response in bridges.

8. ACKNOWLEDGMENTS

The study leading to this paper was part of a continuing project supported by the U.S. National Science Foundation (NSF) under Grant CEE-8108124. The conclusions, however, are those of the authors and do not necessarily present the views of NSF. Dr. Gary Norris is specially thanked for providing the stiffness properties of the pile foundations.

9. REFERENCES

1. M. CHEN and J. PENZIEN 1975 University of California, Berkeley, EERC Report 75-4. Analytical investigation of seismic response of short, single, or multiple span highway bridges.

2. A.G. GILLIES and R. SHEPHERD 1981 Bulletin of Seismological Society of America, Vol. 71, No. 2, 517-530. Dynamic inelastic analysis of a bridge structure.

3. B.M. DOUGLAS, M. SAIIDI, J. RICHARDSON, and J.D. HART 1983 Proceedings of the Fifteenth Joint Meeting of U.S./Japan Panel on Wind and Seismic Effects, UJNR. Results from High-Amplitude Dynamic Tests and Implications for Seismic Design.

4. SAIIDI 1982 ASCE, Journal of the Structural Division, Vol. 108, No. ST5, 1077-1087. Hysteresis models for reinforced concrete.

5. T. TAKEDA, M.A. SOZEN, and N.N. NIELSEN 1970 ASCE, Journal of the Structural Division, Vol 96, No. ST12, 2557-2573. Reinforced Concrete Response to Simulated Earthquakes.

6. P. DeALBA, H.B. SEED, and C.K. CHAN 1976 ASCE, Journal of the Geotechnical Division, Vol. 102, No. GT9, 909-927. Sand liquefaction in large-scale simple shear test.

7. W.B. NACHTRAB and R.L. DAVIDSON 1965 National Academy of Sciences-National Research Council, Highway Research Record No. 76, 83-101. Behavior of elastomeric bearing pads under simultaneous compression and shear loads.

8. W. RAMBERG and W.T. OSGOOD 1943 NACA Technical Note 902. Description of stress-strain curves by three parameters.

9. N.M. NEWMARK 1959 ASCE, Journal of the Engineering Mechanics Division, Vol. 85, No. EM3, 67-94. A method of computation for structural dynamics.

10. B.M. DOUGLAS and J. RICHARDSON 1984 Proceedings of The Eighth World *Conference on Earthquake Engineering*, San Francisco, CA, July 21-28, 8 pp. Maximum amplitude dynamic tests of a highway bridge.

11. J.H. GATES and M.J. SMITH 1982 California Department of Transportation, Report No. FHWA/CA/SD-82/07. Verification of dynamic modeling methods by prototype excitation.

12. B.M. DOUGLAS and G.M. NORRIS 1983 ASCE Journal of Technical Topics in Civil Engineering. Bridge dynamic tests/implications for seismic design.

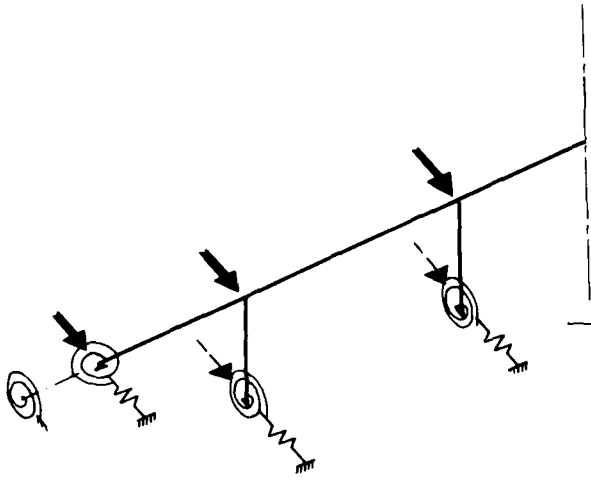

Fig. 1 Idealized Bridge Structure

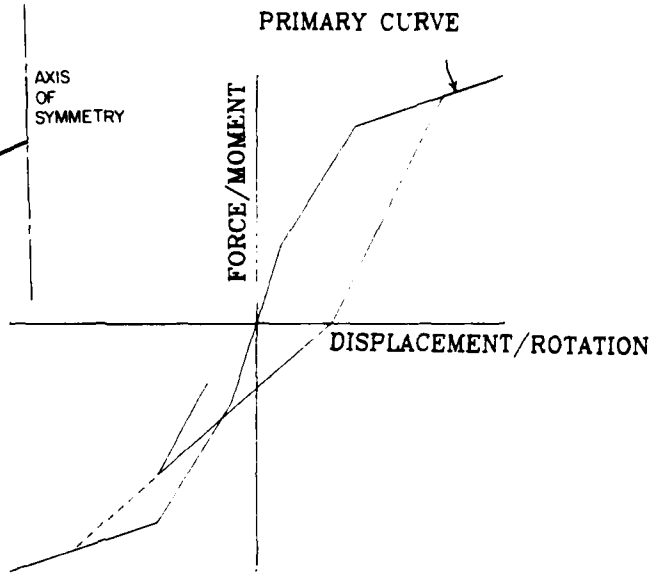

Fig. 2 The Trilinear Hysteresis Model (TQ-Hyst)

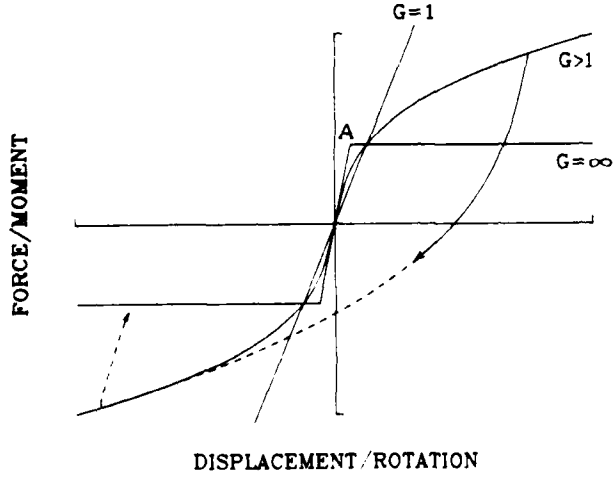

Fig. 3 The Ramberg-Osgood Model

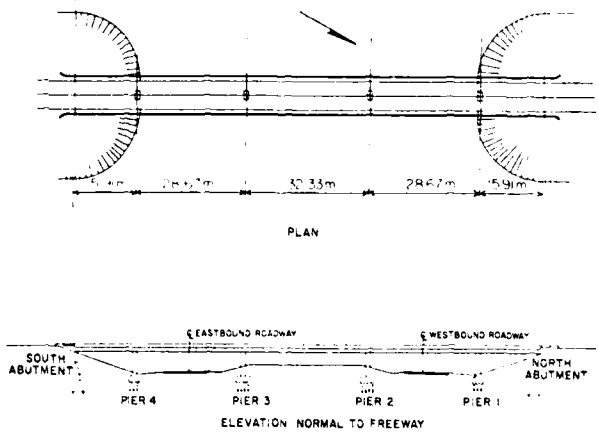

Fig. 4 The Rose Creek Bridge

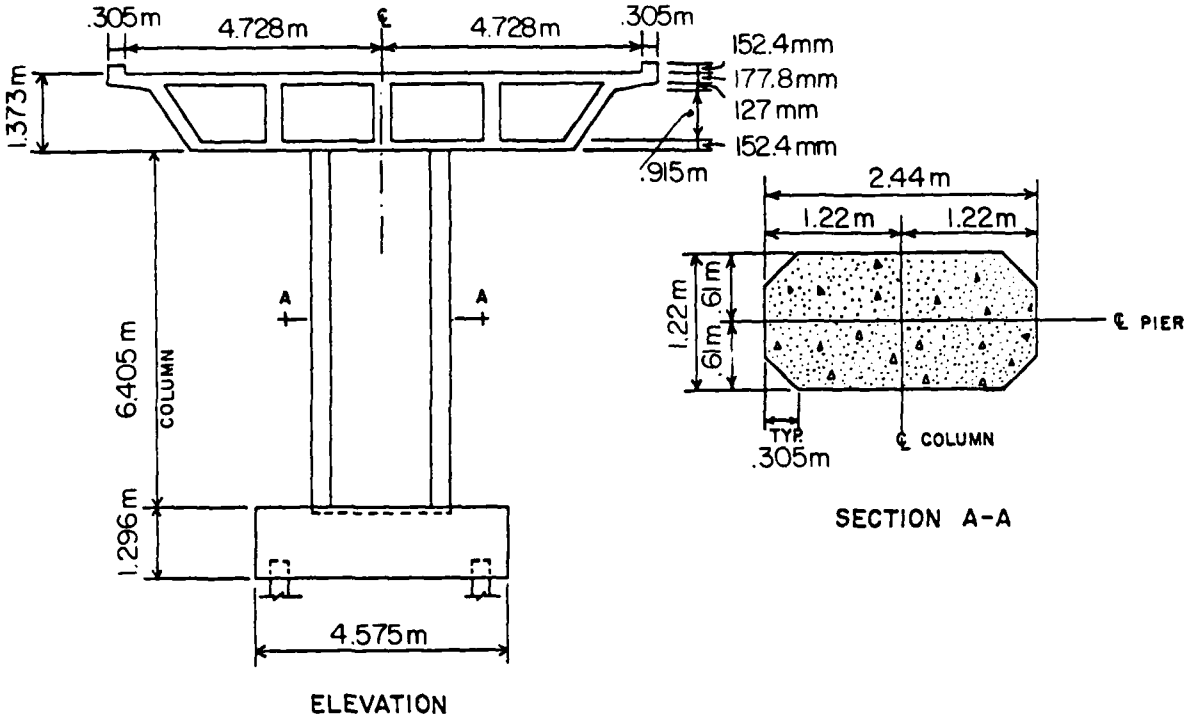

Fig. 5 Pier and Deck Dimensions

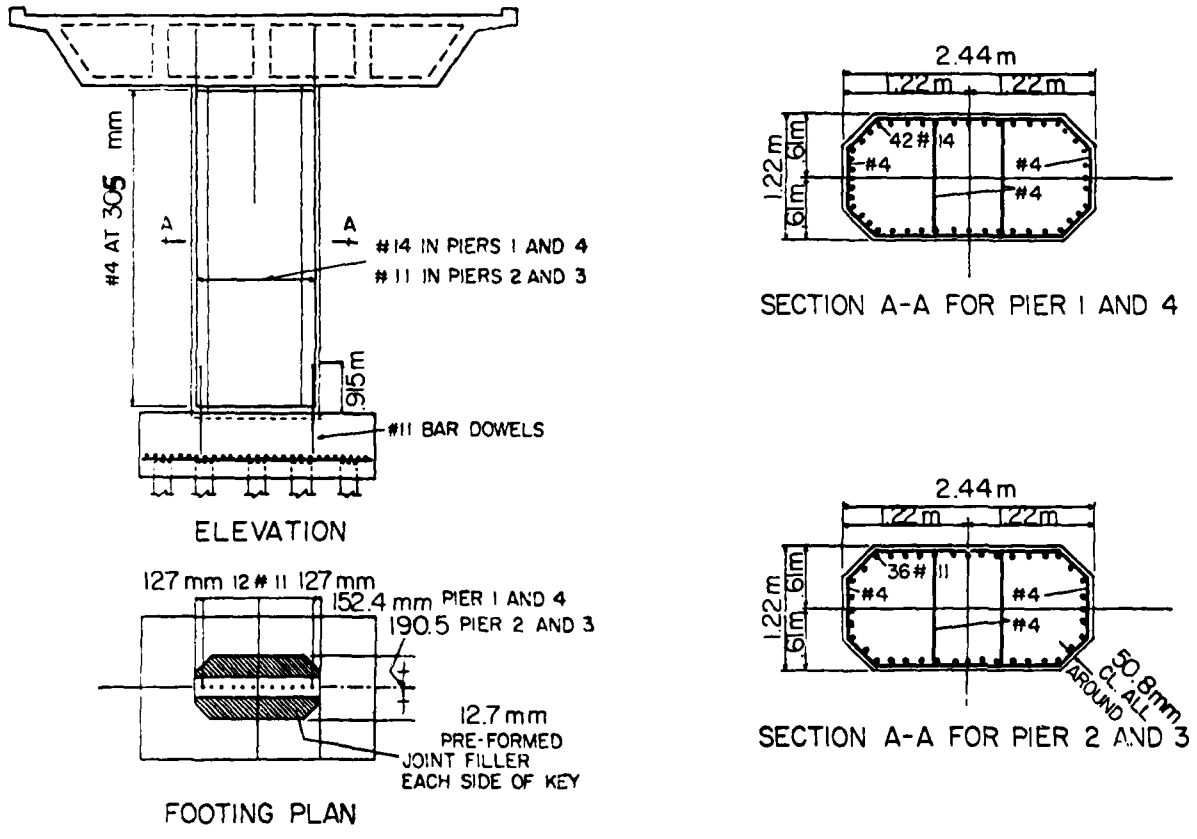

Fig. 6 Detail of Pier Reinforcement

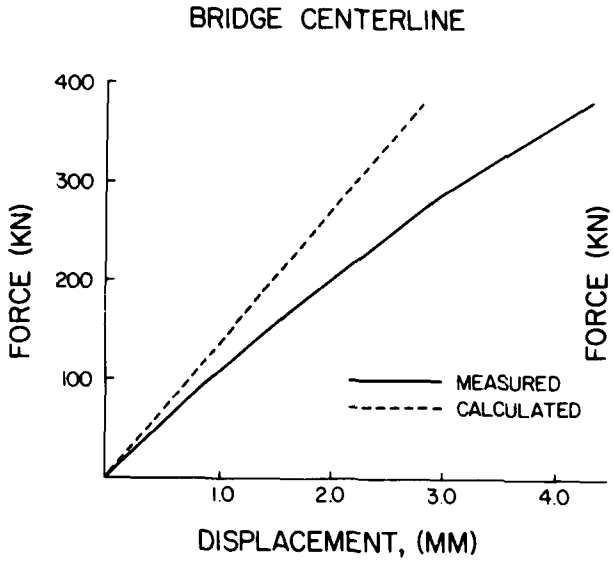

Fig. 7 Static Response at the Deck Center

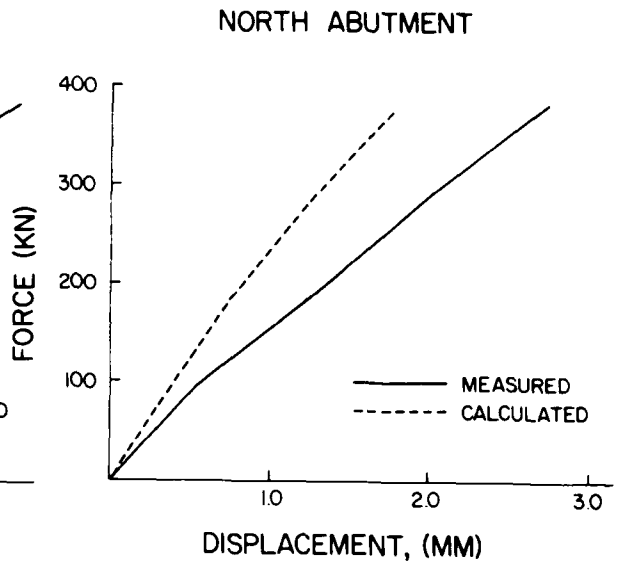

Fig. 8 Static Response at the North Abutment

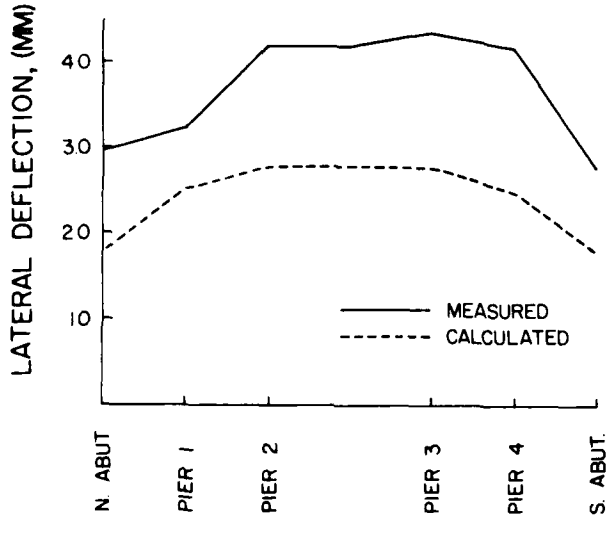

Fig. 9 Plan View of Deflection for the Maximum Load

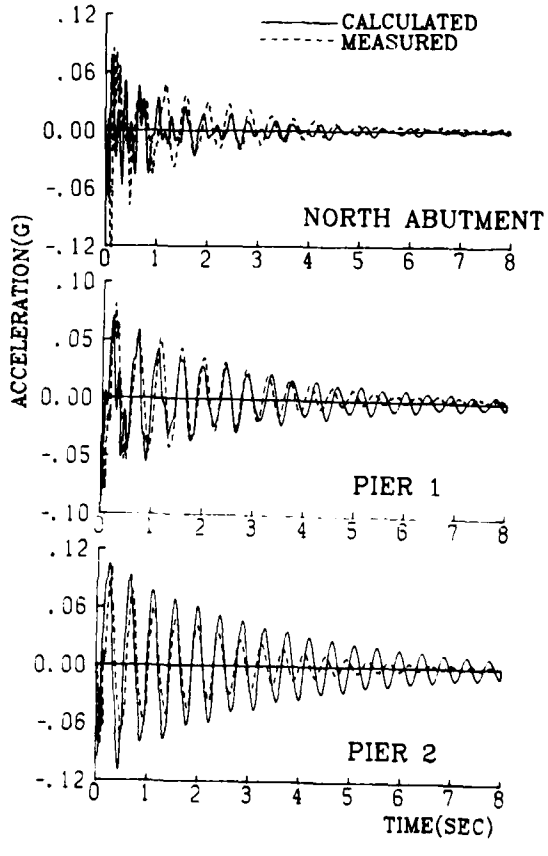

Fig. 10 Acceleration Histories

ELASTIC-PLASTIC RESPONSE OF ROOFTOP FRAMES TO DISTRIBUTED AND CONCENTRATED SHOCK LOAD: EXPERIMENTAL RESULTS AND THEORETICAL PREDICTIONS

M S J Hashmi

Department of Mechanical and Production Engineering
Sheffield City Polytechnic, Sheffield, England

1. INTRODUCTION

The most commonly used structural elements in engineering, ie cantilevers, beams, columns, rings or a combination of one or more of these elements, are sometimes designed to withstand sudden dynamic loads. However, there are structures which are often subjected to dynamic overloads purely by accident. Although the chances of dynamic overload occurring may be very small, it is this situation which is of most concern to the design and safety engineer.

The behaviour of framed structures under impulsive load has been the subject of interest to many researchers and relevant literature shows that, prior to 1956, research on the subject was mainly concerned with the elastic response of frames to transient forces[1,2]. Later, Di Maggio[3] studied the elasto-plastic response of frames when plastic conditions develop at a number of points in the structure. Tanaka[4] studied the response of a moving plastic portal frame, when the base of the frame was suddenly stopped, thus causing a decelerating motion in the plane of the frame.

Rawlings[7] has applied the dynamic rigid-plastic analysis, previously used for studying beams, to the study of the dynamic plastic behaviour of steel frames. He has also studied the influence of concentrated masses attached at different positions on the frame. Stewart et al[8] carried out an experimental investigation into the in-plane response of model frames when a concentrated dynamic load was applied to the side. Similar investigations, but withblast loads, were carried out by Takahashi et al[9,10]. In these tests the applied load was of the order of the ordinary static collapse load. Although the deformation response in these tests appeared to be of a modal type, the determination of the deflection response required the inclusion of elastic effects because of low load density.

Johnson and Martin[11] studied the inelastic behaviour of a rectangular portal frame, having a concentrated mass attached to the centre of the beam, when an impulsive load was applied to the mass and delivered in a direction perpendicular to the plane of the frame. Other tests on frames have been reported by Bodner[12] who observed that the dominant deformations were of a modal type. Burgman and Rawlings[13] studied the dynamic behaviour of pin jointed frames subjected to large concentrated dynamic overloads. They studied the various collapse modes of the frames and also considered the buckling behaviour of the members in compression.

Hashmi and Al-Hassani[14] studied the elastic-plastic response behaviour of rectangular frames subjected to distributed impulsive load. Their experimental results compared well with theoretical predictions obtained using a numerical technique presented earlier in reference [15].

Martin[16] developed a simple iterative procedure for determining mode shapes of structures of rigid perfectly plastic material subjected to dynamic loading. The technique was subsequently extended to include geometrically linear homogeneous viscous beams[17] and non-linear beams and frames[18] by Griffin and Martin. Experimental results were reported by Bodner and Symonds[19] of tests on mild steel frames theoretical analysis of which was subsequently presented by Symonds and Raphanel[20].

In a recent paper Hashmi[21] presented results of experiments on unrestrained triangular frames made of aluminium which were subjected to distributed and concentrated impulsive loads. In the present study experimental results are presented of tests on aluminium and mild steel frames subjected to distributed and concentrated impulsive loads. The effect of extra mass attached to the frame on the response mode is studied experimentally and theoretically. The effect of material strain rate sensitivity is also studied theoretically using the numerical technique the details of which has been previously described in reference [15].

2. EXPERIMENTAL WORK

Experiments were carried out on aluminium and mild steel rooftop frames by applying distributed and concentrated impulsive loads respectively.

2.1 Distributed Loading

The distributed impulse was obtained using the magnetic loading technique[14]. This is a technique of loading structures by means of high transient magnetic field which is produced by the discharge of a bank of capacitors through a robustly constructed conductor made to conform closely to the structural member. The deforming forces arise from the interaction of the induced currents in the structural member and the high transient magnetic field which exists in the gap between the member and the loading conductor. The absence of mechanical contact forces and the ability to control the leading pulse in shape, distribution and magnitude make this loading method superior to other methods.

For this type of loading, 0.9 mm thick half hard aluminium sheets were cut into 12.5 mm wide strips which were bent to form rooftop frames having dimensions as shown in Fig 1. Each frame was rigidly held by adjustable clamps and brought near to the loading conductor so that only the area to be loaded was adjacent to the conductor. The loading situations considered in this study are shown in Fig 1 for rooftop frames (a) without, and (b) with the attached mass.

Measurement of the impulse delivered to each frame was obtained from the swing of a ballistic pendulum onto which the frame was mounted.

2.2 Concentrated Loading

Concentrated impulsive load was obtained by use of explosive detonator which was attached onto the frame by means of adhesive tapes. Layers of polymer sheet were introduced in between the detonator and the surface of the frame to prevent any localised damage. The impulse produced by the detonator was calibrated by means of a pendulum. For this type of loading the frames were made out of 1.9 mm thick and 10.5 mm wide mild steel strips. The overall dimensions of the frames and the various loading configurations are shown in Fig 2. Concentrated impulse was applied at the midspan of the (a) slanting side, and (b) vertical side of the rooftop frames.

Similar loading configurations were repeated having extra mass attached at different locations on to the frame.

The stress-strain properties of the materials of the frames were determined from quasi-static tensile tests on specimens prepared from aluminium and mild steel strips and the results are shown in Fig 3.

In order to study the transient deformation mode of the frames high speed photographs were taken of a number of different loading cases using a high speed camera. Synchronisation of the camera with the onset of the deformation process was facilitated by a built-in micro-switch which sets off the event at the desired maximum speed of the camera.

3. RESULTS AND DISCUSSIONS

3.1 Distributed Impulsive Loading

The deformation responses of aluminium rooftop frames, with and without attached mass, subjected to impulsive load distributed over one of the slanting sides were recorded operating the high speed camera at a rate of 6,000 frames/sec. The finite-difference numerical technique reported in reference [15] was used to simulate the response mode of these frames. The equivalent lumped mass models are shown in Fig 4(a) and (b). In Fig 4(a) which corresponds to the loading configuration shown in Fig 1(a), the frame is represented by 37 mass points and an initial velocity is assigned to the masspoints 10 to 18. Similarly, the equivalent lumped mass model for the rooftop frame with attached extra mass and loaded as shown in Fig 1(b) is represented by 37 mass points as shown in Fig 4(b). The concentrated attached mass is represented by the larger mass at mass point 30. In both cases the initial speeds of v_x = 18.5 m/sec and v_z = 24.1 m/s were deduced from the measured impulse delivered to the frames by the loading unit.

In Fig 5(a) a series of profiles of a frame loaded in the manner depicted in Fig 1(a) are shown corresponding to various time instants after the onset of the deformation process. This frame was subjected to a distributed impulse of 0.098 N-s. The response of this frame was predicted theoretically and a comparison of the theoretical and experimental instantaneous profiles 3.2 milliseconds after the onset of the process is made in Fig 5(b).

The deformation response of a rooftop frame carrying extra mass of 22 grams and subjected to impulsive load distributed over one of its slanting sides in the manner shown in Fig 1(b) was also recorded using high speed camera. Fig 6(a) shows a number of profiles of a rooftop frame with attached mass corresponding to different instants of time after the onset of the process. Comparison of the experimentally observed and theoretically predicted instantaneous profiles for this frame subjected to a distributed impulse of 0.098 N-s can be seen in Fig 6(b).

The effect of the extra mass on the response mode is demonstrated in Figs 5 and 6. Without any attached mass the frame tends to deform as a whole, each element undergoing substantial deflection. The frame with the attached mass, on the other hand, deforms in a manner such that gross deformation is mainly confined to the loaded member of the frame.

It is also evident from these figures that the theoretically predicted deformation mode closely matches those observed experimentally for the frames with and without attached mass.

3.2 Concentrated Impulsive Loading

Mild steel rooftop frames were subjected to concentrated impulsive load in the manner shown in Fig 2. Computer simulation of the response mode was carried out based on the equivalent lumped mass model as shown in Fig 7. The whole frame is represented by 43 mass points and where appropriate, the extra mass is represented by a larger mass on the lumped mass model. The concentrated impulse is represented by initial velocity of 77 m/s over two mass points. Three different magnitudes of impulse were obtained by introducing different thicknesses of the polymer sheet between the detonator and the surface of the frame.

The final profiles of rooftop frames subjected to concentrated impulses of 0.385, 0.352 and 0.282 N_S imparted at the midpan of one of the slanting sides are shown in Fig 8(a). Fig 8(b), on the other hand, shows the final profiles of similar frames subjected to the same magnitudes of concentrated impulses as in the previous case but imparted at the midspan of one of the vertical sides. In order to observe the effect of the added concentrated mass and its location on the response mode mild steel frames were subjected to concentrated load in the same manner as before but each frame having a mass of 62 g attached at a different location. In Fig 9(a) the final profiles of rooftop frames with a mass attached at different location are compared with that of a rooftop frame without any attached mass but subjected to the same concentrated impulse of 0.385 N_S at the midspan of one of the slanting sides. Final profiles of similar rooftop frames with and without added mass but subjected to the same concentrated impulse at the midspan of one of the vertical sides are shown in Fig 9(b). It is evident from Fig 9 that the deformation mode is very much influenced by the presence as well as the location of the attached extra mass. The effect is the least when the mass is attached at the top of the vertical side opposite to the side of the frame onto which the impulsive load is applied.

The deformation response of mild steel rooftop frames without and with attached mass were recorded using high speed camera. Figs 10(a) and (b) show series of instantaneous profiles depicting the deformation mode after the onset of the loading process of a rooftop frame without and with attached mass respectively. The frame in Fig 10(a) was subjected to a concentrated impulse imparted at the midspan of one of the slanting sides whilst the frame in Fig 10(b) was subjected to a concentrated impulse imparted at the midspan of one of the slanting sides, the extra mass of 22 g being attached at the top end of the near vertical side. Both frames were subjected to the same impulse of 0.282 N-s.

The response modes of these frames were predicted theoretically using the finite difference numerical technique with and without taking account of the effect of material strain rate sensitivity. Fig 11(a) shows comparison of the experimentally observed and theoretically predicted deformation profiles of the frame shown in Fig 10(a) 1.5 millisecond after the onset of the deformation process. Similar comparison for the frame with attached mass is shown in Fig 11(b). The strain rate sensitivity effect of the material of the frame was incorporated according to the equation,

$$\sigma_d = \sigma_s \left[1 + \left(\frac{\dot{\varepsilon}}{D}\right)^{1/p}\right]$$ where the values of D and p were taken to be 50,000 s^{-1} and 2.5 respectively as suggested in reference [22].

It is evident from Fig 11(a) and (b) that the theoretically predicted results agree closely with those obtained experimentally for mild steel

rooftop frames. The theoretical instantaneous profiles predicted with and without incorporating the effect of material strain rate sensitivity were found to be practically the same and indistinguishable as separate profiles in Figs 11(a) and (b). Calculations were repeated with values for D and p as 40.4 s^{-1} and 5 according to reference [23] and this time some appreciable difference was observed in the predicted profiles at 1.5 milliseconds. The predicted final profiles, however, were observed to be slightly influenced by the strain rate sensitivity.

4. CONCLUSIONS

Aluminium and mild steel rooftop frames were subjected to distributed and concentrated impulsive loads respectively. It has been observed that the location of the point of application of the load and the presence of attached extra mass has significant effect on the collapse mode of the frames.

It has also been shown that the theoretically predicted deformation mode matches closely with those observed experimentally for aluminium frames and also for mild steel frames. The effect of strain rate sensitivity on the instantaneous deformation profiles was found to be significant for this type of rooftop frames.

APPENDIX

A finite difference numerical technique was employed to theoretically analyse the gross deformation response of the frames before and after fracture takes place. The method has been described in detail elsewhere[15] and only a short account will be presented here giving the main governing equations. If the two dimensional structure moves in the x-y plane only and s is the length measured along the axis of the structure then a typical element may be as shown in Fig. 12(a). This element is acted upon by the axial force, N, the transverse shear force Q and the bending moment M. Additionally the inertia forces due to accelerations $\ddot{u}$ in x and $\ddot{v}$ in y direction will also be present.

The resulting force and moment equations of equilibrium for an element are

$$\frac{\partial}{\partial s}(N \cos\theta) - \frac{\partial}{\partial s}(Q \sin\theta) - m\ddot{u} = 0 \qquad (1)$$

$$\frac{\partial}{\partial s}(N \sin\theta) + \frac{\partial}{\partial s}(Q \cos\theta) - m\ddot{v} = 0 \qquad (2)$$

and

$$\frac{\partial M}{\partial s} - Q = 0 \qquad (3)$$

Equations (1)-(3) may be written in finite-difference form and the resulting equations apply to the lumped-parameter model as shown in Fig.12(b). This model simplifies the actual structure into a mass-link system. The mass of each small element of the structure is represented by a concentrated point mass connected to the other masses by light links which transmit axial forces, shear forces and bending moments. The links are assumed to have the same strength properties as that of the actual structure, the cross-section of which is assumed to consist of n discrete, evenly spaced and equal cross-sectional area, layers of material which can carry normal stresses.

Under the action of the forces, therefore, the position of each mass in the model identifies the position of an element of the actual structure. The finite difference equations for an element at the ith position are

$$N_{i+1}\cos\theta_{i+1} - N_i\cos\theta_i - Q_{i+1}\sin\theta_{i+1} + Q_i\sin\theta_i - m_i\ddot{u}_i = 0, \quad (4)$$

$$N_{i+1}\sin\theta_{i+1} - N_i\sin\theta_i + Q_{i+1}\cos\theta_{i+1} - Q_i\cos\theta_i - m_i\ddot{v}_i = 0 \quad (5)$$

and $$M_i - M_{i-1} - Q_i\Delta s_i = 0. \quad (6)$$

Equations (4)-(6) apply to all the masses around the structure and give the instantaneous values of $u_{i,j}$ and $v_{i,j}$ for any time t_j, when coupled with the following relationship between acceleration and displacement in finite difference notation,

$$u_{i,j+1} = \ddot{u}_{i,j}(\Delta t)^2 + 2u_{i,j} - u_{i,j-1}$$

and $$v_{i,j+1} = \ddot{v}_{i,j}(\Delta t)^2 + 2v_{i,j} - v_{i,j-1}$$

The time increment is defined through

$$\Delta t = t_{j+1} - t_j.$$

The link length Δs_i and its angle θ_i may then be expressed in terms of the co-ordinates $u_{i,j}$ and $v_{i,j}$ which in turn permits the calculation of strain in each link. It then remains to connect the strain thus obtained with the axial force N_i and bending moment M_i using appropriate stress-strain properties given by

$$\sigma = f(\varepsilon,\dot{\varepsilon}).$$

Having determined the values of N and M at all the mass point locations and for all the links the cycle of computation is repeated until plastic deformation ceases.

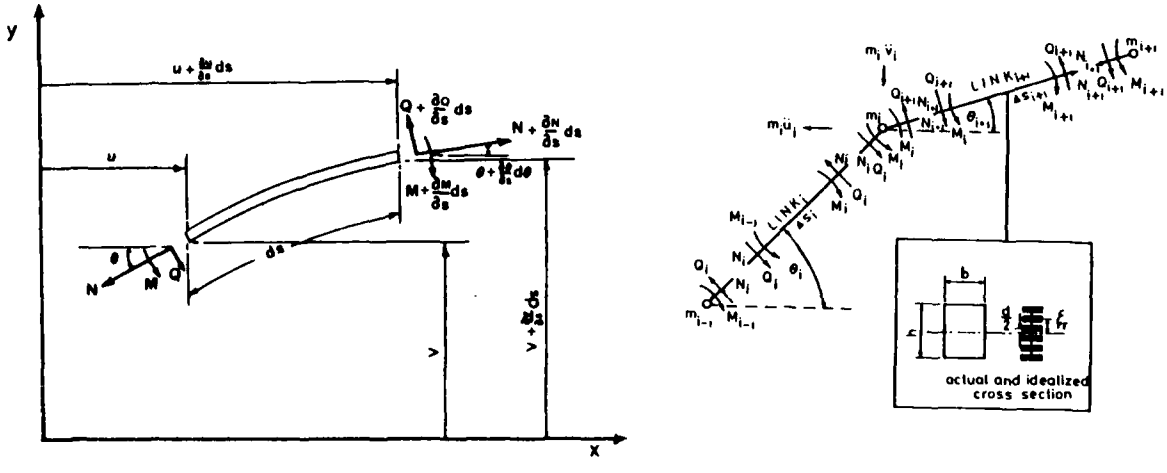

Fig. A1 showing (a) an element of the structure in x-y plane, and (b) the equivalent lumped-parameter model

REFERENCES

1. S Timoshenko, 1928. Vibration Problems in Engineering. New York: D Van Nostrand.

2. G L Rogers, 1953. An Introduction to Dynamics of Framed Structures. New York: John Wiley & Sons Inc.

3. F L Di Maggio, 1958. J.Eng'g.Mech.Div.,Proc. ASCE, 84, No EM3, Dynamic elastic-plastic response of rigid frames.

4. H Tanaka, 1960. Technical Report No 60, Brown University, Plastic deformation of square portal frames under horizontal load.

5. B Rawlings, 1964. J.Struct.Div. ASCE, 90, No ST3, p 265. Dynamic plastic analysis of steel frames.

6. B Rawlings, 1964. Proc. Instn. of Civil Engrs., 29, p 389, Impact tests on model steel frames.

7. B Rawlings, 1964. J.Mech.Eng'g.Science, 6, No 4, Mode Changes in frames deforming under impulsive loads.

8. W C Stewart, P E Rowe and P J Pabl, 1965. Technical Report DSR 5135 (AD628063) MIT. Dynamic tests of model steel structures.

9. S K Takahashi and R K Chin, 1965. Technical Report R336, US Naval Civil Eng'g. Laboratory. Calif., Static and dynamic behaviour of pinned base portal frames.

10. S K Takahashi and R K Chin, 1965. Technical Report R336, US Naval Civil Eng'g. Laboratory. Calif., Static and dynamic behaviour of fixed base portal frames.

11. G L Johnson and J B Martin, 1969. Int. J. Solids & Structures, 5 p 1171, The permanent deformation of a portal frame subjected to a transverse impulse.

12. S R Bodner, 1968. Proc. of Eng'g. Plasticity Conference, Cambridge University Press. Deformation of rate sensitive structures under impulsive loading.

13. J B Burgman and B Rawlings, 1968. Int.J.Mech.Sci., 10, p 967, Dynamic plastic analysis of pin-jointed frames.

14. M S J Hashmi and S T S Al-Hassani, 1975. Int.J.Mech.Sci., 17, p 513, Large deflexion response of square frames to distributed impulsive loads.

15. M S J Hashmi, S T S Al-Hassani and W Johnson, 1972. Int.J.Mech.Sci., 14, p 843, Large deflexion elastic-plastic response of certain structures to impulsive loads: Numerical solutions and experimental results.

16. J B Martin, 1981. Meccanica 16, p 42, The determination of mode shapes for dynamically loaded rigid-plastic structures.

17. P D Griffin and J B Martin, 1982. J.Structural Mech. 10, p 93, Finite element analysis of dynamically loaded homogeneous viscous beams.

18. P D Griffin and J B Martin, 1983. Int.J.Mech.Sci., 25, p 15, Geometrically non-linear mode approximations for impulsively loaded homogeneous beams and frames.

19. S R Bodner and P S Symonds, 1969. Int. J. Solids Structures 15, p 1, Experiments on dynamic plastic loading of frames.

20. P S Symonds and J L Raphanel, 1979. Proc. Conf. on Mechanical Properties of Materials at High Rates of Strain. Institute of Physics Conf. Ser No 47, p 277, Large deflections of impulsively loaded plane frames - extensions of the mode approximation technique.

21. M S J Hashmi, 1982. Proc. 1st Int. Modal Analysis Conf. p 550, Orlando, USA. Experimental and theoretical study of the gross deformation response of unrestrained frames subjected to concentrated and distributed impulsive loads.

22. M S J Hashmi, 1980. J. of Strain Analysis, IMechE, 15, p 201, A technique of assessing strain rate sensitivity of a mild steel at room temperature and strain rates of up to 10^5 per second.

23. P S Symonds, 1967. Brown University, Report BU/NSRDC/1-67, Survey of Methods of analysis for plastic deformation of structures under dynamic loadings.

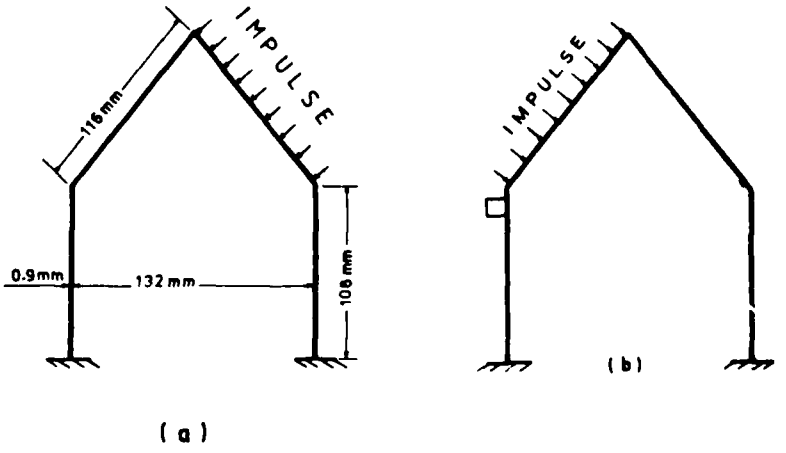

Fig 1 Loading configurations of rooftop frames subjected to distributed impulse

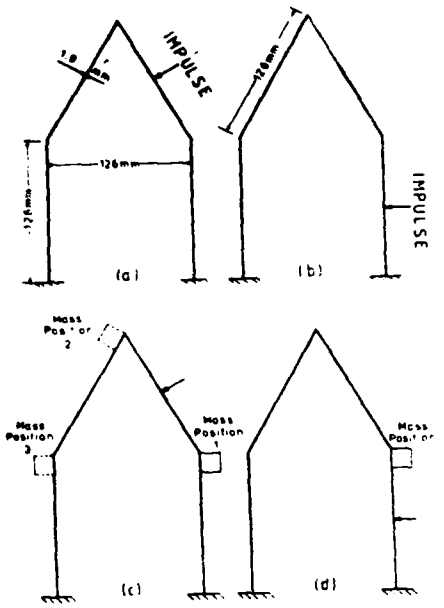

Fig 2 Loading configurations of rooftop frames subjected to concentrated impulse

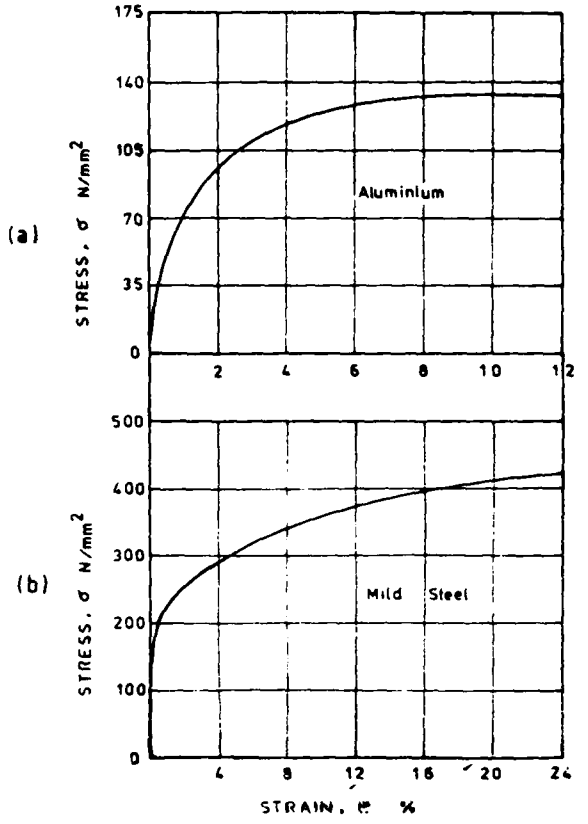

Fig 3 Stress-strain properties of (a) aluminium and (b) mild steel

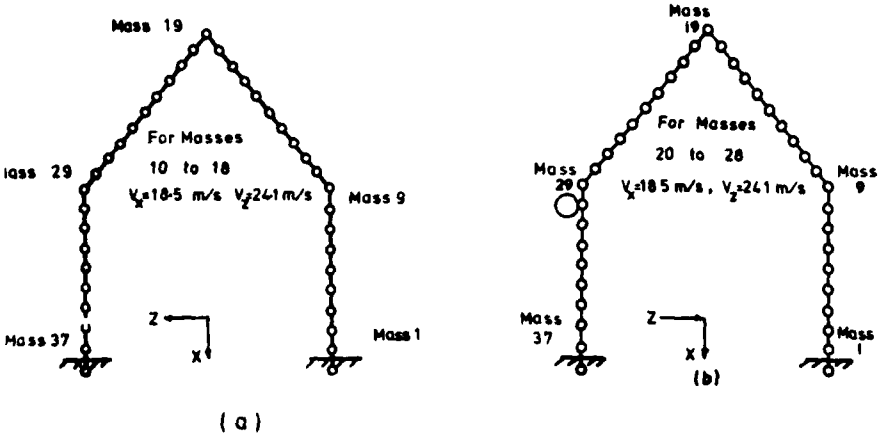

Fig 4 Equivalent lumped mass models for distributed impulsive loading

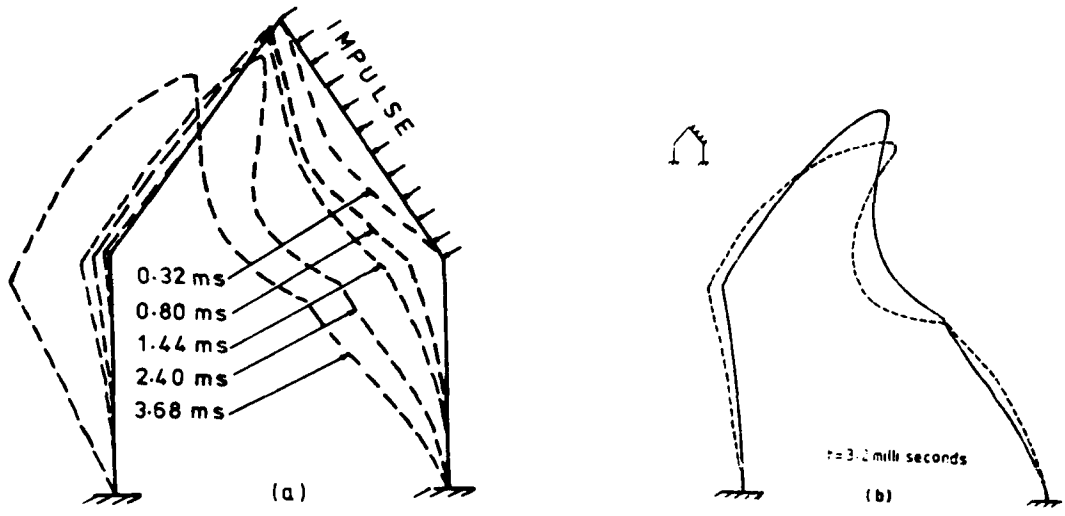

Fig 5 (a) Profiles showing deformation mode,
(b) Comparison of theoretical and experimental profiles.

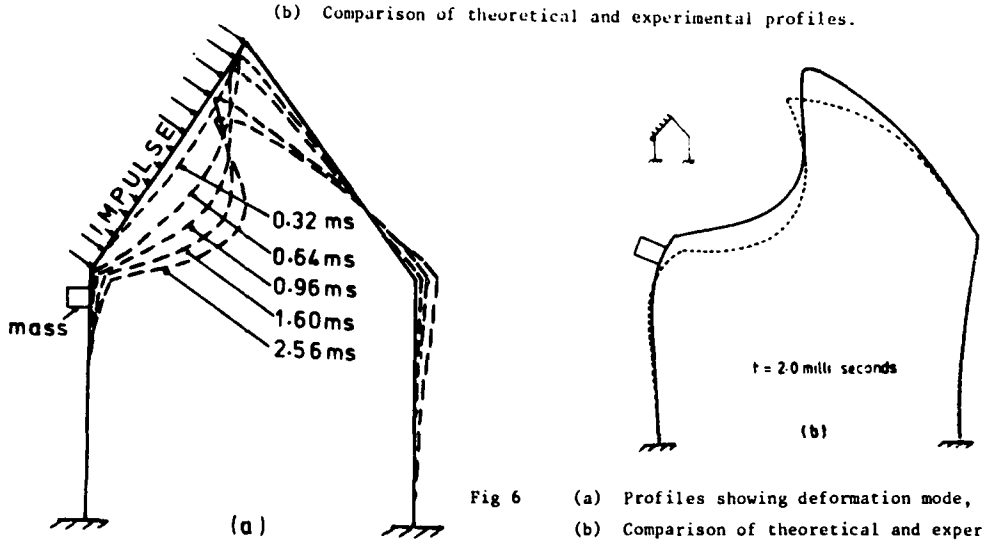

Fig 6 (a) Profiles showing deformation mode,
(b) Comparison of theoretical and experimental profiles.

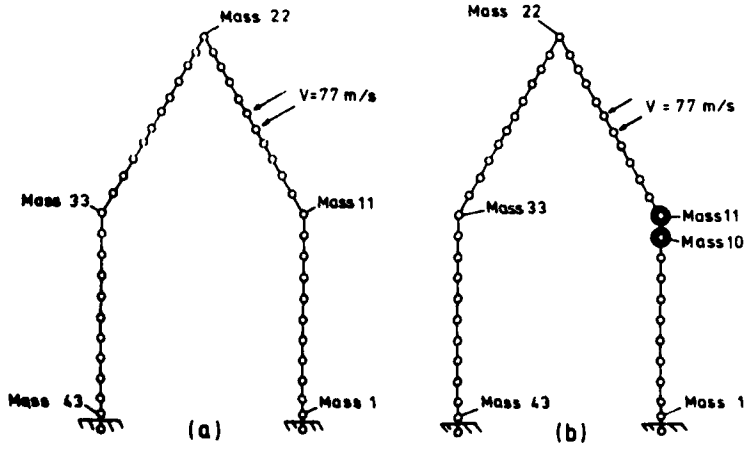

Fig 7 Equivalent lumped mass models for concentrated impulsive loading

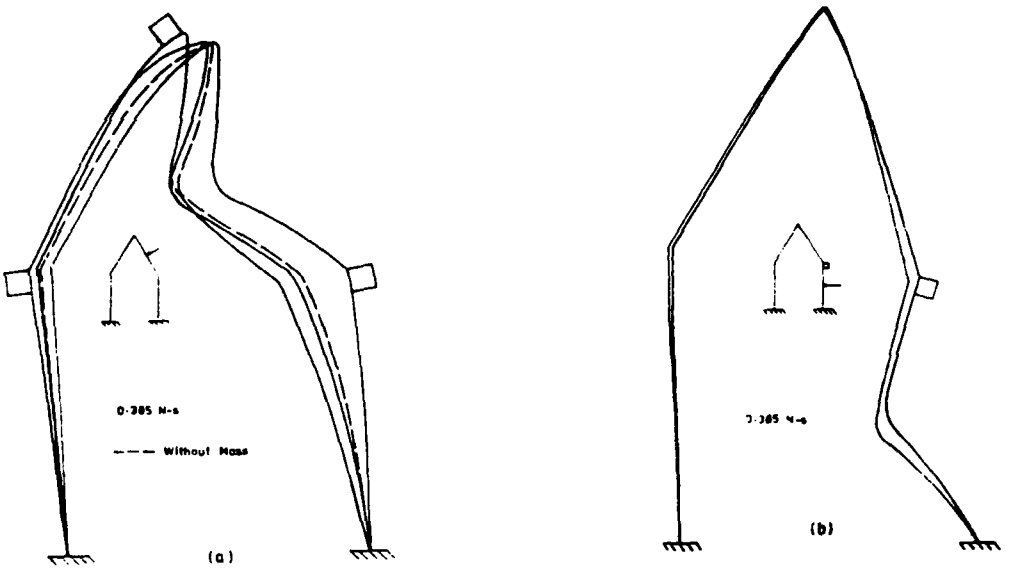

Fig 8 Final profiles of rooftop frames subjected to concentrated impulsive load at the (a) slanting (b) vertical side.

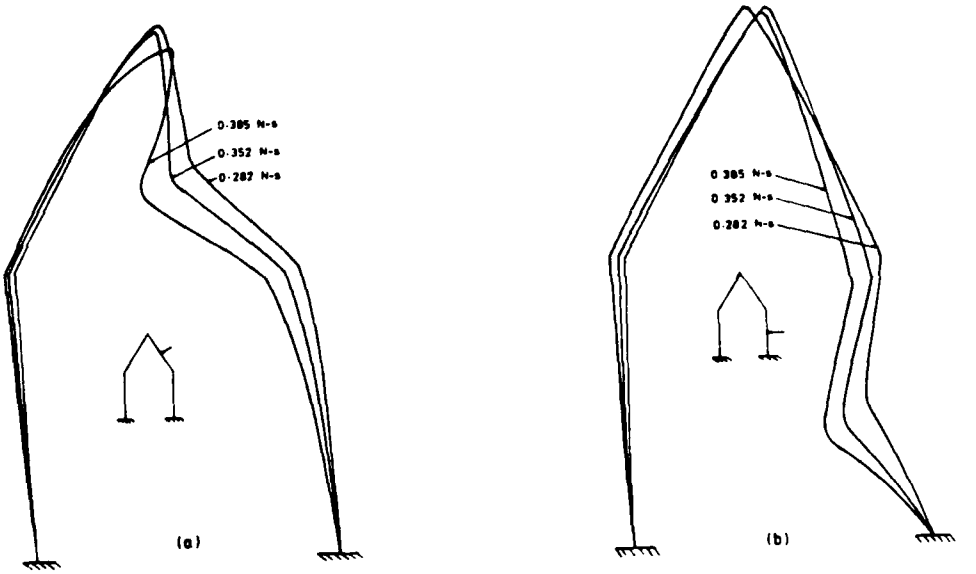

Fig 9 Effect of added mass on the deformation mode of rooftop frames subjected to concentrated impulsive load at the (a) slanting (b) vertical side.

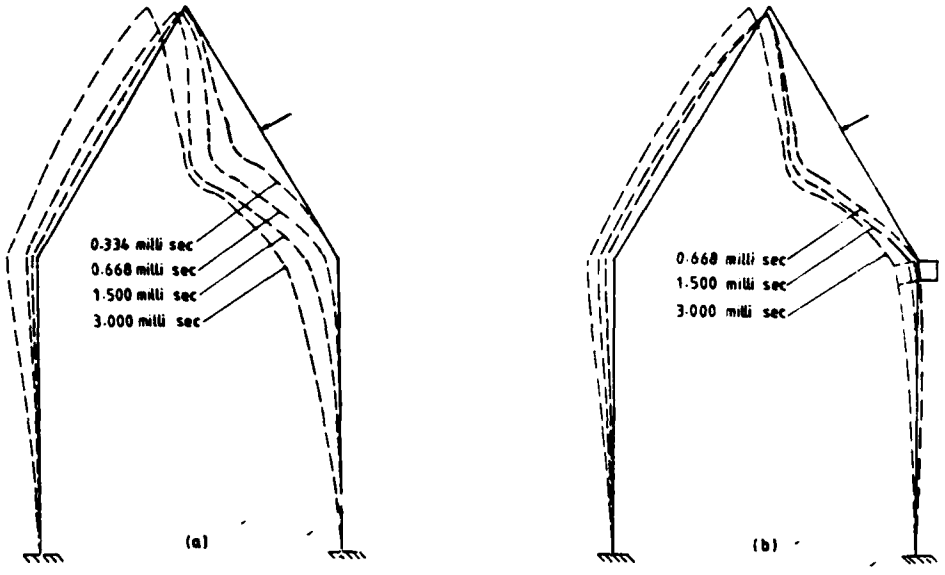

Fig 10 Showing experimental deformation modes of a rooftop frame (a) without and (b) with attached extra mass.

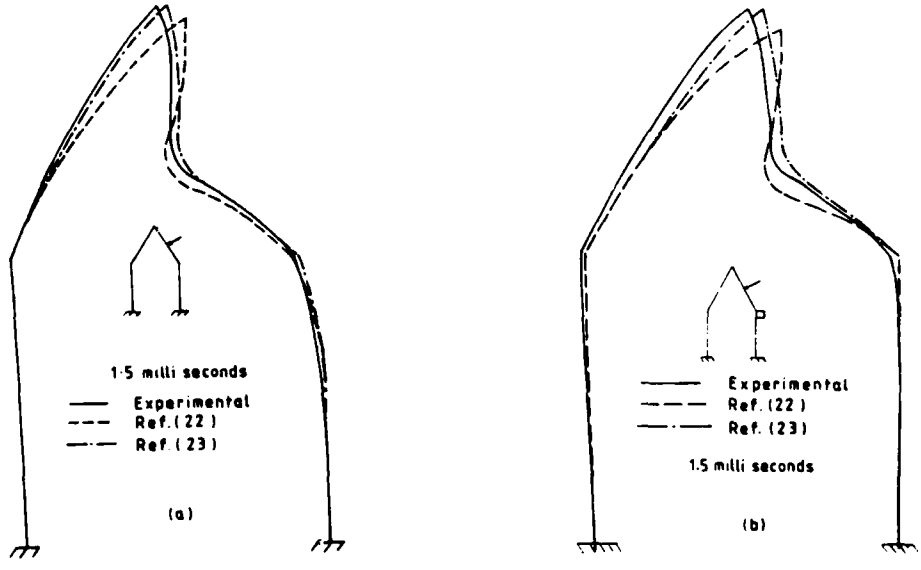

Fig 11 Showing comparison of theoretical and experimental instantaneous profiles of rooftop frames (a) without and (b) with attached extra mass.

11. RANDOM VIBRATION

RESEARCHES IN RANDOM VIBRATION

J.D. Robson

University of Glasgow (Professor Emeritus)

1. INTRODUCTION

1.1 General

The aim of this lecture is to give an indication of the research in Random Vibration carried out at Glasgow University in the Department of Mechanical Engineering during the period 1965-1982. In the time now available it is possible to give no more than an indication, but the adoption of a somewhat superficial approach does make possible a sort of completeness and may help to render the lecture digestible by those who are not entirely familiar with the intricacies of random vibration analysis. The references given in the text should make it possible for those who wish for further details to find them.

During the period under review the team working on random vibration at Glasgow has always been small, and the permanent members of staff have had many other matters to occupy them. Other research workers have become available only from time to time, and the way in which the work has developed has depended very much on current individual interests and availability. Nevertheless it is possible looking back to detect some sort of pattern, the work being devoted as far as possible to unravelling the more immediate complications arising in the application of random vibration theory to practical problems.

While this work has always been motivated by the needs of application it cannot be claimed that it has always had a strong and immediate effect on industrial practices; probably its greatest influence has been as a contribution to the increasing awareness of random matters which now prevails. Yet even where it has not been actually applied the work remains always applicable, and it is possible that this very brief exposure may suggest further possibilities to those currently involved in application.

The work now to be described may for convenience be divided into three parts, to which the next three sections of this presentation correspond. Section 2 will deal with the application of basic theory to the responses of road-vehicles to road roughness. Section 3 will treat more general aspects of the multivariate responses of linear systems subjected to random excitation. Section 4 is devoted to a number of separate problems where the simplifying assumptions of process Gaussianity and system linearity are not permissible.

1.2 Basic Theory

In random vibration the designation of any theory as basic must involve a highly arbitrary decision. The subject depends fundamentally on the concepts of probability theory, and most of the basic concepts of orthodox vibration analysis remain relevant. While this must be accepted it is nevertheless convenient to regard the starting point of the subject as the description of a stationary random process by autocorrelation function or spectral density, and the initial result which relates response and excitation spectral densities by making use of the system's known properties under harmonic excitation. Certain details of definition

differ between individual writers, and the following statement of basic analytical results provides a good opportunity to establish the definitions which are to be used here.

Figure 1 shows the basic situation where a single random excitation P(t) is applied to a linear vibratory system giving rise to a response x(t). If P(t) is a member function of a stationary Gaussian random process $\{P(t)\}$ it is describable by the autocorrelation function $R^P(\tau)$ and spectral density $S^P(f)$, where

$$R^P(\tau) = E\left[P(t)P(t+\tau)\right], \qquad (1)$$

$$S^P(f) = \int_{-\infty}^{\infty} R^P(\tau) e^{-i2\pi f\tau} d\tau. \qquad (2)$$

(The process $\{x(t)\}$ has of course similar descriptions $R^x(\tau)$, $S^x(f)$.) With $S^P(f)$ defined as in (2) the mean-square value of P(t) is given by

$$E\left[P^2(t)\right] = \int_{-\infty}^{\infty} S^P(f)\, df. \qquad (3)$$

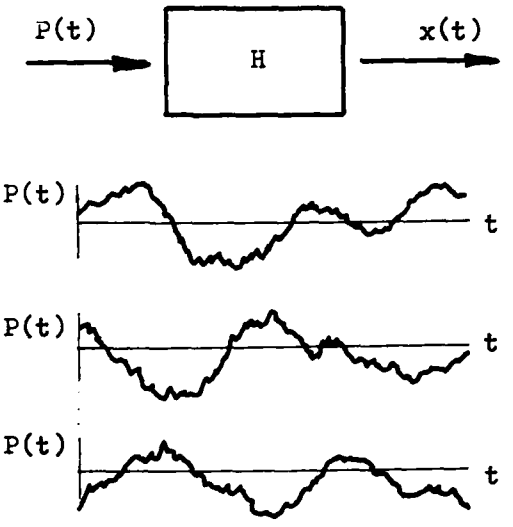

Figure 1. Basic System

For a linear system under single excitation the relationship between response and excitation spectral densities is given by

$$S^x(f) = \left|H(f)\right|^2 S^P(f) \qquad (4)$$

where H(f) is the harmonic influence function of the system.

With multi-excitation systems one must have regard also to cross correlation functions and cross spectral densities. If the excitations are $P_1(t)$ and $P_2(t)$ these are defined by

$$R^P_{12}(\tau) = E\left[P_1(t)\, P_2(t+\tau)\right], \qquad (5)$$

$$S^P_{12}(f) = \int_{-\infty}^{\infty} R^P_{12}(\tau)\, e^{-i2\pi f\tau} d\tau. \qquad (6)$$

The response relationships are then more complex: for the case of two excitations (with arguments omitted for the sake of brevity)

$$S^x_{11} = H^*_{11} H_{11} S^P_{11} + H^*_{11} H_{12} S^P_{12} + H^*_{12} H_{11} S^P_{21} + H^*_{12} H_{12} S^P_{22} \qquad (7)$$

where H_{12} (for example) is the harmonic influence function connecting the response $x_1(t)$ with excitation $P_2(t)$.
Where there are two responses $x_1(t)$, $x_2(t)$ the cross spectral density $S^x_{12}(f)$ is given by

$$S^x_{12} = H^*_{11} H_{21} S^P_{11} + H^*_{11} H_{22} S^P_{12} + H^*_{12} H_{21} S^P_{21} + H^*_{12} H_{22} S^P_{22}. \qquad (8)$$

There is no difficulty in principle in setting out similar response relationships for greater numbers of excitations and responses, and these are often needed in practice. In such cases there is a strong incentive to take advantage of the conciseness of matrix notation, which adapts itself particularly well to spectral relationships. With

$$\underset{\sim}{S}^P = \begin{bmatrix} S^P_{11} & S^P_{12} & \cdots & S^P_{1m} \\ S^P_{21} & S^P_{22} & \cdots & S^P_{2m} \\ \vdots & \vdots & & \vdots \\ S^P_{m1} & S^P_{m2} & \cdots & S^P_{mm} \end{bmatrix}, \quad \underset{\sim}{S}^x = \begin{bmatrix} S^x_{11} & S^x_{12} & \cdots & S^x_{1n} \\ S^x_{21} & S^x_{22} & \cdots & S^x_{2n} \\ \vdots & \vdots & & \vdots \\ S^x_{n1} & S^x_{n2} & \cdots & S^x_{nn} \end{bmatrix}$$

and

$$\underset{\sim}{H} = \begin{bmatrix} H_{11} & H_{12} & \cdots & H_{1m} \\ H_{21} & H_{22} & \cdots & H_{2m} \\ \vdots & \vdots & & \vdots \\ H_{n1} & H_{n2} & \cdots & H_{nm} \end{bmatrix}, \qquad (9)$$

the response relationship is simply

$$\underset{\sim}{S}^x = \underset{\sim}{H}^* \, \underset{\sim}{S}^P \, \underset{\sim}{H}^T. \qquad (10)$$

The above equations may be said to constitute the basic theory of random vibration, but there is one more quantity which must be mentioned here because it appears frequently in the account that follows - the coherency γ^2. This is defined, typically by

$$\gamma^2 = \frac{S_{12} \, S_{21}}{S_{11} \, S_{22}} \quad ; \qquad (11)$$

it gives a sort of nondimensional measure - at each frequency f - of the cross spectral density, and so a measure of the degree of interaction between two random signals. It can be shown that the coherency is always between 0 and 1; the coherency of a single input, acting alone, and any resulting response is exactly 1 provided that the system is linear.

2. VEHICLE RESPONSE

2.1 The Basic Problem

The response of a vehicle to the undulations of the road surface over which it travels appears to be a straightforward embodyment of the results of the previous section, for it is a matter of simple kinematics once the speed of the vehicle is known to convert road profiles expressed as functions of horizontal distance to imposed displacements expressed as functions of time. This is only so, of course, if the vehicle is travelling at constant velocity, if the vehicle-system is nearly-enough linear, and if the road profiles considered can be modelled as realisations of stationary random processes. Moreover the response descriptions obtained in terms of spectral densities are really only adequate if the random processes concerned have Gaussian distributions.

Whether these implicit assumptions are acceptable can only be decided by the comparison of theoretically-determined spectra with those obtained from experimental measurements, and it was with such comparisons that the work commenced.[1] The profiles of typical stretches of road were carefully measured (with surveying instruments); the vehicle response spectra were then predicted, using manufacturer's figures for the vehicle's dynamic parameters (apart from damping, which was too variable and needed to be established in conditions close to those of the experiment). The resulting spectra were then compared with spectra obtained from vertical responses measured as the vehicle was driven at constant speed along the surveyed stretch of

road.

The simple random vibration response relationships, (4) and (7), were in fact found to provide a useful means of predicting response spectral densities, though the accuracy of the results depended very much on the sophistication of the vehicle-model adopted in analysis. Accuracy could be improved by adopting a more complex vehicle-model, and also by regarding the system as possessing two (or four) excitations corresponding to the motions imposed by the road at the respective wheel-pairs (or wheels). As might be expected the need for a more sophisticated model depended on circumstances: in certain situations a model based on a single road-profile excitation was quite good enough, but sometimes it was necessary to have regard to the separate inputs at front and rear, and sometimes also to those at near-side and off-side.

There were practical difficulties however in employing this technique when separate allowance had to be made for near-side and off-side excitations. It was not unduly difficult to obtain reliable spectral descriptions for single profiles of particular roads, or even to obtain typical spectra for particular types of road, but it proved much more difficult to obtain complete spectra for <u>pairs</u> of profiles. The determination of cross spectral densities for offside and nearside profiles calls for much greater accuracy of measurement than does the determining of the corresponding direct spectral densities. The individual surveying of profile-pairs provided suitable data for a small number of roads and trackwidths, but such a technique is not practicable if a large number of profile-pairs have to be treated. Those interested in the details of these comparisons are referred to reference [1].

It was from the work described above that two later interests developed: the description and modelling of typical road surfaces, and response prediction for a vehicle whose speed was not constant.

2.2 Surface Description and Modelling

Response predictions can only be as good as the excitation information on which they are based. For the purpose of laboratory comparisons the obtaining of accurate excitation spectra presents little difficulty because measurement of a particular road-surface can be carried out to any desired accuracy. But the vehicle manufacturer is not much interested in the performance of his vehicles on one particular road; it is the vehicles' behaviour "on motor-ways" or "on country roads" that concerns him. It is therefore a prerequisite to the practical use of valid random vibration response theory that <u>typical</u> excitation descriptions be available. For this purpose it is not essential that the descriptions be precise descriptions of typical roads: it is sufficient that the descriptions themselves be typical - and preferably in a form which lends itself easily to analysis.

For this purpose the mathematical modelling of profiles and surfaces is of considerable importance; not only can the fixing of model parameters give any desired spectral properties, but it can be made very simple to vary these parameters and so to investigate responses to a large number of different road-surfaces. There are intrinsic difficulties however and these only become apparent when the problem is investigated. Simple models were first developed in reference [2], and the problems of surface description were explored more fully in [3,4,5].

It is not difficult to provide a satisfactory profile model, and this may be all that is required in certain applications. All that is

needed is to express the spectral density of the profile, $\mathcal{S}(n)$ in terms of the wave-number n (n being measured in cycles per unit distance, instead of the more familiar cycles per unit time). For many purposes a description of the form

$$\mathcal{S}(n) = c\, n^{-w} \qquad (12)$$

may be used, with $w \triangleq 2.5$, and c dependent on the type of road [5]. For cases where a greater degree of sophistication is needed, a bilinear relationship of the form

$$\left.\begin{array}{ll} \mathcal{S}(n) = c_1\, n^{-w_1} & |n| \leqslant n_0 \\ \qquad\quad c_2\, n^{-w_2} & |n| \geqslant n_0 \end{array}\right) \qquad (13)$$

has been proposed [2].

In contrast the modelling of an entire surface might appear impossibly demanding, but simplicity can be achieved here too by having recourse to the concept of isotropy. Briefly the assumption that a road surface is isotropic implies that all profiles, irrespective of plan position or orientation, have identical spectral densities. Thus once isotropy has been assumed - and the assumption justified - all that remains is to describe the individual profiles. Then from the given profile spectral density the cross spectal densities applicable to any pair of points on the surface can easily be deduced. The profile description can be based on the models of (12) or (13), but a spectral density based on actual measurement can be used if it is thought that there is any advantage in doing this.

Isotropic surfaces possess one important characteristic which has to be taken into account. Arbitrarily chosen profile spectra are not necessarily compatible with the definition of isotropy, and specific compatibility criteria must be satisfied. Moreover the profile spectral density has to be defined over the whole range of wave-number from zero to infinity, because determination of the cross spectral densities involves integration between these limits. The restrictions are fully explained in [3]. If descriptions of the form of (12) or (13) are used it is only necessary that the spectral density outside the range of wave-numbers which are of practical interest be chosen to satisfy the compatibility criteria - though simply to make these zero is not acceptable.

A mathematical model is only useful if it provides a realistic description, and it might be thought that real road-surfaces are most unlikely to be isotropic: certainly many country roads are bumpier near the verge, and most roads are linearly generated and worn. There surely must be roads for which isotropy is not applicable. Nevertheless the cross spectra for pairs of points predicted on the assumption of isotropy have often agreed well with those based on measurement [4,5]. Particularly if account is taken of the possibility of errors in the determination of cross spectra based on measurement, isotropy-based descriptions have much to commend them.

2.3 Responses at Variable Speeds

While the response of a vehicle which travels at constant speed must be of considerable interest to the manufacturer, vehicles do also operate at non-constant speeds. And though the response of an accelerating vehicle must be expected to be a more complicated study than that of a vehicle travelling at constant velocity, this state of operation cannot reasonably be ignored.

However, though one might feel constrained while treating the constant-velocity problem to simulate as closely as possible the dynamic properties of a real vehicle, the adoption of a greatly simplified vehicle model seemed justified while studying the additional effects of acceleration - provided of course that the dominant parameters of the simplified system (natural frequency and damping ratio in particular) were as close as possible to those of a real vehicle.

The response of a single-freedom vehicle model traversing a random profile in a state of uniform acceleration was therefore investigated [6]. With realistic vehicle accelerations it was found that the mean-square vehicle responses at any given velocity depended very little on the magnitude of the acceleration. The problem was later investigated again using a rather different approach [7], and similar conclusions were obtained.

Other forms of acceleration were also investigated [7,8] including the case of a vehicle travelling at a randomly-varying speed. This last problem arose through the need to assess errors in experiments in which a vehicle was driven at a supposedly constant speed.

3. MULTIPLE RESPONSE SPECTRA

It was our involvement in multiple response instrumentation of experimental vehicles, together with the interest of some of our colleagues in the deployment of very large numbers of transducers on offshore structures, which led to work on the interpretation of multiple response records, or in effect on the properties of the spectra of multiple responses. This work ranged from practical enquiries into the recovery of small but important responses which were masked by other signals to the establishment of the complex inter-relationships which connect the elements of the response spectral density matrix.

3.1 Signal Conditioning

The responses of a structure to random excitation are measured for many reasons, one of these being to identify - and if necessary to eliminate - individual sources of excitation. Some particular responses may be better indicators of a particular source than others, but their significance is often obscured by the presence there of response to another more powerful source. In such circumstances it is useful to be able to "condition" a response signal, to remove from it all effects which are coherent with one or more of the other response signals. The theory of conditioning was examined in [9] and a new interpretation of the relationships between conditioned signals and the original signals was provided.

Suppose a multivariate random process to consist of components x_1, x_2, x_3, ... Components x_2, x_3, ... can be conditioned with respect to x_1 by dividing each of them into two parts, one fully coherent with x_1 and the other quite uncoherent with it. This is indicated in Figure 2, where the signals x_{2c1}, x_{3c1}, ... are fully coherent with x_1, and the signals x_{2u1}, x_{3u1}, ... are quite uncoherent with it.

The spectral densities of the uncoherent parts can easily be expressed in terms of the spectral densities of the original components. Denoting the original spectral densities by S^x_1, S^x_{12}, etc., and the spectral density of x_{2u1}, etc., by $S^x_{2.1}$, etc., it can be shown that

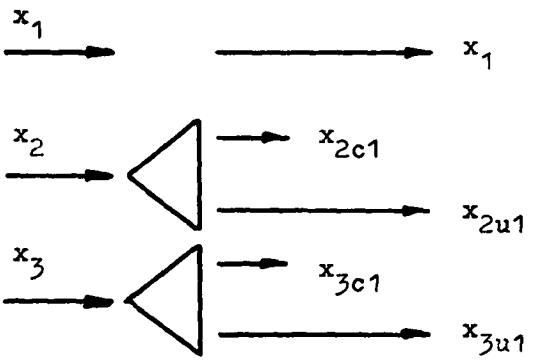

Figure 2. Separation of parts uncorrelated with x_1 from x_2 and x_3.

$$S^x_{2.1} = S^x_2 - \frac{S^x_{21} S^x_{12}}{S^x_1} \quad . \tag{14}$$

This can be done also with cross spectral densities, so that for example

$$S^x_{23.1} = S^x_{23} - \frac{S^x_{21} S^x_{13}}{S^x_1} \quad . \tag{15}$$

Thus all response spectra can be stripped of all the effects of coherency with a chosen signal x_1.

The formulation of the conditioning relations in terms of matrices is rewarding [10,11], in particular as making explicit the importance of the rank of the response spectral density matrix in respect of consecutive applications of the conditioning operation. (For example, use might be made of the doubly-conditioned spectral density $S^x_{3.12}$). It is found that each conditioning reduces the rank of the spectral density matrix by one. As very few normal modes contribute to the response at any frequency, the response spectral density matrix is usually of low rank (see the following section), so that the consecutive conditioning of responses is of limited applicability.

3.2 Rank and Order of Spectral Density Matrices

The separate spectral densities - direct and cross - of multiple responses, which form the elements of a response spectral density matrix, are separately computable but are not necessarily independent. The off-diagonal elements, being cross spectral densities, do of course make up complex conjugate pairs, but other relationships can be inferred from the form of the matrix response relationship

$$\underset{\sim}{S}^x = \underset{\sim}{H}^* \, \underset{\sim}{S}^P \, \underset{\sim}{H}^T. \tag{10 bis}$$

No matrix product can be of rank greater than the rank of any of its factors. The response spectral density matrix $\underset{\sim}{S}^x$ cannot therefore be of greater rank than that of the excitation spectral density matrix $\underset{\sim}{S}^P$, and this may well be very small.

If the order of $\underset{\sim}{S}^x$ is greater than the rank of $\underset{\sim}{S}^P$ there must be rank deficiencies in $\underset{\sim}{S}^x$, which imply linear relationships between its rows (or columns). If for example the rank of $\underset{\sim}{S}^P$ is 2 and the order of $\underset{\sim}{S}^x$ is 4, then there must be two relationships connecting the (complex) elements of the various rows together. Taking these relationships together with the known complex conjugate relationships of the cross spectral densities, it is found that the full 16 elements of the 4x4 matrix can all

be deduced if only 7 are computed directly, as indicated in Figure 3. Such relationships were explored in [12].

(a) Complex $\underset{\sim}{H}$

$$\begin{bmatrix} \cdot & x & x & x \\ \cdot & \cdot & x & x \\ \cdot & \cdot & \cdot & x \\ \cdot & \cdot & \cdot & x \end{bmatrix}$$

(b) Real $\underset{\sim}{H}$

$$\begin{bmatrix} \cdot & x & x & \cdot \\ \cdot & \cdot & x & x \\ \cdot & \cdot & \cdot & \cdot \\ \cdot & \cdot & \cdot & \cdot \end{bmatrix}$$

Figure 3. Response Spectral Density Matrices of Order 4 and Rank 2. Direct computation of the marked elements gives rise to the rest.

In general the harmonic influence matrices $\underset{\sim}{H}$ are complex. When $\underset{\sim}{H}$ is real, however, the consequences of any rank deficiency become much more marked, and the interrelationships much more stringent. For example, with a response matrix of order 4 and rank 2 as before, it is found that all 16 elements can be deduced if only four are known. It is not true however that any set of elements of the quoted minimum numbers have this property; the basic set of elements must be chosen with care, as were those of Figure 3.

Familiarity with the vibration of physical systems may encourage the belief that harmonic influence functions are usually complex, for dynamic components usually influence phase as well as magnitude. This is the case if physically occurring excitations $\underset{\sim}{P}$ and responses $\underset{\sim}{x}$ are considered. But the situation is different if the response relationships are formulated in a manner which makes explicit the separate modal contributions; then real $\underset{\sim}{H}$'s are both common and practically relevant.

The contribution of the several normal modes can be made explicit by introducing normal coordinates $\underset{\sim}{\xi}$ and corresponding generalised forces $\underset{\sim}{\Xi}$, related to $\underset{\sim}{x}$ and $\underset{\sim}{P}$ by

$$\underset{\sim}{x} = \underset{\sim\sim}{d}\,\underset{\sim}{\xi} \quad , \quad \underset{\sim}{\Xi} = \underset{\sim\sim}{e}\,\underset{\sim}{P} \tag{16}$$

where $\underset{\sim\sim}{d}$, $\underset{\sim\sim}{e}$ are real. $\underset{\sim}{\xi}$ and $\underset{\sim}{\Xi}$ then have a diagonal harmonic influence matrix $\underset{\sim\sim}{\alpha}$, assuming the coordinates to be uncoupled. (This last assumption is common, though not always valid. Care must be taken to ensure that it is applicable in any particular application.) This relationship is illustratrated in the block diagram of Figure 4; it is characteristic of vibratory systems that at any particular frequency only a small number of modes contribute significantly to the response, so that only a very few α- blocks need to be included.

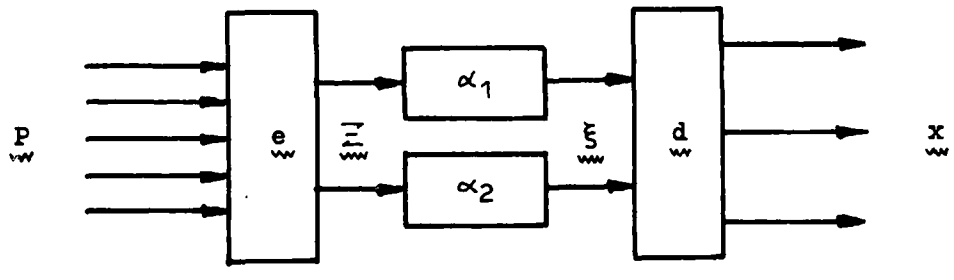

Figure 4. Block Diagram Showing Modal Response Contributions

The first equation of (16) constitutes a relationship with a real harmonic influence function, because the elements of $\underset{\sim}{d}$ are necessarily real; the columns of $\underset{\sim}{d}$ comprise the real (undamped) normal modes of the system. And because of the typically low order of $\underset{\sim}{\xi}$, and so of $\underset{\sim}{S}^{\xi}$, the spectral response matrix $\underset{\sim}{S}^{x}$ for any large number of transducers is likely to possess a considerable rank deficiency. In such a case only a very small number of the elements of the spectral density matrix need to be directly computed.

It is worth noting that the small number of modes which usually contribute significantly to the response at any frequency imposes a low rank on $\underset{\sim}{S}^{x}$ irrespective of the (possibly) high rank of $\underset{\sim}{S}_{p}$. It is still true that the rank of $\underset{\sim}{S}^{x}$ cannot be greater than that of $\underset{\sim}{S}_{p}$, but the requirement concerning the rank of $\underset{\sim}{S}^{\xi}$ then becomes more stringent.

3.3 System Identification

Response spectra taken from offshore structures, arising from their exposure to ocean waves, can often be used to estimate approximately simple dynamic properties of a structure. Almost any single response spectrum will give an indication of the system's fundamental natural frequency, and the shape of the peak gives an indication of the damping in the fundamental mode. It is natural to wonder whether more precise and detailed information about the dynamic properties of the structure might be obtained through more lavish and careful deployment of transducers.

Without quantitative information about the excitation it has to be accepted that such inferred knowledge of the dynamic properties of the structure will be limited, and our work on this subject was concentrated on an attempt to define these limits. This proved surprisingly difficult but it raised some interesting points.

The problem was seen as essentially divided into two parts. It was first necessary to establish the extent to which the accurately-known response spectra of a computer modelled structure could be used to determine the structure's characteristics. After this it would be necessary to explore whether the inaccuracies inseparable from the determination of response spectral densities on actual offshore structures would permit inferences of useful accuracy.

References [13,14] approach the first part of the problem, [14] demonstrating that - in the notation of Figure 4 - the α's and the columns of the $\underset{\sim}{d}$-matrix can be inferred with precision from the precisely known response spectral densities of a simulated two-freedom system subjected to white-noise excitation. (The assumption of a white excitation is not as artificial as it might appear if attention is confined to a small range of frequency, as is to be preferred on other grounds.) This technique was found to be effective even when individual response peaks could not be distinguished on the spectrum by inspection alone. However the analysis used involved the assumption that uncoupled normal coordinates were applicable: this might well not be true in circumstances where such a refined technique would be of most value, and more is still to be said on this subject.

One limitation on the information obtainable from response spectra is already apparent from Figure 4. Even if the generalised force spectral densities $\underset{\sim}{S}^{z}$ could be found, it would not be possible to proceed from them to the spectral densities of the physical excitations $\underset{\sim}{S}^{p}$; without information on the elements of $\underset{\sim}{e}$ these are not uniquely defined.

3.4 Analytical Devices

Matrix notation is only a shorthand to facilitate the algebraic treatment of equations, and it cannot be claimed that results obtained through its use are otherwise unobtainable. Nevertheless, matrix notation can make results more readily apparent - quite apart from its making available the use of such concepts as rank. The two following examples illustrate this well.

a) Spectral Inequalities All spectral density matrices are known to be non-negative-definite, and this fact imposes a series of inequations on the values of its element spectral densities. (See reference [15])

Because of its non-negative-definiteness the spectral density matrix

$$\underset{\sim}{S}_{ww} = \begin{bmatrix} S_{11} & S_{12} & \cdots & S_{1n} \\ S_{21} & S_{22} & \cdots & S_{2n} \\ \vdots & \vdots & & \vdots \\ S_{n1} & S_{n2} & & S_{nn} \end{bmatrix} \tag{17}$$

must satisfy the condition

$$\det \underset{\sim}{S}_{ww} \geq 0. \tag{18}$$

But this condition must also be satisfied by all the spectral density matrices which can be formed by discarding corresponding pairs of rows and columns from (17) and so providing the spectral density matrices for smaller numbers of components. Each of these new matrices must be non-negative definite, and they too must satisfy (18).

It follows therefore that, typically,

$$\left.\begin{aligned} & S_{11} \geq 0 \\ & S_{11}S_{22} - S_{12}S_{21} \geq 0 \\ & S_{11}S_{22}S_{33} + S_{12}S_{23}S_{31} + S_{13}S_{32}S_{21} - S_{31}S_{22}S_{13} - S_{21}S_{33}S_{12} \\ & \qquad - S_{23}S_{11}S_{32} \geq 0 \\ & \text{etc.} \end{aligned}\right\} \tag{19}$$

The first of (19) is simply a statement of the well-known fact that all direct spectral densities are positive. The second of (19) confirms that all coherencies are less than (or equal to) unity. The third of (19) and the other higher-order inequalities are unfamiliar results which may well prove important in certain circumstances. For example, a "typical" spectral density matrix, introduced into a computation to demonstrate a procedure, cannot have its cross elements allocated arbitrarily: they must conform to (19).

It should be noted that the subscripts introduced in (19) are typical and not complete. In a fourth order spectral density matrix, for example, it is necessary to satisfy six second-order inequalities, and four third-order inequalities, as well as the single fourth-order inequality.

b) Further Spectral Response Relationships The relationship between the response spectral matrix $\underset{\sim}{S}^{x}_{ww}$ and the excitation spectral matrix $\underset{\sim}{S}^{p}_{ww}$ is

is easy enough to remember, and it contains a great deal of information. But other relationships are sometimes needed: we may also be interested in the cross spectral density matrix $\underset{\sim}{S}^{xP}$ which includes such mixed cross spectral density elements as that applicable to the two signals x_1 and P_2 - that is S^{xP}_{12}. The adoption of intermediate coordinates increases the variety of unfamiliar response relationships that may be required.

Reference [16] presents a simple technique for setting up the correct response relationship between any pair of connected spectral density matrices. It makes use of the limited analogy which exists between the random vibration response problem and that in which a harmonic excitation is applied to the same system.

The technique is based on the loose correspondence between the spectral density matrix $\underset{\sim}{S}^{xP}$ of the random vibration problem and the matrix product $\underset{\sim}{x}^*\underset{\sim}{P}^T$ of the discrete-frequency problem - it being assumed in the usual way that $\underset{\sim}{P} \propto e^{i\omega t}$.

Suppose that the relationship sought is that between the cross spectral density matrix $\underset{\sim}{S}^{xP}$ and the response spectral density matrix $\underset{\sim}{S}^{xx}$. The analogy gives

$$\left.\begin{aligned} \underset{\sim}{S}^{xP} &\longleftrightarrow \underset{\sim}{x}^*\underset{\sim}{P}^T \\ \underset{\sim}{S}^{xx} &\longleftrightarrow \underset{\sim}{x}^*\underset{\sim}{x}^T \end{aligned}\right) \qquad (20)$$

and the usual rules for discrete-frequency response give

$$\underset{\sim}{x} = \underset{\sim}{H}\,\underset{\sim}{P}. \qquad (21)$$

Successive use of (20) and (21) gives

$$\underset{\sim}{S}^{xx} \longrightarrow \underset{\sim}{x}^*\underset{\sim}{x}^T = \underset{\sim}{x}^*(\underset{\sim}{H}\,\underset{\sim}{P})^T = \underset{\sim}{x}^*\underset{\sim}{P}^T\underset{\sim}{H}^T \longrightarrow \underset{\sim}{S}^{xP}\,\underset{\sim}{H}^T. \qquad (22)$$

This analogy must not be taken too far: there can be no complete analogy between a random process and a harmonic function of time. For this restricted use however the analogy is quite reliable.

4. NON-IDEAL SYSTEMS AND PROCESSES

This title is used here to embrace all those random vibration situations where the assumptions of the basic theory are not tenable, due to processes departing from the Gaussian or systems failing to be linear. (A further non-ideal problem - a non-stationary one - has already been considered in section 2.) Just as the assumption of linearity is justified in a great number of practically occurring vibration problems of all types, so a great number of practically occurring random processes can be treated as Gaussian. But some systems must be treated as nonlinear and some processes as non-Gaussian; the analyst must be prepared for them - not necessarily in combination, though the application of a Gaussian excitation to a nonlinear system almost inevitably gives rise to a non-Gaussian response. It seemed important to initiate work in this field.

In this section a more general theory of the description and response of random processes will be introduced, applicable to all random processes whether Gaussian or non-Gaussian. Following this three separate studies of non-ideal processes or systems will be described: work on the symmetry properties of higher order correlation functions and spectral densities, a new method of description for a class of non-Gaussian random processes, and a study of the (second order) response spectra of a Duffing-type

nonlinear spring-mass system subjected to random excitation.

4.1 General Theory of Description and Response

Description of a random process by its spectral density conceals the essential fact that all descriptions of random processes are - and must be - probabilistic, and furthermore of some complexity. Averages simplify description, but to describe a random process adequately these must cover not only mean- and mean-square-values but also all the averages of all the products made up from instantaneous values at all given instants of time. Confining attention to stationary random processes greatly simplifies the problem, but even here the full description of a random process $\{x(t)\}$ by means of averages requires the specification of a whole sequence of autocorrelation functions in terms of the delay variables τ_1, τ_2, τ_3, ...:

$$\left.\begin{aligned} R^x(\tau) &= E[x(t)\ x(t+\tau)] \\ R^x(\tau_1,\tau_2) &= E[x(t)\ x(t+\tau_1)\ x(t+\tau_2)] \\ R^x(\tau_1,\tau_2,\tau_3) &= E[x(t)\ x(t+\tau_1)\ x(t+\tau_2)\ x(t+\tau_3)] \\ &\text{etc.} \end{aligned}\right\} \qquad (23)$$

for all combinations of τ_1, τ_2, τ_3, ...

This sequence did not arise when autocorrelation functions were first discussed in section 1.2 because the higher order descriptions were not needed. Though for a Gaussian random process the higher-order autocorrelation functions do exist and are meaningful, it is a special property of a Gaussian process that all higher-order descriptions can be inferred from the second order description. This constitutes a very great simplification, which is lost when non-Gaussian processes are considered.

Spectral densities corresponding to (23) are obtained by Fourier transformation, but the greater number of τ-variables calls for higher-order Fourier transforms. These give rise to a sequence of spectral densities which are functions of several frequencies.

Thus we have

$$\left.\begin{aligned} S^x(f) &= \int_{-\infty}^{\infty} R^x(\tau)\ e^{-i2\pi f\tau}\,d\tau \\ S^x(f_1,f_2) &= \int\int_{-\infty}^{\infty} R^x(\tau_1,\tau_2)\ e^{-i2\pi(f_1\tau_1+f_2\tau_2)}\,d\tau_1 d\tau_2 \\ S^x(f_1,f_2,f_3) &= \iiint_{-\infty}^{\infty} R^x(\tau_1,\tau_2,\tau_3)\ e^{-i2\pi(f_1\tau_1+f_2\tau_2+f_3\tau_3)}\,d\tau_1 d\tau_2 d\tau_3 \\ &\text{etc.} \end{aligned}\right\} \qquad (24)$$

The second of (24) is called the bi-spectral density, followed by the tri-spectral density, and so on.

The response relationships applicable to the higher-order spectral densities are naturally more complicated than those for the second order, though perhaps less so than might have been expected. We are not concerned with them here, however. A catalogue of useful response relationships is to be found in reference [17].

4.2 Symmetry Properties of Higher-Order Descriptions

It is a consequence of the definitions of higher-order auto-correlation functions and spectral densities that symmetries exist. These are not simple reflections however and can be very complex. An understanding of them is essential to those concerned with the application of higher-order descriptions because they can greatly reduce the task of computation. Thus, for example, computation of $S^x(f_1,f_2)$, the bi-spectral density of a process $\{x(t)\}$, over only one-eighth of the f_1,f_2-plane enables it to be inferred over the remaining seven-eighths.

Such possibilities are most easily appreciated by considering the bi-autocorrelation function $R^x(\tau_1,\tau_2)$. It is plain from the definition that the τ-variables may be interchanged so that

$$R^x(\tau_2,\tau_1) = R^x(\tau_1,\tau_2); \tag{25}$$

the value for a given combination of τ_1,τ_2 is equal to that for the same combination of τ_2,τ_1. But more complex symmetries emerge from a little manipulation of the definition. Because $\{x(t)\}$ is stationary

$$\begin{aligned} R^x(\tau_1,\tau_2) &= E\left[x(t)\ x(t+\tau_1)\ x(t+\tau_2)\right] \\ &= E\left[x(t-\tau_1)\ x(t)\ x(t+\tau_2-\tau_1)\right] \\ &= R^x(-\tau_1,\ \tau_2-\tau_1), \end{aligned} \tag{26}$$

and a value computed for a given combination τ_1,τ_2 is also applicable to the combination $-\tau_1,\tau_2-\tau_1$, and also to $-\tau_2,\tau_1-\tau_2$ by a similar argument.

Similar symmetries exist for bi-spectral densities, and it can be shown that

$$\begin{aligned} S(f_1,f_2) &= S(f_2,f_1) \\ &= S(f_1,-f_1-f_2) = S(-f_1-f_2,f_1) \\ &= S(f_2,-f_1-f_2) = S(-f_1-f_2,f_2). \end{aligned} \tag{27}$$

Figure 5 shows the implications of (27) on the f_1,f_2-plane, the points A,

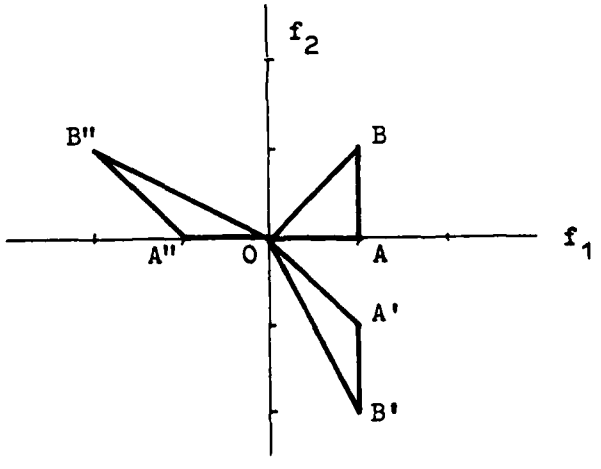

Figure 5. Symmetries of Bi-Spectral Density. The triangle OAB transforms into OA'B' and OA"B".

A',A'' all having the same value of bi-spectral density, and the points B, B',B'' all having the same value. Thus the triangle OAB may be said to transform into the triangle OA'B' and into the triangle OA''B''. If the values of the bi-spectral density are known over the triangle OAB they are known also over the other two. This together with the simple symmetry property of reflection in the line $f_1=f_2$ ensures that if the values of the bi-spectral density are computed for the one-eighth-plane which subtends the angle AOB at the origin, then the values for one-half of the plane are known. The other half comes immediately from the fact that

$$S(-f_1,-f_2) = S^*(f_1,f_2). \tag{28}$$

The symmetries for higher-order descriptions are necessarily much more complicated, though the need for making use of them is still more pronounced. These have been explored, for nonstationary as well as stationary descriptions, up to the fourth order. The symmetry mappings form well-defined groups, in terms of the mathematical theory of groups, and the group-theoretical properties are emphasised in reference [18].

Examples of bi- and tri-spectra of a particular non-Gaussian random process will be found in the next section.

4.3 A Quasi-Gaussian Random Process

Just as the study of nonlinear vibration is much concerned with quasi-linear theory, it is to be expected that quasi-Gaussian theory will prove relevant to the study of non-Gaussian random processes. It offers a considerable simplification, where it can be justified, and it is likely to be justified in many practical applications.

Reference [19] approaches quasi-Gaussian random processes by considering the response of a simple quasi-linear spring element to Gaussian excitation. The spring considered has a polynomial spring-law which can be varied by changes to the coefficients, and the various response spectral densities can be expressed in terms of these coefficients. This work serves two purposes. Firstly it provides typical examples of the higher-order descriptions of a physically-realisable quasi-Gaussian random process, and secondly because the coefficients of the spring-law can be used to define the random process, it provides a convenient model of a quasi-Gaussian random process and can be given any desired overall properties - for example skewness and kurtosis.

It is shown that if a stationary Gaussian excitation $\{x(t)\}$ having spectral density $S^x(f)$ is applied to an element with spring-law

$$y = x + \alpha x^2 + \beta x^3 \tag{29}$$

the first three spectral densities of the response $\{y(t)\}$ are

$$\left.\begin{aligned}
S^y(f) &= S^x(f)\,(1 + 6\beta\sigma_x^2) \\
S^y(f_1,f_2) &= 2\alpha\left[S^x(f_1)\,S^x(f_2) + S^x(f_1)\,S^x(f_1+f_2) + S^x(f_2)\,S^x(f_1+f_2)\right] \\
&\quad + \alpha\sigma_x^2\left[\delta(f_1)\,S^x(f_2) + \delta(f_2)\,S^x(f_1) + \delta(f_1+f_2)\,S^x(f_1)\right] \\
S^y(f_1,f_2,f_3) &= S^x(f_1,f_2,f_3)\left[1 + 12\beta\sigma_x^2\right] + 6\beta\left[S^x(f_1)\,S^x(f_2)\,S^x(f_3)\right. \\
&\quad \left. + S^x(f_1+f_2+f_3)\left\{S^x(f_1)\,S^x(f_2) + S^x(f_1)\,S^x(f_3) + S^x(f_2)\,S^x(f_3)\right\}\right]
\end{aligned}\right\} \tag{30}$$

The singularities of the second of (30) arise because $\{y(t)\}$ has a non-zero mean-value; this can be eliminated by basing analysis on covariances instead of correlations, as a result of which all the terms containing $\alpha\sigma_x^2$ vanish.

If in the above example the excitation is given a band-limited white spectral density defined by

$$\begin{aligned} S^x(f) &= S_1 \qquad |f| \leq f_c \\ &= 0 \qquad |f| > f_c \end{aligned} \tag{31}$$

and the mean value of $\{y(t)\}$ is suppressed as above the spectral density and bi-spectral density are as shown in Figure 6.

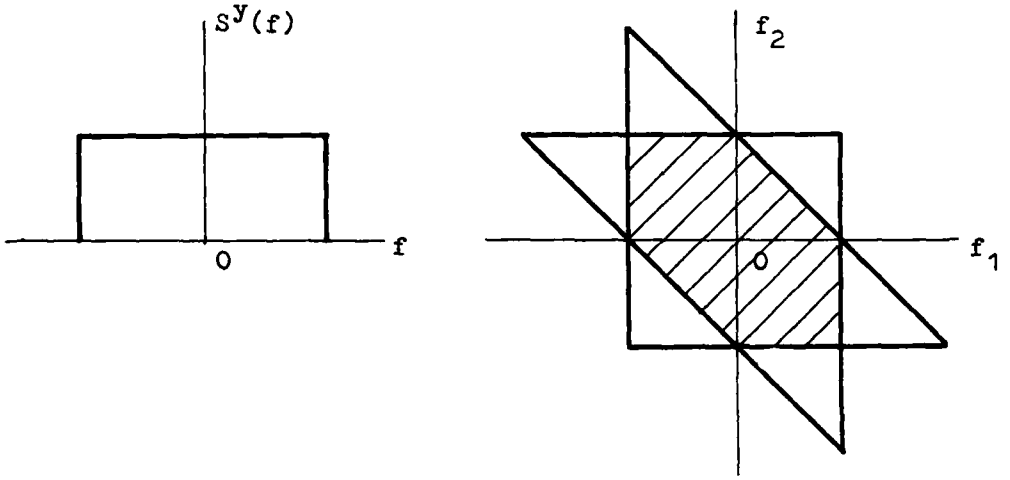

Figure 6. Second and Third Order Spectral Densities of Non-Gaussian Response.
Second Order: $S^y(f) = S_1(1 + 12\beta S_1 f_c)$.
Third Order: $S^y(f_1,f_2) = 6\alpha S_1^2$, $3\alpha S_1^2$, 0, respectively on shaded plateau, adjacent triangles, and elsewhere.

Reference [19] gives the values of the coefficients necessary to reproduce desired values of skewness and kurtosis.

4.4 Response Spectra of Duffing System

Even when the familiar (second order) spectral density does not provide a complete description of a random process it must nevertheless form an important part of the full description. And it is in any case always of some interest to the engineer; it is always true, for example, that over a given frequency range $f_1 \leq f \leq f_2$

$$2\int_{f_1}^{f_2} S^x(f)\,df = E\left[x^2(t)\right]. \tag{32}$$

Practically ocurring spring-mass systems cannot always be relied on to be effectively linear; yet there is little information in the literature on the response spectral densities of nonlinear systems, except for cases where the departure from linearity is small. Unfortunately for a nonlinear system the form of the response curve obtained under discrete-

frequency excitation, characteristic though it is, offers little clue to the form of the response spectrum under random excitation.

It seemed desirable to remedy this deficiency,and work has been in progress recently with the object of establishing at least the (second-order) response spectra arising from a Duffing-type spring-mass system under white and band-limited-white random excitations. It was not deemed practicable to obtain this information through analytical procedures, and results were obtained instead by analysing the response of a computer-simulated nonlinear system to random excitation.

The spectra obtained will be presented, for a repesentative range of system parameters, in reference [20]. The spectra were found to possess a characteristic near-triangular form, and an approximate straight-line representation has been devised which can easily be set up when the system parameters are known. It was interesting that having discarded the established analytical techniques of the Focker-Planck and Equivalent Linearisation methods as a means of obtaining spectral densities, these two methods proved, in combination, a most valuable adjunct in the interpretation and application of the computed results.

5. CONCLUSION

The work which has been described so very briefly in this paper has been carried out over a period of time by a number of different researchers who have between them embodied a very wide range of interests, talents and aspirations. It is not surprising that in these circumstances the directions of the different researches are very various also. At least this vatiety has made for a wide coverage of the subject of random vibration.

But it should be apparent from this presentation in a single paper that there has been an underlying unity provided by the basic framework of the subject. The topics have all arisen from the need to extend application or understanding beyond the scope of the basic theory of random vibration. It cannot be pretended that all possible extensions have been covered, but there should be enough examples here to illustrate the manner of and scope for extension. Extension of the basic theory in this way is rarely a trivial matter, but the scope of the subject and the resources available ensure that it is rarely impossible.

It is in the nature of a paper like this that the author is principally a reporter of the work of others. And it must be apparent that it is simply not possible to do justice to the expenditure of so many expert man-years in so small a compass. But the names of the real contributors are explicit in the references, and it is presumed that each topic is adequately presented in the relevant publication. The present author is glad to acknowledge the contribution of all the workers involved, and particularly that of Dr D.B. Macvean and Dr C.J. Dodds who as members of the permanent staff of the Mechanical Engineering Department of the University of Glasgow have played a crucial part in the implementation of most of the work described here. Thanks are also due to those who provided funds and facilities in one form or another, primarily the University of Glasgow, and the Science and Engineering Research Council.

REFERENCES

1. C.J.DODDS and J.D.ROBSON 1970 Proc 13th FISITA Congress, 17.2D Response of vehicle components to random road surface undulation.

2. C.J.DODDS and J.D.ROBSON 1973 Journal of Sound and Vibration 31, 175-183 The description of road surface roughness.

3. K.M.A.KAMASH and J.D.ROBSON 1977 Journal of Sound and Vibration 54, 131-145 Implications of isotropy in random surfaces.

4. K.M.A.KAMASH and J.D.ROBSON 1978 Journal of Sound and Vibration 57, 89-100 The application of isotropy in road surface modelling.

5. J.D.ROBSON and K.M.A.KAMASH 1977 The Dynamics of Vehicles. Amsterdam: Swets and Zeitlinger. 222-228 Road surface description in relation to vehicle response.

6. V.J.VIRCHIS and J.D.ROBSON 1971 Jounal of Sound and Vibration 18, 423-427 Response of an accelerating vehicle to random road undulation.

7. K.SOBCZYK and D.B.MACVEAN 1976 Stochastic Problems in Dynamics. London: Pitman 412-432 Nonstationary random vibrations of systems travelling with variable velocity.

8. K.SOBCZYK, D.B.MACVEAN and J.D.ROBSON 1977 Journal of Sound and Vibration 52, 37-49 Response to profile-imposed vibration with randomly-varying traversal velocity.

9. C.J.DODDS and J.D.ROBSON 1975 Journal of Sound and Vibration 42, 243-249 Partial coherence in multivariate random processes.

10. S.MAHALINGAM, D.B.MACVEAN and J.D.ROBSON 1980 Journal of Sound and Vibration 68,313-316 Residual spectral densities: a matrix approach.

11. D.B.MACVEAN, S.MAHALINGAM and J.D.ROBSON 1980 Journal of Sound and Vibration 69, 487-490 A general matrix approach to residual spectra.

12. S.MAHALINGAM, D.B.MACVEAN and J.D.ROBSON 1980 Journal of Sound and Vibration 69, 461-476 Interdependence of the spectral densities of multiple responses.

13. J.A.FITZPATRICK 1980 Euromech 131 (Identification Problems in Structural Dynamics) Identification of normal modes in a two-freedom system.

14. J.D.ROBSON, H.WALUKIEWICZ and D.B.MACVEAN 1981 Integrity of Offshore Structures London: Applied Science Publishers 71-84 Inferences from structural response records.

15. J.D.ROBSON 1979 Journal of Sound and Vibration 63, 466-468 Consequences of the non-negative definiteness of the spectral density matrix.

16. J.D.ROBSON 1975 Journal of Sound and Vibration 40, 285-286 The derivation of multivariate spectral density relationships by means of the harmonic analogue.

17. J.D.ROBSON 1980 Journal of Sound and Vibration 73, 312-315 The response relationships of random vibration analysis.

18. H.WALUKIEWICZ and D.B.MACVEAN (In preparation) Symmetry groups and fundamental regions in the description of random processes

19. J.D.ROBSON 1981 Journal of Sound and Vibration 76, 169-177 A simplified quasi-Gaussian random process model based on nonlinearity

20. E.M.THANIOTIS, D.B.MACVEAN and J.D.ROBSON (In preparation) Response spectral densities of a nonlinear system subjected to broad-band random excitation.

SOME CLOSED-FORM SOLUTIONS IN RANDOM VIBRATION OF TIMOSHENKO BEAMS

Isaac Elishakoff and David Livshits

Department of Aeronautical Engineering
Technion - Israel Institute of Technology
Haifa, Israel

Abstract

Random vibration of simply supported uniform Timoshenko beams is considered under stationary space- and time-wise ideal white noise excitation. An approximate differential equation is used with both shear distortion and rotary inertia included, but with the term which takes the simultaneous action of these effects, omitted. A closed-form solution is derived for the displacement and velocity space-time correlation function of the Timoshenko beam with transverse damping, generalizing the corresponding result by Eringen for the classical Bernoulli-Euler beam. Closed-form solutions are also derived for beams with structural or Voigt damping mechanisms. The mean-square value of the stress diverges for both the classical and Timoshenko beams with transverse damping, but converges for the beam possessing structural damping.

The main finding of this study is identity of the space-time correlation functions of displacement according to the refined Timoshenko theory and the classical Bernoulli-Euler theory, when joint action of rotary inertia and shear deformation is neglected. This remarkable coincidence takes place for beams possessing (a) transverse viscous damping, (b) Voigt damping, or (c) combined rotary and transverse viscous damping.

1. INTRODUCTION

Random vibration of structures has been treated in a series of papers in the last 25 years or so. Eringen [1] analyzed the behaviour of viscously damped beams and plates through the normal mode method, and in certain cases obtained closed-form solutions for the output quantities. In particular, he considered the classical Bernoulli-Euler beam, governed by the differential equation

$$EI \frac{\partial^4 w}{\partial x^4} + c \frac{\partial w}{\partial t} + \rho A \frac{\partial^2 w}{\partial t^2} = q(x,t) \tag{1}$$

$q(x,t)$ being the space- and time-wise ideal white noise with the following space-time correlation function (so-called "rain-on-the-roof" excitation)

$$R_q(x_1,x_2,t_1,t_2) = \frac{R}{\ell} \delta(x_2-x_1)\, \delta(t_2-t_1) = \frac{R}{\ell} \delta(\zeta)\delta(\tau) \tag{2}$$

where R is some positive constant, ℓ - the span of the beam, ζ - the spacing of the observation cross-sections, τ - the time lag. The beam was taken simply supported at its ends with mode shapes

$$\phi_j(x) = \sin \frac{j\pi x}{\ell} \tag{3}$$

Utilizing the normal mode approach, Eringen derived the closed-form expression for the mean-square displacement

$$d^2(\zeta) = \frac{R\ell^2}{6EIc} \xi^2(1-\xi^2) \quad , \quad \xi = \frac{x}{\ell} \tag{4}$$

The derivation of this expression is also recapitulated in Ref. 2.

Eringen showed that the mean-square normal stress diverged attributing this divergence to inadequacy of the classical beam theory.

In a subsequent paper Samuels and Eringen [3] demonstrated that transverse and rotary viscous dampings acting in concert produce a finite mean-square stress in a Timoshenko beam, mean-square displacements derived via the Timoshenko and Bernoulli-Euler theories differing by less than 5%. It was concluded accordingly that the Bernoulli-Euler beam theory represents an adequate model for studying random vibration of beams when only the mean-square displacements were desired; if the mean-square stress also was looked after, it was necessary to use the improved theory by Timoshenko (see also Ref. 4).

A further contribution in this context is due to Crandall and Yildiz [5], who showed that the response of a uniform beam to stationary random excitation depended largely on the dynamical model postulated, on the damping mechanism employed by the material, and on the nature of the random excitation process. Mean square displacements, slopes, bending moments and shear forces were compared for combinations of four beam models comprising three different damping mechanisms and random loading with autocorrelation function as per Eq. (2). The beam variants were the Bernoulli-Euler beam, the Timoshenko beam, and two intermediates, namely the Rayleigh beam (rotary inertia included, shear deformation neglected), and its reverse (shear deformation included, rotary inertia neglected) referred to as the "pure shear beam". The damping mechanism variants were transverse viscous damping, rotary viscous damping, and Voigt damping. It was found that certain mean-square response quantities were finite (for a time-wise ideal white noise excitation) even though the input possessed an infinite mean-square. At the same time, some of the responses turned out to be unbounded (see Table).

Table [4]

Beam model	Response variable	Transverse viscous damping	Rotary viscous damping	Transverse and rotary viscous damping	Voigt damping
Bernoulli-Euler beam	Displacement	converges	converges	converges	converges
	Stress	diverges	converges	converges	diverges
Rayleigh beam	Displacement	converges	converges	converges	converges
	Stress	diverges	converges	converges	converges
"Pure Shear" beam	Displacement	converges	diverges	converges	converges
	Stress	converges	diverges	converges	converges
Timoshenko beam	Displacement	converges	diverges	converges	converges
	Stress	diverges	diverges	converges	converges

Crandall and Yildiz considered also the variant of band-limited white noise with upper cut-off frequency ω_c. For the cases of unbounded response they studied its growth pattern as function of ω_c, and some of their results are reproduced in the accompanying table which indicates whether the

mean-square displacement and the mean-square stress converge or diverge. Because of the complexity of the integrals involved, these results were originally formulated in order-of-magnitude values with respect to the damping parameters and the serial number of the term, which also represents the appropriate mode.

In an earlier study [6] by the present writers, close-form solutions were obtained for the classical Bernoulli-Euler beam under "rain-on-the-roof" excitation. Here we present closed-form solutions for the Timoshenko beam, apparently for the first time. An approximate differential equation is employed with both shear deformation and rotary inertia included but with their joint effect neglected. The analysis also sheds further light on results of earlier studies.

2. THEORY

2.1 Basic Equations

The differential equation governing free vibration of the Timoshenko beam reads

$$EI\frac{\partial^4 w}{\partial x^4} + \rho A\frac{\partial^2 w}{\partial t^2} - \rho A r^2\frac{\partial^4 w}{\partial x^2 \partial t^2} - \frac{EI}{k'AG}\rho A\frac{\partial^4 w}{\partial x^2 \partial t^2} + \frac{\rho A r^2}{k'AG}\rho A\frac{\partial^4 w}{\partial t^4} = 0 \qquad (5)$$

The first two terms represent the classical Bernoulli-Euler theory; the last three are contributed respectively - and in that order - by rotary inertia, shear deformation, and their interaction. Following Timoshenko [7] and Clough Penzien [8], let us study the relative contribution of the fifth term in determining the natural frequency. For a beam simply supported at its ends, the mode shapes are given by Eq. (3), which on substitution in (5) yields the following equation for the frequency parameter

$$\left(\frac{j\pi}{\ell}\right)^4 - p^4 - p^4 r^2\left(\frac{j\pi}{\ell}\right)^2\left(1+\frac{E}{k'G}\right) + j^4 r^2\left(p^4 r^2\frac{E}{k'G}\right) = 0 \qquad (6)$$

Here, the first two terms yield the natural frequency of the classical Bernoulli-Euler beam

$$\omega_{j,cl} = \frac{j^2\pi^2}{\ell^2}\left(\frac{EI}{\rho A}\right)^{1/2} \qquad (7)$$

The third term in Eq. (6) is the principal contribution of rotary inertia and shear deformation, represented respectively by the quantities 1 and $E/k'G$ in the brackets. For a beam made of conventional materials and with rectangular cross-section, the value of $E/k'G$ is about 3, so that shear deformation is about three times as important as rotary inertia. This rules out both the Rayleigh model, which neglects shear deformation altogether, and the "shear" beam for which the error is smaller but still of order of 25%. However, for an I beam, with the same thicknesses of the web and flange, and also the same depth and width, Cowper's [9] formula yields

$$k' = \frac{490(1+\nu)}{1656+1663\nu} = 0.26 \quad , \quad \frac{E}{k'G} = 10$$

for Poisson's ratio $\nu = 0.3$. In this case the effect of rotary inertia can be neglected.

Timoshenko [7] and Clough and Penzien [8] showed that the last term Eq. (6) is of secondary importance for practical cases in which $jr/\ell < 1$.

Accordingly, we shall omit it as well as the last term in the governing differential Eq. (5).
This omission yields for the natural frequency the approximate expression

$$\omega_{j,T} = \left(\frac{j\pi}{\ell}\right)^2 \frac{EI}{\rho A}\left[\frac{1}{1+r^2(j\pi/\ell)^2(1+E/k'E)}\right]^{1/2} \tag{8}$$

The expression in square brackets representing part of the correction for the rotary inertia and shear deformation. This correction is more important for higher mode numbers j and for beams with higher slenderness ratio ℓ/r.

We now proceed to treat the beam under the loading (2) using the approximate differential equation with a view to a closed-form solution*.

2.2 Transverse Viscous Damping

In this case the governing differential equation reads

$$EI\frac{\partial^4 w}{\partial x^4} + \rho A\frac{\partial^2 w}{\partial t^2} + c\frac{\partial w}{\partial t} - \alpha\frac{\partial^4 w}{\partial x^2 \partial t^2} = q(x,t) \tag{9}$$

where

$$\alpha = \rho A r^2\left(1 + \frac{E}{k'G}\right) \tag{10}$$

Representing $q(x,t)$ and $w(x,t)$ as series

$$q(x,t) = \sum_{j=1}^{\infty}\int_{-\infty}^{\infty} Q_j(\omega)\phi_j(x)e^{i\omega t}d\omega$$

$$w(x,t) = \sum_{j=1}^{\infty}\int_{-\infty}^{\infty}\frac{Q_j(\omega)}{L_j(\omega)}\phi_j(x)e^{i\omega t}d\omega \tag{11}$$

we readily find, substituting Eqs. (11) in Eq. (9)

$$L_j(\omega) = \rho A[(\omega_{j,T}^2 - \omega^2)\alpha_j + 2i\zeta_j\omega_{j,T}\omega] \tag{12}$$

where $\omega_{j,T}$ is as per Eq. 8, and

$$\alpha_j = 1 + \left(\frac{j\pi}{\ell}\right)^2 r^2\frac{\alpha}{\rho A} = 1 + \left(\frac{j\pi}{\ell}\right)^2 r^2\left(1+\frac{E}{k'G}\right) \tag{13}$$

$$c = 2\rho A\zeta_j\omega_{j,T} \tag{14}$$

The normal-mode method yields the following expression for the mean-square displacement

*Should the question be asked "Is it reasonable to seek an exact solution through an approximate differential equation?", the answer is yes. Indeed, who would attempt approximate solution of simple linear differential equation of bending of a beam, despite the fact that the equation itself is inexact?

$$E[w^2(x,t)] = \frac{R}{\pi(\rho A \ell)^2} \sum_{j=1}^{\infty} \left(\sin \frac{j\pi x}{\ell}\right)^2 \int_{-\infty}^{\infty} \frac{d\omega}{(\omega_{j,T}^2 - \omega^2)^2 \alpha_j^2 + 4\zeta_j^2 \omega_{j,T}^2 \omega^2} \tag{15}$$

Now

$$\int_{-\infty}^{\infty} \frac{d\omega}{(\omega_{j,T}^2 - \omega^2)^2 \alpha_j^2 + 4\zeta_j^2 \omega_{j,T}^2 \omega^2} = \frac{\pi}{2\zeta_j \alpha_j \omega_{j,T}^3} \tag{16}$$

or, bearing in mind Eq. (14),

$$\int_{-\infty}^{\infty} \frac{d\omega}{(\omega_{j,T}^2 - \omega^2)^2 \alpha_j^2 + 4\zeta_j^2 \omega_{j,T}^2 \omega^2} = \frac{\pi\rho A}{c\alpha_j \omega_{j,T}^2} \tag{17}$$

Comparison of Eqs. (7) and (8) reveals that

$$\alpha_j \omega_{j,T}^2 = \omega_{j,cl}^2 \tag{18}$$

whence

$$E[w^2(x,t)] = \frac{R}{\pi\rho A \ell^2} \sum_{j=1}^{\infty} \left(\sin \frac{j\pi x}{\ell}\right)^2 \frac{\pi}{c\omega_{j,cl}^2} \tag{19}$$

and therefore should coincide with Eringen's classical Eq. (4). This implies that when the joint effect of shear deformation and rotary inertia is neglected, but their proper contributions are taken into account, the mean-square displacement of the Timoshenko beam is identical to that of the Bernoulli-Euler beam. This remarkable "exact" result is in agreement with the numerical calculations by Samuels and Eringen [3] who found that the difference between these theories does not exceed five percent (see Fig. 2 in Ref. 3 and Figs. 66.3 and 66.4 in Ref. 4).

Since the mean-square displacements predicted by the classical and refined theory coincide, the mean-square stresses do the same; they turn out to be divergent for both, the Bernoulli-Euler and Timoshenko beams.

On the other hand, the mean-square velocities for these beams differ, as is shown below. In fact,

$$E[\dot{w}^2(x,t)] = \frac{R}{\pi(\rho A \ell)^2} \sum_{j=1}^{\infty} \left(\sin \frac{j\pi x}{\ell}\right)^2 \int_{-\infty}^{\infty} \frac{\omega^2 d\omega}{(\omega_{j,T}^2 - \omega^2)^2 \alpha_j^2 + 4\zeta_j^2 \omega_{j,T}^2 \omega^2} \tag{20}$$

The integral equals

$$\int_{-\infty}^{\infty} \frac{\omega^2 d\omega}{(\omega_{j,T}^2 - \omega^2)^2 \alpha_j^2 + 4\zeta_j^2 \omega_{j,T}^2 \omega^2} = \frac{\pi}{2\alpha_j \zeta_j \omega_{j,T}} = \frac{\pi\rho A}{\alpha_j c} \tag{21}$$

and consequently

$$E[\dot{w}^2(x,t)] \quad \frac{R}{\rho A \ell^2 c} \sum_{j=1}^{\infty} \left(\sin \frac{j\pi x}{\ell}\right)^2 \frac{1}{\alpha_j} \tag{22}$$

Denoting

$$\delta = \frac{r^2\pi^2}{\ell^2}\left(1 + \frac{E}{k'G}\right) \tag{23}$$

we obtain

$$E[\dot{w}^2(x,t)] \frac{R}{\rho A \ell^2 c} \sum_{j=1}^{\infty} \left(\sin \frac{j\pi x}{\ell}\right)^2 \frac{1}{1+\delta j^2} \tag{24}$$

and resorting to the familiar sum [Ref. 8, Eq. 1.445.2]

$$\sum_{j=1}^{\infty} \frac{\cos jx}{j^2+\beta^2} = \frac{\pi}{2\beta} \frac{\cosh \beta(\pi-x)}{\sinh \beta\pi} - \frac{1}{2\beta^2}, \text{ for } 0<x<2\pi \tag{25}$$

we have

$$E[\dot{w}^2(\xi,t)] = \frac{R}{2\rho A \ell^2 c} \frac{\ell/r}{\gamma \sinh(\ell/r\gamma)} \sinh\left[\frac{\ell}{r\gamma}(1-\xi)\right]\sinh\left(\frac{\ell}{r\gamma}\xi\right) \tag{26}$$

where $\xi = x/\ell$ is the nondimensional axial coordinate and

$$\gamma = \left(1 + \frac{E}{k'G}\right)^{1/2} \tag{27}$$

Taking [9]

$$k' = \frac{10(1+\nu)}{12+11\nu}$$

we find $E/k'G = 3.12$ and $\gamma = 2.03$. For a beam of rectangular cross-section $r = h/12^{1/2} = 0.289h$, where h is the depth of the cross-section. Then, at the middle cross-section $\xi = {}^1/_2$

$$E[w^2(\tfrac{1}{2},t)] = \frac{R}{2\rho A \ell^2 c} \frac{3.46\ (\ell/h)}{2.03 \sinh\ (1.705\ \ell/h)} \sinh^2(0.8525\ \ell/h) \tag{28}$$

For $\ell/h \gg 1$, we have

$$\sinh^2(0.8525\ \ell/h) \simeq \frac{1}{2} \sinh\ (1.705\ \ell/h) \tag{29}$$

and the mean-square velocity is obtained as

$$E[\dot{w}^2(\tfrac{1}{2},t)] = \frac{0.4265\ R}{\rho A \ell^2 c} \left(\frac{\ell}{h}\right) \tag{30}$$

whereas for the classical beam it diverges. Indeed, as the slenderness ratio increases, the natural frequencies of the Timoshenko beam tend to those of the Bernoulli-Euler beam and for $\ell/h \to \infty$ Eq. (30) yields an infinite mean-square velocity.

2.3 Timoshenko Beam with Structural Damping

The governing equation reads

$$E(\frac{\partial}{\partial t})I \frac{\partial^4 w}{\partial x^4} + \rho A \frac{\partial^2 w}{\partial t^2} - \alpha_0 \frac{\partial^4 w}{\partial x^2 \partial t^2} = q(x,t) \tag{31}$$

where $\partial/\partial t$ is a time-differentiation operator and

$$\alpha_0 = \rho A r^2 (1 + \frac{E_0}{k' G_0}) \quad , \quad e^{-i\omega t} E(\frac{\partial}{\partial t}) e^{i\omega t} = E_0(1+i\mu) \tag{32}$$

Poisson's ratio is assumed constant, μ is the structural damping coefficient. The frequency response function is

$$H_j(\omega) = \frac{1}{\rho A \alpha_j [\omega_{j,T}^2 (1+i\mu) - \omega^2]} \tag{33}$$

The displacement space-time correlation function at zero time lag becomes

$$R_w(x_1,x_2,0) = \frac{R}{\pi(\rho A \ell)^2} \sum_{j=1}^{\infty} \sin \frac{j\pi x_1}{\ell} \sin \frac{j\pi x_2}{\ell} \frac{1}{\alpha_j^2} \int_{-\infty}^{\infty} \frac{d\omega}{(\omega_{j,T}^2 - \omega^2)^2 + \omega_{j,T}^2 \mu^2} \tag{34}$$

or

$$R_w(x_1,x_2,0) = \frac{R\ell^4}{\pi^6 E_0 I (\rho A E_0 I)^{1/2}} \frac{[1+(1+\mu^2)^{1/2}]^{1/2}}{\mu[2(1+\mu^2)]^{1/2}} \times$$

$$\times \sum_{j=1}^{\infty} \sin \frac{j\pi x_1}{\ell} \sin \frac{j\pi x_2}{\ell} \frac{1}{j^6} \frac{1}{[1+(\frac{r\pi}{\ell})^2 j^2 \gamma^2]^{1/2}} \tag{35}$$

For the mean-square displacement we have

$$E[w^2(\xi,t)] = \frac{R\ell^4}{\pi^6 EI (\rho A E_0 I)^{1/2}} \frac{[1+(1+\mu^2)^{1/2}]^{1/2}}{\mu[2(1+\mu^2)]^{1/2}} \sum_{j=1}^{\infty} (\sin j\pi\xi)^2 \frac{1}{j^6} \frac{1}{[1+(\frac{r\pi}{\ell})^2 j^2 \gamma^2]^{1/2}} \tag{36}$$

The corresponding expression $R_w(x_1,x_2,0)$ for the Bernoulli-Euler beam is obtained by putting formally $\gamma=0$, in Eq. (36) which yields

$$R_w(x_1,x_2,0)_{cl} = \frac{R\ell^4}{\pi^6 EI (\rho A E_0 I)^{1/2}} \frac{[1+(1+\mu^2)^{1/2}]^{1/2}}{\mu[2(1+\mu^2)]^{1/2}} \sum_{j=1}^{\infty} \sin \frac{j\pi x_1}{\ell} \sin \frac{j\pi x_2}{\ell} \frac{1}{j^6} \tag{37}$$

The summation of this series is given in [6]. The maximum mean-square displacement is (see Eq. 27 there)

$$E[w^2(\tfrac{1}{2},t)]_{cl} = \frac{R\ell^4}{960\, E_0 I(\rho A E_0 I)^{1/2}} \frac{[1+(1+\mu^2)^{1/2}]^{1/2}}{\mu[2(1+\mu^2)]^{1/2}} \tag{38}$$

Closed summation of (36) for the Timoshenko beam is apparently unfeasible. The appropriate terms in series (37) for the classical beam are multiplied by the factor $1/[1+(r\pi/\ell)^2 j^2 \gamma^2]^{1/2}$ as the mode number increases. In these circumstances it is reasonable to compare the contribution of the first mode for the Timoshenko beam with the closed-form solution (38) for the classical beam

$$E[w^2(\tfrac{1}{2},t)]_T \simeq \frac{R\ell^4}{\pi^6 E_0 I(\rho A E_0 I)^{1/2}} \frac{[1+(1+\mu^2)^{1/2}]^{1/2}}{[2(1+\mu^2)]^{1/2}} \frac{1}{[1+(r\pi/\ell)^2\gamma^2]^{1/2}} \tag{39}$$

The ratio of the mean-square displacements is

$$\eta = \frac{E[w^2(\tfrac{1}{2},t)]_T}{E[w^2(\tfrac{1}{2},t)]_{cl}} \simeq \frac{960}{\pi^6\,[1+(r\pi/\ell)^2\gamma^2]^{1/2}} \tag{40}$$

For a rectangular cross-section η equals 0.982 at $h/\ell=0.1$ and 0.937 at $h/\ell=0.2$, i.e. the difference between the Bernoulli-Euler and Timoshenko models is about 6.7%.

2.4 Timoshenko Beam with Voigt Damping

The governing differential equation is

$$E_0 I(1+\epsilon\frac{\partial}{\partial t})\frac{\partial^4 w}{\partial x^4} + \rho A \frac{\partial^2 w}{\partial t^2} - \alpha_0 \frac{\partial^2 w}{\partial x^2 \partial t^2} = q(x,t) \tag{41}$$

where α_0 is as per Eq. (32) and Poisson's ratio is again assumed constant. The frequency response function is in this case

$$H_j(\omega) = \frac{1}{\rho A \alpha_j[\omega_{j,T}^2(1+\epsilon i\omega) - \omega^2]} \tag{42}$$

Therefore

$$R_w(x_1,x_2,0) = \frac{R}{\pi(\rho A\ell)^2} \sum_{j=1}^{\infty} \sin\frac{j\pi x_1}{\ell} \sin\frac{j\pi x_2}{\ell} \int_{-\infty}^{\infty} \frac{d\omega}{\alpha_j^2[(\omega_{j,T}^2-\omega^2)^2+\omega_{j,T}^4\epsilon^2\omega^2]} \tag{43}$$

The integral equals $\pi/\alpha_j^2\epsilon\omega_{j,T}^4$. However,

$$\alpha_j\omega_{j,T}^2 = \omega_{j,cl}^2$$

and as a consequence, the displacements space-time correlation function for the Timoshenko beam coincides with its classical counterpart, given by Eq. (38) of Ref. [6].

For the velocity space-time correlation function the appropriate integral equals

$$\frac{\pi}{\alpha_j^2 \varepsilon \omega_{j,T}^2} = \frac{\pi}{\alpha_j \varepsilon \omega_{j,cl}^2}$$

Thus

$$R_w^{\cdot}(x_1,x_2,0) = \frac{R\ell^2}{\rho AEI\varepsilon\pi^4} \sum_{j=1}^{\infty} \frac{1}{j^4} \frac{1}{1+\alpha_j^2} \sin\frac{j\pi x_1}{\ell} \sin\frac{j\pi x_2}{\ell} \tag{44}$$

and for the mean-square velocity the following closed-form expression is obtainable

$$E[\dot{w}^2(x,t)]_T = E[w^2(x,t)]_{cl} -$$

$$- \frac{R\ell^2}{\rho AEI\varepsilon\pi^4} \left[\frac{\alpha\pi}{2}^2 \xi(1-\xi) + \frac{\alpha\pi\alpha^{1/2}}{2\sinh(\pi/\alpha^{1/2})} \sinh\frac{\pi}{\alpha^{1/2}}(1-\xi) \sinh\frac{\pi}{\alpha^{1/2}}\xi\right] \tag{45}$$

2.5 Timoshenko Beam with Rotary and Transverse Damping

Instead of Eq. (9) we have

$$EI\frac{\partial^4 w}{\partial x^4} + \rho A\frac{\partial^2 w}{\partial t^2} + c\frac{\partial w}{\partial t} - \alpha\frac{\partial^4 w}{\partial x^2 \partial t^2} - d\frac{\partial^3 w}{\partial x^2 \partial t} = q(x,t) \tag{46}$$

where d is the rotary damping coefficient. The formalism of the normal mode method yields

$$E[w^2(x,t)] = \frac{R}{\pi(\rho A\ell)^2} \sum_{j=1}^{\infty} \left(\sin\frac{j\pi x}{\ell}\right)^2 \int_{-\infty}^{\infty} \frac{d\omega}{(\omega_{j,T}^2-\omega^2)^2\alpha_j^2+4\zeta_j^2\omega_{j,T}^2\omega^2} \tag{47}$$

where

$$2\zeta_j\omega_{j,T} = \frac{c_{eq}}{\rho A} = \frac{c+d(j\pi/\ell)^2}{\rho A}$$

Therefore, in analogy with Eq. (16), we obtain

$$E[w^2(x,t)] = \frac{R}{\pi(\rho A\ell)^2} \sum_{j=1}^{\infty} \left(\sin\frac{j\pi x}{\ell}\right)^2 \frac{\pi}{2\alpha_j\zeta_j\omega_{j,T}^3}$$

$$= \frac{R}{\pi(\rho A\ell)^2} \sum_{j=1}^{\infty} \left(\sin\frac{j\pi x}{\ell}\right)^2 \frac{\pi\rho A}{\alpha_j c_{eq}\omega_{j,T}^2} \tag{48}$$

Here again the product $\alpha_j\omega_{j,T}^2$ equals $\omega_{j,cl}^2$ and the Timoshenko beam result coincides with the classical beam result, reported in Ref. [6].

A remarkable conclusion is, that mean-square value of the stress also coincides with that of the Bernoulli-Euler beam derived in Ref.[6]. That is, the mean-square stress is the Timoshenko beam diverges, when only transverse damping is present. Addition of the rotary damping however small improves the situation so that under this combined transverse and rotary damping the mean-square stress converges. This conclusion was originally arrived at by Samuels and Eringen [3] and also Crandall and Yildiz [5] and are reconfirmed by the present writers.

3. Acknowledgements

This work was supported in part by the Technion Fund for Promotion of Research.

4. References

1. A.C. ERINGEN 1957 Journal of Applied Mechanics 24, 46-52. Response of beams and plates to random loads.

2. I. ELISHAKOFF 1983 Probabilistic Methods in the Theory of Structures. New York: Wiley-Interscience, pp. 406-408.

3. J.C. SAMUELS and A.C. ERINGEN 1956 Journal of Applied Mechanics 25, 496-500. Response of a simply supported Timoshenko beam to a purely random Gaussian process.

4. A.C. ERINGEN 1962 In Handbook of Engineering Mechanics. W. Fluegge, Ed., New York, McGraw-Hill, pp. 66.13-66.16. Stochastic Loads.

5. S.H. CRANDALL and A. YILDIZ 1962 Journal of Applied Mechanics 31, 267-275. Random vibrations of beams.

6. I. ELISHAKOFF and D. LIVSHITS 1983 Department of Aeronautical Engineering, Technion - Israel Institute of Technology, TAE-Rept. 521. Some closed-form solutions in random vibration of Bernoulli-Euler beams.

7. S.P. TIMOSHENKO 1928 Vibration Problems in Engineering. London: Constable and Company, p. 231.

8. R.W. CLOUGH and J. PENZIEN 1975 Dynamics of Structures. New York: McGraw-Hill, pp. 298-301, 318-320.

9. G.R. COWPER 1966 Journal of Applied Mechanics 33, 335-340. The shear coefficient in Timoshenko's beam theory.

10. I.S. GRADSHTEYN and I.M. RYZHIK 1980 Tables of Integrals, Series and Products. New York: Academic Press.

RANDOM VIBRATION OF DISCRETE, PERIODIC COUPLED FRAME-WALL SYSTEMS

G. Oliveto and A. Santini

Istituto di Scienza delle Costruzioni
Università di Catania

1. INTRODUCTION

The structural strength of tall buildings is often provided by a coupled frame-wall system with the frame supporting most of the vertical loads and the horizontal loads shared in some measure between the frame and the wall. For design purposes, the knowledge of the shear forces and bending moments in the frame and in the wall is of the utmost importance and also the knowledge of the displacements due to horizontal actions. The main sources of horizontal forces in buildings are wind and earthquake excitations. This paper will consider the response of coupled frame-wall systems to earthquake motions although, with minor alterations, the procedure may also be applied to wind excitations.

The problem of evaluating the response of coupled shear-wall systems to earthquake excitations has been the object of several investigations in the past but some contributions have also appeared recently [1], [2], [3], [4]. Early investigations [1] have considered the response to static forces which are provided by many seismic codes as alternative means for assessing the seismic strength of some types of structures. More recently [2], [3], [4], dynamic analyses have been presented aiming at the evaluation of the frequencies of vibration which may be used in conjunction with either the response spectra or the mode superposition method. However both the static and the dynamic analyses have been performed on continuum equivalent models which may give a picture of the qualitative behaviour of the system but may not provide results of sufficient accuracy for design and analysis. Surprisingly enough, analyses of discrete models, to which the system is amenable quite naturally, have not been presented, perhaps because those have been looked upon as trivial exercises! However discrete models of the shear type frame have been presented extensively in literature and analysed for static [5] and dynamic [6] loadings of both a deterministic and random nature.

The analyses of the response of periodic shear type frames to earthquake excitations modelled as stationary random processes was presented by A.C. Eringen [6] and extended to some nonstationary random processes by Y.K. Lin [7]. In this paper the method developed by Y.K. Lin will be applied to periodic frame-wall systems.

2. THE PHYSICAL AND MATHEMATICAL MODELS

A coupled frame-wall system consists in its most elementary form, of a frame and a wall connected at regular intervals by inextensible rods as shown in fig.1. The connecting rods are provided in actual buildings by the floor slabs which may be considered inextensible because of their large in-plane stiffness. In continuum equivalent models the wall is treated as an Euler-Bernoulli beam and the frame as a shear beam [1]. The connecting rods are split and spread to form a curtain providing a continuous rigid constraint against mutual displacements of the wall and the frame. The shear stiffness of the beam equivalent to the frame is obtained by analysing the behaviour of a panel of shear type frame and replacing the actual rotations by the average one along the height of the panel. Both these operations, by violating compatibility alter the identity of the physical problem and should be avoided as can be done by analysing the discrete model of the structure.

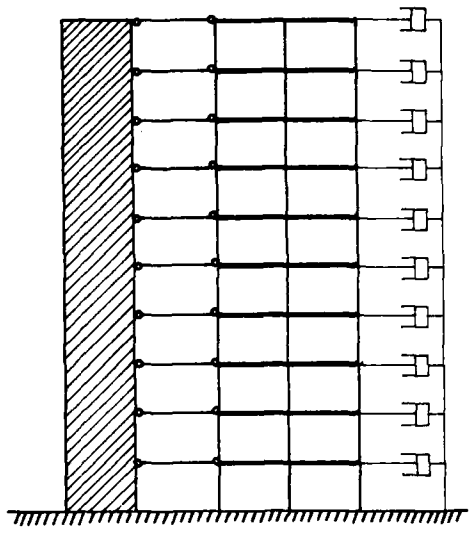

Fig.1 Coupled Frame-Wall System

In what follows the ground floor will be denoted by the suffix 0 and the subsequent floors will be numbered from 1 to N. The geometrical and mechanical properties will be considered constant at each storey but varying from storey to storey. Later this variability will be removed but it will be clear how to proceed in the general case at the price of some additional computational effort. The shear stiffness of the frame at the i-th storey will be denoted by

$$K_i = 12 \sum_{j=1}^{n} (E_j^f I_j^f / h^3)_i$$

where h is the height of the storey, E_j^f and I_j^f are Young's modulus and the second moment of area of the j-th column and n is the number of columns in the frame. Expressions for K_i are available also for frames which are not, or may not be considered, of the shear type, [1]. At the same storey let E_i^w and I_i^w be the corresponding properties for the wall.

2.1 The field matrix

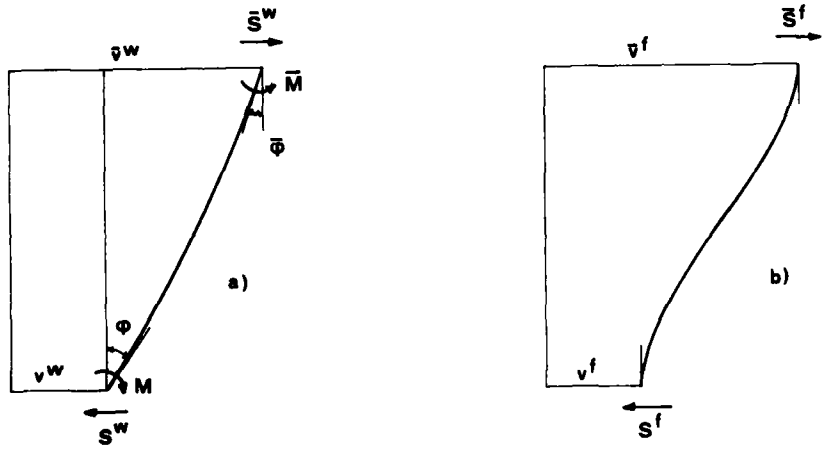

Fig.2 Forces and displacements related by the field matrices
a) for the wall, b) for the frame

A field matrix relates forces and displacements at the top of a storey to those at the bottom. In the present case the field matrices may be written as follows for a wall and a frame segment corresponding to the same storey, fig.2.

$$\begin{bmatrix} \bar{S} \\ \bar{M}/h \\ \bar{\phi}R/h^2 \\ \bar{v}R/h^3 \end{bmatrix}_i^w = \begin{bmatrix} 1 & 0 & 0 & 0 \\ 1 & 1 & 0 & 0 \\ -1/2 & -1 & 1 & 0 \\ -1/6 & -1/2 & 1 & 1 \end{bmatrix}_i^w \begin{bmatrix} S \\ M/h \\ \phi R/h^2 \\ vR/h^3 \end{bmatrix}_i^w$$

$$\begin{bmatrix} \bar{S} \\ \bar{v}R^w/h^3 \end{bmatrix}_i^f = \begin{bmatrix} 1 & 0 \\ \rho & 1 \end{bmatrix}_i^f \begin{bmatrix} S \\ vR^w/h^3 \end{bmatrix}_i^f$$

$$\rho = \frac{R^w}{R^f} \quad ; \quad R^f = EI^f(1+i\alpha)$$

$$R^w = EI^w(1+i\beta) = R$$

Here w and f stand for wall and frame respectively and the subscript i refers to the storey number. Hysteretic damping in the wall and in the frame is taken into account through the parameters α and β respectively.

For the subsequent developments it is convenient to replace the 4x4 and the 2x2 field matrices by a single 4x4 matrix. This can be done because the lateral displacements in the frame and in the wall are identical at floor levels and both the shear forces may be expressed in terms of their sum and of the remaining variables. Therefore, by enforcing the equalities

$$v^f = v^w = v$$

$$S^f = S^w = S$$

and after some algebraic manipulations the following relationships may be written

$$\begin{bmatrix} \bar{S} \\ \bar{M}/h \\ \bar{\phi}R/h^2 \\ \bar{v}R/h^2 \end{bmatrix}_i = \begin{bmatrix} 1 & 0 & 0 & 0 \\ C & E & G & 0 \\ B & D & E & 0 \\ A & B & C & 1 \end{bmatrix}_i \begin{bmatrix} S \\ M/h \\ \phi R/h^2 \\ vR/h^2 \end{bmatrix}_i \qquad (1)$$

where

$$d = 2(1-6\rho)$$

$$A = 2\rho/d \qquad D = (1+6\rho)/d$$

$$B = 3A \qquad E = -4(1+\rho)/d$$

$$C = -6A \qquad G = 12/d$$

and M, $\bar{M}$, φ, $\bar{\Phi}$, still denote bending moments and rotations at the ends of a wall segment . The shear forces in the wall and in the frame are given by the following expressions

$$S^w = -6(2\rho S+M/h-2\varphi R/h^2)/d$$

$$S^f = 2(S+3M/h-6\varphi R/h^2)/d$$

2.2 The point matrix

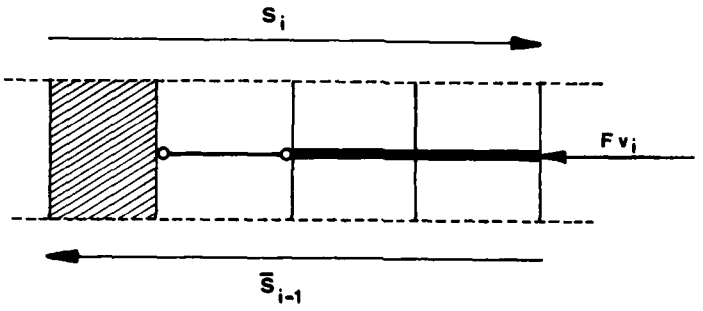

Fig.3 Horizontal forces on a system segment

A point matrix effects transfer across a floor providing the following relationships between the field variables at the top of a segment of structure to those at the bottom of the following one, fig.3.

$$\begin{bmatrix} S \\ M/h \\ \varphi R/h^2 \\ vR/h^3 \end{bmatrix}_i = \begin{bmatrix} 1 & 0 & 0 & F \\ 0 & 1 & 0 & 0 \\ 0 & 0 & 1 & 0 \\ 0 & 0 & 0 & 1 \end{bmatrix}_{i-1} \begin{bmatrix} \bar{S} \\ \bar{M}/h \\ \bar{\Phi}R/h^2 \\ \bar{v}R/h^3 \end{bmatrix}_{i-1} \qquad (2)$$

(i=2,...,N-1)

In the above matrix the coefficient

$$F = -h^3(m\omega^2-ic\omega)/R$$

accounts for inertia and viscous forces at floor levels.

2.3 The transfer matrix

The relationship (1) and (2) may be written in compact form as

$$\underline{z}_{i-1} = F_{i-1}\underline{z}_{i-1}$$

$$\underline{z}_i = P_{i-1}\underline{z}_{i-1}$$

where F_{i-1} and P_{i-1} denote the field and point matrices respectively. By combining the above equations it may be written

$$\underline{z}_i = P_{i-1}F_{i-1}\underline{z}_{i-1} \quad \text{or} \qquad \underline{z}_i = T_{i-1}\underline{z}_{i-1} \tag{3}$$

where the transfer matrix T_{i-1} may be given as follows

$$T_{i-1} = P_{i-1}F_{i-1} = \begin{bmatrix} 1+FA & FB & FC & F \\ C & E & G & 0 \\ B & D & E & 0 \\ A & B & C & 1 \end{bmatrix}_{i-1}$$

By applying equation (3) recurrently it may be found that

$$\underline{z}_i = T_{i-1}T_{i-2}\cdots T_o\underline{z}_o \tag{4}$$

For a periodic structure, being $T_{i-1}=T_{i-2}=\ldots=T_o=T$, equation (4) may be written as follows

$$\underline{z}_i = T^i\underline{z}_o \tag{5}$$

2.4 The state vector at the base

In the state vector $\underline{z}_o$ the shear force S_o and the bending moment M_o are unknown, the rotation φ_o is zero and the displacement v_o may be prescribed as a unit sinusoidal ground motion, i.e. $v_o(t)=\exp[i\omega t]$. Equation (5) may be partitioned as follows by separating forces and displacements in the state vectors

$$\begin{bmatrix} \underline{f}_i \\ \underline{d}_i \end{bmatrix} = \begin{bmatrix} T^i_{ff} & T^i_{fd} \\ T^i_{df} & T^i_{dd} \end{bmatrix} \begin{bmatrix} \underline{f}_o \\ \underline{d}_o \end{bmatrix} \tag{6}$$

This when written for the top floor becomes

$$\begin{bmatrix} \underline{0} \\ \underline{d}_N \end{bmatrix} = \begin{bmatrix} T^N_{ff} & T^N_{fd} \\ T^N_{df} & T^N_{dd} \end{bmatrix} \begin{bmatrix} \underline{f}_o \\ \underline{d}_o \end{bmatrix} \tag{7}$$

By solving the first of equations (7) it may be found that

$$\underline{f}_o = -T^N_{ff}T^N_{fd}\underline{d}_o$$

or

$$\underline{z}_o = \begin{bmatrix} -T^N_{ff}T^N_{fd} \\ I \end{bmatrix} \underline{d}_o$$

The vectors $\underline{z}_i$, which may therefore be evaluated for a prescribed unit sinusoidal motion, take the physical meaning of frequency response functions and may be used to evaluate the structural response to random excitations such as earthquake motions.

3. MODELLING THE EARTHQUAKE MOTION

At an early stage of seismic engineering, earthquake accelerations have been modelled as stationary random processes. Nowadays more realistic models which take into account the nonstationary nature of the phenomenon are used

instead, [7], [8]. Amplitude modulated random processes, i.e. stationary random noises multiplied by a deterministic modulation function, are widely accepted models for seismic accelerations. For such models the time-dependent frequency response function may be written as follows

$$M_k(t,\omega) = \int_o^t c(t-u)h_k(u)\exp[-i\omega u]\,du \tag{8}$$

where $c(t-u)$ is the modulation function and $h_k(u)$ is the impulse response function related to the stationary frequency response function $H_k(\omega)$ through the well-known relationship

$$h_k(u) = \frac{1}{2\pi}\int_{-\infty}^{\infty} H_k(\omega)\exp[i\omega u]\,d\omega \tag{9}$$

The cross-correlation function of any two output processes $O_k(t)$ and $O_m(t)$ is given by

$$E[O_k(t_1)O_m(t_2)] = \int_{-\infty}^{\infty} M_k(t_1,\omega)M_m^*(t_2,\omega)\exp[i\omega(t_1-t_2)]\,S_{vo}(\omega)\,d\omega \tag{10}$$

where a star denotes complex conjugation and $S_{vo}(\omega)$ is the spectral density of the input stationary random process before modulation. In the present model $S_{vo}(\omega)$ is the spectral density of the ground displacement random process, not that of the ground acceleration which is being used in most seismic engineering analyses. However $S_{vo}(\omega)$ may be easily obtained for a stationary random process from $S_{\ddot{v}o}(\omega)$ as follows, [9].

$$S_{vo}(\omega) = \omega^{-4}S_{\ddot{v}o}(\omega) \tag{11}$$

In most seismic engineering analyses $S_{\ddot{v}o}(\omega)$ is associated either to a white noise or to a band limited white noise or to a filtered white noise random process, [8], and in all cases does not vanish at the zero frequency. This results in a singularity in the spectral density of the displacement process which will cause inconveniences in the evaluation of the cross-correlation functions of the output processes through equation (10). To avoid these inconveniences one might use as input process some sort of filtered white noise for which $S_{\ddot{v}o}(\omega)$ goes to zero more quickly than ω^4 or at least at the same rate. Another alternative which will be followed here requires a reformulation of the problem in such a way that the acceleration process is accepted as input instead of the displacement process. This may be done by splitting the absolute displacement in two parts corresponding to the ground displacement $v_o(t)$ and to the displacement relative to the ground $y(t)$ respectively, that is

$$v(t) = v_o(t) + y(t)$$

By also introducing amongst the state variables the inertia forces associated to the ground acceleration and by observing that traditionally in earthquake engineering viscous damping is associated to the relative velocities only [10], the transfer matrix may be reformulated as follows

$$\begin{bmatrix} S \\ M/k \\ \varphi R/h^2 \\ yR/h^3 \\ m\ddot{v}_o \end{bmatrix}_i = \begin{bmatrix} 1+FA & FB & FC & F & 1 \\ C & E & G & 0 & 0 \\ B & D & E & 0 & 0 \\ A & B & C & 1 & 0 \\ 0 & 0 & 0 & 0 & 1 \end{bmatrix}_{i-1} \begin{bmatrix} S \\ M/h \\ \varphi R/h^2 \\ yR/h^3 \\ m\ddot{v}_o \end{bmatrix}_{i-1} \tag{12}$$

where the state vectors have been reported for the sake of clarity.

4. SPECTRAL DECOMPOSITION OF THE TRANSFER MATRIX

The evaluation of the state vector $\underline{z}_i = T^i \underline{z}_o$ requires the computation of the powers of the transfer matrix T. If the transfer matrix is not constant, then $T_i = T_{i-1} T_{i-2} \ldots T_o$ must be evaluated by performing the product of i transfer matrices in the order given above. In many engineering applications the matrix T turns out to be either constant for the overall system or constant for each substructure in which the overall system can be decomposed. In such cases it may be convenient to perform a spectral decomposition of the transfer matrix which considerably simplifies the computation of its powers. Let $\lambda_j, \underline{\varphi}_j, \underline{\psi}_j$, be respectively the eigenvalues, the right-hand eigenvectors and the left-hand eigenvectors of matrix T, then unless T is defective the following expansion holds, [11],

$$T = \sum_{j=1}^{5} \lambda_j \underline{\varphi}_j \underline{\tilde{\psi}}_j \tag{13}$$

provided that the eigenvectors have been normalized so that

$$\underline{\tilde{\varphi}}_j \underline{\psi}_j = 1 \tag{14}$$

In the equations (13) and (14) a $\sim$ denotes transposition. Furthermore it can be proved that any power of T may be written as follows

$$T^n = \sum_{j=1}^{5} \lambda_j^n \underline{\varphi}_j \underline{\tilde{\psi}}_j \tag{15}$$

As it has been pointed out by Y.K. LIN, [7], [12], the determinant of a transfer matrix is always equal to unity and its eigenvalues are reciprocal pairs. For the problem at hand one eigenvalue is real and equal to unity while the remaining four are reciprocal couples. Therefore by writing these latters as

$$\lambda = \exp[\pm i\theta]$$

it turns out that

$$\cos\theta = 1/4\left[(2+2E+FA) \pm \left[4+4E^2+F^2A^2-8E+20FA+4FEA\right]^{1/2}\right]$$

providing the required eigenvalues. The right-hand and left-hand eigenvectors associated to these pairs may be written as follows

$$\varphi(\lambda) = w \begin{bmatrix} (1-\lambda)(1-2E\lambda+\lambda^2) \\ -C(1-\lambda)^2 \\ B(1-\lambda^2) \\ -A(1+4\lambda+\lambda^2) \\ 0 \end{bmatrix} \tag{16}$$

$$\psi(\lambda) = w \begin{bmatrix} (1-\lambda)(1-2E\lambda+\lambda^2) \\ -FB(1+\lambda) \\ FC\ (1-\lambda) \\ -F(1-2E\lambda+\lambda^2) \\ -(1-2E\lambda+\lambda^2) \end{bmatrix} \tag{17}$$

The eigenvectors associated with the eigenvalue $\lambda_5=1$ may be written in the form

$$\tilde{\Phi}_5 = \begin{bmatrix} 0 & 0 & 0 & -1/F & 1 \end{bmatrix}$$

$$\tilde{\Psi}_5 = \begin{bmatrix} 0 & 0 & 0 & 0 & 1 \end{bmatrix}$$

4.1 The limit case of zero frequency

It should be noticed that at the zero frequency one pair of reciprocal eigenvalues become real and equal to unity, the corresponding eigenvectors become singular and the matrix T becomes defective. However expansions (13) and (15) still hold in the limit. In fact let λ_3 and $\lambda_4=\lambda_3^*$ be the eigenvalues which become equal to 1 at the zero frequency. Their contribution to expansions (13) and (15) may be written as follows

$$\begin{bmatrix} 1 & 0 & 0 & 0 & n \\ 0 & 0 & 0 & 0 & -a \\ a & 0 & 0 & 0 & b \\ c & a & 0 & 1 & e \\ 0 & 0 & 0 & 0 & 0 \end{bmatrix} \qquad (18)$$

where

$$a = B(1-E); \quad b = a(2n-1)/2; \quad c = an$$

$$e = -a/(1-E)/6 + an(n-1)/2 + 1/F$$

The contribution of the remaining pair of reciprocal eigenvalues $\lambda_1=E-\sqrt{E^2-1}$ and $\lambda_2=\lambda_1^*=E+\sqrt{E^2-1}$, may be given as follows:

$$\begin{bmatrix} 0 & 0 & 0 & 0 & 0 \\ c_n & e_n & g_n & 0 & c_{25} \\ c_{31} & d_n & e_n & 0 & c_{35} \\ c_{41} & c_{42} & c_n & 0 & c_{45} \\ 0 & 0 & 0 & 0 & 0 \end{bmatrix} \qquad (19)$$

with

$$c_n = C\sin(n\theta)/\sin\theta$$

$$e_n = \cos(n\theta)$$

$$g_n = G\sin(n\theta)/\sin\theta$$

$$d_n = D\sin(n\theta)/\sin\theta$$

$$c_{25} = a\left[\cos(n-1)\theta + \cos(n\theta)\right]/(1+\cos\theta)$$

$$c_{31} = -a\cos(n\theta)$$

$$c_{35} = -a\left[\cos(n-1)\theta - \cos(n\theta)\right]/(1-\cos\theta)$$

$$c_{41} = 2aB\sin(n\theta)/\sin\theta$$

$$c_{42} = -aE\cos(n\theta)/\cos\theta$$

$$c_{45} = a\left[\cos(n-1)\theta + \cos(n\theta)\right] / \left[6(1-E)(1+\cos\theta)\right]$$

$$\cos\theta = E$$

Finally the contribution of the 5th eigenvalue to expansions (13) and (15) is given below:

$$\begin{bmatrix} 0 & 0 & 0 & 0 & 0 \\ 0 & 0 & 0 & 0 & 0 \\ 0 & 0 & 0 & 0 & 0 \\ 0 & 0 & 0 & 0 & -1/F \\ 0 & 0 & 0 & 0 & 1 \end{bmatrix} \qquad (20)$$

The singularity introduced by the term -1/F, being F=0 at the zero frequency, is cancelled by an apposite term in the coefficient e of matrix (18).

5. PREDICTION OF THE MAXIMUM RESPONSE

The prediction of the maximum response is of utmost importance in seismic engineering. When the excitation is a random process this prediction can be made only on a probabilistic base. It has been shown [8] that the peak response may be expressed in terms of the standard deviation of the response $\sigma_y(s)$ and of the peak response factor $r_{s;p}$ through the equation

$$y_{s;p} = r_{s;p}\,\sigma_y(s)$$

where $y_{s;p}$ is the level of the response parameter which has probability p of not being exceeded during an earthquake of duration s. By defining the evolutionary spectral density of the response as

$$S_y(t,\omega) = M(t,\omega)M^*(t,\omega)S_{\ddot{v}_o}(\omega)$$

and its moments as

$$\lambda_{i,y}(t) = \int_{\infty}^{\infty} \omega^i S_y(t,\omega)\,d\omega$$

it may be shown [8] that the peak response factor $r_{s;p}$ can be calculated approximately through the equation

$$r_{s;p} = \left[2\log\left[2n\left[1-\exp(-\delta_e\sqrt{\pi\log 2n})\right]\right]\right]^{1/2}$$

where

$$n = \frac{1}{2\pi}\Omega_y(s)s_o(-\log p)^{-1}$$

$$\delta_e = \delta_y(s)^{1+b}$$

$$\Omega_y(s) = (\lambda_{2,y}/\lambda_{0,y})^{1/2}$$

$$\delta_y(s) = \left[1-\lambda^2_{1,y}/(\lambda_{0,y}\lambda_{2,y})\right]^{1/2}$$

$$m = \sigma_y^2(s)/\sigma_y^2(s/2)$$

$$s_o/s = \exp[-2(m-1)]$$

$$b = 0.2$$

A full account on this subject together with references to the original literature sources may be found in the already quoted paper by E. Vanmarcke [8].

6. NUMERICAL APPLICATIONS

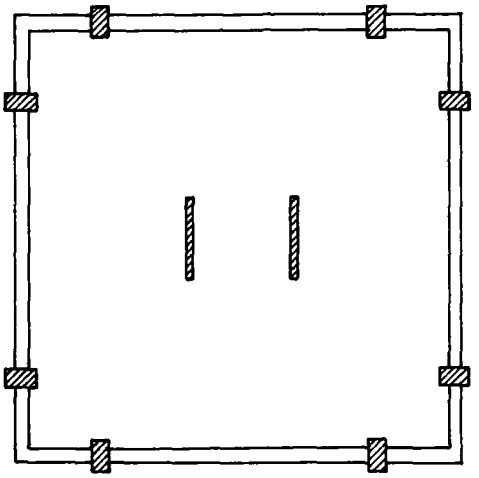

Fig.4 Floor plan of the analysed structure (from ref. [1])

Some numerical applications have been carried out with reference to the structure considered by A.C. Heidebrecht and B. Stafford Smith [1]. This is a 12 storey structure with the floor plan reported in fig.4, a total height H=36m, an interstory height h=3m and $E=2\times10^7 KN/m^2$ for both wall and frame. Two different analyses were presented in ref. [1] each corresponding to a different evaluation of the lateral stiffness of the frame. For sake of brevity only the analyses corresponding to the first case of ref. [1] will be presented here. The relevant parameters for the following analyses are the bending rigidity of the walls given by $EI=3.75\times10^6 KN\cdot m^2$ and the shear stiffness of the frame given by $K=9.87\times10^3 KN/m$. Only viscous damping has been introduced in the analyses in the Rayleigh fashion. The mass and stiffness proportional damping terms have been evaluated to provide a 5% effective damping ratio in both the first and the second mode.

6.1 Characteristics of the excitation process

A band limited white noise with a cut-off frequency of 25 Hz has been used as the stationary exitation process in the numerical applications. The duration and the spectral density introduced in the calculations are respectively

$$t_{max} = 25 \text{ s}$$

$$S_{\ddot{v}}(\omega) = 54.44 \text{ cm}^2/\text{s}^3 \qquad \text{for } \omega \leq 25 \text{ Hz}$$

$$S_{\ddot{v}}(\omega) = 0 \qquad \text{for } \omega > 25 \text{ Hz}$$

These values are considered as representative of the El-Centro 1940 and of other earthquakes of similar duration and intensity, [13], [14].

Fourier spectra of actual earthquake records, [15], show that the frequency content and the associated power are negligible beyond the assumed cut-off frequency. The modulation function which has been used in the analyses of the transient response is as follows

$$c(t) = 1 \qquad \text{for } t \leq t_{max}$$

$$c(t) = 0 \qquad \text{for } t > t_{max}$$

6.2 Stationary response

The analysis of the stationary response has been performed as reported in paragraph 5 by assuming all formulae as time-independent and therefore setting m=1. The peak response has been calculated for all the quantities of physical interest and for no exceedance probabilities of 50% and 95% respectively. The results referring to the overall shear are reported in fig.5. These show for both probabilities an increase of the peak interstorey shear from the top to the base pointing to a predominant contribution of the first mode as should be expected. However contributions up to the sixth mode are included as may be seen by comparing the natural frequencies of the system, reported in table I, and the cut-off frequency of the excitation process. The peak displacement reported in fig.6 shows an increase from the bottom to the top floor also pointing to a predominant contribution of the first mode.

Table I. Natural frequencies of the system

number	value (Hz)
1	0.53
2	2.01
3	4.81
4	9.03
5	14.68
6	21.75
7	30.15
8	39.67
9	49.90
10	60.02
11	68.77
12	74.71

The diagrams of fig.7 and fig.8 show how the peak shear is shared between the frame and the wall. It may be seen that at high and intermediate storeys the peak shear in the frame is higher than that in the wall while the opposite occurs at the lower storeys. Moreover, the peak shear at the bottom storey is higher in the wall than in the combined system, suggesting that at lower storeys

the frame may be pushing on the wall. Finally the peak bending moments and rotations in the wall are reported in fig.9 and fig.10 respectively. The peak bending moment shows an increase from the top, remains almost constant at intermediate levels and increases rapidly at the lower storeys. The peak rotation increases from the bottom, up to a certain level and then decreases almost unperceivably up to the top.

6.3 Transient response

The results presented so far do not account for the transient nature of the excitation process and may therefore overestimate the actual response. Some additional computations are required to predict the transient response as summarized in paragraph 5. The transient variance of the top displacement and of the base shear have been evaluated at different times and represented in fig.11 and fig.12, respectively, as fractions of their stationary values. They show a steep initial growth and a subsequent knee with a gradual decline in the rate of increase. After the excitation ceases to exist these show a quick decrease attaining negligible values in very short times. The reduction of the peak transient response, as compared to the stationary one, is due to the reduction of both the variance $\sigma(t)$ and of the peak factor $r_{s;p}$. The values of the peak factors calculated for the total shear and the storey displacement have been reported in table II for the transient and stationary responses allowing for the comparison.

Table II. Peak factors (s = 25 sec, p = 95%)

Storey number	total shear		displacement	
	stationary	transient	stationary	transient
0	3.96	3.92	-	-
1	3.84	3.80	3.64	3.60
2	3.80	3.77	3.61	3.57
3	3.78	3.74	3.57	3.53
4	3.77	3.73	3.54	3.50
5	3.76	3.72	3.51	3.47
6	3.76	3.73	3.48	3.43
7	3.77	3.74	3.44	3.40
8	3.79	3.75	3.40	3.36
9	3.79	3.76	3.37	3.33
10	3.90	3.84	3.36	3.32
11	3.98	3.96	3.37	3.33
12	-	-	3.40	3.35

Finally the peak response factors for the total shear and the storey displacements have been reported in fig.13 and fig.14, respectively, superimposing the stationary to the transient results for a direct comparison.

ACKNOWLEDGEMENTS

This work has been financially supported by grants of the National Research Council (CNR) and of the Ministry of Education (MPI).

REFERENCES

1. A. C. HEIDEBRECHT and B. STAFFORD SMITH 1973 Journal of the Structural Division, ASCE, Vol. 99, No. ST2. Approximate Analysis of tall Wall-Frame Structures.

2. A. K. BASU and A.K. NAGPAL 1980 Journal of the Structural Division, ASCE, Vol. 106, No.ST5. Frame-Wall Systems with Rigidly Jointed Link Beams.

3. A.K. BASU, A.K. NAGPAL and A.K. NAGAR 1982 Journal of the Structural Division, ASCE, Vol. 108, No. ST6. Dynamic Characteristics of Frame-Wall Systems.

4. A.K. BASU and G.Q. DAR 1982 Earthquake Engineering and Structural Dynamics, Vol. 10 615-631. Dynamic Characteristics of Coupled Wall-Frame Systems.

5. T. VON KARMAN and M. BIOT 1940 Mathematical Methods in Engineering. New York: Mc Graw-Hill.

6. A.C. ERINGEN 1958 Proceedings, 3rd U.S. National Congress of Applied Mechanics 141-151, Response of Tall Buildings to Random Earthquakes.

7. Y.K. LIN 1976 Mechanics Today, Vol 3, edited by S. Nemat-Nasser, Pergamon Press 93-124. Random Vibration of Periodic and Almost Periodic Structures.

8. E.H. VANMARCKE 1976 Seismic Risk and Engineering Decisions, C. Lommitz and E. Rosenblueth Editors, Elsevier, Amsterdam. Structural Response to Earthquakes.

9. D.E. NEWLAND 1975 Random Vibration and Spectral Analysis London: Longman.

10. R.W. CLOUGH and J. PENZIEN 1975 Dynamics of Structures. New York: Mc Graw-Hill.

11. J.H. WILKINSON 1965 The Algebraic Eigenvalue Problem. Oxford: Clarendon Press.

12. Y.K. LIN and T.J. MC DANIEL 1969 J. Engng. Ind. 91 1133-1141. Dynamic of Beam Type Periodic Structures.

13. G. AHMADI 1983 Int. J. Engng. Sci. Vol. 21, No 2, pp 93-102. Stochastic Earthquake Response of Structures on Sliding Foundation.

14. G.N. BYCROFT 1960 J. Engng. Mech. Div. ASCE 86, EM2, pp 1-16.

15. R. BERARDI, A. BERENZI and F. CAPOZZA 1981 Convegno del Progetto Finalizzato "Geodinamica" del CNR. Udine, 12-14 Maggio. Campania-Lucania Earthquake on 23 November 1980. Accelerometric Recordings of the Main Quake and Related Processing.

PEAK STATIONARY RESPONSE

—— p = 95%
--- p = 50%

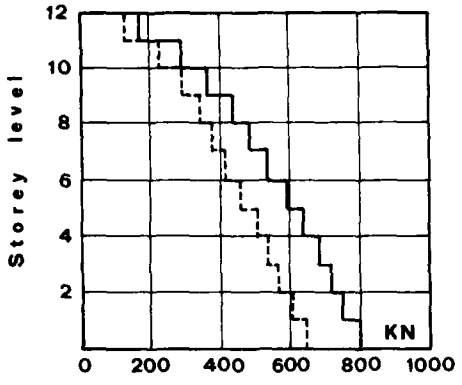

Fig.5 Total shear force

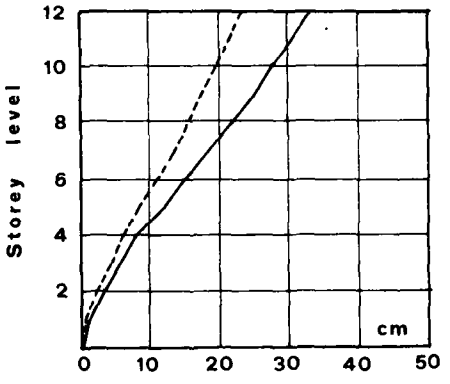

Fig.6 Displacement

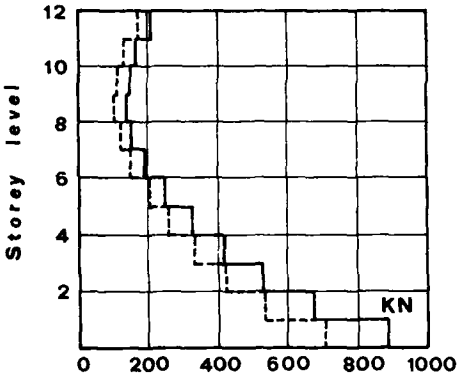

Fig.7 Shear force (wall)

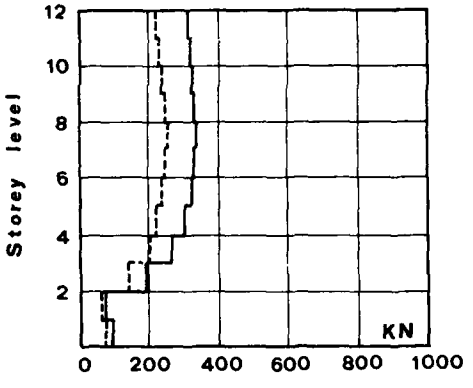

Fig.8 Shear force (frame)

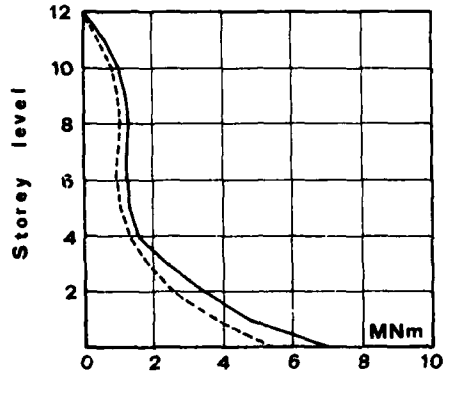

Fig.9 Bending moment (wall)

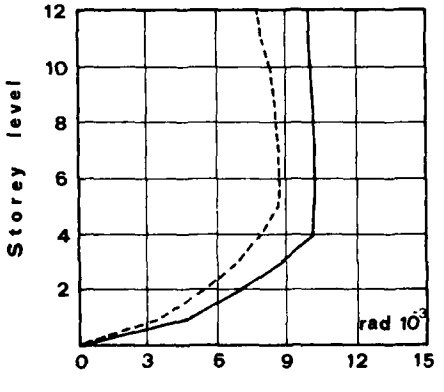

Fig.10 Rotation (wall)

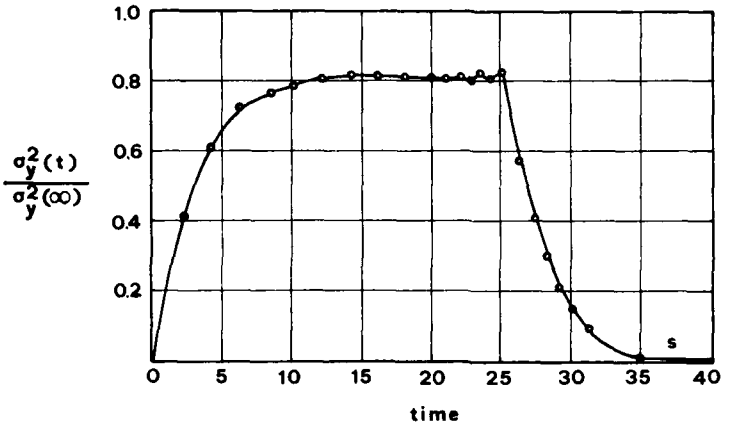

Fig.11 Variance of the top displacement

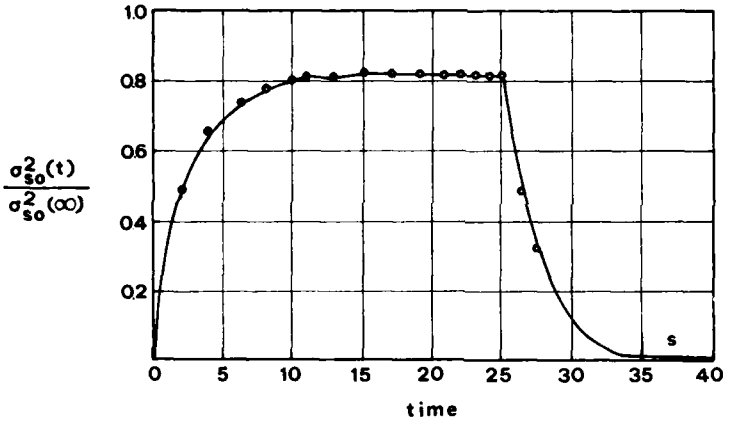

Fig.12 Variance of the total shear force at the base

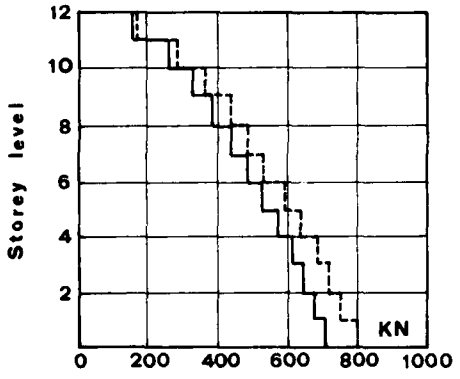

Fig.13 Peak total shear force
—— transient
--- stationary

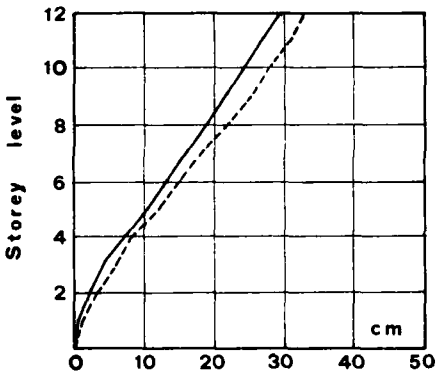

Fig.14 Peak displacement
—— transient
--- stationary

12. ROAD VEHICLES

DYNAMIC ANALYSIS OF VEHICLES WITH NONLINEAR SUSPENSION PROPERTIES[a]

John A. Lyons[1] and Levon Minnetyan[2]

Department of Civil and Environmental Engineering
Clarkson College of Technology
Potsdam, New York 13676
U.S.A.

1. INTRODUCTION

The analysis of complicated structural systems with both linear and nonlinear components by a conventional direct time-history integration of the equations of motion presents a formidable computational problem. The nonlinear force-displacement behavior, commonly known as material or constitutive-type nonlinearity, of one or more of the structural components may necessitate the reformulation as well as the solution of the system equations of motion at each time step. For many practical structures, the computational effort required is often too great to facilitate an economical solution. Clearly, a more efficient procedure would be of value. In this work, one such method is presented, as well as the results of an investigaiton of its use in solving a typical problem in the analysis of a particular class of structural systems.

The structural systems for which the present method, which will be referred to hereafter as the HYBRID method, appears to be well suited are those with a relatively small number of discrete but significant nonlinear components. Typically, these nonlinear elements are connected to the remaining linear-elastic substructures at a relatively small number of nodes. Further, the response of the nonlinear components is primarily affected by the lowest (most fundamental) frequencies and modes of vibration of the linear-elastic regions of the structure. Also characteristic of such structural systems is that the response of the linear-elastic substructures, which are generally quite complex, is sensitive to the higher vibration frequencies and modes. Determination of the internal forces, of particular interest in the design of such structures, is especially sensitive to inaccuracies in the analysis. Thus smaller time steps and a more accurately defined finite-element model are required to meaningfully determine the response of the complex linear-elastic substructures. A loosely categorized class of structural systems is thus identified. In what follows, these structures will be referred to as Complex Linear-Elastic Substructures with Discrete Nonlinear Components (CLS/DNC). Examples belonging to this class of structures include linear-elastic vehicle systems with nonlinear suspensions. Also included are such structures as taxiing aircraft or high speed rocket sleds. These structures have relatively large and complex linear-elastic regions coupled together by energy dissipating nonlinear couplers. Other examples may include space stations with vibration damping systems, or earthquake resistant buildings incorporating nonlinear fuse elements.

An aircraft taxiing over an irregular runway profile is an immediate

[a]Research sponsored by the Air Force Office of Scientific Research, Air Force Systems Command, USAF, under Grant Number AFOSR-82-0216. The United States Government is authorized to reproduce and distribute reprints for Governmental purposes notwithstanding any copyright notation thereon.

[1]Graduate Student

[2]Assistant Professor

candidate for analysis by the present HYBRID method. It is readily seen that this structure is a CLS/DNC type structure. The aircraft superstructure is essentially a highly complex linear-elastic substructure, and the suspension system (landing gear) is composed of a comparatively small collection of discrete nonlinear components which behave in a significantly nonlinear manner. It is known from past experience with such systems that the modelling of the linear substructure (aircraft) must be quite detailed, and that the higher vibration frequencies and modes are of importance in obtaining useful results from the dynamic simulation. It has also been found that the response of the nonlinear components is rather insensitive to the effects of the higher frequency modes of vibration of the linear elastic substructures. In essence, the response of the linear substructures and the nonlinear suspension components is decoupled with respect to all but the lowest vibration frequencies and modes [1].

The HYBRID method seeks to take advantage of this effective decoupling in the higher modes. The method incorporates a time-history analysis for the nonlinear response with a frequency domain analysis of the linear modes. First the time-history analysis including the nonlinear components and a small number of linear modes is conducted. Partial decoupling of the nonlinearities from the rest of the structure constitutes the second step. The remaining linear dynamic subsystem is analyzed through the frequency domain under external forces and interactions from the nonlinear components. Development of the HYBRID method for the analysis of a typical CLS/DNC structure is the subject of this paper.

2. NUMERICAL IMPLEMENTATION OF THE HYBRID METHOD

The HYBRID method is first evaluated by its application to a simple two-dimensional vehicle structure that is taxiing over an irregular runway profile. The vibration problem for the unconstrained vehicle is solved by an eigensolution algorithm based on the generalized Jacobi method with eigenvalue shifts and subspace iterations [2]. The solution of the eigenproblem supplies the vibration mode shape, natural frequency and generalized mass data which is needed both in time-history and frequency domain analyses. A validated computer program, TAXI, developed at the Air Force Flight Dynamics Laboratory [3], is used to perform the time-history analysis and to determine the nonlinear suspension strut forces. Typical nonlinear load-deflection relationships are used to represent the suspension gear properties [4]. A typical vehicle model that consists of twelve simple beam elements supported by nonlinear suspension struts is depicted in Fig. 1.

2.1 Computation of Time-History Nonlinear Forces

After the solution of the vibration eigenvalue problem for the unconstrained linear elastic vehicle structure, the equations of dynamic equilibrium are written in terms of the modal coordinates η

$$[M]\{\ddot{\eta}\} + [C]\{\dot{\eta}\} + [K]\{\eta\} = [\phi]^T\{F-F_s\} \qquad (1)$$

where

$[M]$ = generalized mass matrix
$[C]$ = modal damping matrix
$[K]$ = generalized stiffness matrix
$[\phi]$ = mode shape matrix
$\{F\}$ = applied external loading

The nonlinear load-displacement and load-velocity characteristics of suspension struts are taken into account in terms of the additional F_s nonlinear forces that depend upon the displacement and the rate of displacement of the landing

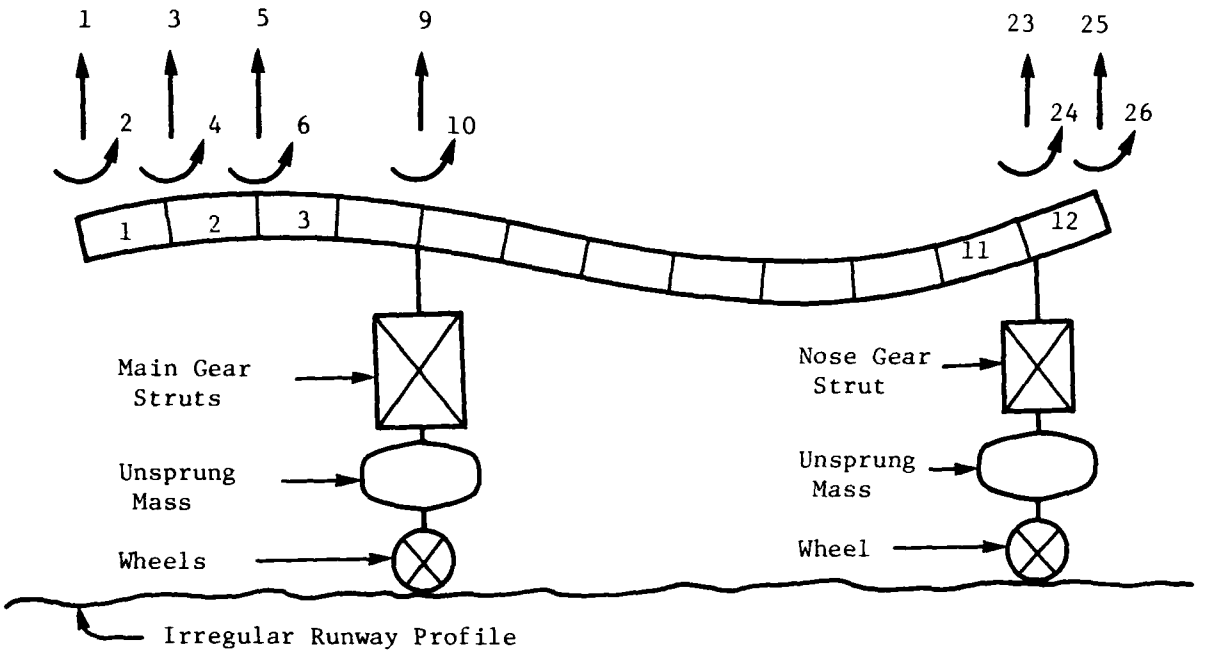

Fig. 1. Simple Beam Vehicle Model

gear. Accordingly, the nodal displacements corresponding to the landing gear attachment points must be calculated at each step during time-history integration to determine the F_s strut forces. Nevertheless, it is advantageous to formulate the generalized vibration problem with the unconstrained aircraft structure to make the rigid body modes orthogonal to the flexible modes and render the generalized mass matrix diagonal. With proper scaling of the mode shape vectors, the generalized masses corresponding to the rigid body modes become the aircraft total mass and mass moment of inertia [1].

The nonlinear force time-histories are first computed using Eq. (1) including a small number of flexible modes of the vehicle structure. For practical vehicle simulations it has been demonstrated that typically 5 to 10 flexible modes are satisfactory for the estimation of nonlinear suspension response [5]. Assuming that the response of the nonlinear components is contained primarily in the lowest modes permits a relatively efficient (in terms of computational effort) evaluation of these force-histories by direct integration. However, the dynamic response of the linear-elastic substructures, which in practical cases may be very large and complex, generally requires a highly detailed mathematical model and the necessary inclusions of the contributions from many modes. Using direct integration for the calculation of the dynamic response of displacements and internal forces or stresses to the accuracy required for such structures may involve an extremely large computational effort. This effort may be so large as to render a direct integration response solution impractical. An alternative to direct integration for the response analysis of complex linear-elastic structures is afforded by the use of frequency domain analysis. A greater number of modes can be considered at this second stage without concern for the time domain discretization refinement.

2.2 Frequency Domain Analysis for the Linear Structural Response

The basic conditions that permit a frequency domain analysis are that the nonlinear suspension strut forces are determined and the linear vehicle structure is represented by orthogonal generalized coordinates. At the beginning of the linear analysis, the previously determined nonlinear suspension forces are converted to the frequency domain by Discrete Fourier Transformation (DFT). The DFT coefficients are defined as [1,6]

$$C_n(\bar{\omega}_n) = \Delta t \sum_{\tau=0}^{N-1} F(\tau) e^{-2\pi i n\tau/N}; \quad n=0,\ldots,N-1 \tag{2}$$

where

$i = \sqrt{-1}$
$\Delta t = T/N$
T = total time period considered (includes an attached period of $F(t)=0$ to take into account the periodic nature of DFT)
τ = time step number
n = frequency step number
N = number of discrete time intervals in T
$\bar{\omega}_n$ = forcing frequency
$C_n(\bar{\omega}_n)$ = complex coefficients that define the discretized harmonic amplitude function in the frequency domain

The complex frequency response function, $H_j(\bar{\omega}_n)$, for each jth generalized structural mode under the forcing frequency $\bar{\omega}_n$ is defined as [6]

$$H_j(\bar{\omega}_n) = \frac{1}{-\bar{\omega}^2 M_j + i\,\bar{\omega}_n C_j + K_j} \tag{3}$$

where

M_j, C_j, K_j = jth generalized modal mass, damping, and stiffness, respectively

It can be shown that the total response of a system to any forcing input can be written by means of an inverse Fourier transformation. The displacements of the jth modal coordinate are given by [6]

$$\eta_j(\tau) = \mathrm{Re}\left\{\frac{\Delta\bar{\omega}}{\pi} \sum_{n=0}^{N-1} H_j(n) C_j(n) e^{2\pi i n\tau/N}\right\} - \frac{1}{K_j N} \sum_{\tau=0}^{N-1} F(\tau) \tag{4}$$

where

$\Delta\bar{\omega} = \dfrac{\bar{\omega}_N}{N}$ = frequency domain discretization step size

The structure nodal coordinate displacements can be obtained from the modal superposition equations

$$\{u(\tau)\} = [\phi]\{\eta(\tau)\} \tag{5}$$

Other response parameters such as stresses or loads developed in various structural components can be evaluated directly from the displacements, u. The elastic forces {f} which resist the deformation of the structure are given directly by the displacements and the structure stiffness coefficients

$$\{f(\tau)\} = [k]\{u(\tau)\} \tag{6}$$

where [k] is the structure nodal coordinate stiffness matrix. To obtain the internal forces at particular locations in the vehicle structure, the elemental stiffness matrices and the corresponding element vertex displacements are used.

$$\{f'(\tau)\} = [k']\{u'(\tau)\} \tag{7}$$

where prime indicates the quantities that are defined with respect to elemental vertex coordinates.

3. SIMULATED RESPONSE OF A SIMPLE VEHICLE MODEL

The intent in this work is to model a simple vehicle traversing an uneven surface. Nevertheless, the simple beam vehicle model physical properties are chosen such that the total mass and vibration characteristics are similar to a typical fighter aircraft. This choice enables the realistic utilization of the suspension system modelling routines included in the computer program TAXI [4].

The dynamic input for the vehicle model is provided by its traverse over an irregular runway profile. The traverse takes place at a velocity of 44 feet/second and lasts for 5.2 seconds. This represents a total runway length of 229 feet. From the starting point (horizontal station 0 feet) until the taxiing vehicle model arrives at station 106 feet, the surface is perfectly smooth. At horizontal station 106, a 4 foot 'up-ramp' is encountered. This ramp slopes from zero elevation to 1.5 inches elevation at station 110. Past station 110, the ramp ends and the profile is again perfectly smooth and horizontal until station 180 is reached. Here, a 'down-ramp' begins, defined exactly as a mirror image of the up-ramp just described. The ramp ends at station 184, and the profile is smooth until the end of the traverse at station 229. This runway profile is an idealization of the standard AM-2 runway repair mat.

As a first trial analysis for the vehicle model and dynamic input just defined, an attempt is made to validate a basic assumption of the HYBRID method: that the response of the nonlinear components is essentially decoupled from all but the lowest flexible modes of the elastic substructure. For this purpose, the simple beam vehicle is modelled with 12 beam elements as depicted in Fig. 1. When the orthogonal transformation to modal coordinates is applied to this 26 degree of freedom system only the first 12 flexible modes are deemed sufficiently accurate for further analysis.

To determine the validity of the assumption that the nonlinear component response is affected primarily by the lowest modes of vibration, three trial response calculations are conducted. For the first calculation, the number of flexible modes to be included in the time-history analysis for the determination of the nonlinear strut forces is set to 12. In the second and third response calculations, the flexible mode content is reduced to six, and then to four The time step Δt used in the time-history analysis step is 0.00025 seconds. Stability and convergence studies have determined this stepsize to be sufficiently small for all numerical results presented in this paper [7].

The flexible mode content used in the frequency domain step is always set to 12. This is in keeping with the intended function of this step in a practical application. This function is the detailed response calculation of the elastic substructure which typically requires the inclusion of many more modes than does the time-history calculation of the nonlinear component response. The frequency domain step receives the nonlinear force time-history data at time increments $\Delta\tau$ of 0.002 seconds. The significant dynamic loading takes place only when the vehicle model is encountering the 78 foot long AM-2 runway repair mat. At the 44 foot/second velocity of the traverse, this takes 1.77 seconds for each of the two landing gear struts. But, since this loading is not periodic (as is required for frequency domain analysis) it must be made

AD-A143 301 PROCEEDINGS OF THE INTERNATIONAL CONFERENCE ON RECENT ADVANCES IN STRUCTU..(U) SOUTHAMPTON UNIV (ENGLAND) INST OF SOUND AND VIBRATION RESEAR.. M PETYT ET AL. 4/6

UNCLASSIFIED 1984 F/G 20/11 NL

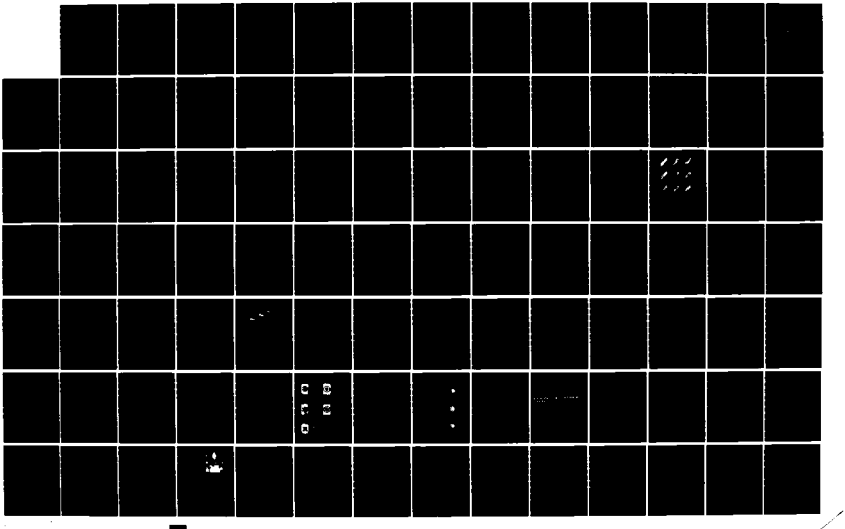

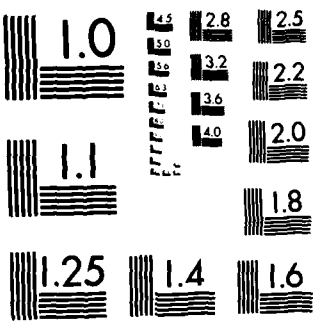

so by attaching a relatively long period of zero loading [6]. A total of N=4096 increments of $\Delta\tau$=0.002 seconds each is specified to define an extended loading period T of 8.19 seconds. Convergence studies have shown that not much improvement is to be gained by using a larger value of T [7].

In the typical structures considered in this paper, the response of the nonlinear components is assumed to be contained primarily in the lowest modes. This assumption is based on the actual measured response of certain dynamically tested structures with discrete nonlinearities (such as instrumented aircraft) [8]. To determine the validity of this assumption that the nonlinear component response is affected primarily by the lowest modes of vibration, three trial response calculations were conducted. For the first calculation, the number of flexible modes to be included in the time-history analysis for the determination of the nonlinear strut forces was set to 12. In the second and third response calculations, the flexible mode content was reduced to six, and then to four. The results of these simulations verify that the response of the nonlinear components is essentially affected only by the lowest 6 modes of the linear vehicle [1,7]. There is also evidence that the number of flexible modes needed at the first stage of the HYBRID method is independent of the complexity of the vehicle structure or the refinement of its discretized model [7]. Thus, one major conclusion drawn from these initial studies was that for the vehicle model considered, the nonlinear force response is affected primarily by the lowest half dozen or so flexible modes of the linear substructure.

In Figs. 2 and 3 simulations are presented which depict the present stage of refinement of the HYBRID method as compared to conventional time-history results. In these figures the HYBRID simulations are represented by the solid lines and the TAXI simulations are given by the broken curves. Fig. 2 depicts the comparison of the HYBRID and TAXI simulations for the internal shear force at coordinate 5 and Fig. 3 compares the bending moment simulations at coordinate 6. The coordinate numbers represent the internal force response locations as referenced in Fig. 1. The response predicted by the HYBRID method does not differ significantly from the response computed by conventional time-history analysis, as conducted by the TAXI program. Thus, the contention of this paper in demonstrating the HYBRID method as a viable alternative to the more traditional time-history analysis has been accomplished. However, the general procedural aspects of the overall numerical solution presented here must be significantly improved before the method can be used efficiently for realistic transient response simulations. In particular, conducting a frequency domain analysis for the entire response period is not practical. Breaking down the total time history into smaller segments would be more effective in terms of the proper utilization of available computer memory to achieve a better representation of the frequency response. A subdivision of the total time period can be accomplished by considering the fundamental nonlinear response period as one unit of time in which a frequency domain analysis is conducted. This approach would also allow the implementation of a HYBRID-Iterative procedure in which frequency domain analysis is conducted interactively with conventional time history analysis.

Finally, it is believed that the HYBRID procedure can be quite useful for the transient response analysis of complex structures with nonlinear components. Nonetheless, much work needs to be done to establish the optimal numerical details of this procedure.

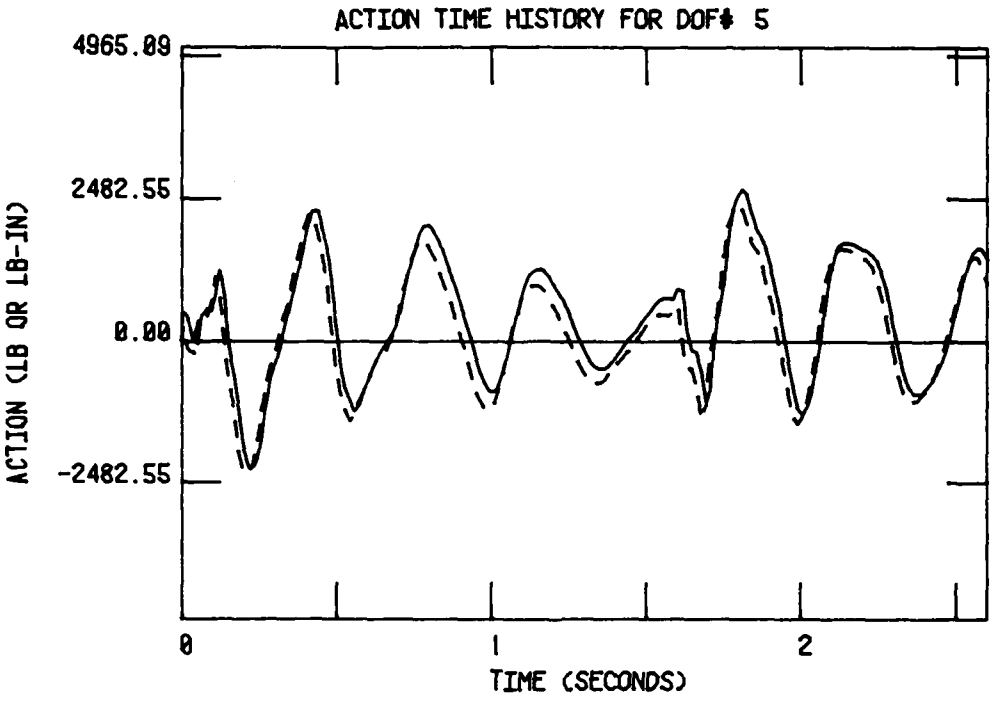

Fig. 2. Comparison of Shear Force Response Simulations

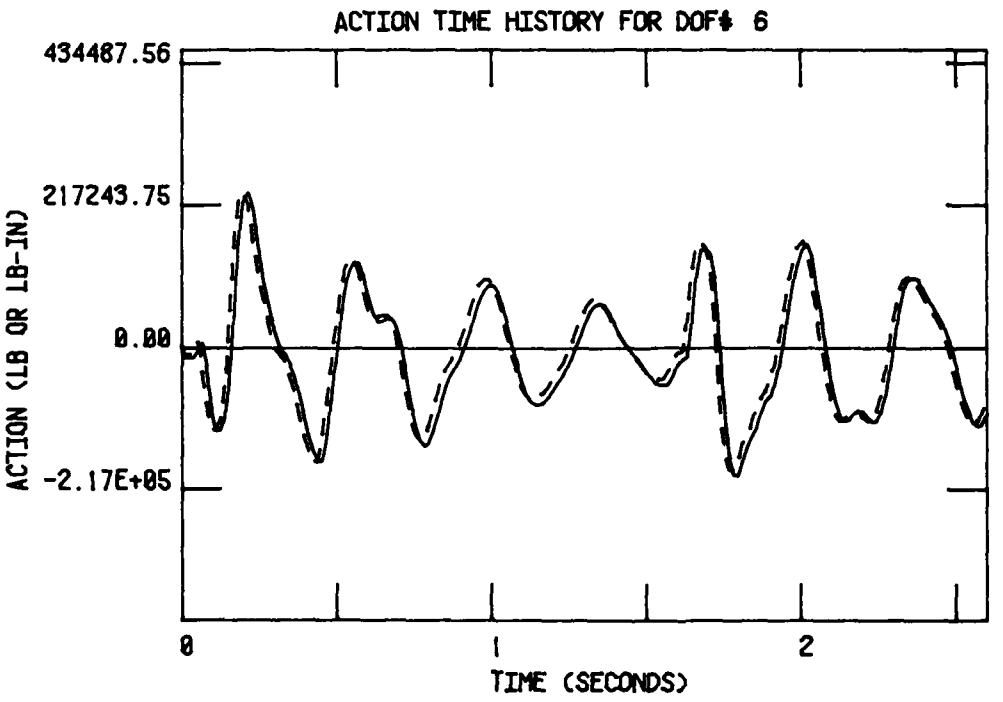

Fig. 3. Comparison of Bending Moment Response Simulations

4. REFERENCES

1. L. MINNETYAN, J.A. LYONS and T.C. GERARDI 1983 53rd Shock and Vibration Bulletin, Part 2, 63-77. Dynamic Simulation of Structural Systems with Isolated Nonlinear Components.

2. K.-J. BATHE 1982 Finite Element Procedures in Engineering Analysis, Prentice Hall.

3. A.G. GERARDI 1977 AFFDL-TR-77-37, Air Force Flight Dynamics Laboratory, Wright-Patterson AFB, Ohio. Digital Simulation of Flexible Aircraft Response to Symmetrical and Asymmetrical Runway Roughness.

4. T.G. GERARDI and J.T. RIECHERS 1981 Report No. AFWAL/FIBE-81-1. Test and Evaluation of the High Pressure Strut Concept on the F-4 Main Landing Gear.

5. T.G. GERARDI and L. MINNETYAN 1982 AGARD Conference Proceedings No. 236, Aircraft Dynamic Response to Damaged and Repaired Runways. Status of computer simulations of USAF aircraft and an alternative simulation technique.

6. R.W. CLOUGH and J. PENZIEN 1975 Dynamics of Structures. McGraw-Hill.

7. J.A. LYONS 1983 M.S. Thesis, Department of Civil and Environmental Engineering, Clarkson College of Technology. Simulation of the Dynamic Response of Structures with Discrete Constitutive Type Nonlinearities by a New Hybrid Method.

8. T.G. GERARDI and D.L. MORRIS 1982 52nd Shock and Vibration Bulletin, Part 3, 131-143. An Assessment of the A-10's Capability to Operate on Rough Surfaces.

A STATE SPACE APPROACH TO THE ANALYSIS OF NONSTATIONARY, NONLINEAR RANDOM VIBRATION WITH PARTICULAR APPLICATION TO THE PROBLEM OF VEHICLES ON ROUGH GROUND

R.F. Harrison and J.K. Hammond

Institute of Sound and Vibration Research
University of Southampton

1. INTRODUCTION

The dynamic response of vehicles to uneveness in the underlying surface on which they are travelling is of obvious engineering interest both for reasons of ensuring structural integrity and to ensure safe handling and a comfortable ride. The problem has therefore received a great deal of attention in the literature over a number of years.

Clearly 'uneveness' may take various forms, for instance one may describe a badly potholed road as uneven. However, this class of problem is generally best treated as a deterministic one. Another type of uneveness is that which admits only a statistical description, i.e., it may be regarded as a realisation of a random process and it is this class of uneveness, termed roughness throughout this paper, which is of interest here. In general, a rough surface is 'perceived' by the vehicle as a non-stationary random process when regarded as a temporal (time dependent) input due either to inhomogeneity (spatial non-stationarity) in the surface roughness or to variations in the vehicle velocity, or both. Analysis of the response of vehicles to such processes is further complicated by inherent non-linearity in their dynamics, rendering exact statistical analysis analytically intractable.

Previously, analysis of the non-stationary response of vehicles modelled by linear dynamics has been successfully accomplished (for a single input and the surface roughness considered homogeneous) by classical impulse response techniques or by an evolutionary spectral method in the spatial domain, while, to the best of the authors' knowledge the non-stationary, non-linear vehicle problem has not been successfully tackled at all, unless perhaps by numerical simulation. There exists, therefore, no unified approach to this very general problem and furthermore the problems of multiple inputs (wheels) and spectral representation for the non-stationary, linear case, have been largely ignored and so it was felt that the whole problem should be re-addressed in an attempt to provide a unified approach. This paper presents just such an approach, drawing on selected parts of the thesis by Harrison [1].

The methods presented have been developed using a 'systems' approach. Basically this approach assumes that the physical systems to be analysed admit a state-space representation (i.e., representation by ordinary differential equations) following which a large body of powerful, analytical techniques are available.

The vehicle dynamics are modelled by ordinary differential equations in the time domain whilst the excitation process is modelled by a differential equation, cast in the spatial domain and driven by a spatially 'white' process. The key novel feature is the linking of the two domains via the vehicle's variable velocity enabling the dynamic equations to be augmented by the excitation ones (having time variable coefficients). The link is made by drawing on some results from the theory of generalised functions. For linear systems, the analytical techniques referred to above become immediately applicable, in

particular, differential equations governing the first two statistical moments may be derived for both single and multiple inputs. Furthermore, this augmented system, after some further analysis becomes amenable to evolutionary spectral representation (i.e., decomposition of power in a signal over frequency at each time instant). Hitherto, the particular class of non-stationarity associated with the vehicle problem has not responded to this approach.

Non-linear systems may also be written in the state-space form, but obviously the linear theory no longer has application. However, the linearization technique known as statistical linearization is well suited to the linear systems approach mentioned above, since the linearized elements depend on the instantaneous mean and variance of the system response and, hence, fit directly into the formulation. Using this technique in conjunction with the space domain excitation model enables the approximate analysis of non-linear systems subject to non-stationary random excitation to be carried out.

It is not proposed to give a review of other approaches to this problem. This has been discussed in an earlier paper by Hammond and Harrison [2].

2. THEORY

This section briefly describes the general theory applicable to the class of process described above for both linear and non-linear systems. The following section will show how this relates to the vehicle problem.

2.1 Linear Systems

Consider a linear dynamical system described by the state equation

$$\dot{\underline{x}} = A(t)\underline{x} + B(t)\underline{w}(t); \qquad \underline{x}(t_o) \tag{1}$$

where $\underline{x}$ is an n dimensional state vector
and $\underline{w}$ is an m dimensional zero mean white noise vector with

$$E\left[\underline{w}(t_1)\underline{w}^T(t_2)\right] = Q(t)\delta(t_1 - t_2) \tag{2}$$

$A(t)$, $B(t)$ and $Q(t)$ are (possibly time varying) matrices of appropriate dimension.

It is well known that the first and second moments of $\underline{x}$ may be expressed as solutions of differential equations (see ref. [2]). For example, the zero lag covariance matrix $P(t) = E\left[\underline{x}(t)\underline{x}^T(t)\right]$ satisfies

$$\dot{P} = A(t)P + PA^T(t) + B(t)Q(t)B(t); \quad P(t_o). \tag{3}$$

Both (1) and (3) require appropriate initial conditions, $\underline{x}(t_o)$ and $P(t_o)$.

If input $\underline{w}(t)$ is 'non white' then it is often possible to consider a shaping filter representation for the input and model it as the output of another dynamical system that is white noise driven. The original process is then augmented by the second system to yield an overall white noise driven system for which the above theory applies.

It is essentially this concept that requires further generalisation for our purposes, namely that the input $\underline{w}(t)$ may have a very different form. More specifically, in a number of physical problems it may occur that the input

process to a system is more naturally described in some domain other than time. For instance, in the problem of vehicle motion on rough ground, it is convenient to consider the excitation process as a spatial process. Another problem, namely that of noise sources moving relative to an observer, is very conveniently formulated by considering the noise to be a function of the time frame of the source (see Hammond *et al* [3]). In both of these cases, a non-linear distortion of the independent variable axis occurs as a result of considering the natural domain of the excitation process as a function of time. For instance, in the vehicle problem, the space variable may be considered as a function of time, the two domains being related by the vehicle velocity. This distortion introduces a non-stationarity into the excitation process as 'perceived' by the vehicle or observer even if the underlying excitation is homogeneous. This class of non-stationarity is usually referred to as 'frequency modulated'.

It is emphasised that the linking of the two domains is central to all the work herein, enabling a large number of different situations to be treated in a unified way. In this section, however, the physical interpretation of such models is ignored whilst the theoretical ideas are presented.

The aim here is to augment a system, whose temporal response is required and whose equations are therefore cast in the time domain, with an excitation process which has a shaping filter representation in some domain other than time, s, say (not necessarily space) but which may itself be regarded as a function of time, i.e., $s = s(t)$.

Consider the system given by:

$$\dot{\underline{x}} = A(t)\underline{x} + B(t)\underline{i}(t); \qquad \underline{x}(t_o) \tag{4}$$

where $\underline{i}(t)$ denotes an input to the system.

Let us express $\underline{i}(t)$ in terms of another vector $\underline{u}$ which is *primarily a function of* s, and where the notion of time only occurs when we allow s to be written as a function of time. We shall denote $\underline{u}(s)$, when regarded as a function of time, as $\tilde{\underline{u}}(t) = \underline{u}[s(t)]$ and write

$$\underline{i}(t) = L(t)\tilde{\underline{u}}(t).$$

It is now necessary to express $\underline{u}(s)$ in shaping filter form *in the* s *domain*, i.e., we write

$$\underline{u}(s) = F(s)\underline{v}(s) + E(s)\underline{w}(s) \tag{5}$$

where

$$\frac{d\underline{v}(s)}{ds} = C(s)\underline{v}(s) + D(s)\underline{w}(s); \qquad \underline{v}(s_o) \tag{6}$$

$\underline{w}(s)$ is a 'white in s' vector and the other matrices and vectors introduced are of appropriate dimension.

Now, in order to augment (4) with (5) and (6), it is first necessary to make a formal change of variable and substitute $s = s(t)$, $s_o = s(t_o)$ into (5) and (6) and convert the differentiation operation accordingly, i.e., $\frac{d}{ds}(\ ) = \frac{1}{\dot{s}(t)}\frac{d}{dt}(\ )$, yielding

$$\tilde{\underline{u}}(t) = \tilde{F}(t)\tilde{\underline{v}}(t) + \tilde{E}(t)\underline{w}(s(t)) \tag{7}$$

$$\frac{d}{dt}\tilde{\underline{v}}(t) = \dot{s}(t)\tilde{C}(t)\tilde{\underline{v}}(t) + \dot{s}(t)\tilde{D}(t)\underline{w}(s(t)); \quad \tilde{\underline{v}}(t_o) \tag{8}$$

where $\tilde{}$ denotes a function of s regarded as a function of time.

Equation (4) may now be augmented to yield

$$\frac{d}{dt}\begin{bmatrix}\underline{x}\\ \tilde{\underline{v}}\end{bmatrix} = \begin{bmatrix}A & BL\tilde{F}\\ 0 & \dot{s}(t)\tilde{C}\end{bmatrix}\begin{bmatrix}\underline{x}\\ \tilde{\underline{v}}\end{bmatrix} + \begin{bmatrix}BL\tilde{E}\\ \dot{s}(t)\tilde{D}\end{bmatrix}\underline{w}(s(t)); \quad \begin{bmatrix}\underline{x}(t_o)\\ \underline{v}(t_o)\end{bmatrix} \tag{9}$$

This is a form similar to equation (1) but with one important difference, namely, the driving term, because of the variable transformation, is now, in general, a 'non-stationary white-noise' having a non-linearly dilated time axis.

By redefining variables, equation (9) may be written as

$$\dot{\underline{x}} = A(t)\underline{x} + B(t)\underline{w}(s(t)); \qquad x(t_o) \tag{10}$$

and it is this equation that forms the basis of the various analyses presented. (N.B. $A(t)$, $B(t)$ in (10) are *not* the same as those in (1).)

2.1.1 Equations for the evolution of the first and second order moments

In this section two differential equations governing the evolution of the mean vector and zero-lag auto covariance matrix, are presented (refer to [1, 2] for proofs). These equations constitute the time domain method for the non-stationary analysis of linear systems.

If the mean value of the white process is given by $E[\underline{w}(s)] = \underline{\nu}(s)$ then the equation governing the mean vector, obtained by taking the expectation of (10), is given by

$$\dot{\underline{\mu}} = A(t)\underline{\mu} + B(t)\tilde{\underline{\nu}}(t); \qquad \underline{\mu}(t_o). \tag{11}$$

The differential equation governing the propagation of the zero-lag covariance matrix $P(t)$ may be shown to be

$$\dot{P} = A(t)P + PA^T(t) + B(t)\tilde{Q}(t)B^T(t)/\dot{s}(t); \quad P(t_o) \tag{12}$$

with $\dot{s}(t) > 0$. It may be argued that in many cases the singularity at $\dot{s}(t) = 0$ is removable and simple zeros are permitted, i.e., $\dot{s}(t) \geq 0$. Equation (12) is very similar to (3); however, it differs in one important respect, which is the factor of $\dot{s}^{-1}(t)$ in the third term.

2.2 Non-linear Systems

For a class of non-linear systems it is possible to use statistical linearisation and combine it with the state formulation above and so consider the approxi-

mate evolution of the mean and covariance of the response of the non-linear system. This is very briefly summarised below and reference is made to [1] for full details.

The dynamic system is now written

$$\dot{\underline{x}} = \underline{f}(\underline{x}) + B\underline{i}(t); \qquad \underline{x}(t_o) \tag{13}$$

i.e., (4) is generalised. $\underline{i}(t)$ has its previous meaning with equations (5)-(8) holding as before.

The augmented system is *non-linear and time variable* (due to the variable $\dot{s}(t)$) and in order to use the results of the previous section the non-linearity is approximated using statistical linearisation writing

$$\underline{f}(\underline{x}) \simeq \underline{n}_o + N_1\underline{x}. \tag{14}$$

n_o and N_1 are found by least squares techniques (e.g., ref. [4]) and may be shown to depend on the means and variances to be found, thus yielding a set of *non-linear* equations for the means and variances of the augmented system (see Chap. 4 of ref. [1]). This method of solution is referred to as the CADET method (ref. [4]) abbreviating the phrase Covariance Analysis by DEscribing function Technique.

2.2.1 Covariance equivalence and evolutionary spectra

An important aspect that has arisen out of the above discussions relates to an interpretation of equation (10). (For convenience assume $w(s(t))$ is a scalar process.) From the derivations above it is possible to argue that

$$E\{w[s(t_1)]w[s(t_2)]\} = \frac{\delta(t_1 - t_2)}{\dot{s}(t)}, \quad \text{if } \dot{s} > 0 \tag{15}$$

i.e., $w[s(t)]$ has the covariance characteristics of a *non-stationary* white noise $w_1(t)/\sqrt{\dot{s}(t)}$, say, where $w_1(t)$ is white and stationary with $E[w_1(t_1)w_1^1(t_2)] = \delta(t_1 - t_2)$. In this sense, $w[s(t)]$ is 'covariance equivalent' to $w_1(t)/\sqrt{\dot{s}(t)}$, and accordingly we can also conceive of a vector $\underline{x}_1(t)$ that is covariance equivalent to $\underline{x}(t)$ (in (10)) satisfying

$$\frac{d}{dt}\underline{x}_1(t) = A(t)\underline{x}_1(t) + B(t)\frac{w_1(t)}{\sqrt{\dot{s}(t)}} \tag{16}$$

From this it follows that the evolutionary spectral density (matrix) for $\underline{x}_1(t)$ may be expressed starting with the spectral form for $w_1(t)$. Full details are given in reference [3].

3. VEHICLE EXAMPLE

For simplicity a single degree of freedom dynamic system is chosen as a representation for a vehicle (see Fig. 1) having a (non-linear) damper $f_2(\dot{z})$. The spring $f_1(z)$ is assumed linear. The damping is taken to consist of a (small) linear term and a nonlinearity of the form

$$f_2(\dot{z}) = \begin{cases} \dot{z}^2 & \dot{z} \geq 0 \\ -r\dot{z}^2 & \dot{z} < 0 \end{cases} \tag{17}$$

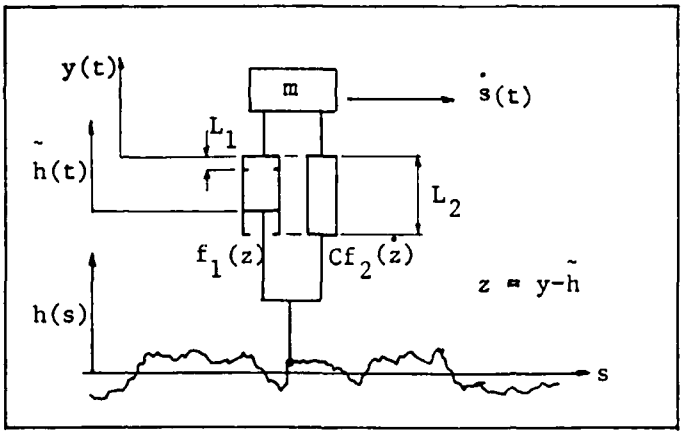

Fig. 1 Simplified undercarriage model.

where $\dot{z}$ $(= \dot{y} - \dot{\tilde{h}})$ is the relative or closure velocity. $y(t)$ is the absolute mass displacement and $\tilde{h}(t)$ is the ground profile, a functio· of space, regarded as a function of time, as before.

A second order spatial shaping filter model for the height profile is taken as

$$\frac{d^2}{ds^2} h + (\alpha + \beta)\frac{d}{ds} h + \alpha\beta h = k\, w(s) \qquad (18)$$

where α is the cut-off wavenumber of the ground profile spectrum, β is the cut-off wavenumber of the 'rolling contact filter' (see [1]) and k $(= \sqrt{2\alpha}\ \beta\sigma)$ ensures that the variance of the true ground profile $= \sigma^2$, so that the variance of $h(s) = \beta\sigma/(\alpha + \beta)$.

The justification for this second order model is given in [1].

Only some results are presented here, the details of the combination of the dynamics and road being found in [1]. Sample results for the case of a vehicle undergoing constant acceleration from rest is shown in Figs. 2. σ^2 denotes the ground roughness variance; $\gamma = C/m$; ω_o is the undamped natural frequency of the (linear part) of the system; ζ relates to the (light) linear damping; a is the acceleration in m/s^2; Both the mean and variance are normalised closure displacements relative to σ, i.e.,

$$\mu_1 = E\left[\frac{z}{\sigma}\right] \quad \text{and} \quad p_{11} = E\left[\frac{(z - \mu_1)^2}{\sigma^2}\right].$$

Figure 2 depicts the non-stationary behaviour of the mean and variance of normalised, relative displacement for both symmetric and asymmetric configurations.

The 'smooth' line is the result of the solution of the CADET (plus shaping filter) approach and the more ragged line the result of ensemble averaging 2000 simulations. 99% confidence limits are given for the simulation results. Notice that in each case the variance of response (Figs. 2a and 2c) exhibit similar characteristics, although in the symmetric case the amplitudes are lower and the non-stationary behaviour slightly less vigorous, i.e., the 'peak' is broader and the decay less steep. Naturally, the mean value for the symmetric case is zero

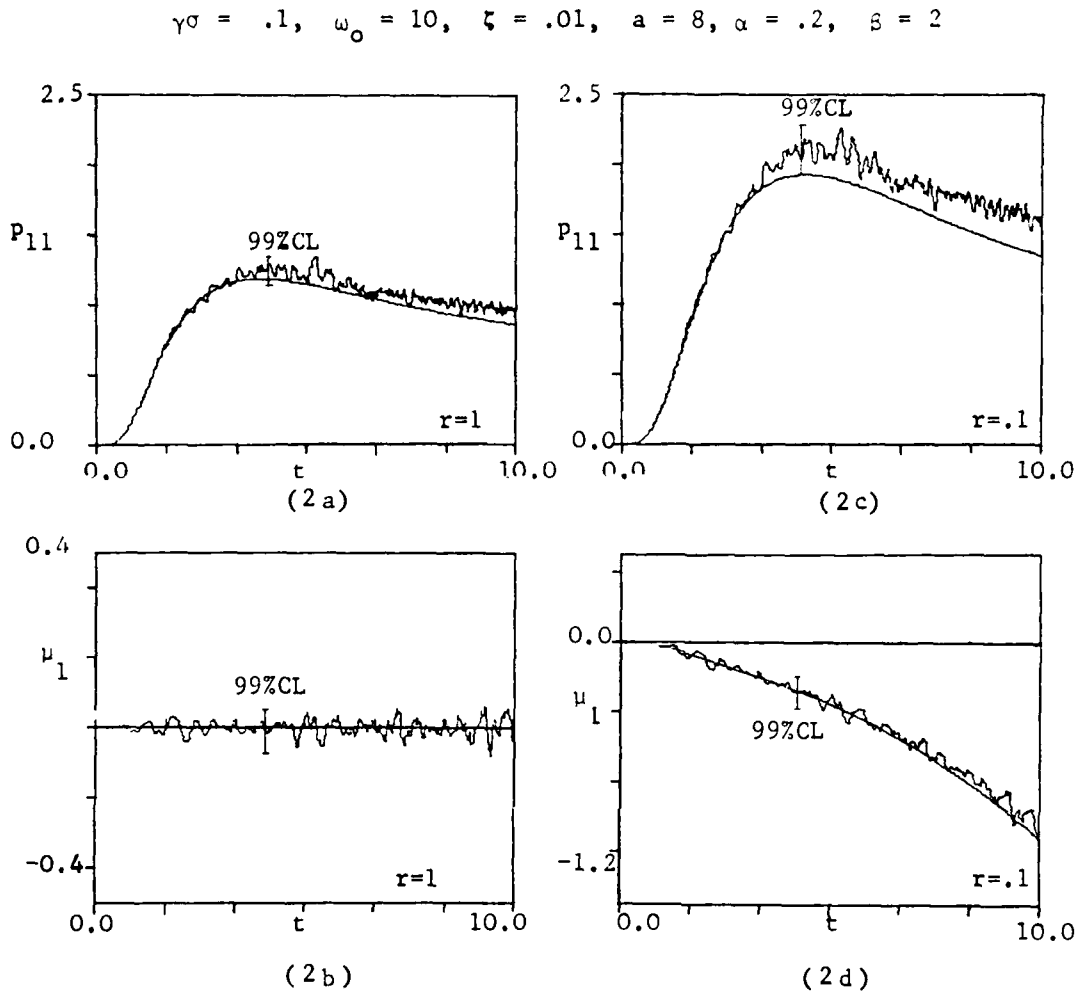

Fig. 2. Normalised mean and variance of response, quadratic damping - constant acceleration.

(Fig. 2b) and as would be expected from the asymmetric case (Fig. 2d) the mean value becomes increasingly negative as time (hence velocity) increases.

It is clear that the CADET results lie close to the simulated values (2000 realisations) and that the approximate results are of comparable accuracy to the simulation. It is also apparent that as time (velocity) increases, the accuracy of the CADET results decreases.

4. CONCLUDING REMARKS

This paper has presented the basis of a unified approach to the treatment of the response of vehicles travelling over rough ground and the discussion of the basic theory has been the prime consideration. Several aspects have been omitted in the interests of brevity, specifically three important aspects are noted below.

(i) It has been *assumed* that spatial shaping filters are satisfactory descriptors for rough ground. This aspect has been treated in some depth in ref. [1] where rough ground profiles have been analysed using maximum entropy spectral analysis methods to yield auto regressive shaping filters, which in turn have been converted to continuous domain state space forms so as to tie in with the theoretical formulation.

(ii) The evolutionary spectral forms for covariance equivalent processes have been alluded to. This, too, has been applied in ref. [1] to the vehicle problem and evolutionary spectra for the response of accelerating vehicles have been computed.

(iii) Multiwheel systems introduce particular difficulties. These have been considered in [1] where analytic and computational techniques are presented to deal with the problem.

REFERENCES

1. R.F. HARRISON 1983 Ph.D. Thesis, ISVR, University of Southampton. The Nonstationary Response of Vehicles on Rough Ground.

2. J.K. HAMMOND and R.F. HARRISON 1981 Trans. ASME Journal of Dynamic Systen Measurement and Control, Sept. 245-250. Nonstationary response of vehicles on rough ground - A state space approach.

3. J.K. HAMMOND, Y.H. TSAO and R.F. HARRISON 1983 Proc. Int. Conf. Acoustics, Speech and Signal Processing, Boston. Evolutionary spectral density models for random processes having a frequency modulated structure.

4. A. GELB and R.S. WARREN 1972 AIAA Conference on Guidance and Control, Stanford, Calif. AIAA Paper No. 72-875. Direct statistical analysis of non-linear systems - CADET.

13. RAILWAY VEHICLES

DYNAMIC MODELLING OF RAILWAY TRACK AND WHEELSETS

S L Grassie

Department of Engineering
University of Cambridge

1. INTRODUCTION

Our understanding of the dynamics of railway track and of the wheels and vehicles which run over it has increased enormously in the last decade. This development has been demanded by railway administrations themselves: faster trains require better standards of track, but have also caused damage of unforeseen severity. This damage has arisen largely from dynamic loading caused by wheelflats, railjoints, dipped welds, corrugation, poorly ballasted sections of track and the like. An understanding of track movement can suggest improved designs of track and ways in which present maintenance costs can be reduced. The development of more sophisticated mathematical models of track and wheelset has been made feasible by the computing resources which are now commonly available, but need not always be exploited to their fullest extent.

The purpose of this paper is to discuss some of the developments which have been made in modelling the system of vehicle and track, what results and conclusions have been drawn from these investigations, and some areas in which is inadequate. The emphasis here is on the vertical dynamic response, although consideration is also given to lateral and longitudinal dynamics. It is important to the practising engineer who has an inelastic timetable and meagre computing resources to know when the sophistication of complex models is unnecessary: this paper discusses what should be included in a model and what is superfluous.

The frequency range of interest is 5 - 2000 Hz because it has been found [1] that these frequencies are the most significant for dynamic loading of track. The components of the system are considered in a downward sequence from the vehicle in Section 2, through the wheel/rail contact in Section 3 to the track in Section 4. The components are combined in Section 5 and a review of the subject is made in Section 6.

2. MODELLING THE VEHICLE

The unsprung mass of a vehicle (Fig. 1) includes the wheelset, brakes, bearing boxes and the like, which are attached to the bogie by the primary suspension. Jenkins et al [2], in an investigation of vertical dynamic forces between wheel and rail, quote values of the unsprung mass and primary suspension stiffness per axle of a British Rail (BR) Class 87 locomotive to be 3160 kg and 3.3 MN/m respectively. It is reasonable to assume that the unsprung mass is increasingly well isolated from the rest of the vehicle at frequencies above its 5 Hz resonance on the suspension, and that this is the case for lateral and longitudinal motion as well as for vertical. The bogie therefore exerts just a dead load P_o on the unsprung mass. The dynamic response of the unsprung mass at higher frequencies is the concern of this section.

2.1 Radial Excitation

It has generally been accepted that the wheelset is adequately modelled as a rigid body for radial excitation at the wheel tread. At frequencies below 50 Hz the effective mass for excitation at a single wheel can be taken as half the total unsprung mass (i.e. about 1600 kg). Using this assumption, Jenkins et al [2] have obtained reasonable agreement between calculated and observed low frequency forces under a passing locomotive.

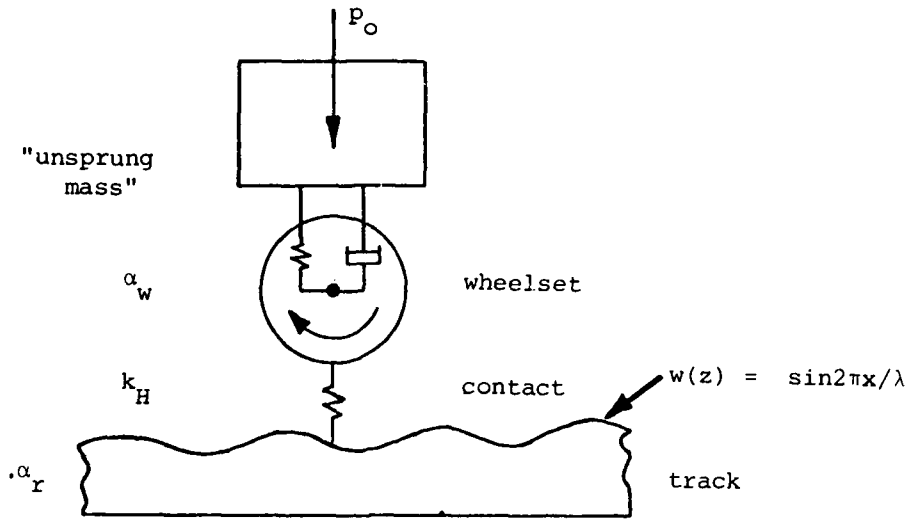

Fig. 1: Model of unsprung mass on track

Remington [3] shows experimental data of the radial response of a wheel mounted in a standard US Pullman bogie. For frequencies in the range 50 - 1000 Hz he finds that the wheel is adequately modelled as a mass equal to the wheel mass plus ⅓ of the axle mass. At higher frequencies, the wheel rim moves increasingly on the radial flexibility of the web: a better model of the wheel is then an infinite beam of the same cross-sectional dimensions as the rail. Munjal and Heckl [4] represent the wheel as a thin ring bending in its own plane, but do not support this with experimental data.

A typical BR wheelset has been represented by the idealised wheelset of Fig. 2 [5]. The model wheelset is assumed to be undamped, which is justified by the fact that the damping factor in each mode of a freely-supported BR wheelset lies in the range 2×10^{-4} to 110×10^{-4} [6]. It was found that resonances of the free wheelset affect its response only in narrow frequency ranges, and that it is otherwise modelled adequately as the mass of a single wheel: this is typically 350 kg. Deformation in the plane of the wheel was neither modelled nor examined experimentally. Because a wheelset is not held freely in its bearings, it is reasonable to include some of the axle mass in the effective mass of the wheel. Remington [3] suggests that ⅓ of the axle mass be included, while a figure of ½ is suggested elsewhere [7].

The author is aware of no published data to show at what frequency vibration of the wheelset becomes decoupled from that of the rest of the unsprung mass. At present, the best model of a typical locomotive wheel is a rigid body of 1600 kg mass below 50 Hz and 500 kg mass above this frequency.

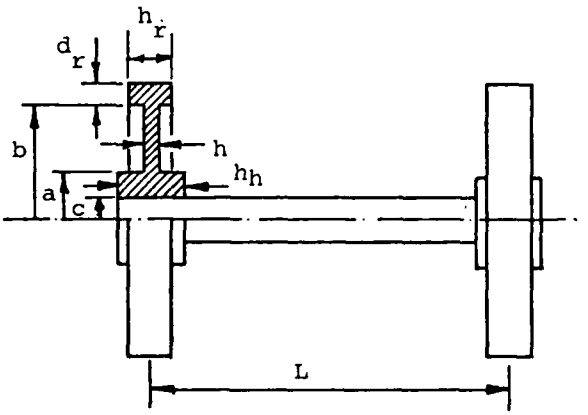

Fig. 2: Idealised wheelset

2.2 Lateral Excitation

The majority of analyses of lateral excitation of a railway wheel have arisen from a concern with wheel/rail noise. Because the wheel web is an efficient radiator of acoustic energy, both Arai [8] and Remington [3] have represented the wheel as a thin disc. However, Remington found no model for the lateral impedance of a wheel excited at its tread.

Barlow [9] has developed a finite element model of a BR wheelset and has obtained excellent agreement between observed and calculated natural frequencies. However, general use of such a technique is limited by the large computing resources which are required.

The idealised wheelset shown in Fig. 2 has been used to calculate the dynamic response of a wheel to a lateral force applied at the tread [5]. It was found that the wheel rim is isolated by the flexible web from the rest of the wheelset at modest frequencies of excitation. Hence, for lateral excitation the wheelset can be represented as a thin ring with the same dimensions as those of the wheel rim.

2.3 Longitudinal Excitation

An experiment is described in [7] in which a longitudinal force was applied to the wheel tread of a vehicle standing on the track. It was found that the wheel is adequately represented, for frequencies greater than 50 Hz, as a rigid body with effective mass

$$M_{we} = M_w \frac{1 + M_a/M_w}{1 + (1 + M_a/M_w)(r/k)^2} \qquad (1)$$

where M_w is the actual wheel mass, M_a the effective unspring mass at the wheel centre, k the radius of gyration of the wheel and r the wheel radius. Reasonable agreement was obtained with experiment by taking M_a equal to half the axle mass ($\sim$ 115 kg); the effective mass M_{we} so calculated is 150 kg for a typical 36" BR wheel.

3. MODELLING THE CONTACT

Because both wheel and rail are elastic bodies, there is deformation at their point of contact. The dimensions of the contact patch (typically 14 mm × 10 mm) are small compared to dimensions of wheel and rail, and it is therefore reasonable to assume in calculation that the contacting bodies are elastic half spaces and that the force is applied at a point.

3.1 Normal Deformation

The normal deformation of elastic bodies in contact has been studied extensively. For contact on the railhead, the deformation is adequately described by Hertz. The approach of the bodies is [10], [11],

$$\delta = (9P^2/16E^{*2}R_e)^{1/3} \qquad (2)$$

where $E^* = E/2(1 - \nu^2)$

and $R_e = \sqrt{R'R''}$

The normal load is P; $E/(1 - \nu^2)$ is the plane strain elastic modulus; R' and R" are the relative radii of curvature of the surfaces. The contact stiffness is

$$k_H = dP/d\delta = (6E^{*2}R_eP)^{1/3} \qquad (3)$$

Non-linearity of the contact deformation should be included in any calculation in which relative displacements of wheel and rail are large: in particular, at railjoints and with wheelflats, total unloading of the contact often occurs. For this reason British Rail include the non-linearity in all of their recent calculations [12, 13]. However, if relative displacements of wheel and rail are small, the contact stiffness can be taken as constant. This assumption, which has been used by Grassie et al [1, 14] and Sato [15], greatly simplifies analysis while retaining the important features of the dynamic response. For typical BR parameters (transverse railhead radius R' = 300 mm; wheel radius R" = 450 mm; dead load P_o = 100 kN), $k_H \cong 1.5$ GN/m.

The contact stiffness is high compared to other stiffnesses in the system: for example, the stiffness of the railpad separating rail and sleeper is 250 MN/m (section 4). A rough estimate of the frequency above which the contact flexibility should not be ignored is that of resonance of the unsprung mass on the contact stiffness, i.e. $f = (1/2\pi)\sqrt{k_H/M_w} \cong 275$ Hz. Neglect of the contact flexibility is a shortcoming in some work on high frequency dynamics [16, 17] because contact forces are overestimated, while its inclusion in considering low frequency dynamics is an unnecessary sophistication [18].

3.2 In-plane Deformation

The deformation under a tangential force of stationary elastic bodies in contact has been studied by Mindlin [19], who found that the tangential stiffness is approximately the same as the normal stiffness. This was also found in an experiment with a vehicle standing on the rail [7].

Transmission of a rapidly-varying tangential force between a rolling wheel and the rail is at present an area of research. However, if the rolling length over which the tangential force changes is long compared to the contact dimensions, rolling can be regarded as a series of steady states [20]. Steady-state rolling contact is well understood and the theory has been reviewed by Kalker [21].

Because of local elastic deformation there exists a small difference in relative velocity, called 'creep', between a rail and a steadily rolling wheel transmitting traction. If the longitudinal displacement of wheel relative to rail at their point of contact is u_x, the longitudinal creep is

$$\xi_x = \dot{u}_x/v$$

where v is the forward velocity of the wheel. The dependence of longitudinal traction on creep is given approximately by the formula

$$\xi_x = \frac{3\mu N(4 - 3\nu)}{16Ga^2}\left[1 - \left(1 - \frac{T_x}{\mu N}\right)^{1/3}\right] \qquad (4)$$

where T_x is the longitudinal traction, μN is the limiting traction, a is the radius of the circular contact patch, and $G = E/2(1 + \nu)$ [22]. The exact theory, which involves elliptic integrals, is given by Kalker [23].

The creep curve for a typical railway case is shown in Fig. 3. For small creep, the curve is linear and the traction is given by

$$T_x = C_x\xi_x = C_x\,\dot{u}_x/v \qquad (5)$$

where $C_x = 16Ga^2/(4 - 3\nu)$ is the longitudinal creep coefficient. If the traction is small, the steady creep behaviour may be represented by a dashpot of strength C_x/v between wheel and rail. For slowly varying tractions, the contact is adequately represented by the spring-dashpot model of Fig. 3(b) in which the spring represents

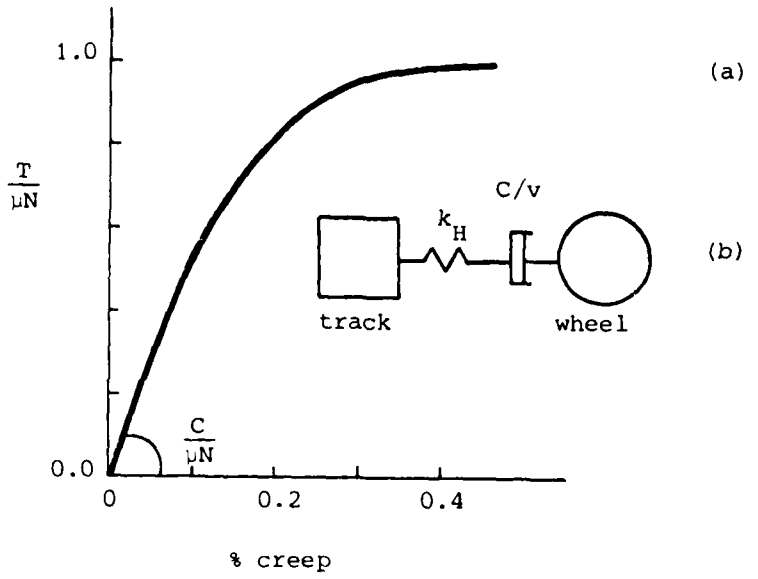

Fig. 3: (a) Typical creep curve
(b) Contact model for small, slowly-varying traction

the static contact stiffness k_H.

The equation for transverse creep corresponding to eqn. (4) for longitudinal creep is

$$\xi_y = \frac{3\mu N(4 - \nu)}{16Ga^2}\left[1 - \left(1 - \frac{T_y}{\mu N}\right)^{1/3}\right] \qquad (6)$$

where T_y is the transverse traction [22].

4. MODELLING THE TRACK

Conventional railway track comprises a rail which is supported periodically on sleepers which rest in ballast. Use of concrete rather than wooden sleepers has become common, and a resilient railpad is then used for mechanical and electrical isolation between rail and sleeper.

Our present concern is with track of this sort. The dynamics of other sorts of track have received less attention. The low frequency dynamics of elevated guideways which use discrete concrete slabs supported at their ends have been considered by Wormley et al [24 - 26]. Sato [15] has investigated the dynamics of railway track laid on a continuous concrete slab.

4.1 Vertical Excitation

Research on track dynamics has concentrated on the vertical response. For this purpose the track model which has traditionally been used is that of an infinite Euler beam on a continuous, distributed, elastic support representing the ballast; in some analyses damping is included in the support (Fig. 4(a)). The mass of the sleepers has generally been lumped in with that of the rail; where only high frequencies are of interest, the rail alone has been taken as the beam and the support stiffness taken as that of the elastic rail fastenings [3, 16].

Both Hetenyi [27] and Fryba [28] have written at length about beams on

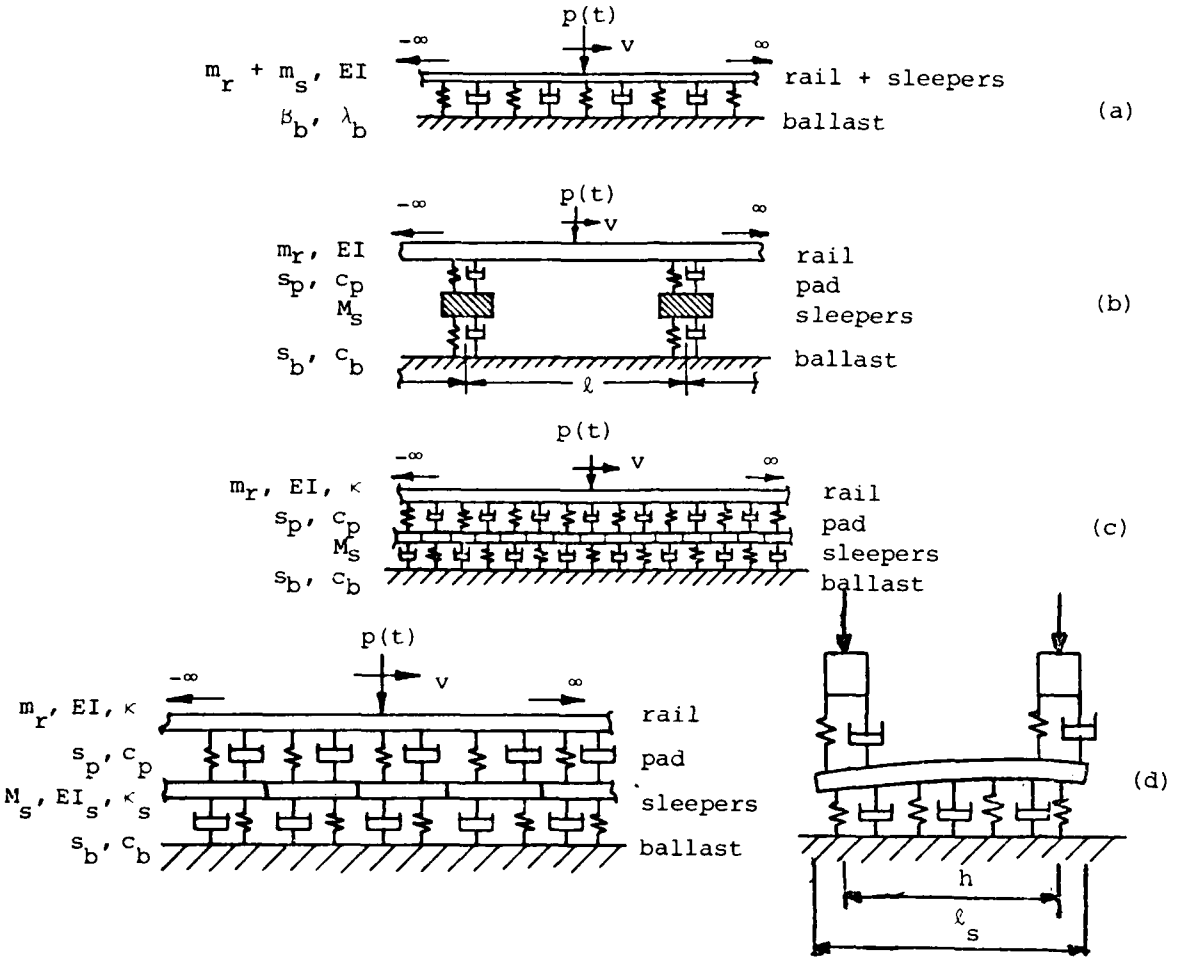

Fig. 4: Track models

(a) Euler beam; damped, elastic support
(b) Euler beam; discrete support
(c) Timoshenko beam; continuous, two-layer, damped, elastic support
(d) Timoshenko beam; continuous layer of flexible sleepers

elastic foundations, and it has been shown [14] that this is a good model for track laid on wooden sleepers. Weitsman [29] and Torby [30] have used the model to provide reassurance that the ballast may be considered as acting in both tension and compression despite the fact that on poor track the sleepers may not be supported when they are on the 'bow wave' ahead of the train. The model has been used to calculate the so-called 'critical speed' of railway vehicles. This speed, which is essentially the minimum speed at which bending waves propagate along the rail, is commonly regarded as limiting the operating speed because the rail would not deflect ahead of the train. Kerr [31] has reviewed work in this area, and Kenney [32] has shown that movement both at and above the critical velocity may be possible provided that there is some damping in the support. On typical BR track, wave speeds greater than ten times the speed of any present vehicle have been measured [14]. It follows that for most purposes deformation of the track under a moving load can be calculated as if the load were stationary.

Although this simple model has been much used, it has several deficiencies when used for the dynamics of modern railway track at the frequencies considered here. In particular it neglects:

(a) periodic support of the rail;
(b) the resilient railpad between rail and sleeper

(c) the flexibility of the sleeper;
(d) shear deformation and rotary inertia of rail and sleeper.

The seriousness of these deficiencies depends upon the purpose of the model and the frequency range of interest: for example, it is impossible to calculate sleeper strains with a model which ignores sleeper flexibility. Notwithstanding such details of the response, the single most serious shortcoming of the conventional model is neglect of the railpad flexibility [14]. Above a frequency of 300 Hz there is substantial relative movement of rail and sleeper on the pad, and it must be included in any realistic model.

A model which includes both the railpad and the discrete, periodic support is shown in Fig. 4(b). A similar model in which the railpad is neglected is considered by Munjal and Heckl [17]. The rail is considered to be an infinite Euler beam; pad and ballast are regarded as springs and dashpots in parallel; the sleeper is massive. The need to include the discrete nature of the rail support depends primarily upon the wavelength of bending waves in the rail. When a transverse harmonic force is applied to the rail, energy is carried away from the point of application by travelling waves. As the waves travel further from the point of application, their amplitude decreases because energy is absorbed both by the support and by vibration of each element of the rail. At low frequencies, the wavelength is long: any deflection of the track under an applied force thus involves many bays of sleepers and the amplitude of deformation depends little on position of the applied force in the sleeper span. This is illustrated in Fig. 5, which shows the direct receptance to a point force which is applied to the railhead at two positions in a sleeper span. The receptance is calculated from the model of Fig. 4(b) using the method of transfer matrices [14].

The bending wavelength decreases with frequency. At the 'pinned-pinned' resonant frequency

$$f = \frac{1}{2\pi}\left(\frac{\pi}{\ell}\right)^2 \sqrt{\frac{EI}{m_r}}\,, \qquad (7)$$

where EI is the bending stiffness and m_r the mass per unit length of the rail, the wavelength is twice the sleeper spacing ℓ. At this frequency, which is about 950 Hz for the typical parameters of Fig. 5, motion of the rail is part standing wave, with the rail effectively pinned at sleepers, and part travelling wave. At the antinode of vibration midway between sleepers, the receptance is large, while at a sleeper the receptance is small. The observed pinned-pinned resonance in Fig. 5 is at a lower frequency than calculated from eqn. (7), which neglects shear and rotatory inertia of the rail. There is excellent agreement between experiment (770 Hz) and calculation (766 Hz) when these are included.

The discrete support significantly affects the track response only in a rather narrow frequency range close to the pinned-pinned resonant frequency. Its effect upon the response of the track under a moving wheel is also small (Section 5). Therefore, usually a track model can be used in which the railpad is included, but the support is continuous. With a continuous model it is easier to make good the other deficiencies of the simple model of an Euler beam on an elastic foundation.

In the model of Fig. 4(c), the railpad and ballast are continuous, uniform layers of stiffness and viscous damping; the sleepers are represented by a layer of elemental masses and the rail is a Timoshenko beam: shear deformation and rotary inertia of the rail are thus included. A similar model in which the rail is modelled as an Euler beam has been used by Sato [15]. The direct receptance calculated from the Timoshenko beam model [14] is shown in Fig.5. The continuous model is incapable of showing the pinned-pinned resonance, but the receptance agrees well at other frequencies with that calculated from the model with discrete

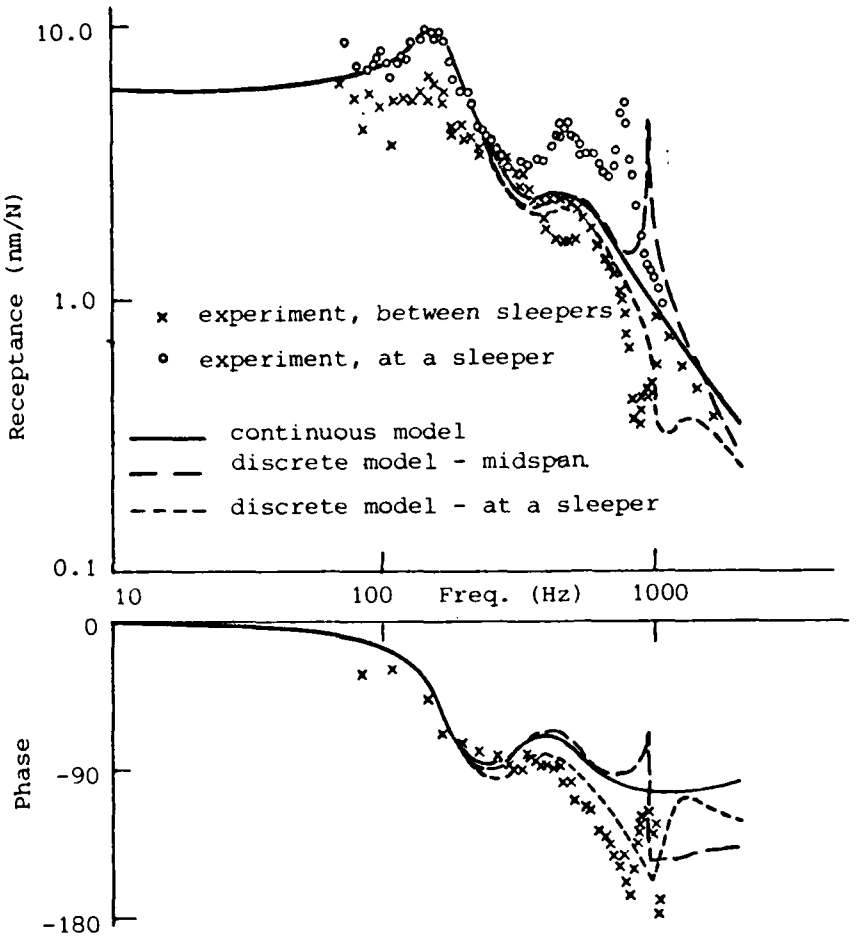

Fig. 5: Vertical direct receptance of track

Parameters for theory:

m_r = 56 kg/m	s_p = 280 MN/m	c_p = 63 kNs/m
M_s = 110 kg	s_b = 180 MN/m	c_b = 82 kNs/m
EI = 4.86 MNm^2	κ = 0.34	ℓ = 0.7 m

supports and with experimental data. Shear and rotatory inertia become more significant the greater is the ratio of depth of beam to effective length (the semi-wavelength in this case), and thus become more significant as the frequency increases. Their effect is to increase deformation of the rail.

Two areas of high response, at 150 Hz and 470 Hz, are shown by the model of Fig. 4(c). The behaviour at these track resonances can be illustrated by considering both the rail and the sleepers to be massive. The first resonance of this two mass system is of the masses moving almost in phase on the ballast, while at the second resonance the two masses move almost in antiphase on the flexibility of the pad. Because the sleepers are ever more nearly stationary at frequencies above 470 Hz, a reasonable estimate of the rail response at such frequencies is obtained by considering it to be a beam supported to earth on a continuous railpad.

If the detailed response of the support is of interest, this must be represented in greater detail than in the model of Fig. 4(c). A track model is shown in Fig. 4(d) in which the sleepers are not rigid but are a continuous layer of Timoshenko beams, with bending stiffness across the track and zero bending stiffness along the track, resting on a viscously-damped, elastic layer. This model, which in other respects is identical to that of Fig. 4(c), is discussed in

[1]. Although it appears to be three-dimensional, analysis of the model is simplified by the fact that the response to general harmonic excitation of the two rails can be regarded as a synthesis of motion involving symmetric and asymmetric modes of the sleepers. Therefore, the motion of only one rail need be considered, with symmetric and asymmetric sleeper modes treated separately.

In the models of Fig. 4 the track is infinite in extent and the response to a harmonic point force is calculated by analytical methods. A track model which uses modal analysis has been developed by British Rail for the majority of their requirements and is described by Clark et al [12, 13]. It represents the rail as an Euler beam supported through railpads on discrete sleepers which rest in ballast; both railpad and ballast are viscously damped springs. To this extent the BR model is identical to that of Fig. 4(b). It differs in that only twenty bays of track are considered and the sleepers are modelled as Euler beams which vibrate only in their symmetric modes. Natural frequencies and normal modes of this finite length of track are found using the algorithms of Wittrick and Williams [33, 34], and the response is calculated numerically by modal analysis. A measure of the computing resources required is that 126 modes of the 20-span model are found between 80 Hz and 3 kHz.

A common feature of both the BR model and those of Fig. 4 is that the characteristics of both ballast and pads are constant for the length of the track. On good track this assumption should be substantially correct, while on poorer track the response is calculated adequately for most purposes. However, occasionally there exists a 'hung' sleeper where the ballast has deteriorated to such an extent that the sleeper is virtually unsupported. Such sites are often associated with a more fundamental problem: for example, poor welds, bad formation and 'wet beds'. Nonetheless, not only do they represent a severe test for the sleeper and fastening system, but also such 'soft spots' can create undesirable vertical motion of the unsprung mass [35] and thus exacerbate an existing problem. This problem is being investigated by the author and Mr S J Cox of Pandrol Ltd. using the model shown in Fig. 6. In this model the track is considered as comprising two semi-infinite spans which are supported on pads, sleepers and ballast of normal characteristics; joining these two spans is a length of track whose support is different. The case of greatest interest is that in which the ballast is absent, but in principle the support could be modified in any prescribed way. Work on this model is in progress.

4.? Lateral Excitation

A beam on an elastic foundation (Fig. 4(a)) has been used to represent the lateral as well as the vertical dynamics of railway track [3]. It has been shown that this is a reasonable model for the lateral dynamics of track laid on wooden sleepers in the frequency range 50 - 1200 Hz [36]. Timoshenko [37] has calculated

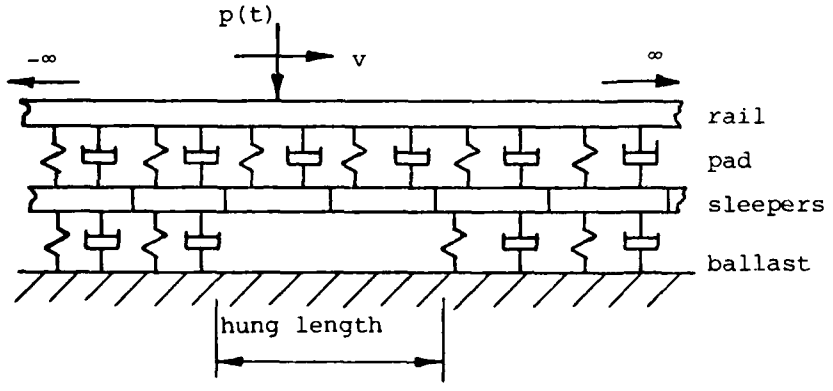

Fig. 6: Model for track with 'hung' sleepers

the deflection and stresses in a rail under a lateral point forces by assuming that the rail both twists and bends on its uniform, continuous, elastic support. An extension of this model to examine the lateral dynamic response at low frequencies is straightforward [38].

Clark and Foster [39] consider torsion to be the principal mode of deformation of the rail under a lateral force. They represent a finite number of spans of track by three modes of vibration. These modes are (a) twisting of the complete length of track in phase on the torsional support stiffness; (b) the first torsional 'pinned-pinned' mode, in which the semi-wavelength of the torsional wave is equal to the sleeper spacing; (c) the second torsional 'pinned-pinned' mode, in which the wavelength of the torsional wave is equal to the sleeper spacing. Because of the prominence of the pinned-pinned modes in this model, it predicts a track response which is strongly dependent on position of the applied force in the sleeper span.

In an experiment on BR track laid with railpads on concrete sleepers, it was found that there is significant distortion of the rail cross section at frequencies greater than 300 Hz [36]. The experimental data strongly suggested that the railhead is undergoing lateral bending vibrations which are substantially independent of the railfoot, while the web of the rail acts as a foundation spring. As a consequence, the rail is significantly more flexible laterally than is predicted by a model in which the complete rail cross section bends about its neutral axis. The dynamic response of this track in the frequency range 100 - 1000 Hz is satisfactorily represented by the two-layer foundation model of Fig. 4(c). In this case, the railhead is the Timoshenko beam, the railfoot is a continuous layer of elemental masses, while both the pad and the rail web are continuous, viscously-damped, elastic layers. It is assumed that the ballast is sufficiently flexible in shear and the sleepers sufficiently massive for them to be stationary at these frequencies. Calculation and experimental data for the direct receptance are shown in Fig. 7. It is predicted that at the resonance of 150 Hz both head and foot move almost in phase on the railpad, while at the resonance at 450 Hz they move almost in antiphase on the web. The resonance at 370 Hz for excitation between sleepers and a corresponding antiresonance for excitation at a sleeper occur because of the discrete nature of the support. This behaviour is discussed in Section 4.1 and is not shown by a model with a continuous support.

The author is not aware of any track model in the literature for both lower (0 - 150 Hz) and higher (100 - 2000 Hz) frequencies. Because of the complex distortion of the rail section at high frequencies, it is unlikely that a single, simple model would be adequate for both frequency ranges. For higher frequencies, the model of Fig. 4(c) is adequate, while for lower frequencies the combined bodily flexure and torsion can be represented by appropriate beams on elastic foundations. The effect of the discrete support can be analysed by the transfer matrix method described in [14]: whereas the fourth order bending equation gives rise to a 4 × 4 transfer matrix, the second order torsion equation gives simply a 2 × 2 transfer matrix; computation is straightforward.

4.3 Longitudinal Excitation

The longitudinal dynamic response of railway track has been considered by Grassie et al [7]. The track is adequately represented as an analogue of Fig. 4(c) in which the rail is an infinite bar, resting on a uniform, continuous support with two viscously-damped elastic layers and a layer of elemental masses. The driving point receptance thus calculated is compared to experiment in Fig. 8.

At low frequencies the track behaves as a spring: the driving point receptance to a static load is

$$\alpha = 1/(4\beta_t AE)^{1/2} \qquad (8)$$

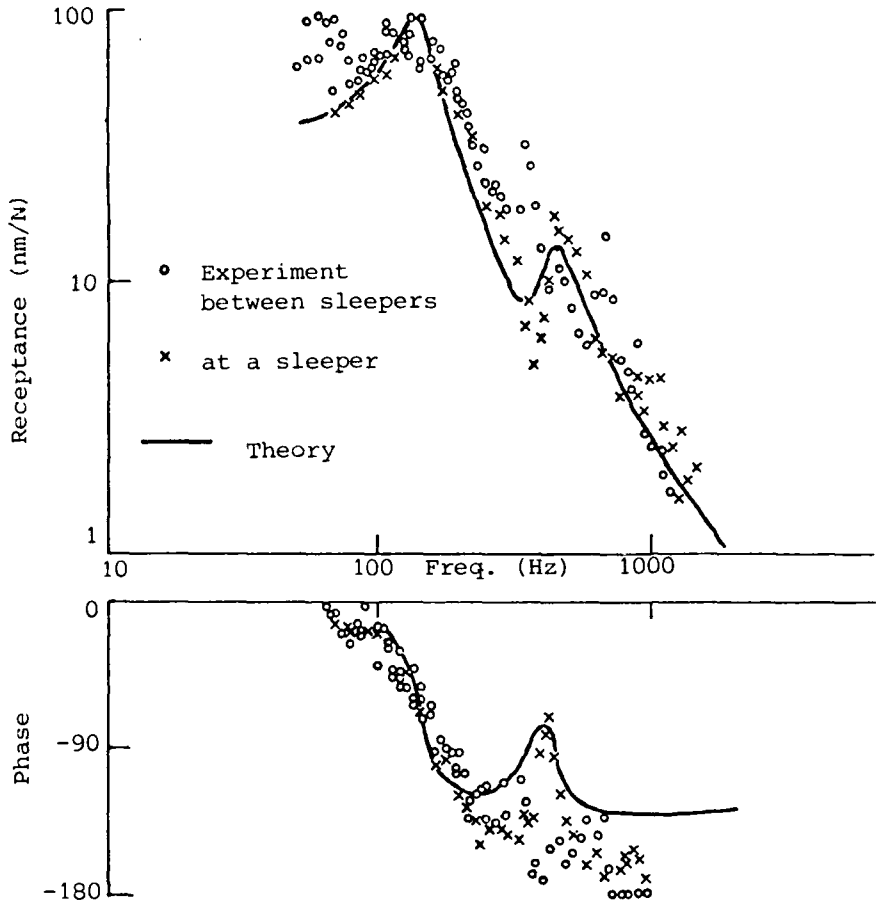

Fig. 7: Lateral direct receptance of track

Parameters for theory

m_{head}	= 28 kg/m	β_{web}	= 96.0 MN/m^2	λ_{web}	= 5.2 kNs/m^2
m_{foot}	= 28 kg/m	β_{pad}	= 48.7 MN/m^2	λ_{pad}	= 15.7 kNs/m^2
EI	= 0.3 MNm^2	κ	= 0.833		

where $\beta_t = \beta_p\beta_b/(\beta_p + \beta_b)$

β_p and β_b are the stiffnesses of the pad and ballast per unit length of track, A is the cross-sectional area of the rail and E its Young's modulus. At high frequencies the response is primarily that of the rail alone; the receptance is inversely proportional to frequency, while its phase lag approaches 90 degrees. The track behaves like a dashpot: its receptance at frequency ω is

$$\alpha \approx -\frac{j}{2m_r\omega}\sqrt{\frac{\rho}{E}} \qquad (9)$$

where m_r is the mass per unit length of the rail and ρ its density. The track is represented well by these two elements, the spring of eqn. (8) and the dashpot of eqn. (9), in parallel. The receptance thus calculated is shown in Fig. 8 for comparison with that calculated from the more elaborate model.

A discrete track model is described in [7]. However, the effect of the discrete support is small because the longitudinal wave speed is high (5180 ms). The first 'pinned-pinned' resonant frequency occurs at 3700 Hz for a sleeper spacing of 0.7 m.

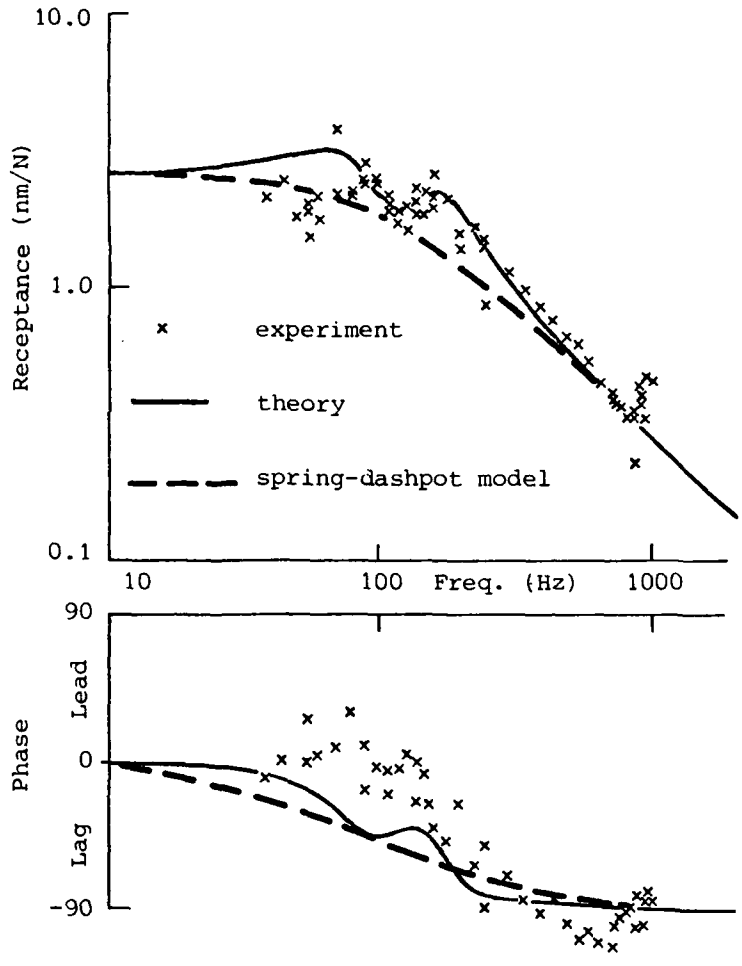

Fig. 8: Longitudinal direct receptance of track

Parameters for theory

m_r = 56 kg/m s_p = 34 MN/m c_p = 8.6 kNs/m

M_s = 120 kg s_b = 35 MN/m c_b = 52 kNs/m

ℓ = 0.7 m

5. DYNAMICS OF THE COMBINED SYSTEM

In the preceding sections of this paper, dynamic models have been described for the components of the wheel/rail system: the wheel, the contact between wheel and rail, and the railway track itself. The response of a stationary wheel on a rail to dynamic forces in the plane of the contact is discussed in [5]: the author is aware of no other published work on this subject. The vertical dynamics of the system have by contrast received great attention and have been investigated in two fundamentally different ways:

(a) a generalised, non-linear analysis, in which a single model is constructed which can be used for any prescribed forcing function and over a broad frequency range;

(b) a linear analysis, in which different models are used to reveal different aspects of the response.

The most sophisticated example of the former technique is in the work of Clark et al [12, 13] of British Rail. Examples of linear analysis can be found in the work by Sato [15] and by Grassie et al [1, 14] at Cambridge University (CU).

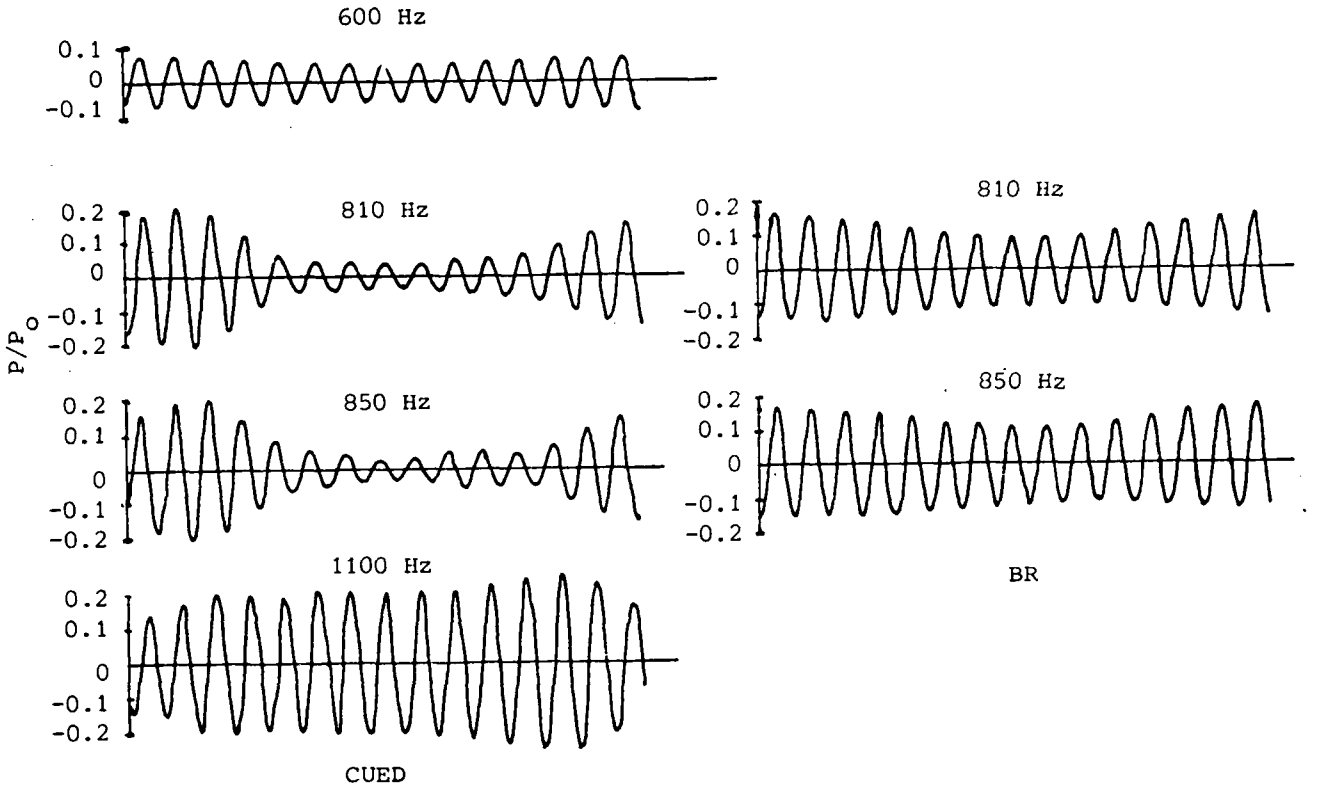

Fig. 9: Vertical dynamic contact force through a sleeper span

Parameters for theory

m_r = 54.4 kg/m	s_p = 200 MN/m	c_p = 37 kNs/m
M_s = 143 kg	s_b = 46.6 MN/m	c_b = 37 kNs/m
EI = 4.84 MNm^2	ℓ = 0.75 m	
M_w = 1680 kg	k_H = 1.5 GN/m	P_o = 86.2 kN
Δ = 0.01 mm	λ = 50 mm	

A comparison is made here between results of the BR and CU techniques.

Models of the components of the system have been described, and in each case the response to an applied force is found. When a wheel rolls over a rail, this force is not known *a priori*, but arises from dynamic interaction of the components of the system excited by roughness of the railhead and wheel. For the linear models, it is convenient to consider the roughness to be a sinusoidal corrugation of wavelength λ and amplitude Δ (Fig. 1). The response to non-sinusoidal irregularities can then be found from the harmonic response by Fourier analysis. The vertical dynamic contact force $p(t) = Pe^{j\omega t}$ arising from a wheel rolling at velocity v over a sinusoidal irregularity is given by the formula

$$\frac{P}{k_H \Delta} = \frac{-1}{1 + k_H(\alpha_r + \alpha_\omega)} \qquad (10)$$

where α_r and α_ω are the receptances of track and wheel respectively, k_H is the linear contact stiffness and $\omega = 2\pi v/\lambda$. A similar result for the tangential contact force using the simple contact model of Fig. 3(b) is

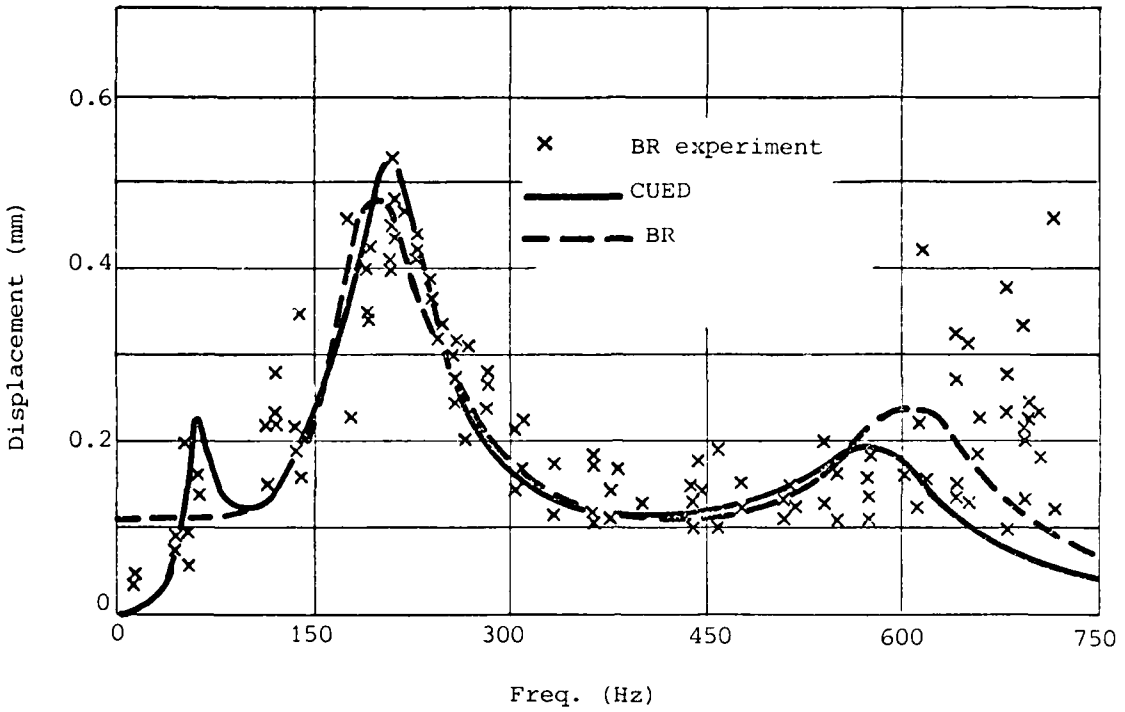

Fig. 10: Sleeper end displacement

Parameters for CU theory

m_r = 56 kg/m	s_p = 250 MN/m	c_p = 26 kNs/m
M_s = 293 kg	s_b = 50 MN/m	c_b = 51 kNs/m
EI = 4.86 MNm^2	κ = 0.34	ℓ = 0.63 m
EI_s = 3.75 MNm^2	κ_s = 0.833	ℓ_s = 2.5 m
h = 1.5 m	λ = 60 mm	Δ = 0.115 mm
M_w = 380 kg	k_H = 1.21 GN/m	

$$\frac{P}{k_H \Delta} = \frac{-1}{1 + k_H(\alpha_r + \alpha_\omega - j\lambda/2\pi C)} \qquad (11)$$

where C is the appropriate creep coefficient for the rolling wheel. This reduces to the formula of eqn. (10) for a stationary wheel. Δ is the amplitude of the relative displacement which is imposed between wheel and rail.

If the track model includes the discrete support at sleepers, the track receptance α_r varies periodically at sleeper spacing and the contact force does likewise. A method is described in [14] for calculating the dynamic contact force between a steadily rolling wheel and a sinusoidally-corrugated rail in these circumstances for the CU model of Fig. 4(b). The contact force so calculated is compared in Fig. 9 with calculations made using the BR model for several corrugation-passing frequencies. These frequencies span the pinned-pinned resonance discussed in Section 4.1. The effect of this resonance is to modulate the response at sleeper pitch. Because the CU model has less damping in the pinned-pinned mode than the BR model, greater modulation is predicted by the former. The agreement otherwise is good. Modulation is much reduced at frequencies far from that of the pinned-pinned resonance.

The BR model and the CU model of Fig. 4(d) can be used to calculate sleeper displacements. A comparison is made in Fig. 10 between calculated sleeper end displacements and experimental data obtained by Dean of BR [40]. Agreement between the calculated displacements, and between calculation and experiment, is good.

6. CONCLUSIONS

Several dynamic models of the wheel/rail system have been described for excitation in the frequency range 5 - 2000 Hz. Although no single model is completely satisfactory throughout the whole frequency range, different models can be used satisfactorily for different aspects of the dynamic response.

The wheelset vibrates independently of the rest of the unsprung mass of the bogie at frequencies above about 50 Hz. Above this frequency, the wheel is represented adequately as a rigid body for vertical and longitudinal excitation and as a thin, elastic ring for lateral excitation. There is inadequate experimental data available on the dynamic response in the frequency range 5 - 100 Hz.

There is elastic deformation at the contact between wheel and rail. The associated flexibility, although small compared to track flexibilities, should not be ignored for frequencies of excitation above 250 Hz. There is a similar flexibility for deformation in the plane of contact between a stationary wheel and the rail. For small, slowly-varying tangential forces, the contact is adequately modelled as a series combination of the contact spring and a dashpot which represents the effects of creep. Study of rapidly varying tangential forces in rolling contact is the subject of current research.

Track is usually represented for vertical motion as an Euler beam on a uniform, distributed, elastic foundation. This model is deficient in several respects; in particular it ignores:

(a) the discrete support of the rail at sleepers;
(b) the flexible railpad between rail and sleepers;
(c) flexibility of the sleeper;
(d) shear deformation and rotatory inertia of the rail and sleeper.

Models developed at British Rail and at Cambridge University satisfy some of these deficiencies. The BR model includes flexible, discrete sleepers and railpads; its dynamic response is found by modal analysis. It has the attraction of being part of a general-purpose computer program for the dynamics of the wheel/rail system. Its disadvantage for the general user is its complexity and cost in computing resources.

Both BR and CU models have shown that discrete support of the sleepers introduces a pinned-pinned resonance and some modulation of the contact force at sleeper pitch. However, the modulation is not large, and is particularly subdued in the BR calculations because the pinned-pinned resonance is well damped. Away from this frequency the track is represented well by a much simpler, continuous model in which railpad, flexible sleepers and ballast are distributed uniformly along the track. If only high or low frequencies are of interest, or if the detailed response of the support is of no concern, even simpler models can be used.

For lateral excitation of the track, a model is proposed for the frequency range 100 - 2000 Hz in which the railhead rests on a uniform, continuous, two-layer support. Because the rail both twists and bends, and at high frequencies the cross-section distorts significantly, no simple model is available for the frequency range 0 - 2 kHz.

For longitudinal excitation, the track is represented well as an infinite rod on a uniform, continuous, two-layer support. It is modelled adequately by the parallel combination of a spring which represents the longitudinal track stiffness and a dashpot which takes account of energy radiated in longitudinal wave motion.

REFERENCES

1. S L GRASSIE and S J COX 1984 Proceedings of Institution of Mechanical Engineers, Series D (to appear). The dynamic response of railway track with flexible sleepers to high frequency vertical excitation.

2. H H JENKINS, J E STEPHENSON, G A CLAYTON, G W MORLAND and D LYON 1974 Railway Engineering Journal, 3, 2-16. The effect of track and vehicle parameters on wheel/rail vertical dynamic forces.

3. P J REMINGTON 1976 Journal of Sound and Vibration, 46, 359-379. Wheel/rail noise - Part I: characterization of the wheel/rail dynamic system.

4. M L MUNJAL and M HECKL 1982 Journal of Sound and Vibration, 81, 477-489. Some mechanisms of excitation of a railway wheel.

5. S L GRASSIE, R W GREGORY and K L JOHNSON 1982 Journal of Mechanical Engineering Science, 24, 103-111. The behaviour of railway wheelsets and track at high frequencies of excitation.

6. D J WILLIAMS and T M DAWN 1977 British Rail R & D Division, Derby. Wheel/rail noise: investigation of the modes of vibration of a static 36 inch nominal diameter railway wheelset.

7. S L GRASSIE, R W GREGORY and K L JOHNSON 1982 Journal of Mechanical Engineering Science, 24, 97-102. The dynamic response of railway track to high frequency longitudinal excitation.

8. H ARAI, S HAYASHI, S MOURI, S SATO and Y ZENOU 1977 Japanese Railways Quarterly Report, 18, 55-61. Dynamic characteristics of wheel and of wheel/rail noise.

9. R H BARLOW 1975 Railway Technical Centre, Derby, BR Technical Note EMMA 75. Natural frequencies of axisymmetric structures using NEWPAC.

10. K L JOHNSON 1982 Proceedings of Institution of Mechanical Engineers, 196, 363-378. One hundred years of Hertz contact.

11. S P TIMOSHENKO and J N GOODIER 1934 Theory of Elasticity, 414-420. New York: McGraw-Hill.

12. S G NEWTON and R A CLARK 1979 Journal of Mechanical Engineering Science, 21, 287-297. An investigation into the dynamic effects on the track of wheelflats on railway vehicles.

13. R A CLARK, P A DEAN, J A ELKINS and S G NEWTON 1982 Journal of Mechanical Engineering Science, 24, 65-76. An investigation into the dynamic effects of railway vehicles running on corrugated rails.

14. S L GRASSIE, R W GREGORY, D HARRISON and K L JOHNSON 1982 Journal of Mechanical Engineering Science, 24, 77-90. The dynamic response of railway track to high frequency vertical excitation.

15. Y SATO 1977 Japanese Railways Quarterly Report, 18, 109-114. Study on high-frequency vibrations in track operated with high-speed trains.

16. E K BENDER and P J REMINGTON 1974 Journal of Sound and Vibration, 37, 321-334. The influence of rails on train noise.

17. M L MUNJAL and M HECKL 1982 Journal of Sound and Vibration, 81, 491-500. Vibration of a periodic rail-sleeper system excited by an oscillatory, stationary, transverse, point force.

18. H C MEACHAM and D R AHLBECK 1969 Journal of Engineering for Industry, 91. 803-816. A computer study of dynamic loads caused by vehicle-track interaction.

19. R D MINDLIN 1949 Journal of Applied Mechanics, 71, 259-268. Compliance of elastic bodies in contact.

20. J J KALKER 1970 Journal of Applied Mechanics, 92, 677-688. Transient phenomena in two elastic cylinders rolling over each other with dry friction.

21. J J KALKER 1979 Vehicle System Dynamics, 5, 317-358. Survey of wheel-rail rolling contact theory.

22. K L JOHNSON 1958 Journal of Applied Mechanics, 80, 339-346. The effect of a tangential contact force under the rolling motion of an elastic sphere on a plane.

23. J J KALKER 1966 Wear, 9, 20-38. Rolling with slip and spin in the presence of dry friction.

24. W S CHIU, R G SMITH and D N WORMLEY 1971 Journal of Dynamic Systems, Measurement and Control, 93, 25-34. Influence of vehicle and distributed guideway parameters on vehicle-guideway dynamic interactions.

25. H H RICHARDSON and D N WORMLEY 1974 Journal of Dynamic Systems, Measurement and Control, 96, 169-179. Transportation vehicle/beam-elevated guideway dynamic interactions.

26. J E SNYDER and D N WORMLEY 1977 Journal of Dynamic Systems, Measurement and Control, 99, 23-33. Dynamic interactions between vehicles and elevated, flexible, randomly irregular guideways.

27. M HETENYI 1946 Beams on Elastic Foundations. Ann Arbor: University of Michigan Press.

28. L FRYBA 1972 Vibration of Solids and Structures under Moving Loads. Groningen: Noordhof International Publishing Company.

29. Y WEITSMAN 1970 Journal of Applied Mechanics, 92, 1019-1030. On foundations that react in compression only.

30. B J TORBY 1975 Journal of Applied Mechanics, 97, 738-739. Deflection results from moving loads on a beam that rests upon an elastic foundation reacting in compression only.

31. A D KERR 1974 Journal of Applied Mechanics, 96, 841-848. The stress and stability analyses of railroad track.

32. J T KENNEY 1954 Journal of Applied Mechanics, 76, 359-364. Steady-state vibrations of beams on elastic foundations for a moving load.

33. W H WITTRICK and F W WILLIAMS 1971 Quarterly Journal of Mechanics and Applied Mathematics, 24, 263-284. A general algorithm for computation of natural frequencies of elastic structures.

34. F W WILLIAMS 1971 Quarterly Journal of Mechanics and Applied Mathematics, 24, 285-310. Natural frequencies of repetitive structures.

35. G A CLAYTON, G H COPE and C O FREDERICK 1978 Railway Engineers' Forum, Institution of Civil Engineers, London, 20 November. Interaction of vehicle and track.

36. S L GRASSIE, R W GREGORY and K L JOHNSON 1982 Journal of Mechanical Engineering Science, 24, 91-95. The dynamic response of railway track to high frequency lateral excitation.

37. S P TIMOSHENKO 1926 Second International Congress of Applied Mechanics, Zurich, 407-418. Method of analysis of statical and dynamical stresses in rails.

38. S L GRASSIE 1980 PhD Thesis, University of Cambridge. The corrugation of railway track.

39. R A CLARK and P FOSTER 1983 Proceedings of Symposium on Rail Corrugation, Berlin, 23-24 June. Mechanical aspects of rail corrugation formation.

40. P A DEAN 1981 Railway Technical Centre, Derby, BR Technical Memorandum TM CES 11. Dynamic track response to short wavelength corrugations.

TWO THEORETICAL MODELS FOR WAVE PROPAGATION IN RAILS

W. Scholl

Institut für Technische Akustik
Technische Universität Berlin

1. INTRODUCTION

As trains get faster and louder there is an increasing interest in all mechanisms participating in noise generation by rail traffic. One of the main acoustic sources seems to be the rail.

The intention of this paper is to give a basic survey on wave propagation in rails under idealized conditions, which means particularly without sleepers and without any surrounding medium.

As the complete three-dimensional description was considered to be too voluminous, two simpler models were developped, which are two-dimensional and supplement each other. The "three-layers-model" describes the sound propagation along the rail, including the influence of the shape of the cross section. The "cross-section-model" covers modes with propagation and displacements within the cross-sectional area.

Moreover the first nine types of waves were determined experimentally on a 1.7m long piece of rail of type UIC 60.

2. THREE-LAYERS-MODEL

2.1 Description

In order to get a simple two-dimensional model for wave propagation along a rail, an infinitely long strip was used, divided into three parallel tangent layers representing head, web, and foot of the rail (Fig.1).

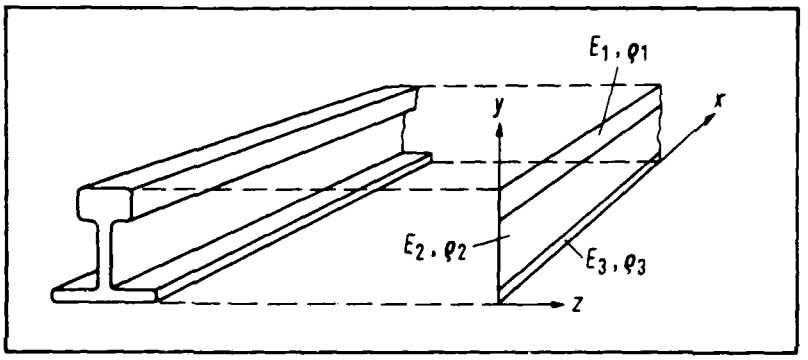

Fig.1. Rail and three-layers-model

Though the rail is homogeneous as for density and Young's modulus, different values were assigned to the three bands, proportional to the width of the corresponding rail part, thus regaining the lost information about the cross-sectional profile.

This model captures wave types with motions and forces restricted to the plane of the strips, i.e. mainly vertical flexural and shear waves, longitudinal waves and related higher modes.

It must be kept in mind, however, that all points over the width of the rail, which are represented by the same strip point, have to be in phase. That means, no wave propagation transverse to the plane in question is allowed. This condition is violated with increasing frequency first at the rail foot, the exact limit depending

on the present type of wave.

2.2 Analysis

An easy representation of the structure-borne sound field can be given by using two scalar potential functions Φ and Ψ, standing for the dilatational and rotational part of the field. Together they can form all existing wave types without limitation of the ratios of cross-sectional dimensions to wave-length [1,2,3].

Assuming harmonic time dependence and homogeneous, isotropic medium, Φ and Ψ have to satisfy the wave equations

$$\Delta\Phi + k_c^2 \Phi = 0 \tag{1a}$$

$$\Delta\Psi + k_t^2 \Psi = 0. \tag{1b}$$

k_c is the dilatational wave number and k_t is the rotational (shear) wave number of the infinite elastic medium, given by

$$k_c^2 = \frac{\omega^2 \rho}{G} \frac{1-2\mu}{2-2\mu} \quad \text{and}$$

$$k_t^2 = \frac{\omega^2 \rho}{G}$$

with angular frequency ω, density ρ, Poisson's ratio μ, and shear modulus G (including dissipation factor). Velocities and stresses can be written in terms of Φ and Ψ as

$$v_x = \frac{\partial\Phi}{\partial x} + \frac{\partial\Phi}{\partial y} \tag{2a}$$

$$v_y = \frac{\partial\Psi}{\partial y} - \frac{\partial\Psi}{\partial x} \tag{2b}$$

$$\sigma_y = \frac{2G}{j\omega} \left(\frac{\partial^2\Phi}{\partial y^2} + \frac{\mu}{1-2\mu} \left(\frac{\partial^2\Phi}{\partial x^2} + \frac{\partial^2\Phi}{\partial y^2}\right) - \frac{\partial^2\Psi}{\partial x \partial y}\right) \tag{2c}$$

$$\tau_{xy} = \frac{G}{j\omega} \left(2\frac{\partial^2\Phi}{\partial x \partial y} + \frac{\partial^2\Psi}{\partial y^2} - \frac{\partial^2\Psi}{\partial x^2}\right). \tag{2d}$$

We now suppose a given pressure wave along the upper edge of the head strip of the rail:

$$\sigma = \sigma_o e^{-jk_x x}.$$

In each strip a set of waves will appear with the same given x-wave number and both positive and negative y-wave numbers due to reflection at the edges of the strips:

$$\Phi = \Phi_+ e^{-jk_{cy} y} e^{-jk_x x} + \Phi_- e^{jk_{cy} y} e^{-jk_x x} \tag{3a}$$

$$\Psi = \Psi_+ e^{-jk_{ty} y} e^{-jk_x x} + \Psi_- e^{jk_{ty} y} e^{-jk_x x}. \tag{3b}$$

Introducing Eqs.(3) into wave equations (1) yields the unknown y-wave numbers as

$$k_{cy}^2 = k_c^2 - k_x^2$$

$$k_{ty}^2 = k_t^2 - k_x^2.$$

There are twelve unknown constants left, i.e. Φ_+, Φ_-, Ψ_+, Ψ_- in three strips. But there are also twelve boundary conditions as follows:

$$\left.\begin{aligned} \sigma_{y,\,head} &= 0 \\ \tau_{xy,head} &= 0 \end{aligned}\right\} \quad \text{evaluated at the uppermost edge}$$

$$\left.\begin{aligned} \sigma_{y,head} &= \sigma_{y,web} \\ \tau_{xy,head} &= \tau_{xy,web} \\ v_{x,head} &= v_{x,web} \\ v_{y,head} &= v_{y,web} \end{aligned}\right\} \quad \text{evaluated at the edge between head and web}$$

$$\left.\begin{aligned} \sigma_{y,web} &= \sigma_{y,foot} \\ \tau_{xy,web} &= \tau_{xy,foot} \\ v_{x,web} &= v_{x,foot} \\ v_{y,web} &= v_{y,foot} \end{aligned}\right\} \quad \text{evaluated at the edge between web and foot}$$

$$\left.\begin{aligned} \sigma_{y,foot} &= 0 \\ \tau_{xy,foot} &= 0 \end{aligned}\right\} \quad \text{evaluated at the lowest edge}$$

These conditions can be expressed in terms of the unknown quantities by Eqs.(2) and Eqs.(3), and the resulting set of linear equations may be solved numerically, for example. It is now easy to compute the velocities and stresses all over the three-layers-model by just substituting the found potentials - as given by Eqs.(3) - into Eqs.(2).

2.3 Results

The above-mentioned analysis was used to investigate a model of an UIC 60 type rail [4]. The stimulating wave was varied in a wide range of frequencies and wave lengths, the pressure amplitude being constant. Whenever a chosen combination of frequency and wave length coincides with that of a natural wave of the rail there is a resonance. Five different types of natural waves were detected within the audible frequency range. Fig.2 shows typical examples of each mode, which could be described - starting from the top - as vertical flexural wave, quasilongitudinal wave, 2nd longitudinal and 2nd flexural modes (with one longitudinal nodal line), and 3rd longitudinal mode (with two longitudinal nodal lines). Note that at 2.6 kHz (and even below) there is strong deformation of the cross section, so that simple homogeneous beam models would fail here.
For more details see [5].

3. CROSS-SECTION-MODEL

3.1 Description

This second model completes the investigations by introducing modes of the rail with displacements and stresses also perpendicular to those of the three-layers-model.

If one considers the cross-sectional view of a rail only, one

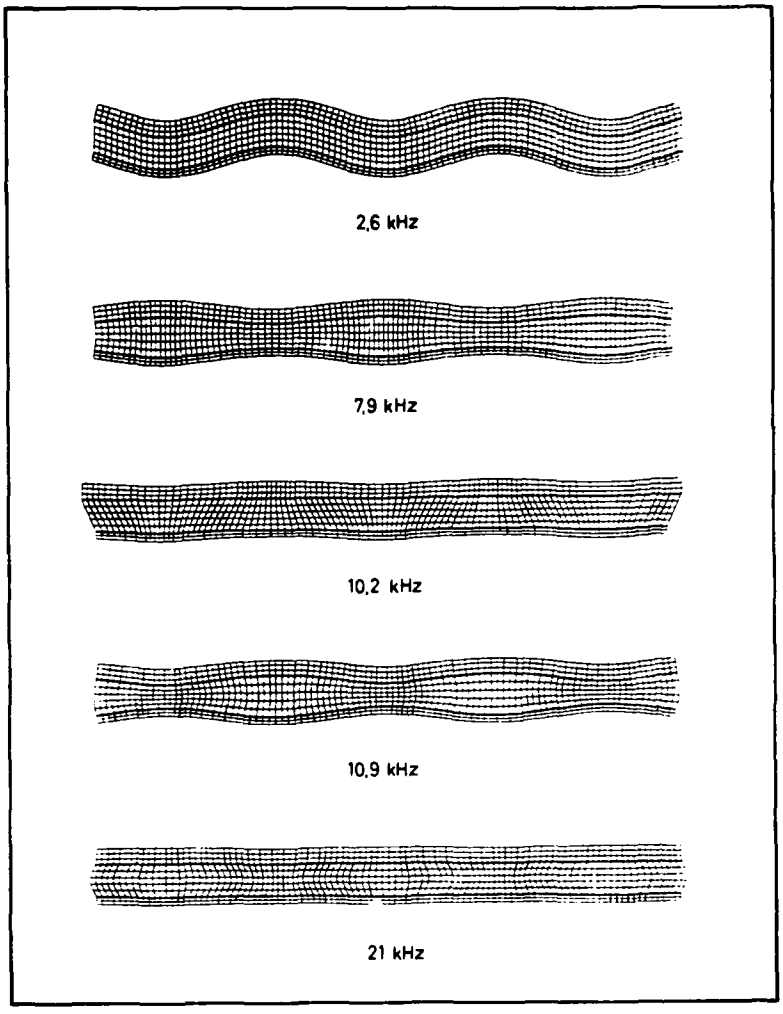

Fig.2. Natural waves of the three-layers-model (side-view of rail)

can think of it as a composition of one-dimensional bars belonging to the left and right halves of the rail foot, to the web, and to the head respectively (Fig.3). It is assumed that there are bending and longitudinal waves propagating along the bars, with displacements restricted to the cross-sectional plane. Since the model is only two-dimensional, it represents the case of zero wave number or infinite wave length along the actual rail, that means, the model yields the natural waves of the rail at their cutoff frequencies. Those types with zero cutoff frequency appear as static displacements of the undeformed cross section and don't supply much information therefore. Such types are the horizontal and vertical flexural waves along the rail as well as the torsional wave. At low frequencies these could be investigated much easier anyway, using one single homogeneous bar as a model.

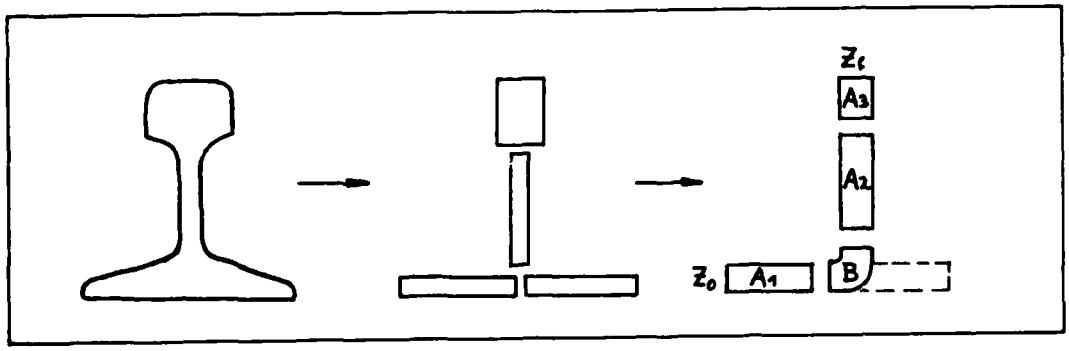

Fig.3. Cross-section-model. From left: rail shape, corresponding beam-system, calculated chain

3.2 Analysis

The treatment of flexural and longitudinal waves in homogeneous beams is well known [1]. For each bar there are six unknown amplitudes: bending moment M and bending angle ß, transverse force Q and transverse displacement η, as for the bending wave, and longitudinal force F and longitudinal displacement ξ, as for the longitudinal wave. Altogether twenty-four unknowns in four beams. There are just as many boundary conditions, demanding equality of corresponding displacements and vanishing net forces at the "inner" boundaries, and vanishing forces or displacements, depending on possible supports, at the external foot or head ends.

Though this settles the problem, a particular method is outlined here, which reduces the set of twenty-four equations to a product of four 6x6-matrices and a set of three equations in three variables.

Let x denote any fixed point of a beam within x = o at its 'input' and x = ℓ at its 'output'. Let Z_x be the 'state at x', a vector constituted by the six forces and displacements, evaluated at x. Then any such state of the beam can be expressed in terms of its input state [1],

$$Z_x = A_x \cdot Z_o, \tag{1}$$

by evaluating the general bending and longitudinal wave solutions of forces and displacements at 0 and x and eliminating the six unknown constants. A_x is a 6x6 matrix. In particular the output state of a beam is

$$Z_\ell = A_\ell \cdot Z_o \ . \tag{2}$$

To link two aligned beams, one simply equates the output of the first with the input of the second, $Z_{\ell 1} = Z_{o2}$, and obtains from Eq.(2)

$$Z_{\ell 2} = A_{\ell 2} \cdot Z_{o2} = A_{\ell 2} \cdot Z_{\ell 1} = A_{\ell 2} \cdot A_{\ell 1} \cdot Z_{o1},$$

the combination of beams obviously being represented by the product of their matrices.

The beam system, corresponding to the rail shape, was interpreted in such a way as a chain of elements (Fig.3) for which holds (a bit condensed)

$$Z_\ell = A_3 \cdot A_2 \cdot B \cdot A_1 \cdot Z_o = R \cdot Z_o \ . \tag{3}$$

B is the 'transfer' matrix of the right half of the foot, where input and output both are at the same beam end, at right angles, and depend on the given opposite end boundary conditions. The analysis of B is similar to that of the A-type. R is the resultant product matrix, depending on given material and geometric constants and frequency.

In case of vanishing forces at all external beam ends Eq.(3) becomes in detail

$$\begin{pmatrix} \eta_\ell \\ ß_\ell \\ \xi_\ell \\ 0 \\ 0 \\ 0 \end{pmatrix} = \begin{pmatrix} \cdot & \cdot & \cdot & \cdot & \cdot & \cdot \\ \cdot & \cdot & \cdot & \cdot & \cdot & \cdot \\ \cdot & \cdot & \cdot & \cdot & \cdot & \cdot \\ r_{41} & r_{42} & r_{43} & \cdot & \cdot & \cdot \\ r_{51} & r_{52} & r_{53} & \cdot & \cdot & \cdot \\ r_{61} & r_{62} & r_{63} & \cdot & \cdot & \cdot \end{pmatrix} \begin{pmatrix} \eta_o \\ ß_o \\ \xi_o \\ 0 \\ 0 \\ 0 \end{pmatrix} \tag{4}$$

The blank entries in R are unimportant, either being multiplied by zero or belonging to the unemployed set of equations. The fully written rest is a homogeneous set of linear equations in η_o, β_o, ξ_o yielding natural frequencies and associate initial sets (η_o, β_o, ξ_o) whenever its determinant equals zero. In all these cases the complete shapes of vibration can be calculated by analogous application of Eqs.(1) and (3), the chain being formed only up to the just examined point x.

To avoid redundancy in practice one should not set up the product matrix R explicitly but only the interesting left half. For this, one replaces $Z_o = (\eta_o, \beta_o, \xi_o, 0, 0, 0)^T$ by

$$Z_o' = \begin{pmatrix} 1 & 0 & 0 \\ 0 & 1 & 0 \\ 0 & 0 & 1 \\ 0 & 0 & 0 \\ 0 & 0 & 0 \\ 0 & 0 & 0 \end{pmatrix}$$

and performs Eq.(3) starting from the right-hand side, dealing with 6x3 matrices all the time [6].

Finally this method allows changing the boundary conditions at the external foot and head ends quite simply by changing Z_ℓ or Z_o (and B, if the right foot end is involved).

3.3 Results

The above-mentioned analysis served to investigate a cross-section-model of an UIC 60 type rail. Fig.4 shows some computed examples of natural modes and frequencies for either free, clamped, and pinned ends of the rail foot, the rail top being free in all cases.

It should be kept in mind that the clamped and pinned conditions of the model are valid c o n t i n u o u s l y along the actual rail and thus can't be compared directly to the usual clamping to sleepers. But their examination may basically show the effect of different mountings of the rail.

4. EXPERIMENTS

An UIC 60 rail piece of 1.7 m length was suspended 'free' from two flexible steel wires. By harmonic excitation at one end all determinable natural frequencies were succesively tuned in and each time the whole surface of the rail was scanned with an acceleration pickup, recording amplitude, direction, and phase shift. Hence the natural shapes of vibration were reconstructed. In the frequency range up to 12 kHz nine different kinds of waves were found, which are shown in Fig. 5. Table 1 gives a short summary of their main features and their respective model representations. The difference between frequencies of analogous modes are due to arbitrarily chosen wave lengths along the rail.

As can be seen, the two models reproduce nearly all natural waves within the investigated frequency range. The two exceptions, torsional and horizontal flexural waves, could be treated, at low frequencies, by equating the rail with a homogeneous bar, as said before.

This work has been sponsored by the German 'Bundesminister für Forschung und Technologie'. I like to thank Prof.Heckl for his help.

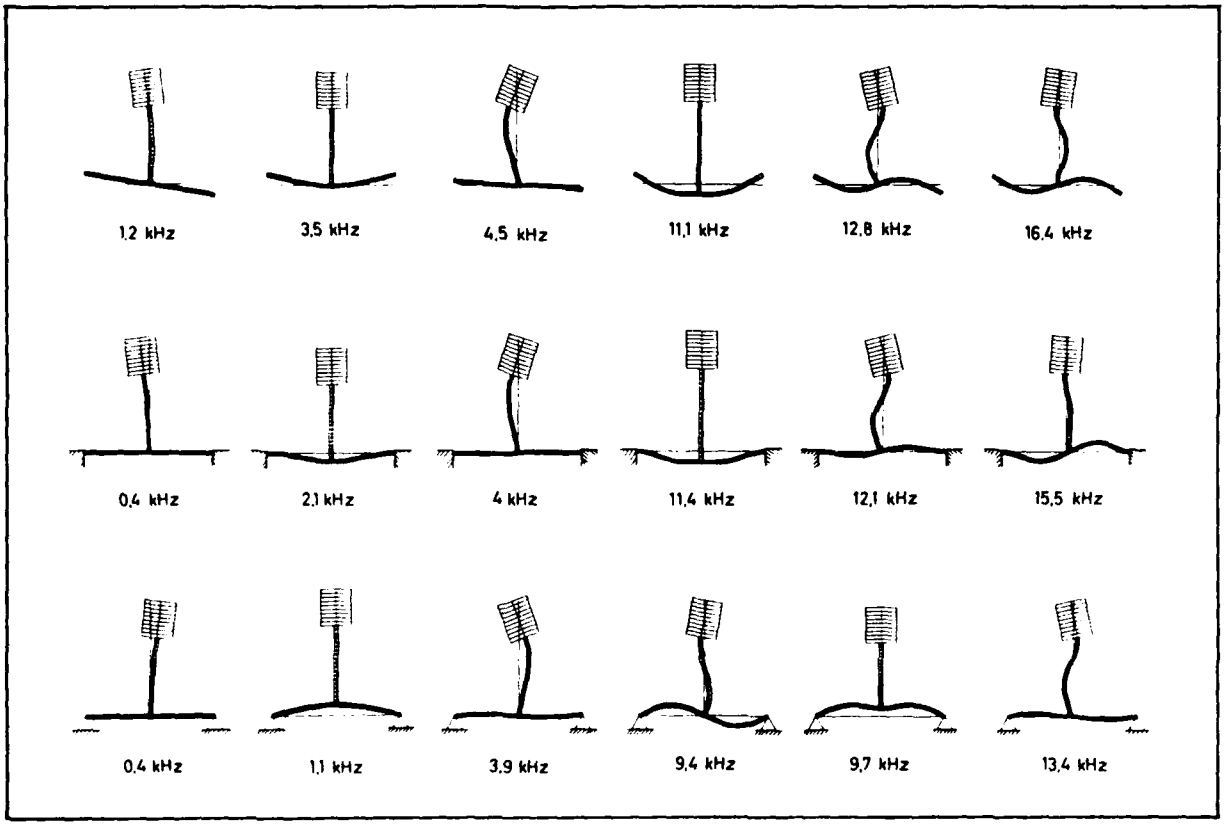

Fig.4. Natural modes of the cross-section-model

experiment (Fig.5)	3-layers (Fig.2)	cross-section (Fig.4)	character (along the rail)
3.3 kHz	2.6 kHz	-	vertical flexural
4.5 kHz	7.9 kHz	-	longitudinal
6 kHz (upper row)	1o.2 kHz	-	longitudinal, 2^{nd} mode
out of meas.range?	1o.9 kHz	11.1 kHz	'head against foot'
out of meas.range	21 kHz	-	longitudinal, 3^{nd} mode
6 kHz (middle row)	-	3.5 kHz	'foot only'
o.8 kHz	-	-	horizontal flexural
o.5 kHz	-	-	torsional
1.6 kHz	-	1.2 kHz	torsional, 2^{nd} mode
4.4 kHz	-	4.5 kHz	more complicated
12.1 kHz	-	12.8 kHz	more complicated

Tab.1. Analogous modes of experiment and theoretical models

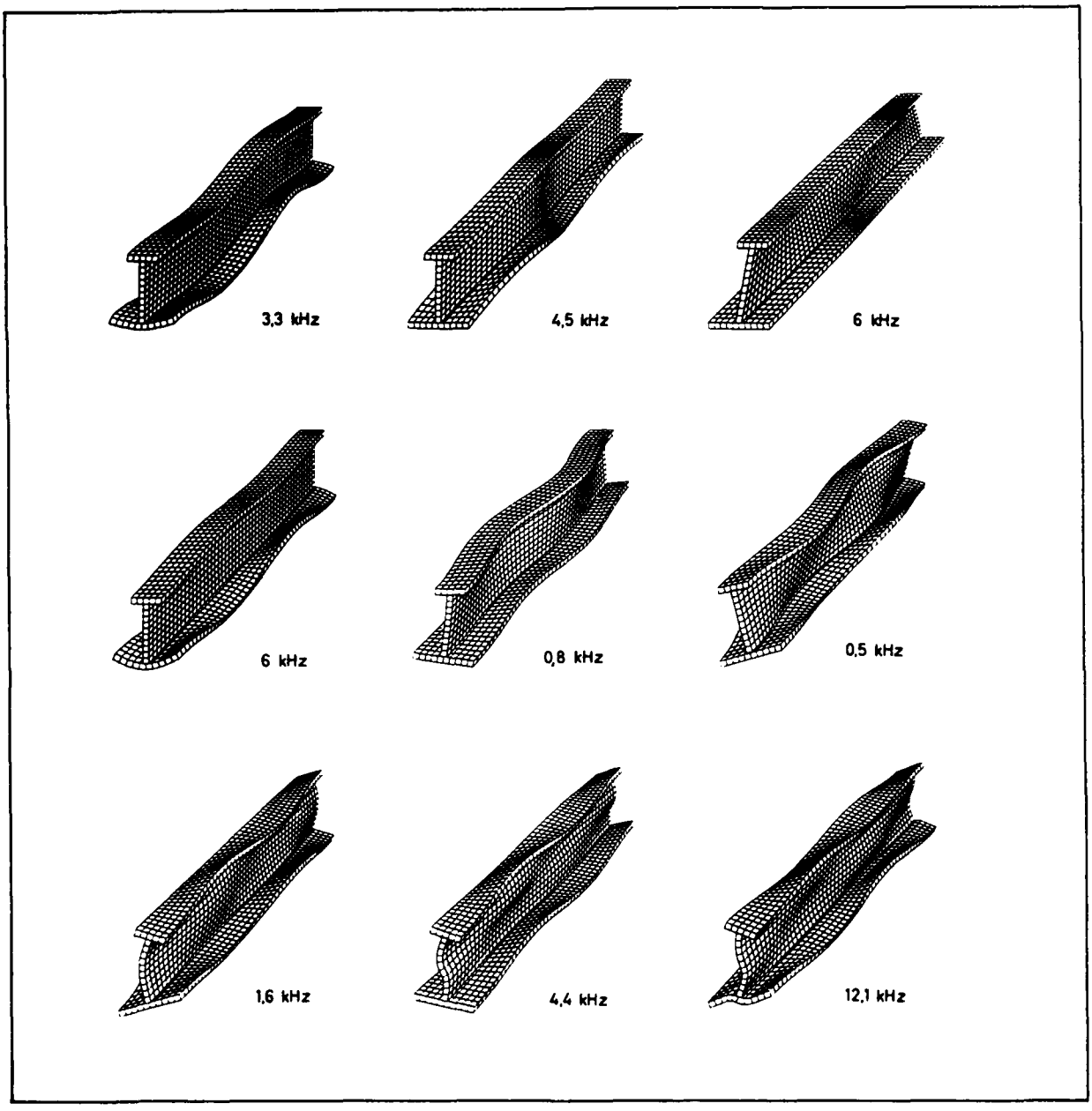

Fig.5. Experimentally determined natural waves of the rail (wave lengths unified for better comparability)

5. REFERENCES

1. L. CREMER and M. HECKL 1967 Körperschall. Berlin: Springer Verlag.

2. L.M. BREKHOVSKIKH 196o Waves in layered media. New York, London: Academic Press, p. 15.

3. T.R. MEEKER and A.H. MEITZLER 1964 Physical Acoustics, Vol.I, Part A. New York, London: Academic Press, p. 111.

4. F. FASTENRATH 1977 Die Eisenbahnschiene. Berlin: Verlag Wilhelm Ernst u. Sohn.

5. W. SCHOLL 1982 Acustica 52, 10-15. Schwingungsuntersuchungen an Eisenbahnschienen.

6. R. ZURMÜHL 1958 Matrizen. Berlin: Springer Verlag.

DYNAMICS AND STABILITY OF TRAIN-TRACK-SYSTEMS

R. Bogacz and K. Popp

Institute of Fundamental Technological Research
Polish Academy of Sciences,
Warsaw, Poland

Institute of Mechanics
University of Hanover,
Hanover, Germany

1. INTRODUCTION

The development of tracked high-speed transportation systems, e.g. fast wheel-rail-sytems with operational speeds up to 260 km/h or fast magnetically levitated trains with speeds up to 400 km/h, is enforced in several countries. With increasing travelling speed the dynamic interaction between vehicles and guideway becomes more and more important. Thus, there is a strong need for simple but reliable models for such systems in order to study the dynamical effects.

The aim of this paper is to introduce several linear and nonlinear models for train-track-sytems and to investigate their dynamical behaviour. The models are useful to examine the vertical dynamics as well as the lateral dynamics. The track-subsystem is modelled as an infinite Bernoulli-Euler-beam on an elastic foundation, while the train-subsystems consists of different continuous or lumped models which are infinite or finite in length, respectively. Both subsystems are in relative motion to each other with constant velocity. The suspension is modelled by linear springs and in some cases also by nonlinear springs.

The mathematical description of the different train-track-models depends on the modelling of the subsystems. It consists either of two coupled partial differential equations or a set or ordinary differential equations coupled with a partial differential equation. The solution is obtained applying the concept of travelling waves. Special attention is paid to the stationary solution and its stability.

The stability analysis for linear system is performed by investigating the roots of the resulting characteristic equation. Critical travelling speeds can be calculated depending on the system parameters. Explicit results are obtained in the case of vanishing damping. The influence of nonlinear suspension springs is also analyzed and the stability of the resulting limit cycles is discussed. The results obtained by comparatively simple models are believed to remain valid also for more complex systems and provide an insight into the problem of the dynamic stability of real train-track-systems.

2. SHORT LITERATURE REVIEW

Before we start the analysis, a short review of the available literature shall be given. The classical problem of an infinite Bernoulli-Euler-beam (flexural rigidity EI, mass per unit length μ) on a Winkler foundation (foundation constant c) under the action of a simple moving force F, travelling with constant speed U, was first addressed by Timoshenko [1, 1926]. The beam deflection $w(x,t)$, $-\infty < x < \infty$, $t>0$, is governed by the wellknown partial differential eq.

$$EI \frac{\partial^4 w(x,t)}{\partial x^4} + \mu \frac{\partial^2 w(x,t)}{\partial t^2} + cw(x,t) = F\delta(x-Ut), \qquad (1)$$

where δ denotes the Dirac 'function'. The steady-state solution was obtained by Ludwig [2, 1938], Dörr [3, 1943], [4, 1948], Kenney [5, 1954] and reviewed by Frýba [6, 1972] and Panovko, Gubanova [7, 1967]. It turns out that in the subcritical case $U < U_{cr}$, $U_{cr} = \sqrt[4]{4cEI/\mu^2}$, the steady-state solution w_∞ is a symmetric travelling wave, where the amplitudes are decreasing exponentially with the distance $\xi = x - Ut$ from the force location,

$$w_\infty(\xi) = \frac{Fe^{-\alpha|\xi|}}{4\alpha\sqrt{cEI}} \left(\cos\beta\xi + \frac{\alpha}{\beta}\sin\beta|\xi|\right), \tag{2}$$

$$\alpha = \sqrt{1 - (U/U_{cr})^2}\ \sqrt[4]{c/(4EI)}\ , \quad \beta = \sqrt{1 + (U/U_{cr})^2}\ \sqrt[4]{c/(4EI)}\ .$$

Usual design parameters for railway tracks result in critical velocities $U_{cr} >> U$. Thus, the subcritical case is of technical importance. However, the critical speed can be reduced by the action of additional axial forces, as pointed out by Kerr [8, 1972]. The supercritical case yields waves expanding from the force location with smaller wave lengths and amplitudes in front of the load as behind it. This case is discussed exhaustively in [3], and also in [4], [5], including the effect of viscous damping. The transient solution of (1) was investigated by Nowacki [9, 1963] and given in closed form by Stadler, Shreeves [10, 1970], where also the steady-state solution is discussed in detail.

There are various extensions of the classical problems towards more realistic models for railway tracks. A tensionless Winkler foundation was investigated in an analog-computer study by Criner, McCann [11, 1953], where only small differences of the beam deflection were found compared to the classical model with the same loading. Another paper devoted to this subject is due to Chorus, Adams [12, 1979]. Different beam models on a Pasternak foundation have been compared by Saito, Terasawa [13, 1980]. Though the Bernoulli-Euler beam theory compared to Timoshenko beam theory and the exact two-dimensional elastic theory gives extremely inconsistent results in front of the load for $U > U_{cr}$, it seems to be reliable for all velocities excluding the foregoing region. A periodic mass and stiffness distribution along the beam was investigated by Popp, Müller [14, 1982] in order to approximate the effects of sleepers in a railway track. Again, for realistic system parameters the differences compared to the classical model turned out to be very small. Thus, the classical model (1) seems to be quite appropriate for the investigation of real railways tracks.

However, from the application point of view, more realistic load models are required. The classical problem with a moving harmonic force $F(t) = F_0\cos\omega t$ instead of a constant force was investigated by Mathews [15, 1958], [16, 1959], also regarding the effect of viscous beam damping. Chonan [17, 1978] solved the corresponding problem for Timoshenko beams and compared the results. The effect of a moving mass has been discussed by Frýba [6, 1972]. He also solved the problem of rail excitation through a flat spot on a wheel which carried a secondary mass-spring-damper system cf. [18, 1960]. The problem of the stability of a rolling wheel on a rail has been investigated in recent papers by Korb [19, 1980] and Brommundt, Gao [20, 1983].

In contrast to the reviewed literature, the present paper is devoted to load models with more than one contact point. As a limit case of a long train, an infinite moving beam will be investigated in detail. On the other hand, the case of a moving lumped system with two contact points will be analyzed. Superposition of the solution for this system may provide insight in the dynamical behaviour of trains of finite length.

3. SYSTEM MODELS

In the development of tracked high-speed transportation systems it is of great interest to study the stability behaviour of the train-track-models listed in Table 1, where equivalent models for the lateral dynamics (left) and vertical dynamics (right) as well as train models of infinite length (above) and finite length (below) are shown. From the mathematical point of view, the vertical dynamics can be deduced from the corresponding lateral dynamics by superposition of an appropriate static load. In a first part, train models of infinite length will be analyzed, cf. model 1 and 2. Beside the detailed investigation of linear elastic foundations, also the effect of nonlinear elastic foundations will be discussed. In a second part, train models of finite length will be analyzed , see model 3, 4, 5. Since model 2 and 4 are limit cases of model 1 and 3, respectively, and model 5 follows from model 3 by appropriate superposition, we confine our investigations to analyze the models 1 and 3. Throughout the analysis Bernoulli-Euler beam theory will be applied and damping will be neglected, although it is always physically present.

4. INTERACTION OF TWO FINITE BEAMS ON ELASTIC FOUNDATION DUE TO RELATIVE MOTION

4.1 System dynamics in case of linear elastic foundations

We consider model 1, cf. Table 1, composed of two infinite continuous beams $j,j = 0,1$, where beam 0 moves with constant velocity U_o relative to beam 1. Each beam (flexural rigidity E_jI_j, mass per unit length μ_j, longitudinal force T_j, $T_j>0$ means compression and $T_j<0$ means tension) is supported by a linear elastic foundation (foundation constant c_j). Two reference frames with coordinates (x_1,x_2) and $(\overset{*}{x}_1,\overset{*}{x}_2)$ are used, attached to beam 1 and 0, respectively. For undisturbed motion the beam displacements $w_j(x_1,t)$ in x_2-direction are assumed to be zero. The equations of motion with respect to the (x_1,x_2)-frame read

$$E_1I_1 \frac{\partial^4 w_1}{\partial x_1^4} + T_1 \frac{\partial^2 w_1}{\partial x_1^2} + \mu_1 \frac{\partial^2 w_1}{\partial t^2} + p_f(x_1,t) - p_1(x_1,t) = 0$$

$$p_f(x_1,t) = c_1 w_1(x_1,t) \ . \tag{3}$$

$$E_oI_o \frac{\partial^4 w_o}{\partial x_1^4} + T_o \frac{\partial^2 w_o}{\partial x_1^2} + \mu_o\left(\frac{\partial^2 w_o}{\partial t^2} + 2U_o \frac{\partial^2 w_o}{\partial x_1 \partial t} + U_o^2 \frac{\partial^2 w_o}{\partial x_1^2} \right) - p_o(x_1,t) = 0. \tag{4}$$

Here, p_j, $j = 0,1$, denotes the pressure which acts on beam j due to the disturbed motion of the beams. From the condition of conformity it follows

$$p_1(x_1,t) = -p_o(x_1,t) = c_o(w_o - w_1) \ . \tag{5}$$

In order to simplify the analysis we describe eq. (4) in the moving $(\overset{*}{x}_1,\overset{*}{x}_2)$-frame, where

$$x_1 - \overset{*}{x}_1 - U_o t = 0 \ , \quad x_2 - \overset{*}{x}_2 = 0 \ . \tag{6}$$

Then eq. (4) takes the form

$$E_oI_o \frac{\partial^4 \overset{*}{w}_o}{\partial \overset{*}{x}_1^4} + T_o \frac{\partial^2 \overset{*}{w}_o}{\partial \overset{*}{x}_1^2} + \mu_o \frac{\partial^2 \overset{*}{w}_o}{\partial t^2} + c_o(\overset{*}{w}_o - \overset{*}{w}_1) = 0 \ . \tag{7}$$

To solve the set of eqs. (3), (5), (7) together with the condition (6), we are looking for a steady-state solution in the form of travelling waves,

$$w_j = A_j\, e^{i k_j (x_1 - v_1 t)} \quad , \quad \overset{*}{w}_j = \overset{*}{A}_j\, e^{i \overset{*}{k}_j (\overset{*}{x}_1 - v_2 t)} \quad , \tag{8}$$

$$-p_j = (-1)^j\, P e^{i k_j (x_1 - v_1 t)} \quad , \quad j = 0,\ 1 \ .$$

Making use of relation (6) we find

$$A_j = \overset{*}{A}_j \quad , \quad \overset{*}{k}_j = k_j = k \quad , \quad \mathrm{Im}(k) = 0 \ , \quad j = 0,1 \ , \tag{9}$$

$$v_1 - v_2 - U_o = 0 \ . \tag{10}$$

Introducing (8) into (3), (5), (7) and regarding (9), (10) it follows

$$A_1 = \frac{P}{\mu_1 k^2 (R_1^{\,2} - v_1^{\,2})} \quad , \quad R_1^{\,2} = \frac{1}{\mu_1} \left(E_1 I_1 k^2 - T_1 + \frac{c_1}{k^2}\right) \quad , \tag{11}$$

$$A_o = \frac{-P}{\mu_o k^2 (R_o^{\,2} - v_2^{\,2})} \quad , \quad R_o^{\,2} = \frac{1}{\mu_o} \left(E_o I_o k^2 - T_o\right) \quad , \tag{12}$$

$$P = c_o (A_o - A_1) \ . \tag{13}$$

The condition of a unique solution of (11) - (13) with respect to A_o, A_1 yields a relation between $v_1^{\,2}$ and $v_2^{\,2}$. With the abbreviations

$\eta = \dfrac{\mu_1}{\mu_o}$ and $\alpha^2 = \dfrac{c_o}{\mu_o k^2}$ it follows

$$\frac{1}{\eta (R_1^{\,2} - v_1^{\,2})} - \frac{v_2^{\,2} - R_o^{\,2} - \alpha^2}{\alpha^2 (R_o^{\,2} - v_2^{\,2})} \equiv F_1(v_1^{\,2}) - F_2(v_2^{\,2}) = 0 \ . \tag{14}$$

Fig. 1 shows qualitatively a plot of the functions $F_1(v_1^{\,2})$, $F_2(v_2^{\,2})$ and $F_1(v_1^{\,2}) = F_2(v_2^{\,2})$. Eq. (14) in combination with (10) constitutes the characteristic equation of the problem under consideration

$$\Phi(v_1, v_2) \equiv F_1(v_1^{\,2}) - F_2(v_2^{\,2}) = 0 \quad , \quad v_1 - v_2 - U_o = 0 \ . \tag{15}$$

4.2 Stability analysis

In the present case without damping the solution (8) cannot become asymptotically stable, independent of the value of the velocity U_o. Stability of the steady-state solution (8) requires $\mathrm{Im}(v_\nu) = 0$, $\nu = 1,2$, and instability is given if $\mathrm{Im}(v_\nu) < 0$, $\nu = 1$ or $\nu = 2$. Now we will analyze the stability behaviour depending on the velocity U_o. First we observe that stability is given if and only if there exist four different real roots $v_\nu^{(n)}$, $\nu = 1,2$, $n = 1,2,3,4$ of eq. (15). If there exist only two real roots $v_\nu^{(1)}$, $v_\nu^{(2)}$, then in view of relation (10) the remaining complex roots must have the form

$$v_1^{(3)} = r_1 + is\ ,\quad v_2^{(3)} = r_2 + is\ ,$$
$$v_1^{(4)} = r_1 - is\ ,\quad v_2^{(4)} = r_2 - is\ , \tag{16}$$

which leads to instability.

The regions S_I of U_o for which

$$S_I = \{U_o: \exists v_\nu,\ \mathrm{Im}(v_\nu) \neq 0,\ \ \phi(v_\nu, U_o) = 0\} \tag{17}$$

we will call instability regions. The following subset S_{ID} of S_I,

$$S_{ID} = \{U_o: \exists v_\nu,\ \mathrm{Im}(v_\nu) \neq 0,\ \ \mathrm{Re}(v_\nu) = 0,\ \ \phi(v_\nu, U_o) = 0\}\ , \tag{18}$$

determines the parameters of divergent instability. Since the analytical determination of critical parameters is complicated we use a geometrical approach, see e.g. Fig. 2. The critical values of U_o which result in boundaries of the instability region S_I are determined in a v_1, v_2-plane by the straight lines $v_2 = v_1 - U_o$ tangent to the curves obtained from (14). In the range $S = \{U_o: U_o \in [U_{1cr}, U_{2cr}]\}$, cf. Fig. 2, the solution (8) describes waves with amplitudes increasing in time. Beside this solution exists also a trivial solution, thus, according to Liapunov's instability criterion the range S is the range of instability, $S = S_I$.

Now we will determine the instability regions for particular cases. It can be shown from the form of the characteristic curves in a v_1, v_2-plane that for R_o^2, R_1^2, $\alpha^2 \in [0, \infty)$ the region of instability S_I is bounded by

$$|R_o| + |R_1| \leq |U_{1cr}| \leq \sqrt{(\eta+1)\ R_1^2 + \frac{R_o^2}{\eta}}\ ,\quad |U_{2cr}| \geq \sqrt{R_o^2+\alpha^2} + \sqrt{R_1^2 + \frac{\alpha^2}{\eta}} \tag{19}$$

The limit case $\alpha^2 = \dfrac{c_o}{\mu_o k^2} \to \infty$ describes a stiff connection between beam 0 and 1. In this case U_{1cr} reaches a finite limit value, while U_{2cr} tends to infinite.
The case $R_o^2 = E_oI_ok^2 - T_o = 0$ belongs to a moving beam 0 with rigidity equal to zero. For $T_o = 0$, $E_oI_o = 0$ the case of a moving chain of densily distributed oscillators without mass interaction can be gained, cf. model 2 in Table 1. The corresponding v_1,v_2-plane is shown in Fig. 2. Estimates of critical velocities for this case can be found from (19) substituting $R_o^2 = 0$. It should be noted that R_o^2 can even be negative but bounded

$$R_o^2 > R_{ocr}^2 = -\frac{\eta\alpha^2 R_1^2}{\eta R_1^2 + \alpha^2}\ . \tag{20}$$

The critical value R_{ocr}^2 can be found from the existence of a stability region in the neighborhood of $U_o = 0$, i.e. from $F_1(v_1^2=0) = F_2(v_2^2=0,\ R_o^2=R_{ocr}^2)$. For corresponding v_1,v_2-plane is shown in Fig. 3. Thus, $R_o^2 < 0$ yields

$$U_{1cr}^2 \in \left(R_1^2 + \frac{\alpha^2}{\eta}\frac{R_o^2}{\alpha^2+R_o^2}\ ,\quad (\eta+1)\ R_1^2 + \frac{R_o^2}{\eta}\right]\ . \tag{21}$$

It follows, that e.g. a breaking train can become unstable for $U_o > U_{1cr}$, where U_{1cr} may be very small. The latter is a wellknown fact from train accidents.

4.3 The effect of nonlinear elastic foundations

In case of nonlinear foundation characteristics the determination of critical travelling speeds for given wave amplitudes is possible only in some particular cases, cf. Bogacz, Kaliski [21, 1964] and Bogacz [22, 1968], where the problem of self-excitation of nonlinear oscillators moving along a beam has been investigated. We study this case using the analogy with a discrete system of two degrees of freedom and apply the concept of modal or limit lines in a w_o, w_1-configuration plane, cf. Rosenberg [23, 1962]. We assume an approximation of the nonlinear foundation characteristics by two odd terms of a Taylor series expansion, which yields in contrast to (3), (5)

$$p_f = c_1(w_1 + \delta_1 w_1^3) \quad , \tag{22}$$

$$p_1 = -p_o = c_o\,[(w_o - w_1) + \delta_o(w_o - w_1)^3] \, . \tag{23}$$

Here, $\delta_j > 0$ and $\delta_j < 0$, $j = 0,1$, characterize a hardening and softening foundation characteristic, respectively. Assuming the solution of the equations of motion in form of travelling waves and applying one of the approximation methods, e.g. Galerkin's method, we obtain the characteristic equation. In contrast to the linear case the relations for v_1^2 and v_2^2 depend on the wave amplitudes A_1 and A_o,

$$v_1^2 = R_1^2 \{1 + \delta_1 A_1^2 - \frac{\alpha^2}{\eta}(\lambda-1)\,[1 + \delta_o a_1^2 (\lambda-1)^2]\} \tag{24}$$

$$v_2^2 = R_1^2 \{\frac{R_o^2}{R_1^2}\,\alpha^2(1-\frac{1}{\lambda})\,[1 + \delta_o A_1^2(\lambda-1)]\} \quad , \tag{25}$$

where $\lambda = \frac{w_o}{w_1} = \frac{A_o}{A_1}$. Utilizing (24) and (25) in connection with (15) we determine the equation of limit lines in the form

$$\phi_n(\lambda, A_1, U_o) = 0 \, . \tag{26}$$

Now, the limit lines can be plotted in a w_o, w_1-plane for given system parameters. The results are shown for two supercritical cases in Fig. 4 ($U_o^2 = 2R_1^2$) and Fig. 5 ($U_o^2 = 16R_1^2$). If there exists a equipotential line,

$$H = H(\lambda, A_1) = \text{const.} \quad , \tag{27}$$

tangent to the limit line, then the point of tangency B, determines the trajectory of the limit cycle. If the curvature of the limit line in B is greater than the curvature of the equipotential line, then the limit cycle is unstable, $B \equiv B_I$, in the opposite case the limit cycle is stable, $B \equiv B_S$, as can be seen from small changes of the potential energy density H.

For $U_o^2 = 2R_1^2$, cf. Fig. 4, the trivial solution is unstable. The wave amplitudes increase in time until the energy level $H = H_S$ and a stable limit cycle B_S is reached. This holds true for hardening as well as for softening foundation characteristics. For $U_o^2 = 16\,R_1^2$, cf. Fig. 5, the trivial solution is stable in a small neighborhood near the origin of the configuration plane in

either case. However, for the hardening foundation characteristic there exist two limit cycles. A stable one, B_S, with energy level H_S and an unstable one, B_I, with energy level H_I. For $H_I \leq H < H_S$ the system becomes unstable, otherwise it is stable.

5. INTERACTION OF A MOVING LUMPED SYSTEM WITH AN INFINITE BEAM ON A LINEAR ELASTIC FOUNDATION

We consider model 3, cf. Table 1, which consists of a one degree-of-freedom vehicle (mass m, spring constants c) with two contact points (distance L), moving on an infinite beam supported by a linear elastic foundation. The remaining parameters and the reference frames are specified analogously to Section 4. First we analyze the case of a single periodic contact force F(t) acting at pdint $\overset{*}{x}_1=0$, cf. Mathews [15, 1958]. The corresponding equation of motion reads,

$$E_1 I_1 \frac{\partial^4 \overset{*}{w}_1}{\partial \overset{*}{x}_1^4} + T_1 \frac{\partial^2 \overset{*}{w}_1}{\partial \overset{*}{x}_1^4} + \mu_1 \left(\frac{\partial^2 \overset{*}{w}_1}{\partial t^2} - 2 U_o \frac{\partial^2 \overset{*}{w}_1}{\partial \overset{*}{x}_1 \partial t} + U_o^2 \frac{\partial^2 \overset{*}{w}_1}{\partial \overset{*}{x}_1}\right) + c_1 \overset{*}{w}_1 - p_1(\overset{*}{x}_1 t) = 0,$$

$$p_1(\overset{*}{x}_1,t) = F(t)\,\delta(\overset{*}{x}_1) = Pe^{-i\omega t}\,\delta(\overset{*}{x}_1)\ . \tag{28}$$

The solution can be composed of two parts,

$$\overset{*}{w}_1(\overset{*}{x}_1,t) = \overset{*}{W}_1(\overset{*}{x}_1,t)\,H(-\overset{*}{x}_1) + \overset{*}{W}_2(\overset{*}{x}_1,t)\,H(\overset{*}{x}_1)\ , \tag{29}$$

where $H(\overset{*}{x})$ is the Heavyside unit function, i.e. $H(\overset{*}{x}) = 1$ if $\overset{*}{x} > 0$ and $H(\overset{*}{x}) = 0$ if $\overset{*}{x} < 0$. The functions $\overset{*}{W}_1$ and $\overset{*}{W}_2$ fulfill the following compatibility condition at $\overset{*}{x}_1=0$:

$$\frac{\partial^n \overset{*}{W}_1}{\partial \overset{*}{x}_1^n} = \frac{\partial^n \overset{*}{W}_2}{\partial \overset{*}{x}_1^n}\ ,\quad n = 0,\ 1,\ 2\ ,$$

$$E_1 I_1 \left(\frac{\partial^3 \overset{*}{W}_1}{\partial \overset{*}{x}_1^3} - \frac{\partial^3 \overset{*}{W}_2}{\partial \overset{*}{x}_1^3}\right) + Pe^{-i\omega t} = 0\ . \tag{30}$$

Utilizing the functions B_ν, C_ν, $\nu = 1,2$, the solution can be obtained in the form

$$W_1(\overset{*}{x}_1,t) = [B_1(r_1\overset{*}{x}_1) + C_1(r_2\overset{*}{x}_1)]e^{-i\omega t},$$
$$W_2(\overset{*}{x}_1,t) = [B_2(r_3\overset{*}{x}_1) + C_2(r_4\overset{*}{x}_1)]e^{-i\omega t}\ . \tag{31}$$

Here, r_n, $n = 1,2,3,4$, are the roots of the characteristic equation

$$E_1 I_1 r^4 + (T_1 + \mu_1 U_o^2)\, r^2 - 2 i \mu_1 U_o \omega r + c_1 - \mu_1 \omega^2 = 0\ . \tag{32}$$

From the condition of radiation it follows $\mathrm{Re}(r_n) > 0$ for $n = 1,2$ and $\mathrm{Re}(r_n) \leq 0$ for $n = 3,4$. Introducing (31) in (30), (29), we obtain a relation

between beam deflection $\overset{*}{w}_1(\overset{*}{x}_1,t)$, force $F(t)$, velocity U_o and frequency ω. In steady-state the time dependece cancels out and it follows

$$\left.\frac{\overset{*}{w}_1(\overset{*}{x}_1,t)}{F(t)}\right|_{t\to\infty} = \frac{\overset{*}{w}_{1\infty}(\overset{*}{x}_1)}{P} = G(\overset{*}{x}_1,\ \omega,\ U_o)\ . \tag{33}$$

For free elastic waves the relation between wave velocity $\overset{*}{v}$ and wave number k reads

$$\overset{*}{v}^2 = (E_1I_1k^4 - Tk^2 + c)/\mu k^2\ , \tag{34}$$

which leads to the critical velocity U_{cr},

$$\left.\frac{\partial \overset{*}{v}}{\partial k}\right|_{\overset{*}{v}=U_{cr}} = 0 \Rightarrow U_{cr}^2 = \sqrt{\frac{4c_1E_1I_1}{\mu_1^2}} - \frac{T_1}{\mu_1}\ . \tag{35}$$

Now we analyze model 3 of Table 1. Since symmetry is assumed, the equation of motion for the mass m takes the simple form

$$m\frac{d^2y}{dt} + F_c(t) = 0\ , \tag{36}$$

$$F_c(t) = c[2y(t) - \overset{*}{w}_1(-\tfrac{L}{2},\ t) - \overset{*}{w}_1(\tfrac{L}{2},\ t)], \tag{37}$$

where y characterizes the mass displacement and $F_c/2$ denotes the contact force in x_2-direction. The beam equation is given by (28), where the load reads

$$p_1(\overset{*}{x}_1,t) = \tfrac{1}{2}F_c(t)\ \delta(-\tfrac{L}{2}) + \tfrac{1}{2}F_c(t)\ \delta(+\tfrac{L}{2})\ . \tag{38}$$

For steady-state motion from (36), (37) is follows

$$\left.\frac{2c-m\omega^2}{c} = \frac{\overset{*}{w}_1(-\frac{L}{2},t) + \overset{*}{w}_1(\frac{L}{2},t)}{y(t)}\right|_{t\to\infty}\ . \tag{39}$$

Using (33), (37) and (39) we obtain the characteristic equation in the form

$$\frac{2c-m\omega^2}{cm\omega^2} = 2G(0,\ \omega,\ U_o) + G(L,\ \omega,\ U_o) + G(-L,\ \omega,\ U_o). \tag{40}$$

For $U_o^2 < U_{cr}^2$ the function $G(\overset{*}{x}_1,\ \omega,\ U_o)$ reads

$$\begin{aligned} G(\overset{*}{x}_1,\ \omega,\ U_o) = {} & [G_R(|\overset{*}{x}_1|,\ \omega,\ U_o) + i\ G_I(|\overset{*}{x}_1|,\ \omega,\ U_o)]\ H(\overset{*}{x}_1) + \\ & [G_R(|\overset{*}{x}_1|,\ \omega,\ U_o) - i\ G_I(|\overset{*}{x}_1|,\ \omega,\ U_o)]\ H(-\overset{*}{x}_1)\ . \end{aligned} \tag{41}$$

Here,

$$G_R = (4k^2 - \varepsilon_1^2 + \varepsilon_2^2)[\varepsilon_1^{-1} \exp(-\varepsilon_1|\overset{*}{x}_1|) + \varepsilon_2^{-1} \exp(-\varepsilon_2|\overset{*}{x}_1|)] \cos k \overset{*}{x}_1/N +$$

$$+ 4k^2 [\exp(-\varepsilon_1|\overset{*}{x}_1|) + \exp(-\varepsilon_2|\overset{*}{x}_1|)] \sin k|\overset{*}{x}_1|/N,$$

$$G_I = (4k^2 + \varepsilon_1^2 - \varepsilon_2^2)[\varepsilon_1^{-1} \exp(-\varepsilon_1|\overset{*}{x}_1|) - \varepsilon_2^{-1} \exp(-\varepsilon_2|\overset{*}{x}_1|)] \sin k|\overset{*}{x}_1|/N -$$

$$- 4k^2 [\exp(-\varepsilon_1|\overset{*}{x}_1|) - \exp(-\varepsilon_2|\overset{*}{x}_1|)] \cos k \overset{*}{x}_1/N ,$$

$$N = 2E_1I_1[(4k^2 + \varepsilon_1^2 - \varepsilon_2^2)^2 + 16\, k^2\varepsilon_2^2] , \tag{42}$$

$$2k^2 - \varepsilon_1^2 - \varepsilon_2^2 = (\mu_1 U_o^2 + T_1)/E_1I_1, \quad k(\varepsilon_1^2 - \varepsilon_2^2) = \mu_1 U_o \omega/E_1I_1 ,$$

$$(k^2 + \varepsilon_1^2)(k^2 - \varepsilon_2^2) = (c_1 - \mu_1\omega^2)/E_1I_1,$$

$$k = |\mathrm{Im}(r_n)|, \quad n = 1,2,3,4, \quad \varepsilon_1 = |\mathrm{Re}(r_1)|, \quad \varepsilon_2 = |\mathrm{Re}(r_2)| .$$

Since $G_I(0, \omega, U_o) = 0$ holds and due to symmetry the characteristic equation (40) for $U_o^2 < U_{cr}^2$ reduces to

$$\frac{2\alpha_o^2 - \omega^2}{m\alpha_o^2\omega^2} - 2\, G_R(0, \omega, U_o) - 2G_R(L, \omega, U_o) = 0 , \tag{43}$$

where $\alpha_o^2 = c/m$. Now we discuss briefly the stability behaviour of the steady-state solution. To check stability we apply a small disturbance and put $\omega = \Omega - i\varepsilon_o$, ε_o small, into (43). This yields

$$\Omega^2 - \varepsilon_o^2 - \frac{2\alpha_o^2}{1+2m\alpha_o^2[G_R(o)+G_R(L)]} = 0 , \tag{44}$$

$$2\varepsilon_o\Omega = 0 . \tag{45}$$

For $\varepsilon_o \neq 0$ it follows, that in case of $U_o^2 < U_{cr}^2$ the only instability may occur at $\Omega = 0$. Other instability boundaries are not found. For $U_o^2 = U_{cr}^2$ a similar situation is given as in the case of a lumped system interacting with a string, cf. Bogacz [24, 1979], but much more complicated because of the nonlinear relation between wave number and wave velocities. Thus, in the present case without damping the steady-state solution may become unstable for velocities $U_o^2 \geq U_{cr}^2$, similarly to the case of the interaction between two continuous beams.

6. CONCLUDING REMARKS

For the dynamic analysis of an infinite beam on an elastic foundation under the action of a moving infinite beam or a moving lumped subsystem of finite length, the wave approach is appropriate and yields results of practical importance. The methods applied and the results obtained for comparatively simple models can be extended to more complex systems and, thus, provide insight into the problem of the dynamic stability of real train-track-systems.

7. REFERENCES

1. S. TIMOSHENKO 1926 Proc. 2nd. Int. Congr. Appl. Mech., Zürich, 407-418. Method of Analysis of Statical and Dynamical Stresses in Rail.

2. K. LUDWIG 1938 Proc. 5th. Int. Congr. Appl. Mech., 650-655. Deformation of a Rail Elastically Supported and of Infinite Length by Loads Moving at a Constant Horizontal Velocity.

3. J. DÖRR 1948 Ing.-Archiv 14, 167-192. Der unendliche, federnd gebettete Balken unter dem Einfluß einer gleichförmig bewegten Last.

4. J. DÖRR 1948 Ing.-Archiv 16, 287-298. Das Schwingungsverhalten eines federnd gebetteten, unendlich langen Balkens.

5. J.T. KENNEY 1954 J. Appl. Mech. 21, 359-364. Steady-State Vibrations of Beams on Elastic Foundation for Moving Load.

6. L. FRÝBA 1972 Vibrations of Solids and Structures Under Moving Loads. Groningen: Noordhoff.

7. Y.G. PANOVKO and I.I. GUBANOVA 1967 Stability and Oscillation of Elastic Systems: Modern Concept, Paradoxes and Errors. Moskau: Nauka, Engl. Transl.: NASA TT F-751, 1973.

8. A.D. KERR 1972 Int. J. Mech. Sci. 14, 71-78. The Continuously Supported Rail Subjected to an Axial Force and a Moving Load.

9. W. NOWACKI 1963 Dynamics of Elastic Systems. New York: Wiley.

10. W. STADLER and R.W. SHREEVES 1970 Quart. Journ. Mech. and Appl. Math. 23, 197-208. The Transient and Steady-State Response of the Infinite Bernoulli-Euler Beam with Damping and an Elastic Foundation.

11. H.E. CRINER and G.D. McCANN 1953 J. Appl. Mech. 20, 13-22. Rails on Elastic Foundations Under the Influence of High-Speed Travelling Loads.

12. J. CHOROS and G.G. ADAMS 1979 J. Appl. Mech. 46. 175-180. A Steadily Moving Load on an Elastic Beam Resting on a Tensionless Winkler Foundation.

13. H. SAITO and T. TERASAWA 1980 J. Appl. Mech. 47, 879-883. Steady-State Vibrations of a Beam on a Pasternak Foundation for Moving Loads.

14. K. POPP and P.C. MÜLLER 1982 Z. angew. Math. u. Mech. 62, T65-T67. Ein Beitrag zur Gleisdynamik.

15. P.M. MATHEWS 195° Z. angew. Math. u. Mech. 38, 105-115. Vibrations of a Beam on Elastic Foundation.

16. P.M. MATHEWS 1959 Z. angew. Math. u. Mech. 39, 13-19. Vibrations of a Beam on Elastic Foundation II.

17. S. CHONAN 1978 Z. angew. Math. u. Mech. 58, 9-15. Moving Harmonic Load on an Elastically Supported Timoshenko Beam.

18. L. FRÝBA 1960 Z. angew. Math. u. Mech. 40, 17o-184. Schwingungen des unendlichen, federnd gebetteten Balkens unter der Wirkung eines unrunden Rades.

19. J. KORB 1980 VDI-Berichte Nr. 381, 99-104. Parametererregung beim Rad-Schiene-System.

20. E. BROMMUNDT and S. GAO 1983 to appear in Z. angew. Math. und Mech. 64. Zur Stabilität des auf einer Schiene rollenden Rades.

21. R. BOGACZ and S. KALISKI 1964 Proc. Vibr. Probl. 5. Stability of Motion of Nonlinear Oscillators Moving along a Beam on an Elastic Foundation.

22. R. BOGACZ 1968 Proc. Vibr. Probl. 9, 55-77. Interaction between a Moving Set of Nonlinear Oscillators and a Travelling Wave.

23. R.M. ROSENBERG 1962 J. Appl. Mech. 29, 7-14. The Normal Modes of Nonlinear n-Degree-of-Freedom Systems.

24. R. BOGACZ 1979 Nonlin. Vib. Probl. 19, 240-250. On Self-Excitation of Moving Oscillator Interacting at Two Points with a Continuous System.

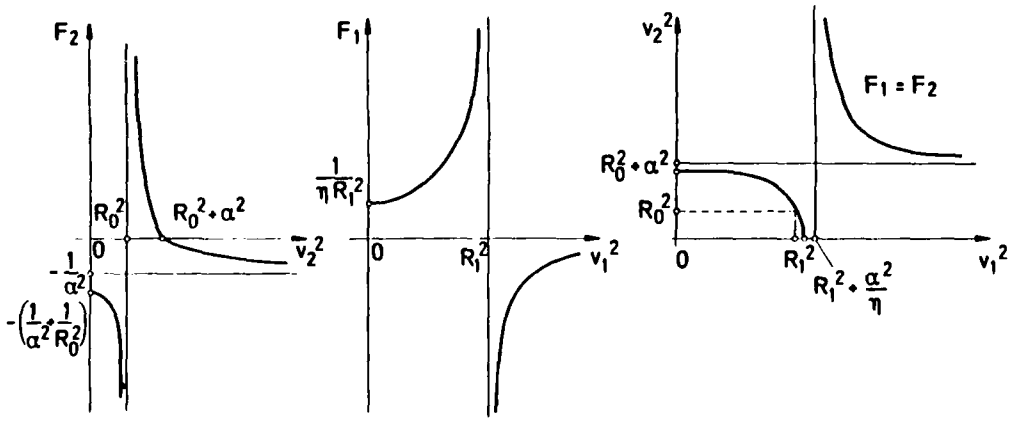

Fig. 1

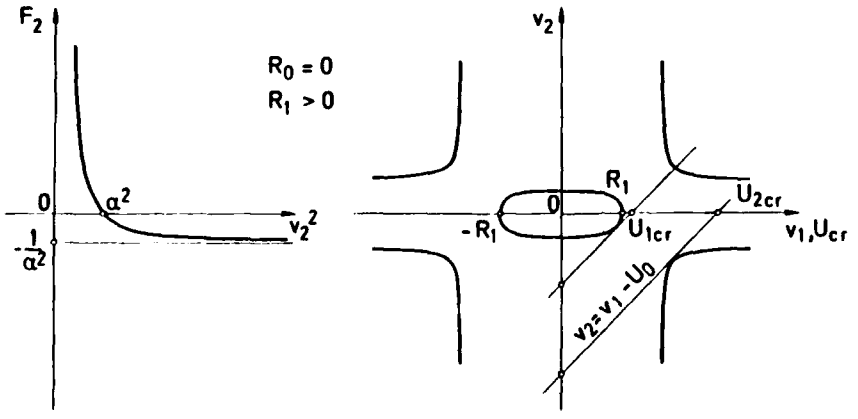

Fig. 2

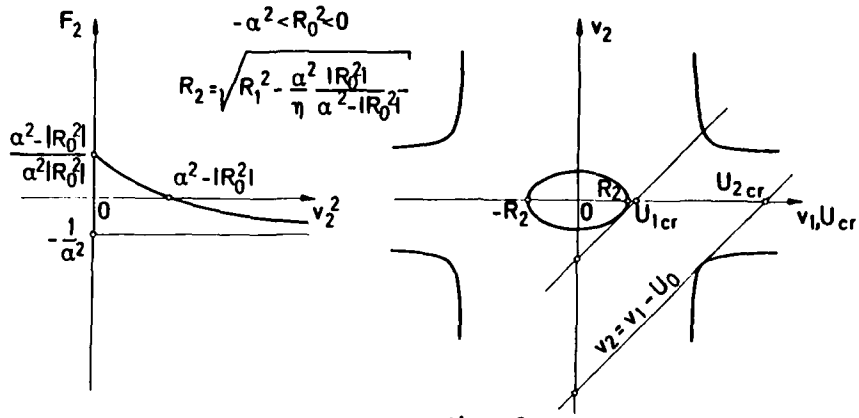

Fig. 3

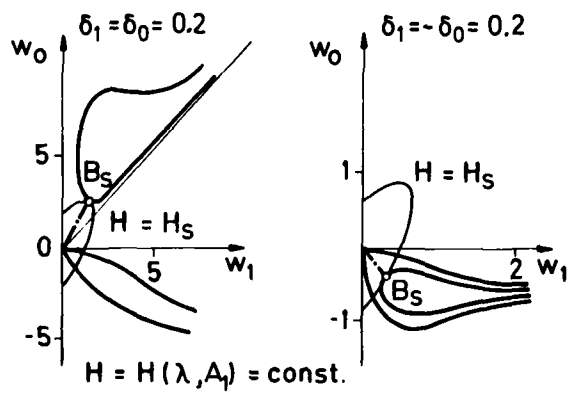

$U_0^2 = 2R_1^2$ $R_0^2 = 0$, $\alpha^2 = 0.5R_1^2$, $\eta = 0.5$

Fig. 4

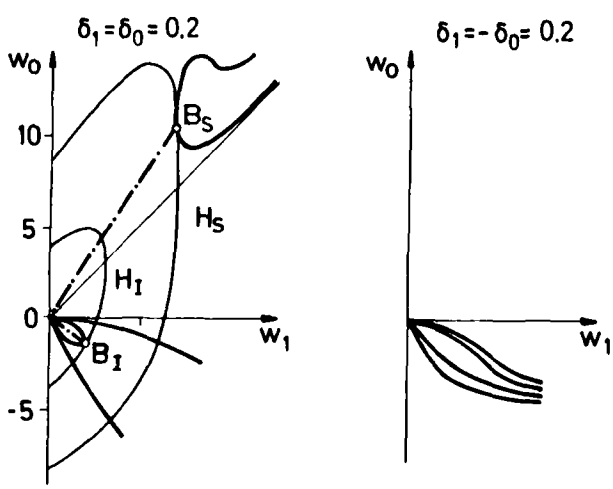

$U_0^2 = 16R_1^2$ $R_0^2 = 0$, $\alpha^2 = 0.5R_1^2$, $\eta = 0.5$

Fig. 5

TABLE 1 : SYSTEM MODELS

LATERAL MOTION	VERTICAL MOTION
1. 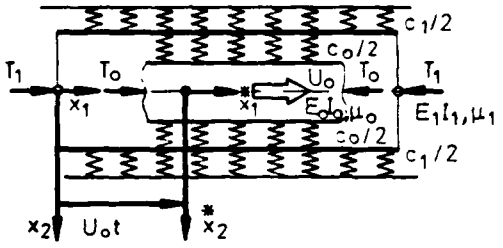	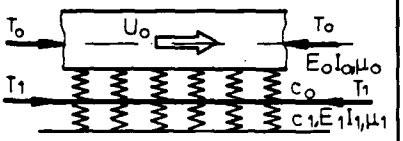
2. 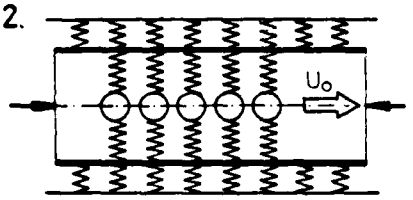	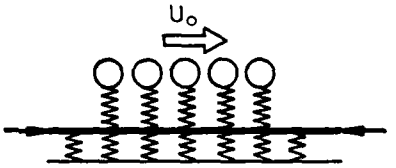
3. 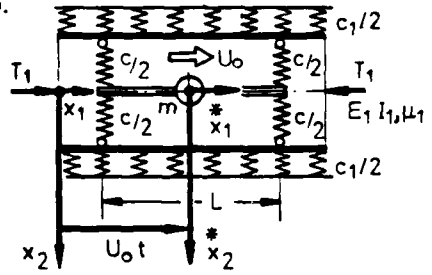	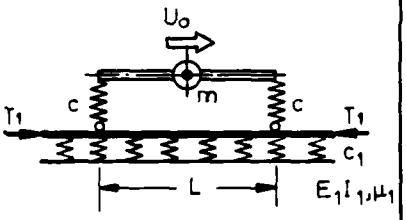
4. 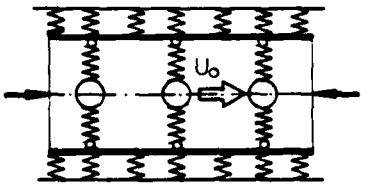	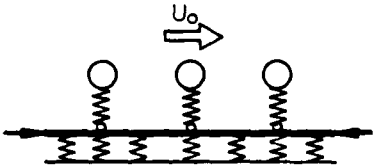
5. 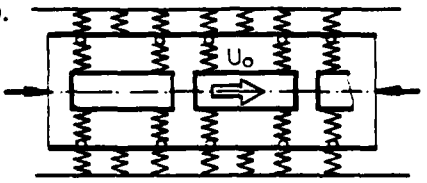	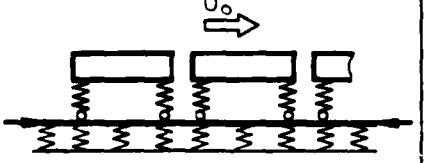

ASSESSMENT OF THE GENERATING MECHANISMS AND CHARACTERISTICS OF WHEEL/RAIL NOISE VIA STUDY OF A ROLLING DISC

N.S. Ferguson and R.G. White
Institute of Sound and Vibration Research
University of Southampton

1.0 INTRODUCTION

Wheel/Rail noise has been the subject of much investigation over recent years and as these investigations have developed, attention has been directed towards the use of models based upon representation of practical wheels and rails. This study models the wheel as a thin disc and is concerned with the excitation and response of the disc in flexural vibration rather than in-plane vibration. Other investigators who have examined the Free Vibration characteristics (see Irretier [1], Sato [2] and Arai [3]) have included rotary and shear deformation into the analyses but these can be neglected here.

Most of the previous work on the forced vibration has been experimental, and in this study an anlytical model is presented, for the forced vibration response of a rotating disc with inclusion of the effect of rolling contact. For the cause of the excitation to the disc various sources have been examined; rigid body forces generated by a rolling disc and surface interaction forces due to the roughness of the rolling surface are the main causes studied.

2.0 FREE VIBRATION CHARACTERISTICS

2.1 Clamped-Free Disc

The equation governing the free vibration of a thin disc in flexure is given, in polar coordinates, by

$$D\nabla^2 w + \rho h \frac{\partial^2 w}{\partial t^2} = 0 \qquad (1)$$

The solution of Equation (1) for various boundary conditions is given by Leissa [4]. The boundary conditions assumed in this study are that the disc is free everywhere on it's outer periphery i.e. no forces or moments, and that internally at some radius it is clamped, this models the attachment of the disc to a central rigid axle. Solving Equation (1) gives the natural frequencies ω_{mn} of free vibration, m,n corresponding to the natural modeshape with m nodal circles and n nodal diameters as given by

$$\phi_{mn}(r,\theta) = (A_{mn}J_n(k_{mn}r)+B_{mn}Y_n(k_{mn}r) + C_{mn}I_n(k_{mn}r) + D_{mn}J_n(k_{mn}r)) \times \cos n\theta \qquad (2)$$

for the even modes in θ and

$$\phi'(r,\theta) = (A_{mn}J_n(k_{mn}r) + B_{mn}Y_n(k_{mn}r) + C_{mn}I_n(k_{mn}r) + D_{mn}J_n(k_{mn}r)) \times \sin n\theta \qquad (3)$$

for the odd modes in θ, k_{mn} the corresponding wavenumbers and $A_{mn}, B_{mn}, C_{mn}, D_{mn}$ are the modeshape coefficients.

2.2 Additional Constraint on the Outer Periphery

Initial consideration of a disc in contact with a surface has been to model the contact as restraining the disc to having no displacement at the point on the outer periphery where contact occurs. Two methods of analysis were used to model the additional constraint; those being the Lagrange Multiplier method and the extended Rayleigh-Ritz method, the latter being the one described here.

The extended Rayleigh-Ritz method, as described by Webster [5], transforms the strain and kinetic energy expressions for the disc whose displacement is described by a series of functions. The expresssions are transformed by the equation governing the constraint, namely

$$\sum_{i=1}^{N} \phi_{mn}(r=R,\ \theta=0) = 0 \qquad (4)$$

the constraint being at (R,0) in polar coordinates. The matrix equation is then solved in the same way as for the Rayleigh-Ritz method.

2.3 Addition of the In-Plane Loading

In addition to the constraint as a disc rests on its outer edge is an in-plane load due to its own mass. The stress distribution which this creates is given by Carlin [7] and this is modelled as an additional strain energy term in the extended Rayleigh-Ritz method.

The additional strain energy term due to the in-plane loading is expressed as

$$U^1 = \tfrac{1}{2} \sum_k \sum_\ell q_k(t)\ q_\ell(t)\ R_{k\ell}$$

$R_{k\ell}$ given by the expression for the strain energy in the modes k with ℓ. One then has the standard determinantal equation for the natural frequencies as

$$\det\left| [K'] - \omega^2 [M] \right| = 0 \qquad (5)$$

where $|K'|$ is the matrix whose terms are given by

$$K'_{ij} = \{K_{ij} + R_{ij}\}\ ,$$

K_{ij} being the standard stiffness matrix elements and $[M]$ the standard mass matrix

To include the effect of the constraint one applies the extended Rayleigh-Ritz method to the above expressions and transforms the matrices $[K']$ and $[M]$ subject to the constraint equation.

Figures 1 and 2 respectively show the wavenumber k plotted against the loading parameter PR/D, P the load on the disc with modulus of rigidity D and outer radius R, for the disc with the in-plane loading with and without constraint on the periphery at the point of application of the load. With no loading, P=0, one observes the difference between the set of wavenumbers k_{mn} for the unconstrained disc and the set for the constrained case; for higher loading one observes the effect of the constraint in reducing the amount that the wavenumbers decrease as the loading increases.

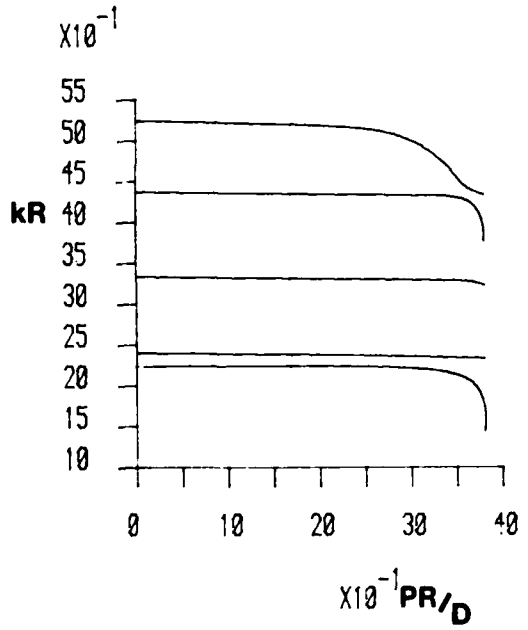

FIG.1

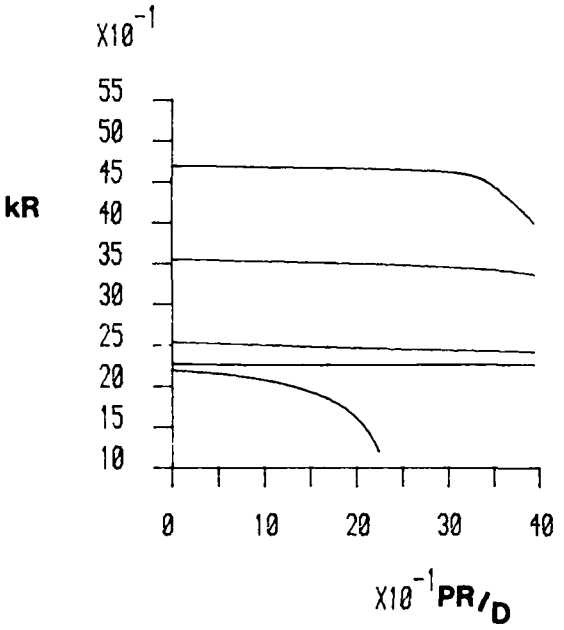

FIG.2

3.0 FORCED VIBRATION CHARACTERISTICS

3.1 Brief Outline of Modal Analysis

In this approach the modeshapes of free vibration of the disc are used to evaluate the forced vibration response of the rotating disc, as initially investigated by Johnson [8]. The response of the disc is given in series form as

$$w(r,\theta,t) = \sum_s q_s(t)\phi_{mn}(r,\theta)+p_s(t)\phi'_{mn}(r,\theta) \qquad (6)$$

$\phi_{mn}(r,\theta)$, $\phi'_{mn}(r,\theta)$ being the orthonormal modeshapes as in (2) and (3) and $q_s(t)$, $p_s(t)$ being the generalised coordinates which describe the response of the disc in these modes. One then has the corresponding Lagrange equations of motion for these modes as

$$M_o\ddot{q}_s(t) + K_s q_s(t) = F_s(t) \qquad (7)$$

and

$$M_o\ddot{p}_s(t) + K_s p_s(t) = F'_s(t) \qquad (8)$$

for the even and odd modes in θ respectively, ignoring structural damping and $F_s(t)$ $F'_s(t)$ being the corresponding generalised forces for the modes.

Due to orthogonality of the modes no cross-terms exist in the expressions (7) and (8) and an approximation as used by Johnson [7], exists to include the effect of rotation of the generalised stiffness terms K_s although this effect is neglected here as Ω, the angular rotational speed, is relatively low. Internal damping can be included by the inclusion of a complex stiffness term $K_s(1+j\eta)$, where η is the loss factor for each mode of vibration unless more specific information is known.

3.2 Response to Harmonic Excitation

For a point applied laternal harmonic force $Fe^{j\omega t}$ acting on the outer periphery of a disc rotating at constant angular velocity Ω one has the generalised forces as

$$F_s(t) = \int \rho h\, F e^{j\omega t}\delta(r-R)\delta(\theta-\Omega t)\,\phi_{mn}(r,\theta)\,dA$$

$$= \rho h\, Fe^{j\omega t}\,\phi_{mn}(R,\Omega t) \qquad (9)$$

similarly for the odd modes in θ, rotating with the disc,

$$F'_s(t) = \rho h\, Fe^{j\omega t}\,\phi'_{mn}(R,\Omega t) \qquad (10)$$

Substituting into equations (7) and (8) for $q_s(t)$ and $p_s(t)$ and substituting into equation (6) for the response of the disc as

$$w(r,\theta,t)= \sum_s \frac{\phi_{mn}(r)\phi_{mn}(R)FR}{2M_o}\left\{\frac{e^{j((\omega+n\Omega)t-n\theta)}}{\omega_{mn}^2-(\omega-n\Omega)^2}+\frac{e^{j((\omega-n\Omega)t+n\theta)}}{\omega_{mn}^2-(\omega-n\Omega)^2}\right\} \qquad (11)$$

Similarly one has the response of the disc for a harmonic moment $Moe^{j\omega t}$ applied about the O1 and O3 axis as

$$w(r,\theta,t) = \sum_s -\frac{M_o\phi_{mn}(r)}{2M_o}\left(\phi_{mn}(R)+R\left(\frac{d\phi_{mn}(R)}{dr}\right)\right)\times$$

$$\left\{\frac{e^{j((\omega+n\Omega)t-n\theta)}}{\omega_{mn}^2-(\omega+n\Omega)^2}+\frac{e^{j((\omega-n\Omega)t+n\theta)}}{\omega_{mn}^2-(\omega-n\Omega)^2}\right\} \qquad (12)$$

for the moment applied about the O1 axis, and which is tangential to the edge of the disc and in the plane of the disc, and

$$w(r,\theta,t)= \sum_s \frac{M_o R\, \phi_{mn}(r)\phi_{mn}(R)}{2M_s} \left\{ \frac{e^{j((\omega+n\Omega)t-n\theta)}}{\omega_{mn}^2-(\omega+n\Omega)^2} - \frac{e^{j((\omega-n\Omega)t+n\theta)}}{\omega_{mn}^2-(\omega-n\Omega)^2} \right\} \qquad (13)$$

for the moment applied about the O3 axis, which is along the radial line $\theta=\Omega t$ ($\theta_o=0$), both with their origin at $\theta=\Omega t$.

3.3 Approximate Solutions

Using the Galilean transformation $\theta_o=\theta-\Omega t$ one can express the responses as given in (11), (12) and (13) in terms of θ_o fixed in space. These solutions show that in general the modes do not exhibit stationary modeshapes in space, however when $\omega>>n\Omega$, ω the frequency of the harmonic excitation, one has the solutions in the s^{th} mode, corresponding to the $(m,n)^{th}$ mode as

$$w_s(r,\theta_o,t) = \frac{FR\phi_{mn}(r)\phi_{mn}(R)}{M_s} \cdot \frac{e^{j\omega t}\cos n\theta_o}{\omega_{mn}^2-\omega^2} \qquad (14)$$

$$w_s(r,\theta_o,t) = -\frac{M_o\phi_{mn}(r)}{M_s} \left(\phi_{mn}(R)+R\frac{d\phi_{mn}(R)}{dr}\right) \frac{e^{j\omega t}\cos n\theta_o}{\omega_{mn}^2-\omega^2} \qquad (15)$$

$$w_s(r,\theta_o,t) = -j\frac{M_o R\, \phi_{mn}(r)\phi_{mn}(R)}{M_s} \frac{e^{j\omega t}\sin n\theta_o}{\omega_{mn}^2-\omega^2} \qquad (16)$$

corresponding to the three cases (11), (12) and (13). In all these cases stationary modal patterns will be observed in cases with a lateral force and a harmonic moment about the O1 axis an antinode occurs at $\theta=\Omega t$ whilst a nodal line exists for the moment applied about the O3 axis.

3.4 Spatial Filtering

In contact of elastic bodies, as in the disc on a surface, one has contact over an area not solely at one point so any forces must act over an arc of the outer periphery. This spatial variation in the force is introduced by the use of a Fourier series in θ_o to replace the delta function. An example relevant to the rolling disc is for the force to act over a small arc of the periphery, $-\varepsilon<\theta_o<\varepsilon$, and follows a parabolic variation described by

$$F_o e^{j\omega t}\left(1-\theta_o^2/\varepsilon^2\right) \qquad (17)$$

Using the Fourier series in θ_o for $(1-\theta_o^2/\varepsilon^2)$ and applying in the previous analysis gives the solution for the displacement of the disc as

$$w(r,\theta,t) = \frac{2Fe^{j\omega t}R}{\varepsilon^2} \sum_s \frac{\phi_{mn}(r)\phi_{mn}(R)}{n^2 M_s} \left(\frac{\sin n\varepsilon}{n} - \varepsilon\cos n\varepsilon\right) \times$$

$$\left\{ \frac{e^{j((\omega+n\Omega)t-n\theta)}}{\omega_{mn}^2-(\omega+n\Omega)^2} + \frac{e^{j((\omega-n\Omega)t+n\theta)}}{\omega_{mn}^2-(\omega-n\Omega)^2} \right\} \qquad (18)$$

Comparing (18) to (11) one has the additional factor for the response in the $(m,n)^{th}$ mode as

$$\frac{4}{n^2\varepsilon^2}\left(\frac{\sin n\varepsilon}{n} - \varepsilon \cos n\varepsilon\right) \qquad (19)$$

which for large values of n tends to zero but for $n\varepsilon$ small this is approximately constant and equal to $4\varepsilon/3$.

4.0 MODELLING THE INTERACTION BETWEEN THE DISC AND ROLLING SURFACE

4.1 Contact Theory

Initially, in the non-rotating case, the contact was modelled as pinning the disc which corresponds to an infinitely stiff Hertzian spring for the contact. In reality this is too strict a constraint for as the disc rolls lateral motion is possible. To model the interaction Hertzian contact theory and Rolling contact theory are applied. For no creepage occurring the lateral motion can be modelled by the application of an elastic Hertzian spring (see Grassie [8] for details). Where creepage occurs, creepage being relative motion of the materials in the disc and the surface over which it rolls, rolling contact theory describes the forces and displacements generated. Approximating the contact area for the disc and the surface as being rectangular one has the corresponding creepage coefficients relating the generated forces to the lateral, longitudinal or spin creepage which occurs.

In the lateral direction, which is of main interest, one has from Rolling contact theory (see Kalker [10])

$$T_y = E_{ab}\, C_{22}\gamma_2 \qquad (20)$$

T_y the lateral force due to lateral creepage only, no spin average occurring, a,b the semi-major and minor axes of the contact area, C_{22} the creep parameter as calculated by Kalker and γ_2 the lateral creepage. The lateral creepage being the ratio of the difference in the lateral velocity of the materials in the contact area to the mean rolling velocity V approximated by the forward velocity of the disc.

In the model applied the difference in lateral velocities is approximated by that due to the lateral vibration of the disc given by $w(r,\theta=\Omega t,t)$ for the contact at time t. As the contact area is small to first approximation the creepage can be modelled as an equivalent viscous damper c applied at the one point $(R,\Omega t)$ and whose value is given by

$$c = \frac{E_{ab}\, C_{22}}{V} \simeq \frac{E_{ab}\, C_{22}}{\Omega R} \qquad (21)$$

Using this model as $\Omega \to 0$ the condition is that of pinning the disc while as $\Omega \to \infty$ the damper decreases in effect on the disc.

4.2 Inclusion of Contact into the Forced Vibration Model

For a rotating disc with an attached damper and elastic spring, as given in Figure 3, undergoing forced vibration, the response of the disc is found using the Receptance method (as described by Bishop [10]) for a harmonic lateral force $Fe^{j\omega t}$ applied at point 1. The point receptance α_{11} for the disc in this configuration is

$$\alpha_{11} = \frac{\beta_{11}\,\gamma_{11}}{\beta_{11} + \gamma_{11}} \qquad (22)$$

β_{11} the point receptance of the disc with no attachments and γ_{11} the point receptance of the system composed of a spring and viscous damper in parallel which is given as

$$\gamma_{11} = \frac{1}{K+j\omega c} \qquad (23)$$

α_{11} is given expression (11) as $w(R,\Omega t,t)/Fe^{j\omega t}$. The response of the disc at any other point 2(r,θ) can also be found using the transfer receptance.

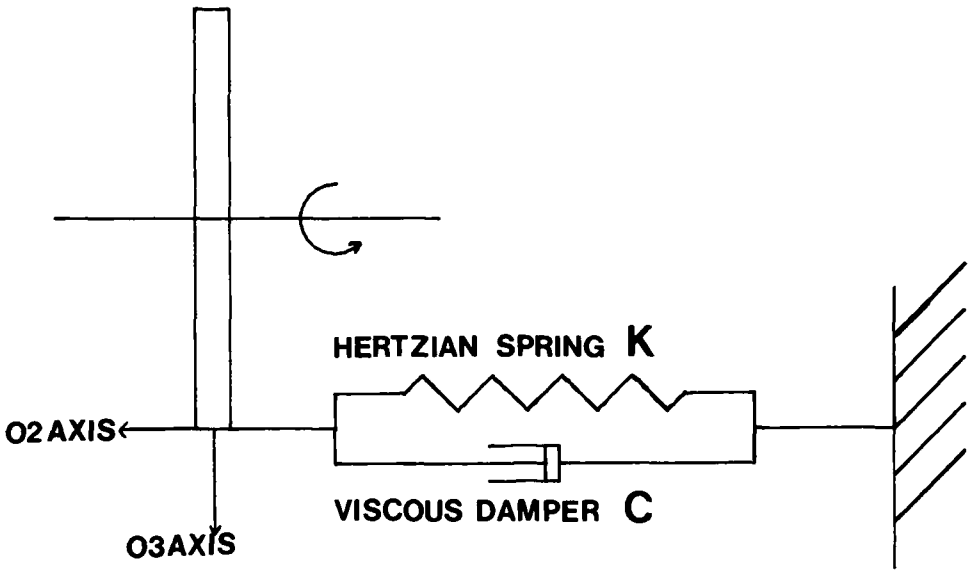

FIG.3

A plot of the modulus of the point receptance $|\alpha_{11}|$ is given in Figure 4 for the frequency range 100Hz-1KHz for a thin disc, 1.5×10^{-3}m thick, outer radius 0.12m clamped centrally at a fifth of it's outer radius. K, the value of the Hertzian spring is given as 1.0×10^{7} N/m for the contact and the value of c as a function of r as $c=1.225 \times 10^{-1}/\Omega$, for Ω= 10 to 100 rads/sec.

5.0 SOURCES OF EXCITATION

5.1 Rigid Body Forces

As described by Meirovitch |11| if a rolling disc is perturbed from rolling in a vertical plane and is rolling at a sufficiently high value of Ω to retain stability the disc will oscillate at a frequency ω given by

$$\omega^2 = \frac{4}{5R} \{3\Omega^3 R - g\omega\} \qquad (24)$$

The actual lateral force on the disc given by the reaction of the surface will also be at the same frequency ω. As seen from the expression above this value is essentially a low frequency component of the possible excitation of the disc.

5.2 Friction and Roughness Forces

One possible cause of friction, which normally acts in a direction opposite to the direction of motion of two bodies against one another, is considered to be adhesion of the two bodies over some part of the contact area. Another cause is material being deformed and displaced in the two bodies to produce resistance to the motion (see Halling [12]). In the latter case where friction is due to the surface asperities one has a possible excitation of the rolling disc over a rough surface. This has been investigated for a smooth disc rolling over a rough surface composed of circular asperities. As the contact area moves across the surface one can predict the forces on individual asperities and evaluate forces and moments acting on the disc over the contact area. A lateral force can be

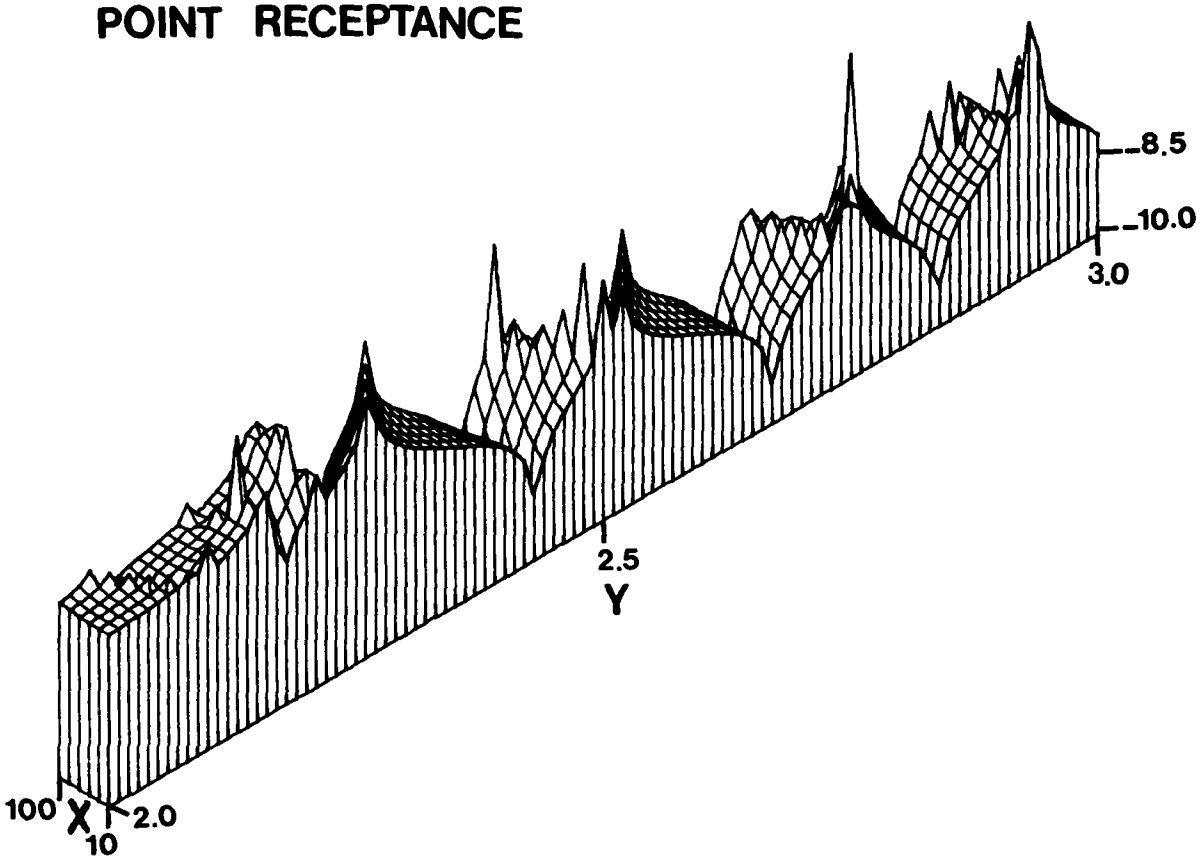

X=RADS/S Y AXIS=LOG10(FREQ(HZ)) **FIG.4**

calculated due to material deformation which occurs across the contact width over each individual asperity. Further investigation is continuing in order to find the power spectrum of these forces and moments so applying the solutions as given in Section 3. One can predict the response of the disc as it rolls over the surface.

6.0 CONCLUSIONS

Analyses of the free and forced vibration characteristics of a rolling disc have been presented in this paper. Whilst one realises the simplified models are not very representative of a wheel/rail system the studies have given an insight into the vibration generation in rolling bodies. The influences such as loading, contact effects, rotation etc. can be clearly seen in the results from the analyses performed.

7.0 ACKNOWLEDGEMENTS

The authors gratefully acknowledges the financial support provided for this research by the Research and Development Division of the British Railways Board at the Railway Technical Centre, Derby, England.

REFERENCES

1. H.IRRETIER, 1983. Journal of Sound and Vibration, 87, No.2, 161-178. The natural and forced vibrations of a wheel disc.

2. S.SATO and H.MATSUHISA, 1981. Bulletin of the Japanese Society of Mechanical Engineers, 24, No.191, 849-853. Wheel Flexural Vibration including the effects of shear deformation and rotatory inertia.

3. H.AKAI, 1978. Internoise 78, 767-770. Study on Dynamic Characteristics of wheel concerned with wheel/rail noise.

4. A.W.LEISSA, 1969, NASA Report No.160. The Vibration of Plates.

5. J.J. WEBSTER, 1968. Int Journal of Mech Sciences 7, 571-582. Free Vibrations of Rectangular Curved Panels.

6. J.F. CARLIN, 1975. Journal of Eng. for Industry, 97 No.1, 37-48. Effect of Tensioning on Buckling and Vibration of Circular Saw Blades.

7. D.C. JOHNSON, 1952. Aircraft Engineering 24, 271-273. Forced Vibration of a Rotating Elastic Body.

8. S.L GRASSIE, R.W. GREGORY and K.L. JOHNSON, 1983. Journal of Mech. Eng. 24 No.2, 103-111. The behaviour of railway wheel sets and track at high frequencies of excitation.

9. J J KALKER 1973. Delft Progress Report No.1. Simplified Theory of Rolling Contact.

10. R.E.D. BISHOP, and G.M.L. GLADWELL and S. MICHAELSON, 1965. The Matrix Analysis of Vibration. Cambridge University Press.

11. L. MEIROVITCH, 1970 Methods of Analytical Dynamics, McGraw Hill.

12. J HALLING, 1975. Principles of Tribology. MacMillan Press Ltd.

ON THE ACOUSTICALLY OPTIMAL DESIGN OF RAILWAY WHEELS [1)]

H. Irretier und O. Mahrenholtz

Institut für Mechanik, Universität Hannover

The squealing noise of railway wheels during the passage through curves is an important subject in the field of sound radiation in street-traffic. Measurements and frequency analysis show that this squealing noise is caused by the bending vibrations of the wheel disk excited by stick-slip between the wheel rim and the rail. Consequently from the acoustical point of view in the design of railway wheels it is of importance to know the coherence between the constructional parameters of the wheel disk and its acoustical quantities.

In the present study the radiated sound pressure and power of a wheel disk due to axial harmonic excitation at one point at the rim is calculated. On the basis of the subjective human feeling of sound pressure the radiated sound power, integrated over the important frequency range, is determined and acoustical quality factors for the various types of wheel disks are specified.

1. INTRODUCTION

One of the parts of a tracked transit system which radiates most sound are the steel wheels of the rail vehicle. Especially when the wheel traverses a sharp curve, it often emits an intense, high-pitched squeal. This noise is extremely disturbing since it consists of pure tones emitted at frequencies at which the human ear is most sensitive.

Frequency analysis of the noise show that the bending vibrations of the wheel are the source of the radiated sound. This was pointed out by Stappenbeck [1], Albert and Raquet [2], Rudd [3], Hübner [4] and Sato and Matsuhisa [5], [6].

The natural vibrations of the wheel disk had been first discussed by Stappenbeck [1]. He perceived that the bending vibrations of the wheel are responsible for the high-pitched squeal. Later Albert and Raquet [2] confirmed this. Rudd [3] and Hübner [4] found that the wheel performes self-sustained oscillations, based on the bending modes of the wheel. In two papers [5], [6] Sato and Matsuhisa studied the bending vibration of the wheel and the sound radiation coefficients for natural vibrations of the disc. They found good agreement between their numerical results and laboratory tests. A recent paper given by Heiss[7] shows a very detailed study of the eigenfrequencies and modes of a railway wheel. Investigations of the sound radiation of circular plates were performed by Alper and Magrab [8] who calculated the sound pressure and sound power of an axisymmetric vibrating plate with one side sea-water loaded, and by Hansen and Bies [9] who determined the radiation efficiency of a clamped plate vibrating in its natural modes. Seybert and Bowles [10] studied the sound radiation efficiency of a beam vibrating in its natural modes.

The forced vibration of a wheel disk have so far been studied only on the basis of simple models consisting of annular plat s with constant, linearly or

---

1) The study was supported by the Ministry of Research & Technology BMFT, Federal Republic of Germany. The authors are thankful for this support which enables them to carry out the present investigation.

exponentially varying thickness and an axisymmetric exciting force. The most important papers, which however are limited to axisymmetric vibrations were given by Reismann [11], Snowdon [12] and Irie, Yamada and Aomura [13].

In the present study a more general model is employed, which includes the sound radiation by forced vibrations of a railway wheel including the extreme thickness variation of the wheel in the radial direction. First, numerical results for the eigenfrequencies and mode shapes are compared with laboratory tests by a holographic technique. Then, the mechanical impedance and the acceleration spectrum for hysteretic damping are calculated and again compared with test results. Finally, the sound radiation quantities - the spatial directivity pattern, the sound pressure weighted according to the evaluation curve A (DIN IEC 651), the sound power and the radiation efficiency - are determined for the practical important frequency range.

Calculations for different wheel disks show the dependence of the sound power frequency response curve on different parameters of the system. By integrating the weighted sound power over the frequency range an acoustical quality factor is determined and compared for various types of wheel disks.

2. THE NATURAL VIBRATIONS OF THE WHEEL DISK

Figure 1 shows the axisymmetric wheel disk considered. Its mid-plane is assumed to be planar and points on it are defined by the polar coordinates r and φ. The outer radius of the disk is r_a, its inner radius μr_a, and $h(r)$ is its thickness at radial distance r from its centre.

The material of the disk is assumed to be homogeneous and linear-elastic, described by Young's modulus E, Poisson's ratio ν, and the density of the material ρ. A linear theory for the displacements is applied.

For the description of the bending vibrations a finite element approximation is used to calculate the natural frequencies and the mode shapes. Following Mindlin's thick plate theory [14], which takes into account the effect of shear deformation and rotary inertia, the deformation of the disk is described by

$$\underline{w} = \underline{w}(r,\varphi,t) = [w \ \gamma_r \ \gamma_\varphi]^T \ , \tag{1}$$

where t denotes time, w is the mid-plane deflection (Figure 1) and γ_r and γ_φ are the angles of cross-section in radial and circumferential direction, respectively.

At first, the natural vibrations of the wheel disk with a completely free outer edge are considered. For the undamped case, they are described by the natural circular frequency $\omega_{k\ell}$ for the ℓ-th natural vibration with k nodal diameters and the modes

$$\underline{\tilde{W}}_{k\ell} = \underline{\tilde{W}}_{k\ell}(r,\varphi) = \begin{bmatrix} \tilde{W}_{k\ell}(r,\varphi) \\ \tilde{\Gamma}_{rk\ell}(r,\varphi) \\ \tilde{\Gamma}_{\varphi k\ell}(r,\varphi) \end{bmatrix} = \begin{bmatrix} W_{k\ell}(r) \cos k\varphi \\ \Gamma_{rk\ell}(r) \cos k\varphi \\ \Gamma_{\varphi k\ell}(r) \sin k\varphi \end{bmatrix} \tag{2}$$

i.e. the natural motion of the disk takes the form

$$\underline{w} = \underline{w}(r,\varphi,t) = \underline{\tilde{W}}_{k\ell}(r,\varphi) \exp(j\omega_{k\ell}t) \ . \tag{3}$$

For the calculation of the natural frequencies $\omega_{k\ell}$ and the mode shapes $\underline{\tilde{W}}_{k\ell}$ a finite element approximation for the disk is applied according to the rectangular thick plate finite element described by Pryor, Barker and Frederick in [15] and the ring thick plate finite element given by Wilson and Kirkhope [16]. Within each ring element the deformations are approximated by the polynomials (index $k\ell$ dropped out)

$$\begin{aligned} W(r) &= a_1 + a_2 r + a_3 r^2 + a_4 r^3 \\ \psi_r(r) &= a_5 + a_6 r \\ \psi_\varphi(r) &= a_7 + a_8 r \end{aligned} \tag{4}$$

where $\psi_r = \frac{dW}{dr} + \Gamma_r$ and $\psi_\varphi = -k\frac{W}{r} + \Gamma_\varphi$ are the total angles of shear deformation of cross-section in radial and circumferential direction, respectively. Following the well-known steps of finite element derivation the eigenvalue problem

$$(-\omega^2 \underline{M} + \underline{K})\underline{q} = \underline{0} \tag{5}$$

originates for the entire wheel disk which yields the natural circular frequencies $\omega_{k\ell}$ and the corresponding eigenvectors $\underline{q}_{k\ell}$ from which the modes $\underline{\tilde{W}}_{k\ell}$ can be calculated.

3. THE FORCED VIBRATIONS OF THE WHEEL DISK

The most convenient way to calculate the forced vibrations of the disc due to harmonic excitation is the technique of modal transformation. This method starts either from the finite element model described above or directly from the equation of motion of the non-discretized continuum. Here, the latter way is chosen because of some advantages for the description.

The equation of motion for the displacement vector $\underline{w}$ given in equation (1) can be set up in the form

$$\underline{M}\frac{\partial^2 \underline{\bar{w}}}{\partial t^2} + (1 + g\frac{\partial}{\partial t})\,\underline{D}^{r\varphi}[\underline{\bar{w}}] = \underline{\bar{f}} = [\bar{f}\ 0\ 0]^T \tag{6}$$

where now damping is introduced by the coefficient g and consequently the displacement vector $\underline{\bar{w}}$ and the vector of axial load $\underline{\bar{f}}$ are interpreted as complex quantities. The mass matrix $\underline{M}$ and the matrix $\underline{D}^{r\varphi}$ of differential operators follow from Mindlin's plate theory [14] and are given in [17].

The assumed, harmonic excitation - a concentrated axial force F acting at the disk rim at the point r_s, φ_s (Figure 1) - is described by

$$\underline{\bar{f}} = \underline{F}\exp(j\Omega t) = [F\ 0\ 0]^T \exp(j\Omega t)\ . \tag{7}$$

This force causes a vibration of the wheel disk, for which the displacement vector can, provided that the damping is small, be expressed by the modal expansion

$$\underline{\bar{w}} = \sum_{k=0}^{\infty}\sum_{\ell=0}^{\infty} \bar{c}_{k\ell}\,\underline{\tilde{W}}_{k\ell}(r,\varphi)\exp(j\Omega t)\ , \tag{8}$$

where $\bar{c}_{k\ell}$ are unknown, complex coefficients and $\underline{\tilde{W}}_{k\ell}$ the k/ℓ-mode shape of the undamped system as calculated above.

Applying the well-known steps of modal transformation technique the equations (6), (7), (8) yield

$$\underline{\bar{w}} = F \sum_{k=0}^{\infty} \sum_{\ell=0}^{\infty} \frac{\tilde{W}_{k\ell}(r,\varphi)\ \tilde{W}_{k\ell}(r_s,\varphi_s)}{\alpha_{k\ell}(\bar{\omega}_{k\ell}^2 - \Omega^2)} \exp(j\Omega t) \quad , \tag{9}$$

where the complex frequency

$$\bar{\omega}_{k\ell} = \omega_{k\ell}(1+jg\Omega) \tag{10}$$

is introduced and $\alpha_{k\ell}$ is a factor corresponding to the normalisation of the eigenvectors.

From equation (9) follows the mid-plane deflection $\bar{w}$, its velocity $\bar{v} = j\Omega\bar{w}$ and its acceleration $\bar{a} = -\Omega^2\bar{w}$.

The impedance $\bar{Z}$ of the disk is then given by the ratio of the exciting force to the mid-plane velocity. It is normalized with respect to the impedance $j\Omega M$ of a rigid body which has the same mass M as the disk, which yields the dimensionless impedance

$$\bar{\phi} = \bar{\phi}(r_s,\varphi_s,r,\varphi) = -\left\{ 2\pi\rho \int_{\mu r_a}^{r_a} rhdr \cdot \sum_{k=0}^{\infty} \sum_{\ell=0}^{\infty} G_{k\ell}(r_s,\varphi_s,r,\varphi) \frac{\nu_{k\ell}^2}{(1-\nu_{k\ell}^2)+j\eta} \right\}^{-1} \tag{11}$$

where now hysteretic damping $\eta = g\Omega = \text{const}$ is introduced, the Green's function is given by

$$G_{k\ell}(r_s,\varphi_s,r,\varphi) = \frac{\tilde{W}_{k\ell}(r,\varphi)\ \tilde{W}_{k\ell}(r_s,\varphi_s)}{\int_0^{2\pi} \int_{\mu r_a}^{r_a} \rho h \left[\tilde{W}_{k\ell}^2 + \frac{h^2}{12}(\tilde{\Gamma}_{rk\ell}^2 + \tilde{\Gamma}_{\varphi k\ell}^2)\right] rd\varphi dr} \tag{12}$$

and $\nu_{k\ell}$ is the frequency ratio $\nu_{k\ell} = \Omega/\omega_{k\ell}$.

4. THE SOUND RADIATION OF THE WHEEL DISK

The problem of the wheel sound radiation is a special case of the general problem of surface radiation. To find acceptable good results in the main interesting frequency range from 800 Hz to 8000 Hz (normal railway wheel) a special solution of the Huygens-Helmholtz-scalar wave equation can be applied to determine the acoustic quantities of the wheel. This solution is known as the Rayleigh-Integral [18, 19, 20] which, however, has a boundary condition that prevents the equalization of pressure at the wheel rim, that is it provides a baffled radiator. Since a railway wheel is not baffled, an error is produced in relation to a free radiator by using this solution. The magnitude of this error depends on the frequency range for which the acoustical quantities are determined. As shown by Meixner and Fritze [21] we can state for a usual railway wheel that the error in the spatial pressure distribution in the angle range $\Theta < 75^o$ (Figure 2) and in the radiated sound power is less than 1 dB in the frequency range from 800 Hz to 8000 Hz. This seems to be a sufficient accuracy for all practical purposes.

4.1 The radiated sound pressure

The vibrating mid-plane A of the wheel (Figure 2) is assumed to be surrounded by an infinite baffle. On the vibrating mid-plane the normal velocity amplitude is $\bar{v} = \bar{v}(r,\varphi) = j\Omega\bar{w}$ where the deflection $\bar{w}$ follows from equation (9), while on the baffle $\bar{v} = 0$. The procedure now is to represent the mid-plane A by a distribution of infinitesimal small piston sources dA . Each source has a normal velocity $\bar{v}$ and contributes an incremental pressure $d\bar{p}(\tilde{r})$ at a distance $\tilde{r}$ from the source (Figure 2). The integral of $d\bar{p}(\tilde{r})$ over the plane A yields the total pressure in the observer point (R,α,θ) in the farfield $(\bar{v}/\tilde{r} \approx \bar{v}/R)$:

$$\bar{p}(R,\alpha,\theta) = \frac{j\Omega\rho_L}{2\pi R} \int_0^{2\pi} \int_{\mu r_a}^{r_a} \bar{v}(r,\varphi) \cdot \exp(-j \frac{\Omega}{c_L} \tilde{r})\ r\,dr\,d\varphi \quad , \tag{13}$$

where ρ_L is the density of the air, c_L the velocity of sound in the air, $\tilde{r}$ the distance between the piston source and the observer point.

By introducing the approximation $r \ll R$ for the farfield, which yields $\tilde{r} \approx R - r\cos\psi\sin\theta$ (Figure 2), and the sound pressure

$$\bar{p}_o(R) = \frac{j\Omega\rho_L}{2\pi R} q_o \exp(-j\frac{\Omega}{c_L} R) \tag{14}$$

of a single piston source with the reference sound flow q_o, the radiated sound pressure of the wheel disk takes the form

$$\bar{p}(R,\alpha,\theta) = \bar{d}(\alpha,\theta) \cdot \bar{p}_o(R) \tag{15}$$

where

$$\bar{d}(\alpha,\theta) = \frac{1}{q_o} \int_0^{2\pi} \int_{\mu r_a}^{r_a} \bar{v}(r,\varphi) \exp(j \frac{\Omega}{c_L} r\cos\psi\sin\theta)\ r\,dr\,d\varphi \tag{16}$$

is the dimensionless spatial directivity pattern of the wheel disk. When the expressions $q_o = \pi(1-\mu^2)\, r_a^2\, v_o$ and $v_o = F / \sqrt{\rho\, h_o\, B_o}$ are introduced for the reference sound flow of the piston source (inner radius μr_a, outer Radius r_a), where h_o is a characteristic thickness and $B_o = Eh_o^3/12(1-\nu^2)$ the bending stiffness of the wheel disk, the spatial directivity pattern given in equation (16) is a characteristic quantity which only depends on the material and geometrical data of the system.

For comparison of the radiated sound pressure of various types of wheel disks the sound pressure level

$$L_p = 20\lg\ (|\bar{p}|/p_o)\ [dB] \tag{17}$$

is introduced where $p_o = 2 \cdot 10^{-4}$ µbar is the reference sound pressure.

4.2 The radiated sound power

The radiated sound power is now derived from the numerically integrated acoustical intensity in a wheel disk surrounding hemisphere (Figure 2), far from the centre of the wheel. The effective acoustical intensity is given by the

expression

$$\vec{I}^{eff} = \vec{I}^{eff}(R,\alpha,\theta) = \frac{1}{2} \mathrm{Re}\ \{\bar{p}(R,\alpha,\theta) \cdot \vec{\bar{v}}_L^{*}(R,\alpha,\theta)\} \tag{18}$$

where the factor 1/2 results from the time average for the case of harmonic vibration considered here and $\vec{\bar{v}}_L^{*}(R,\alpha,\theta)$ is conjugate complex to the sound velocity $\vec{\bar{v}}_L = \vec{\bar{v}}_L(R,\alpha,\theta)$ at the observer point on the hemisphere (Figure 2). Using the dynamical equation

$$\vec{\bar{v}}_L = -\frac{1}{j\rho_L \Omega} \mathrm{grad}\ \bar{p} \tag{19}$$

and introducing the pressure distribution from above, the radial component $\vec{\bar{v}}_{LR}$ of $\vec{\bar{v}}_L$ takes the form

$$\vec{\bar{v}}_{LR} = \frac{q_o}{2\pi R} \cdot \bar{d} \cdot \left(\frac{1}{R} + j\frac{\Omega}{c_L}\right) \cdot \exp\left(-j\frac{\Omega}{c_L}R\right)\ \vec{e}_R \ . \tag{20}$$

The equations (14) and (20) show that in the farfield, which is only considered here, p and $\vec{\bar{v}}_{LR}$ are in phase because of $1/R \ll \Omega/c_L$ and it follows for the radial component of the acoustical intensity

$$\vec{I}_R^{eff} = \frac{1}{2}\frac{\rho_L}{c_L}\left(\frac{\Omega}{2\pi R}\right)^2 q_o^2\ |\bar{d}|^2 \cdot \vec{e}_R \ . \tag{21}$$

The radiated sound power follows from integration over the hemisphere to

$$P_H = \int_0^{2\pi}\int_0^{\pi/2} I_R^{eff} \cdot R^2 \sin\theta\ d\theta\ d\alpha \tag{22}$$

which is the radiated sound power in one half sphere. The whole radiated power is given by $P = 2P_H$.

Again a dimensionless sound power quantity is introduced using the reference sound power $P_o = 10^{-12}$ W. The sound power level is then given by

$$L_P = 10\,lg(P_H/P_o)\ [dB] \ . \tag{23}$$

4.3 The radiation efficiency

Another important quantity for the description of the acoustical properties of the disk is the radiation efficiency σ . It describes the ratio of the radiated sound power of the disk to that one radiated from a nondeformable plane A vibrating with the effective disk velocity v_{eff} i.e.

$$\sigma = \frac{P_H}{\rho_L c_L A\, v_{eff}^2} \ , \tag{24}$$

where v_{eff}^2 is given by

$$v_{eff}^2 = \frac{1}{2A}\iint_A |\bar{v}|^2\, dA = \frac{1}{2r_a^2(1-\mu^2)\pi}\int_0^{2\pi}\int_{\mu r_a}^{r_a} |\bar{v}(r,\varphi)|^2\, r\,dr\,d\varphi \ . \tag{25}$$

Thus, the radiation efficiency describes the radiated sound power of the real vibrating disk in relation to that one of a rigid plane of equal size.

4.4 An acoustical quality factor

The acoustical quantities described above are objectively calculated values and do not take into consideration the frequency dependent human sensibility for sound intensity. Moreover, they are frequency dependent quantities and not an integral measure for the whole frequency range of importance. To introduce an acoustical quality factor [22] for a wheel disk, which radiates squealing noise, first, the sound pressure $\bar{p}$ is weighted with the evaluation curve A (Figure 3) according to DIN IEC 651 [25]. Consequently, as a corresponding valuation factor for the sound power the square of the evaluation curve is introduced. Secondly, an integration is performed over the frequency range. Thus, the acoustical quality factor is defined as

$$G = \frac{1}{\Omega_{max} - \Omega_{min}} \int_{\Omega_{min}}^{\Omega_{max}} P_H(\Omega)\ \chi_A^2\ (\Omega)\ d\Omega \quad , \tag{26}$$

where the sound power follows from equation (22) and χ_A is the evaluation curve shown in Figure 3.

As a dimensionless quantity the acoustical quality level

$$L_G = 10\ \ell g\ (G/P_o)\ [dB] \tag{27}$$

is introduced to compare various types of wheel disks. Thus, the 'optimal' wheel disk which radiates only the diminutive reference sound power P_o in the whole frequency range is described by $L_G = 0$.

5. NUMERICAL RESULTS

All numerical results are gathered from the report [22].

5.1 Natural vibrations

At first, the finite element model was tested with help of a wheel disk model which was measured on a holographic test stand. The model, typical for a realistic wheel disc, is shown in Figure 4 where the finite element approximation consisting of 7 ring elements with constant or linear varying thickness is plotted, too. The material of the model was steel with the material properties $E = .206 \cdot 10^6\ N/mm^2$, $\rho = .785 \cdot 10^{-8}\ Ns^2/mm^4$ and $\nu = .3$.

Table 1 shows a comparison between test and numerical results for the lowest eigenfrequencies $f_{k\ell} = \omega_{k\ell}/2\pi$ for the test model. For the numerical calculations the two extreme assumptions 'clamped' and 'free' were introduced for the inner boundary. For the case 'free' the natural vibrations $k/\ell = 0/0$ and $1/0$ do not exist. The numerical results only show a distinct difference for the zero and one nodal diameter modes because of the different assumptions for the inner radius boundary conditions, whereas for higher nodal diameter modes the results are nearly independent from the conditions introduced at the disk's hub. This tendency is confirmed by the test results. The only measured frequency of the zero and one nodal diameter modes is f_{10} and differs from the calculated value more than 100% because it was not possible in the tests to reach a fully rigid clamped disk hub. For the higher nodal diameter modes with $k \cdot 2$, however, the results show a good agreement between the measured and calculated values.

The numerical results show that it is necessary to include the effects of rotary inertia and shear deformation, here in the sense of Mindlin's plate theory. Other mechanical models which neglect these effects are not sufficient to describe the wheel disk's bending vibrations as pointed out by Irretier [24].

For the interpretation of the natural vibration behaviour and later of the forced vibration response and the sound radiation properties of the wheel disk, it is necessary to consider its mode shapes. For this purpose, the modes $\tilde{W}_{k\ell}(r,\varphi)$ of the wheel disk model, calculated from the finite element procedure, were compared with experimental results derived from holographic tests where the time average holographic technique was used. Five representative results are shown in the Figure 5. The holographic photos as well as the calculated forms of the modes with $\ell = 0$ nodal circles show that these modes are characterized by a large displacement of the thick disk rim which is typical for all the mode shapes with $\ell = 0$. On the other hand, the modes for $\ell = 1$ show a large movement of the web while the rim motion is small and in opposite phase to the web. This latterfact can be well observed from the holographic results as well as from the calculated ones.

The mode shapes show that the wheel disk vibrations with $\ell = 0$ are mainly responsible of the squealing noise because for them the excitation at the contact area between the wheel and the rail is applied in the region of large deflection. Thus, high energy input occurs while for the modes with $\ell = 1$ the rim deflection remains small and the energy input is much less.

5.2 Forced vibrations

The forced vibrations are considered next where now a real wheel disk (Figure 6) was investigated for which some test results for the dynamic response were given by KRUPP [23] determined from laboratory tests. The wheel was harmonically excited at the rim by a shaker, and the amplitude F of the exciting force as well as the acceleration amplitude $|\bar{a}_p|$ at the point of excitation (r_s=450 mm, φ_s=0) were recorded by pick-ups. The applied finite element approximation for the calculations consists again of 7 ring elements and is shown in Figure 6, too, where one model is plotted for the new, unused state of the wheel disk, for which the tests were carried out, and a second one describing an used state with strongly worn disk rim.

The comparison of the test and the numerical results for the new state are given in Table 2 and show an extremely good accuracy of the mechanical model. The differences of the results are less than 1%. The calculations for the used state, for which no test results exist, point out that those vibrations where the disk rim has large amplitudes (cp. Figure 5) i.e. ℓ=0 , the decrease of the eigenfrequencies is between 15% and 20%. This might be an important fact considering the absorber technique to reduce the squealing noise of wheel disks. The eigenfrequencies with ℓ=1 nodal circles change also considerably from the new to the used state whereas the higher eigenfrequencies of those modes characterized by large deflections of the thin disk web are altered slightly.

The amplitude $|\bar{a}_p|$ of the measured and calculated acceleration at the point of excitation is shown in Figure 7 as a function of the exciting frequency. For the calculation 60 modes were used for the modal transformation i.e. all eigenfrequencies up to 12000 Hz. Below 300 Hz the test and numerical results differ considerably from each other because of different boundary conditions at the hub in the tests and the calculations. However, for freqencies higher than 300 Hz, which is the important range for the sound emission, the agreement between the test and the numerical results is rather satisfactory even for the magnitude of the acceleration and not only for the peaks itself.

For a frequency range up to 3000 Hz Figure 8 shows the acceleration $|\bar{a}_p|$

for various damping coefficients. The sharp resonance peaks corresponding eigenfrequencies of the wheel disk (cp. Table 2) are nearly completely smoothed out even for low values of damping. Nevertheless, the acceleration level close to resonance frequencies is much higher compared with the other frequency ranges.

Finally, the plot in Figure 9 describes the normalized input impedance $|\phi_p|$ according to equation (11) when $r=r_s$, $\varphi=\varphi_s$ for the wheel disk [23] shown in Figure 6, again for the undamped case $\eta=0$. The well-known fact of decrease of the impedance in the resonance points and infinite values at the anti-resonance frequencies is visible from the plot and declares the large energy input at the resonance frequencies and consequently the corresponding frequency spectrum of the emitted squealing noise.

5.3 Radiated sound pressure

The spatial distribution of the radiated sound pressure of the wheel disk is governed by the spatial directivity pattern given by equation (16) which describes, related to the reference sound pressure $\bar{p}$ from equation (14), the pressure at one observer point in the direction of $\bar{R}^o$ (Figure 2).

For very small damping coefficients two spatial directivity patterns for the considered wheel disk [23] of Figure 6 are plotted in the Figures 10a and 10b, where the first one is calculated for resonance between the exciting frequency and the 3/0-eigenfrequency and the second one for no resonance conditions. We notice the enormous difference of the magnitudes of the radiated sound pressure (cp. the scales in Figure 10a and 10b) and the existence of strongly marked maxima in some directions and nearly vanishing pressure levels in other directions, respectively. The more the exciting frequency removes from an eigenfrequency all the more the pronounced directivity character of the radiated sound pressure is smoothed out, which is indicated in Figure 10b in comparison to Figure 10a.

Introducing damping into the system yields, because of the phase relations between the exciting force and the velocity field $\bar{v}(r,\varphi)$ of the disk's midplane, an asymmetry of the directivity pattern as shown in Figure 10c, where a damping coefficient of $\eta = 0{,}05$ is taken for the calculation. The magnitude of the radiated sound pressure for the considered resonance is reduced approximately by a factor 500 compared with the nearly undamped case (cp. the scales in Figure 10a and 10c).

The spatial directivity pattern is a rather important characteristic of the considered wheel disk, especially when tests are performed to identify its resonance frequencies from radiated sound pressure measurements. For example, in Figure 11 the radiated sound pressure level L_p according to equation (17) is plotted for the wheel disk considered before, for the two spatial directions $\alpha=0^o/\theta=0^o$ and $\alpha=90^o/\theta=30^o$ and a distance $R=r_a$ from the wheel disk's center. We notice that from the first curve only two resonance frequencies can be identified while from the second one more than two can be perceived. However, the important main resonance frequency $f_{30}=830.7$ Hz, which is visible in the acceleration-frequency-curve in Figure 8, does not occur neither in the first nor in the second sound pressure level curve in Figure 11. Thus, this resonance frequency would not be identified by sound pressure measurements performed in these two spatial directions because of the discussed directivity character of the sound pressure distribution.

5.4 Radiated sound power

Because of the strongly marked directional characteristic in wide frequency ranges the radiated sound pressure of the wheel disk is unfit for a qualification of different constructions of wheel sets and a quantification of noise mole-

station in the surroundings. Hence, the radiated sound power through a hemisphere around the wheel disk is quoted to describe the acoustical qualities of the wheel disk.

Figure 12 shows for the wheel disk [23] of Figure 6 the sound power level according to equation (23) for an exciting force amplitude of F=IN. We recognize from the curves for the undamped case[1] that now each resonance peak occurs in the spectrum in contrast to the considerations concerning the sound pressure. This fact, of course, is caused by the integration over the sound pressure according to equation (22) to determine the sound power. The difference between the objective sound power and that one weighted by χ_A corresponding to DIN IEC 651 [25] is relatively small in the considered frequency range.

The damping effect reduces strongly the resonance peaks of the sound power, especially for higher frequencies, which is pointed out by the corresponding curve in Figure 12.

5.5 Sound power and acoustical quality factor for various types of wheel disks

The last step of considerations is to compare the acoustical properties of different types of wheel disks which carry out bending vibrations as described in this paper. Four types of wheel disks are considered, shown in Figure 13. The first one was discussed before in this paper; is was decribed by KRUPP [23] and is indicated as 'type N'. The first alternative construction, the 'type A', has the same hub and web as the first one, but a thicker rim. The third wheel disk, denoted as 'type B', is characterized by a much thicker hub and web compared to the first two types. Finally, 'type C' consists only of the disks rim. The last model may be considered as an approximation of a wheel disk where the disk's rim is separated from the web by a ring consisting of rubber, and so mainly the rim is excited to bending vibrations.

The sound power-level-spectra for the four types of wheel disks are plotted in Figure 14 for damping values of η=.0001 and η=.05 (only type 'N'). The damping effect is only significant near the resonance peaks while the average sound power level is hardly influenced. From this fact follows that by damping only the - of course dominant - resonance peaks can be reduced but not the basic sound power level.

The comparison of the various types of wheel disks shows that 'type B' (thick wheel hub and web) radiates a high sound power level. 'Type C' (only disk rim) yields the best results, even lower sound power levels as the damped 'type N'. This result is caused by the distinctly smaller surface and consequently smaller sound radiating mid-plane of the wheel disk.

The acoustical quality level L_G corresponding to equation (27) for the four types of wheel disk is given in Table 3. The frequency range for the integration performed in equation (26) is bounded by Ω_{min} = 0 Hz and Ω_{max} = 3000 Hz. From Table 3 we notice that the wheel disk 'type B' is unfavourable as to the radiated sound power. The reason for this is a strong decrease of the input impedance in the range 2000-3000 Hz caused by the small rim mass and the large web stiffness.

For the case η=.0001, 'type A' is much better than 'type N' because the high input impedance if the thick rim has a positive influence on the sound radiation. The same effect, of course, occurs by damping as the corresponding quality factor for the wheel disk 'type N' shows. However, damping coefficients up to η = .05 seldom exist in practice provided special damping mechanisms

---

[1] The finite values of the sound power even for the undamped case are due to the finite frequency steps in the calculations.

like absorber are brought into the system.

The best quality factor occurs for the ring wheel 'type C' as aspected from the sound power curve in Figure 14. The quality factor level is even much better than the strongly damped wheel disk 'type N'.

The examples show that the acoustically optimal design of wheel disks may not only be based on damping raising measures but also on constructional provisions during the design period.

6. CONCLUSIONS

The acoustical characteristics of various types on wheel disks have been considered. The applied finite element approximation based on Mindlin's thick plate theory yields good results for the natural and forced vibrations which was proved by laboratory tests. The calculated sound pressure distribution shows distinct directivity characteristic at resonance frequencies. Thus, it is in general not possible to find all eigenfrequencies of the wheel disk from a measurement of sound pressure at only one observer point. As opposed to that, the sound power gives resonance peaks at all eigenfrequencies of the wheel disk.

The comparison of different types of wheel disks show a significant influence of the constructional parameters on the sound power level of the bending vibrations and on the acoustical quality factor. A weak disk web and a stiff disk rim with large mass seems to be the best compromise for an acoustically optimal wheel disk with respect to squealing noise.

7. REFERENCES

1. H. STAPPENBECK 1954 Zeitschrift VDI 96, 171-175. Das Kurvengeräusch der Straßenbahn - Möglichkeiten zu seiner Unterdrückung.

2. H. ALBERT and E. RAQUET 1979 Verkehr und Technik 1, 27-31. Gummigefederte Räder in Leichtbauweise zur Geräuschminderung der U-Bahn-Fahrzeuge der Hamburger Hochbahn AG.

3. M.J. RUDD 1976 J. Sound Vib. 46, 381-394. Wheel/Rail Noise - Part II: Wheel Squeal.

4. H. HÜBNER 1978 Glas. Ann. ZEV 102, 336-342. Schallgedämpfte Eisenbahnräder im städtischen Nahverkehr.

5. S. SATO and H. MATSUHISA 1978 Bull. JSME 21, 1475-1481. Study on the Mechanism of Train Noise and its Counter Measure - Characteristics of Wheel Vibration.

6. H. MATSUHISA and S. SATO 1979 Bull. JSME 22, 1626-1631. Study on the Mechanism of Train Noise and its Countermeasures (Part II; The Effect of Velocity and Load, and the Characteristics of Sound Radiation).

7. P. HEISS 1982 Report of the Institut für Verkehrsplanung und Verkehrswegebau, Technische Universität Berlin. Theoretisches Modell zum Schwingungsverhalten eines Eisenbahnrades im akustischen Bereich.

8. S. ALPER and E.B. MAGRAB 1970 J. Acoust. Soc. Am. 48, 681-691. Radiation from the Forced Harmonic Vibrations of a Clamped Circular Plate in a Acoustic Fluid.

9. C.H. HANSEN and D.A. BIES 1976 J. Acoust. Soc. Am. 60, 543-555. Optical Holography for the Study of Sound Radiation from Vibrating Surfaces.

10. A.F. SEYBERT and P.J. BOWLES 20.09.-23.09.1981 8th ASME Des. Eng. Techn. Conf. Hartford (U.S.A.). The Radiation of Sound from Mass-Loaded and Stiffened Beams.

11. H. REISMANN 1968 J. Appl. Mech. 35, 510-515. Forced Motion of Elastic Plates.

12. J.C. SNOWDON 1970 J. Acoust. Soc. Am 47, 882-891. Forced Vibration of Internally Damped Circular Plates with Supported and Free Boundaries.

13. T. IRIE, G. YAMADA and S. AOMURA 1980 Int. Mech. Sci. 22, 99-107. The Steady State Response of a Mindlin Annular Plate of Varying Thickness.

14. R.D. MINDLIN 1951 J. Appl. Mech. 73, 31-38. Influence of Rotary Inertia and Shear on Flexural Motions of Isotropic, Elastic Plates.

15. W. PRYOR, R.M. BARKER and D. FREDERICK 1970 J. Eng. Mech. Div. EM6, 967-983. Finite Element Bending Analysis of Reissner Plates.

16. G.J. WILSON and J. KIRKHOPE 1976 Transactions of the ASME, 1008-1013. Vibration Analysis of Axial Flow Turbine Disks Using Finite Elements.

17. H. IRRETIER and M. STEGIC 1981 Report 1/81 of the Institute of Mechanics, University of Hannover, 1-15. Eigenschwingungen einer Kreisringplatte mit einem elastisch gestützten Punkt am Außenrand.

18. P.M. MORSE and K.U. INGARD 1968 McGraw-Hill, Inc. Theoretical Acoustics.

19. A. SOMMERFELD 1942/43 Annalen der Physik 42, 389-420. Die frei schwingende Kolbenmembran.

20. L. CREMER 1975 Springer Verlag Berlin, Heidelberg, New York, 2. Aufl. Vorlesungen über technische Akustik.

21. J. MEIXNER and U. FRITZE 1949 Zeitschrift für angewandte Physik 1, 535-542. Das Schallfeld in der Nähe der frei schwingenden Kolbenmembran.

22. H. IRRETIER, O. MAHRENHOLTZ and E. SCHNEIDER 1983 Report for the BMFT. Rechenmodell zur schalltechnischen Optimierung des Radsatzes.

23. Rep. KRUPP 1979 Untersuchungsbericht Q-V 13045. Ermittlung der Eigenschwingungsformen und -frequenzen eines Rades für Schienenfahrzeuge bei Anregung mit einem elektrodynamischen Schwingungserreger.

24. H. IRRETIER 1983 J. Sound and Vibrations 87, 161-177. The Natural and Forced Vibrations of a Wheel Disk. 3rd. Int. Workshop on Railway and Tracked Transit System Noise, Colorado (U.S.A.) 1981.

25. DEUTSCHES INSTITUT FÜR NORMUNG E.V. Internationale Elektronische Kommission, DIN IEC 651, 7-8.

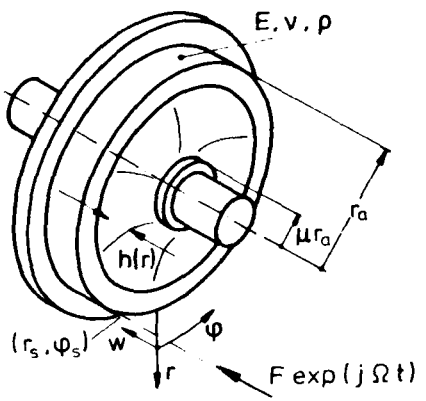

Fig. 1: Wheel disk with axial harmonic excitation; notations

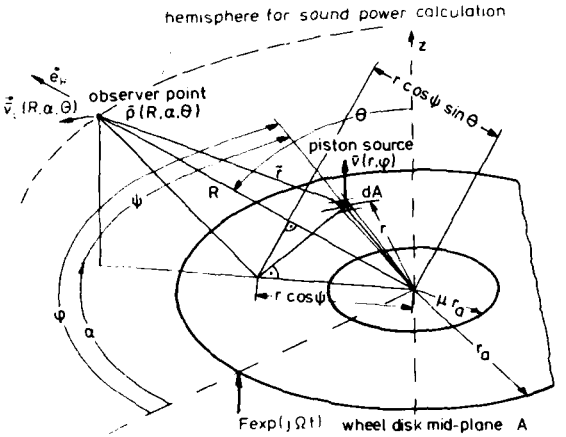

Fig.2: Sound pressure radiation of the wheel disk mid-plane

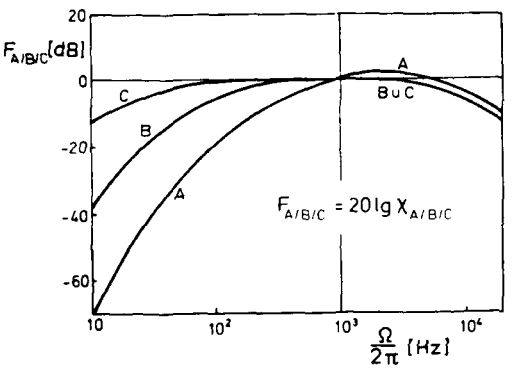

Fig. 3: Frequency evaluation curves A/B/C DIN IEC 651 for radiated sound pressure

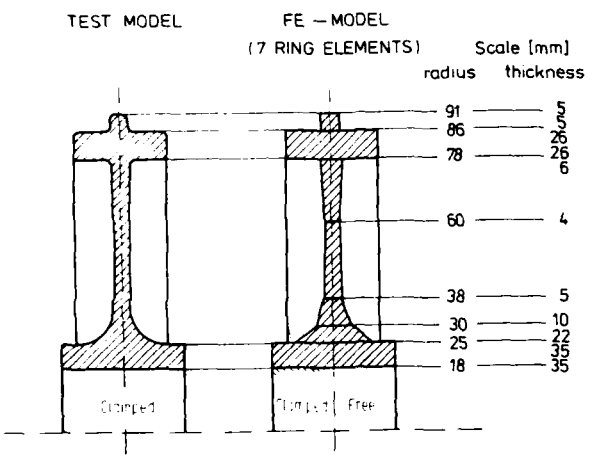

Fig. 4: Test model and finite element model for comparison of eigenfrequencies and mode shapes

Mode		Test results	Numerical results			
k	ℓ	'Clamped'	Clamped	error [%]	Free	error [%]
0	0	---	1287	---	---	---
	1	---	8090	---	2294	---
1	0	416	953	129.0	---	---
	1	---	8451	---	3580	---
2	0	1668	1656	0.7	1641	1.6
	1	---	9609	---	8540	---
3	0	4595	4571	0.5	4570	0.5
	1	11413	11464	0.4	11281	1.2
4	0	8543	8488	0.6	8488	0.6
	1	14121	13855	1.9	13812	2.2
5	0	13113	12972	1.1	12972	1.1
	1	17275	16743	3.1	16733	3.1

Tab. 1: Measured and calculated eigenfrequencies $f_{k\ell}$ [Hz] of the test model (Figure 4)

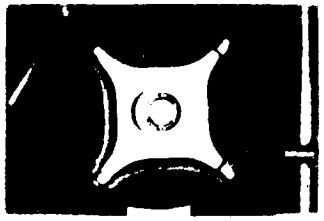

Fig. 5: Measured and calculated mode shapes $\tilde{W}_{k\ell}$ and corresponding eigenfrequencies $f_{k\ell}$ of the test model (Figure 4)

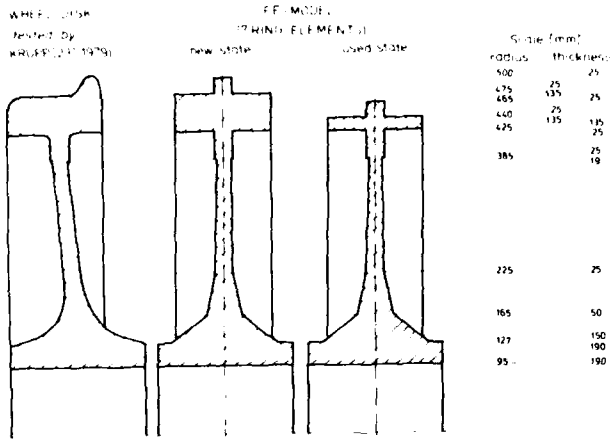

Fig. 6: Wheel disk [23] and finite element models

Mode k	ℓ	Test results (KRUPP 23)	Numerical results (new state)	error [%]	Numerical results (used state)	Alteration [%] against 'new state'
2	0	297	299.0	.67	259.8	-13.1
	1	-	1763.5		1655.4	- 6.1
	2	-	3200.9		3584.0	12.0
3	0	833	830.7	-.28	681.8	-17.9
	1	-	2102.9		1829.5	-13.0
	2	-	3552.5		3826.8	7.7
4	0	1546	1548.2	.14	1291.3	-16.6
	1	-	2512.2		2134.5	-15.0
	2	-	4059.5		4221.1	4.0
5	0	2356	2377.1	.90	2125.7	-10.6
	1	-	2990.9		2504.5	-16.3
	2	-	4690.0		4646.0	- 0.9

Tab. 2: Eigenfrequencies $f_{k\ell}$[Hz] of a real wheel disk [23] in new and used state; test and numerical results

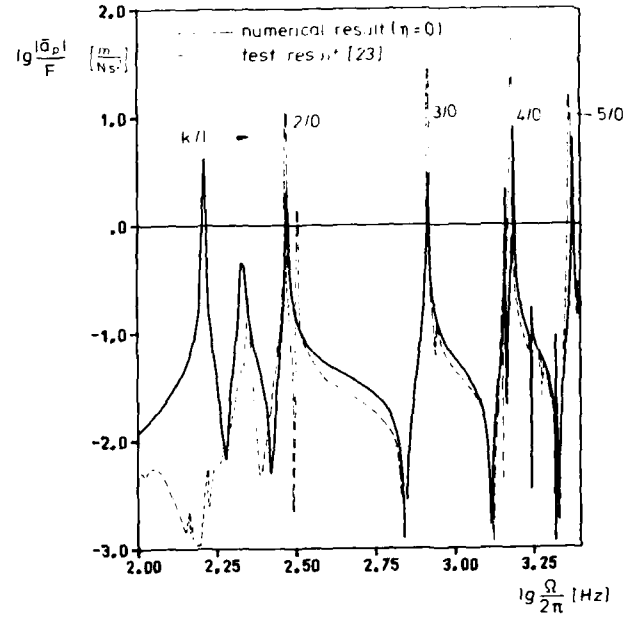

Fig. 7: Acceleration-frequency-curve at the rim of wheel disk [23]; test and numerical results (undamped)

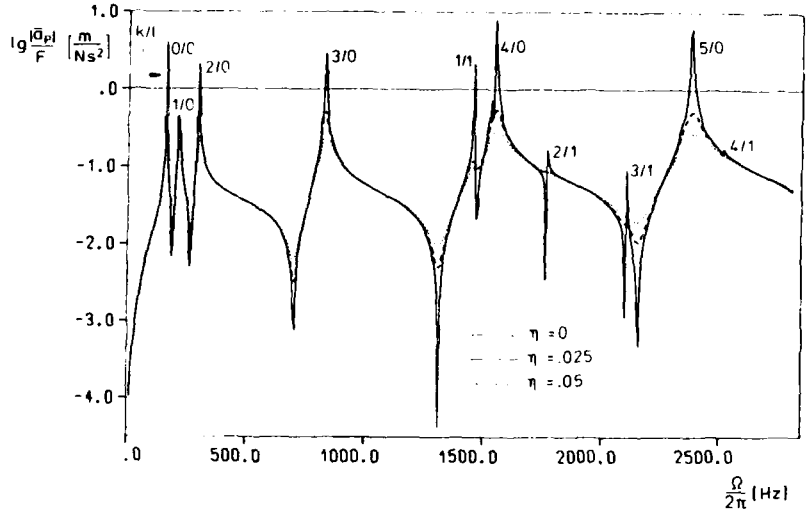

Fig. 8: Acceleration-frequency-curve at the rim of wheel disk [23] for different damping coefficients; numerical results

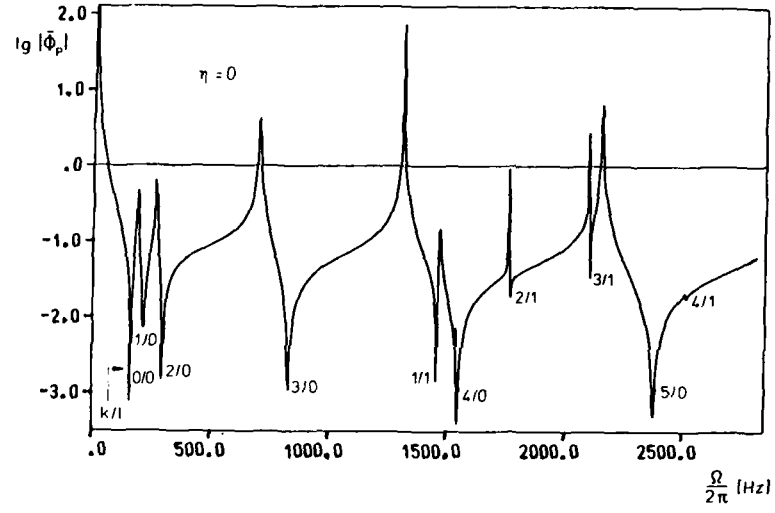

Fig. 9: Input impedance-frequency-curve at the rim of wheel disk [23]; numerical results (undamped)

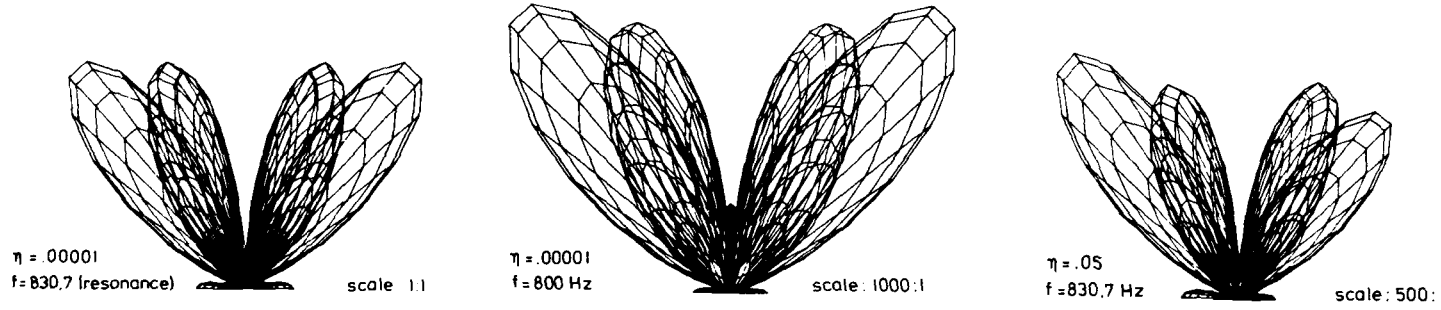

(a) (b) (c)

Fig. 10: Spatial directivity pattern of wheel disk [23] excited at the rim for different frequencies and damping coefficients; numerical results (view from $\alpha = -90^{\circ}$, $\theta = 90^{\circ}$)

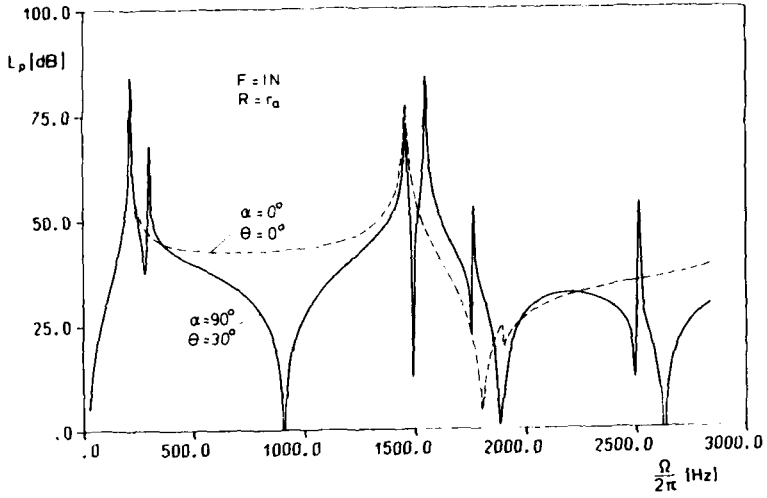

Fig. 11: Sound pressure level-frequency-curve of wheel disk [23] for various angles of radiation; numerical results (undamped)

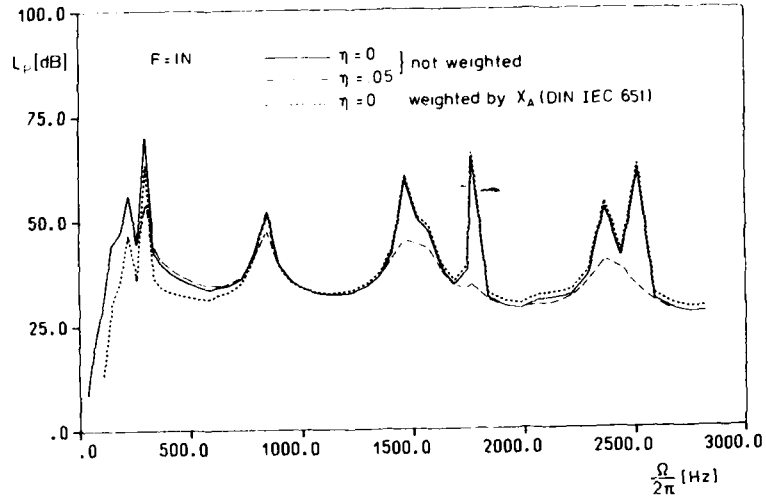

Fig. 12: Sound power level-frequency-curve of wheel disk [23] for various damping coefficients; numerical results

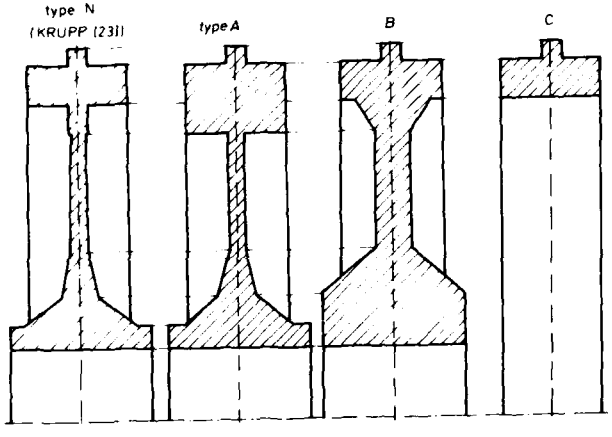

Fig. 13: Various types of wheel disk for comparison of sound emission

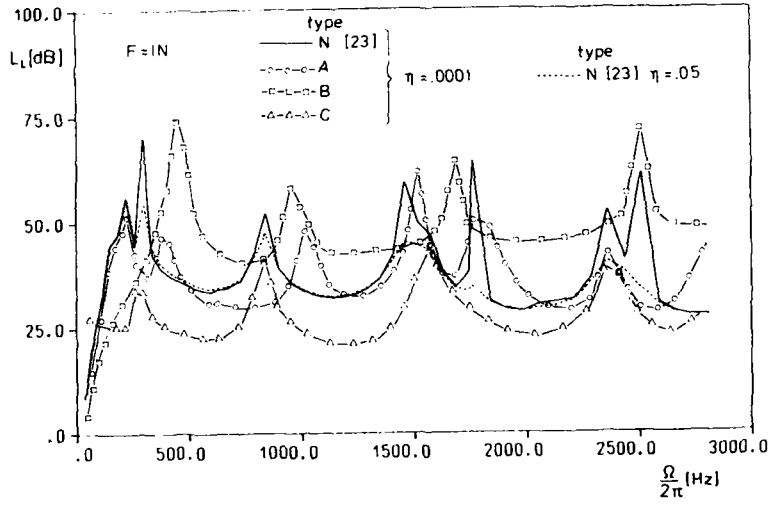

Fig. 14: Sound power-frequency-curves of various types of wheel disks; numerical results

Type	η	L_G[dB]
N	.0001	52.5
	.05	38.3
A	.0001	47.4
B		59.6
C		32.9

Tab. 3: Acoustical quality level for various types of wheel disks

14. AEROSPACE STRUCTURES AND/OR FATIGUE

GALILEO SPACECRAFT MODAL TEST AND EVALUATION OF TESTING TECHNIQUES

Jay-Chung Chen

Jet Propulsion Laboratory
California Institute of Technology
Pasadena, California
USA

1. INTRODUCTION

Designing a structure that will be able to survive a prescribed dynamic environment is generally accomplished today by using an analytical model of the structure. Since many structural systems will not be subjected to their design dynamic environments prior to their commission, it is very important that the analytical model be able to predict the behavior of the physical system quite accurately. Although advancements in modern analytical techniques and the ever-increasing capabilities in computer technology make it possible for engineers to model a physical system to any desired degree of accuracy, cost and schedule constraints preclude such an approach in the design process. Thus, an engineering model for the purpose of the design analysis process will always be an approximate representation of the physical system.

For aerospace payload structural systems, where the responses and loads dictate the design and thus the size and weight of the structure, the accuracy of the analytical model is of major importance because of the stringent weight constraints. A so-called test-verified analytical model is always required for the final verification loads analysis. The modal test, from which the natural frequencies, mode shapes, modal damping and other dynamic characteristics are determined experimentally, is used to verify the analytical model. The comparisons of various modal characteristics, such as the natural frequencies and mode shapes obtained from the modal test and its corresponding analytical predictions, define the accuracy of the analytical model.

A successful modal test involves three integrated phases; namely, pre-test analysis of the test article, the actual testing and data acquisition, and the test/analysis correlation of the results. The pre-test analysis is required for the design of the test including the proper instrumentation distribution, external excitation selection and the frequency range to be covered. The post-test correlation is necessary for defining the accuracy of the model as well as for structural parameter identification procedure in which the analyst can improve upon the analytical model systematically by using the test results. The actual testing and data acquisition is of course the most important aspect in this integrated effort.

In ~~the present~~ paper, the Galileo spacecraft modal test requirements will ~~be~~ described. Also, the associated pre-test activities from which the test is designed will ~~be~~ presented.

2. TEST ARTICLE AND TEST OBJECTIVES

The Galileo is an interplanetary spacecraft whose mission is to conduct scientific exploration of the planet Jupiter. It is to be launched by the space shuttle and a modified Centaur Upper Stage in 1986. Figure 1 is a schematic of the Galileo in the modal test configuration with its major components indicated. The Galileo is a dual-spin spacecraft with substantial amount of weight distributed on the appendages. Figure 2 shows the Galileo core structure wi spun and

despun parts identified. Also, Figure 2 shows those components which are hidden inside the core structure. The total weight of the spacecraft is approximately 5300 lbs., and its distribution is shown in Table 1. A finite element model using NASTRAN code was constructed to perform the loads analysis for structural system design [1]. The model consists of approximately 10,000 static degrees-of-freedom and 1600 mass degrees-of-freedom. It is precisely this model which will be verified by the modal test.

The principal objective of the modal test is to verify the analytical model by comparing the experimentally determined modal characteristic such as the natural frequencies and mode shapes to those obtained from the analytical model. Usually, the model is a finite element representation of the structural system. It should be noted that the comparison or the verification is not made on the model itself, which consists of mass, stiffness and damping matrices, but rather on the eigenvalues and eigenvectors calculated from the model. These analytically predicted eigenvalues and eigenvectors must be interpreted as the physical characteristics of the system. And the modal test should be designed in such a way that these dynamic characteristics can be readily measured from the test. In addition to predicting the eigenvalues and eigenvectors, the analysis can yield other valuable information which can be used as criteria for the verification of the model.

Specifically, the objectives of Galileo spacecraft modal test are:

(1) Generally evaluate the dynamic characteristics of the Galileo structure in the launch configuration.

(2) Obtain from the measured data the following reduced data

a) natural frequencies
b) mode shapes
c) orthogonality checks
d) residual mass
e) modal damping
f) modal forces in selected members
g) cross-orthogonality check
h) generalized forces

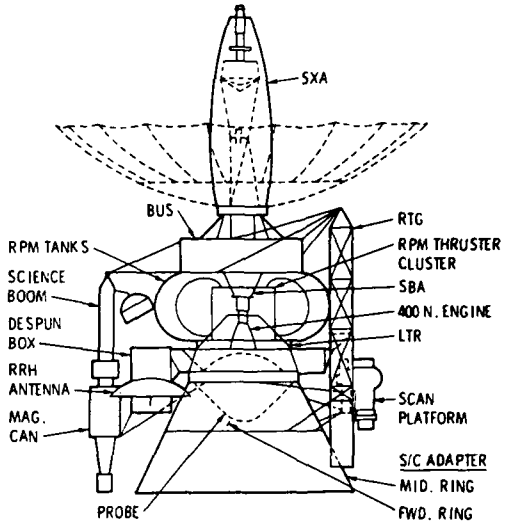

Figure 1. Galileo Spacecraft Modal Test Configuration

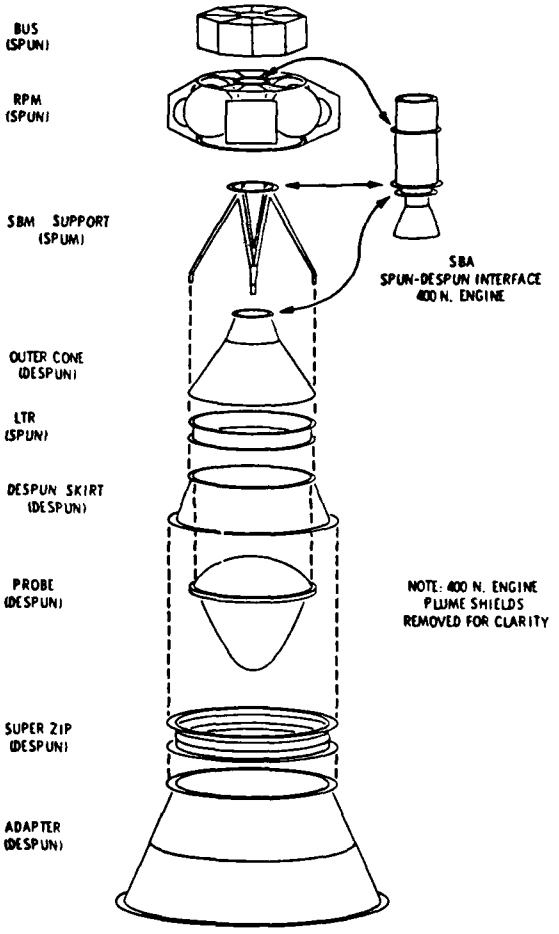

Figure 2. Galileo Spacecraft Core Structures

(3) Define the degree of non-linearity of the dynamic characteristics (frequency and damping) as a function of excitation level.

(4) Provide data to verify the analytical model used for loads analysis.

These measured and reduced quantities will be used in the test-analysis correlation [2], and the analytical model accuracy requirement effort [3].

Table 1. Major Subsystems

Subsystem	Mass* (kg)	Weight* (lbs)
High Gain Antenna	49.5	109.1
Bus	272.5	600.7
Retro Propulsion Module (RPM)	1216	2681
Despun Box	110.4	243.3
RRH	6.0	13.2
Bay E	14.5	32.0
Science Boom	76.6	168.8
Scan Platform	96.4	212.5
+x RTG	80.2	176.9
-x RTG	77.2	170.2
Probe	341.8	753.4
Spin Bearing	43.1	95.1
Inner Cone		
LTR		
Despun Cone	52.8	116.3
S/C Adapter	50.1	110.6

*Quantities are approximate, they may not reflect the numbers used in the model.

3. PRE-TEST ANALYSIS

Although the mathematical model used in the loads analysis is large in terms of number of degrees-of-freedom, the number of modes that are significant in the loads calculation [4,5] is small. In other words, only a finite number of modes within a certain frequency range are needed to be test verified. These modes and their frequency range are to be determined on a basis such that the loads analysis model can be sufficiently verified by the modal test results. For this purpose, pre-test analyses are performed.

Table 2 shows the first 70 natural frequencies predicted by the model. It was these 70 modes that were included in the response/loads analysis in the design process. Although the frequency range is up to almost 83 Hz, it is nevertheless a modal truncation. The very first question will be whether these 70 modes can adequately represent the actual physical system. And the second question will be how many modes should be experimentally tested such that a sufficient verification can be achieved.

The first question can be answered by examining the forcing functions used in the loads analysis. The loads analysis model must consist of sufficient modes such that all the components in the forcing function frequency spectrum will be covered by the spacecraft modes. For instance, Fig. 3 shows the Galileo/launch vehicle interface acceleration in the longitudinal direction which is one of the forcing functions used in the loads analysis. The shock spectra of the interface acceleration appears that major frequency contents are within 30 Hz.

Therefore, the loads analysis with 70 modes modal truncation which is up to 80 Hz should be more than adequate as far as computational accuracy is concerned. As for how many modes should be tested, the concept of effective mass will be used as a criterion. Briefly, if number of modes is equal to number of degrees-of-freedom, the total effective mass will be equal to the rigid-body mass. However, if fewer modes are used, the total effective mass will be less than the rigid-body mass. Therefore, effective mass can be used as a measure for the completeness for number of modes participating in the loads analysis. Effective mass for each individual mode comparing to the total effective mass can be used to gage the importance of that mode. Usually, modes involving global motion will have larger effective mass than those local modes. Table 3 shows the effective mass up to 21st mode whose frequency is 35.21 Hz. The effective mass is normalized by the corresponding rigid-body mass; therefore it can be viewed as

percentage completeness for number of modes. The summation of each effective mass is the indication of how sufficient is the modal truncation. For instance, the first mode contributes 32% and 67% of effective mass in x and θ_y direction, respectively. It is obvious that the first mode is indeed a major important one as one would guess intuitively. On the other hand, the tenth mode contributes very little in the effective mass. One may conclude that the tenth mode must be a local mode which is usually difficult to measure in a modal test. After considering 21 modes, more than 80% of the effective mass is accounted for except in the z and θ_z direction. It is common that more modes are required to accumulate sufficient effective mass in the directions of longitudinal translation and rotation with respect to longitudinal axis. Another interesting phenomenon is the fact that many local modes with negligible effective mass appear as low frequency modes such as the 10th, the 13th to the 18th modes and modes with larger effective mass appear as high frequency modes, such as the 19th and 21st modes. This is contrary to a similar interplanetary spacecraft whose first twelve modes accounted for over 90% of the total effective mass [2]. Although it appears that to test measure the first 21 modes is sufficient for the model verification, many local modes will be among them. From Table 2, it is clear that the system has high modal density together with the higher proportion of local modes; the modal test will not be an easy one. To understand the behavior of the system becomes even more important.

Table 2. Frequency Prediction

Mode No.	Freq (Hz)	Mode No.	Freq (Hz)	Mode No.	Freq (Hz)
1	12.78	25	37.49	49	53.42
2	13.04	26	38.48	50	53.90
3	16.59	27	40.22	51	54.58
4	17.45	28	40.54	52	56.02
5	18.42	29	41.34	53	56.45
6	19.36	30	41.60	54	56.76
7	19.77	31	41.93	55	63.35
8	20.86	32	42.09	56	63.89
9	21.94	33	42.16	57	65.07
10	22.69	34	42.25	58	67.94
11	22.88	35	42.33	59	68.35
12	28.01	36	42.78	60	69.04
13	29.11	37	43.38	61	69.94
14	29.51	38	43.48	62	71.02
15	31.17	39	44.08	63	71.63
16	31.44	40	45.23	64	72.56
17	31.44	41	47.25	65	73.38
18	31.90	42	48.43	66	75.04
19	33.44	43	48.89	67	76.07
20	34.57	44	49.74	68	76.55
21	35.21	45	49.98	69	80.19
22	35.99	46	50.23	70	82.88
23	36.07	47	50.89		
24	36.47	48	51.38		

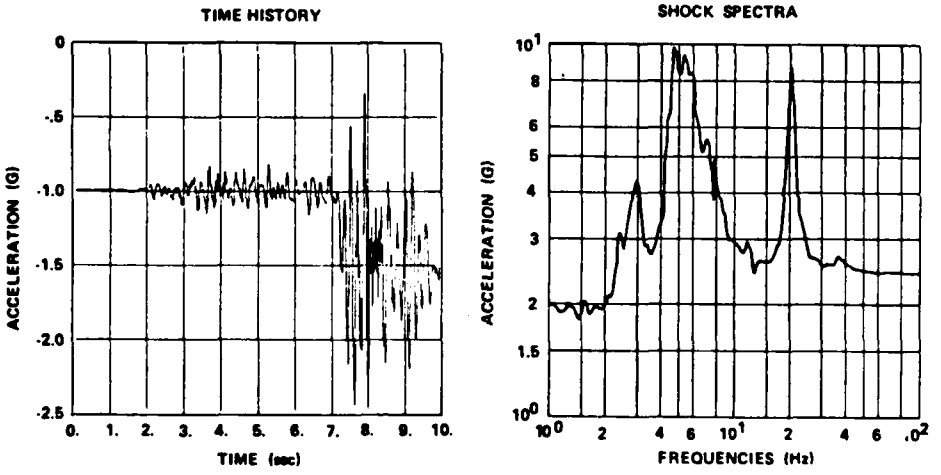

Figure 3. Launch Vehicle/Spacecraft Interface Longitudinal (Z) Direction Acceleration

Table 3. Effective Mass of TAM

DOF / Mode	x	y	z	θ_x	θ_y	θ_z
1	.3239	.0046	.0001	.0067	.6701	.0007
2	.0028	.3519	.0002	.6678	.0067	0
3	.0569	.0018	.0001	.0005	.0189	.2719
4	.0038	.3392	.0004	.2434	.0024	.0009
5	.1135	.0018	0	.0015	.1118	.0130
6	.0343	.0844	.0016	.0143	.0204	.0008
7	.1520	.0026	.0003	0	.0813	.0171
8	.0031	.0003	.0021	.0005	.0002	.2785
9	0	.0006	.0723	.0024	.0001	.0098
10	.0001	.0005	.0117	.0003	0	0
11	.0001	.0012	.1225	.0013	0	.0021
12	.1453	.0002	.0020	0	.0395	.0141
13	.0006	.0008	0	.0001	.0004	.0037
14	.0007	.0067	0	.0011	.0001	.0009
15	0	0	0	0	0	0
16	0	0	0	0	0	0
17	0	0	0	0	0	0
18	.0001	.0004	.0002	0	.0001	.0009
19	.0059	.0030	.4144	.0002	.0015	0
20	.0009	.0051	.0642	.0001	.0002	.0007
21	.0048	.0010	.0738	.0001	.0011	.0001
SUM	.8488	.8061	.7659	.9403	.9548	.6152

The frequency range of interest and number of modes to be verified have been indicated by the examination of forcing functions and the effective mass. Another factor, the maximum modal responses which are obtained from the modal equations by applying the generalized forcing functions, can be used in establishing the order of importance of each mode to be tested. Table 4 lists the summation of effective mass over six directions for each mode and the maximum model acceleration obtained by using the interface accelerations as forcing functions. In general the modes which possess larger effective mass summation have large maximum modal responses. Indeed, the 13th to 18th modes, whose effective masses are negligible, have very small modal responses. One exception is the 10th mode, whose modal acceleration is substantial despite the very small effective mass. However, by carefully examining the forcing function shock spectra it is found that a large amplitude component exists at the resonance frequency, 22.69 Hz. Therefore, it is reasonable that the modal response of this local mode will be large because of the high level forcing functions at the modal frequency. The implication is that the 10th mode, although of local nature, is important nevertheless. Therefore, the test verification for this local mode cannot be ignored. It is expected that large amplitude responses or loads will occur at the local component for this mode. Design modification may become necessary for loads reduction. It is particularly desirable in this case because of the sharpness of the peak in the shock spectra. A small shift of natural frequency can drastically

reduce the responses. In order to do this, this local mode must be accurately predicted and test verified. The effective mass as well as the modal acceleration as listed in Tables 3 and 4, respectively, can be used to construct a list of mode importance for the purpose of modal test priorities.

The results of this understanding of the modal characteristics of the loads model helped in the design of the modal test such as the instrumentation distribution and external excitation selection. After careful consideration, it was determined that 162 channels of accelerometer measurements as well as 118 channels of strain gauge measurements will be taken during the test. The instrumentation distribution is such that all the important modal displacements and modal forces can be measured with sufficient resolution.

Table 4. Modal Acceleration

Mode	Freq (Hz)	Effective Mass Summation	Modal Acceleration
1	12.78	1.01	2.00 (g)
2	13.04	1.03	8.52
3	16.59	.35	-1.36
4	17.45	.59	-8.14
5	18.42	.24	1.19
6	19.36	.16	3.15
7	19.77	.25	-1.62
8	20.86	.29	-1.33
9	21.94	.09	4.25
10	22.69	.01	-1.39
11	22.88	.13	4.42
12	28.01	.20	-2.26
13	29.11	.01	.21
14	29.51	.01	.60
15	31.17	0	0
16	31.44	0	-.07
17	31.44	0	-.06
18	31.90	0	-.20
19	33.44	.43	6.35
20	34.57	.07	2.46
21	35.21	.08	2.75

4. TEST-ANALYSIS MODEL

The purpose of the test analysis model (TAM) is to relate the test measured results to the analytical predictions and to assist in the test data reduction. In general, the number of degree-of-freedom in the loads analysis model is order to magnitude greater than the number of measurements to be made during testing, such as the case of Galileo modal test in which 162 response measurements are made as compared to 10,000 degrees-of-freedom in the loads analysis model. For test-analysis correlation, one may use the 162 measurements to extrapolate and map the motions of entire 10,000 degrees-of-freedom.

On the other hand, a new condensed model can be constructed such that its degrees-of-freedom will be compatible with the test measurements. This condensed model is called the Test-Analysis Model, TAM. For Galileo modal test, the TAM is obtained by Guyon reduction method to collapse the mass and stiffness matrices in the loads analysis model onto 162 degrees-of-freedom matrices. The TAM must be so adjusted that all the modal characteristics predicted by the loads model should be reproduced by TAM within the range of interest. Table 5 shows the comparison of frequencies and generalized effective mass for the modes predicted by the TAM and the corresponding loads analysis model. It should be noted that the mass distribution in the loads analysis model has been altered to reflect the referee fluids used in the propellant tasks. This is the reason that frequencies in Table 2 and Table 5 are different. In general, the TAM retained high degree of fidelity compared to the loads model predictions.

The TAM, a much smaller model compared with the loads analysis model, is used to assist the modal test by predicting the target mode natural frequencies, shown in Table 6, as well as the optimal shaker locations. Also, TAM will be used in the data reduction such as the orthogonality check, effective mass by test modes, cross orthogonality and kinetic energy distribution.

Table 5. Frequency and Effective Mass Comparisons for TAM and Loads Model

TAM			Loads Model		
Mode	Freq (Hz)	Eff. Mass (kg)	Mode	Freq (Hz)	Eff. Mass (kg)
1	13.22	796.0	1	13.23	786.2
2	13.44	840.0	2	13.50	841.0
3	16.93	142.5	3	16.94	143.4
4	17.90	858.0	4	17.99	852.0
5	18.89	291.0	5	18.98	281.0
6	19.92	293.0	6	19.93	298.0
7	20.58	391.1	7	20.39	395.8
8	21.46	6.0	8	21.47	10.1
9	22.67	120.2	9	22.60	176.2
10	23.62	394.0	10	23.54	391.1
11	28.69	344.6	11	28.84	360.3
13	30.26	15.9	13	30.34	16.6
18	34.26	1091.5	18	34.40	1043.8
23	37.69	55.1	19	35.56	17.1
19	36.06	345.2	20	36.18	176.2
22	37.33	5.9	21	36.76	25.1

Table 6. TAM Prediction

Mode	Frequencies (Hz)	Description
1	13.22	Global bending in X
2	13.44	Global bending in Y
3	16.93	Science boom in X
4	17.90	SXA in Y
5	18.89	SXA in X
6	19.92	-X RTG in Z
7	20.58	+X RGG in Z
8	21.46	Oxidizer 2 in X-Y
9	22.67	±X RTG in Z
10	23.62	Probe in Y
11	28.69	Science in Y
12	29.76	Damper and Science Boom in Y
13	30.26	SXA Local in X-Y
14	31.38	SXA Local in X
15	32.40	SXA Local in Y
16	32.69	Probe in X
17	33.15	Damper in X
18	34.26	Oxidizer in Z
19	36.06	Relay Antenna in Y
20	36.53	Thruster Boom in Y
21	37.35	Thruster Boom in Y

5. TEST DESCRIPTION AND RESULTS

The multi-shaker sine dwell technique was chosen as the primary method for the Galileo spacecraft modal test. An interactive computer program is developed to automate the tuning procedure. On-side data reduction including frequency, mode shape, modal force, orthogonality, cross-orthogonality, effective mass and damping are performed immediately after the data are acquired.

Excitation of the test article is accomplished with an integrated system of eight 25 lb. Ling electrodynamic shakers. Each system provides separate power supplies for the field and armature current, however, the control of the multi-shaker system can be accomplished by a single console. Each shaker is attached with an impedance package which consists of a load cell for measuring the shaker force and an accelerometer for measuring the driving point response. Figure 4 shows the test article with shakers attached.

In addition to the shaker forces and driving points motion, the response measurements by the 162 accelerometers and strain measurements by 118 strain gauges are made for the mode shape and modal forces survey. The output of each accelerometer and each strain gauge is conditioned and fed into a data acquisition system with analog to digital conversion device and anti-aliasing filtering circuits. During the test various quantities such as real v.s. imaginary part

of the response, shaker forces v.s. responses, energy or power plots to assist the tuning of the mode. Once a target mode is satisfactorily tuned, the response data of all instruments are acquired and written to a file. Next, the excitation is cutoff and subsequent decay responses of accelerometers are recorded. The acquired data are processed immediately and the results are printed out and copied onto tapes together with the raw data for future data reduction.

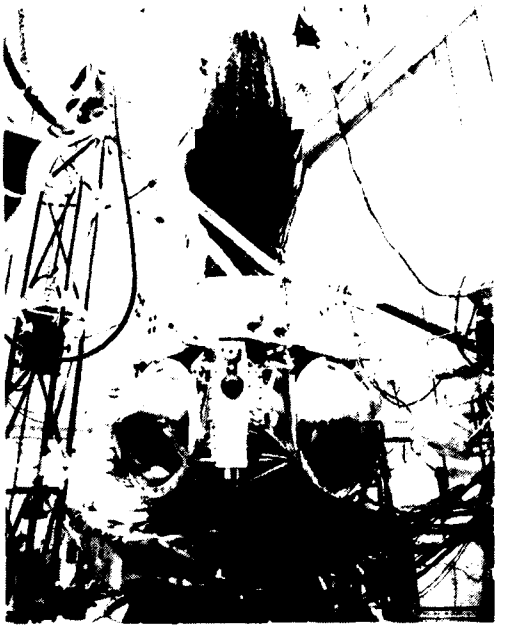

Figure 4. Test Article with Shaker Attached

Although the classical multi-shaker sine dwell method was chosen by the Galileo project for its modal testing, various other advanced modal testing methods were performed. These methods require extensive data processing to compute the transfer functions from which the modal parameters such as the natural frequencies, dampings and mode shapes are obtained by curve fittings. These methods include the single point random, multi-point random, slow sine sweep (SWIFT), fast sine sweep (CHIRP) and tuned sine sweep. The transfer functions obtained by different methods exhibits different characteristics such as shown in Figures 5 and 6 which are from the single point random and multi-point random, respectively. The transfer function from the multi-point random method has a tendency of keeping the peaks at a constant level, thus maintaining the mode shape measurement at same amplitude level. Accelerometer measurement at low level tends to contain more errors. Figures 7 and 8 shows the transfer function obtained by SWIFT and CHIRP method which, again, demonstrate different characteristics.

Fourteen independent modes were obtained by the sine dwell method. The measured frequencies and dampings are listed in Table 7. Similar results from the 4 shaker random method are listed in Table 8 for 26 modes. The very first question will be how complete in terms of number of modes these methods provide. The percentage of effective mass will be used as the criterion for comparison. Table 9 and 10 list the effective mass by mode for the sine dwell method and random method, respectively. The random method provides modes whose effective mass is 10 to 20 percent more than those from the sine dwell method. Also in Table 3 and 4, those modes with less than 10% of the total effective mass in any one of the six directions are identified as local modes whose motions are predominantly local components.

Next, the goodness of the measured mode shapes will be examined by the orthogonality check which is shown in Tables 11 and 12 for the sine dwell and random method, respectively. From Table 11 it shows that mode shapes from sine swell method are not very "clean" because of the presence of large off-diagonal terms. Those off-diagonal terms with magnitude equal or more than 0.10 are "boxed". Orthogonality check is a very effective gauge for checking the "cleanness" of the global modes because usually large amplitude motion is associated with large mass points. On the other hand, for local modes, large amplitude motion is associated with small masses and large masses have small amplitude motion whose accuracy will be less than those large amplitude motion. Therefore, the coupling between the local modes and global modes or between local modes themselves are difficult to be completely orthogonal. This usually shows up as large off-diagonal terms for the local modes. If disregard the local modes,

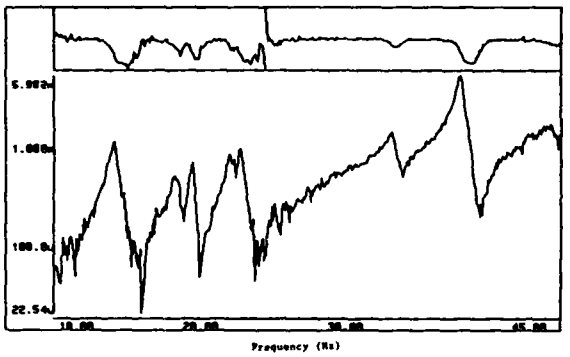

Figure 5. Transfer Function From Single-Point Random Method

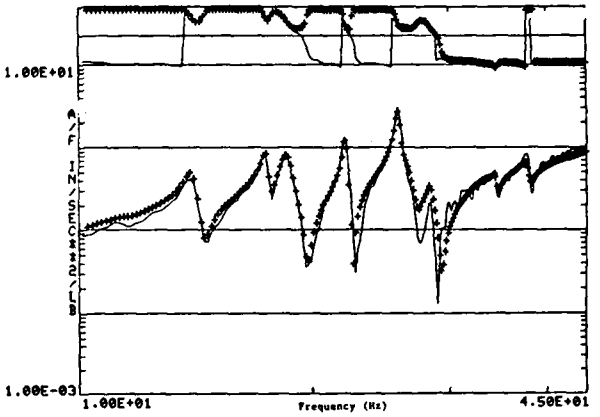

Figure 6. Transfer Function From Multi-Point Random Method

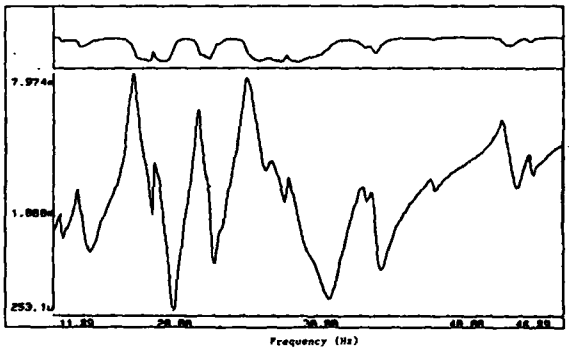

Figure 7. Transfer Function From "SWIFT" Method

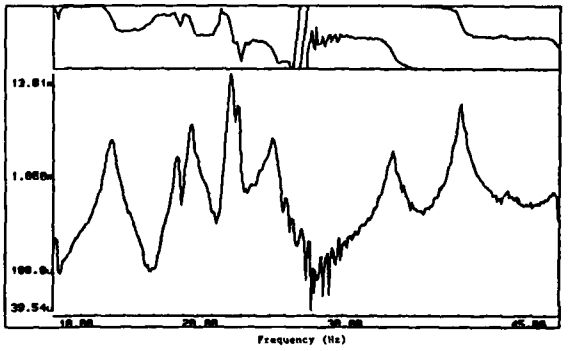

Figure 8. Transfer Function From "CHIRP" Method

Table 11 shows an even worse orthogonality check with large numbers populated in most of the off-diagonal terms. These global modes are not completely orthogonal. From Table 12 a different picture can be seen for the modes obtained by the random method. If only the global modes are considered, very few large numbers appear in the off-diagonal terms. Furthermore, except for the couplings between mode 1 and mode 3, and, mode 7 and mode 8, all the off-diagonal terms are less than 0.05. This is, indeed, very good indication that the global modes are orthogonal as they should be according to the theory. Of course, the validity of orthogonality is dependent on the correctness of the mass matrix used. Since same mass matrix is used for the comparison, the resulting trend should be valid.

In order to made a mode by mode comparison, the cross-orthogonality will be used to identify the modes from one method with respect to the ones from the other method. Table 13 shows the cross-orthogonality between modes from sine dwell and random methods. Modes with coupling term near 1.00 indicate they are similar in shape. Identification is made by boxing the coupling terms. For certain modes with close similarity of shapes with more than one mode from the other group, the identification is made by other considerations such as the closeness of the natural frequencies and characteristics of the modes. Table 14 is the summary of the mode by mode comparison with natural frequency, damping and maximum effective mass within that mode listed. The best correlation is SD1503 and MSR18 with everything almost identical.

Table 7. Multi-Shaker Sine Dwell Modal Test Results

MODE	FREQUENCY	DAMPING	DESCRIPTION
101	13.109	.0176	HGA in x
201	12.696	.0159	HGA in y
301	18.588	.0152	Sci. Boom in x
404	17.409	.0028	Core Bending in x, y
501	17.762	.0125	Core Bending in -x, y
601	21.670	.0054	RPM in x
702	23.656	.0188	RTG in z, in phase
803	25.161	.0102	Damper x-y
902	26.116	.0118	Sci. Boom in z
1503	37.923	.0059	Bounce in z
1801	42.527	.0049	-x thruster in y
2002	42.200	.0042	+x thruster in y
2050	23.103	.0121	-x RTG in z
2902	29.711	.0145	-x RTG in y

Table 8. Four Shaker Random Modal Test Results

MODE	FREQUENCY	DAMPING	DESCRIPTION
1	11.460	.0298	HGA in y
2	14.017	.0166	HGA in x
3	17.444	.0088	Core Bending in y
4	18.544	.0178	Core Bending in x
5	19.326	.0092	Sci. Boom in x
6	22.057	.0049	±RTG in z out of phase
7	22.524	.0095	±RTG in z, in phase
8	25.191	.0103	±RTG, Sci. Boom in z
9	25.796	.0066	Core Bending x, y
10	26.363	.0197	Probe in y
11	27.835	.0204	Sci. Boom (+)/ RRH (-) in y
12	28.288	.0107	RRH in y
13	30.497	.0353	Probe in y/Scan P in z
14	31.840	.0287	Damper in x
15	33.421	.0149	Probe in x
16	33.757	.0114	Probe in x/S.P. in z
17	34.497	.0074	Sci. Boom x, z
18	37.910	.0057	z mode core (+)/ Appendiges (-)
19	39.138	.0458	±x thruster in y, in phase
20	39.768	.0117	Sci. Boom in +y, -x
21	41.727	.0183	Engine in y, x, +x thruster in -y
22	42.348	.0280	Engine in y, -x
23	42.360	.0074	Engine in x, y, z
24	44.611	.0062	±x thrusters in y, in phase
25	44.977	.0048	±x thrusters in y, out of phase
26	46.002	.0038	±x thrusters in y, in phase

6. CONCLUDING REMARKS

The Galileo spacecraft is a large complex structural system and as a test article a large number of measurement are assigned to be acquired. Extensive and detailed pre-test analysis is performed for the preparation of its modal test. Also, very thorough post test correlation effort will be conducted. The primary objective is, of course, the verification of the Galileo loads analysis model and its updating or modification by the test results if necessary. However, it also provides an unique opportunity to evaluate some of the modern modal test technique.

Based on the above comparisons, a preliminary evaluation of the multi-shaker sine dwell method versus the multi-shaker random method can be concluded as:

1. Random method provides more modes for completeness.

2. Global modes from random method are more orthogonal than those from the sine dwell method.

3. Mode by mode comparison indicates a good agreement between the modes from the two methods in terms of natural frequencies and dampings.

4. Cross orthogonality indicates that for some modes, disagreement in mode shape may be substantial.

Table 9. Effective Mass for Multi-Shaker Sine Dwell Method

MODE	FREQUENCY	x	y	z	θ_x	θ_y	θ_z
201	12.70	0.3	8.7	0.0	23.1	0.9	0.0
101	13.11	13.3	0.3	0.0	0.6	33.5	0.0
501	17.76	9.6	26.5	0.1	31.5	10.9	0.2
404	17.40	13.8	19.1	0.0	25.2	18.3	0.4
301	18.60	0.0	0.0	0.0	0.0	1.9	20.2
601	21.67	42.4	0.3	0.1	0.3	39.6	2.4
*2050	23.10	0.0	2.6	4.0	1.2	0.4	0.1
* 702	23.66	0.0	0.6	6.7	1.1	0.0	0.0
803	25.16	0.8	0.0	0.2	0.0	0.3	23.2
* 902	26.12	0.1	0.1	5.7	0.2	0.0	4.3
*2902	29.71	1.0	0.8	0.0	0.1	0.1	6.5
1503	37.92	0.2	0.2	45.8	0.0	0.2	0.1
*2002	42.20	0.1	0.0	0.4	0.0	0.0	0.0
*1801	42.53	0.0	0.0	1.2	0.0	0.0	0.1
		81.6	59.3	64.1	83.3	106.2	57.5

*Denote for local modes

Table 10. Effective Mass for Four Shaker Random Method

MODE	FREQUENCY	x	y	z	θ_x	θ_y	θ_z
1	11.46	0.7	4.8	0.0	14.8	1.5	0.0
2	14.02	22.7	0.2	0.4	0.7	48.0	0.0
3	17.44	1.8	41.6	0.3	52.1	1.7	0.0
4	18.54	18.6	0.5	0.2	0.6	17.2	4.7
5	19.33	0.0	0.2	0.0	0.1	0.6	19.4
6	22.06	21.3	2.9	0.3	1.3	14.2	1.3
7	22.52	3.6	14.8	1.5	5.4	1.5	0.9
8	25.19	0.0	1.7	12.5	0.1	0.0	1.6
9	25.80	1.3	0.8	1.9	0.8	0.6	22.0
*10	26.36	0.0	3.3	0.0	0.4	0.0	0.3
*11	27.84	0.1	0.1	3.8	0.0	0.1	1.7
*12	28.29	0.3	0.4	0.0	0.1	0.0	0.7
*13	30.50	0.7	0.0	5.7	0.9	0.0	0.0
*14	31.84	0.2	0.5	0.1	0.2	0.1	7.1
15	33.42	13.3	0.0	0.9	0.1	3.8	0.2
*16	33.76	3.8	0.7	0.1	0.1	1.2	4.6
*17	34.50	0.8	0.2	0.0	0.0	0.2	2.2
18	37.91	0.1	0.2	45.6	0.1	0.1	0.0
*19	39.14	0.2	0.0	9.8	0.2	0.2	1.0
*20	39.77	0.2	6.3	0.2	4.9	0.1	2.7
*21	41.73	0.0	0.0	1.1	0.0	0.0	0.6
*22	42.35	0.0	1.5	0.0	0.6	0.1	0.0
*23	42.36	0.1	0.7	0.1	0.8	0.0	0.0
*24	44.61	0.2	2.1	0.0	1.2	0.2	0.6
*25	44.98	0.2	0.4	1.0	0.4	0.1	0.0
*26	46.00	0.0	0.9	0.0	1.0	0.1	0.2
		90.4	84.5	85.6	87.2	92.5	72.0

*Denote for local mode

However, the biggest difference between the two method is the time required for completing the test. The sine dwell method required weeks and random method took few hours for the case of Galileo modal test.

ACKNOWLEDGEMENT

The paper presents the results of one phase of research carried out at the Jet Propulsion Laboratory, California Institute of Technology, under Contract NAS7-100 sponsored by NASA.

REFERENCES

1. J.C. CHEN, J.A. GARBA, M. SALAMA and M. TRUBERT 1980 Jet Propulsion Laboratory Publication 80-37. A Survey of Load Methodologies for Shuttle Orbiter Payloads.

2. B.K. WADA, J.A. GARBA and J.C. CHEN 1974 The Shock and Vibration Bulletin 44, Part 2. Naval Research Laboratory, Washington DC, 125-164; also published as JPL Technical Memorandum 33-690. Development and Correlation: Viking Orbiter Analytical Dynamic Model with Modal Test.

Table 11. Orthogonality Check for Multi-Shaker Sine Dwell Method

MODE	201	101	501	404	301	601	2050	702	803	902	2902	1503	2002	1801
201	1.00	.32	.20	-.04	0	.03	-.02	-.02	-.01	0	.01	-.01	.01	-.01
101		1.00	.10	.04	.05	.15	.08	-.01	-.02	0	0	-.01	0	.01
501			1.00	-.19	.16	-.17	-.04	-.01	.01	0	-.01	.02	.01	0
404				1.00	.15	-.20	-.16	.04	.01	.02	0	-.02	-.01	-.03
301					1.00	-.22	-.13	.02	.04	-.05	.01	.02	.03	.02
601						1.00	-.26	-.06	-.08	.08	0	-.02	-.02	-.01
2050							1.00	.60	.01	-.07	-.01	-.05	0	.02
702								1.00	.08	-.19	-.02	-.01	-.01	0
803									1.00	.12	0	.02	.03	.01
902										1.00	0	0	.02	.02
2902											1.00	-.09	-.05	-.05
1503												1.00	0	-.02
2002													1.00	.20
1801														1.00

*Shaded numbers are local modes.

Table 12. Orthogonality Check for Four Shaker Random Method

MODE	1	2	3	4	5	6	7	8	9	10	11	12	13	14	15	16	17	18	19	20	21	22	23	24	25
1	1.00	.02	-.10	.04	-.03	-.04	.04	-.04	-.02	-.01	.02	0	-.07	.02	0	.01	.01	-.01	-.01	-.02	-.05	0	.05	.06	.03
2		1.00	.02	-.04	.04	-.04	0	-.02	-.02	0	-.01	0	-.03	.05	0	.01	-.01	.03	.02	-.01	.02	0	-.02	.02	0
3			1.00	.01	-.03	-.02	.01	.01	0	.04	-.03	.02	-.07	-.02	.01	.01	.01	-.01	-.01	-.22	.03	-.06	.08	.06	.01
4				1.00	.05	-.04	.01	-.07	-.02	-.02	.04	-.10	-.06	.19	0	-.02	.01	.01	.02	-.06	.02	.01	-.06	-.01	-.02
5					1.00	.05	.02	-.01	-.02	.02	-.19	.17	0	.08	-.02	-.02	.01	.03	-.01	-.16	.03	.02	.01	-.05	-.02
6						1.00	-.03	-.02	.02	-.07	.04	.06	.07	.02	.09	.09	-.02	.01	-.03	-.09	.03	-.03	.07	-.03	-.03
7							1.00	.07	-.04	-.14	-.02	-.04	.04	-.01	-.04	-.05	0	0	.02	-.03	-.01	0	.01	.03	.03
8								1.00	-.04	.21	-.19	0	-.02	.01	0	-.01	.04	0	-.01	.01	0	0	.02	0	.01
9									1.00	.03	-.12	-.10	-.03	.44	.09	.09	-.07	-.03	-.05	-.10	0	-.01	.05	.08	.01
10										1.00	.33	-.08	-.35	-.03	-.04	.01	-.04	-.01	-.03	-.06	-.03	0	.02	.02	.01
11											1.00	.60	-.23	.07	-.04	.02	0	-.03	-.01	-.07	.01	-.09	.05	0	-.04
12												1.00	.05	.05	.03	.03	.03	.01	-.03	-.09	.08	.19	.09	-.04	-.19
13													1.00	-.05	0	.20	-.02	.07	-.19	-.03	.14	-.04	.04	-.14	-.11
14														1.00	.26	.33	.22	.13	-.10	-.05	.01	-.01	.10	.05	-.11
15															1.00	.50	-.09	.01	-.19	-.13	.18	-.05	.13	-.19	-.19
16																1.00	-.06	0	-.18	-.14	.14	.01	.12	-.12	-.11
17																	1.00	0	.06	.07	-.04	-.04	-.02	.03	-.02
18																		1.00	-.66	.06	.13	-.01	0	-.02	-.02
19																			1.00	.01	-.08	-.06	-.14	-.13	.10
20																				1.00	-.37	.43	-.34	.29	.07
21																					1.00	-.59	-.23	-.56	-.01
22																						1.00	-.30	.17	.03
23																							1.00	-.16	-.07
24																								1.00	.17
25																									1.00

*Shaded numbers are local modes.

Table 13. Cross Orthogonality Between Sine Dwell and Multi-Shaker Random Methods

Mode	1	2	3	4	5	6	7	8	9	10	11	12	13	14	15	16	17	18	19	20	21	22	25
201	1.00	-.02	-.06	.06	-.04	.01	.02	-.04	.02	0	.03	.01	-.07	.05	.01	.01	.03	0	-.02	-.06	-.01	-.03	.07
101	.39	1.00	-.06	-.26	.13	.01	-.01	-.03	-.02	0	0	-.01	-.03	.04	-.01	-.02	-.01	0	-.01	-.04	.02	-.02	.02
501	.33	-.08	-1.00	-.35	.10	.08	-.01	0	-.02	.06	.07	-.04	.08	-.03	0	0	-.02	0	.01	.22	-.05	.07	-.07
404	-.12	-.13	.63	-1.00	.25	.01	-.01	.10	.08	-.01	-.06	-.01	.03	-.12	0	.02	.03	-.02	-.01	-.13	0	-.06	.13
301	0	-.03	.09	.08	1.00	.06	.01	-.01	-.02	.02	.07	.08	.01	.07	0	-.01	.02	.03	-.01	-.14	.01	.05	-.01
601	.09	.27	.10	.22	-.22	-1.00	.31	.09	-.10	-.04	-.07	.02	-.04	-.06	-.09	-.10	-.03	-.02	.02	.02	.05	-.03	-.06
2050	-.06	.25	.03	.18	-.22	.99	.87	.34	-.18	.57	.10	-.06	-.20	-.07	-.10	-.07	-.01	-.10	.06	-.11	-.03	0	.03
702	-.05	0	.04	-.04	.04	.24	.53	1.00	-.10	.70	.27	-.05	-.31	.02	-.11	-.10	.03	0	.02	-.06	-.06	0	.02
803	-.05	-.04	-.04	0	.06	.06	-.03	.12	1.00	.15	-.12	-.09	-.04	.35	.05	.07	-.29	.01	-.08	-.13	.01	-.02	.05
902	.01	-.03	-.05	-.06	-.08	.01	.03	.43	.13	-.62	-1.00	.03	.42	-.07	.11	.08	0	-.02	.06	.03	.03	-.01	
2902	.07	.02	.04	.05	.11	.06	-.05	-.06	.02	0	.25	.34	-.38	-.30	-.99	-.65	-.23	-.24	.91	-.11	-.03	-.72	.27
1503	-.02	-.03	-.03	0	.02	.02	.01	-.01	-.02	-.03	-.04	.01	.09	.09	-.02	-.02	-.01	1.00	-.45	.05	.12	-.02	-.01
2002	.06	.01	.01	.03	.03	0	-.01	-.05	.07	.03	-.03	-.11	.02	.08	.11	.12	-.12	.03	1.00	.33	.61	.68	.18
1801	-.01	.06	.03	.09	.02	-.02	-.02	0	.03	0	-.05	0.06	.23	.25	-.04	0	.03	-.04	.86	.65	-.47	.71	1.00

Note: Shaded numbers indicate questionable coupling.

3. J.C. CHEN 1982 Proc. AIAA/ASME/ASCE/AHS 23rd Structures, Structural Dynamics and Materials Conference, New Orleans, LA. Analytical Model Accuracy Requirements for Structural Dynamic Systems.

4. M. TRUBERT and M. SALAMA 1980 AIAA Journal, 15(8), 988-994. Generalized Shock Spectra Method for Spacecraft Loads Analysis.

5. J.C. CHEN, M.R. TRUBERT and J.A. GARBA 1983 Proc. AIAA/ASME/ASCE/AHS 24th Structures, Structural Dynamics and Materials Conference, Lake Tahoe, Nevada, Paper 83-0818. Time Domain Response Envelope for Structural Dynamic Systems.

Table 14. Sine Dwell and Multi-Shaker Random Methods Comparison Summary

MODE		FREQUENCY		DAMPING		MAX. EFFECTIVE MASS	
SD	MSR	SD (Hz)	MSR (Hz)	SD	MSR	SD, %	MSR, %
201	1	12.70	11.46	.0159	.0298	θ_x = 70	θ_x = 68
101	2	13.11	14.02	.0176	.0166	θ_y = 70	θ_y = 67
501	3	17.76	17.44	.0125	.0088	θ_x = 40	θ_x = 53
404	4	17.41	18.54	.0028	.0178	x = 18	x = 44
301	5	18.59	19.33	.0152	.0092	θ_z = 91	θ_z = 96
601	6	21.67	22.06	.0054	.0049	x = 50	x = 52
2050	7	23.10	22.52	.0121	.0095	y = 31	y = 53
702	8	23.66	25.19	.0188	.0103	z = 80	z = 79
803	9	25.16	25.80	.0102	.0066	θ_z = 95	θ_z = 80
902	11	26.12	27.84	.0118	.0204	z = 55	z = 66
2902	15	29.71	33.42	.0145	.0149	θ_z = 77	x = 73
1503	18	37.92	37.91	.0059	.0057	z = 99	z = 99
2002	19	42.20	39.14	.0042	.0458	z = 80	z = 86
1801	25	42.53	44.98	.0049	.0048	z = 92	z = 48

ACOUSTIC FATIGUE LIFE OF ADHESIVE BONDED STRUCTURES SUBJECTED TO ACOUSTIC LOADS

H. F. Wolfe
Technical Manager, Acoustics and Sonic Fatigue Group
AFWAL/FIBE, Wright-Patterson Air Force Base, Ohio 45433

and

I. Holehouse
Engineering Staff Specialist
Rohr Industries, P. O. Box 878, Chula Vista, California 92012

1. SUMMARY

Acoustic fatigue damage to riveted metallic structures in aircraft due to high intensity noise has been recognized as a problem and design criteria have been developed to prevent such damage. However, very little design criteria are available for bonded and composite structures subjected to high intensity noise. A summary of the work completed in acoustic fatigue prediction techniques for weldbonded aluminum, adhesive bonded aluminum and adhesive bonded graphite-epoxy structures is discussed. These structures are more complex than riveted structures, more difficult to analyze and exhibit many different modes of failure which require a more detailed study to predict the sonic fatigue lifetime. Adequate performance under static loading did not guarantee adequate performance under dynamic loading. Some prediction methods have been developed for certain failure modes in adhesive bonded aluminum and graphite-epoxy bonded skin-stiffened structures. Further investigations are needed to adequately predict the acoustic fatigue life of adhesive bonded and graphite-epoxy aircraft structures.

2. INTRODUCTION

Acoustically induced fatigue failures in aircraft operation have been a design consideration for over 25 years. The problem was introduced with the advent of the turbojet engine which produced high intensity acoustic pressure fluctuations on aircraft surfaces. As engine performance requirements increased, the intensity of the acoustic pressures increased. Airframe minimum weight requirements resulted in higher stresses in structural components. The number of acoustic fatigue failures began to grow at a rapid rate until adequate design criteria were developed and used in the design process.

Similar fatigue failures have occurred in other regions of high intensity pressure fluctuations. These have occurred in regions of separated flow, behind protuberances such as air brakes, and in surface areas near the plane of propeller rotation. Failures have also occurred from the fluctuating pressure induced when bomb bay doors are opened during high speed flight.

The oscillating pressures from various noise sources produced a resonant response of the structural components such as external skin panels, frames, ribs and spars which results in rapid stress reversals in the structure. If these stresses have sufficient magnitude, fatigue failures occur.

Acoustic fatigue failures have resulted in unacceptable maintenance and inspection burdens associated with the operation of the aircraft. In some cases, sonic fatigue failures have resulted in major redesign of aircraft structural components.

Accurate prediction methods are needed to determine the acoustic fatigue life of structures. The approach has been semiempirical using analysis, acoustic testing of panels and vibration shaker testing of cantilever beam coupons. This combination of theoretical relationships, statistical relationships and test data for a particular structural configuration and material is used to predict the acoustic fatigue life of aircraft structures. A broad base of general design information for riveted structures in the form of nomographs and equations based upon combined analytical and experimental approaches was developed and is summarized in AGARDograph No. 162, Reference [1]. Experience has shown that these design data and prediction techniques are generally adequate for riveted structures and form a basis for developing prediction techniques for advanced structural concepts.

Three types of structural joints are discussed in this paper. These are the conventional riveted joint, the weldbonded joint and the adhesive bonded joint. The primary components of the joints are shown in Figure 1.

3. WELDBONDED STRUCTURAL CONCEPTS

Weldbonded structural joints in this paper are defined as thin plates or skins attached to back-up structures or stiffeners using a combination structural adhesives and spot welds. In general, weldbonded structures offer reduced manufacturing costs and improved fatigue life. This paper addresses the sonic fatigue life which can be quite different than the fatigue life under mechanical loading.

In 1972 three full scale A-7 wing outer panel trailing structures were tested which in service are subjected to buffeting loads [2]. These loads were acoustically simulated in a test chamber. Three identical structures were fabricated using two weldbonding techniques and one structure using the conventional rivet methods for comparison purposes. Fatigue failures in the riveted structure initiated around the rivet heads. Fatigue failures in the weldbonded structures were located in the skin along the edge of the stiffeners. The comparisons of weldbonded structures with riveted structures are dependent on the criteria selected and the type of weldbond system. One criterion is the test time until first failure. First failure is defined as the visual observation of a crack without the aid of magnification. The test times to first failure for both weldbonded structures and the riveted structure were observed to be approximately equal. Another criterion is the amount of cracking. Both weldbonded structures exhibited less cracking at the end of five to ten lifetimes than did the riveted structure. Although the fatigue failures of the weldbonded structures were quite different from the riveted structure, the fatigue lifetimes were relatively close.

Several programs with test coupons and test panels were conducted to develop prediction techniques for weldbonded structures similar to those developed for riveted structures. A combination of theoretical relationships, statistical relationships and test data for a particular weldbond system is used to predict the acoustic fatigue life. The fatigue life of the material and the response of the structure are usually determined using cantilever beam coupons and panels. The cantilever beam coupon test provides fatigue and damping data. The test coupons are a section of the more complex panel, including the stiffener. These coupons are vibrated at resonance on an electro-mechanical shaker to generate alternating bending stresses in the beam representative of the bending stresses produced by acoustic excitation. A typical shaker test set-up is shown in Figure 2. Strain gages are installed on the skin at locations of maximum strain. A low level sine sweep is usually performed to determine the natural frequencies and modes of the beam. Fatigue tests are usually conducted using a narrowband random excitation centered at the first or second bending modal frequency. The root-mean-square (RMS) strain level is held

constant. The test article is inspected frequently to determine the time of failure. The cycles-to-failure is determined by multiplying the time to failure by the response frequency. Stress versus cycles-to-failure (S-N) curves are developed for each weldbond system. The cantilever beam coupon tests are simpler and less costly than panel tests. The coupon fatigue data are considered supplemental to the data from panel tests. These tests have been extremely beneficial in screening candidate weldbonded systems before fabricating full-scale and much more costly test panels.

S-N curves were developed for the following weldbond system: Whittaker X6800 adhesive with a spot weld etch surface preparation. The curves, developed using cantilever beam coupons, are shown in Figure 3. The skin thickness for each curve is noted, since the peel stress in the adhesive is dependent upon the skin thickness. Fatigue failure initiated with a delamination of the adhesive along the bondline followed by a crack in the spot weld. A change in the surface preparation significantly affected the fatigue life of the beam coupons tests as shown in Figure 4. The weldbonded coupon with metal bond etch surface preparation produced longer lifetimes than those with the spot weld etch surface preparation. Therefore, the steps in the fabrication process became very important in the fatigue life. The fatigue life data is shown in terms of bending moments to permit a direct comparison of different skin thicknesses. Very little benefit was gained by using the spot weld with this type of loading, since crack initiation depended on the adhesive system.

Three and four bay, flat and curved test panels were fabricated identically to the C-140 aircraft fuselage construction except that rivets were replaced by weldbonding with a spot weld etch surface preparation. These panels were tested in an acoustic test chamber with a wideband random excitation similar to that produced by the engines. The S-N curve developed from test panels is shown in Figure 5. Comparing the S-N curve obtained from the weldbonded panels with the riveted data, a shorter fatigue life can be expected with this type of surface preparation. Most of the weldbond sonic fatigue work sponsored by the U.S. Air Force is summarized in Reference [3].

4. ADHESIVE BONDED ALUMINUM STRUCTURAL CONCEPTS

To establish a data baseline for high strength structural adhesives, American Cyanamid FM137 adhesive/BR127 primer with a metal bond etch surface preparation was selected for evaluation. This was a common adhesive system used in production including the L-1011 wide body aircraft.

Mode shapes are generally obtained experimentally to determine response frequencies and locations of maximum strain. An example of a contour plot obtained for one modal pattern of a three bay adhesive bonded aluminum panel is shown in Figure 6. Comparisons were made with similar riveted construction. No major differences were noted in the dynamic response of the bonded and riveted panels tested. This was also the case in the modal analysis comparison with similar weldbonded panels. The S-N curves developed from cantilever beam coupon tests using FM137 adhesive are shown in Figure 7. Two types of failures were encountered: skin failures and cohesive bond failures. A cohesive bond failure is defined as one in which part of the adhesive remains on both adherends after failure. An adhesive bond failure is defined as a complete separation of the adhesive from one adherend while remaining on the other adherend. Generally, adhesive failures are considered undesirable, since they are unpredictable. A much lower fatigue strength resulted from adhesive failure modes than cohesive failure modes.

Adhesive bonded panels using the C-140 fuselage design were tested in an acoustic test chamber. Fatigue cracks in the stiffeners, as shown in Figure 8 ended the test before the bond system could be evaluated. The fatigue life of the stiffener was about equal to that obtained with riveted construction.

As additional stress durable adhesive systems were developed, more programs were undertaken to determine the benefits of adhesive bonded structural concepts. One program that advanced the state-of-the-art of adhesive technology was called Primary Adhesively Bonded Structural Technology (PABST). The sonic fatigue part of the program investigated the following adhesive/primer bond systems: American Cyanamic FM73/BR127, Narmco M1133/BR127, 3M AF55/XA3950, and Hysol EA9628/EA9202 with phosphoric acid anodized aluminum adherends. Two failure curves were developed from cantilever beam coupon data. A fatigue curve for skin failures in the aluminum adherend is shown in Figure 9. Compared with riveted data, a higher fatigue life in the skin can be expected at the lower stress levels. At the higher stress level, the fatigue life is about equal. A fatigue curve for the cohesive bond failure is shown in Figure 10 in terms of bending moment. Included in these data is a weldbonded coupon using Goodrich PE-130 adhesive, which showed a comparable life with the other adhesive systems tested. No general comparison with riveted design can be made until the skin thickness is known, which also determines the mode of failure in the adhesive bonded structure. Increasing the skin thickness in a bonded structure increases the peel stress in the adhesive which can shorten the fatigue life of the adhesive while increasing the fatigue life of the skins.

A sonic fatigue analysis of the PABST structure, using the acoustic loads for the take-off condition from measured YC-15 flight test data, indicated that the structure would not withstand the 50,000 hour service life. This was based upon coupon data with a correction factor for panel data. The critical structure was a large bay size with heavy gage thickness [2 ft (60.96 cm) by 2 ft, 0.070 in (0.178 cm) thick]. Accelerated sonic fatigue tests of the structure were conducted in a plane progressive wave tube facility. Results from the panel tests show that the prediction with the coupon data was fairly accurate. A typical example of the panels tested is shown in Figure 11. Fatigue failures were found in the adhesive bondline and in back-up structures. Fatigue curves for the coupon data and the panel data are shown in Figure 12.

The bonded surfaces were examined after fatigue failure by separating the joint under static load. The bonded surfaces produced under dynamic excitation were noticeably different from those produced under static loading as shown in Figure 13. Under static load, the failure was characterized by separation midway through the thickness of the adhesive film; whereas, under dynamic load, the adhesive separated closer to the surface of the adherend. While the reason for the crack location is not known, consistent and predictable behavior was found whenever the failure was cohesive within the adhesive and not in the primer, oxide layer or adherend.

Some of the fractured adhesive surfaces were evaluated using a scanning electron microscope (SEM). The adhesives, primer and oxide layers have distinct morphological features easily distinguishable. An example of a cohesive bond failure is shown in Figure 14. A full range of fracture mechanisms were found: cracking, cavitation and shear banding, which indicated that the adhesive performed satisfactorily.

Another area of concern was quality control since different results often were obtained when test structures were fabricated by different manufacturers using the same standard. Since bond failures within the primer were a common problem, an investigation was conducted with cantilever beam coupons with different primer thicknesses, adhesive thicknesses and surface preparation. The fatigue results are shown in Figure 15. The fatigue data indicated that the FM73/BR127 adhesive/primer system was essentially insensitive to variation in primer thicknesses and the type of adherend surface treatment. The thicker adhesive samples showed a somewhat shorter fatigue life and showed evidence of interfacial failure, namely, adhesive to primer failure and primer to oxide

AD-A143 301 PROCEEDINGS OF THE INTERNATIONAL CONFERENCE ON RECENT ADVANCES IN STRUCTU..(U) SOUTHAMPTON UNIV (ENGLAND) INST OF SOUND AND VIBRATION RESEAR.. M PETYT ET AL. 5/6

UNCLASSIFIED 1984 F/G 20/11 NL

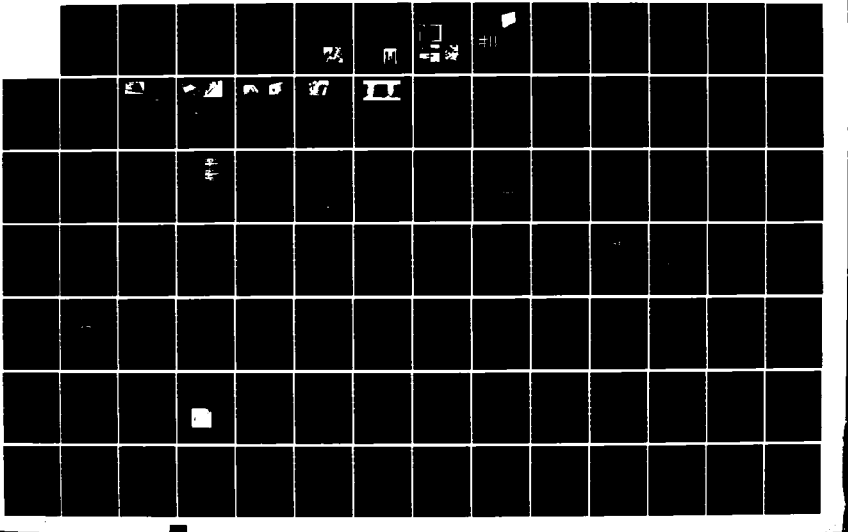

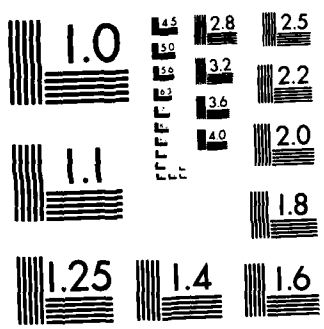

failure. Most of the adhesive bonded stiffened skin sonic fatigue work is summarized in Reference [3] and [4].

5. ADHESIVE BONDED ALUMINUM HONEYCOMB

Adhesive bonding is the conventional method of joining the face sheets and the core for aluminum honeycomb sandwich structures. Extensive sonic fatigue tests have been performed on such structures in progressive-wave tubes (PWT) [5]. These tests have involved various adhesives having widely varying peel strengths and lap shear properties. The results of these tests and the subsequent service history in high intensity acoustic environments (above 170 dB for 50,000 hours) have consistently shown that the adhesive bond is not the mode of failure. This is not to imply that adhesive bonds never fail nor that an adhesive's structural properties are unimportant. A properly designed honeycomb panel utilizing one of the current widely used aircraft structural adhesives will not usually experience adhesive bond failures unless there is a bond quality problem. Variations in peel strength and lap shear strength, within the range of typical adhesives, will not affect sonic fatigue life. However, if the bond quality is degraded due to moisture or porosity for example, it has been found that rapid fatigue failures occur in the adhesive bond even when static tests such as lap shear, peel and flatwise tension indicate good bond quality. This problem is discussed further in the next section.

6. ADHESIVE BONDED GRAPHITE-EPOXY (G/E) STRUCTURES

Recent extensive sonic fatigue and shaker testing on bonded G/E structures [6] demonstrated the importance of adhesives in developing light-weight aircraft structures. Comparisons between the sonic fatigue resistance of riveted aluminum and bonded graphite structures showed the bonded graphite offers a 2:1 weight savings. While this structural advantage is due largely to the graphite material, rather than the joining process, it could not be achieved without effective fatigue resistant adhesives. Since composite structures exhibit much larger deflections than metal structures, the adhesives used must display a combination of high strength and good elastomeric properties.

The adhesive selected for the program described in Reference 6 was 3M's AF147. The graphite pre-preg was Hercules AS-3501. AF147 is an elastomeric adhesive with a high fracture toughness. It cures at 350^{0}F and has a lap shear strength of 4,500 lb/in^2 (3.10 x 10^7 Pascals) based on the manufacturer's literature. A corresponding value of 3,430 lb/in^2 (2.37 x 10^7 Pascals) was measured from specimens cut from a sonic fatigue test panel.

Test specimens were skin-stringer configurations, typical of aircraft fuselage structures, consisting of G/E zee stiffeners and skins secondarily bonded together. These specimens comprised sub-element shaker test specimens [3 in by 9 in (7.62 cm by 22.9 cm) skin section with a 3 in long zee section bonded along the center] and multi-bay panels [2 ft by 3 ft (61 cm by 91 cm) skins with various stiffener spacings, skin thicknesses and curvatures]. The shaker specimens were subjected to random mechanical loading and the sonic fatigue test panels were subjected to random acoustic loading in a PWT. Early shaker and PWT results were characterized by premature delamination of the stiffeners from the skins, with no damage occurring to the graphite fibers. This type of failure clearly indicated inadequate strength in the adhesive joint. Visual inspection of the failed joints revealed some porosity. Since these specimens had met or exceeded the usual industry adhesive acceptance criteria, it became apparent that these criteria were not adequate to determine the sonic fatigue capabilities of an adhesive joint. Quality acceptance criteria applied to the failed specimens included percent weight of resin, void percent by volume, flatwise tension and lap shear. Also an ultrasonic inspection was made.

The observation that the static strength properties of bonded joints do not adequately reflect the dynamic high cycle fatigue characteristics is substantiated by Reference 4, in which identical specimens exhibited different modes of failure under static and dynamic loads. Under static loads failures occurred in the adherend, whereas under dynamic loads the failures occurred in the adhesive itself. Also small variations in static strength properties often resulted in large variations in sonic fatigue life, but only when the static strength variations are due to process and/or quality variables. Corresponding static strength variations due to the basic strength characteristics of the adhesive system do not appear to affect sonic fatigue life. Similar observations have been made on other joining methods such as brazing and diffusion bonding.

In Reference 6, the graphite specimens experienced premature dynamic fatigue failures, with visual evidence of porosity, an investigation was carried out to determine the cause of failure and the relationship between the porosity and static strength. Modifications were made to the bonding process which reduced the porosity by 75%. However, the corresponding increase in lap shear strength was only 2%. Nevertheless, when sonic fatigue tests were performed on panels before and after modifying the bonding process, there were dramatic changes in fatigue lives and also in the mode of failure. Figure 16 shows a failed sonic fatigue test panel prior to modifying the bonding process. The failure is in the adhesive and the photograph shows the sub-structure separated from the skin without any significant graphite fiber damage. Figure 17 shows the failed panel after modifying the bonding process. Here the mode of failure has shifted to the skin laminate, evidenced by the extensive graphite fiber damage and broken skin fibers attached to the sub-structure. Neither lap shear, peel strength or flatwise tension values predicted this result. The sonic fatigue life of the two panels ranged from virtually instant failure to 10^7 cycles. The strain-versus-cycles-to-failure data from the panels and beam coupons are shown in Figure 18. The acoustic life of stiffened skin G/E structures can be predicted using this curve and the technique developed to predict the maximum RMS strain [6].

Although the static tests did not indicate the sonic fatigue life nor mode of failure, the sub-element shaker tests did predict the mode of failure and gave good fatigue life versus strain data. Based on the work performed in Reference 6, shaker testing of sub-element specimens appears to be the simplest and least expensive test to establish good bond quality relative to sonic fatigue resistance.

7. RECOMMENDATIONS AND CONCLUSIONS

Very little benefit in sonic fatigue life was gained by the spot weld in the weldbonded structures compared to the adhesive bonded structures. A change in the surface preparation significantly affected the sonic fatigue life of the weldbonded structure tested. The acoustic fatigue life of the weldbonded aluminum structure with the Whittaker X6800 adhesive and spot weld etch surface preparation was significantly shorter than the metal bond etch surface preparation. Apparently the acoustic loads produce a peel stress in the adhesive. Most adhesives have a low peel strength.

The adhesive bonded aluminum panels tested until destruction generally failed in the stiffener. The stiffener design used was identical to riveted design. The design was inadequate to prevent sonic fatigue damage to the stiffeners in adhesively bonded metallic structure. More acoustic fatigue data are needed covering a wider range of stiffener designs.

Double cantilever beam coupon data have been developed for two modes of failure of an adhesive bond aluminum joint: cohesive bond failure of the adhesive and metal fatigue failure of the adherend. The cohesive bond fatigue curve is for a very narrow range of adhesives, generally high strength, brittle and are curved at 250°F (121°C). More work is needed to include a wider range of adhesives and to correlate cantilever beam coupon data with panel data.

Investigations have shown that the static strength properties of bonded graphite-epoxy (G/E) joints do not adequately reflect the random bending fatigue characteristics. Shaker tests of G/E beam coupons have shown virtually a zero random bending fatigue life for an adhesive system while static strength tests and quality control inspections are all acceptable, The non-destructive test techniques available are not sufficient to ensure adequate performance under dynamic loading. Shaker tests or other suitable dynamic tests must be performed on any candidate adhesive bond system to ensure adequate performance under acoustic loads.

A prediction method has been developed for laminated graphite-epoxy stiffened skin design with the adhesive bonded stiffeners. The method is limited to skin-stringer configurations. More work is needed to predict the life of other design configurations and other materials. The shaker tests with random mechanical loading augmented by selective progressive-wave tube tests appear to be the best approach.

Riveted technology prediction methods in general are not valid for adhesive bonded metallic structures and advanced composite structures. Modal analysis techniques are applicable, however, the magnitude and location of the maximum stress in the structure will be different. Many failure modes are possible with the adhesive bonded structures which must be understood. Fatigue curves are needed for each failure mode of interest. Adequate design methods must be produced to prevent the undesirable failure modes. Some of the methods used to solve sonic fatigue problems in riveted structures are not applicable to adhesive bonded structures. For example, increasing the skin thickness to reduce the stress in the skin can increase the peel stress in the adhesive and other stresses in the joint, shortening fatigue life.

Sonic fatigue tests and service experience have shown adhesive bonding to be a highly effective joining process. For some types of structures such as aluminum or composite honeycomb sandwich, co-cured and integrally cured composites, it is the only viable attachment method. In stiffened metal structures, the effectiveness of bonding compared to mechanical fasteners will depend upon the skin thickness. As skin thicknesses decrease, 0.04 in (0.102 cm) and less, adhesive bonds become more effective, whereas, riveted structures begin to encounter "knife-edges" and the fatigue notch factor increases. With thicker skins, 0.080 in (0.203 cm) and up, the fatigue resistance of riveted joints increases, and adhesive joints begin to become less fatigue resistant. Consequently, it seems that any comparison of the two design methods should account for skin thickness.

The methodology associated with predicting the acoustic fatigue life is more complex in adhesive bonded metallic structures and composite structures since the failure modes and mechanisms are quite different and more sensitive to design and manufacturing methods than are riveted configurations. The testing requirements should be identified and defined in greater detail. Standardized test methods should be established to permit comparisons among the different investigators. Manufacturing methods, process control, quality control techniques and nondestructive evaluation techniques should be standardized to ensure consistent performance of the structures.

8. REFERENCES

1. A.G.R. THOMSON and R. F. LAMBERT 1972 AGARD-AG-162, Advisory Group for Aerospace Research and Development, 7 Rue Ancelle 92200 Neuilly Sur Seine, France, "Acoustic Fatigue Design Data" Parts I through IV

2. J.M. CRADDOCK 1973 Vought Systems Division, LTV Aerospace Corp. Report No.2-22320-3R-4 (AD-918-212L), "Evaluation of Weldbonding for Joining Thin Gage Aircraft Structures"

3. K.R. WENTZ and H.F. WOLFE 1978 Journal of Engineering Materials and Technology, Transactions of the ASME, "Development of Random Fatigue Data for Adhesively Bonded Weldbonded Structures Subjected to Dynamic Excitation"

4. H.F. WOLFE, C.L. RUPERT and H.S. SCHWARTZ 1982 AIAA Journal of Aircraft, Vol 19, Number 7, P. 581 AIAA Dynamics Specialists Conference, Paper No. 81-0627-CP, Atlanta, Georgia, "Evaluation of Bonding Parameters on Random Fatigue Life of Bonded Aluminum Joints"

5. J.R. BALLENTINE et. al. 1968 AFFDL-TR-67-156, AF Flight Dynamics Laboratory, Wright-Patterson AFB, Ohio, "Refinement of Sonic Fatigue Structural Design Criteria"

6. I. HOLEHOUSE 1980 AFFDL-TR-80-3019 (AD-A084897), AF Wright-Aeronautical Laboratories, Wright-Patterson AFB, Ohio, "Sonic Fatigue Design Techniques for Advanced Composite Aircraft Structures"

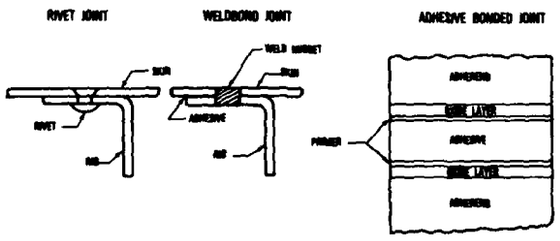

Figure 1 Components of a Riveted Joint, Weldbond Joint and Adhesive Bonded Joint

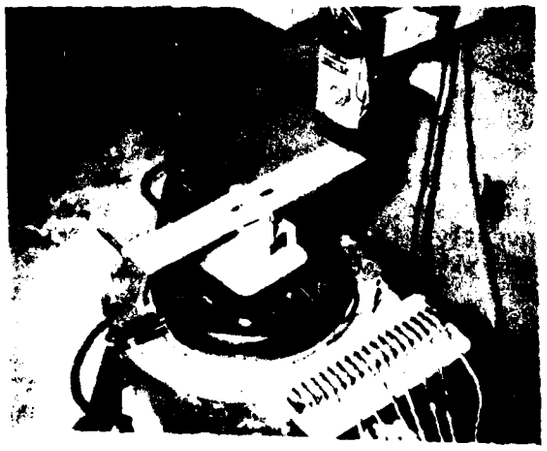

Figure 2 Test Set-Up For Beam Coupons

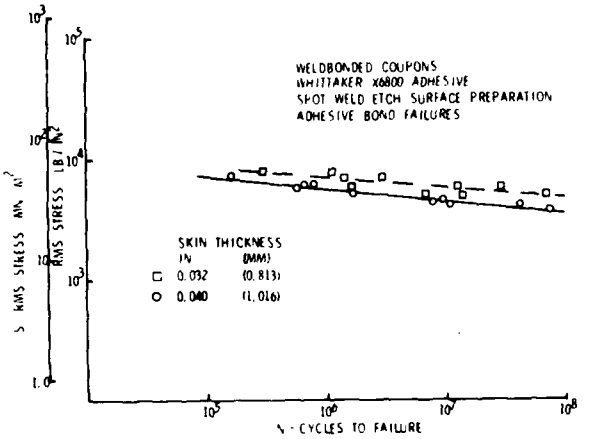

Figure 3 Weldbonded Coupon S-N Curve Whittaker X6800 Adhesive, Spot Weld Etch Surface Preparation

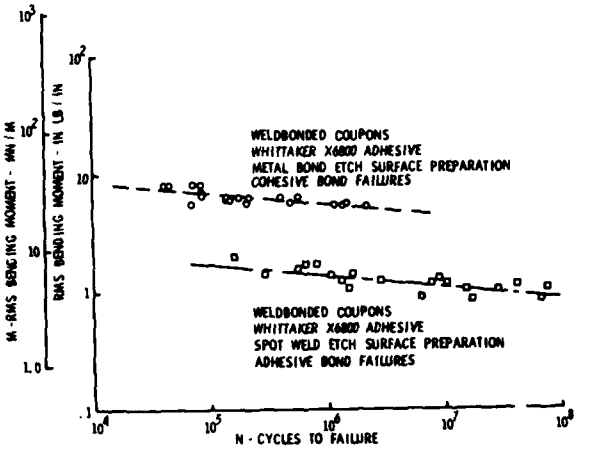

Figure 4 Weldbonded Coupon M-N Curve, Comparison of Two Adhesive Systems

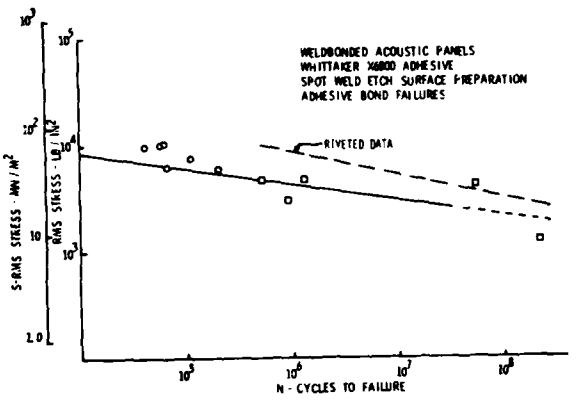

Figure 5 Weldbonded Panel S-N Curve, AFFDL Data, Whittaker X6800 Adhesive, Spot Weld Etch Surface Preparation

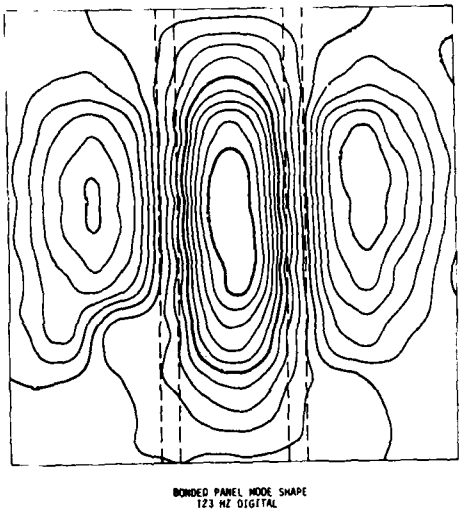

Figure 6 Contour Plot of Three Bay Adhesively Bonded Panel Mode Shapes

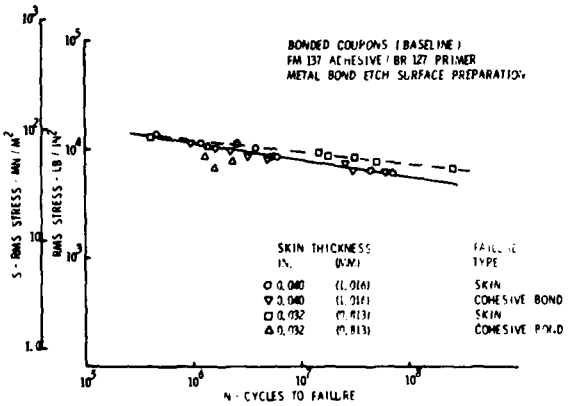

Figure 7 Bonded Coupon S-N Curve, FM-173 Adhesive BR-127 Primer, Metal Bond Etch Surface Preparation

Figure 8 Intermediate Segment Failures, Bonded Acoustic Test Panel, FM-173 Adhesive BR-127 Primer, Metal Bond Etch Surface Preparation

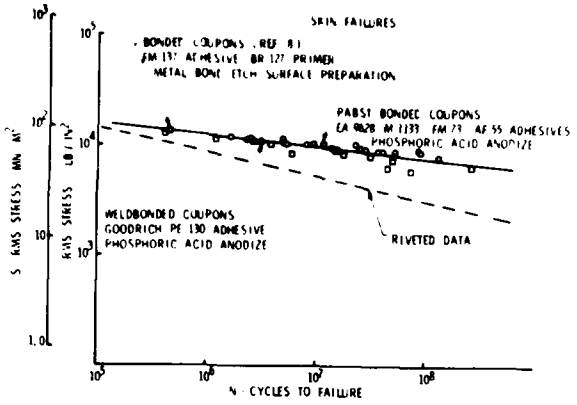

Figure 9 Skin Failure Data, Three Adhesive Systems

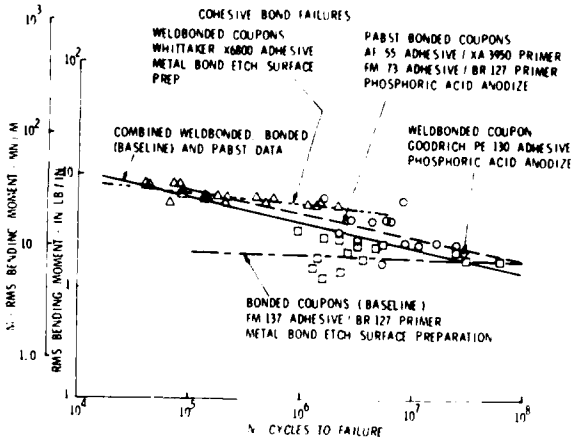

Figure 10 Bonded Coupon M-N Curves and Combined Cohesive Failure Curve

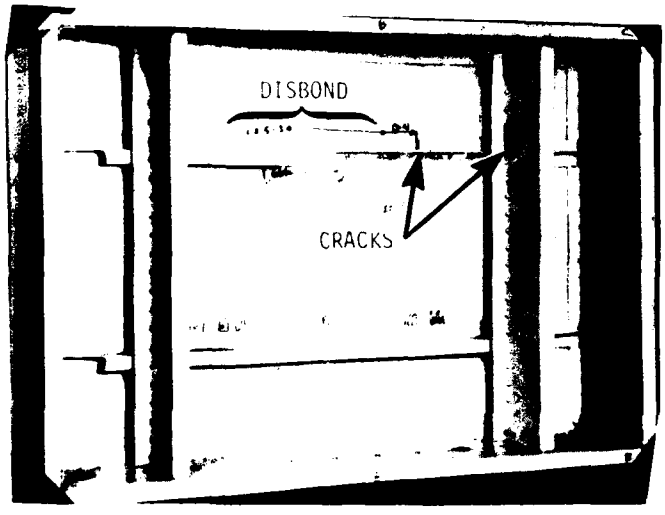

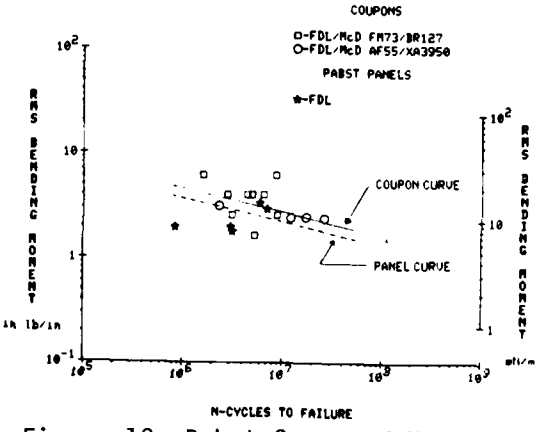

Figure 12 Pabst Coupon M-N Curve and Pabst Panel Curve

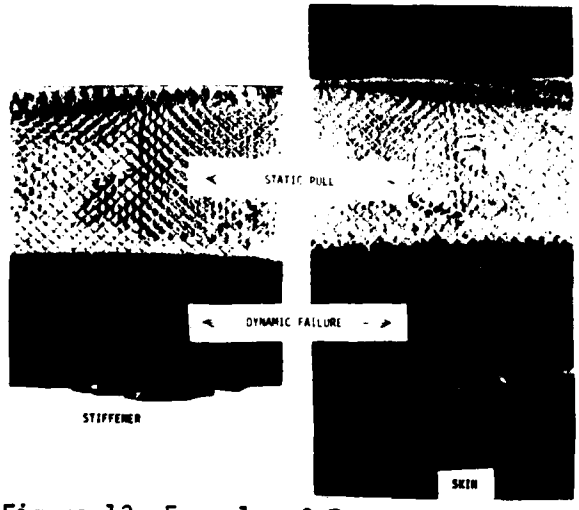

Figure 13 Example of Fractured Adhesive Surfaces Under Static and Dynamic Loads

Figure 14 Photomicrograph Example of Cohesive Bond Fracture of FM-73/BR-127 Bond System

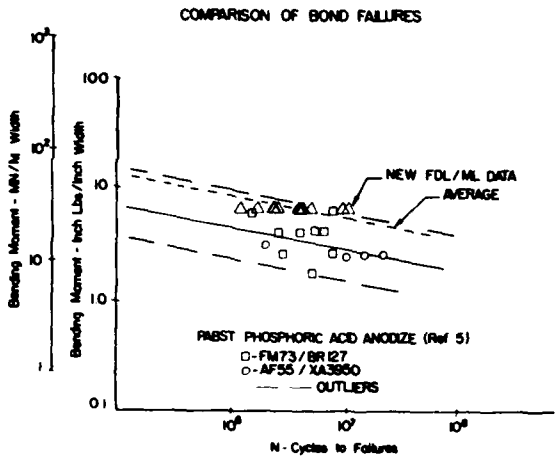

Figure 15 Comparison of FDL/ML Bond Failures With Pabst Data

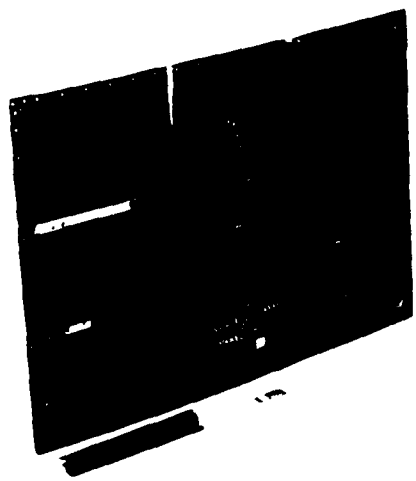

Figure 16 Graphite-Epoxy Panel With Adhesive Bond Failures

Figure 17 Graphite-Epoxy Laminate Fatigue Failures, Back Face

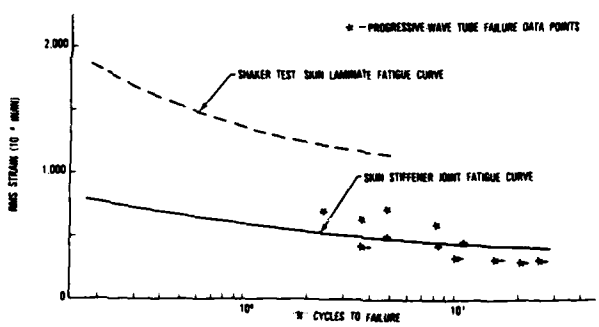

Figure 18 Strain Versus Cycles-To-Failure, Panel & Coupon Tests, Graphite-Epoxy Laminate

DYNAMIC RESPONSE AND ACOUSTIC FATIGUE* OF STIFFENED COMPOSITE STRUCTURE

J. Soovere

Lockheed-California Company
Burbank, California, USA

1. INTRODUCTION

Aircraft structure ma.. rom graphite/epoxy (Gr/E) composites offer a significant weight savings .. :r comparable aluminum alloy structures. The initial application of these composites has been restricted to low load-carrying lightweight structures such as ailerons, flaps, elevators, slats, and fairings to gain in service experience at low risk. The Gr/E composites may also be used in lightly loaded fuselage structures on some vertical/short takeoff and landing (V/STOL) aircraft. For minimum weight, the fuselage structure will be required to operate well into the post-buckling region, with initial buckling just above 1g.

These lightweight structures are very often subjected to a high level jet noise environment, especially during takeoff and landing, which can produce high random vibration stresses in these structures. High cycle fatigue failures, commonly referred to as acoustic fatigue failures, have occurred in these structures [1] , [2] as a result of the random vibration stresses. The V/STOL fuselage can also be subjected, simultaneously, to a thermal environment. Other environmental factors such as moisture penetration, impact damage and lightning strikes may degrade the performance of these structures in a high noise environment.

The compression and shear buckling loads experienced by the fuselage structure introduce peel loads at the skin-stiffener interface similar to those produced by jet noise. Initial studies with Gr/E composites [3] indicated that fasteners provided an improved acoustic fatigue life over structural bonding. For this and other practical reasons, initial application of Gr/E composites to transport aircraft, such as the L-1011 composite aileron [4] , [5] in Figure 1, used mechanical fasteners. Bonding has also been used on some experimental Gr/E acoustic fatigue panels [3] , [6]. Integrally stiffened Gr/E panels [7] , [8] , [9] , [10] , where the skin and stiffeners are cocured, represent the next stage in this development. The peel strength and, therefore, the acoustic fatigue life of these integrally stiffened structures can be further improved by the use of stitching [8] , [11].

This paper summarizes the results obtained from acoustic fatigue and dynamic response tests and the L-1011 composite aileron and integrally stiffened Gr/E panels. The nature of the damping in integrally stiffened composite panels, its theoretical prediction and its implication on internal noise are briefly discussed.

2. COMPOSITE AILERON TEST PROGRAM

The composite aileron was fabricated with a minisandwich skin [4] , [5] in which the Gr/E face sheets were separated by a syntactic (SYNT) core containing glass microballoons. Cocured doublers were located on the inner face sheet at the rib locations. The covers were attached to the Gr/E cloth ribs, and the front and rear spars with fasteners.

*Performed in part under Contracts N62269-80-C-0239, NADC, and NAS 1-15069, NASA, and in part with Lockheed-California Company funding.

The composite aileron test program included the development of random fatigue data by means of double and single cantilever coupons representing the skin-spar and the skin-rib interfaces and the rib bend radius. Typical measured strain distributions [4] are illustrated in Figure 2. The results of these coupon random fatigue data [5] , including the effects from a built-in void adjacent to a fastener head, a single impact damage (0.88 kilogram-meter) adjacent to a fastener head, moisture conditioning and elevated temperature (82°C), are summarized in Figure 3.

In the early design, core compression was experienced along the edges of the doubler [4] , [5] which produced a premature separation of the doubler from the skin along these edges at lower random strain levels (Figure 3). Improvements in the fabrication procedure eliminated this problem [5]. Consequently, the random fatigue data (Figure 3), which involved failures in the outer face sheets adjacent to the countersunk fastener heads, were considered to be more representative of the improved design.

Modal studies conducted on a representative section of the composite aileron, using impedance head hammer tap and loudspeaker excitations, indicated very low damping ratios (Table 1) even after damage [5] from simulated lightning strikes (Figure 4). The damage was mostly confined to the visible surface damage area with very little interlaminar damage. All of the modes dropped in frequency by a small amount, reflecting, in view of the amount of damage sustained, the redundant nature of the composite structure.

The random fatigue data were used, in conjunction with the results of a nonlinearity test, to select the accelerated proof test random spectrum level (Figure 5). Nonlinear panel response (Figure 6) was obtained during the proof test. The measured strains, when compared with the random fatigue data, indicated that the composite aileron would be free of acoustic fatigue failures throughout its design life.

3. COMBINED ACOUSTIC AND SHEAR LOADS

Acoustic fatigue tests were conducted on an integrally J-stiffened Gr/E minisandwich (Figure 7) and a monolithic (Figure 8) panel near initial shear buckling [7] , [10]. Both integrally stiffened panels were designed to an initial shear buckling load of 1786 kilograms per meter (Table 2). The analysis was performed with an anisotropic finite element program (STRAP 5) developed by the Lockheed-California Company. In general, good agreement was obtained between the predicted and measured buckling loads for the three bay monolithic panel and similar four bay monolithic panels tested in another program [12]. The tooling used affected the thickness of the minisandwich panel skin which resulted in a higher measured initial buckling load. Good agreement was obtained between the predicted and measured mode shapes, the latter obtained from Moire fringe patterns measured in the test facility illustrated in Figure 8. The monolithic panel buckled mode shape contained five antinodes in each of the three bays whereas the minisandwich panel exhibited two antinodes only in the large center bay.

The initial buckling was measured with a noncontacting displacement transducer located at an antinode. The initial buckling load was determined from the discontinuity in the load displacement curve [7] , [10] , and from the frequency-load curve (Figure 9). The increase in the damping ratio (Figure 10) in both the critical and noncritical modes, on approaching initial buckling, made it difficult to trace the variation of the modal frequencies through buckling with the impedance head hammer tap method. The higher the critical mode number, the greater the difficulty. This increase in damping on approaching buckling, was previously [13] observed in axial compression tests on stiffened aluminum panels. The damping was also found to be nonlinear in the compression load region. The same result can also be expected for stiffened composite panels under axial compression load.

In spite of the high damping near initial buckling, the overall strain was increased by approximately thirty percent (Figure 11) at the critical location on both panels, when excited with broad band random acoustic loading. Nonlinear response (Figure 12) was obtained in both panels at the higher sound pressure levels.

4. COMBINED ACOUSTIC AND THERMAL ENVIRONMENTS

The effect of a 121°C thermal environment on the sonic fatigue life of integrally stiffened Gr/E panels, representative of potential fuselage structure, was investigated [7] , [9] using two advanced J-stiffened monolithic panels and two advanced blade stiffened orthogrid panels, illustrated in Figures 13 and 14, respectively. These panels were also designed to an initial shear buckling load of 1786 kilograms per meter (Table 2). The panels were mounted, in turn, into a steel test frame in which the thermal expansion was matched biaxially to that of the composite panel. In the modal studies, heat was applied to the outer surface of the panels by six infrared lamps and the excitation was provided by impedance head hammer taps at preselected grid points. The excitation and the corresponding displacement were analyzed within the Hewlett-Packard HP 5451C Fourier Analyzer to obtain the resonant frequencies, damping ratios and mode shapes.

The measured fundamental mode shape for both panels is illustrated in Figure 15. The fall-off in the resonant frequencies with temperature (Figure 16), observed for both panel configurations, is due to thermally induced bi-axial compression loads in the skin, introduced by differences in the thermal expansion of the Gr/E frames and skin because of differences in their fiber orientations. The temperature does not appear to have affected the damping in both the monolithic and the orthogrid panels (Table 3). The fundamental mode damping ratio in the orthogrid panel is, however, an order of magnitude greater than that in the monolithic panel. The damping in the higher order panel modes is more comparable and very low for both panels.

One panel of each design was acoustic fatigue tested at ambient temperature and the other at a temperature of 123°C. Heat was supplied by a specially designed quartz lamp heater panel, mounted inside the progressive wave tunnel. An overall sound pressure level of 167 dB (Table 4) was used to fail the room temperature orthogrid panel (Figure 14). In contrast, the room temperature and elevated temperature monolithic panels were failed with an overall sound pressure level between 160.8 to 164 dB. The difference in the sound pressure level required to produce the same long side rms strain (Table 4) in the orthogrid and monolithic ambient temperature panels can be attributed to the effect expected from the differences in their fundamental mode damping, even in the presence of nonlinear panel response (Figure 17). The failure obtained with the orthogrid panel does not reflect the true capability of the design since these panels contained stress concentrations at the ends of the longitudinal stiffeners (Figure 14) where the failure was initiated.

In spite of some indications that the temperature of 123°C could affect the sonic fatigue life, the results are considered inconclusive on account of the small sample size. The current room temperature semi-empirical analysis method [6] did not predict the rms strains in the room temperature panels with any degree of accuracy (Table 4). The main reason is thought to be the omission of damping in the above method although differences in the spectrum shape of the random noise may also be a contributing factor.

5. RANDOM FATIGUE DATA FOR INTEGRALLY STIFFENED Gr/E PANELS

Random fatigue data were developed with double cantilever coupons (Figure 18), representing the skin-longitudinal stiffener interface, for the integrally stiffened monolithic (Figure 19) and orthogrid (Figure 20) panels at room temperature. The monolithic coupon data exhibited higher rms strain (Figure 19) levels than the bonded panel data in reference [6]. The monolithic panels could withstand even higher strains than the corresponding coupons. Stitching (Figure 18), also illustrated in cross-section in (Figure 21), increased the failure strain level by approximately 70 percent, comparable to the improvement measured in static peel tests [11].

The orthogrid coupons (Figure 20) achieved an rms strain level comparable to that measured in the composite aileron skin at a KT of 1, and that achieved with stitching in the monolithic coupon. The composite aileron and the orthogrid panel had the same fiber orientation in the face sheets. The orthogrid panel failed well below the coupon strain level indicating the magnitude of the stress concentration at the ends of the axial stiffeners.

6. THEORETICALLY PREDICTED DAMPING FOR THE ORTHOGRID PANELS

Fastener related damping has been eliminated in integrally stiffened composite panels while the material damping is very small, usually below viscous damping ratio of 0.001 for Gr/E composites. Consequently the only source of significant damping is acoustic radiation, once the energy loss to the surrounding structure has been minimized. A characteristic of acoustic radiation is that the damping is high in the fundamental mode and falls off with increase in mode number due to the cancellation effect [14]. Furthermore, the acoustic radiation is proportional to panel area and should be very large in the fundamental mode of a large single panel. These conditions have been met by the damping ratios in Table 3. The predominant contribution of acoustic radiation to the damping has also been confirmed with stiffened composite honeycomb panels [15]. The orthogrid panel represents an ideal example for demonstrating the above conclusion. The simplified expression in reference [14], for the viscous damping ratio produced by acoustic radiation from a simply supported panel, was used. The measured and predicted damping ratio in Figure 22 are in reasonable agreement, particularly for the fundamental mode, when considering the simplicity of the analysis.

7. CONCLUSIONS

The importance of developing nonlinear analysis capability for design purposes has been demonstrated since composite structures can sustain high vibration levels, in the nonlinear response region, over a wide range of combined loads and environmental conditions without failure. All of the random fatigue data exhibited a fatigue limit just beyond 10^7 cycles, an important consideration for the design of acoustic fatigue resistent composite structures. The acoustic fatigue resistance in integrally stiffened composite structures can be considerably improved by attention to detailed design at the critical locations. In this respect, the integrally stiffened panels are considered to be superior to secondary bonded panels. Since the damping in integrally stiffened composite panels is due to acoustic radiation, the transmission of turbulent boundary layer noise, through the lighter weight integrally stiffened composite fuselage structure, could be significantly increased, over current fuselage structure, for the same density of acoustic sidewall treatment. A compensating increase in the sidewall treatment density could eliminate much of the weight-saving achieved with composite fuselage structure.

REFERENCES

1. T.R. RIEBEN 1957 WADC-TR-57-513. Sonic Fatigue Testing and Development of Aircraft Panels.

2. E.J. RICHARDS 1960 WADC-TR-59-676. An Introduction to Acoustic Fatigue.

3. M.J. JACOBSON 1972 AFFDL-TR-71-126. Advanced Composite Joints; Design and Acoustic Fatigue Characteristics.

4. J. SOOVERE 1980 The Shock and Vibration Bulletin, No. 50, Part 4. Sonic Fatigue Testing of NASA L-1011 Composite Aileron.

5. J. SOOVERE 1982 Journal of Aircraft, 19, No. 4. Sonic Fatigue Testing of an Advanced Composite Aileron.

6. I. HOLEHOUSE 1980 AFWAL-TR-80-3019. Sonic Fatigue Design Techniques for Advanced Composite Aircraft Structures.

7. J. SOOVERE 1982 NADC-78169-60. Effect of Acoustic, Thermal and Shear Loading on Flat Integrally Stiffened Graphite/Epoxy Fuselage Panels.

8. M.J. JACOBSON 1981 NADC-81045-60. Fatigue of V/STOL Composite Fuselage Panels Under Acoustic-Thermal Environments.

9. J. SOOVERE 1983 24th Structures, Structural Dynamics and Materials Conference, Lake Tahoe, Nevada, USA. The Effect of Acoustic-Thermal Environments on Advanced Composite Fuselage Panels.

10. J. SOOVERE 1983 Second United States/Japan Conference on Composite Materials NASA-Langley Research Center, Hampton, Virginia, USA. Dynamic Response of Flat Integrally Stiffened Graphite/Epoxy Panels Under Combined Acoustic and Shear Loads.

11. J. SOOVERE 1980 LR 29410; 1982 LR 30126; Lockheed Reports. Acoustic Response of Composite Panels Under Combined Loading - Parts 1 and 2.

12. R.B. OSTROM 1981 NADC-78137-60. Post-Buckling Fatigue Behavior of Flat, Stiffened Graphite/Epoxy Panels Under Shear Loading.

13. J. SOOVERE and S.T. CHIU 1976 AFFDL-TR-76-68. Effects of Combined Acoustic and Flight Loads on Crack Growth.

14. D.J. MEAD 1964 AFML-TR-65-284. The Effect of Certain Damping Treatments on the Response of Idealized Aeroplane Structures Excited by Noise.

15. J. SOOVERE Ph.D. Thesis, University of Southampton. Dynamic Response of Acoustically Excited Stiffened Composite Honeycomb Panels (In Preparation).

TABLE 1. MODAL FREQUENCIES AND DAMPINGS

UNDAMAGED AILERON		AFTER SIMULATED LIGHTNING STRIKES	
FREQUENCY, Hz	VISCOUS DAMPING RATIO	FREQUENCY, Hz	VISCOUS DAMPING RATIO
96.4	0.0042	91.18	0.0063
125.9	...	109.2	0.0038
134.3	0.0040	119.2	0.0067
149.0	0.010	126.6	0.0065
...	...	129.7	0.0091

TABLE 2. INITIAL SHEAR BUCKLING LOAD

TYPE OF PANEL	LENGTH mm	WIDTH mm	THICKNESS mm	SKIN LAYUP	N_{XYCR} Kg/M	
					STRAP 5	TEST AVERAGE
J-Stiffened Monolithic	546	152	0.89	$(45/0/\overline{90})_s$	1821*	1759**
	533	180	1.02	$(45/0/-45/90)_s$	1893*	1789 - 1841
J-Stiffened Minisandwich	533	304	1.52	$(45/0/-45/SYNT)_s$	1839*	2419 - 2682
Advanced J-Stiffened Monolithic	737	180	1.02	$(45/0/-45/90)_s$	1839*	--
Advanced Orthogrid	660	254	1.40	$(45/0/-45/SYNT)_s$	1839*	--

* Target Value 1786 Kg/M
** Reference [12]
Subscript s means symmetrically laminated.

TABLE 3. MONOLITHIC AND ORTHOGRID PANEL RESONANT FREQUENCIES AND VISCOUS DAMPING RATIOS

	MONOLITHIC PANEL						ORTHOGRID PANEL					
	J2				J1		01				02	
	AMBIENT TEMPERATURE		123 DEGREES CENTIGRADE TEMPERATURE		AMBIENT TEMPERATURE		AMBIENT TEMPERATURE		123 DEGREES CENTIGRADE TEMPERATURE		AMBIENT TEMPERATURE	
MODE NUMBER	FREQUENCY Hz	DAMPING RATIO	FREQUENCY Hz	DAMPING RATIO	FREQUENCY Hz	DAMPING RATIO	FREQUENCY Hz	DAMPING RATIO	FREQUENCY Hz	DAMPING RATIO	FREQUENCY Hz	DAMPING RATIO
1,1	178.9	0.0058	154.1	0.0046	160.52	0.0043	171.3	0.0473	159.3	0.0402	178.3	0.0393
2,1	262.9	0.0020	225	0.0036	243.1	0.0026	273.2	0.0226	242.5	0.0079	273.4	0.02354
3,1	324.25	0.0025	281.9	0.0042	303.9	0.0030	370.9	0.0015	293.7	0.0132	373.4	0.0028
4,1 Center Bay	389.0	0.0009	341.8	0.0032	359.7	0.0026	460.8	0.0043	394.7	0.0034	457.5	0.0064
4,1 All Bays In Phase	434.4	0.0044	388.7	0.0028	397.8	0.0089	--	--	--	--	--	--
All Bays Out-Of-Phase	--	--	461.1	0.0012	487.1	0.0040	--	--	--	--	--	--

TABLE 4. SUMMARY OF SONIC FATIGUE REST RESULTS AND ANALYTICAL PREDICTIONS

	TEST RESULTS						ANALYSIS [6]			
PANEL NUMBER	OVERALL NOISE LEVEL AT PANEL LOCATION dB	NOISE SPECTRUM LEVEL AT PANEL LOCATION dB/Hz	MAXIMUM RMS STRAIN μ mm/mm LONG SIDE	MAXIMUM RMS STRAIN μ mm/mm SHORT SIDE	TEST TIME HOURS/ MINUTES	NUMBER OF CYCLES	LONG SIDE RMS STRAIN μ mm/mm	FIXED FIRST MODE FREQ. Hz	NUMBER OF HOURS/ MINUTES	NUMBER OF CYCLES
J1	157.4	130.9	717	680	5/0*	7.2×10^6	--	--	--	--
	161.0	134.5	900	850	5/0*	7.2×10^6	503	200	6/25	3.9×10^6
	163.4	136.9	1300	1250	0/10**	2×10^5	663	200	0/43	5.2×10^5
J2***	158.4	131.3	460	581	5/0*	5×10^6	--	--	--	--
	160.8	134.3	573	704	3/14**	3.2×10^6	492	200	6/15	4.5×10^6
02	167.0	140.5	490	830	2/20**	2.94×10^6	998	151	0/24	$<2 \times 10^5$****
01***	167.0	140.5	566	745	4/39*	5.86×10^6	998	151	0/24	$<2 \times 10^5$****

*No Failure
**Panel Failed in Sonic Fatigue
***123°C Temperature
****No Test Data in Reference [6] Below 2×10^5

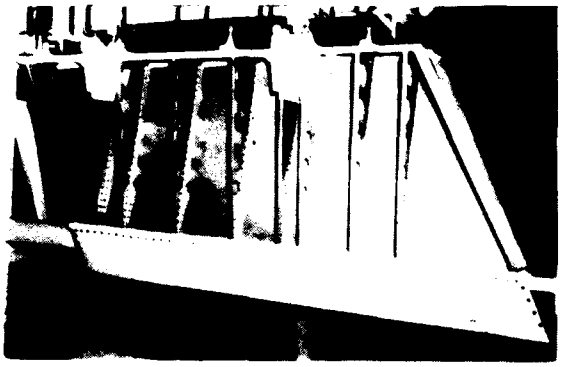

Figure 1. L-1011 Composite Inboard Aileron with the Lower Cover Removed

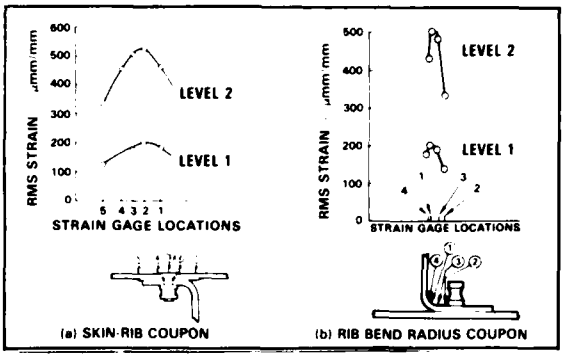

Figure 2. Typical Measured Strain Distribution

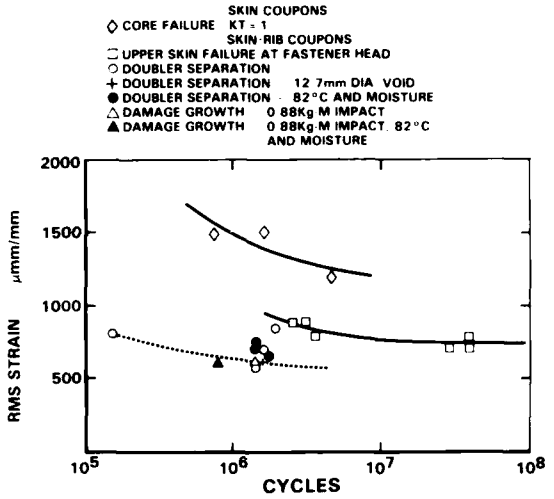

Figure 3. Random Fatigue Data for the Skin and the Skin/Stiffener Interface

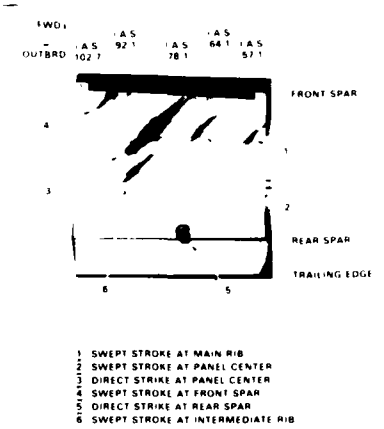

Figure 4. Exterior of Composite Aileron After Lightning Strike Tests

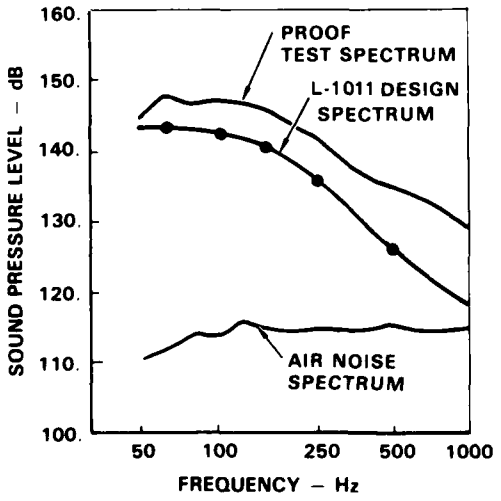

Figure 5. Inboard Aileron Design, Proof Test, and Air Noise 1/3-Octave Band Spectra

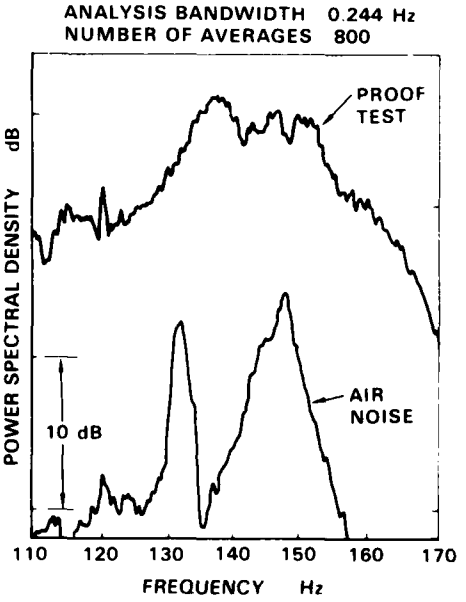

Figure 6. Narrow-Band Analysis of Aileron Strain Data

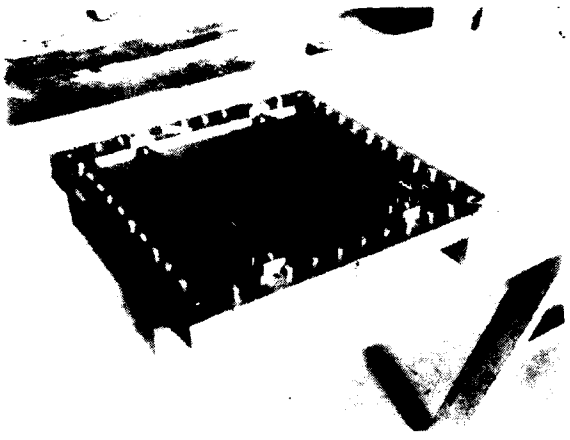

Figure 7. Reverse Side of Shear Frame Showing Stiffener Pivot Attachments - J-Stiffened Minisandwich Panel

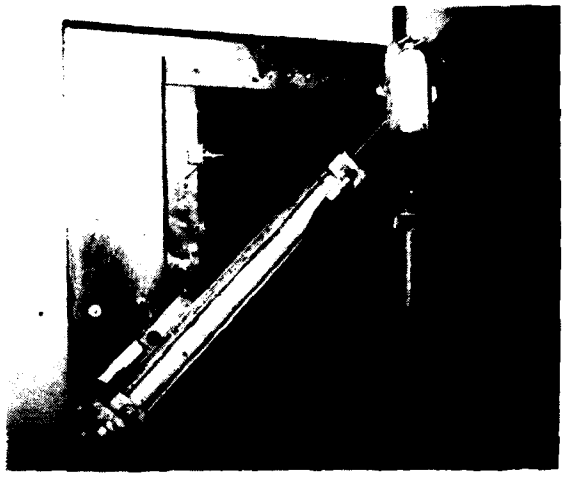

Figure 8. Load Frame in Acoustic Progressive Wave Tunnel Wall Configured for Shear Load - J-Stiffened Monolithic Panel

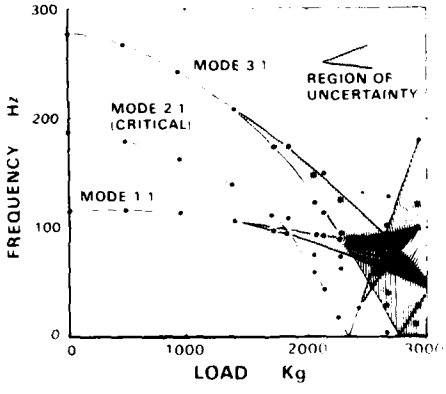

Figure 9. J-Stiffened Minisandwich Panel Frequency Variation as a Function of Jack Load

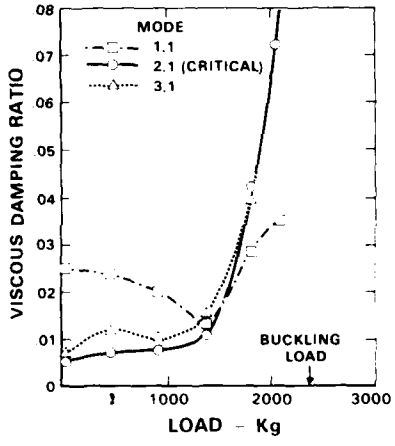

Figure 10. Variation of Damping with Jack Load for J-Stiffened Minisandwich Panel

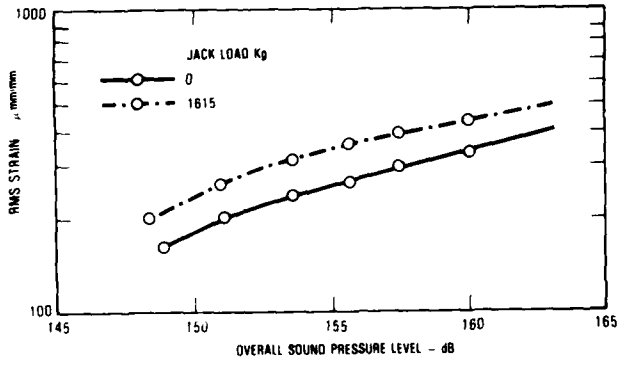

Figure 11. Variation of Overall Sound Pressure Level - J-Stiffened Monolithic Panel

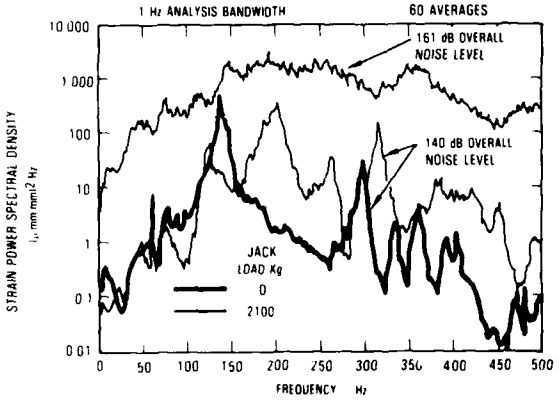

Figure 12. Strain Power Spectral Density for J-Stiffened Minisandwich Panel

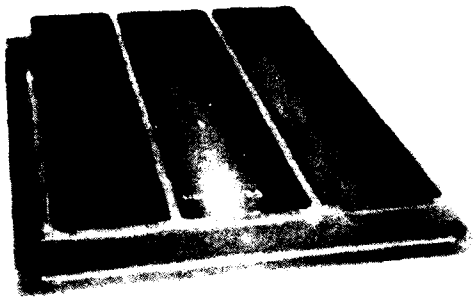

Figure 13. J-Stiffened Monolithic Graphite/Epoxy Panel

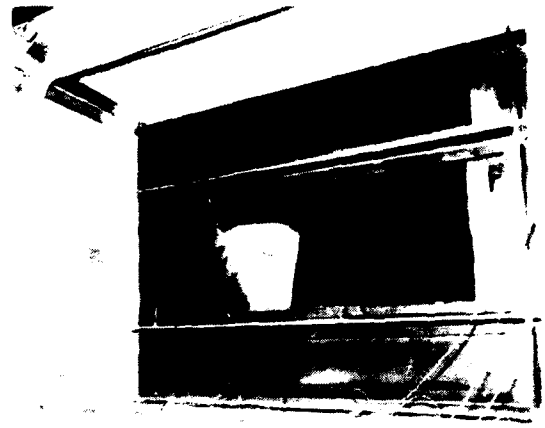

Figure 14. Acoustic Failure in Blade Stiffened Orthogrid Graphite/Epoxy Panel

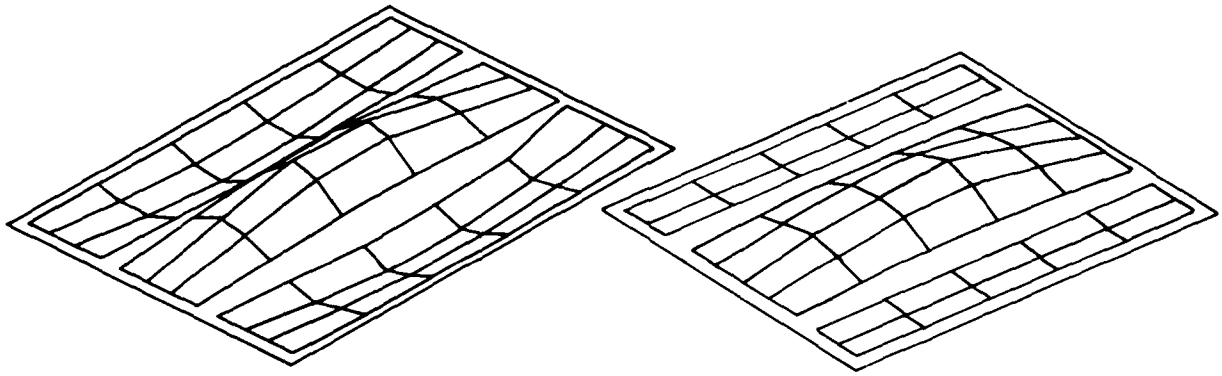

(a) Monolithic Panel

(b) Orthogrid Panel

Figure 15. Measured Panel Fundamental Mode Shape

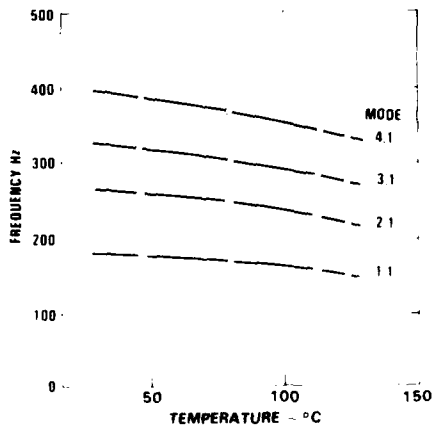

Figure 16. Variation of Modal Frequencies with Temperature - Monolithic Panel

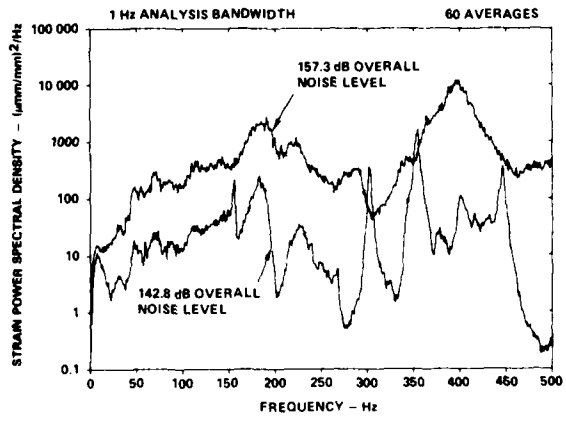

Figure 17. Typical Strain Power Spectral Densities for Monolithic Panel

Figure 18. Unstitched and Stitched Coupons Mounted on Electromagnetic Shaker

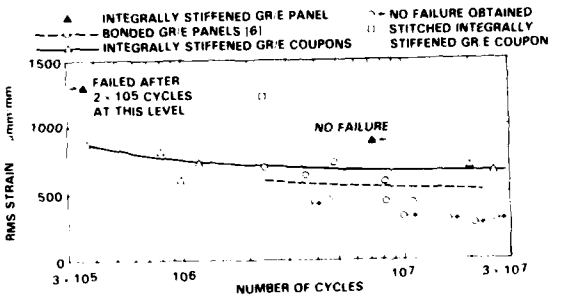

Figure 19. Ambient Temperature Random Fatigue Data from Monolithic Panels and Coupons

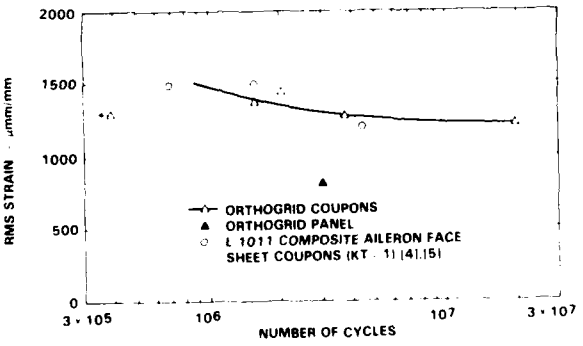

Figure 20. Ambient Temperature Random Fatigue Data from Orthogrid Coupons and Panel

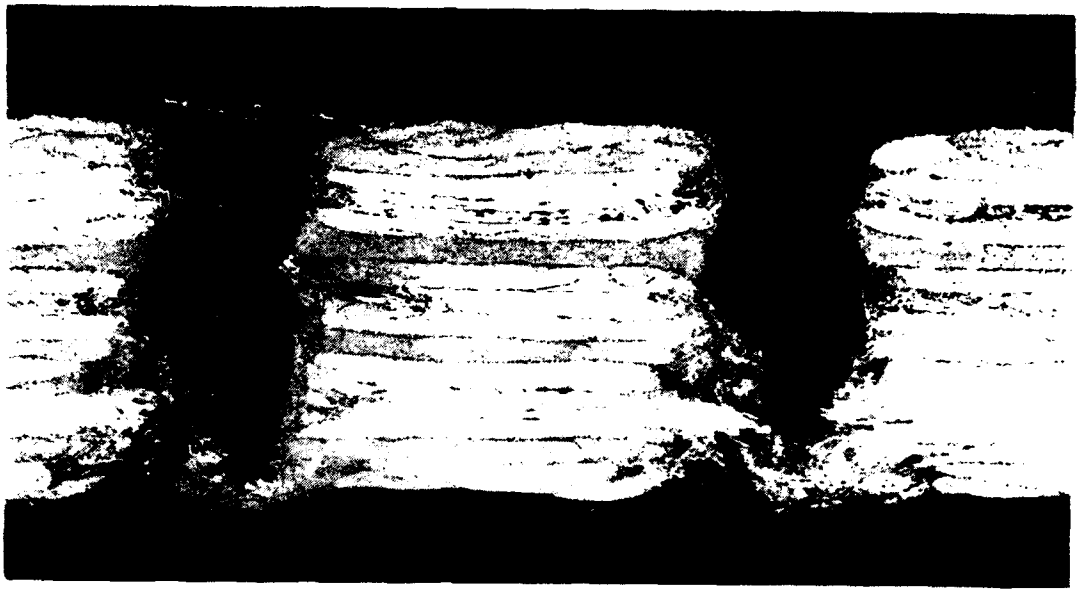

Figure 21. Sectional Micrograph Through Stiffener Flange and Panel Along the Stitch Line - X25 Magnification

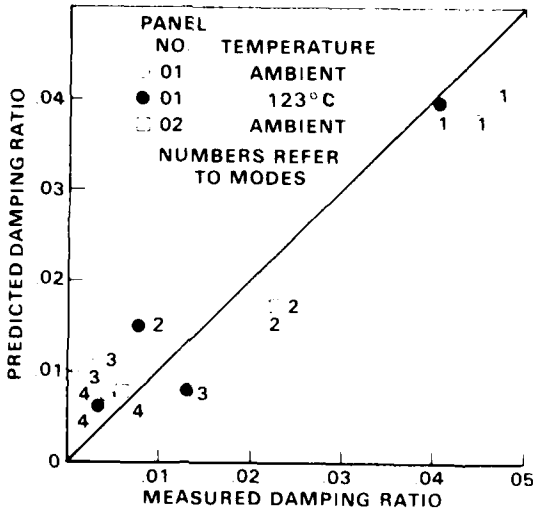

Figure 22. Comparison of Predicted and Measured Orthogrid Panel Damping

SONIC FATIGUE DESIGN METHOD FOR THE RESPONSE OF CFRP STIFFENED-SKIN PANELS

Ian Holehouse, Engineering Staff Specialist
Ronr Industries, California, U.S.A.

1 INTRODUCTION

This paper describes the development of a semi-empirical method to estimate the structural response of cfrp stiffened-skin panels when subjected to random acoustic loading. The objective was to provide a method suitable for practical use in the design of cfrp airplane structures, utilizing the results from the work described in References 1 and 2.

A combined analytical and experimental programme was conducted in order to investigate the dynamic response of carbon-fibre reinforced plastic (cfrp) skin-stringer panels to random acoustic excitation. A range of multi-bay panels was subjected to high intensity noise environments in a progressive-wave tube, and finite-element analyses carried out on the test panel designs, generating static strains and frequencies. Multiple stepwise regression analyses were then used in combination with graphical evaluations in order to develop empirical relationships between measured response strains from the sonic fatigue tests and various combinations of panel configuration parameters. From these regression analyses, design equations were developed assuming both linear structural behaviour and also taking into account non-linear behaviour with respect to the acoustic loading. A design method was then formulated based on these analyses which represented the test data with the greatest accuracy. It was found that the natural frequencies of the cfrp panels were adequately predicted by the frequency equation in Reference 3, substituting cfrp elastic modulus and density values for the corresponding values for metals. Figure 1 gives the test panel configurations and calculated and measured frequencies.

Particular attention was given to the need to use physical criteria in evaluating data points and regression results, in contrast to relying on statistical criteria. In general it was easier to satisfy statistical tests of significance, than to satisfy requirements for acceptable structural behaviour. Accordingly, statistically accurate representations of structural response data can be developed that have no practical use due to illogical relationships between the design variables, response levels and applied loads.

Strain and acoustic spectrum levels were found to be unsuitable for regression analysis due to large variations that did not significantly correlate to panel configuration parameters nor to fatigue lives. Overall rms levels, on the other hand, did correlate significantly to variations in panel configuration parameters, and fatigue lives. This aspect of the data was partially attributed to the major strain spectrum levels often contributing less than 25 percent of the corresponding overall response levels, based on integrated spectral density plots.

2 REGRESSION ANALYSIS

Regression analysis is a statistical method for investigating functional relationships between variables, based on sample data. It is particularly suitable for data that are imprecise and where there is a need to statistically optimize relationships. The basic approach is to use samples of data to calculate an estimate of a proposed relationship and then to evaluate the fit using statistics such as "F" and "t" tests, in addition to evaluating the accuracy with which the proposed relationship estimates the required quantity based on differences between measured and estimated values. The accuracy required in this work exceeded the statistical requirements, necessitating careful attention to the physical significance of the relationships between variables.

The regression analyses performed utilized a multiple-stepwise regression computer programme, involving a forward selection procedure for the independent variables, with the provision for eliminating variables, as in backward elimination procedures. In order to obtain a linear response equation, the dependent variable is Overall RMS Strain divided by the Overall Sound Pressure Level. For a non-linear equation, the dependent variable is just "Overall RMS Strain," with the "Overall Sound Pressure Level" as an independent variable, i.e.:

$$\text{Linear:} \quad \frac{\varepsilon_{rms}}{SPL} = \text{fn}\ (b,\ t,\ R) \qquad (1)$$

$$\text{Non-Linear:} \quad \varepsilon_{rms} = \text{fn}\ (SPL,\ b,\ t,\ R) \qquad (2)$$

where ε_{rms} = overall rms strain
b = stringer spacing
t = skin laminate thickness
R = radius of curvature.

The coefficients in the regression equations subsequently obtained, were evaluated for their proximity to values having physical significance and, where appropriate, modified to reflect such values. For example, a panel configuration parameter having an exponent of 0.499 was subsequently represented by the square root of that parameter. The resulting equation, comprising several independent varibles having modified coefficients, was then used as a single independent variable in subsequent regression analyses. The estimating accuracy of the modified equation was then evaluated in relation to the physical significance of its format, particularly in regard to dimensional balance. Regression analyses typically generate equations that do not have balanced dimensions, thereby requiring that the input parameters be expressed in the same units as those used in the regression analysis, or modifying the equation's coefficients for a given set of units.

Although such a procedure is likely to reduce the apparent accuracy with which the final estimating equation represents the data, it offsets the effects of correlation between the original independent variables (multicollinearity). Regression analysis of collinear data often produces ambiguous results, making it impossible to accurately evaluate the individual effects of a particular independent variable on the regression equation. Problems of this type were encountered in this work.

2.1 Elimination of Outliers

The regression analysis initially used eighty-two data points given in References 1 and 2. Some of these data points were subsequently identified as being incompatible with the data as a whole and were eliminated.

The usual procedure for eliminating outliers is to identify those data points having the largest percent deviation between the "estimated" and "actual" values and removing them from the analysis. This invariably results in a more accurate equation. However, the improvement in "accuracy" must be carefully weighed against the impact of the reduced data base.

Rejecting data on this basis is a reasonable procedure when dealing with data about which little or nothing is functionally known, such as "public opinion" type surveys. However, when dealing with technical data, it is often necessary to impose functional limitations in order to define acceptable data points. In this programme, the impositions made on the data were that the response strain levels must increase with increasing sound pressure level, stringer spacing (b) and radius of curvature (R); and must decrease with increasing skin laminate thickness. Such an approach sometimes results in rejecting data points where the percent deviation of the estimated value is not large. An illustration of the importance of this is given in Figure 2. The four points w, x, y and z represent response strain values for four different skin thicknesses. The line drawn 1 ---- 1 represents a computed regression relationship showing strain increasing with skin thickness. Based on a table of residuals, data point "z" appeared to be an outlier. Elimination of point "z" resulted in a new regression line 2 ---- 2 , which had greater statistical accuracy than the first line. Since it is known that strain decreases with increasing thickness, it can be seen that the regression analysis resulted in an illogical relationship. In addition, by removing an outlier on the basis of statistical accuracy, the incorrect trend of the regression was worsened. By plotting the data prior to regression, and knowing that strains decrease with increasing skin thickness, it is obvious that data point "w" is the main outlier and not point "z." When point "w" was removed, the new regression line was 3 ---- 3 , which shows a more reasonable relationship. This example illustrates the importance of checking data for technical inconsistencies prior to regression analysis, preferably by graphical means. It also demonstrates the danger in allowing statistical decisions to replace technical ones. It should be remembered that regression analyses have an inherent tendency to reinforce existing trends.

2.2 Development of the Regression Model

In developing a single design method for both flat and curved panels, using regression analysis, it was necessary to determine a numerical value for the radius of curvature of a flat panel. Since regression analysis deals entirely with numerical values, using a very high value to represent an infinite radius of curvature must be avoided. Originally, a value of R = 10,000 inches was used, resulting in a very small regression coefficient for this variable. Since the response differences between the flat and the R = 90-inch curved panels were relatively small, it seemed likely that a much lower number than 10,000 inches would be appropriate. Various numbers were tried, and also a graphical review of the data was performed. It was determined that R = 150 inches was a satisfactory number to represent the flat panel radius.

The linear response equation obtained from the regression analysis was:

$$\varepsilon_{rms} = \frac{b^{1.1045}\, R^{0.5519}}{t^{1.2069}}\; 10^{\left(\frac{SPL}{20} - 9.08\right)} \qquad (3)$$

The average estimating accuracy of this equation was 23 percent.

The strain response data generatd bythe PWT tests displayed a general level of non-linear response. Although evidence of non-linearity is apparent in various aspects of the response data, such as changes in damping and response frequencies, it is the non-linear increase in overall rms strains with increasing sound pressure levels that has the greatest significance from a practical design standpoint. The correspondong non-linear response equation obtained was:

$$\varepsilon_{rms} = 10^{-7.852} \frac{b^{1.0458} R^{0.4994}}{t^{1.1241}} 10^{\left(\frac{SPL}{23}\right)} \quad (4)$$

where SPL is in decibels and b, t and R are in inches.

This equation had an average estimating accuracy of 22 percent. The proximity of the exponents of the variables to values of physical significance is of interest. The exponents of b and R are very close to unity and one-half respectively, $t^{1.125}$ was the only approximation to a rational number that did not have a significant effect on the estimating accuracy.

By performing a regression analysis on a modified form of the right-hand side of equation 4, the following equation was obtained:

$$\varepsilon_{rms} = \frac{b R^{1/2}}{t^{1.125}} 10^{\left(\frac{SPL - 179}{23}\right)} \quad (5)$$

However, a graphical review of the results from this equation snowed that the exponents of the panel configuration parameters (b, t and R), were significantly different from those indicated by the test data. It nad also been noted that significant variations occurred in the values of tne regression coefficients when minor changes were made to the input data.

This type of ambiguity is usually associated with performing regression analysis using independent variables that exhibit significant correlation with each other, and are therefore not truly independent. This condition is usually referred to as multicollinearity. The regression coefficient of an independent variable is intended to be a measure of the efffect of that variable on the dependent variable (rms strain), with the remaining independent variables held constant. When the degree of correlation between the independent variables makes this conceptually impossible, it follows that tne isolated effects of the independent variables in the regression equation cannot be accurately estimated. Structural design and analysis clearly requires a knowledge of the isolated effects of varying configuration parameters.

Measured rms strains were plotted in turn against stringer spacing (b), skin laminate thickness (t) and radius of curvature (R). The rates of change of b, t and R, with respect to estimated rms strains from equation 5 were then superimposed on tne graphs for comparison purposes. The results are shown in Figures 3, 4 and 5 respectively, where rms strain appears to vary with $b^{1.3}$ to $b^{1.5}$, $t^{1.3}$ to $t^{1.8}$ and the variation with R can be seen to require a different functional relationsnip to that used in equation 5. During subsequent regression analyses, it became apparent tnat thelow exponent of b in equation 5 was associated with tne curved panels. Accordingly, it was decided to perform separate regression analyses on the curved and flat panels.

2.2.1 Derivation of a Flat Panel Response Equation

When using regression analysis to derive a flat panel equation, the results showed fundamental changes indicative of a significant level of incompatibility between the curved and flat panel results. It remained to be determined whether this incompatibility was a fundamental aspect of the test data or due to the representation of the radius of curvature in the regression model, already identified as a problem. The resulting flat panel equation was:

$$\varepsilon_{rms} = \frac{b^{1.318}}{t^{1.364}} \, 10^{\left(\frac{SPL - 169}{24.35}\right)} \qquad (6)$$

Equation 6 was modified to a non-dimensional form in which the exponents of b and t were identical, and the following result obtained:

$$\varepsilon_{rms} = \left(\frac{b}{t}\right)^{4/3} \, 10^{\left(\frac{SPL - 168}{24}\right)} \qquad (7)$$

where ε_{rms} is in micro-strain and b and t can be expressed in any coherent units. SPL is in decibels.

Equation 7 estimates rms strains with an average deviation from the measured values of 9 percent, having a corresponding standard deviation of the residual errors of 22 micro-strain about a mean value of -4. The value of the Durbin-Watson statistic obtained was 1.64. A value greater than 1.45 demonstrates a lack of significant serial correlation in the residual errors.

2.2.2 Effects of Panel Curvature

There remained a need to determine a functional relationship between rms strain and R that would approximate a straight line. It was also apparent that the discontinuity in Figure 5 at the transition from curved to flat panels, resulting from the use of an empirical value of R (150 inches) to represent the flat panel radius, was not accpetable with a relationship of the form $\varepsilon_{rms} \propto R^{0.5}$, as in equation 5.

When drawing the curves shown in Figure 5, it was observed that the best fit was obtained using a hyperbola. It was also found that when the rate of change of R was plotted against rms strain, that the same hyperbolic curves resulted, indicating an exponential relationship. Various exponential functions were graphically evaluated until it was determined that the hyperbolic tangent of a linear function of R should provide an effective representation of curvature. The hyperbolic tangent has appropriate aysmpotic trends for both small and large values of R.

The following relationship was thus proposed:

$$\varepsilon_{rms} = \varepsilon_f \ \text{Tanh} \ F(R) \qquad (8)$$

where ε_f is the rms strain for an equivalent flat panel, obtained form equation 7 and F(R) is a linear function of the radius of curvature. The next step was to derive the coefficients of the function of R such that its hyperbolic tangent approached unity for values of R in the region of 150 inches, and approached zero for a value of R below 30 inches and greater than zero. The derivation was based on the relationships between measured data for the curved panels and the corresponding calculated flat

panel strains. The resulting equation was:

$$\varepsilon_{rms} = \left(\frac{b}{t}\right)^{4/3} 10^{\left(\frac{SPL - 168}{24}\right)} \text{Tanh}\left(\frac{R - 17}{40}\right) \quad (9)$$

where R is in inches.

From equation 9, it can be seen that when R = 17 inches Tanh $(\frac{17 - 17}{40}) = 0$, and $\varepsilon_{rms} = 0$. When R = 150 inches, Tanh $(\frac{150 - 17}{40}) = 0.997$, and ε_{rms} effectively equals the flat panel response. Thus the effects of curvature are included without degrading the accuracy of the estimated flat panel response.
The value of R = 17 inches corresponding to zero rms strain is compatible with the curves shown in Figure 5, and is an intuitively acceptable value. As the radius of curvature decreases, there is a finite value where it becomes unreasonable to consider the structure as on array of curved stiffened panels. The estimating accuracy of equation 9 is given below:

RESIDUAL RMS STRAIN (Measured - Estimated)	Mean ($\mu\varepsilon$)	% DEVIATION	STANDARD DEVIATION ($\mu\varepsilon$)
Flat Panels	-4	9%	22
All Panels	7	11%	36

2.2.3 Effects of Panel Aspect Ratio

Although the panel aspect ratio (a/b) in this programme varied from 1.5 to 3, it was not a true independent variable since the longer side of the skin bays was kept constant at a = 12 inches, while b ranged from 4 inches to 8 inches. Thus it was not possible to use (a/b) as a variable in the regression analyses because it is completely collinear with b. Apart from being obviously pointless, if a regression solution is "forced" in such a situation, a regression coefficient would be obtained for the first of the two correlated variables to be entered, and a regression coefficient of zero would then be obtained for the second variable.

In order to include panel aspect ratio as an independent structural parameter in the design method, Reference 3 was used to quantitify proportional changes in response levels due to variations in aspect ratio, with the intention of formulating a functional relationship suitable for inclusion in equation 9. A plot of aspect ratio versus the proportional change in rms strain was observed to be hyperbolic, and within the range of values of interest, was similar in form to the curve of radius of curvature versus rms strain, obtained in the preceeding section. Accordingly, the hyperbolic tangent of (a/b) was plotted against the corresponding rms strain ratios, and a straight line relationship obtained. The resulting estimating equation was:

$$\varepsilon_{rms} = \left(\frac{b}{t}\right)^{4/3} [4 \text{ Tanh } (a/b) - 1] \, 10^{\left(\frac{SPL - 178}{24}\right)} \text{Tanh}\left(\frac{R - 17}{40}\right) \quad (10)$$

where R is in inches. When using S.I units (R in metres), equation 10 becomes:

$$\varepsilon_{rms} = \left(\frac{b}{t}\right)^{4/3} [4 \text{ Tanh } (a/b) - 1]\ 10^{\left(\frac{SPL - 178}{24}\right)} \text{ Tanh } (R - 0.43) \quad (10a)$$

These equations estimate the rms strains for flat and curved panels for all aspect ratios above unity.

2.3 Design Range and Estimating Accuracy

When evaluating the accuracy of an estimating procedure based on the results of regression analyses, it is important to examine the characteristics of the residual errors, including those associated witn data points classified as outliers. Properties of the residual errors that are of particular interest are strong associations with particular variables (εrms, b, t, R, a/b, SPL), or particular values of these variables, and also their probability distribution about their mean value. Associations with particular variables are usually indicated by the Durbin-Watson statistic, however, this test of correlated errors is limited to observations of successive error values and does not always detect trends that may be observed graphically. The distribution of the residuals can be readily used to establish confidence intervals if they are observed to be normally distributed about their mean value.

Before performing such evaluations, those data points classified as outliers, and therefore excluded from the development of the estimating equation, need to be re-examined. This is particularly relevant in this case where some of the outliers are the result of invalid data (in contrast to data scatter), and some were found to have their measured values accurately predicted by the estimating equation.

Since the magnitude of the residuals naturally increases with themagnitude of the response, it is the characteristics of the proportional difference between themeasured and estimated values that requires scrutiny. These characteristics were therefore observed by examining the ratios of measured to estimated rms strains.

The largest errors were found to be due to a high degree of non-linear response of those panels having 4 ply (0.022 inch) skin laminates. It was apparent that equation 10 did not have an acccurate range extending to skin laminates of less than 6 plies. The size of the residual errors associated with the non-linear behaviour of the 4 ply laminates also distorted the general accuracy of equation 10. It therefore seemed more informative to express the distribution of the residual errors, and the confidence intervals relating to estimating accuracy, without including the 4 ply laminate data, and to make it clear that the scope of the estimating procedure did not include the non-linear response behaviour of skin laminate thicknesses below 0.033 inch (6 plies).

Accordingly, the distribution of the residuals was based on the mean value and standard deviation of the ratios of measured to estimated rms strains for all data points, excluding most of the 4 ply laminate data. Some data points were retained for the 4 ply laminates that corresponded to low acoustic load levels, where the non-linear effects are not excessive. This allows equation 10 to be used to estimate the response of 4 ply skin panels, neglecting their increased degree of non-linear response relative to the other panel configurations. No data poins were excluded on the basis of "scatter" from this final determination of the estimating accuracy of equation 10. The mean value of the ratios of measured to estimated response levels is 0.99, with a standard deviation of 0.14. The corresponding normal distribution curve

is shown in Figure 6, with the individual data points superimposed. Figure 7 shows the estimated rms strains plotted against the corresponding measured values. The dashed lines represent the 90 percent confidence interval. The data point having the highest percent deviation corresponds to that remaining panel having the lowest stiffness, and occurs at the maximum load level. This panel has a 6 ply laminate and displays the same trend towards increasing non-linear response as that shown by the 4 ply laminates, but to a lesser extent. Only three data points have residuals due to "scatter" that exceed two standard deviations, with one of the three exceeding three standard deviations, with a value of 3.3. This corresponds to a 31 percent deviation. This is a surprisingly low level of scatter for sonic fatigue data.

The degree of non-linearity accounted for in equation 10 is equivalent to a 7 dB increase in acoustic loading resulting in a doubling of rms strain, compared to the 6 dB increase that represents a doubling of the load. However, it is clear that the degree of non-linear response is not related only to the level of acoustic loading and rms strain. The 4 ply panel displayed rapidly increasing non-linear response characteristics at response levels that did not produce similar effects on panels having greater stiffness. This is thought to be due to the panel deflections having a greater rate of increase with decreasing panel stiffness, than does the rms strain level. In conventional plate theory, the static stress in a fully-fixed plate under uniform pressure loading varies with $\frac{b^2}{t^2}$, whereas the maximum deflection varies with $\frac{b^4}{t^3}$. The increase in non-linear response effects of the 4 ply laminates was quite pronounced at response levels below the random endurance level for the cfrp panels of 440 micro-strain (Figure 8). However, using equation 10 to size airplane panels having 4 ply skin laminates will not result in conservative designs to the degree indicated by the non-linearity of that response. The 4 ply panel showed evidence of carbon fibre damage during PWT testing response levels lower than was required to produce damage to those panels having thicker skin laminates. It is likely that these premature failures were deflection related, possibly to the extent of producing brittle fibre damage in the high strain and deflection gradient areas adjacent to the stiffeners. If this is a valid observation, taking advantage of the degree of non-linear response of the 4 ply laminates may result in underestimated fatigue lives and premature failures on actual airplane panels. This suggests that it may be appropriate to use equation 10 to design 4 ply panels for practical airplane applications.

The estimating accuracy of equation 10 was compared to three semi-empirical design methods for aluminium panels. These results are shown below:

	REF. 6 (ARCAS)	REFERENCE 7 (CLARKSON)	REFERENCE 5 (BALLENTINE)	EQUATION 10
MEAN	1.073	0.962	0.923	0.99
STANDARD DEVIATION	0.886	0.530	0.296	0.14
SAMPLE SIZE	38	59	28	66

The stated level of estimating accuracy applies to cfrp stiffened skin panels over the following range of design parameters:

Stringer spacing:	4 inches to 8 inches
Skin laminate thickness:	0.033 inch (6 plies) to 0.066 incn (12 plies)
Radius of curvature:	Flat down to 30 inches.
Aspect ratio:	1 to 3 (assumed to be valid for all values above unity)
Stringer types:	Z sections. For J and hat sections, multiply estimated rms strain by 0.75.
Skin laminate ply orientations:	$(0, \pm45)_s$, $(0, \pm45, 90)_s$, $(0_2, \pm45)_s$, $(0, \pm45)_{2s}$. Assumed to valid for quasi-isotropic and most orthotropic laminates.
Damping:	Valid for typical values: 0.017 to 0.04.

3 CONCLUSIONS

An estimating equation has been derived that can be applied in the sonic fatigue design of cfrp skin-stringer panels for airplane applications. The equation estimates rms strain levels for both flat and curved panels, with an average accuracy of 9 percent, having a corresponding 90 percent confidence level of approximately 20 percent. The equation is to used inconjunction with natural frequency estimates using References 3 or 4, and the random fatigue curve shown in Figure 8.

Substantiating information and data for this work can be found in Reference 2.

REFERENCES

1. I. HOLEHOUSE 1980 AFFDL-TR-80-3019. Sonic Fatigue Design Techniques for Advanced Composite Aircraft Structures.

2. I. HOLEHOUSE 1983 Ph.D. Thesis, University of Southampton. Sonic Fatigue Design Techniques for Advanced Composite Airplane Structures.

3. A.G.R. THOMPSON and R.F. LAMBERT 1972 AGARD-AG-162, Advisory Group for Aerospace Research and Development, North Atlantic Treaty Organization. Acoustic Fatigue Design Data.

4. Y.K. LIN 1960 Journal of Applied Mechanics. Free Vibrations of Continuous Skin-Stringer Panels.

5. J.R. BALLENTINE ET AL 1968 AFFDL-TR-67-156. Refinement of Sonic Fatigue Structural Design Criteria.

6. N.R. ARCAS 1969 39th Shock and Vibration Bulletin, Part 63, Naval Research Laboratory, Washington DC. Prediction of Stress and Fatigue Life of Acoustically Excited Aircraft Structure.

7. B.L. CLARKSON 1968 J.R. Aero Soc. 172. Stresses in Skin Panels Subjected to Random Acoustic Loading.

Configuration	Skin Thickness "t" (in.)	Stringer Spacing "b" (in.)	Curvature "R" (in.)	Frequencies (Hz) (3) Agard Fully Fixed	(2) Calc.	(4) Lin	(2) Test
a	0.033	8	Flat	160	139	151	143
b	0.044	8	Flat	202	171	177	170
d	0.066	8	Flat	308	246	281	340
f	0.044	8	30	825	-	1,040	620
g	0.044	8	60	510	398	543	350
h	0.044	8	90	375	318	386	290
i	0.044	4	Flat	674	332	558	800
j	0.044	4	90	824	340	688	950
k	0.044	6	Flat	312	302	292	350
l	0.066	6	90	631	347	592	660
n	0.022	8	Flat	120	94	101	140
p	0.022	8	90	377	219	397	
q	0.022	4	Flat	409	299	363	360
r	0.033	4	60	782	348	777	760
s	0.022	6	30	828	-	1,164	

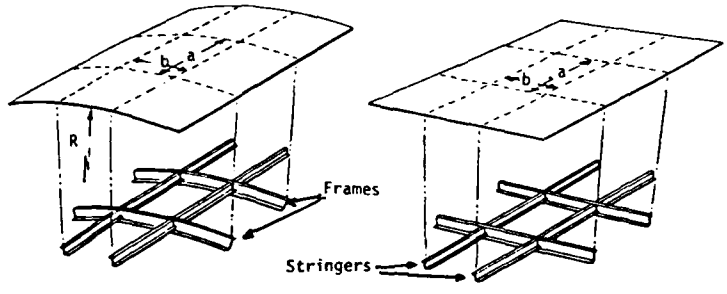

Figure 1. Test Panel Configurations and Natural Frequencies

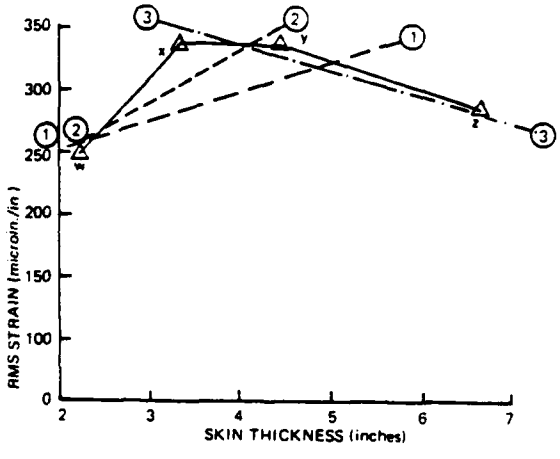

Figure 2. Graphic Illustration of Regression Error

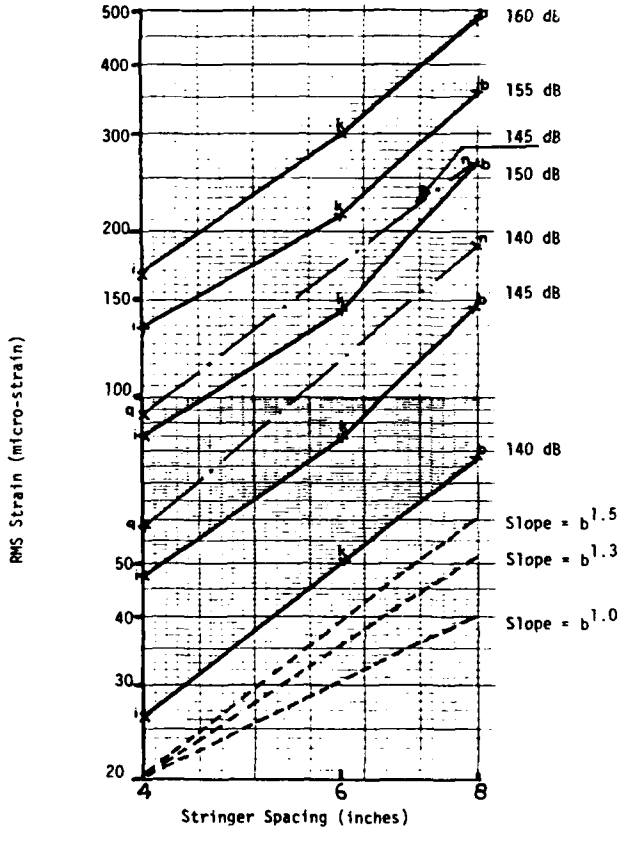

Figure 3. RMS Strain vs Stringer Spacing

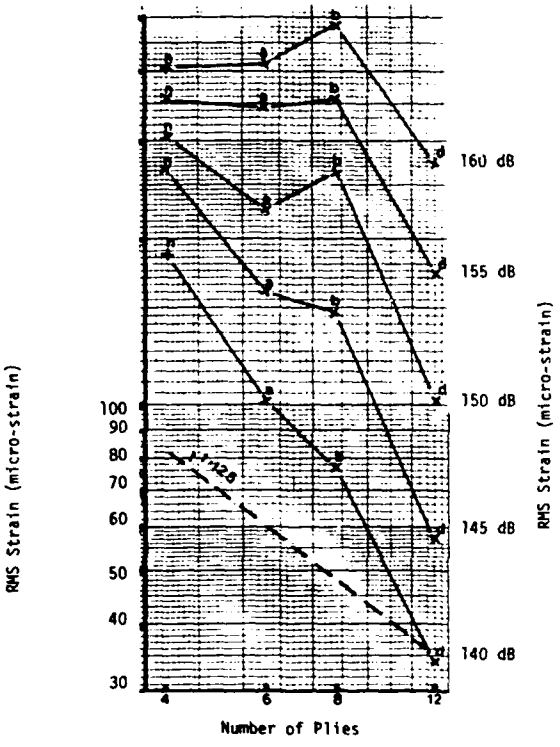

Figure 4 . RMS Strain vs Skin Laminate Thickness

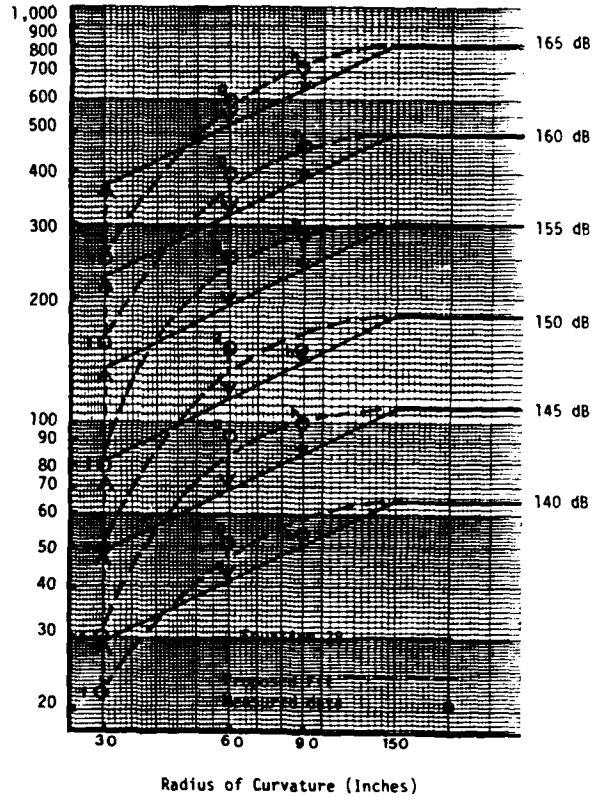

Figure 5 . RMS Strain vs Radius of Curvature (Inches)

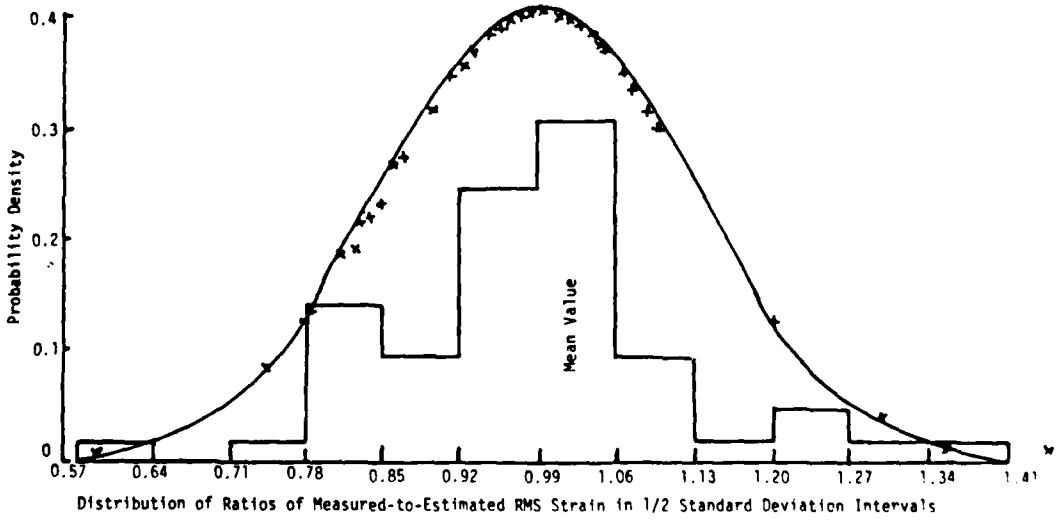

Figure 6 . Distribution of Ratios of Measured to Estimated RMS Strain About the Mean Value

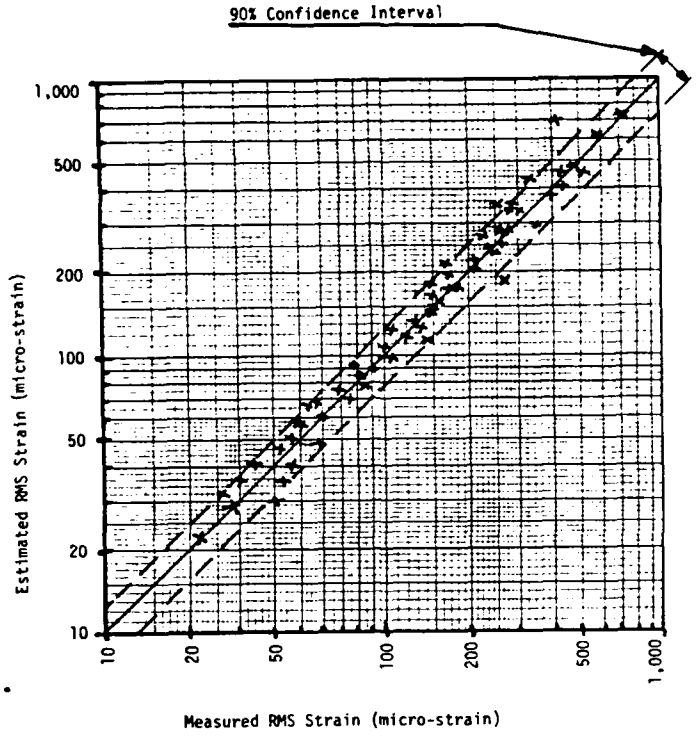

Figure 7. Comparison of Estimated and Measured RMS Strains

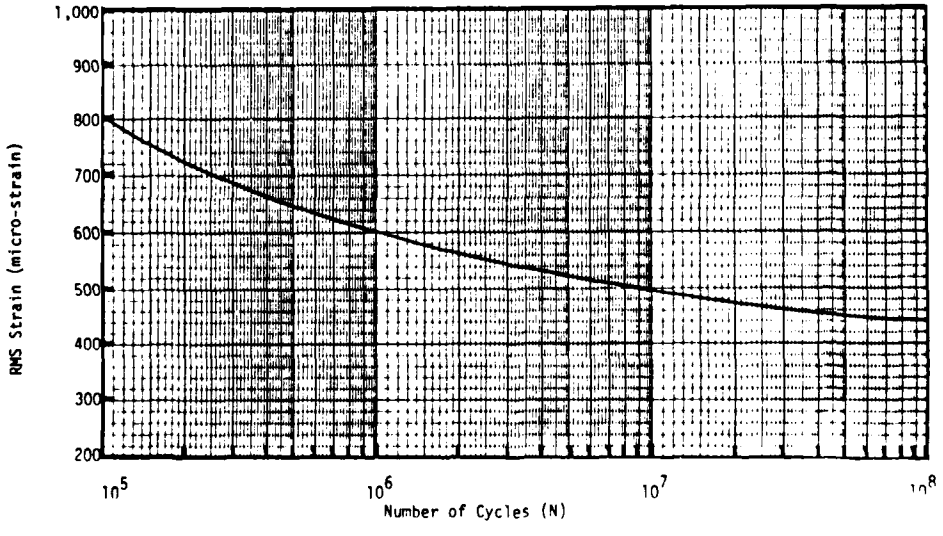

Figure 8 . Random Fatigue Curve for CFRP Stiffened-Skin Panels-RMS Strain vs Cycles to Failure

PREDICTION OF THE DYNAMIC PROPERTIES OF CARBON-GLASS FIBRE SANDWICH HYBRID LAMINATED COMPOSITES

R.D. Adams[1], R.G. Ni[2] and D.X. Lin[3]

1. Department of Mechanical Engineering, University of Bristol, Bristol, U.K.
2. Institute of Aeronautical Materials, Beijing, China.
3. Shaanxi Mechanical Engineering Institute, Xian, China.

1. INTRODUCTION

Some authors [1,2] have developed theories for predicting the flexural behaviour of sandwich beams. Adams and Weinstein [3] made theoretical predictions of the flexural stiffness of sandwich beams and confirmed these by measurements. This approach not only indicated the relationship between the properties of the skin and core of laminated materials, but also some physical insight into the nature of the interface bond stress and the augmented skin stress.

Bert, Wilkins and Gisman [4] presented a method of analysis for predicting the logarithmic decrement for damping in sandwich beams in free vibration from the beam geometry and constituent material properties. A finite element method for computing the dynamic response and the mode shape of three-layer damped plates has been developed by Ioannides and Grootenhuis [5].

Zhang and Zhan [6] worked on the measurement of the mechanical properties for carbon-glass hybrid composites in the form of a sandwich consisting of CFRP skins and a GFRP core. This kind of hybrid composite with a small amount of CFRP for the skins has a much higher flexural modulus than one made solely of GFRP. Also, the impact strength of the hybrid is much higher than that of pure CFRP. Therefore, hybrid composites are a useful class of materials for structural components in which the stresses are mainly flexural.

The purpose of this work is to predict the vibration damping and modulus of sandwich hybrid composite beams, and the resonant frequency, vibration damping and mode shape of sandwich hybrid composite plates in flexure.

2. THEORY

The prediction for the beams is based on the work of Ni and Adams [7]. The hybrid composites used here consist of a symmetrical arrangement of CFRP skins and a GFRP core, which is shown in Fig. 1. The fibre orientation angle

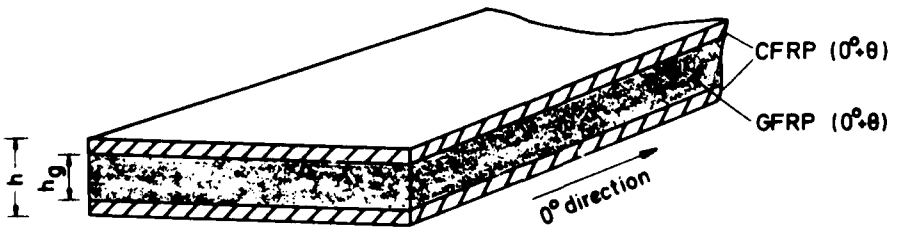

FIG. 1 SECTION OF THE CARBON GLASS-FIBRE/EPOXY HYBRID COMPOSITES

with the principal direction of the beam in both CFRP and GFRP is denoted θ. The hybrid mentioned above is called a unidirectional carbon-glass composite hybrid (CGC).

According to plate theory for laminated composites the flexural modulus matrix components, D_{ij}, can be expressed as

$$D_{ij} = \int_{-\frac{h}{2}}^{\frac{h}{2}} Q_{ij}\, z^2 dz \tag{1}$$

where Q_{ij} is the stiffness matrix and h is the thickness of the beam.

In the case of the hybrid composites used here, equation (1) can be written as

$$D_{ij} = 2\int_{o}^{Rh/2} Q_{ij}^{(G)}\, z^2\, dz + 2\int_{Rh/2}^{h/2} Q_{ij}^{(C)}\, z^2\, dz \tag{2}$$

where R is the volume proportion of GFRP in the hybrid.

By inverting the normalized flexural modulus matrix, the normalized flexural compliance matrix components, C_{ij}, can be obtained. The effective flexural Young's modulus for free vibration, E_{ff}, of the hybrid laminates can then be shown as

$$E_{ff} = \frac{1}{C_{11}} \tag{3}$$

On the basis of the work of Ni and Adams [7], the energy dissipation can be separated into three parts associated with stresses σ_x, σ_y and σ_{xy} in the fibre co-ordinate system, as

$$\Delta Z = \Delta Z_x + \Delta Z_y + \Delta Z_{xy} \tag{4}$$

Then the specific damping capacity of the composites can be expressed as

$$\Psi = \Psi_x + \Psi_y + \Psi_{xy} \tag{5}$$

where

$$\Psi_x = \frac{\Delta Z_x}{Z}, \quad \Psi_y = \frac{\Delta Z_y}{Z}, \quad \Psi_{xy} = \frac{\Delta Z_{xy}}{Z}$$

and Z is the total strain energy.

Further mathematical manipulation leads to the result

$$\Psi_x = \frac{m^2(m^2C_{11}+mnC_{16})}{C_{11}}\left[\Psi_L^{(G)}F^{(G)}R^3+\Psi_L^{(C)}F^{(C)}\,(1-R^3)\right] \tag{6}$$

where $F^{(G)}$ and $F^{(C)}$ are functions of the stiffness and compliance components for glass and carbon, $m = \cos\theta$, $n = \sin\theta$, and $\Psi_L^{(G)}$ and $\Psi_L^{(C)}$ are the longitudinal specific damping capacity of on-axis GFRP and CFRP respectively.

Similarly,

$$\Psi_y = \frac{n^2(n^2C_{11}-mnC_{16})}{C_{11}}\left[\Psi_T^{(G)}F^{(G)}R^3+\Psi_T^{(C)}F^{(C)}(1-R^3)\right] \quad (7)$$

and

$$\Psi_{xy} = \frac{mn\left[2mnC_{11}-(m^2-n^2)C_{16}\right]}{C_{11}}\left[\Psi_{LT}^{(G)}F^{(G)}R^3+\Psi_{LT}^{(C)}F^{(C)}(1-R^3)\right] \quad (8)$$

where the subscripts T and LT denote transverse normal and longitudinal shear values.

The work of Lin, Ni and Adams [8] is used for the prediction of the properties (damping, mode shape and frequency) of the hybrid composite plates used in this work. The method is based on the finite element technique which includes transverse shear deformation, and the damped element model suggested by Adams and Bacon [9] which was extended to involve both transverse shear deformation and rotary inertia effects.

3. EXPERIMENTAL PROGRAMME

The specimens used here were made from carbon HMS/DX-210 and glass/DX-210 prepreg by the hot compression mould method. Details of the specimens are given in Table 1. The method of measuring the modulus and damping of the beams is the

Table 1. Details of the hybrid composite specimens

Specimen	Lay-up	Mean density (g/cm^3)	Volume proportion of GFRP, R	Fibre volume fraction v_f
A	$(C,G,G,G,G)_s$	1.836	0.80	0.512
B	$(C,C,G,G,G)_s$	1.715	0.66	0.451
C	$(C,C,C,G,G)_s$	1.635	0.43	0.438
D	$(C,C,C,C,G)_s$	1.615	0.22	0.485

same as that used in references [7] and [10]. The fundamental symmetric free-free flexural mode of vibration is excited by a coil-magnet pair, the coil being attached to the mid-point of the beam. The flexural Young's modulus is determined from the resonant frequency and the damping from the measured input energy and the stored energy: for the plates, see references [8] and [11]. Here, a transient testing technique is used in which the plate was excited by an impulse and the response measured. A fast Fourier transform method was used to change the data from the time domain to the frequency domain, from which the resonant frequencies and the modal damping could be calculated. The basic data used in the computer programs in this work were corrected for fibre volume fraction by the methods described in reference [12].

4. RESULTS AND DISCUSSION

4.1 Beams

The values of the flexural modulus, E, and specific damping capacity, Ψ, of beam specimens cut at an angle, θ, to the major fibre direction from two extremes of hybrid plates (A and D in Table 1) are shown in Figs. 2 and 3. It is clear that there is good agreement between the theoretical and the experimental values both for E and Ψ. The outer layer of carbon fibres of the 0^o specimen of hybrid D was not perfectly straight, so that the experimental value of flexural

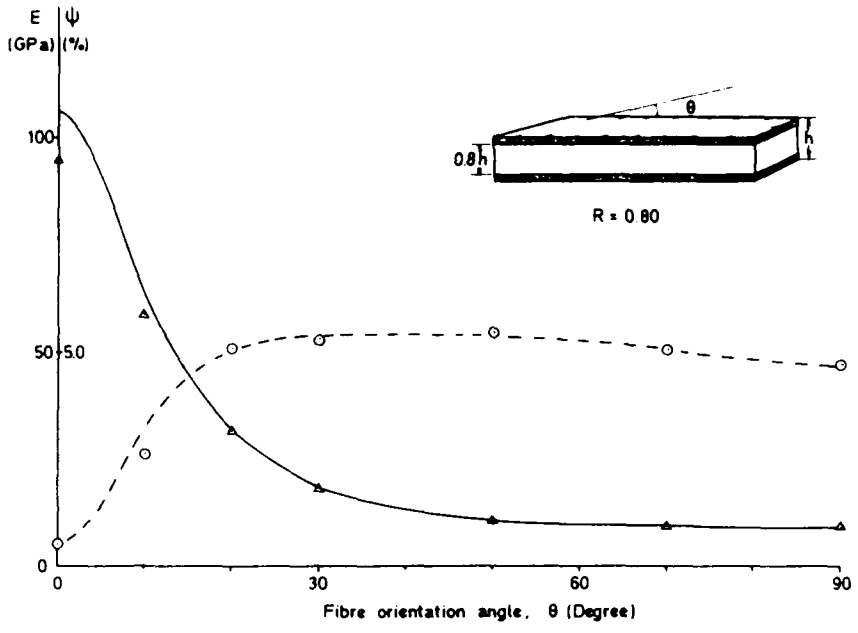

FIG. 2 VARIATION OF FLEXURAL MODULUS E, AND DAMPING Ψ, WITH FIBRE ORIENTATION ANGLE FOR HYBRID A

——— theoretical prediction of E
Δ experimental values of E
------ theoretical prediction of Ψ
O experimental values of Ψ

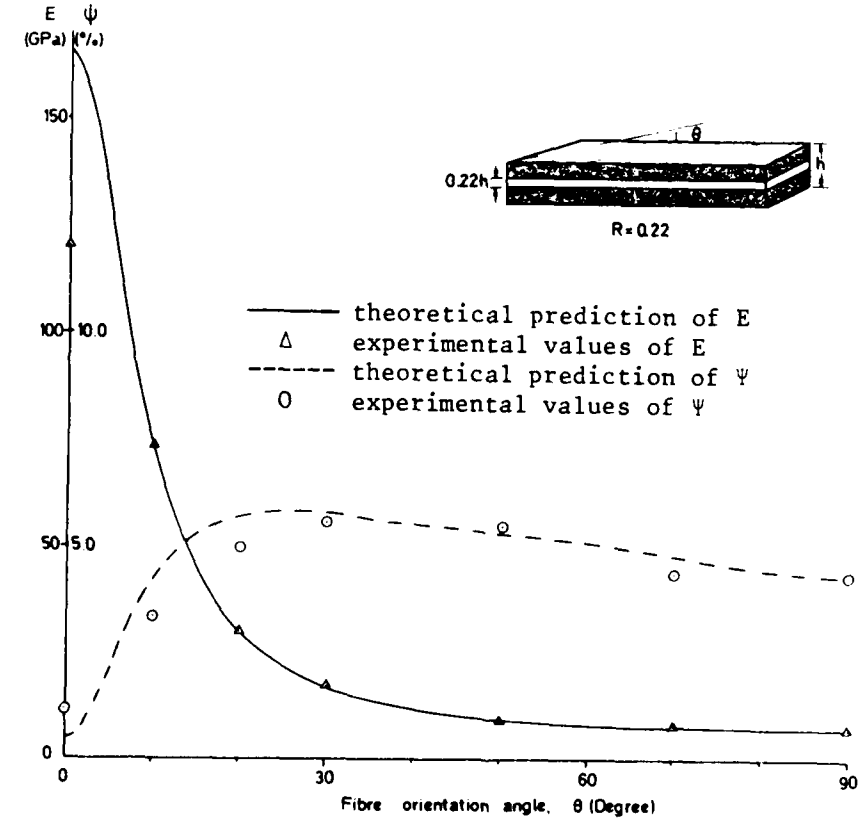

FIG. 3 VARIATION OF FLEXURAL MODULUS E, AND DAMPING Ψ, WITH FIBRE ORIENTATION ANGLE FOR HYBRID D

modulus is significantly lower than the theoretical one and the experimental value of Ψ is higher than predicted.

The theoretical curves for the variation of the flexural modulus E and specific damping capacity Ψ with the volume proportion of GFRP in the hybrid with glass and carbon fibre volume fractions of 0.5 at three different fibre orientations are shown in Fig. 4. It can be seen that in the case of the 0^{o} fibre

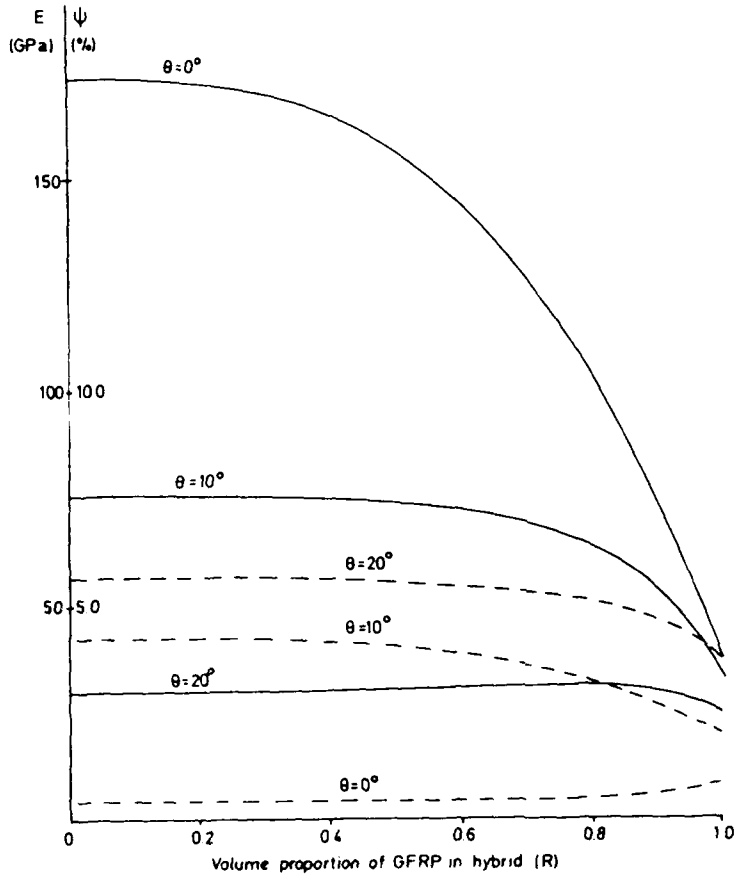

FIG. 4 THEORETICAL PREDICTION OF THE FLEXURAL MODULUS E, AND DAMPING Ψ, WITH THE PROPORTION OF GFRP (R) IN THE HYBRID AT DIFFERENT FIBRE ORIENTATIONS. THE FIBRE VOLUME FRACTION IN BOTH GLASS AND CARBON F.R.P. IS 0.5.
——— theoretical prediction of E ---- theoretical prediction of Ψ

orientation, the flexural modulus of the hybrid, which only has 20 per cent volume of CFRP skins, still has 60 per cent of the flexural modulus of pure on-axis CFRP, but the variation of damping with volume proportion of GFRP is small. In the case of the 10^{o} fibre orientation, the flexural modulus of the hybrid is much lower than that of the 0^{o} fibre orientation (for R = 0.8) but it is still much higher than that of pure GFRP for most of the region of volume proportion of GFRP and the damping of the hybrid is much higher than that of 0^{o} fibre orientation. In the case of the 20^{o} fibre orientation, the flexural modulus of the hybrid is nearly constant, but lower than that of unidirectional, 0^{o} 100% GFRP, which is not to be generally expected. Thus, designers may select hybrids with different volume proportions of GFRP and at different values of fibre orientation.

The differences between theoretical predictions of E and Ψ of unidirectional CGC and cross-plied CGC, where the glass fibre direction in the core is at 90^{o} to the carbon fibre in the skins, with 0.5 of fibre volume fraction at 0^{o} carbon fibre orientation angle are shown in Fig. 5. It can be seen that the difference

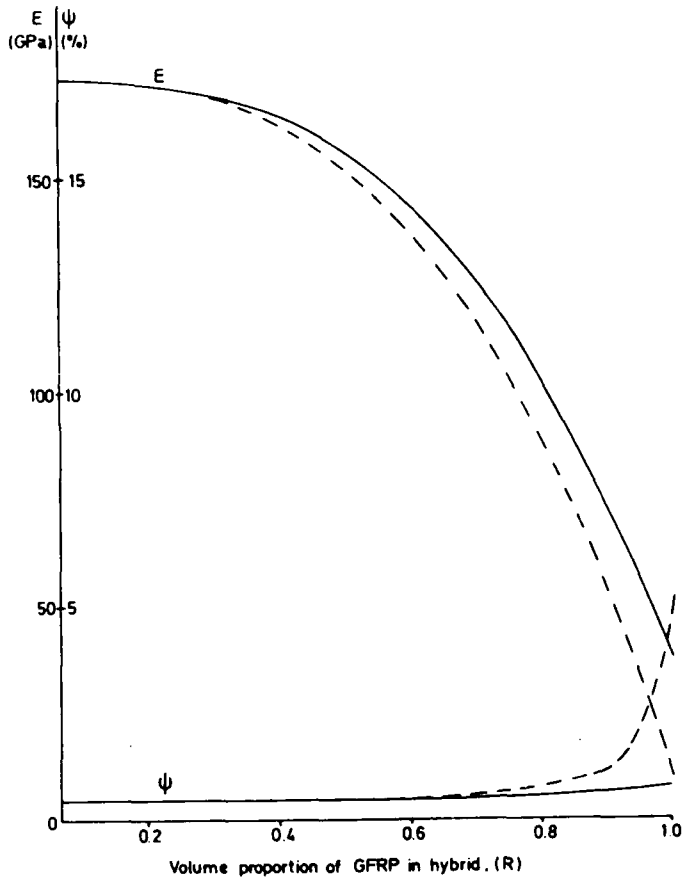

FIG. 5 COMPARISON OF THE VARIATION OF E, AND Ψ OF UNIDIRECTIONAL C.G.C. AND CROSS C.G.C. HYBRID WITH A FIBRE VOLUME FRACTION OF 0.5 AT 0° CARBON FIBRE ORIENTATION ANGLE
——— theoretical prediction of E or Ψ of unidirectional C.G.C.
------ theoretical prediction of E or Ψ of cross C.G.C.

between E and Ψ of the unidirectional CGC and the cross CGC hybrid is small, except when R approaches unity, that is for very fine CFRP skins. In other words, the effect of the core material in this type of hybrid on the modulus and damping of the hybrid in flexure is, in general, not large. This characteristic of the hybrid is of great interest for structural design since it allows some freedom in chosing the orientation of the GFRP core.

4.2 Plates

The results for the natural frequencies, damping values, and mode shapes of the first six modes of the hybrid plates B and C are shown in Figs. 6 and 7. It is evident that there is good agreement between the theoretical and the experimental values of the dynamic properties of both plates.

The damping measurements of the fifth mode were higher than predicted. The reason is that the response of this mode during the transient vibration test was weak and noise is included in the signal. The higher damping measurement of the sixth mode than the predicted value is believed to be due to air damping and extraneous sources of dissipation such as at the supports.

Comparing the sixth mode of the plate and the first mode of the 0° beam from the same plate, and the second mode of the plate and the first mode of the 90° beam, it should be noted that there exists a similar stress situation between

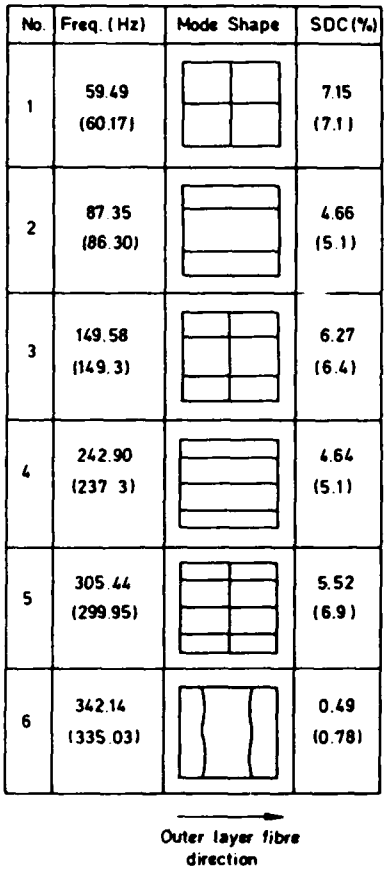

FIG. 6 NATURAL FREQUENCIES AND DAMPING OF VARIOUS MODES OF HYBRID PLATE B EXPERIMENTAL VALUES IN PARENTHESIS.

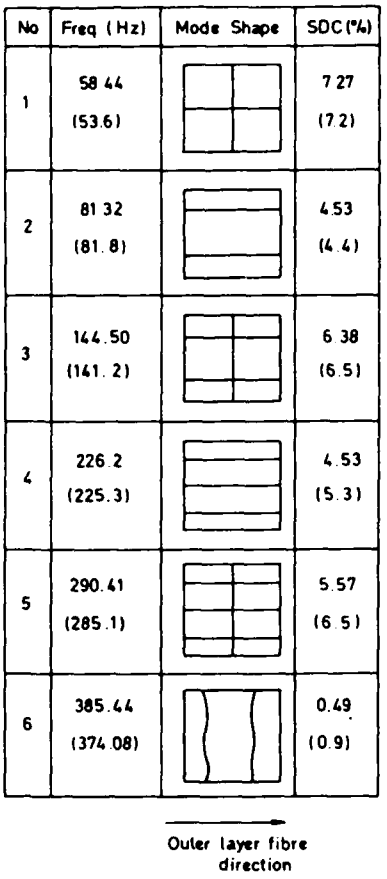

FIG. 7 NATURAL FREQUENCIES AND DAMPING OF VARIOUS MODES OF HYBRID PLATE D EXPERIMENTAL VALUES IN PARENTHESIS.

them since these plate modes of vibration are essentially beam bending modes. Thus, the corresponding values of damping should be close, which is verified by the theoretical predictions listed in Table 2.

Table 2. Comparison between some theoretical damping results of beams and plates

Specimen	Specific damping capacity (%)			
	0° fibre direction beam	6th mode shape of plate	90° fibre direction beam	2nd mode shape of plate
B	0.49	0.49	4.73	4.66
C	0.46	0.49	4.55	4.53

4.3 Economic considerations

Hybrid composites of this type are normally used for economic reasons in the same way that an I-section beam is used: the outer layers carry the bending loads while the core (web) is essentially a shear load carrier. Since the longitudinal and transverse shear properties of carbon and glass fibre composites are similar, hybrids offer attractive possibilities for high-stiffness, low-cost laminates, but there are several parameters which need to be optimised.

In practice, material with a high modulus and low density is usually required for structural components, so the specific modulus, the ratio of modulus to density, is generally of interest to the designer.

On the other hand, if cost is a consideration, then the price of the hybrid will increase with increasing CFRP content.

If specific modulus is less important than modulus, then we can define a new term, the ratio of modulus to cost index, $M_e = E/P$, which we call the economic index of modulus. The variation of this economic index of modulus with volume proportion of GFRP in hybrid composites is shown in Fig. 8.

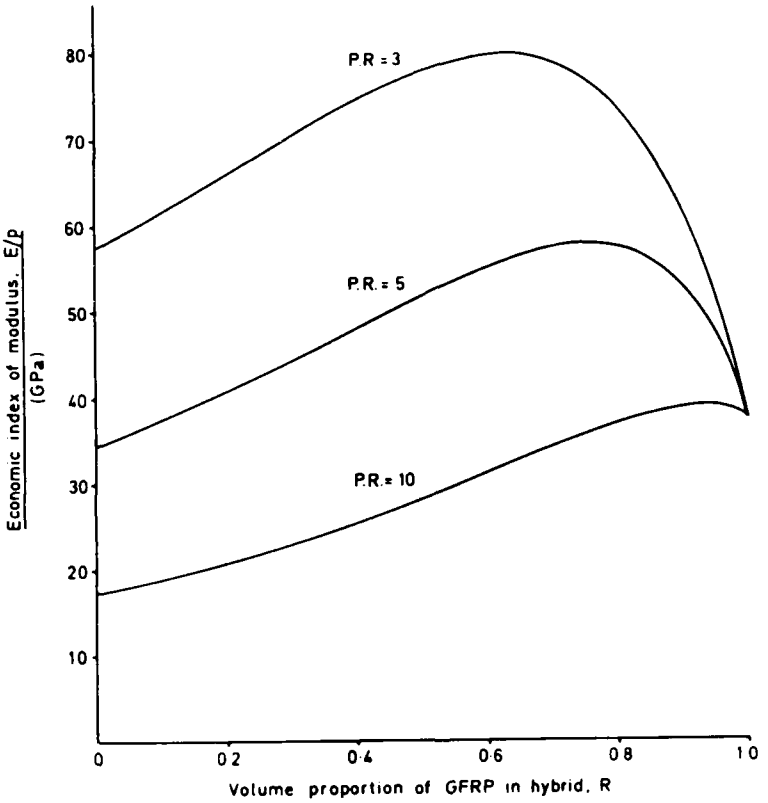

FIG. 8 THE RELATION BETWEEN THE ECONOMIC INDEX OF MODULUS (E/P) AND THE VOLUME PROPORTION OF GFRP IN THE HYBRID AT $V_f = 0.5$ and $\theta = 0^{\circ}$. P IS THE COST INDEX AND P.R. IS THE PRICE RATIO OF CFRP TO GFRP.

CONCLUSIONS

The work of Ni and Adams [7] on beams and the work of Lin, Ni and Adams [8] on plates has been successfully applied to sandwich hybrid laminated composites, which consist of CFRP skins and a GFRP core.

It has been shown that by adding a small amount of CFRP to the surface of GFRP, hybrid composites can be produced which have a much higher flexural modulus and lower density than the original GFRP.

The theoretical analysis indicated that the effect of core material on the modulus and damping of this type of hybrid in flexure is generally not large. It therefore allows some freedom in choosing the orientation of the GFRP core and even different core materials.

A method has been given for assessing the economic value of hybrid composites with respect to the stiffness of a beam in flexure. Choice of the optimum proportions depends on the ratio of the cost of carbon to glass composite.

REFERENCES

1. C.B. NORRIS, W.S. ERICKSEN and W.J. KOMMERS Report No. 1505-A, Forest Products Laboratory, US Dept. of Agriculture. Flexural rigidity of a rectangular strip of sandwich construction.

2. H.G. ALLEN 1967 Trans. J. Plastics Inst., 35, 359. Measurement of shear stiffness of sandwich beams.

3. R.D. ADAMS and A.S. WEINSTEIN 1975 J. Eng. Matls and Technology, Trans. ASME, Series H, 97, 264-270. Flexural stiffness of sandwich beams.

4. C.W. BERT, D.J. WILKINS and W.C. GISMAN 1967 J. Eng. for Industry, Trans. ASME, 662. Damping in sandwich beams with shear-flexible cores.

5. E. IAONNIDES and P. GROOTENHUIS 1979 J. Sound & Vibration, 67(2), 203. A finite element analysis of the harmonic response of damped three-layer plates.

6. X.C. ZHANG and M.Z. ZHAN 1980 Aeronautical Mtls., No. 4, 43, Inst. of Aeronautical Mtls., Peking, China. Mechanical properties of carbon-glass fibre/epoxy hybrid composites.

7. R.G. NI and R.D. ADAMS To be published. Prediction of the vibration damping and elastic moduli of symmetric laminated composites.

8. D.X. LIN, R.G. NI and R.D. ADAMS To be published. Prediction and measurement of the vibration damping parameters of carbon and glass fibre reinforced plastic plates.

9. R.D. ADAMS and D.G.C. BACON 1973 J. Comp. Matls., 7, 402. Effect of fibre orientation and laminate geometry on the dynamic properties of CFRP.

10. R.D. ADAMS and D.G.C. BACON 1973 J. Phys. D: Appl. Phys., 6, 27. Measurement of the flexural damping capacity and dynamic Young's modulus of metal and reinforced plastics.

11. D.X. LIN and R.D. ADAMS To be published. Determination of the dynamic characteristics of structures by transient testing using Zoom-FFT.

12. R.G. NI and R.D. ADAMS To be published. Correction of the basic data for prediction of dynamic properties of laminated composites with fibre volume fraction.

Life Time Prediction Based on the Combined use of Finite Element and Modal Analysis Data

ir. E. Verdonck and Prof. R. Snoeys

Katholieke Universiteit Leuven
Departement Werktuigkunde
Celestijnenlaan 300B
3030 Leuven
Belgium

The knowledge of the stress or strain history at the critical point is essential for the estimation of life time of dynamically loaded structures. Besides the definition of the correct loading pattern, an identification of the mechanical structure is necessary. This identification may be carried out analytically or experimentally. If the structure is available for testing the experimental identification is quite attractive because fewer hypothesis have to be accepted especially with respect to the damping characteristics.

Modal analysis enables to determine the dynamical behaviour experimentally. Hereby the structure is excited by a known dynamical force, and the response is measured at different measurement points, distributed over the structure. The modal parameters (natural frequencies, damping values and mode shapes) are determined using curve-fitting algorithms.

In order to calculate the strain and stress distribution occuring for a particular modal deformation pattern for a part of or the complete structure, a finite element model is used. Then the stresses and strains are found for each particular mode, and consequently combined to derive the stress and strain histories for a particular dynamic loading of the structure.

Once the stress and strain histories are known in the critical area, an appropriate damage rule and counting method is used to find the damage of one loading sequence. The life time is found from the number of loading sequences that can be applied to satisfy the fatigue failure criterion.

This procedure enables one to evaluate the influence on life time of various modifications in structural design, material properties (Young modulus, density and fatigue properties), frequency content and distribution of the dynamical load and damping properties of the stucture. The technique developed here can readily be applied and can be used to optimise life time of various types of mechanical structures.

1. INTRODUCTION

Structures subjected to a persistant dynamical load can fail for stress levels which are considerable lower than these permitted for statical loading. This phenomenon has been studied for a long time and is known under the name "fatigue". When dimensioning against fatigue, the structure has to be designed to obtain an acceptable life time.

To estimate life time, "damage" has to be determinated based on the fatigue behaviour of the material and the strain history in the critical loaded area (this is the area with the highest loads). Damage includes all micro or macroscopic structural changes which has a prejudical influence on the strength and / or the stiffness of the macro structure.

In life time calculations the determination of the dynamical stress components are often based on statically determined stresses and strains. Dynamical deformations caused by alternating loads can be considerably larger than the deformations found by pure statical calculations. While statical deformations only depend on the stiffness of the structure, the dynamical deformations are strongly influenced by the damping. Therefore it is important to include the dynamical behaviour in life time calculations. The method which is proposed here uses the dynamical load and the dynamical behaviour of the structure to construct stress and strain histories.

The experimental method was used to find the dynamical behaviour of the structure. This method has the advantage that it determines the dynamical behaviour of the structure which is closer to the real dynamical behaviour than an analytical method. When the dynamical loads and the dynamical behaviour of the structure are known, the dynamical response of the structure can be found, from which the occurring stress and strain distributions in the structure are determined as a function of time. Proceeding from the strain history in the critical area the accumulated damage is found. A life time prediction theory based on the fatigue behaviour of the material, an adequate cycle counting method and damage accumulation hypothesis enables an estimation of the life time of the structure to be made.

2. DYNAMICAL MODEL

The dynamical behaviour of structures is determined by the equilibrium - equation:

$$\{f\} = [M]\{\ddot{x}\} + [C]\{\dot{x}\} + [K]\{x\} \qquad (1)$$

where: [M] : mass matrix
[K] : stiffness matrix
[C] : damping matrix
{f} : force vector in time domain
{x}, {ẋ}, {ẍ} displacement, velocity and acceleration respectively expressed in the time domain.

This differential equation can be solved. The displacement of point I due to a dynamical force F in point J can be written in the frequency domain as:

$$X_I = \sum_{k=1}^{N} \left[\frac{U_{IJk} + j\,V_{IJk}}{-\mu_k + j\,(w - v_k)} + \frac{U_{IJk} - j\,V_{IJk}}{-\mu_k + j\,(w + v_k)} \right] . F_J \qquad (2)$$

where: I : response point
J : excitation point
k : mode number
N : number of modes
j : complex variable $j = \sqrt{-1}$
X_I : Fourier transform of response at point I
F_J : Fourier transform of force at point J
U_{IJk} , V_{IJk} : real and imaginary part resp. of the modal displacement of point I for excitation in point J for mode k.
v_k : damped natural frequency of mode k
μ_k : decay of mode k
w : frequency

Equation (2) discribes the dynamical behaviour of the mechanical structure. The modal displacements ($(U_{IJk} + j\,V_{IJk})$ for k = 1,2...N, I = all measurement points of the structure and J the excitation point), the natural frequencies v_k and the damping values μ_k are experimentally obtained by a modal analysis test.
The inverse Fourier transformation of formula (2) gives the response at point I of the structure due to a force input at point J.

$$x_I(t) = \int_{\emptyset}^{t} \sum_{k=1}^{N} \left\{ (U_{IJk}+jV_{IJk})\, e^{(\mu_k+jv_k)\tau} + (U_{IJk}-jV_{IJk})\, e^{(\mu_k-jv_k)\tau} \right\} . F_J(t-\tau)\,d\tau \qquad (3)$$

Expression (3) shows that the response can be written as a linear combination of the mode shapes. Hereby the weighting factors are functionsof the complex eigenvalues and the force input function. Simplifying the notations expression (3) can be written as:

$$x_I(t) = 2\,\mathrm{Re}\left(\sum_{k=1}^{N} \Psi_{Ik} \cdot q_k(t)\right) \qquad (4)$$

Where I : a measurement point of the structure with coordinates (x,y,z).

t : time

$x_I(t)$: displacement response in the x direction at point I and time t.

Ψ_{Ik} : modal displacement of point I in the x direction of the k^{th} mode.

$$q_k(t) = \int_{\emptyset}^{t} e^{(\psi_k + j\nu_k)\tau} \cdot F_J(t-\tau)\, d\tau$$

= the k^{th} generalised modal coordinate.

When the force input point M is different from the excitation point J, the modal displacements have to be rescaled.

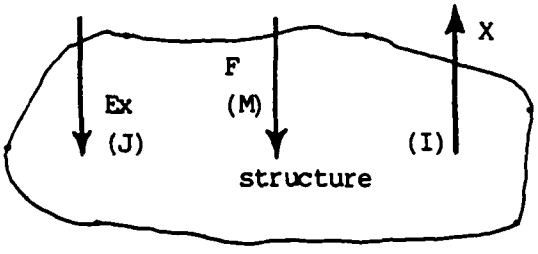

I : response point
J : excitation point
M : force input point

Fig. 1 . Force input in a point different from the excitation point

The modal displacements become:

$$U_{IMk} + j\,V_{IMk} = \frac{(U_{MJk} + j\,V_{MJk}) \cdot (U_{IJk} + j\,V_{IJk})}{(U_{JJk} + j\,V_{JJk})} \qquad (5)$$

3. CALCULATION OF THE STRAINS

For small displacements the normal strain in the x direction is:

$$\varepsilon_{Ix}(t) = \frac{\partial x_I(t)}{\partial x} \qquad (6)$$

Substituting equation (4) into (6), the normal strain distribution in

the x direction can be represented in terms of the sum of modal strains as:

$$\varepsilon_{Ix}(t) = 2\,\mathrm{Re}\left(\sum_{k=1}^{N}\phi_{Ik}\cdot q_k(t)\right) \qquad (7)$$

Where the strain ϕ_{Ik}, is the "modal strain", describes the strain distribution throughout the structure. The x-strain for each mode is:

$$\phi_{Ik} = \frac{\delta\Psi_{Ik}}{\delta x} \qquad (8)$$

Because of the complexity of most structures of interest, it is usually necessary and acceptable to consider the response at only a discrete number of points based on a finite difference model, a finite element model, or test data. Thus, the response functions for displacement $x_I(t)$ and strain become vector functions of time, $\{x(t)\}$ and $\{\varepsilon_x(t)\}$.

4. STRESS AND STRAIN CALCULATION FOR BEAM-LIKE STRUCTURES

Formula (8) may look straightforward but can only be applied in cases where the displacements in the longitudinal direction (x direction) can be measured. For beam-like structures the transversal deformations (z-direction) are more adequate. The calculation of the modal strain distribution from the modal deformations is illustrated for a two-dimensional deformation pattern (in the x-z plane). Hereby the bending deformations are dominating. Looking to the displacements of two successive measurements z_I and z_J, the displacements of points I and J can be characterized by the vectors (Fig. 2):

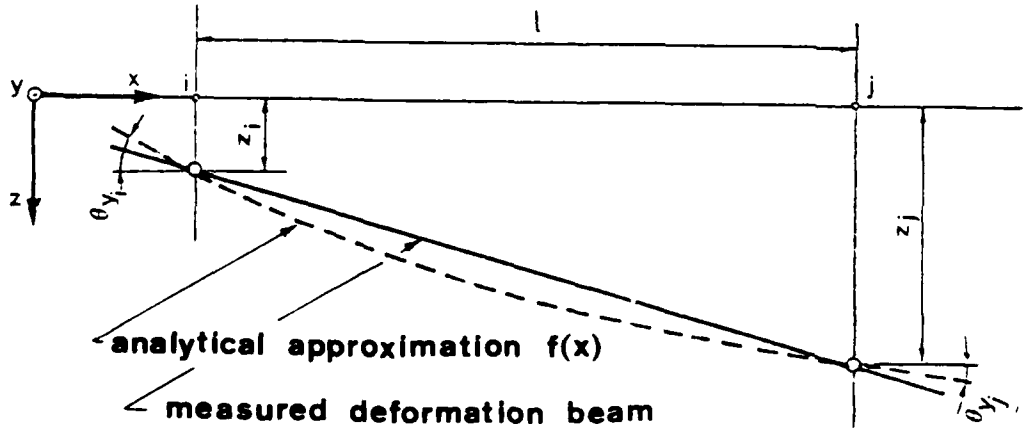

Fig. 2. Analytical approximation of the dynamical beam deformations

$$\{ d_I \} = \begin{Bmatrix} z_I \\ \theta_{yI} \end{Bmatrix} \quad \text{and} \quad \{ d_J \} = \begin{Bmatrix} z_I \\ \theta_{yI} \end{Bmatrix}$$

Whereby: z_I and z_J are the displacements in points I and J in the z-direction.

θ_{yI} and θ_{yJ} are the rotation angles in points I and J around the y-axis.

If the displacements $z_I, z_J \ldots$ can be approximated by the function $f(x)$, than the roation angles can be calculated by:

$$\theta_I = \arctan \left. \frac{df(x)}{dx} \right|_{x=x_I} \cong \left. \frac{df(x)}{dx} \right|_{x=x_I}$$

The strain in the x-direction of a beam is given by the expression:

$$\varepsilon_x = Z \frac{d^2 f(x)}{dx^2} \tag{9}$$

hereby is Z the distance between the neutral axis and the considered axis. Expression (9) is computed for all points of the structure, and the strain distribution is found for each particular mode. The total strain as function of time is found by lineair combination of the modal strains (formula 7).

4.1 Analytical Approximation of Mode Shapes of Beams

To reduce the influence of the measurement noise the mode shapes are approximated by orthogonal polynomials. The generation of orthogonal polynomials has been extensively discused by G. E. Forsythe [5]. Orthogonal polynomials which satisfy the orthogonality relation in the interval [-1,1]:

$$\sum_{k=1}^{N} w(x_k)\, P_i(x_k)\, P_j(x_k) = \delta_{ij} \tag{10}$$

$\delta_{ij} = 1$ for $i=j$

$\delta_{ij} = 0$ for $i \neq j$

Where $P_j(x_k)$: orthogonal polynomial of degree j evaluated in point x_k

$w(x_k)$: weighting function evaluated in point x_k.

The discrete function $y(x_k)$ is approximated by the polynomial:

$$f(x) = \sum_{k=0}^{M} b_j \, P_j(x) \qquad (11)$$

Where M : highest degree of polynomial
j : degree of polynomial
b_j : coefficient of orthogonal polynomial of degree j.

The coefficients b_j are found by the formula:

$$b_j = \frac{\sum_{k=1}^{N} w(x_k) \; P_j(x_k) \; y(x_k)}{\sum_{k=1}^{N} w(x_k) \; (P_j(x_k))^2} \qquad (12)$$

The use of orthogonal polynomials has a number of advantages. When approximating several modes, the polynomials has to be generated only once, because orthogonal polynomials only depend on the evaluation points, which are the same for all modes. The optimal degree of the approximation polynomial can be determined fast, due to the fact that n coefficients of the polynomial of degree n are identical to the n lowest degree coefficients of the polynomial of order n+1.

The second derivate is found by generating the coefficients of the 2^{nd} derivate polynomial. The strain is easely calculated by expression (9).

4.2 Verification of the Modal Strains of a Cantilever Beam

The mode shapes of a cantilever beam made of steel, with a cross section of 15 x 15 mm^2 and a length of 0.85 m has been determinated using modal analysis and finite elements. Table 1. gives a survey of the modal parameters which where found.

mode	eigen frequency (Hz) F.E.	eigen frequency (Hz) M.A.	damping ratio (%) M.A.
1	17.4	16.0	1.15
2	109.1	100.4	0.85
3	305.5	280.9	0.97

Table 1. Modal parameters found by F.E. and M.A.

The resonance frequencies found by modal analysis are a little lower than the resonance frequencies found by F.E. This is due to the compliance in the fixation point. The modal analysis test yields besides values for the resonance frequencies also values for the damping ratio's. Three methods were used to determine the modal strains:

1) Strains where measured and modal strains where found by modal analysis.
2) A finite element modal was made and used to compute the mode shapes and the corresponding modal strains.
3) The strains were calculated from the mode shapes found by modal analysis of the measured accelerations.

Table 2. gives an overview of the strains at the fixated end of the beam. The strains are scaled to a modal displacement of 1 cm at the free end of the beam.

mode	max. strain obtained by F.E.	strain measurements	M.A.
1	$3.82\ 10^{-4}$	$3.53\ 10^{-4}$	$4.45\ 10^{-4}$
2	$2.50\ 10^{-3}$	$2.47\ 10^{-3}$	$2.69\ 10^{-3}$
3	$7.03\ 10^{-3}$	$7.69\ 10^{-3}$	$6.90\ 10^{-3}$

Table 2. Modal strains at the fixated end of a cantilever beam

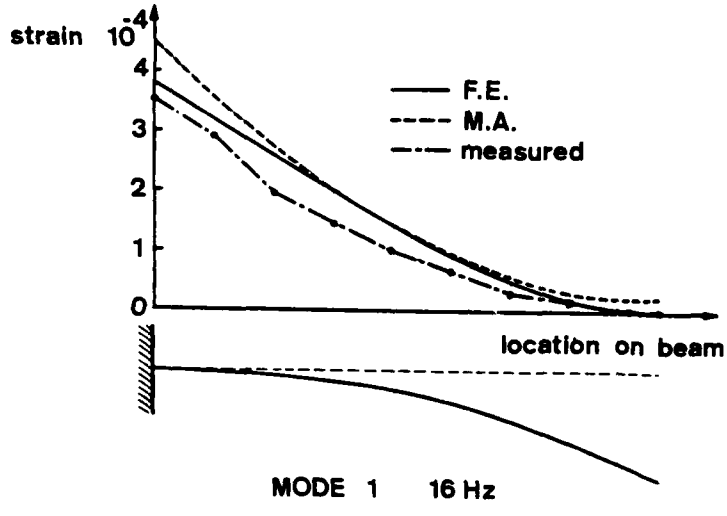

Fig. 3. Modal strain distribution of mode 1, determined by different methods

Fig. 3 shows the strain distributions for mode 1 of a cantilever beam. As it can be seen of Table 2. and Fig. 3 the strains obtained from

F.E. calculations are very close to the measured modal strains. There is an maximum discrepancy of 30% between the strains obtained from differentiation of the modal displacements and the strain measurements.

5. STRESS AND STRAIN CALCULATION BASED ON FINITE ELEMENTS

The method based on double differentiation of the mode shapes can not be used for complex structures. However a finite element model can be of a great help. The finite element method is based on a structural model (finite element model) to compute:

- deformations of a static loaded structure
- dynamical behaviour (eigen frequencies and mode shapes)
- stresses and strains in deformated structures
- ...

The finite element method will be used here to compute the mode shapes of the structure. Stress calculations are carried out to find the modal stresses and strains of the structure. The mode shapes found by finite elements are compared with the mode shapes obtained by modal analysis to find the scale factor. The modal stresses calculated from the finite element model are rescaled accordingly. The modal stresses and strains which are found are used to calculate the stress and strain histories.

6. LIFE TIME PREDICTION OF A TENNIS RACKET

A finite element model of a tennis racket was developed by H. Sol [6]. The model was composed of 92 beam elements and 56 plate elements (Fig. 4). All beam elements have a rectangular hollow cross section. A numerical dynamic analysis has been carried out for the tennis racket in free conditions. Three modal vectors where computed. At the same time a modal analysis test has been carried out. Table 3. summarises the modal parameters which where found.

	FINITE ELEMENTS	MODAL ANALYSIS	
mode number	eigenfrequency Hz	eigenfrequency Hz	damping ratio %
1	105.9	102.7	1.19
2	290.4	294.3	0.67
3	300.5	310.2	0.47

Table 3. Modal parameters determined by finite elements and modal analysis of a tennis racket.

Mode 1 and 3 are bending modes, mode 2 is a torsion mode (Fig. 5).

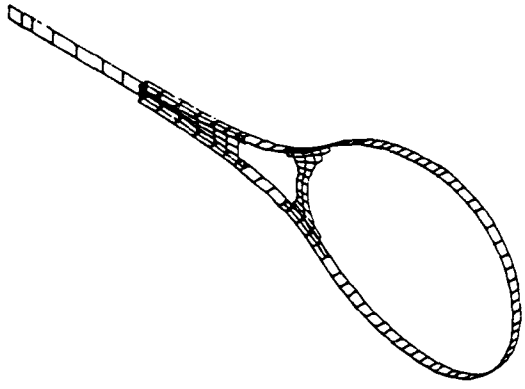

Fig. 4. Finite element model of a tennis racket

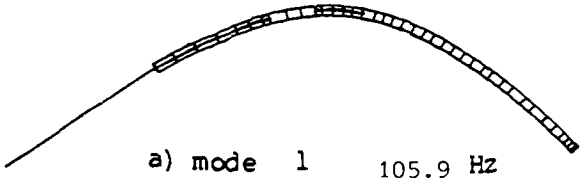

a) mode 1 105.9 Hz

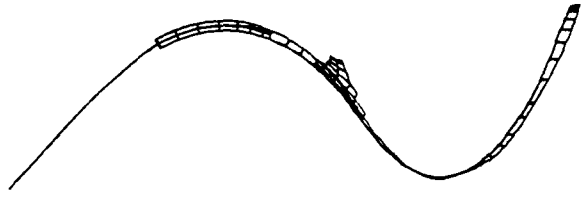

b) mode 2 290.4 Hz

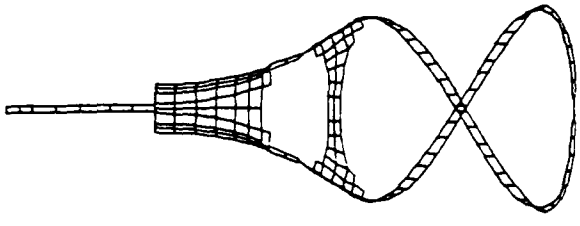

c) mode 3 300.5 Hz

Fig. 5. Mode shape of an tennisracket found by finite elements.
a) single bending
b) double bending
c) torsion

A good correspondence was found between the mode shapes determined by modal analysis and finite elements.

6.1 Calculation of the Strains

The finite element program supports the stress calculation in plate and beam elements. For plate elements the F.E. program enables plotting and listing of the principal stresses.

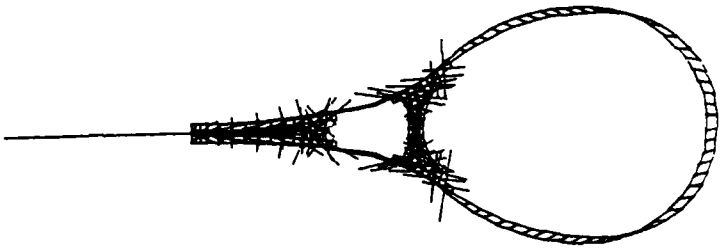

Fig. 6. Principal stresses in the plate elements for mode 1.

As it can be seen from Fig. 6 the stress in the plate elements are maximum for these plate elements which are located near the frame. The modal stresses for the 2nd mode are about one magnitude smaller. Fig. 7 shows the cross section stress distribution of point no 52. It's easily seen that normal stresses are due to the bending. The shear stresses are mainly caused by bending and torsion.

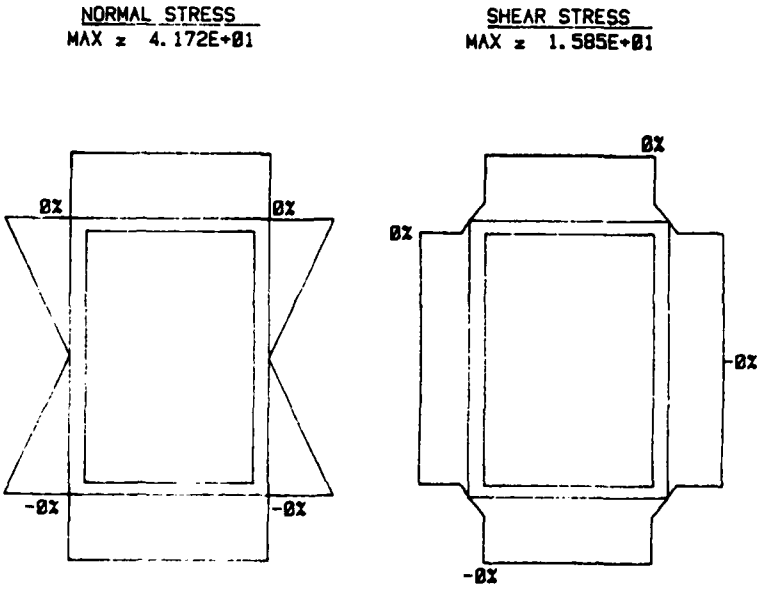

Fig. 7 Stress distribution at point no. 51.

Fig. 8 shows the tensile stress (of the upper axis) all over the tennis racket. The tensile stress is maximum in the centre of the tennis racket. Non zero tensile stress values are found in points located at the top of the tennis racket. Fig. 9 and 10 show the shear stress distribution of points located on the upper axis and the

neutral axis respectively. The shear stress for the first mode is maximum for the cross section located near the connection point of frame and shaft of the tennis racket. The modal stresses where calculated for all mode shapes which where taken into account.

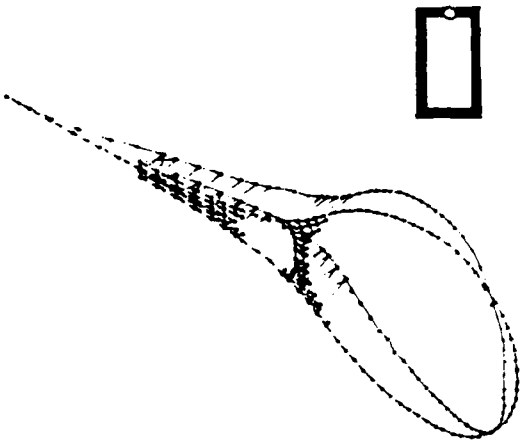

Fig. 8 Tensile stress distribution on the tennis racket, mode 1.

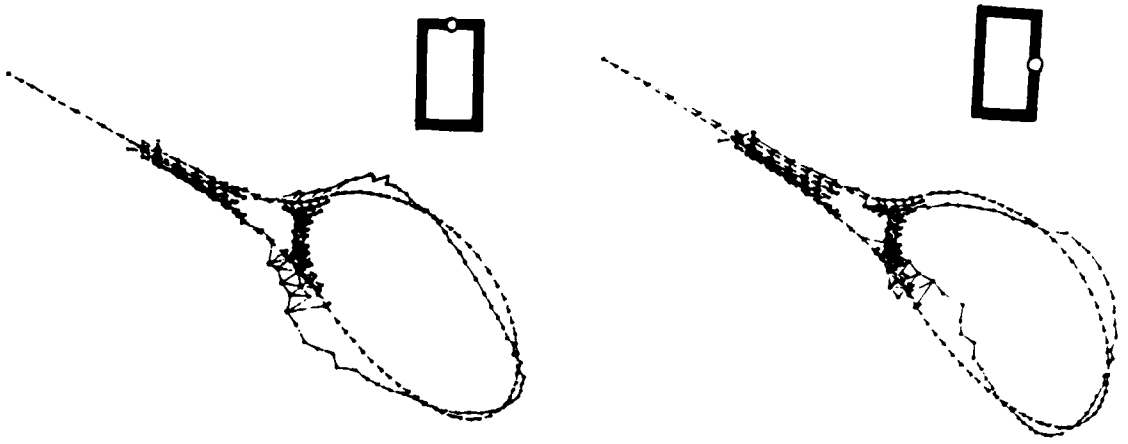

Fig. 9 and 10. Shear stress distribution on the tennis racket, mode 1, in two different locations in the cross section.

6.2 Calculation of the Strain History at the Critical Point

Based on expression (7) the strain distribution was calculated as a function of time. Hereby the tennis racket was subjected to an impact load (ball impact) in the center of the frame of 500 N with a duration of 5 ms. A computer program calculates the strain histories for all points of the tennis racket. The program looks for the location with the highest strain peaks. That point will be considered as the critical point.

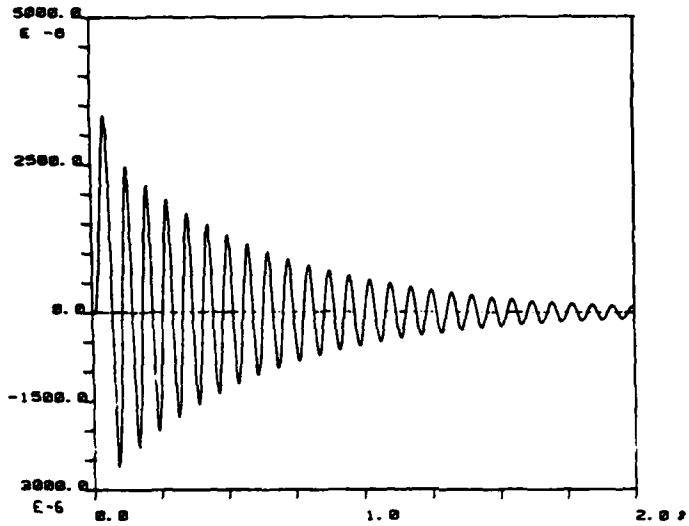

Fig. 11. Strain history at the critical point

Fig. 11 shows the strain history of point 59, which was found as critical point. As it can be seen from Fig. 11, the first mode has a dominant influence in the strain history for that point. However other impact locations can cause other critical points, and other modes can be found dominant.

6.3 Calculation of Life Time

The popular "Rain - Flow" cycle counting algorithm [7] was used to find the cycle types in respect to there amplitude and mean value. Fig. 12 shows the histogram of the cycle types which where found.

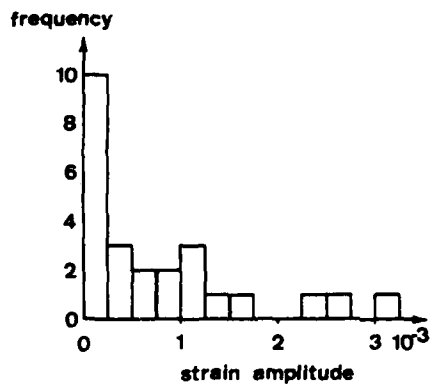

Fig. 12. Histogram of cycles

Damage for each cycle was found using the Wöhler curve corresponding to the aluminium alloy which was used to make the tennis racket. Table 4. gives the damage for each cycle and the accumulated damage.

AMPLITUDE	AVERAGE	DAM.1CYCLE	TOTAL DAM.
.310E-02	.605E-03	.379E-03	.379E-03
.228E-02	.661E-04	.794E-04	.458E-03
.202E-02	.643E-04	.525E-04	.511E-03
.178E-02	.581E-04	.330E-04	.544E-03
.157E-02	.492E-04	.199E-04	.564E-03
.138E-02	.415E-04	.113E-04	.575E-03
.122E-02	.381E-04	.614E-05	.581E-03
.107E-02	.354E-04	.313E-05	.584E-03
.949E-03	.300E-04	.149E-05	.586E-03
.836E-03	.254E-04	.655E-06	.586E-03
.737E-03	.227E-04	.272E-06	.587E-03
.650E-03	.214E-04	.107E-06	.587E-03
.574E-03	.183E-04	.410E-07	.587E-03
.506E-03	.155E-04	.150E-07	.587E-03
.446E-03	.135E-04	.538E-08	.587E-03
.393E-03	.127E-04	.193E-08	.587E-03
.347E-03	.112E-04	.686E-09	.587E-03
.306E-03	.949E-05	.242E-09	.587E-03
.270E-03	.803E-05	.839E-10	.587E-03
.238E-03	.758E-05	.296E-10	.587E-03
.210E-03	.684E-05	.104E-10	.587E-03
.185E-03	.580E-05	.366E-11	.587E-03
.163E-03	.490E-05	.127E-11	.587E-03
.144E-03	.451E-05	.446E-12	.587E-03
.127E-03	.417E-05	.156E-12	.587E-03
.112E-03	.354E-05	.552E-13	.587E-03
.899E-05	.928E-04	.555E-22	.587E-03

Table 4. Damage of each cycle and accumulated damage

A total damage of 0.578 10^{-3} was found. According to the Miner rule a life time of 1730 impacts should be reached.

7. CONCLUSIONS

Modal parameters (resonant frequencies and damping values) and mode shapes gives a complete description of the dynamical behaviour of the structure. For simple structures (beam like structures) the stresses and strains can be calculated from modal analysis data based on acceleration measurements, without the necessity of measuring modal strains. However the process of calculating strains is based on a double numerical differentiation. People who are familiar with numerical techniques know that differentiation is an unstable process and results should be

interpreted with care. The advantage of this method to obtain the modal strains lies in the fact that no F.E. model of the structure is required, and the method is easy to apply.

Better strain distributions can be retrieved when a finite element modal is available. A dynamical analysis should be made and the modal strains calculated.

It is not always necessary to have a F.E. - model of the complete structure. When the critical component is known, only a F.E. ⇒ model of that component is required. The modal deformations of the particular component are found by subjecting that component to its respective modal deformations and calculating the corresponding strain.

F.E. enable the computation of stress - concentration factors which can then be taken into account. Stress concentration factors are very important for life time calculations and should never be neglected.

REFERENCES

1. R. SNOEYS and H. VAN BRUSSEL 1982 K.U. Leuven, Uitg. Universitas Antwerpen, Standaard boekhandel. Dimensioneren tegen vermoeing.

2. H.J. SCHIJVE 1980 Pt/Werktuigbouw 35, 3, 152-161. Vermoeiing onder een veranderlijk wisselende belasting.

3. E. VERDONCK 1982 Proceeding 2 of 7th International Seminar on Modal Analysis, K.U. Leuven. Response Calculation of Dynamical Structures.

4. J.W. YOUNG and J. JOUNIDES Development of Test-derived Strain Modal Models for Structural Fatigue Certification of Space Shuttle Orbiter.

5. G.E. FORSYTHE 1957 J. Soc. Indust. Appl. Math. 5, 2. Generation and Use of Orthogonal Polynomials for Data-fitting with Digital Computer.

6. H. SOL 1983 Een eindig elementenprogramma voor ontwerp van tennisracketten, rapport V. U.B. Tennis (Deel III-B).

7. H.O. FUCHS and R.I. STEPHENS 1980 Metal Fatigue in Engineering. New York: J. Wiley and Sons.

15. MACHINERY

NOISE ENERGY RADIATED FROM ROD-LIKE STRUCTURES

L.C. Chow and J.M. Cuschieri*

Institute of Sound and Vibration Research
University of Southampton

1. INTRODUCTION

Drill rods are highly stressed components transmitting a great deal of energy. Some of the energy input to the rod excites the rod in flexural vibration. However, the fraction of energy that goes into vibration is very small, in the order of 10^{-2}, but this still makes rock drilling a noise hazardous operation [1]. Typically the SPL from a drill rod is about 110 dB 1 m away from the drill. Thus the understanding of the noise generation mechanism in rock drills is important to control the noise other than the exhaust noise if a new generation of quiet rock drills are to be designed. Using an energy accountancy concept, the noise radiated from a solid hexagonal rod and a tubular rod is investigated to obtain the parameters that influence the radiated noise. The operation of the drill is a consecutive series of impacts on the drill rod, thus the tailoring of this impact is investigated for noise control and drilling efficiency.

2. THE NOISE ENERGY CONCEPT AND RESULTS

The noise radiated by a machinery structure due to an impact is estimated using an energy balance between the input, radiated and dissipated energy [2]. The sound radiated from a structure expressed in L_{eq} per event at any frequency is given by:

$$L_{eq}(f_o, \Delta f) = 10 \log E_{escape}(f_o) + 10 \log \left[\frac{\sigma_{rad}}{\sigma_{rad} + (\rho_m/\rho_o c_o) 2\pi f_o d \eta_s} \right] \quad (1)$$

where E_{escape} is the total vibrational energy that escapes into the structure; σ_{rad} is the radiation efficiency at frequency f_o; η_s is the structural loss factor; ρ_m, ρ_o are the density of steel and air, respectively, c_o is the speed of sound in air, and d is a measure of the average component thickness.

For most machine structures the loss factor is relatively high, of the order of 0.01; the above relation is written in A-weighted form as:

$$L_{eq}(A, f_o, \Delta f) = 10 \log E_{escape} + 10 \log(\text{spectral content}) + 10 \log\left(\frac{A\sigma_{rad}}{f_o}\right) - 10 \log \eta_s - 10 \log d + \text{constant} \quad (2)$$

where A is the A-weighting function.

---

*Now at Department of Ocean Engineering, Florida Atlantic University, Boca Raton, USA.

The first two terms in this equation are related to the force spectrum and the structure response, that is,

$$E_{escape}(f_o, \Delta f) = \frac{\Delta f}{\pi f_o} |\dot{F}(f_o)|^2 . \mathrm{Re}\left[\frac{H(f_o)}{j}\right] \quad \text{per impact} \tag{3}$$

$H(f_o)$ is the point response defined by $V(f_o) = \dot{F}(f_o)H(f_o)$, where $V(f_o)$ is the Fourier transform of the normal velocity of the structure at the point of impact and $\dot{F}(f_o)$ is the Fourier transform of the input force derivative.

2.1 The Relevant Parameters in Predicting the Radiated Noise Energy

The force pulse in the time domain can be more readily measured but the use of a frequency analyser is necessary if an energy spectrum of such an impulse is needed. The force derivative spectrum is used because for relatively short impacts it is effectively flat at the dominant frequencies. In this investigation an approximate spectrum shape and magnitude is used [3] to estimate the noise energy radiated from the drill rods.

In estimating the radiated noise in broad bands, an average value for the structure response can be used; the average level being the geometric mean between the resonances and antiresonances. This approach is more justifiable at high frequencies where the modal density is high. For a beam structure the mean point response in flexure is given by [4]:

$$\mathrm{Re}\left[\frac{H(f_o)}{j}\right] = \frac{1}{8\pi S\rho_m \sqrt{2\pi f_o}^3} \left(\frac{S\rho_m}{EI}\right)^{\frac{1}{4}} \tag{4}$$

whereas for a thin cylindrical shell structure the response is

$$\mathrm{Re}\left[\frac{H(f_o)}{j}\right] = \frac{1}{16\sqrt{\frac{\pi}{a} B\rho_s c_\ell f_o}} \tag{5}$$

where $B\rho_s = \dfrac{Ed^4\rho_m}{12(1-\nu^2)}$, $\quad c_\ell = \sqrt{\dfrac{E}{\rho_m}}$ and S is cross-sectional area.

The radiation efficiency of a long circular pipe vibrating in flexure is a function of both the number of acoustic wavelengths in one circumference 'ka', and the radial wavenumber '$k_d a$'. An approximate curve for the radiation efficiency of a circular rod is given by [2]:

$$\begin{aligned} \sigma_{rad} &= 1.55 \times (k_d a)^2 (ka) \quad \text{for} \quad 0 < k_d a < 0.9 \\ \sigma_{rad} &= \frac{ka}{k_d a} \quad \text{for} \quad k_d a > 0.9 \end{aligned} \tag{6}$$

where $k_d a = ka\left(1 - \frac{f_c}{f}\right)^{\frac{1}{2}}$; $\quad f_c = \dfrac{c_o^2}{2\pi c_\ell \bar{\kappa}}$; $\bar{\kappa}$ is the radius of gyration associated with the second moment of area of the cross-section, f_c is the coincidence frequency of the structure and a is the radius of rod.

The structural loss factor is measured rather than estimated for the two rods. When the rods are fixed to other structures the loss factor measured represents both the energy lost within the rod and also the energy that escapes into other structures.

The constant term $10 \log(\frac{\Delta f \, \rho_o c_o}{f_o 2\pi^2 \rho_m})$ is given by -32 dB for a steel structure in air for 1/3 octave band frequency analysis.

2.2 Measurement of Noise with Freely Suspended Drill Rods

The noise measurements were done on a hexagonal rod (22.5 mm A/F) and a hollow cylindrical rod (57.2 mm diameter and 3.2 mm wall thickness) of length 1.33 m. Most of the radiated noise is due to flexural vibrations, thus in the first test a transverse impact force was applied with the rod suspended horizontally. The impact was from a calibrated hammer.

All the terms in equation (2) were either measured or estimated and thus the noise energy radiated per impact could be estimated. The structural loss factor of the rods in this position is low, hence equation (1) is used in predicting the radiated noise energy. Noise measurements were carried out using an array of microphones positioned on an imaginary cylindrical surface 1 m away from the rod. The A-weighted measured sound energy is compared with the estimated results (figures 1.1 and 1.2) and the agreement between the two curves is good. The overall estimated and measured noise levels are very close. The differences between the estimated and measured level in each one-third octave frequency band is because the modal density is low and the resonances in the structure response varies from the mean response, but there is good agreement in the overall noise level.

The loss factor of the rods was increased by applying the damping tape. In this case the loss factor approached more what is obtained in practice when the rods are fixed in the chuck. Comparing the measured and estimated radiated noise levels, the agreement in this case is much better (figures 1.1 and 1.2). The structural loss factor was of the order of 0.001 and thus equation (2) was used to obtain the estimated noise levels.

2.3 Noise Radiation with Drill Rods in Vertical Position

Similar experiments were carried out with the drill rods positioned vertically on a concrete block and excited by a longitudinal impact from a drop mass on the shank end of the rod. Noise measurements were carried out at a distance of 0.5 m from the drill rod.

In this case another estimate for the radiated noise energy was obtained by measuring the spatial average surface velocity over the rod surface, i.e., estimating the radiated noise from $E_{rad} = \rho_o c_o S \sigma_{rad} \langle \bar{v}^2 \rangle$. Comparing the measured noise energy with the estimates using $\langle \bar{v}^2 \rangle$, the measured levels are higher at low and high frequencies. This is because of other background noise from the supporting rig and from the rock rod impact. The acceleration noise level is very low and has no effect on the measured noise levels [5]. Adding the background noise to the estimated radiated noise using $\langle \bar{v}^2 \rangle$, better agreement is obtained between the measured and estimated levels [1].

The noise radiated in this case is still due to flexural vibration, even though the drill rod is impacted longitudinally. The vibrations of the rod due

to Poisson's effect are negligible. This is verified by placing two accelerometers on opposite faces of the rod. The two signals were completely out of phase, indicating that the two surfaces were moving in the same direction, i.e., the rod vibrated only in bending motion.

The flexural motion of the rod is possible because the impact on the rod is not exactly square. This also happens during the drilling operation. Assuming that the impactor mass hits the rod at some angle, then part of the input force is in the transverse direction which excites the flexural modes of the rod. The magnitude of this fraction of the impact force cannot be measured; however an estimate for this angle can be obtained by comparing the radiated noise to an estimate using equation (2). The estimated angle is well within the accuracy of the test rig [1].

The fraction of the energy that is radiated as noise using the $\langle \bar{v}^2 \rangle$ estimates is very small, only 0.045% of the input energy for the hexagonal rod and 0.15% for the cylindrical rod. The reason for the higher fraction of energy for the cylindrical rod is that the latter has a better radiation efficiency. Also the coincidence frequency for the cylindrical rod is lower and the level of the structure response is higher, because of the hollow nature of this rod.

From these results it can be concluded that the energy concept predicts the noise energy radiated to reasonable agreement and thus this concept can be used to investigate ways of tailoring the rod parameters to control the radiated noise energy. One of the methods which will give large reductions in noise is the tailoring of the impact and the structure response. However, the relation between energy transfer through the rods and the impact and rod cross-section must be studied before tailoring of these parameters for noise control is investigated.

3. ENERGY TRANSFER MEASUREMENTS AND RESULTS

The rate of energy transfer through the rod is obtained from the input force pulse and the rod end mobility. In the case of multiple impacts, only the first impact is considered and the subsequent impacts are much smaller in magnitude. Tests on energy transfer were done with the drill rod interfacing different structures: mainly a concrete block and a steel cone on both the large and small ends.

With analogy to the propagation of sound in ducts of varying cross-section, the transmission efficiency is given by [6]:

$$\tau = \frac{4}{\left(\sqrt{\frac{z_1}{z_2}} + \sqrt{\frac{z_2}{z_1}}\right)^2} \qquad (7)$$

where z_1 and z_2 are the impedances of each cross-section, or in the case of structures z_1 and z_2 are the point impedances of the structures at the interface. This relation assumes that there are no losses at the interface of the structures.

The energy transferred through the interface is measured by having a force load cell at the tip of the rod. Then comparing the measured to the theoretical results (table 1) there is a large difference of about 40%. This is because the theoretical values are based on the assumption that there are no losses at the discontinuity. In the case of the rod freely touching the concrete block

the rod rebounds and therefore some of the energy goes back into the rod. Hence the theoretical prediction can only be regarded as an upper bound. When the rod is fixed, better agreement is obtained. There is no rebound of the rod and therefore less losses at the interface.

From the table it can be seen that the percentage of the energy transferred using a cylindrical drill rod is about 2.5 times that using a hexagonal drill rod of smaller cross-sectional area. Thus from these results, the transfer of energy is more efficient using a larger size rod.

The effect of the impact force shape on the energy transferred is investigated by using inserts of aluminium, hardboard, soft PVC, wood and soft rubber to alter the impact contact time. It was observed that the change in the impact shape did not alter the energy transmission efficiency for the case of the cylindrical drill rod, although it did for the hexagonal drill rod. The reason for these results is as follows: by increasing the impact time, the corner frequencies of the force derivative spectrum are shifted to lower frequencies. For the cylindrical rod the mean value of the real part of the mobility is constant with frequencies and thus constant energy is transferred between the top and bottom of the rod. The different impact times do not alter the transmission efficiency at the rod-rock discontinuity. However, for the hexagonal drill rod, the mean value of the real part of the mobility varies with frequency. It is lower at mid to low frequencies, thus more energy is transferred by the rod the shorter the impact time.

3.1 Transmission Efficiency

The transmission efficiency at the rod-rock contact depends on the change of impedance or mobility at the contact point. Matching of the mobility between the rod and the interface will result in a high transmission efficiency. In the tests the optimum efficiency obtained was from the cylindrical drill rod onto the small end of the steel cone, followed by the large end of the cone, the concrete block with fixed end, and the concrete block just touching the rod. The real part of the mobility of the cylindrical drill rod is of the same order of magnitude as the real mobility of the small steel surface area resulting in a high energy transmission efficiency [1].

3.2 Energy Dissipation in the Flexural Vibration

An experiment was carried out to estimate the percentage of input energy that is dissipated in flexural vibration by the rod. With the hexagonal rod impacting the steel cone on the large surface, the dissipated energy is calculated from the definition of the loss factor. The spatial average surface velocity is measured and the dissipated energy is computed using the measured average loss factor of 0.01. The dissipated energy was about 3% of the input energy, thus most of the energy goes into longitudinal vibration.

3.3 Ground Penetration

Tests were carried out to investigate the effect on penetration due to different impact times and force magnitudes. These tests were done in sand but no attempt was made to obtain the parameters of the sand. However, for each impact test the sand is compressed with the same force. The average penetration over five blows was taken in each case. For a constant input force magnitude (fig. 2.1), the results show that increasing the impact time increases the penetration. More energy is available to do work. The increase in penetration is linear with contact time for short impacts, and then the curve levels off as

the contact time continues to increase. For the same drop height (fig. 2.2), i.e., the same energy of blow, the penetration decreased with increasing contact time. The relationship between the penetration and the contact time is not linear.

The penetration of the hexagonal rod is larger than that of the cylindrical rod for the same input force, and this can be attributed to the larger friction because of the larger contact area between the rod and the ground as drill penetration starts.

4. CONCLUSION

From knowledge of the impact force, the rod structural point response, the structural loss factor, radiation efficiency and bulkiness factors, the noise radiated by the rod can be estimated. This equation can also estimate the change in the noise energy level if any of these parameters is altered. Also a bigger size rod radiates more noise, 8 dB(A) higher in this test (fig. 1.3) for the same input force. The radiated noise energy is only a small fraction (less than 1%) of the input energy and has no effect on the operation efficiency of the rod.

The damping of the drill rod is usually high because of friction losses between the rod and rock and the rod and holding chuck; thus a further increase in loss factor is not practical. Hence, other noise control methods, such as changes in the structural response or the impact force, must be used.

Using inserts to tailor the impact, the effect of changes in the duration indicate that from the operation of the drill viewpoint, increasing the contact time increases the amount of energy provided that the force magnitude remains the same. The result of this is that the operation of the drill is not affected even though a larger drill is used and if the impact is long enough, such that there is a mismatch between the modified radiation efficiency peak and the force derivative spectrum peak, then a significant reduction in noise will be obtained.

Consider the energy transfer through the drill rod, the larger the size the better since the transfer of energy depends on the mobility matching at the discontinuity. Also, increasing the size of rod increases the radiated noise for the same input force, but for a constant energy transfer, larger size drill only needs a smaller impact which results in a reduction in the radiated noise energy. However, the resistance in ground penetration also increases and this has to be taken into account in a new design using a larger size rod since this may also affect the drilling efficiency. For the same rod size, the shape of the rod does not have any significant effect on both the transfer of energy and the radiated noise.

For applying these results in practice, consideration of not only the performance of the drill but also the modification cost must be included. Commercial percussive drilling units have an impact rate of over 40 blows per second. The softening of the impact to control the radiated noise is limited. The interval between impacts for 40 impacts/second is of 25 ms, thus by softening the impact, the contact time cannot exceed this interval or it will result in a drop in the drilling performance. This kind of treatment is therefore not always considered to be very popular. However, it must be kept in mind that increasing the contact time also increases the amount of energy transfer, thus the same performance of the drill can be maintained by the proper choice of impact duration and impact rate.

The use of larger size rods also has other disadvantages. Most drill rods used in percussive drilling are standardized in size and various end bits can be fitted appropriate to the particular job. Thus, by using different size rods the operator of the new drill must acquire another set of end bits until all the old drills (standard size drills) are phased out either through age or by legislation, controlling the maximum noise levels in mines. Until this legislation arrives, the operator will be reluctant to carry more tools, and also because of the extra costs involved. However, if it is stressed that the new rods may be more efficient, in the long run the new design drills will be acceptable by operators both for efficiency and noise control.

References

1. L.C. CHOW 1983 University of Southampton, M.Sc. Dissertation. Energy propagation along and noise radiation from impacted rods and tubes with application to rock drilling.

2. E.J. RICHARDS 1981 Journal of Sound and Vibration 76(2), 187-232. On the prediction of impact noise, Part III: Energy accountancy in industrial machines.

3. J.M. CUSCHIERI and E.J. RICHARDS 1983 Journal of Sound and Vibration 86(3), 319-342. On the prediction of impact noise, Part IV: Estimation of noise energy radiated by impact excitation of a structure.

4. E. SKUDRZYK 1980 Journal of the Acoustical Society of America 67, 1105-1135. The mean value method of predicting the dynamic response of complex vibrators.

5. E.J. RICHARDS, A. LENZI and J.M. CUSCHIERI 1983 Journal of Sound and Vibration 90. On the prediction of impact noise, Part VI: The frequency distribution of acceleration noise.

6. L. CREMER and M. HECKL 1973 Structure-borne Sound. Heidelberg, Berlin, New York: Springer-Verlag.

Table 1. Theoretical and measured energy transfer of rods at discontinuity.

% of energy transfer from / Cushion pad inserted	hexagonal rod on concrete block	hexagonal rod on to large end of steel cone	hexagonal rod on to small end of steel cone	hexagonal rod fixed on to concrete block	cylindrical rod on concrete block	cylindrical rod on to large end of steel cone	cylindrical rod on to small end of steel cone	cylindrical rod fixed on to concrete block
no insert	2.2	12.3	21.0	12.5	7.6	34.0	59.0	23.2
aluminium	2.1	11.5	20.5	12.0	8.0	36.5	61.4	22.4
hardboard	1.4	4.0	7.1	4.3	9.5	37.9	70.0	21.4
soft PVC	0.8	2.8	4.9	2.4	9.3	34.6	60.8	23.0
plywood	0.7	2.6	4.8	2.2	7.3	35.0	61.4	21.3
soft rubber	0.3	2.0	4.4	2.0	5.9	35.7	68.5	22.4
Theoretical estimated transmission efficiency in %	5.8	9.0	60.0	14.4	29.0	43.0	98.0	23.0

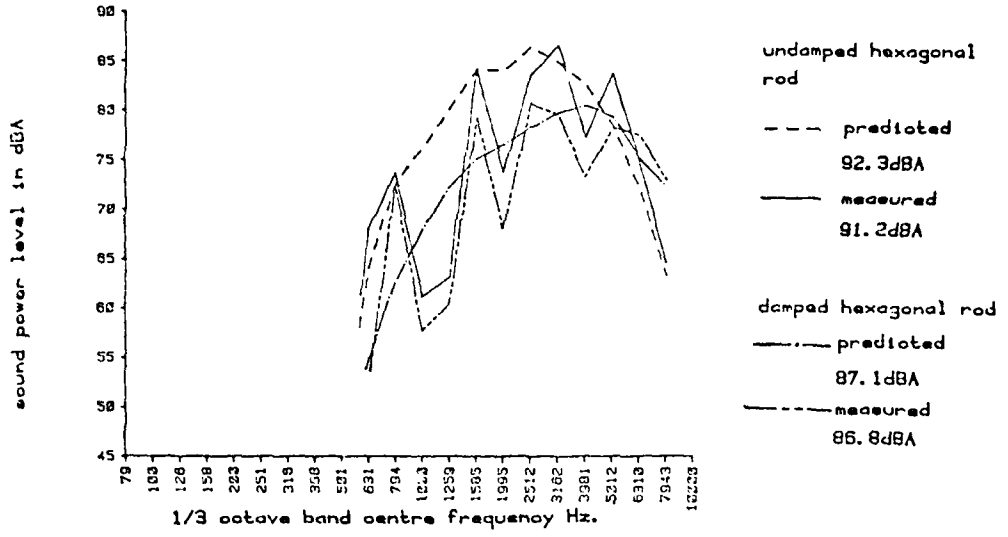

Figure 1.1 Comparison of predicted and measured noise radiation from hexagonal drill rod

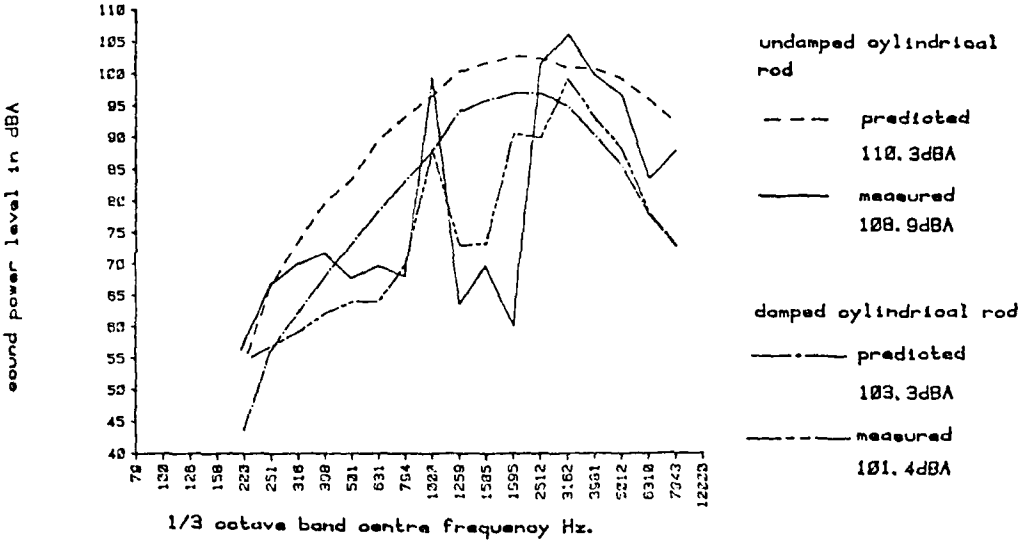

Figure 1.2 Comparison of predicted and measured noise radiation from cylindrical drill rod

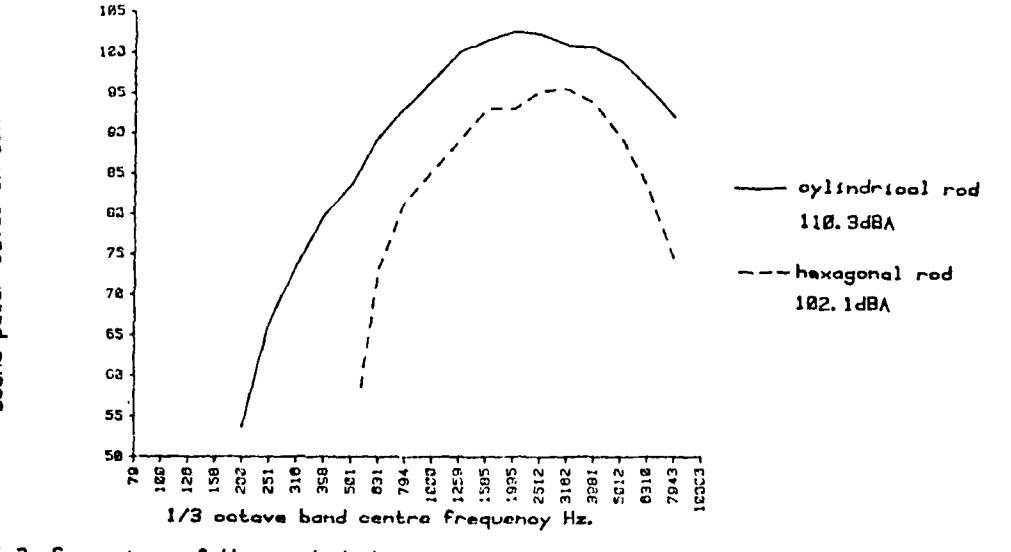

Figure 1.3 Comparison of the predicted noise radiation from the hexagonal and the cylindrical rods

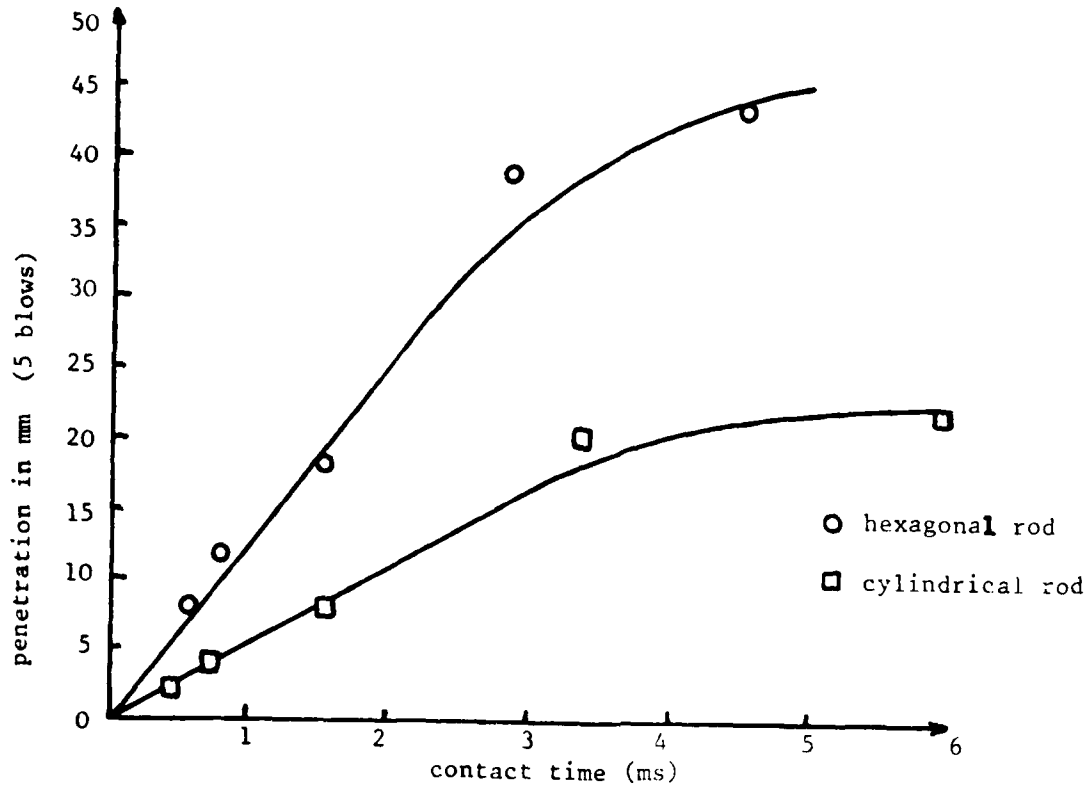

Fig. 2.1 Rod penetration vs pulse contact time (same input force magnitude).

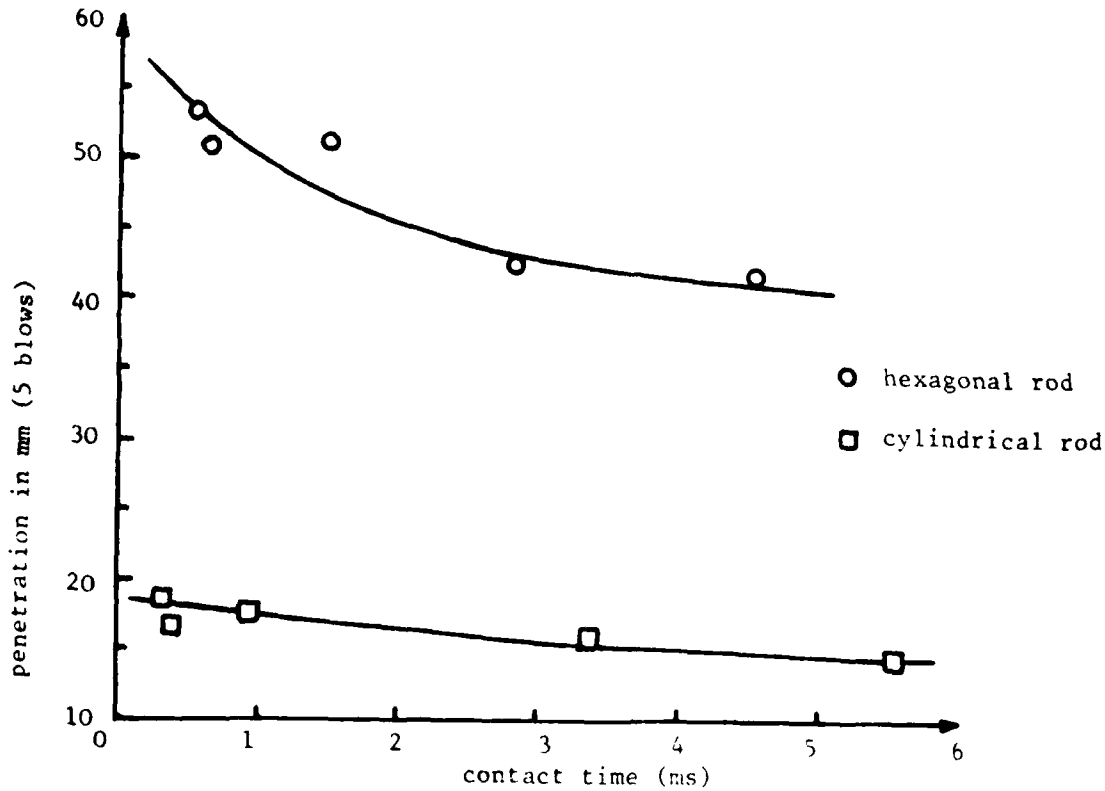

Fig. 2.2 Rod penetration vs pulse contact time (same drop height of hammer).

USING A SCALE MODEL TO INVESTIGATE THE POST FRACTURE STRUCTURAL VIBRATIONS AND NOISE OF A 200 TONNE POWER PRESS

G. Stimpson

Institute of Sound and Vibration Research
University of Southampton

1.0 INTRODUCTION

Power presses are used extensively in the metal working industries for the production of many types of components ranging from small electrical tags to large car body panels. This type of machine often poses a substantial noise problem, the noise emanating basically from the surface vibrations of the press structure. Because of their generally massive construction and the need for continuous access for material or component feeding, they are difficult to quieten by conventional acoustic techniques such as enclosure. Noise control at source offers a much better solution if this can be achieved without compromising working efficiency.

Machinery noise control at source implies control of structural vibration (unless other non-structural sources are present, e.g., air jet or combustion noise, etc.). A detailed knowledge of how the machine operates, how forces are applied to the structure, how the structure responds, vibrates and ultimately radiates noise is required. Mechanical power presses are relatively complex noise producers having many individual sources which combine to give the overall radiated noise. The dominant source, however, during conventional blanking or piercing of metal are the high levels of transient structural vibration induced by the fracture of the workpiece material.

The press structure, having finite stiffness, acts like an enormous spring; it is loaded relatively slowly as the punch contacts the workpiece which deforms first elastically then plastically and begins to shear (see fig. 1). As material shearing continues, the material cross-sectional area is progressively reduced until a point is reached where the remaining material can no longer support the applied load. The material then suddenly fractures and the structure snaps back "unrestrained" and oscillates transiently around its equilibrium position until all the energy has been dissipated. The transient vibration radiates noise and can also lead to high rates of press wear due to the backlash impacts which occur in the drive linkage.

As part of a joint ISVR/CETIM project into power press noise and its control, the noise and vibrational characteristics of a 200 tonne straight-sided mechanical power press are being investigated. Detailed measurements on the actual press posed many practical problems and thus a simplified scale model of the structure was constructed.

The great advantage of a model was not only that it allowed detailed measurements to be made in the laboratory but it provided the capability to study the effects of structural modifications which would be totally unpractical on the full-sized press.

2.0 MODELLING THE PRESS

The model was based on a BRET 200 tonne straight-sided, crankshaft driven, mechanical press of relatively conventional construction. The main frame structure was fabricated from a number of steel plates welded together which made modelling relatively simple.

The aim of the model was not to be an exact replica of the existing press but as an investigative tool representing and isolating the important details of the structural characteristics. As it was only the noise related to the work-piece material fracture which was of prime concern in the current study and as this is related primarily to the material properties and tooling used, it was not necessary to copy the complex drive and operating system of the press. Instead, the model was powered by a simple hydraulic cylinder and hand pump. Also not modelled were complex fabrications at the top of the press, as these served mainly to support and house the drive mechanism. A photograph of the completed model press is shown in figure 2.

2.1 Scaling

A scale of 1/3 on overall dimensions was used. This was chosen so that the model would be small enough for practical measurements in the laboratory and yet still large enough so that the vibration and noise radiation characteristics were truly representative of the actual press. This gave a model height of approximately 1.3 m.

A direct scaling of 1/3 was not used, however, as to maintain equivalent working stresses in the side frames of the structure this would have meant a model with a capacity of over 20 tonnes. In order to reduce model loading to a more practical level ($\sim$ 6 tonnes) a scale of 1/10 was used on material thicknesses.

Although the 1/3 on length and breadth and 1/10 on thicknesses scaling is not a direct dimensional scaling, it does represent approximately a direct vibrational scaling. This is because the natural frequencies of panel vibrations will be approximately the same on the model and full scale for this scaling, thus modal densities and other vibrational characteristics are directly comparable. The actual noise radiation by the model will be quite different, however, as the 1/10 thickness panels will have a correspondingly 10X higher coincidence frequency and thus be far less efficient at radiating sound from low frequency vibrations.

It was therefore more relevant to compare the model vibrations (rather than radiated sound) to those of the full-scale press. Sound radiation from the full-scale press can be predicted from the model by applying measurements of panel vibrations on the model to the actual panel dimensions (hence radiation efficiencies) on the full-size press.

2.2 Loss Factor

The amount of inherent structural damping is a major factor in the vibrational and noise radiation characteristics of machinery structures. It has been shown that for impact excitation of practical structures, noise radiation is directly proportional to the structural loss factor (1).

The loss factors of the various panels of the model were measured and matched (if necessary, by the application of strips of damping tape) to measurements made on comparable panels of the full-scale press. In general the loss factors of the press structure are relatively low (fig. 3), typically $\eta \sim 8 \times 10^{-3}$ because of the welded construction. Thus there was reasonable scope for improvement.

The loss factors were measured by the decay rate method, on the built-up structure. The results, therefore, represent a measure of the rate of energy loss from the particular regions of the structure and are not absolute measures of the damping associated with each individual panel.

3. ESTIMATION OF SOUND ENERGY FROM THE VARIOUS PARTS OF THE MODEL

3.1 From Surface Vibration Measurements

The sound energy radiated (E) from the various parts of the model structure was estimated using the well-known relationship:

$$E = \rho c \, \sigma_{rad} \, S\langle \bar{v} \rangle^2$$

where ρ = air density; c = speed of sound in air; σ_{rad} = panel radiation efficiency; S = panel surface area; $\langle \bar{v} \rangle$ = space-time averaged surface velocity.

The model is well suited to this type of analysis, being constructed from steel plates giving clearly defined panel type radiating areas.

The space and time-averaged surface velocity was calculated from a number of randomly positioned accelerometer measurements on each of the press panels. Excitation of the structure was by piercing 20 mm diameter holes in 2 mm thick hot rolled steel.

As a number of the panels on the model are relatively thin, they will have a correspondingly high coincidence frequency, $\sim$ 8 kHz for the columns and side panels. The majority of the sound energy radiated by these parts of the structure will be radiated, therefore, at frequencies well below the coincidence frequency. Thus, the accuracy of the radiated energy estimations will be very dependent upon the values of radiation efficiency weighting used.

Accurate values of radiation efficiency for panels with complex edge conditions are not available. The best approximations which could be made was to assume panel vibrations with simply supported edge conditions and use the theoretical radiation efficiency formulae quoted by Beranek (2).

3.2 Sound Intensity Measurements

At the same time as the surface vibration measurements were being made on the model, measurements were also made of the near field sound intensity radiated by the structure. Details of the technique are contained in ref. 3 and 4.

Direct measurement of sound intensity, especially from transient noise sources is a relatively newly developed technique and as such its potential and usefulness in machinery noise studies is only just being explored. The concurrent measurements provided an opportunity to compare the intensity technique with the more established method of estimating the radiated sound energy from surface velocity measurements.

3.3 Results

The noise radiated from the various parts of the model estimated by the two techniques is shown in figs. 4 and 5. Some detailed individual differences were apparent but in general agreement was reasonably good in most cases within 3 dB. The total radiated sound energy obtained from both methods gave surprisingly similar results (4.5×10^{-3} J by both methods) and compared well with measurements of the total far field sound energy (6.7×10^{-3}J), see fig. 6.

Comparing the two techniques it was apparent that both methods had inherent advantages and disadvantages for use in noise source location on structures. The obvious major advantage of the intensity technique is that it is the actual acoustic radiation which is being measured and thus eliminating the need for the often approximate radiation efficiency weighting. However, the technique does possess inherent errors at low and high frequencies and also measurements can be contaminated by radiation and reflections from other dominant radiating areas. The surface vibration technique can thus be more effective in isolating closely spaced sources radiating vastly different amounts of sound energy.

3.4 Measurements of Radiation Efficiency

As both the sound radiation from the individual structural panels and their surface vibration was measured, an actual value of radiation efficiency could be obtained, i.e.,

$$\sigma_{rad} = \frac{E_{rad}}{\rho c\, S\langle \bar{v} \rangle^2}$$

E_{rad} from intensity measurements

$\langle \bar{v} \rangle^2$ from surface vibration measurements

Measured values are shown plotted along with theoretical curves for simply supported plates in fig. 7.

In general the results indicated that the thin side panels and columns of the structure were radiating more strongly below coincidence, than was predicted for simply supported plates. It must be concluded that this is due to the complex edge conditions of the panels and the stiffening effect of the welds.

4.0 INCREASING THE STRUCTURAL DAMPING

The structural damping of the model was increased by adding sand into the various hollow sections of the structure. Experiments have shown that sand is a very effective damping medium and very applicable to machinery structures, such as the press, which have numerous internal cavities.

Structural loss factors were increased to $\eta \sim 1 \times 10^{-1}$ by filling with sand as is shown for the columns of the model in fig. 3. This led to a reduction of ~10 dB(A) in the noise radiation when the treatment was applied throughout the structure.

4.1 Prediction of Damping Loss Factors using S.E.A.

Statistical Energy Analysis (S.E.A.) gives a method by which loss factors and vibrational energy distribution within a complex structure can be calculated (5). Such information is very useful in machinery noise control work so that damping treatments for a particular machine can be optimised.

Experiments applying these techniques to industrial type structures and machines are at present under way and are proving very effective in calculating loss factors. The calculated loss factors for the side panel of the model are shown in fig. 8 and show good agreement with the measured values.

5.0 OTHER METHODS OF REDUCING STRUCTURAL RESPONSE

It is the amount of strain energy stored in the structure prior to workpiece material fracture which governs the vibrational energy level which follows (for constant material fracture characteristics). Thus, for a given tooling force the vibration and noise energy level is directly related to the structural stiffness.

Experiments with the model have shown that the bed plate is an important component in the structural response. Placed in bending in the loaded structure it can store a high proportion of strain energy and then act to feed vibrational energy to the rest of the structure. Tests have been carried out with various bed/structure couplings but as yet with little effect on overall response. However, experiments with a stiffened bed plate led to a further 2.2 dB reduction in noise when used with the damped model.

It is the sharp changes of input force on a structure which are the important factors in noise production. In this case the unrestrained structural springback following workpiece material fracture. Smoothing the input force pulse as shown in fig. 9 will lead to substantially reduced structural response and noise.

Modifications to the tooling, sheared punches or reduced punch/die clearances are possibly the simplest method of obtaining a smoothed force history. These methods often prove unacceptable in practice because of reduced component quality or greatly increased tooling costs. An alternative method is to use some form of hydraulic damping or cancellation device to oppose the structural springback.

Tests with these types of system (6) have shown that they can be effective but their efficiency is limited by the effective stiffness of the hydraulic cylinders. Experiments are at present being performed with such a system fitted to the model and results will be presented as available.

ACKNOWLEDGEMENTS

The author acknowledges with thanks CETIM, Senlis, France, who sponsored the project. Also, P. Watkinson, ISVR, who performed the sound intensity measurements and Sun Jincai, ISVR, who performed the SEA calculations.

REFERENCES

1. E.J. RICHARDS 1981 Journal of Sound and Vibration 76(2). On the prediction of impact noise, Part III. Energy accountancy in industrial machines.
2. L.L. BERANEK 1971 Noise and Vibration Control, McGraw Hill Book Co.
3. F.J. FAHY and S.J. ELLIOTT 1981 Noise Control Engineering 17(3), 120-125. Acoustic intensity measurements of transient noise sources.
4. P.S. WATKINSON 1982 IOA Autumn Conference, B6, 1-6.4. Acoustic intensity techniques for transient noise sources.
5. R.H. LYON 1975 Statistical Energy Analysis of Dynamical Systems: Theory and Applications. MIT Press.
6. G.J. STIMPSON 1983 Internoise. Damping out punch press noise.

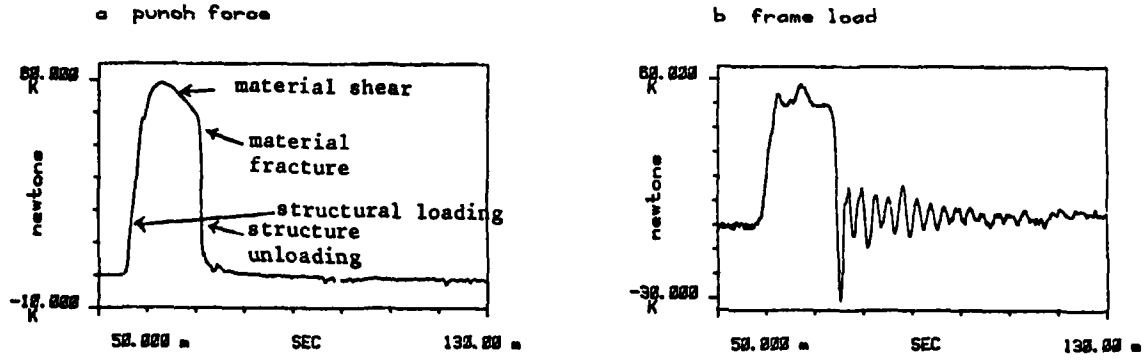

Fig. 1 Force history of normal blanking operation.

Fig. 2 The model press.

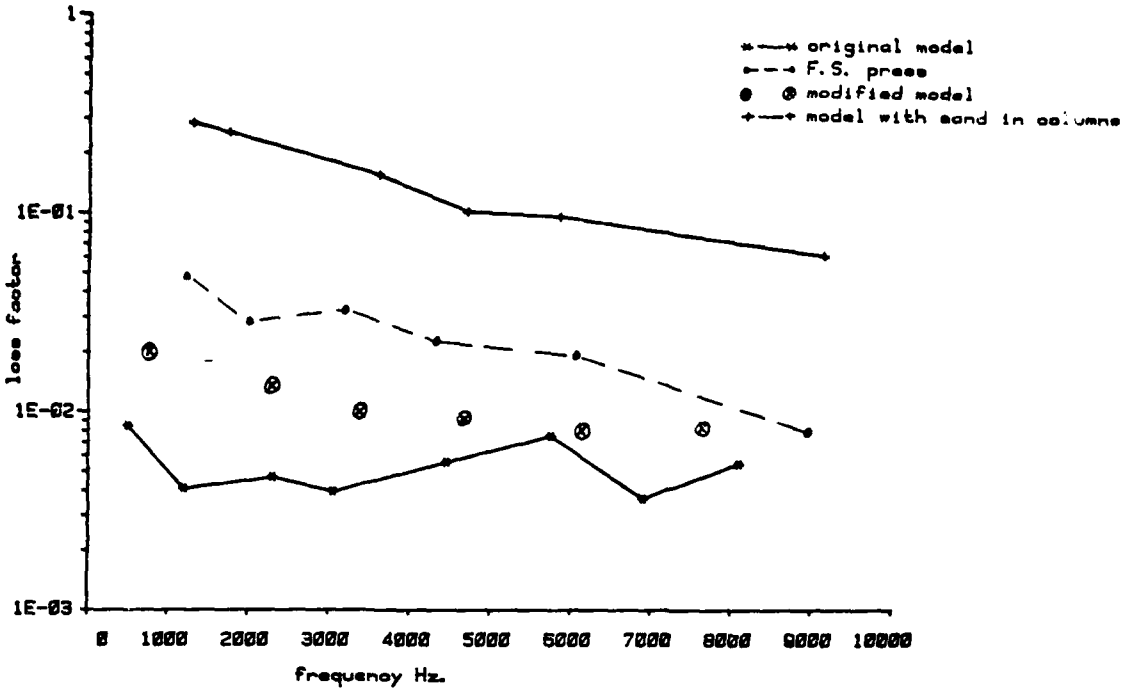

Fig. 3 Loss factors measured on the column

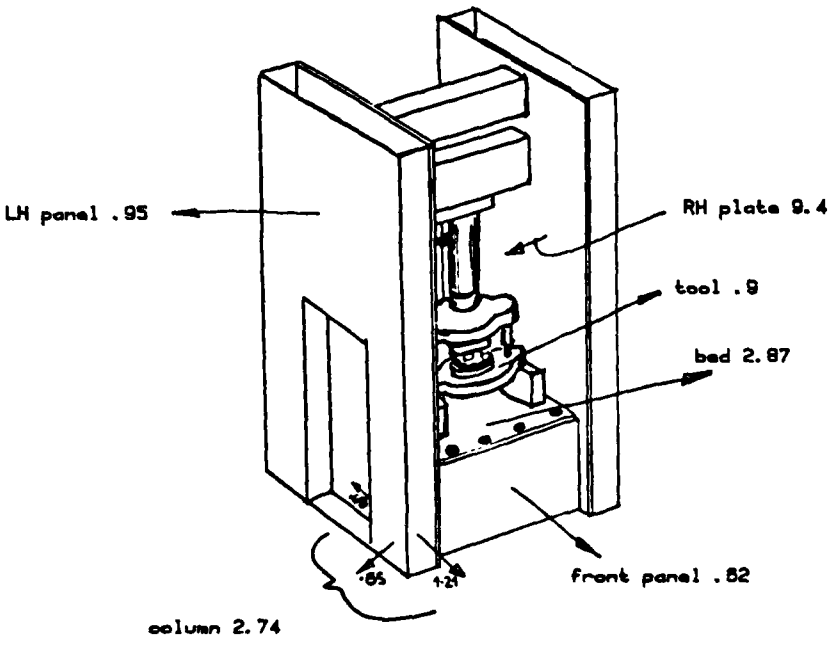

Fig. 4 Radiated sound energy (Joules × 10^{-3}) from surface vibration measurements.

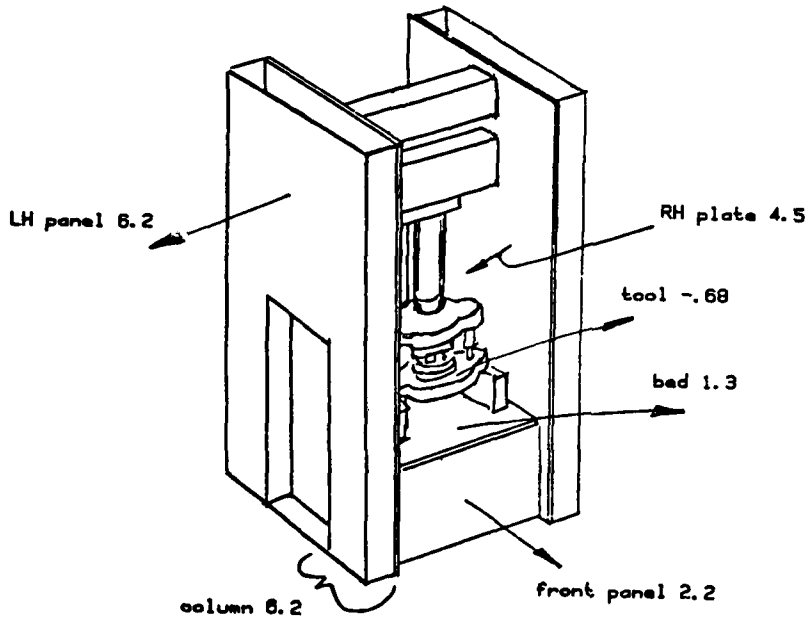

Fig. 5 Radiated sound energy (Joules × 10^{-3}) from intensity measurements.

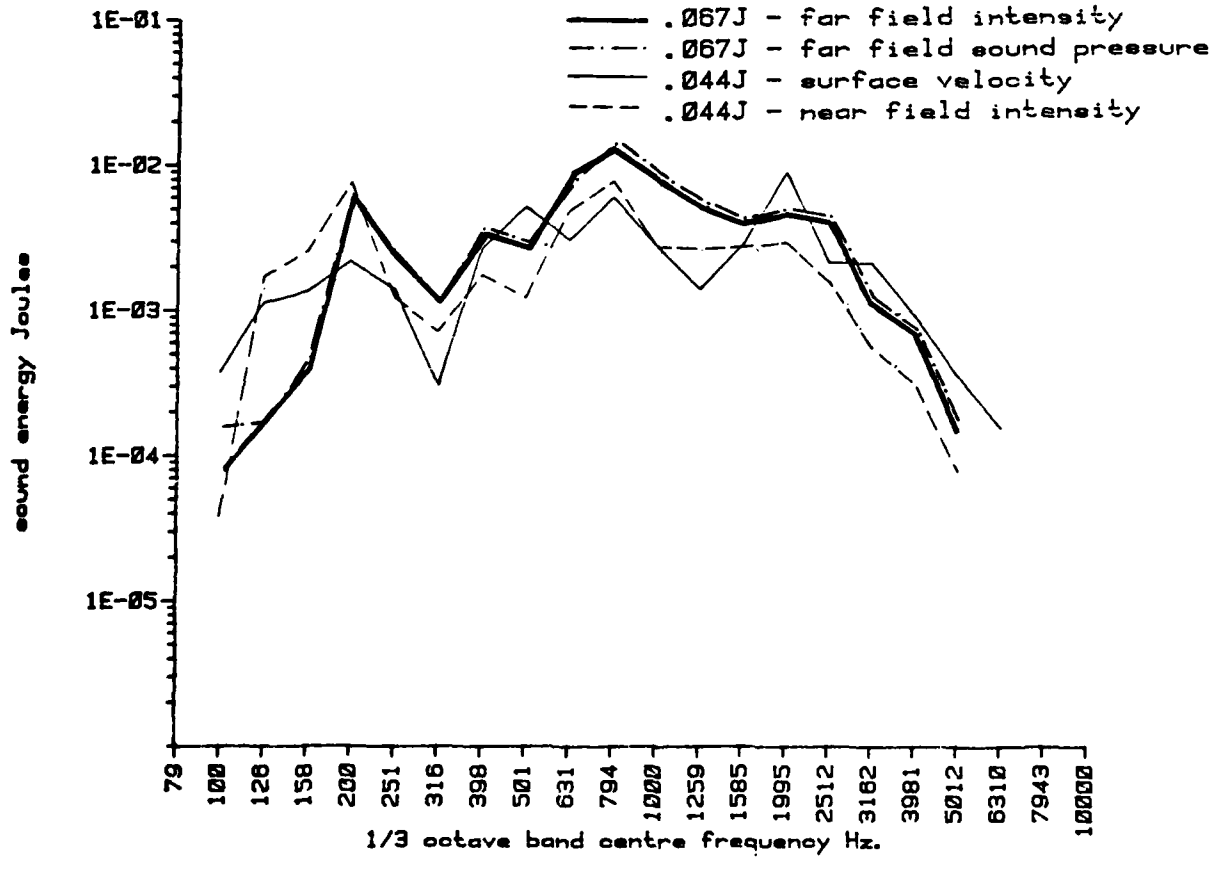

Fig. 6 Total sound energy radiated by the model.

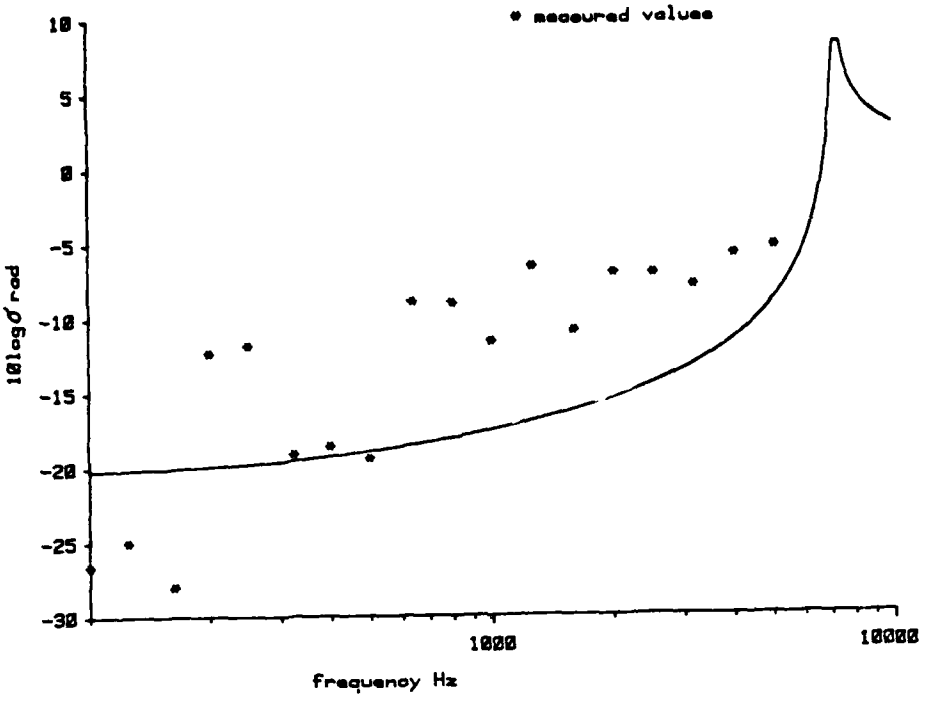

Fig. 7a Radiation efficiency - side plate.

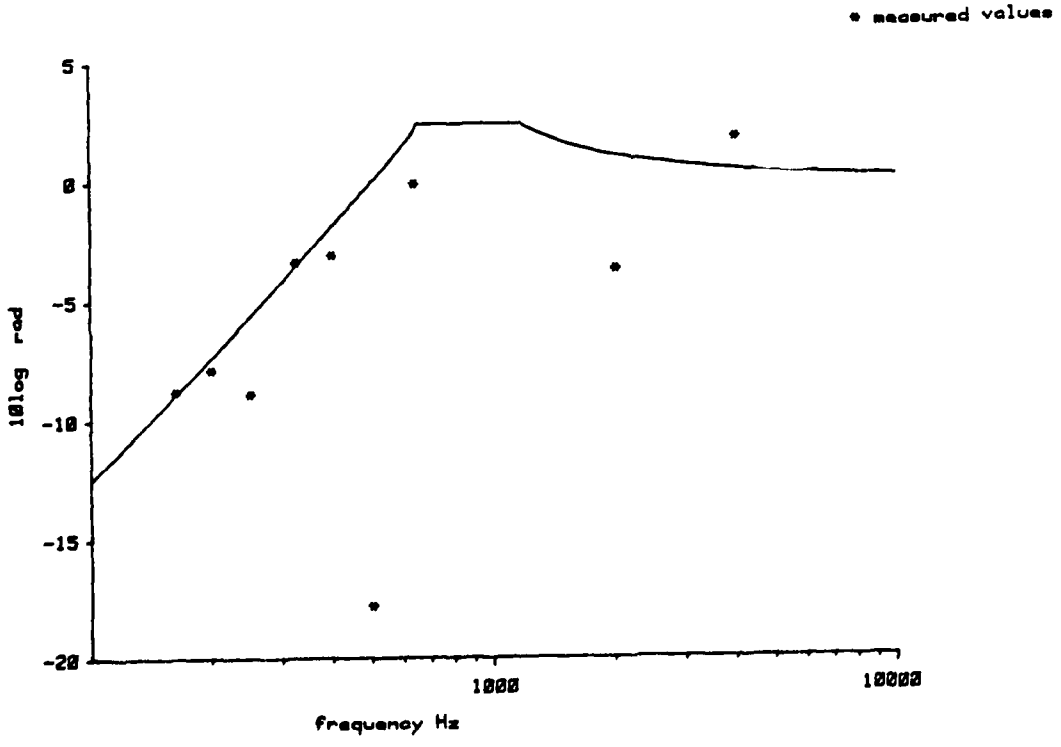

Fig. 7b Radiation efficiency - bed plate.

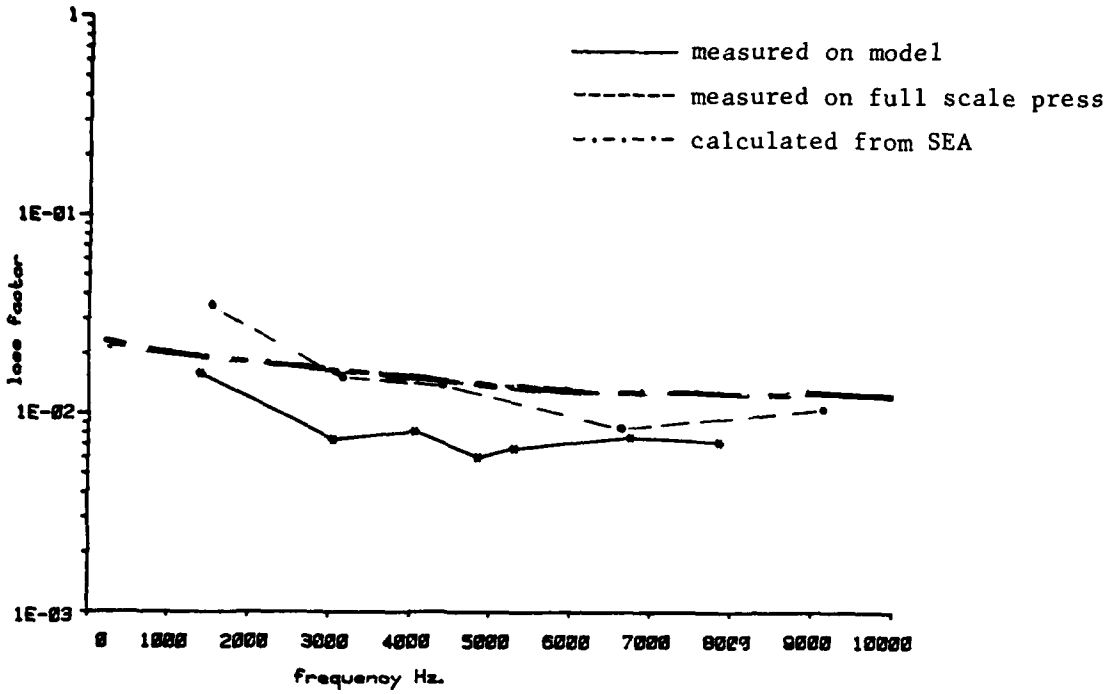

Fig. 8 Measured and predicted loss factors - side plate.

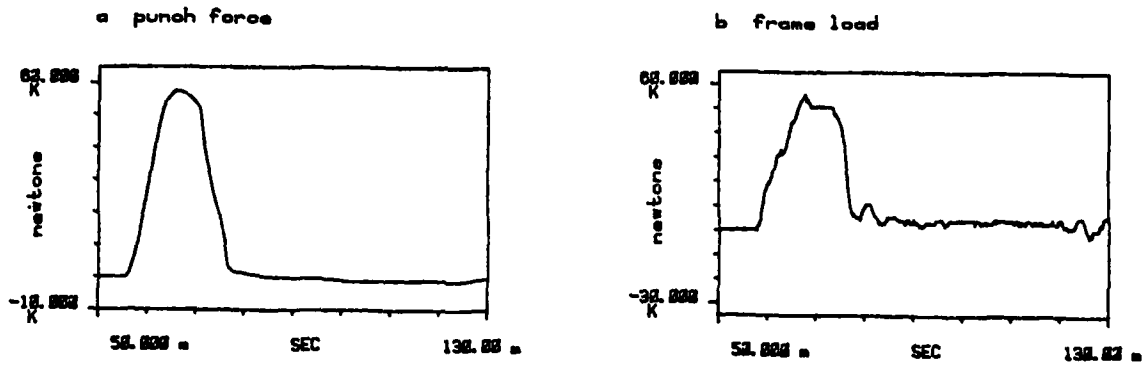

Fig. 9 Force history of smoothed blanking operation

ACTIVE FORCE CONTROL IN MACHINERY NOISE *

J.M. Cuschieri
Department of Ocean Engineering
Florida Atlantic University

*Research performed whilst at the ISVR, University of Southampton, England.

1. INTRODUCTION

The noise radiated from a machine structure is related to the excitation force and the structure response, that is physically the operation of the machine and the machine structure dimensions and shape. Hence to control the noise energy radiated, apart from applying damping, one will have to either modify the excitation force or structure response, by passive or active methods. The use of active vibration control is investigated in this paper.

The damping of a machine structure is usually very high and it is seldom possible to increase the structural loss factor by reasonable amounts to reduce the radiated noise. Also if increasing the damping of the structure is possible, methods of doing so which can withstand the adverse environment of the machine shop must be found. Standard methods such as using viscoelastic material are not very satisfactory and surely their performance will be reduced after only a very short time.

Most machine operations are impulsive in nature and thus one method to control the noise radiated from the machine is to tailor the force pulse, that is to increase the duration of the pulse. However, there may be reasons why this cannot be done and two which are very important are that first if the operation of the machine is cyclic, the duration of the excitation force cannot increase more than the interval between cycles or a portion of the interval due to other operations of the machine. Second, by increasing the duration of the force the machine may be slowed down resulting in lost production.

Thus large reduction in the noise radiated from machine structures can be obtained by either structural changes at the point of impact [1] which can be termed as passive control or by active cancellation of the excitation force. Which of these two methods is most suitable in a particular noise problem will depend on the shape of the excitation force pulse.

If the impact contact time is very short, approximately 1ms, then, in the frequency range where the ear is most sensitive, that is 100Hz to 10kHz, the shape of the force spectrum and consequently the noise radiated will depend on the total shape of the force pulse. Thus in this case the active control system must cancel the whole shape of the pulse to achieve a reduction in noise across the whole frequency range. This will be easy to implement, much more than other forms of control but it is rather impractical, because what it effectively implies is that the control system must generate a force which is equal in magnitude to the excitation force. The whole system must be of the same relative size as the machine under investigation. This would also make such a system very inefficient, thus in this case passive control systems would be more practical. However, if the response of the structure is low in some frequency range, then with a control system, only that part of the force pulse which will influence the spectrum at frequencies where the structural response is high need to be controlled. This will make the control system much more practical since the forces needed may be much lower than those developed by the machine. However, this type of system is more difficult to impliment.

For relatively long force pulses, apporximately 15ms, with very sharp changes in the force (loading of the machine structure) such as in the case of

the operation of a power press [2], then what controls the shape of the force spectrum and thus the radiated noise in the range 100 Hz - 10 kHz is the very large rate of change of force. Hence, a control system only needs to control this large force change. This is similar to the case where only the force in certain frequency ranges needs to be controlled because of the shape of the structural response. This is more of an advantage in this case because the duration of the force is much longer, usually much larger forces are involved, typically for a *small* power process around 50 Tonnes, and to cancel the force completely the active control system must be capable of generating such forces, which is not practical and very inefficient.

Thus active force control systems can have two forms, to either cancel the whole of the force pulse or to cancel the sharp changes in the force. The first method is much easier to implement, because in the second case more precise control is needed to generate the shape of the control force, and this will depend on the force generating system. In previous research, [3, 4] active force control in impulsive systems has not been studied. Active control has only been applied to continuous or quasi-continuous systems with low levels of structural damping. Such systems are not representative of many machinery structures.

In this work a control system to cancel a complete single excitation pulse on a simple structure has been investigated. The system was constructed so that the effects on performance of parameters such as pulse shape, synchronisation and separation could be studied easily.

2. SYSTEM SET UP AND RESULTS

The best position to place a force control system would be as close as possible to the excitation force, in this case all the vibrations in the structure would be eliminated. However, this is not physically possible, and the closest that the control force can be placed to the excitation force would be on the opposite face of the structure. Although this is usually possible it may create problems in retrieving the finished workpiece. An experimental system with the two forces acting on opposite faces of a structure is investigated and the effect on the performance when the two forces are separated by a set distance is also studied.

When the two forces act on opposite sides, potentially the reduction in noise is very high [1] since the modes of excitation that are allowed are of low amplitude and at high frequencies, outside the frequency range of interest. The only modes of vibration that will be allowed are those corresponding to dilation waves, and since the thickness of the structure is usually not more than a few centimetres at the most, the first mode would occur at high frequencies. For a 1 cm thick steel plate, the expected frequency of the first mode is 370 kHz.

The experimental system set up, is to control the noise radiated from a flat plate when impact excited. The duration of the impact is 0.4 ms and thus the control system is set to completely cancel this force, making implementation much easier. The requirements for the control system are that a similar and equal in magnitude control force is applied to the plate in syncrhonisation with the excitation force pulse. The synchronisation between the two forces is essential and this is one problem area, especially because of the very short duration of the impact. The control system must have a very quick response or the operation of the machine must be repetitive within a fraction of a millisecond. This may necessitate the use of better bearings and release mechanisms than the ones that are now in use.

The system set up that eliminated the problem of synchronisation is shown in figure 1. The position of the hammer that is delivering the impact is monitored by an electronic detector, and when it is at a set position it triggers a pulse generating device so that some delay time later when the hammer hits the structure, this pulse triggers the active force system to give a force pulse in synchronization with the excitation pulse. This set up can be used on any machine, by monitoring its operation and triggering at some optimum time before the impact occurs. The control force was generated by an electro-dynamic shaker which was excited by a pulse of duration matching that of the impact. The shaker was not attached to the plate, just to give single pulse. This is one area where further development is necessary, mainly to investigate the response of the shaker to a prerecorded pulse.

The results for the surface velocity and radiated noise energy for a 1cm thick flat plate with the above set up are shown in figure 2 (a) and (b). The reduction with noise level is very high, about 14dB and the reduction is constant throughout the whole frequency range. However, this reduction in noise is lower than expected. If the results are studied carefully it can be observed that the noise energy spectrum is the same in both cases, only with a difference in level. This suggests that the reduction is only partial, that is while the two forces have the same shape, their magnitude is not completely matched. Thus one critical parameter in a force control system is the perfect matching of the excitation and control force both in the time and frequency domain. In the case of cancellation of only the sharp changes, the reduction in the radiated noise will depend on the matching of the force spectra of the excitation force and control force in the frequency range of interest. The theoretical maximum reduction in noise energy that can be achieved should be very high and thus in the further development of an active system, the performance could be further improved.

3. SEPARATION BETWEEN EXCITATION FORCE AND CONTROL FORCE

Since it is not always physically possible to position the excitation force and control force at either the same position or on opposite sides, the effect that a separation distance will have on the performance of the above control system is investigated. The control force is moved along the surface of the plate and the reduction in noise, both total and in one-third octave frequency bands measured, to determine what maximum separation distance is allowed depending on the structure parameters.

The mean, frequency averaged response of a plate structure some distance away from the point of excitation is approximately given by the empirical formula [5]

$$M = M_c \qquad kr \leq 0.63$$

$$= M_c \sqrt{\frac{2}{\pi kr}}\, e^{-j(kr-\pi/4)} \qquad kr > 0.63$$

Where M_c is the characteristic mobility of the plate given by

$$M_c = \frac{1}{8\sqrt{B\rho_s}}$$

B is the bending stiffness
ρ_s is the surface density of the structure
k is the bending wave number
r is the distance from the point of ixcitation.

If the plate is acted upon by two forces, acting in opposite directions, such as in the case of an active force control system the two forces will constitute a torque of magnitude $F\chi$, where F is the magnitude of the forces and

χ the separation, provided that $\chi \leq 0.63/k$. For $\chi > 0.63/k$, the coupling between the two forces decreases as χ increases. This follows from the fact that the response of the plate is flat up to a distance given by $k\chi \leq 0.63$ and then decreases exponentially as χ increases. For large values of separation the two forces will act independently on the plate and it would be expected that the noise radiated from the plate will be 3 dB higher as compared to a single force excitation.

For a plate under torque excitation, the torque structural response H(f) ($H(f) = V(f)/\dot{F}(f)$, V(f) normal velocity, $\dot{F}(f)$ time derivative of excitation force) is independent of frequency while the point force response decreases at 10 dB per decade of frequency [1]. Therefore, at high frequencies the torque response may be higher than the point force response. For a reduction in noise, the frequency at which the torque response and the point response are equal must be outside the frequency range of interest. This frequency depends on the parameters of the structure and the magnitudes of the torque and the force. If it is assumed that the torque has a magnitude $F\chi$ and the point force a magnitude F, then the frequency at which the input energy per unit force for torque and point excitation are equal, varies in the separation. For each separation this frequency is given in figure 3; here the separation distance is given in terms of the number of wavelengths of the structure, $\alpha^4 = Eh^2/(12\rho(1-\nu^2))$ for a flat plate. $\alpha \sim$ wavelength , E = Young's modulus, h = plate thickness, ρ = density, ν = Poisson's ratio.

However, because of the condition $k\chi \leq 0.63$ for the two forces to constitute a full couple, and this condition is frequency dependent, there is another important frequency which also varies with the separation distance. If the excitation force has components at all frequencies, for a set separation the forces are completely coupled up to a specific frequency, given by $k\chi = 0.63$. The variation of this frequency with normalized separation (χ/α) is also shown in figure 3.

Therefore if two forces act on a plate structure in opposite directions, the two forces being equal, and separated by some distance, the noise radiated from the plate at each frequency increases at 6dB per doubling of the separation distance, provided that the condition $k\chi \leq 0.63$ is satisfied. If the two forces are not exactly identical, as in the experimental system investigated in this case, then the radiated noise will be the total of that due to torque excitation and that due to point excitation because the two forces are not exactly identical. However, as the separation increases the condition $k\chi \leq 0.63$ is no longer satisfied and hence the coupling between the two forces decreases, that is the strength of the excitation torque decreases with increase in separation distance. Thus the radiated noise will increase at a slower rate than 6dB per doubling of distance as the separation increases. With this condition, the radiated noise may reach a maximum and then decrease to a level which is 3dB higher than the noise radiated by the structure under the influence of one force, as the separation distance increases.

Some of the noise measurement results for the plate in one-third octave frequency bands for band with various centre frequencies is shown in figure 4. The change of radiated noise with separation distance follows the expected curve as described above. At zero separation, the noise is solely due to the difference between the excitation and control forces. The contribution due to torque excitation should follow the solid line which intersects the level of noise from the plate when excited by a single force at the separation given by curve (i) in figure 3. However, above Kr = 0.63, the measured curve does not follow the solid line since coupling diminishes and the strength of the torque is thus reduced. With further increase of separation, the radiated noise reaches a maximum and then decreases to a level 3dB higher than the level of

noise with one excitation force, when the separation is greater than 25 cm, and the coupling between the two forces is negligible.

Generalising these results for any structure, the performance of an active force control system with some separation between the two forces diminishes as compared to that of no separation. However, up to a certain separation, which is both structural and frequency dependent, the application of a control system, will result in a reduction of the radiated noise over the set up without the active system. For most structures the separation at which $k\chi$ is equal to 0.63 is usually less than the separation which corresponds to equal energy per unit force for both torque and point force excitation, for a particular frequency band. Thus any separation distance which is less than this latter critical distance will give a reduction in the radiated noise energy, and since the coupling between the two forces decreases at this critical distance, then the performance of an active force control system will be an improvement in noise control of the machine even for separation distances slightly less than the critical distance. For structures where the separation distance corresponding to $k\chi = 0.63$ is greater than the critical distance of equal energy per unit force, the performance of the control system very near to critical distance will be very poor.

4. CONCLUSIONS

The results in this investigation show that active force control is possible, and that large reductions in noise energy radiated can be achieved, although the system investigated here would not be ideal in a practical situation. The performance of the system is very critical on the timing of the control and excitation forces. For effective cancellation the shape of the force pulse or its spectrum must be matched exactly and the two opposite forces must act as closely together as possible on the structure. In this investigation the set up was more of a laboratory system and before any new improvements to the system can be made, better methods of implementation have to be found.

One area of work which needs improving and on which there is currently some work going on, is to improve the generation of the control force. At the moment, nothing in the system is included to compensate for the response or transfer function of the shaker. Also better improvement is needed in the synchronisation of the control and excitation force. This will also be one of the main problems in implementing such a system in practical machines and the redesign of certain moving parts and bearing surfaces may be needed to implement this type of noise control. However, because of the very high potential of noise control the research may well be worthwhile in the long run.

REFERENCES

1. CUSCHIERI, J.M. 1983 Ph.D. Thesis, ISVR, Southampton University. A Parametric Study of Impact Noise.
2. STIMPSON, G. 1982 Proc. Institute of Acoustics, Autumn Conference F3. Damping and Cancellation Devices to Reduce Punch Press Noise.
3. ROORDA, J. 1980 Solid Mechanics Archives 5. Experiments in Feedback Control of Structures.
4. SANKAR, S. and GUNTUR, R.R. 1981 Shock and Vibration Bulletin 51 Pneumatic Vibration Control Using Active Force Generators.
5. SKUDRZYK, E. 1968 Simple and Complex Vibratory Systems. Penn. State University Press.

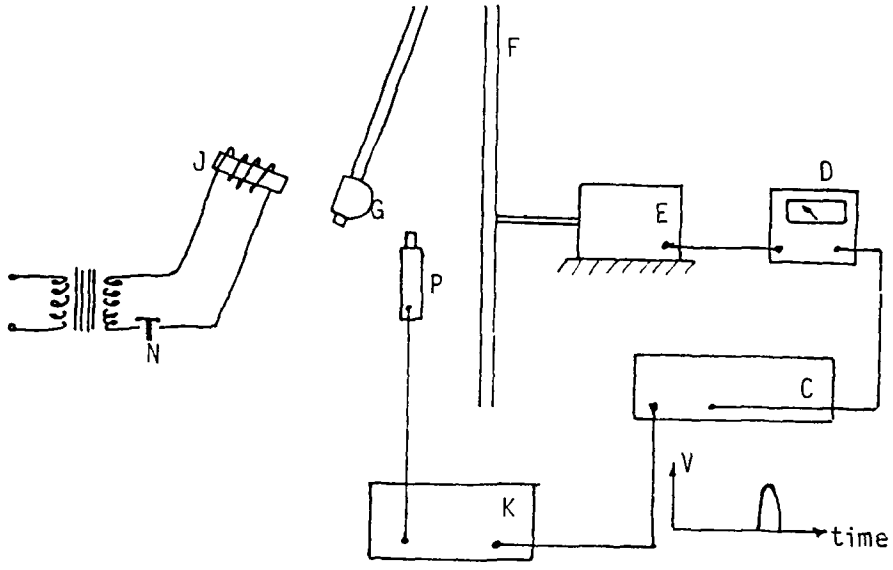

Figure 1. Experimental set-up. C, power amp; D, Ammeter; E, Shaker; F, plate; G, impactor; J, Electromagnet; K, pulse generator; N, spring switch; P, Infrared detector.

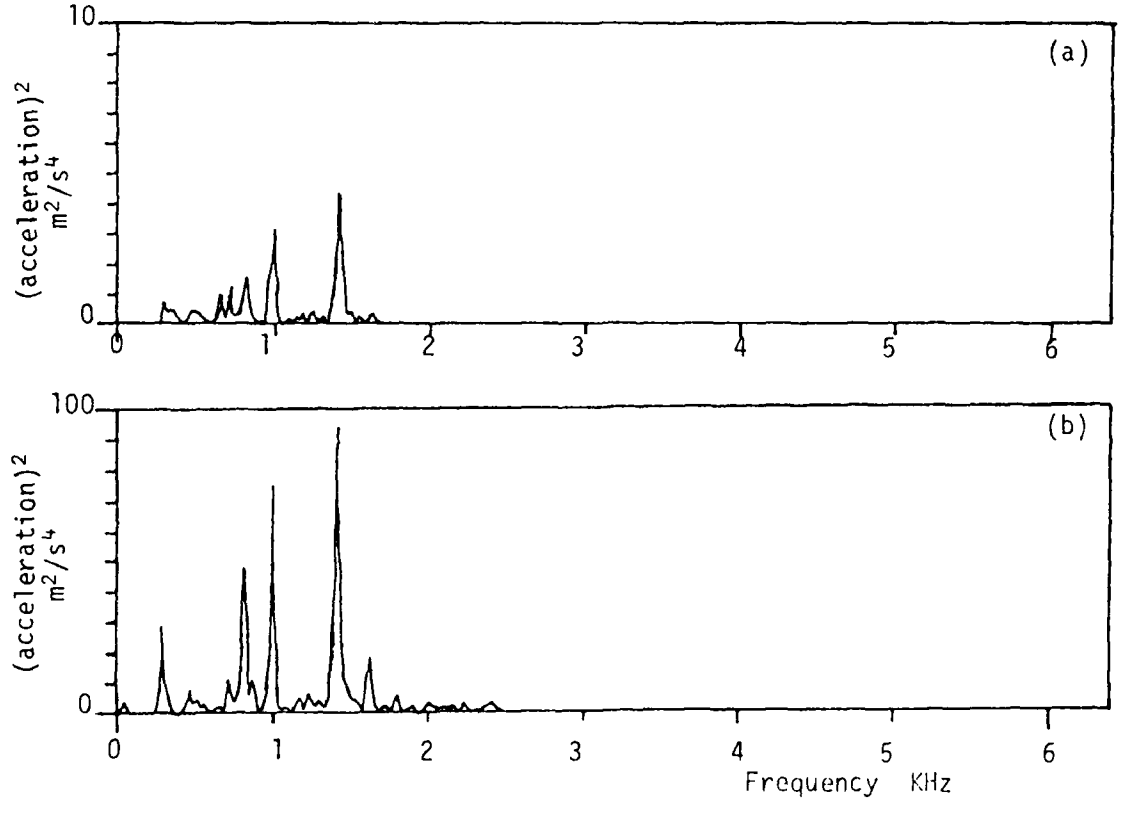

Figure 2(a) Spectrum of plate surface acceleration. (a) with active system; (b) without active system.

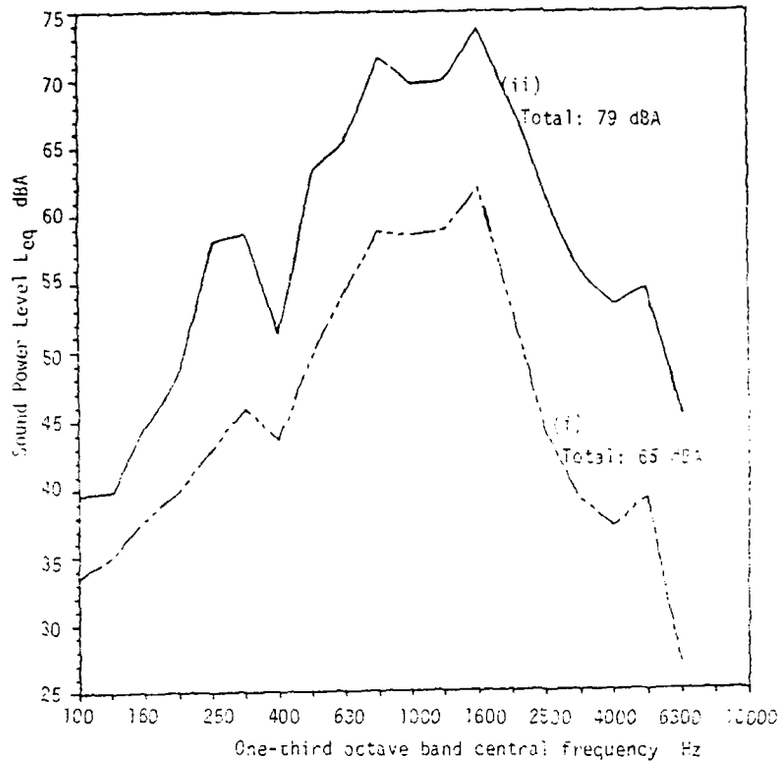

Figure 2(b) Radiated noise in one-third octave frequency bands.
(i) with control system; (ii) without control system.

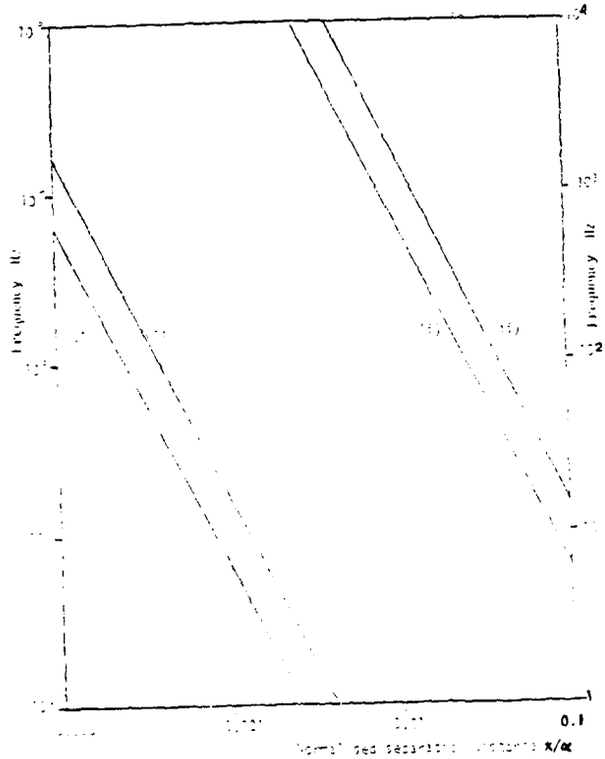

Figure 3.

Change of frequency with separation distance (i) for K_X = 0·63; (ii) frequency at which torque response is equal to point response for plate.

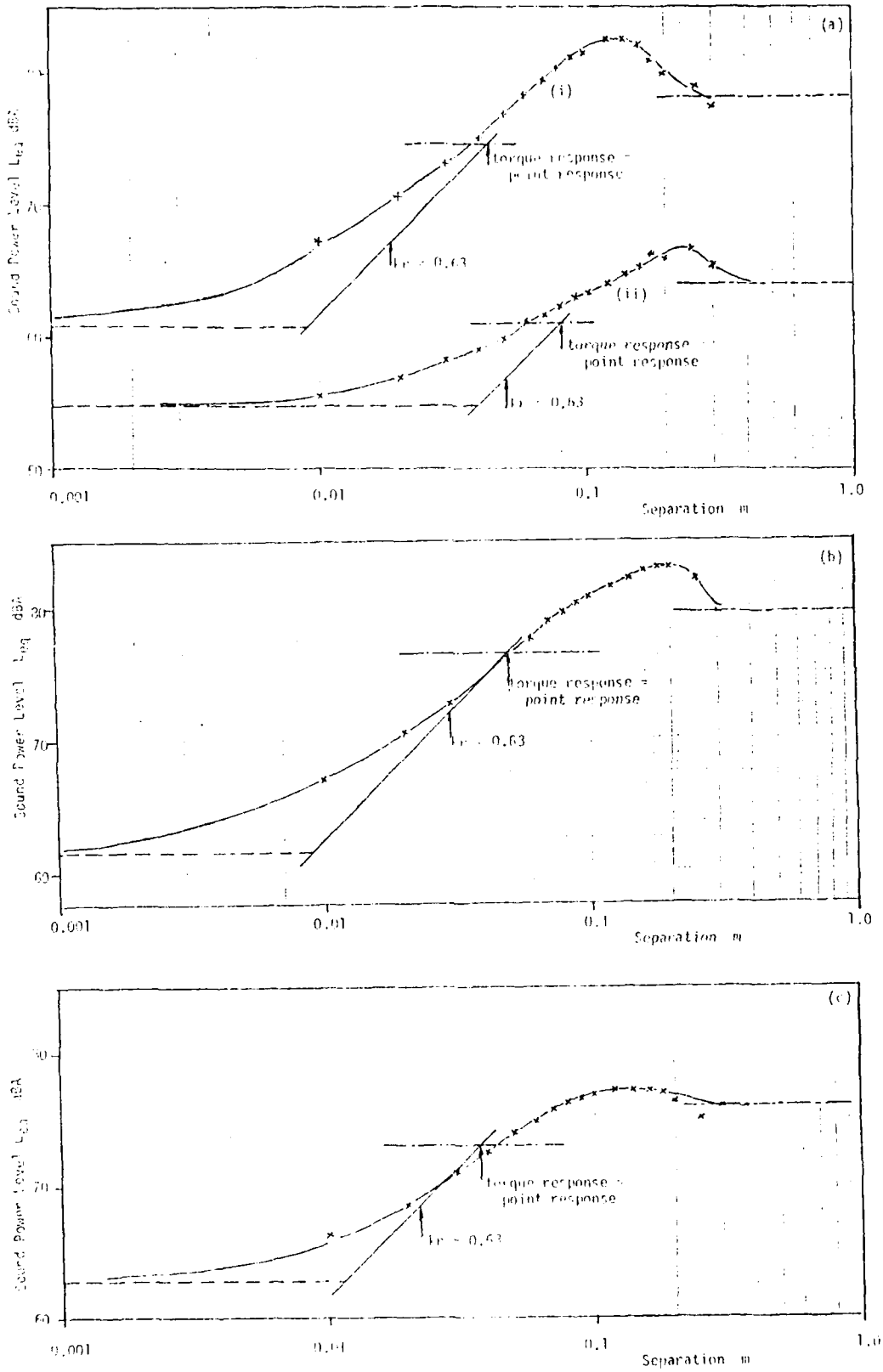

figure 4 . Change of noise radiated with changing separation distance in one-third octave bands. -·-·-, measured; ----, noise level due to excitation at same point; — · —, noise level due to single force excitation; — — —, noise level due to two independent forces; ----, increase of noise due to torque excitation with separation, (6dB per doubling of distance).
(a) (i) 1.25 kHz; (ii) 400 Hz; (b) 1 kHz; (c) 2 kHz.

MODELING THE RELATION BETWEEN STRUCTURAL VIBRATIONS AND RADIATED SOUND

Dr.ir P.SAS, ir. P.Vandeponseele, Prof. R.Snoeys

Katholieke Universiteit Leuven
Afdeling Mechanische Konstruktie en Produktie

1. SUMMARY

Two computational methods for estimating the sound power radiated by mechanical structures are presented. The reported technique fills in the gap between structural vibrations and radiated sound, and enables already in the design stage, accurate assessment of noise reduction measures.
Both methods which are based upon a Helmholtz integral formulation, require the knowledge of the geometry and the modal characteristics of a structure's vibrating surfaces , so that the pressure on the surfaces can be computed.
The first method is limited to flat surfaces and replaces the original source by a distribution of point sources which are easy to integrate over the radiating surface. The second method is more general and accurate but requires considerably more computing time since it includes a closed form integration of the the associated surface integrals.
This paper reviews some principles on acoustic radiation, the concerned algorithms are briefly commented and verification experiments, where close correlation was found between predicted and experimentally determined sound power levels, are presented.

2. INTRODUCTION

The techniques for the reduction of the sound power radiated by mechanical structures such as combustion engines, machine tools, etc... are mainly based upon experimental or empirical approaches. Sound reducing treatments are nearly always derived from more or less elaborate diagnosis measurements. The efficiency of the related treatment can only be experimentally verified after the physical realisation of the sound reducing operation. Seldomly are analytical or numerical algorithms applied to simulate and/or optimize the impact of the noise control treatment on the radiated sound power levels.

Several theoretical studies have been devoted to this subject in the past and have resulted in analytical formulas which are only valid for a limited number of relative simple source geometries such as axisymmetric structures (spheres, cylinders) or flat plates. An analytical solution for the general radiation problem does not exist, numerical solutions on the contrary are conceivable, but apparently have been neglected, due to numerical instability problems and because of the considerable computer power required for real life problems. The number of publications on numerical solutions is only a small fraction of what has been published on analytical solutions.

Yet a radiation model based on an operational numerical solution of the general radiation problem could become a useful design and

diagnosis tool. Indeed, with the aid of such a model, people involved in noise control would be able to predict the impact of structural modifications to the sound power radiated by the modified structure. The objective of our research effort was the development of an acoustic radiation model based on a numerical solution of the Helmholtz integral equation, and the integration of this model into a global sound optimisation philosophy by combining finite element modeling, modal analysis and the mentioned radiation model. The general lay-out of this sound optimisation philosophy is outlined in the following scheme.

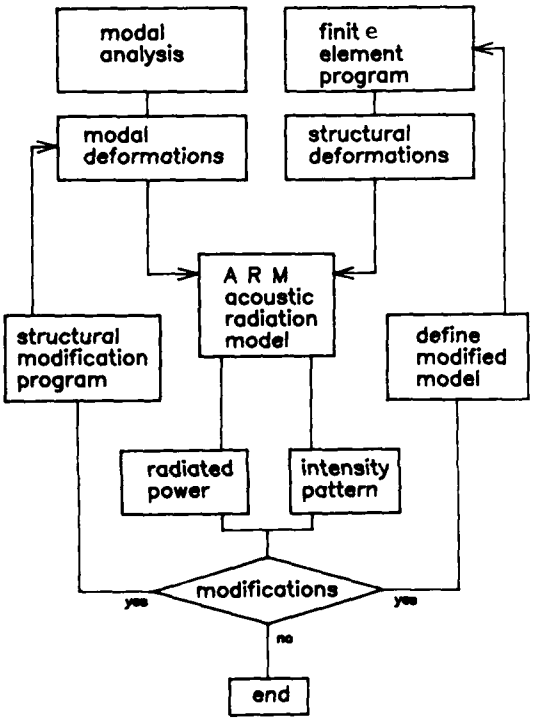

The acoustic radiation model is the center of this approach, it has been conceived such that as well as experimental data (modal analysis) theoretical data, resulting from finite element models, can be treated. The first option yields an optimal tool for judging a new design with regard to its sound production, on condition that a dynamic finite element model of the concerned design is available, which is often the case as more and more design services are equipped with CAD facilities.
The second option is similar but starts from experimentally obtained mode shapes and resonance frequencies. Structural modification programs based upon substructuring and modal synthesis techniques enable the prediction of the impact of structural modifications on those mode shapes and resonance frequencies. The combination of those techniques with the acoustic radiation model yields a useful optimisation tool for solving existing noise problems. For example on a real life structure such as a combustion engine the influence of changing locally the stiffness, mass or damping can be extended to the radiated sound power.

The second approach is the most accurate since it is based upon experimental data where the influence of damping is automatically taken into account. It is however limited to those situations where the concerned structure physically exists.

3. THEORY

The general acoustic radiation problem can be formulated as the following boundary value problem : find the solution for the pressure in an infinite medium, with known density and speed of sound, where an arbitrarily shaped object is immersed. As boundary condition the normal component of the velocity at any surface point of the immersed object is given. It can be shown that a solution of this boundary value problem must satisfy the three dimensional wave equation as well as the Sommerfeld boundary condition [ref. 1,2,3].

Exact solutions of this boundary value problem are possible when the surface represents a level value of a coordinate in one of the few coordinate systems in which the wave equation can be separated [ref.1,2,3,4]. The most general of these exact solutions are probably those for axisymmetric surfaces, where the radial factor of the pressure is a combination of spherical Bessel and Neumann functions while the tangential factor of the pressure is expanded in a series of Legendre functions whose coefficients are determined by the boundary conditions. One of the problems inherent to such exact solution is that the boundary conditions must also be expressed in terms of a series of Legendre functions.

An interesting mathematical property is the fact that, for the given boundary condition, the 3d wave equation can be expressed as an integral equation.

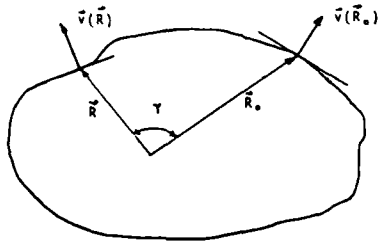

Fig.1 Field lay-out

This implies the introduction of the free-space Green function and the combination of the 3d wave equation with the Gauss-integral theorem which relates a surface and a volume integral. Doing so, one is able to formulate the pressure field at an arbitrary field point as the surface integral of a linear combination of the surface pressure and velocity over the radiating boundary. This integral equation is known as the Helmholtz integral equation (cf fig.1)

$$p(\bar{R}) = - \int_{S_o} [p(\bar{R}_o) \frac{\partial g(|\bar{R}-\bar{R}_o|)}{\partial n_o} + j\omega\rho v(\bar{R}_o) g(|\bar{R}-\bar{R}_o|)] \, dS_o \qquad (1)$$

where $g = \dfrac{e^{jk(|\bar{R}-\bar{R}_o|)}}{|\bar{R} - \bar{R}_o|}$ (free space Green function)

$v(\bar{R})$: structural velocity

Since the only prescribed quantity is the surface velocity, the surface pressure being unknown, the pressure in the field can only be determined by allowing the field point $(\bar{R})$ to approach the radiating surface and by consequently solving the resulting integral equation (Fredhom integral equation of the second kind) for the unknown surface pressure $p(\bar{R}_o)$.

For arbitrary source configurations, with the solution not restricted to a particular frequency range, the surface pressure distribution can only be obtained by solving the Fredholm integral equation numerically. Once the surface pressure obtained, the Helmoltz integral equation becomes a simple integral representation of the pressure at field points not located on the radiating surface, which on his turn can be solved numerically.

The integral equation can be circumvented if we can construct a Green function which satisfies the Neumann boundary conditions. In this case the unknown pressure vanishes under the surface integral, thus reducing the integral equation to a simple integral representation. However a Green function satisfying the Neumann boundary conditions can only be constructed if :

1)The boundery is completely defined by the value of a single coordinate.
2)The wave equation is separable in this coordinate system.

Similar to the exact solution those conditions are only met for simple boundaries such as an infinite plane, cylinder or sphere, if the pressure can be represented by linear conbinations of wave harmonics. The solution for infinite plane sources deserves special attention since it yields the well-known Rayleigh's formula from which it can be concluded that a planar source located in an infinite baffle is equivalent to a distribution of point sources. This principle forms the theoretical basis of the point source model.

$$p(\bar{R}) = - \frac{j\omega\rho}{2\pi} \int_{S_o} \frac{e^{jkr}}{r} \, v(R_o) \, dS_o \qquad (2)$$

4. POINT SOURCE RADIATION MODEL

Since the vibration patterns, originating from finite element models or modal analysis are discrete, they are only determined in a finite number of points distributed over the surface of interest. As a result it will be necessary to approximate the applied surface integral (eq.2) by a summation over those discrete points. This is the equivalent of substituting the vibrating surface by a finite number of point sources. Each of those elementary sources represents a fraction (S_i) of the original surface. The acoustic strength of those sources is given by the product of the partial surface and the structural velocity of the point where the surface was attributed to.
If for example the vibration of a plane surface is given by a pattern of n points, the pressure level for an arbitrary point above the radiation surface is equal to :

$$p_i = - \sum_{i=1}^{n} (jkc \, v_i \frac{1}{2\pi r_i} e^{jkr_i} . \, S_i) \qquad (3)$$

where $r_i = |\bar{R}_i - \bar{R}_o|$

Similar expressions can be derived for the air particle velocity. Consequently the acoustic intensity is easy to derive, since its value is by defenition given by the product of particle velocity and pressure. The acoustic power radiated by a surface is on its turn given by the average of the intensity normal to the surface, multipled by the size of the surface. Equation (3) is only valid if the acoustic environment is reflection free. The influence of eventual reflecting surfaces in the neighbourhood of the radiating surface can therefore be simulated by simply adding image sources at the opposite side of the reflecting surface. The reflection influence is taken into account by adding a supplementary pattern of noise sources to the source lay-out, this supplementary pattern is the image of the original source pattern.

4.1 Accuracy of the Point Source Radiation Model

The accuracy of the radiation model has been verified by comparing the predictions of the radiation model with experimental results. The

results of one of those verification experiments are given in fig 2. This diagram shows the average near field sound intensity levels for the first five resonance frequencies of a constrained plate. A flat plate (50x50x.2cm) was clamped in a concrete block and excited with white noise (0-2000Hz). The near field intensity patterns have been experimentally recorded together with the modal deformation patterns, which served as input for the acoustic radiation model. The intensity measurements have been conducted using a two microphone intensity probe.

As can be noticed from those results, the agreement between experiment and prediction is fairly good. Up to the fourth resonance frequency the accuracy is better than 1dB. The larger error of the fifth resonant frequency is probably due to an insufficient number of source points.

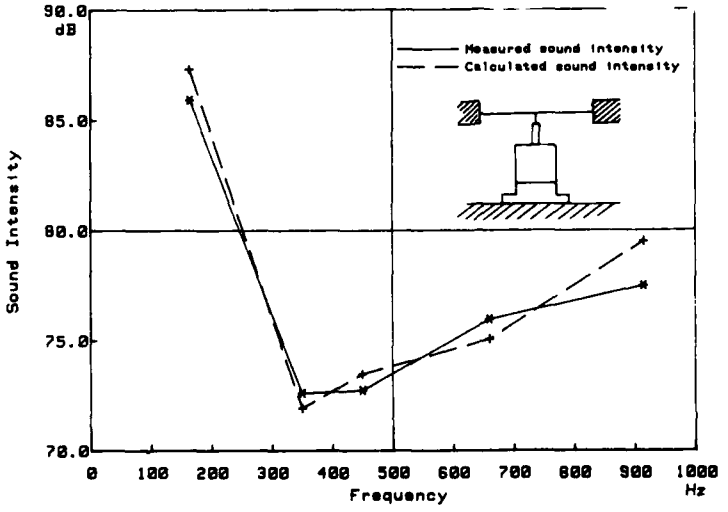

Fig.2 Predicted and measured sound intensity for a clamped plate (50cmx50cm)

4.2 Applications of the Point Source Model

The acoustic radiation model is well suited for purely acoustic purposes. Especially visualising the repercussion on the sound field of parameters such as reflecting surfaces, stiffening ribs or damping layers, among others... can be clarifying.
As an illustration of such an application the transition of near field into far field is determined for some modes of the clamped plate. For that purpose the intensity pattern has been determined by the radiation mode in a plane normal to the clamped plate. The resulting intensity patterns are shown in fig.3. They clearly illustrate that the near field is more extended for the lower frequencies than it is for the higher frequencies. The transition 'near field into far field' is characterised by the disappearance of the hydrodynamical short-circuit phenomenon, all intensity vectors start pointing outwards. A further illustration is given by fig.4 where the predicted intensity patterns for some of the resonant frequencies of a free plate, randomly excited, are represented together with the experimentally measured deformation patterns, which served as input for the radiation model.

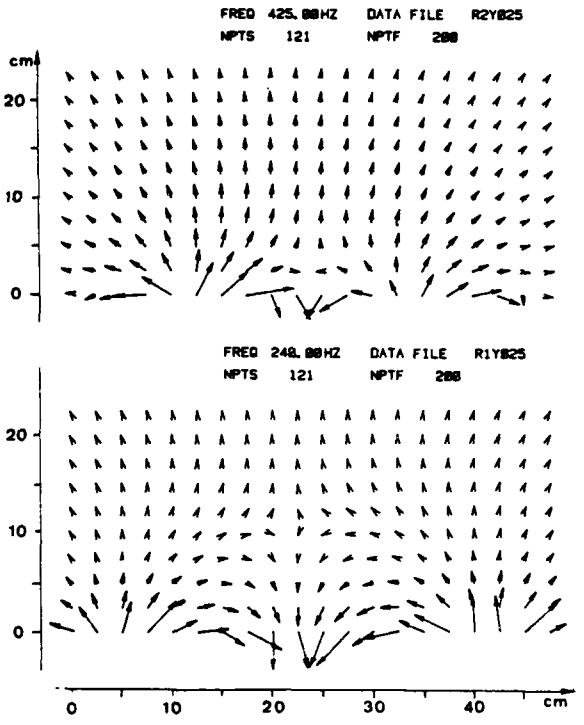

Fig.3 Intensity patterns normal to to a clamped plate

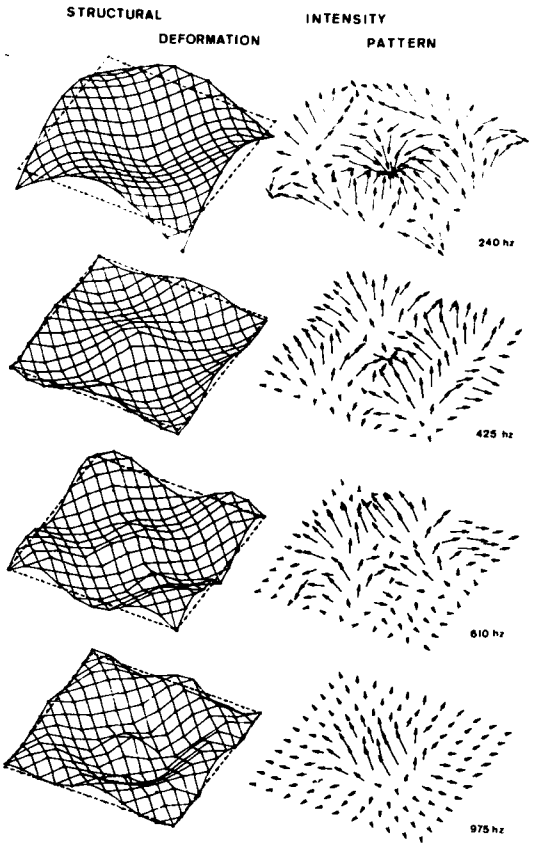

Fig.4 Deformation and intensity patterns for a free plate.

5. GENERAL NUMERICAL SOLUTION OF THE 3-D HELMOLTZ INTEGRAL EQUATION

Searching through literature one will find several papers treating the numerical solution of Rayleighs integral formula (eq.2), but publications treating the numerical solution of the 3-D Helmholtz integral equation (eq.1) are rather scarce.

Concerning the numerical solution of the 3D Helmholtz integral equation, a review of possible solutions for axisymmetric sources has been given by Chertock [ref.6]. Solutions valid for arbitrarely shaped sources are given by Chen and Schweikut [ref.7], Copley [ref.8], Schenck [ref.9], Meyer et al. [ref.10], Burton [ref.11], Terai [ref.12] and recently by Koopman [ref.13].

Schenck [ref.9] was the first to mention the problems caused by the non-uniqueness of the solution at frequencies corresponding to the eigenfrequencies of the associated interior problem. To overcome this problem he introduced the Combined Helmholtz Integral Equation Formulation (CHIEF) where an overdetermined system of algebraic equations is obtained by combining the surface Helmholtz integral formulation with additional equations generated from the interior Helmholtz integral formulation. The difficulty of this approach is the determination of the optimal number and position of the interior points which are used to generate the additional equations. Except for a recent paper of Koopman [ref.13] no application of the combined Helmholtz integral equation formulation has been reported so far.

Another method for overcoming the uniqueness problem was introduced by Burton [ref.10] and has been refined by Meyer et al [ref.11], and later by Terai [ref.12]. This method is based upon the fact that a unique solution for the acoustic pressure can be obtained by solving a modified integral equation consisting of the original integral equation and its differentiated form. This combination yields a unique solution for all frequency values. Unfortunately, the differentiated form of the integral equation contains a strongly singular integral, which cannot be directly integrated. Burton and Mayer approach this problem by using a transformation to interpret the singular integral. This method is efficient but results in a more complicated integral equation which requires more computer power.

For our radiation model the principle of the CHIEF method was preferred, which to our judgment is a reasonable compromise between accuracy, computational effort and versatility. What makes our implementation different from previous investigations is the requi ement that the computational scheme must be compatible with those used in the existing modal analysis and finite element methods. Compared to the method outlined by Koopman [ref.13] a refined near field approximation is used and a more sensitive near-far field transition criterium is introduced.

5.1 Principle

As shown earlier (Sec.2) the pressure at a point R on a closed surface (fig.1) is given by the Helmholtz integral equation (eq.1). By taking the derivative of the free space Green function (9) the integral equation can be rewritten as

$$p(\bar{R}_o) = -\frac{k}{2\pi} \int_{S_o} p(\bar{R}_o) \frac{e^{jkr}}{r} \left(\frac{1}{kr} - j\right)\cos\gamma \, dS_o - \frac{j\rho ck}{2\pi} \int_{S_o} v(\bar{R}_o) \frac{e^{jkr}}{r} \, dS_o \qquad (4)$$

where $r = |\bar{R} - \bar{R}_o|$

$k = 2\pi/\lambda$

Equation (4) could be solved by direct numerical integration, but even for simple sources the computations are unrealistic lengthy. An approximate solution is possible by dividing the source surface S into N planar surface elements. Planar surfaces are far more interesting since integrations over two dimensional surfaces are more tractable and often closed form expressions can be found, thereby avoiding numerical integration. The number of surface elements is chosen such that one can assume that the velocity or pressure distribution over the elements is uniform. Equation (4) can then be written as

$$p(R_i) = \sum_{j=1}^{n} [p(R_j) D_{ij} + v(R_j) M_{ij}] \qquad (5)$$

where p(R) : pressure at the center of element i

$$D_{ij} = -\frac{k}{2\pi} \int_{S_{ij}} \frac{e^{jkr_{ij}}}{r_{ij}} \left(\frac{1}{k\, r_{ij}} - j\right) \cos\gamma_{ij} \, dS_{ij}$$

$$M_{ij} = - j\rho c \frac{k}{2\pi} \int_{S_{ij}} \frac{e^{jkr_{ij}}}{r_{ij}} dS_{ij}$$

If equation (5) is repeated for each centerpoint of all N elements, one obtains a NxN system of linear inhomogeneous equations.

$$[[\delta_{ij}] - [D_{ij}]] [P_j] = [M_{ij}][V_{ij}]^T \qquad (6)$$

where δ_{ij} is the Kronecker delta

This NxN matrix system can be solved for the element pressures by one the appropriate methods. We applied the Householder method since it handles also overdetermined systems, as will be explained later.
Once the pressure on the source surface known it is easy to derive the acoustic power radiated, since on the radiating surface the particle velocity is equal to the surface velocity, the radiated power can be calculated once the surface pressure is known.

5.2 Transition Near Field - Far Field

Further approximations are necessary for the calculation of D and M_{ij}. In order to enable closed form expressions for the integrands of D_{ij} and M_{ij} a series expansion for r is used for large values of kr (far field), while for small values (near field) a truncated Mc Laurin series is used. The transition between the two approximations may not be confused with the, in acoustics currently used, notions of far and near field. The far field represents only the region where the series expansion for r_{ij} is more accurate than the truncated Mc laurin series, and vice versa for the near field. Five terms of the Mc Laurin series have been used for the near field approximation, which is to our judgment an optimum. Closed form solutions for all integrands of the near and far field approximations have been derived. Some of those derivations required the use of additional coordinate transformations but are too lenthy to treat in this context.

Since the approximations of far and near field can be written as closed form integral expressions, the elements of the NxN matrix system (eq.5) are obtained much faster than by direct numerical integration. This is one of the important advantages of this method.

The criterium deciding when to use the near field approximation and when the far field approximation has been empirically derived. A number of test calculations have been carried out to monitor the evolution of the break even point between the far- and nearfield approximation, in function of various field and structure parameters. From this parameter analysis following criterium resulted :

a) for M_{ij} : $(kr)_{krit} = 0.87 \sqrt{kL}$

b) for D_{ij} : $(kr)_{krit} = 2.10 \sqrt{kL}$

The farfield - nearfield criterium is in consequence different for the M_{ij} and D_{ij} approximations.

5.3 Overdetermination of the N × N Matrix System

It is well known [ref.8,9,10] that the Helmholtz integral equation system (eq. 5) will fail to yield the unique solution of the acoustic radiation problem at certain characteristic frequencies. Copley and Schenck [ref.8,9] have shown that these characteristic frequencies are identical to the eigenfrequencies of the corresponding homogeneous interior (Dirichlet) problem. Since the uniqueness problem occurs only at certain frequencies it might be suggested that the problem can be avoided by considering only frequencies which are not close to internal eigenvalues. This is not feasible since the internal eigenvalues are not known a priori and since at higher frequencies the eigenvalue density is so dense that it is almost impossible to stay sufficiently removed from the internal eigenvalues. Moreover since the integral equation is discretized into a system of algebraic equations, there is no longer a specific eigenvalue but a range of values at which the matrix is ill-condidtioned.

Schenck suggested to overcome this non-uniqueness problem by solving an overdetermined sytem of algebraic equations, obtained by combining the system of algebraic equations generated from the standard integral equation (eq.4) with additional equations originating from the internal Helmhotz integral equation

$$\sum_{j=1}^{n} \left| p(R_j) D_{ij} + v(R_j) M_{ij} \right| = 0 \qquad (7)$$

Those additional equations are necessarily associated with points laying inside the source surface. It can be shown that the overdetermined system of equations yields always a unique solution. But in practice the position of those internal points is important. Indeed if those internal points are chosen near the nodal points of the interior eigenfunctions the additional equations fail to provide the necessary constraints to ensure uniqueness. In general both the eigenvalues and nodal lines of the internal problem are unknown so that one has no guidance in selecting the additional internal points. It is therefore suggested to use a sufficient number of internal points.

The Householder method, we retained for solving the matrix system is well suited for handling overdetermined systems, and has therefore been preferred over other methods. The condition number of the matrix is used as an indicator, warning the user at which frequencies singularities occur.

5.4 Accuracy of the General Radiation Model

The accuracy of the general solution of the 3-d Helmholtz integral equation has been verified by comparing the numerical results with analytical formulas or experimental results.

5.4.1 Radiation Efficiency of a Pulsating Sphere

To verify the accuracy of the radiation model, the acoustic power radiated by a pulsating sphere has been predicted by the model and compared to the levels resulting from analytical formulas which can be found in most textbooks on theoretical acoustics. Actually radiation efficiencies have been compared, since they are independant of size and

amplitude of the source (sphere).

The pulsating sphere has been modeled using 72 triangular elements. To illustrate the influence of the overdetermination, the radiation efficiencies have been calculated twice, once without overdetermination, and once with one additional internal point situated at r=0.3R (where R is the radius of the sphere). The results are represented in fig.5 and show close agreement between the predicted and analytical efficiencies.

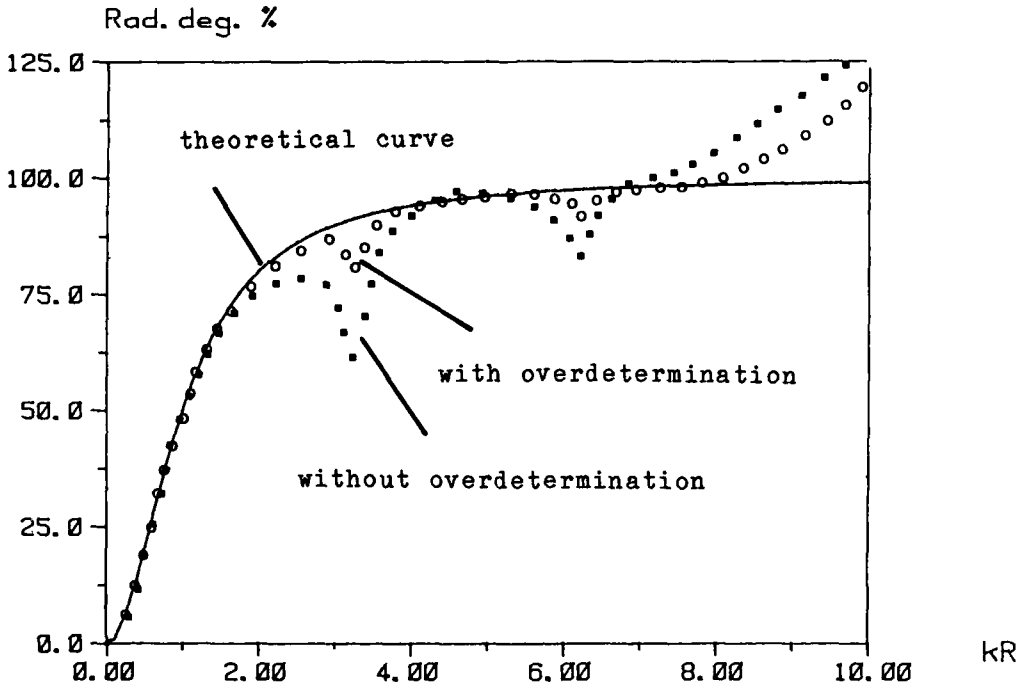

Fig 5. Radiation efficiencies of a pulsating sphere

The pronounced discrepancies between predicted and analytical results at kr=3.4 and kr=6.8 are due to the non-uniqueness problem. Indeed those wavenumbers correspond with the first and the second internal resonance frequency of the sphere. This confirms the fact that the method, we selected for solving the Helmhotz integral equation, yields erroneous results for frequencies around the internal resonances. Overdetermination of the system using additional internal points improves the accuracy (fig.5), but to our judgment further research is required to optimise the position and number of overdeterminations.

5.4.2 Acoustic Radiation of the Oil Sump of a Combustion Engine

A first real life verification test of the radiation model has been carried out on the oil sump of a combustion engine. The oil sump is, because of its size and location one of the noisiest components of combustion engines. The verification test being not yet fully completed, we will report only on some intermediate results.

The experimentally measured vibration amplitudes of the oil sump have been used as input for the radiation model, while the predicted sound power levels have been compared with the measured power levels. Test object was a bare engine block with only the oil sump connected to it. An electromagnetic shaker was used to excite the engine with white noise in the frequency range (0-2000Hz). During excitation the

vibration levels as well as the radiated sound were measured. The vibration levels were derived from acceleration measurents at 82 points all over the structure. Some of those vibration patterns are shown in fig.6.

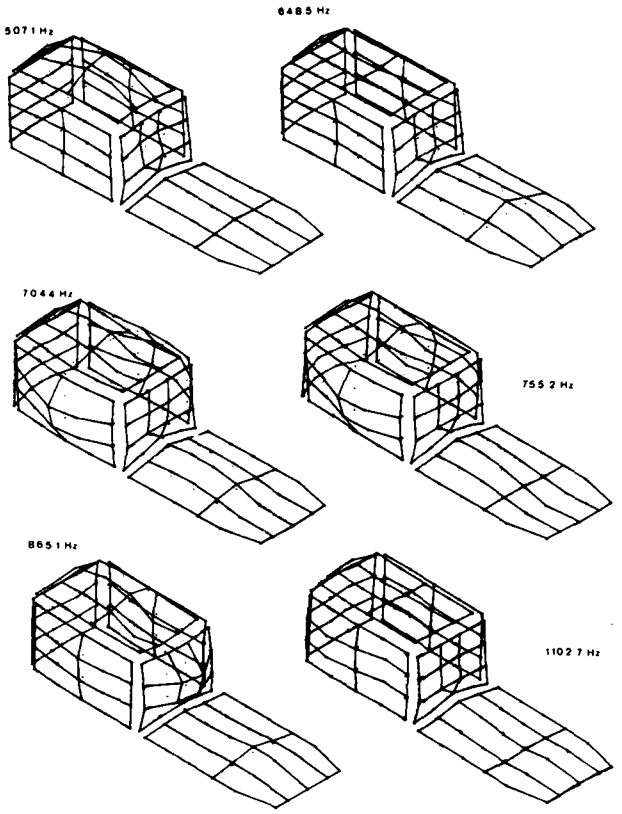

Fig.6 Vibration patterns of an oil sump at resonance frequencies

The experimental sound power levels are based on surface scanned near field acoustic intensity measurements. All surfaces of the oil sump have been scanned with a two microphone acoustic intensity probe, yielding the average intensity for each surface. The sound power radiated by each surface is given by the product of the averaged intensity levels with the size of the considered surface. Summing up the sound power for all the surfaces of the oil sump yields the power radiated by the oil sump. The predicted and measured power levels are summarised in the following table. Only the most pronounced resonance frequencies have been listed.

Freq.	507.1	605	648	670	704	755.2	795	865	1005	1102
Exper.	65.1	62.4	65.8	59.5	66.0	66.5	62.7	68.8	60.4	65.0
Model	64.3	63.1	66.7	60.2	64.8	67.2	62.1	70.2	61.3	63.5

The average difference between experiments and model is +/- .93dB which is an encouraging result. However as we have noticed, by monitoring the condition number of the matrix system, the non-uniqueness problem did not occur for the listed frequencies. Much larger discrepancies between measurement and model predictions might occur for those frequencies where the matrix system is ill-conditioned.

Undoubtly further research and experiments are necessary to verify and improve the accuracy of the radiation model. In the near future we hope to report in detail on the oil sump verification test and on the effect, predicted by the model, of structural modifications on the radiated sound power.

6. REFERENCES

1. M.C. JUNGER and D. FEIT 1972 Sound Structures and their Interaction. Cambridge Massachusetts: MIT Press.

2. P. MORSE and K. UNGARD 1968 Theoretical Acoustics. New York: McGraw Hill.

3. A.D. PIERCE 1981 Acoustics, An Introduction to its Physical Principles and Applications. New York: McGraw Hill.

4. E. SKUDRZYK 1971 Theoretical Acoustics. New York: Springer-Verlag.

5. P. SAS 1981 Doctoral Thesis, Katholieke Univ. Leuven. The Use of Digital Signal Processing Techniques in Acoustic Noise Source Localization, Including Acoustic Intensity Measurements.

6. C. CHERTOCK 1967 J.A.S.A. 36(7). Sound Radiation from Vibrating Surfaces.

7. J. CHEN and G. SCHWEIKERT 1963 J.A.S.A. 35(10). Sound Radiation from an Arbitrary Body.

8. L.G. COPLEY 1968 J.A.S.A. 44(1). Fundamental Results Concerning Integral Representations in Acoustic Radiation.

9. H.A. SCHENCK 1968 J.A.S.A. 44(2). Improved Formulation for Acoustic Radiation Problems.

10. W.L. MEYER, W.A. BELL, B.T. ZINN and M.P. STALYBRASS 1978 Journal of Sound and Vibration 59(2). Boundary Integral Solutions of the Three Dimensional Acoustic Radiation Problem.

11. A.J. BURTON 1976 National Physical Laboratory, Teddington, Middlesex Contract Report No. OC5/535. Numerical Solution of Acoustic Radiation Problems.

12. T. TERAI 1980 Journal of Sound and Vibration 69(1). On the Calculation of Sound Fields around Three Dimensional Objects by Integral Equation Methods.

13. G.H. KOOPMAN and H. BENNER 1982 J.A.S.A. 71(1). Method for Computing the Sound Power of Machines Based on the Helmholtz Integral.

AD-A143 301 PROCEEDINGS OF THE INTERNATIONAL CONFERENCE ON RECENT ADVANCES IN STRUCTU..(U) SOUTHAMPTON UNIV (ENGLAND) INST OF SOUND AND VIBRATION RESEAR.. M PETYT ET AL. 6/6

UNCLASSIFIED 1984 F/G 20/11 NL

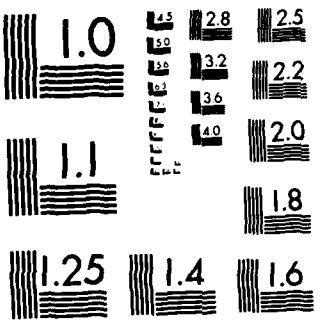

14. P. SAS and R. SNOEYS 1981 Proc. Congress on Recent Developments in Acoustic Intensity Measurements, CETIM, Senlis, France. Visualisation du vecteur d'intensite dans le champ proche.

15. P. SAS, R. SNOEYS and G. DESANGHERE 1982 CIRP Annals, Brugge. Prediction of the Acoustic Intensity Based on Structural Deformations.

16. P. SAS and R. SNOEYS 1982 Proc. IMAC 82, Union College, New York. Prediction of the Acoustic Intensity Based on Mode Shapes.

Research granted by Belgian Government funds as part of the study 'TEST EN DESIGNTECHNIEKEN TER OPTIMALISATIE VAN HET DYNAMISCH GEDRAG VAN MECHANISCHE STRUKTUREN'
Geconcerteerde actie Wetenschapsbeleid 80-85

16. DAMPING

DEVELOPMENT OF THE AEROSPACE STRUCTURES TECHNOLOGY DAMPING DESIGN GUIDE

J. Soovere*, M.L. Drake**, V.R. Miller*** and L.C. Rogers***

1. INTRODUCTION

Aerospace structures and equipment mounted in these structures are required to operate under a wide range of dynamic loads. When structural resonances are excited, the dynamic loads can produce excessive vibration levels in the structures and equipment. These vibration levels can be significantly reduced by increasing the damping in the dominant modes through the application of viscoelastic damping technology.

The above vibration problems are often encountered following some initial in-service exposure. The high cost of subsequent structural changes has made the application of viscoelastic damping technology both attractive and cost-effective in solving these problems. In many instances the reduction in resonant vibration response has been quite dramatic (Figure 1), exceeding that possible with stiffening for the same weight increment [1]. The need for greater accuracy and reliability has extended the application of this technology to guidance systems, optical systems, and circuit boards to name a few. It has been used to reduce the vibration in stiffened aircraft structures and jet engine parts, the cabin noise in the aircraft, the noise emitted by diesel engines, and the noise transmission in buildings. The use of viscoelastic (passive) damping is also expected to increase in space applications, in conjunction with active damping, since the inherent damping is very low in aerospace metals and high modulus graphite/epoxy composites. These latter materials are being used in increasing quantities in space structures.

Vibration testing and data analysis capability has increased dramatically in recent years. The resonant frequencies and damping in structures can now be determined much quicker and with a greater accuracy. The dynamic loads and vibration environments encountered by aerospace structures and equipment are reasonably well known. Damping materials covering a temperature range from -65°F to 1500°F have been developed. The theory [2,3] for simultaneously curve fitting the measured modulus and loss factor for improved accuracy and consistency has been developed for these materials. The basic Ross-Kerwin-Ungar [4] analysis methods for application of viscoelastic damping to beams and plates and the subsequent work by many authors [5,6] have been complimented by the development of finite element methods [7,8] which enable the damping technology to be applied to more complex structural designs. Many successful applications of the viscoelastic damping technology have been reported in the literature. Consequently, it should be possible to anticipate resonant vibration problems and apply the damping technology at the design stage. This approach would not only reduce the cost relative to a subsequent design change, but could also result in a lighter design (Figure 1). This need is becoming more evident as limits of current technology are being approached.

To fully capitalize on this viscoelastic damping technology, it is first necessary to bring all of the pertinent information together in a damping design guide. For a wide appeal, the design guide must be suitable for use by designers. This paper provides a brief outline of such a program, performed

* Lockheed-California Company
** University of Dayton Research Institute
*** Air Force-Wright Aeronautical Laboratory

in three phases, over a period of 34 months. The program will be completed in July 1984.

2. TECHNOLOGY SURVEY

A technological survey was conducted, primarily in the United States, to identify the aerospace companies, government agencies, research institutes, and individuals active in the field of viscoelastic damping technology. A questionnaire was developed to identify the scope of this activity. An eighteen percent response was obtained to the mailed questionnaires. The results indicate a wide field of application (Figure 2) for the damping technology, primarily for vibration control, followed closely by noise control and fatigue suppression (Figure 3). The data in these figures have not been normalized since many of the respondents were involved in more than one field of activity. The classifications of the individuals involved in this activity is indicated in Figure 4. The research and development (R&D) and the management columns combined represent 93 percent of the individuals active in the field. Consequently, most of the design and production activity is also being supported by the R&D engineers. This result indicates a need for greater dissemination of the damping technology, a primary objective of the damping design guide.

3. DAMPING DESIGN GUIDE FORMAT

The damping design guide has been organized into three volumes.

Volume 1 is intended to be a reference volume summarizing the work performed to date on the application of damping technology and the allied fields. It also contains a bibliography of the published articles in these fields and an assessment of future needs.

Volume 2 is intended to be the user oriented design guide. This volume contains a brief introduction to vibration and damping, and a general discussion on how to identify potential vibration problems and how to select the appropriate damping treatment. One chapter will feature design equations/nomograms for predicting the dynamic response of common structural members, both with and without damping treatment. This will be followed by a chapter on worked examples based on successful applications of damping technology. The worked examples are divided into the major fields of application, each introduced by a summary of the problems encountered in that field and followed by a single example for each type of problem.

All of the worked examples and analysis methods have been obtained from literature. The worked examples include a comparison of predicted and measured results such as illustrated in Figures 5 to 7 for circuit boards [9], bolts [10] and exhaust ducts [11], respectively, to name a few. Finite element methods, and results of finite element analysis, involving application of damping, are also included. A typical finite element model of a turbine blade [12] damped with a surface glass treatment is illustrated in Figure 8. A total of 234 elements were used to define the damped blade. The cross-section of the blade (Figure 8b) consisted of fifteen elements for the blade and twelve elements each for the nickel and glass layers. The analysis was performed at temperatures of 800, 925 and 1000° Fahrenheit (427, 296 and 538° Centigrade). The peak damping was obtained at the temperature of 925°F (see Figure 9) in the first mode.

This volume also contains a brief summary of other case histories available in literature for which complete information is not available. The purpose is to broaden the scope of application beyond the worked examples.

Measured damping levels in typical aerospace structures and materials are included for use in the analysis when measured damping data on the actual structures are not available.

Volume 3 contains the damping material data required by the designer. The damping material modules and loss factor are presented in the form of the reduced temperature nomogram [3] (See Figure 10) which is accompanied by a data sheet, Table 1, containing other pertinent information. The use of this standardized data format is explained in the introduction of this volume. The organizations from which these damping materials can be obtained are also listed in this volume.

The damping application can be designed using Volumes 2 and 3. These volumes are intended for use in loose-leaf binders to permit updating of the design methods, in light of experience gained, and of the damping materials which are subjected to change from the normal market pressures.

4. CONCLUSIONS

A design guide is being developed to encourage and permit the application of viscoelastic damping technology at the design stage. It is recognized that the designers will require assistance from dynamicists in the initial use of Volumes 2 and 3 of the design guide until they become familiar with dynamics and viscoelastic damping. They will also require help with finite element analysis, dynamic loads/vibration levels/test specifications, and test methods/data analyses required to verify the performance of the damping treatments, which are usually the responsibility of the dynamics engineer. The widespread use of this relatively specialized, but essential technology is, therefore, dependent upon the assimulation of this technology by dynamics engineers outside the R&D classification. The damping design guide, it is hoped, will speed up this process.

REFERENCES

1. L.C. ROGERS 1978 Conference on Aerospace Polymenic Viscoelastic Damping Technology for the 1980's (L.C.Rogers Editor) Wright-Patterson Air Force Base Report - AFFDL-TM-78-FBA. Damp It: A proposed advanced development program.

2. R.L. BAGLEY 1979 Air Force Materials Lab. TR-79-4103. Application of Generalized Derivatives to Viscoelasticity.

3. L.C. ROGERS 1981 The Shock and Vibration Bulletin, No. 51, Part 1, 55-69, Damping: On modeling viscoelastic behavior.

4. D. ROSS, E.E. UNGAR and E.M. KERWIN, Jr. 1959 Structural Damping, American Society of Mechanical Engineers (J.E. Ruzicka Editor) Damping of plate flexural vibrations by means of viscoelastic laminae.

5. B.C. NAKRA 1976 The Shock and Vibration Digest 8, 3-11. Vibration control with viscoelastic materials.

6. B.C. NAKRA 1981 The Shock and Vibration Digest 13, 17-20. Vibration control with viscoelastic materials - II.

7. M.S. KLUESENER, M.L. DRAKE 1982 The Shock and Vibration Bulletin No. 52, Part 5, Mathematical Modeling: Damped Structure Design Using Finite Element Analysis.

8. C.D. JOHNSON, D.A. KIENHOLZ, and L.C. ROGERS 1981 The Shock and Vibration Bulletin No. 51, Finite Element Prediction of Damping in Beams with Constrained Viscoelastic Layers.

9. J.M. Medaglia 1978 Conference on Aerospace Polymeric Viscoelastic Damping Technology for the 1980's, Wright-Patterson Air Force Base Report AFFDL-TM-78-FBA, SMRD Damping.

10. R.C. Peller, General Dynamics Corvair Division Report, Damping in Mirror Mounts and Composite Structure.

11. J. J. DeFelice, A.D. Nashif 1978 The Shock and Vibration Bulletin, No. 48, Part 2, 75-84, Damping of An Engine Exhaust Stack.

12. Same as Ref 7.

13. D.I.G. Jones 1981 Journal of Aircraft 18, 644-649. An attractive method for displaying material damping data.

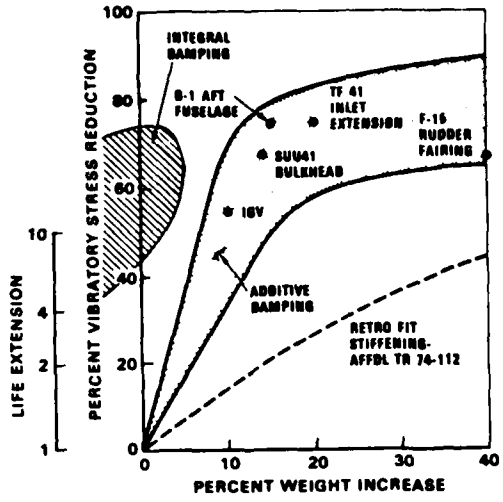

FIG. 1 LIFE EXTENSION OBTAINED WITH ADDITIVE DAMPING ON EXISTING HARDWARE

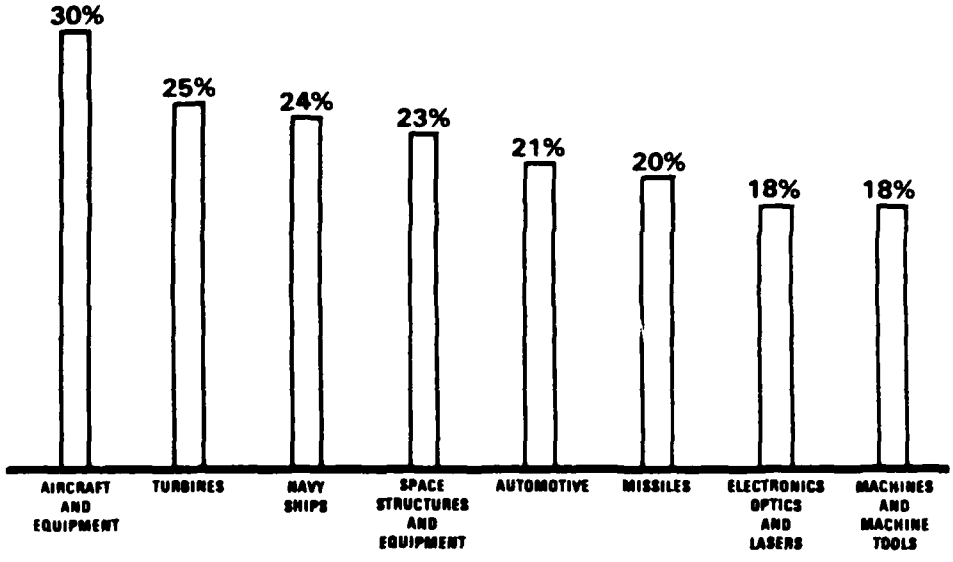

FIG. 2 APPLICATION OF DAMPING TECHNOLOGY

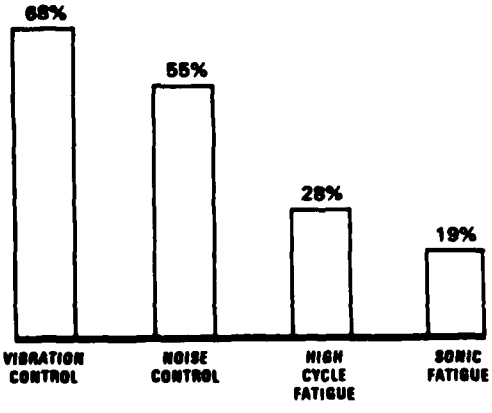

FIG. 3 PURPOSE FOR USE OF DAMPING TECHNOLOGY

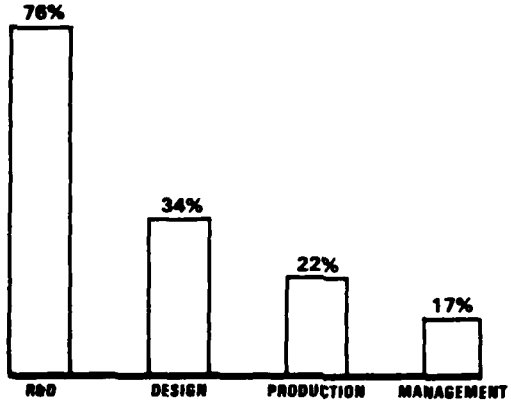

FIG. 4 CLASSIFICATION OF INDIVIDUALS ACTIVE IN THE APPLICATION OF DAMPING TECHNOLOGY

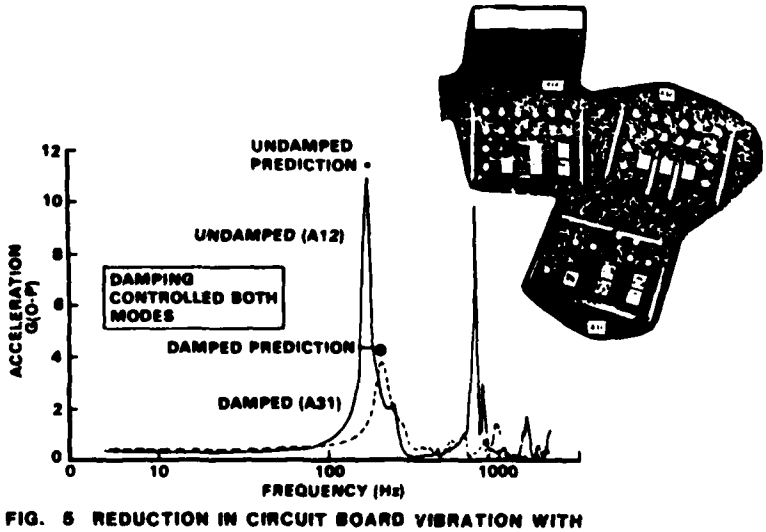

FIG. 5 REDUCTION IN CIRCUIT BOARD VIBRATION WITH ADDITIVE DAMPING

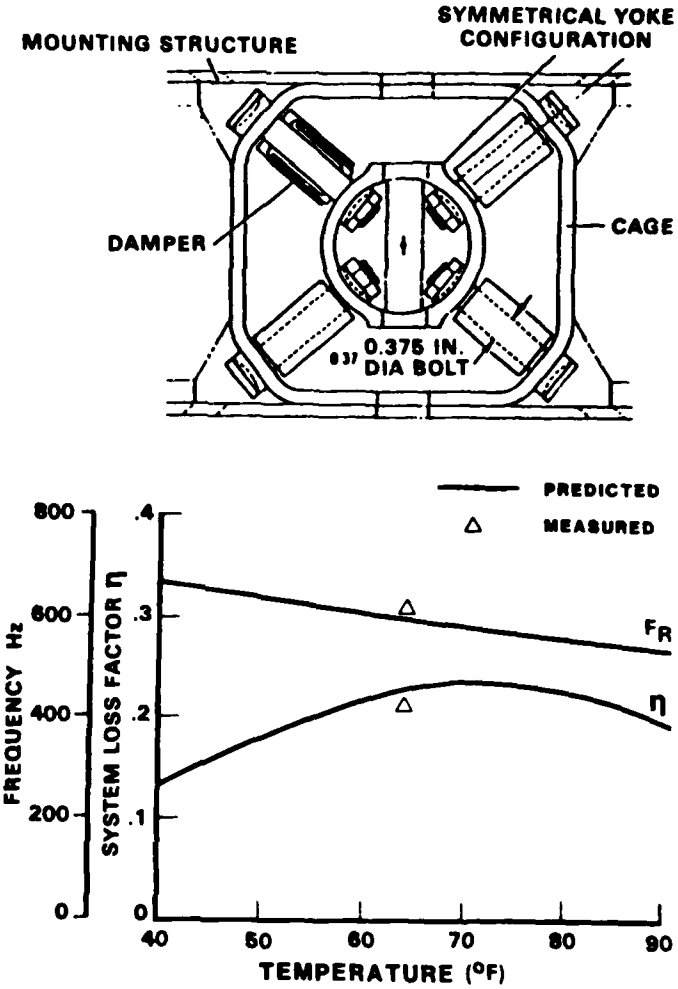

FIG. 6 INCREASE IN LOSS FACTOR OBTAINED WITH DAMPED BOLTS

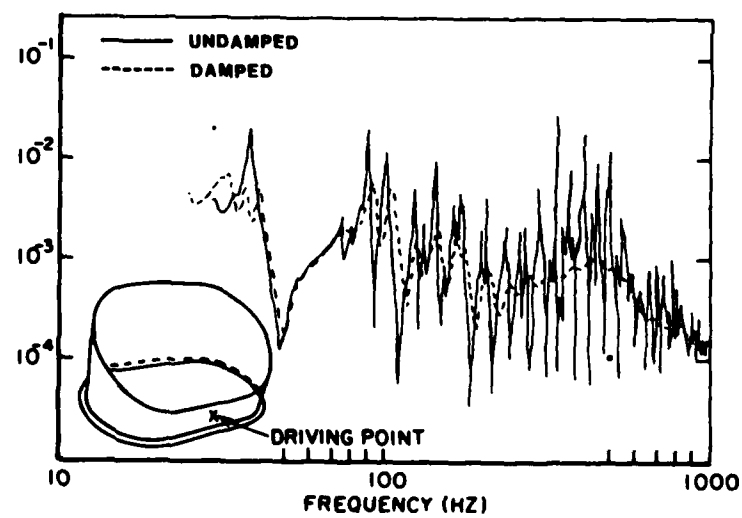

FIG. 7 EFFECT OF DAMPING ON HELICOPTER EXHAUST DUCT VIBRATION

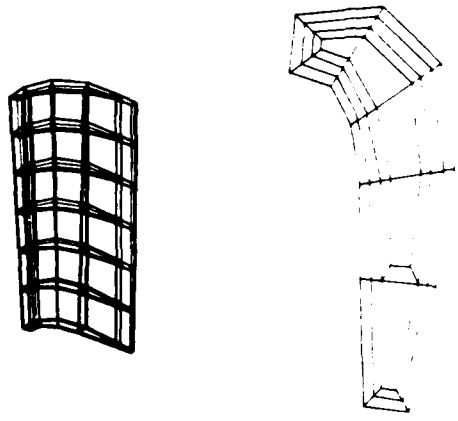

FIG. 8 FINITE ELEMENT MODEL OF TURBINE BLADE

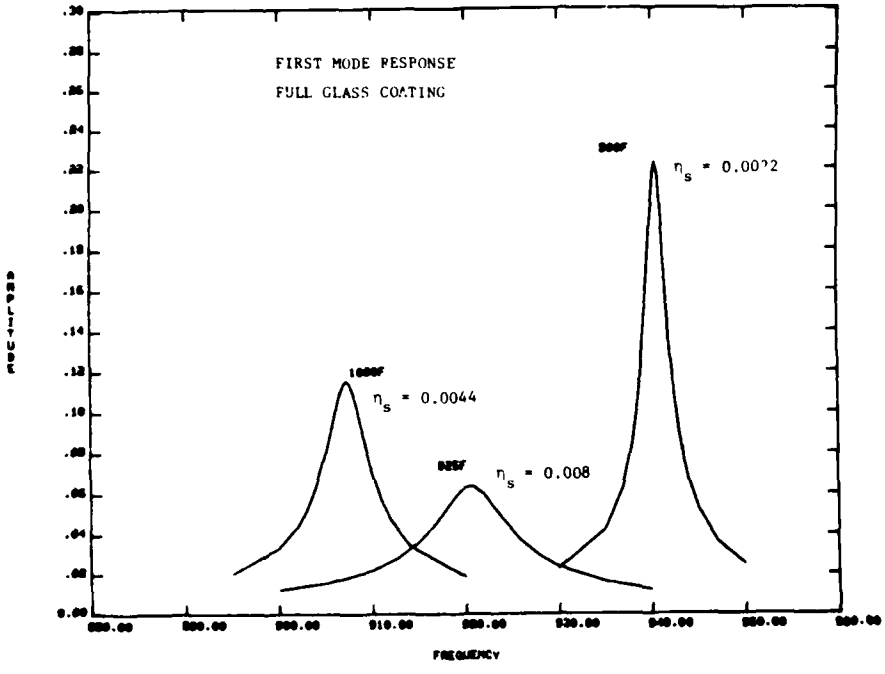

FIG. 9 FIRST MODE BLADE RESPONSE WITH FULL GLASS COATING AT THREE TEMPERATURES

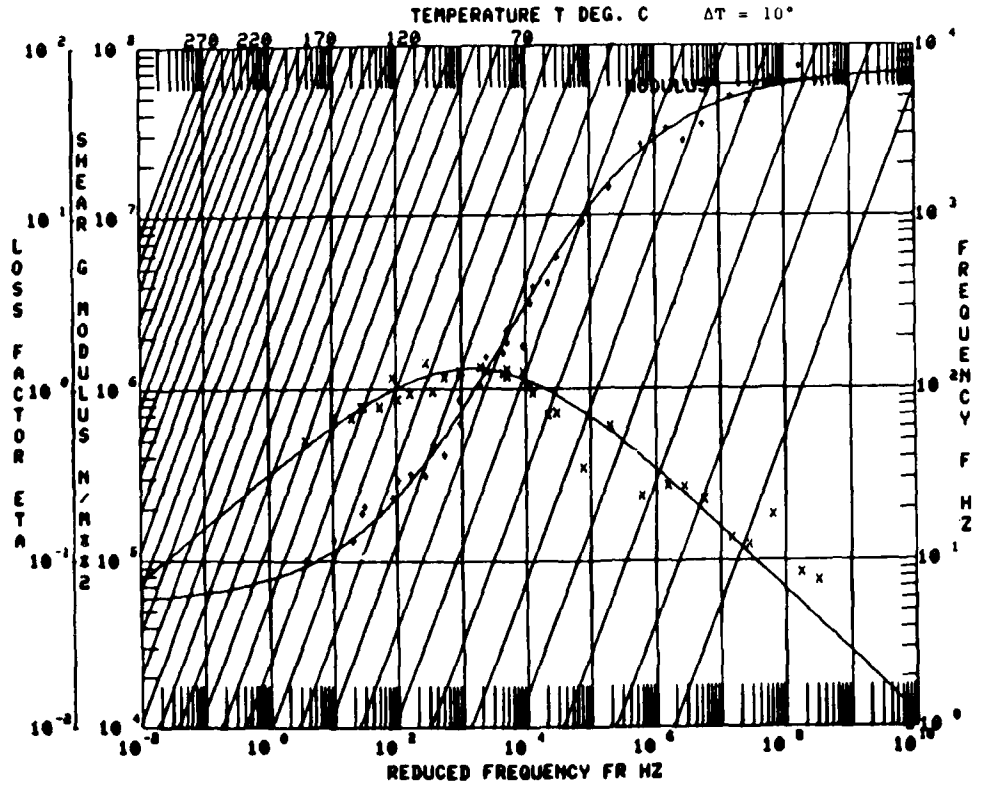

FIG. 10 TYPICAL REDUCED FREQUENCY DAMPING MATERIAL NOMOGRAM

TABLE 1 TYPICAL DAMPING MATERIAL DATA SHEET

MATERIAL MN MANUFACTURER THE SOUNDCOAT COMPANY
MAX LOSS FACTOR η_p 2 1494 MODULUS ⊠ SHEAR ☐ YOUNG S
MODULUS AT η_p 08 PSI 4 13E2 PASCALS
MAX MODULUS 1 94E6 PSI 1 34E9 PASCALS
MIN MODULUS 3 77 PSI 2 6E4 PASCALS
MAX SURVIVAL TEMP LONG TERM NA °F °C
MAX SURVIVAL TEMP SHORT TERM NA °F °C FOR MINUTES
ULTIMATE TENSILE STRENGTH NA PSI PASCALS
DENSITY 030 LBS/IN^3 0 83 G/CC
POISSON S RATIO NA
MAX ALLOWABLE STRAIN LEVEL NA
EFFECTS OF CONTAMINANTS NA
EFFECTS OF RADIATION NA
OUTGASSING NA
THERMAL CONDUCTIVITY NA BTU IN/FT^2 HR °F KCAL/SEC METER °C
CONFORMABILITY EXCELLENT
SUPPLIED AS (FORM) AVAILABLE AS SOUNDFOIL - DAMPING MATERIAL WITH ALUMINUM CONSTRAINING LAYER
BONDING AND/OR APPLICATION PROCEDURE MN IS SELF ADHESIVE AT ROOM TEMPERATURE CLEAN SURFACES TO BE BONDED WITH SOLVENT AND APPLY WITH MODERATE PRESSURE

FREQ. Hz	TEMP FOR η_p °F °C	LOWER LIMIT FOR $\eta \geq 70\% \eta_p$ °F °C	UPPER LIMIT FOR $\eta \geq 70\% \eta_p$ °F °C	MODULUS AT LOWER LIMIT PSI Pa	MODULUS AT UPPER LIMIT PSI Pa
10	21 29 4	-48 -43 3	10 -12 2	1 80E3 1 241E7	8 7E1 6 0E5
100	13 10 6	15 -26 1	61 10 6	1 82E3 1 255E7	8 4E1 5 79E5
1000	54 12 2	21 -6 1	99 37 2	1 83E3 1 262E7	8 4E1 5 79E5

TEST NUMBER 81 01
T_O 10 °C 12 2
MODULUS CURVE PARAMETERS
FROM 2 0E3
MRUM 5 9E6
N 0 3
ML 2 8E4

LOSS FACTOR CURVE PARAMETERS
ETAFROL 2 1
SL 0 4
SH -0 8
FROL 1 3E3
C 1 0

ADDITIONAL COMMENTS

CONTINUUM MODELLING OF DAMPING IN LARGE SPACE STRUCTURES

S. Abrate and C.T. Sun

School of Aeronautics and Astronautics
Purdue University (U.S.A.)

1. INTRODUCTION

Large Space Structures (LSS) are periodic lattices made up of a large number of elements. Their overall appearance may be that of a beam or a plate, and the complexity of their finite element models results from their topological complexity rather than that of their expected behavior. Therefore several investigators have developed equivalent continuum models to simplify linear [1] and nonlinear [2] analyses. These simple models accurately represent the behavior of the original structure for long wavelengths [3].

LSS are subjected to stringent requirements for position, shape and vibration control so that an active control system needs to be implemented. Passive damping in LSS insures the stability of the active control system, allows for higher gains, reduces the bandwidth and therefore the number of sensors and actuators to be used [4]. Sources of damping can be many, among which joint friction and internal damping seem of interest. In this study internal damping will be considered. The formulation of mathematical models including damping effects for discrete and continuous structures are discussed, the damping properties of the equivalent continuum models are determined and results are presented for several examples.

2. MATHEMATICAL DAMPING MODELS

The basic phenomena at the origin of damping are not fully understood and several mathematical models have been proposed each being adequate for certain applications [5]. With differential models, stress, strain and their time derivatives are related through the relation

$$\sum_{k=1}^{n} p_{k-1}\, \sigma^{(k-1)} = \sum_{i=1}^{m} q_i\, \varepsilon^{(i-1)} \qquad (1)$$

where a superscript k designates the kth time derivative. In Eq. (1), with $p_o = 1$, the case n = 1 and m = 2 corresponds to Kelvin's solid, and n = 2 and $m^o = 2$ to a Standard Linear Solid (SLS).

Hysteretic models are used to describe materials for which damping is frequency-independent. For steady state harmonic motion we have

$$\tilde{\sigma} = (E + iE')\tilde{\varepsilon} \qquad (2)$$

where $\tilde{\sigma}$ and $\tilde{\varepsilon}$ refer to the amplitude of stress and strain, E and E' are two material constants.

This model should not be used for transient response calculations since then the principle of causality is violated [5]. The viscous damping model is in disagreement with experimental evidence for high frequencies, and the SLS model is expected to be more realistic.

Experimental data is lacking since tests for aircraft structures applications are generally performed at higher stress levels and frequencies than those of interest for LSS. Then, only the simplest mathematical models

(Kelvin's solid, SLS, hysteretic model) can reasonably be used until more data become available.

3. STRUCTURAL DYNAMIC MODELS

The analysis of trusses and frames is performed using the Finite Element Method (FEM). For viscous damping the equations of motion are

$$[M]\{\ddot{u}\} + [C]\{\dot{u}\} + [K]\{u\} = \{F\} \tag{3}$$

where [M] = mass matrix, [C] = damping matrix, [K] = stiffness matrix, {u} = nodal displacement vector and {F} = external force vector.

For the steady state response of a structure with hysteretic damping, the equations of motion are

$$([K] - \omega^2[M] + i[H])\{\tilde{U}\} = \{\tilde{F}\} \tag{4}$$

where ω is the excitation frequency, [H] is the hysteretic damping matrix and $\{\tilde{U}\}$ and $\{\tilde{F}\}$ are the amplitude vectors of the nodal displacements and external force respectively.

In the case of SLS type of damping, the equations of motion are

$$[D]\{\dddot{u}\} + [M]\{\ddot{u}\} + [C]\{\dot{u}\} + [K]\{u\} = \{F\} \tag{5}$$

To obtain a model for an entire structure damping can be prescribed at the element level according to Eqs. (1-3) and then global matrices are assembled as usual. Another possibility is to prescribe damping at the structure level. When proportional damping is assumed the damping matrix in Eq. (4) takes the form $[C] = \alpha[M] + \beta[K]$. While this assumption allows the modal equations to be uncoupled, there is no justification for it and the coefficients α and β are choosen arbitrarily. Damping matrices can also be formulated so that each mode of the structure has a prescribed damping ratio. Again, tests results or previous experience with similar structures is necessary to select these ratios. Since ground testing of LSS is difficult due mainly to their size [6], and the reliability of test results is questionable, it is difficult to prescribe damping at the structure level. Damping is more conveniently prescribed at the element level.

The formulation of the Timoshenko beam element is extended to the case of viscous damping in [7]. For steady state response analysis, the hysteretic damping model was adjusted so that for the first natural frequency of the system (ω_1), the response matches that obtained when viscous damping is used. That is $[H] = \omega_1[C]$ in equation (4). A plane truss finite element with SLS type damping is formulated using Galerkin's method.

4. EQUIVALENT MODELS

The equations of motion of a Timoshenko beam with SLS type of damping are

$$GA(w'' + \phi') + G'A(\dot{w}'' + \dot{\phi}') + q + p_1\dot{q} = \rho A(\ddot{w} + p_1\dddot{w}) \tag{6}$$

$$GA(w' + \phi) + G'A(\dot{w}' + \dot{\phi}) - EI\,\phi'' - E'I\phi'' + \rho I(\ddot{\phi} + p_1\dddot{\phi}) = 0 \tag{7}$$

where w is the transverse displacement, ϕ the rotation, EI and GA the bending and shear rigidities, ρA the mass per unit length, ρI the rotatory inertia. For viscous damping, set $p_1 = 0$. For hysteretic damping let E and G be complex quantities in the undamped equations of motion.

For a simply-supported beam an analytical solution for the steady state harmonic loading is obtained using modal expansion while for transient analysis the finite element method is used.

The properties of the equivalent Timoshenko beam have to be evaluated from the properties of the original structure. Extending the method proposed in [1] for undamped structures, we isolate a single cell and apply harmonic loading to produce global extension, bending or shear (Fig. 1). In simple cases formulas are obtained for the various coefficients, and for more complex situations a numerical procedure is used.

4.1 Plane Truss with Damping

The equations of motion of the plane truss in Fig. 1, subjected to harmonic loading are

$$([K] + i\omega[C])\ \{\tilde{U}\} = \{\tilde{F}\} \tag{8}$$

for viscous damping. For bending motion for example

$$\{\tilde{U}\} = \{\tilde{U}_1,\ \tilde{U}_2,\ \tilde{V}_2,\ \tilde{U}_3,\ \tilde{V}_3\}\ ,\ \{\tilde{F}\} = \{\tilde{F},\ -\tilde{F},\ 0,\ \tilde{F},\ 0\}$$

Solving Eq. (8) we get $\tilde{U}_1 = \tilde{F}/(\tilde{E}A_1/L)$ where $\tilde{E} = E + i\omega\underline{E}'$, $\underline{E}$ and E' being equal to q_0 and q_1 in Eq. (1). Since the bending moment is $\tilde{M} = \tilde{F}.H$, and the curvature $\Delta\phi/\Delta x = 2(\tilde{U}_1/HL)$, the equivalent complex rigidity $\tilde{M}/(\Delta\phi/\Delta x) = \frac{1}{2}(\tilde{F}/\tilde{U}_1)$ H^2L becomes $\frac{1}{2}\ \tilde{E}A_1H^2$. So the equivalent beam coefficients are

$$\overline{EI} = \tfrac{1}{2}\ EA_1H^2 \quad \text{and} \quad \overline{E'I} = \tfrac{1}{2}\ E'A_1H^2 \tag{9}$$

Following the same procedure for axial and shear deformation we obtain

$$\overline{EA} = 2[EA_1 + (EA_d/\mu)(L/D)^3]\ ,\quad \overline{E'A} = 2[E'A_1 + (E'A_d/\mu)(L/D^3]$$

$$\overline{GA} = 2EA_d(H^2L/D^3)\ ,\quad G'A = 2E'A_d(H^2L/D^3) \tag{10}$$

where $\mu = 1 + 2\ (EA_d/EA_t)(H/D)^3$

For hysteretic damping the same procedure applies and results (9,10) still hold.

4.2 Numerical Determination of Equivalent Damping Properties

Considering a complex cell (Fig. 2), harmonic loadings are applied to produce global extension, bending, torsion or shear deformation (Fig. 3). Using the FEM, this cell can be analyzed directly as described in Sec. 3. In axial motion for example, the axial displacement is $\delta = \delta + i\delta_i$ which corresponds to a strain $\varepsilon = \delta/L = \delta/L + i\delta_i/L$, L being the cell length. For a viscously damped homogeneous bar ($\sigma = E\varepsilon + E'\dot{\varepsilon}$) subjected to a stress $\sigma = \sigma_0\ \exp(i\omega t)$, the strain $\varepsilon = \varepsilon_0\ \exp(i\omega t)$ with $\varepsilon_0 = [G_1(\omega) + iG_2(\omega)]\ \sigma_0$ where $G_1 = E/[E^2 + (\omega E')^2]$, $G_2 = -E'\omega/[E^2 + (\omega E')^2]$ so that $E/E' = -(1/\omega)(G_2/G_1) = (1/\omega)[\mathrm{Im}(\varepsilon)/\mathrm{Re}(\varepsilon)]$.

Since the structure and its equivalent continuum should experience the same strain under the same load, $E'A/EA = -(1/\omega)\delta_i/\delta$ and since the equivalent rigidigy EA is already known from static tests [1], the equivalent damping coefficient E'A is readily obtained.

5. EXAMPLES

For the truss in Fig. 4, the equivalent properties are determined using Eqs. (8-10). The steady state response predicted by direct analysis and the equivalent models are compared in Fig. 5 for viscous, hysteretic and SLS type damping respectively. The damping coefficient is assumed to be $E' = 4\times10^8 N/m^2$ -sec which leads to the equivalent damping properties of the truss beam given by

$$\overline{E'I} = 4.0\times10^5 \text{ N} - \text{m}^2 - \text{sec}$$

$$\overline{G'A} = 8.24\times10^3 \text{ N} - \text{sec} \quad .$$

The transient response to an impulse of duration $1.5\times T_0$ (T_0 = period of first bending mode), is determined by direct time integration for both the original structure and its equivalent model which was in turn discretized in 10 elements. Results in Fig. 6 show good agreement.

A cantilever latticed beam with triangular cross section (Fig. 2) was studied next. Given that $E'/E = 0.001$ for the longitudinal members and $E'/E = 0.005$ otherwise, the numerical procedure of Sec. 4 gives $E'I/EI = 0.00159$ and $G'A/GA = 0.005$.

The steady state response given by the continuum model agrees well with the direct solution as shown in Fig. 7.

REFERENCES

1. C.T. SUN, B.J. KIM and J.L. BOGDANOFF 1981 Proc. AIAA Dynamic Speciality Conference, Atlanta, GA, 523-32. On the Derivation of Equivalent Simple Models for Beam and Plate-like Structures in Dynamic Analysis.

2. S. ABRATE and C.T. SUN 1983 Computers and Structures, 17, (4), 491-497. Dynamic Analysis of Geometrically Nonlinear Truss Structures.

3. S. ABRATE and C.T. SUN 1983 Proc. ASCE EMD Speciality Conference. Wave Propagation in Plane Trusses and Frames.

4. H. HASLEY 1982 Proc. 23rd Struc. Dyn. Matls. Conf., New Orleans, LA. On Passive Damping Mechanisms in Large Space Structures.

5. C.W. BERT 1973 Journal of Sound and Vibration 29(12), 129-153. **Material Damping: An Introductory Review of Mathematical Models, Measures and Experimental Techniques.**

6. C.V. STAHLE 1982 NASA CP 2258 In Modelling Analysis and Optimization Issues for Large Space Structures. Analysis and Testing of Large Space Structures.

7. L.A. ROUSSOS, M.W. HYER and E.A. THORNTON 1982 AIAA Journal 20(6). **Finite Element Model with Nonviscous Damping.**

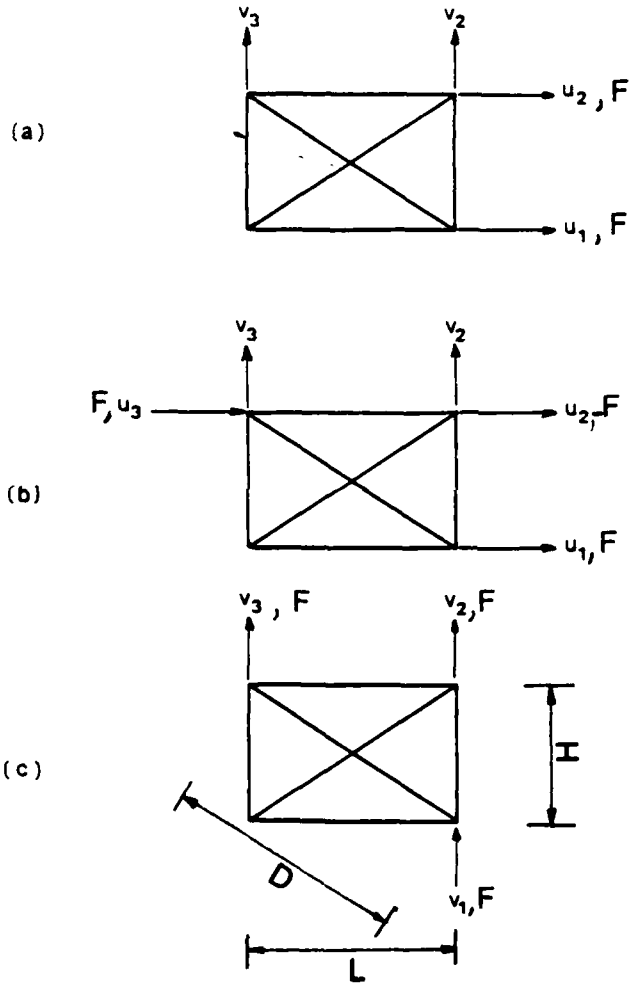

Figure 1: Testing of a typical cell: a) axial force applied, b) bending moment applied, c)transverse shear force applied

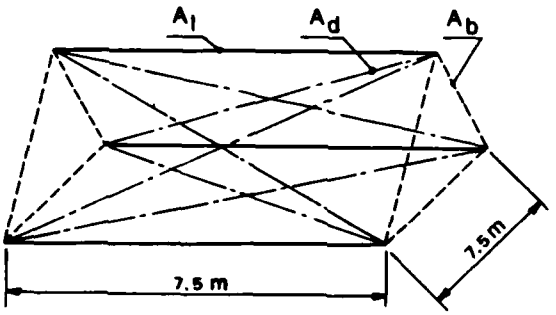

$E = 71.7 \times 10^9 \ N.m^{-2}$
$\rho = 2768 \ kg.m^{-3}$
$A_l = 80 \times 10^{-6} m^2$
$A_d = 40 \times 10^{-6} \ m^2$
$A_b = 60 \times 10^{-6} \ m^2$

Figure 2: Typical cell for the lattice beam with triangular cross section

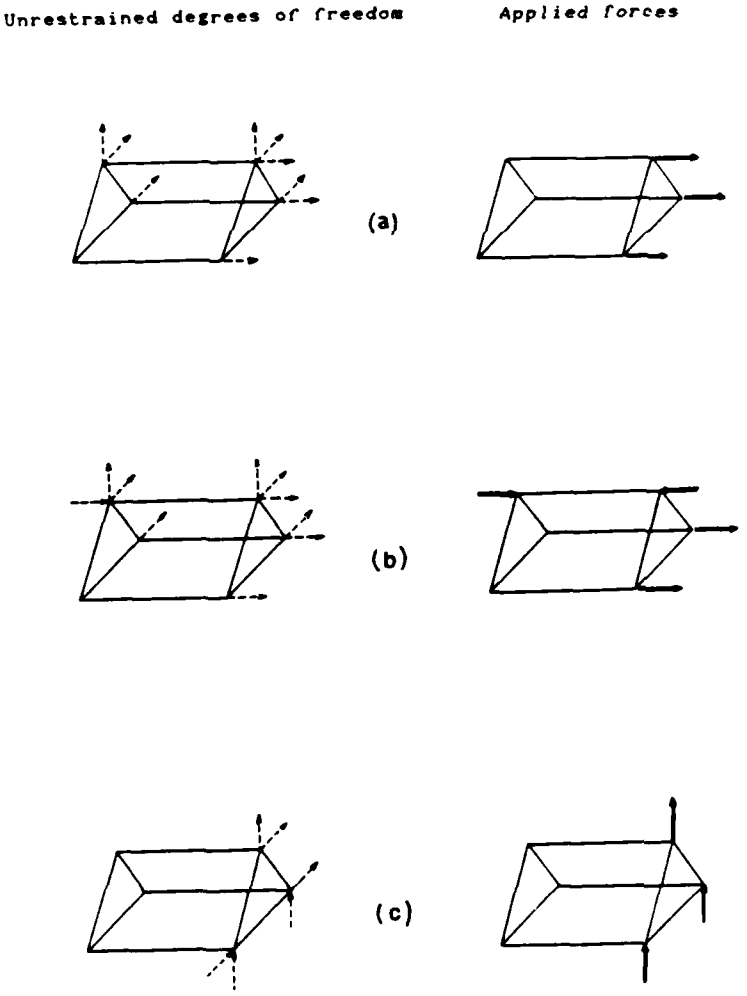

Figure 3: Testing of a complex cell:
a) extension, b) bending, c) transverse shear

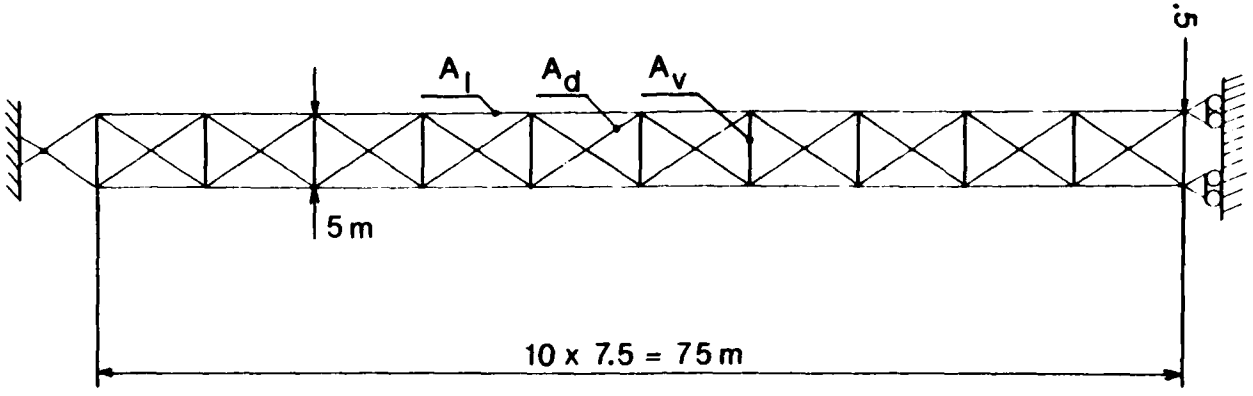

$E = 71.7 \times 10^{9}\ N.m^{-2}$
$\rho = 2768\ kg.m^{-3}$
$A_l = 80 \times 10^{-6} m^2$
$A_d = 40 \times 10^{-6}\ m^2$
$A_v = 60 \times 10^{-6}\ m^2$

Figure 4: Simply supported truss

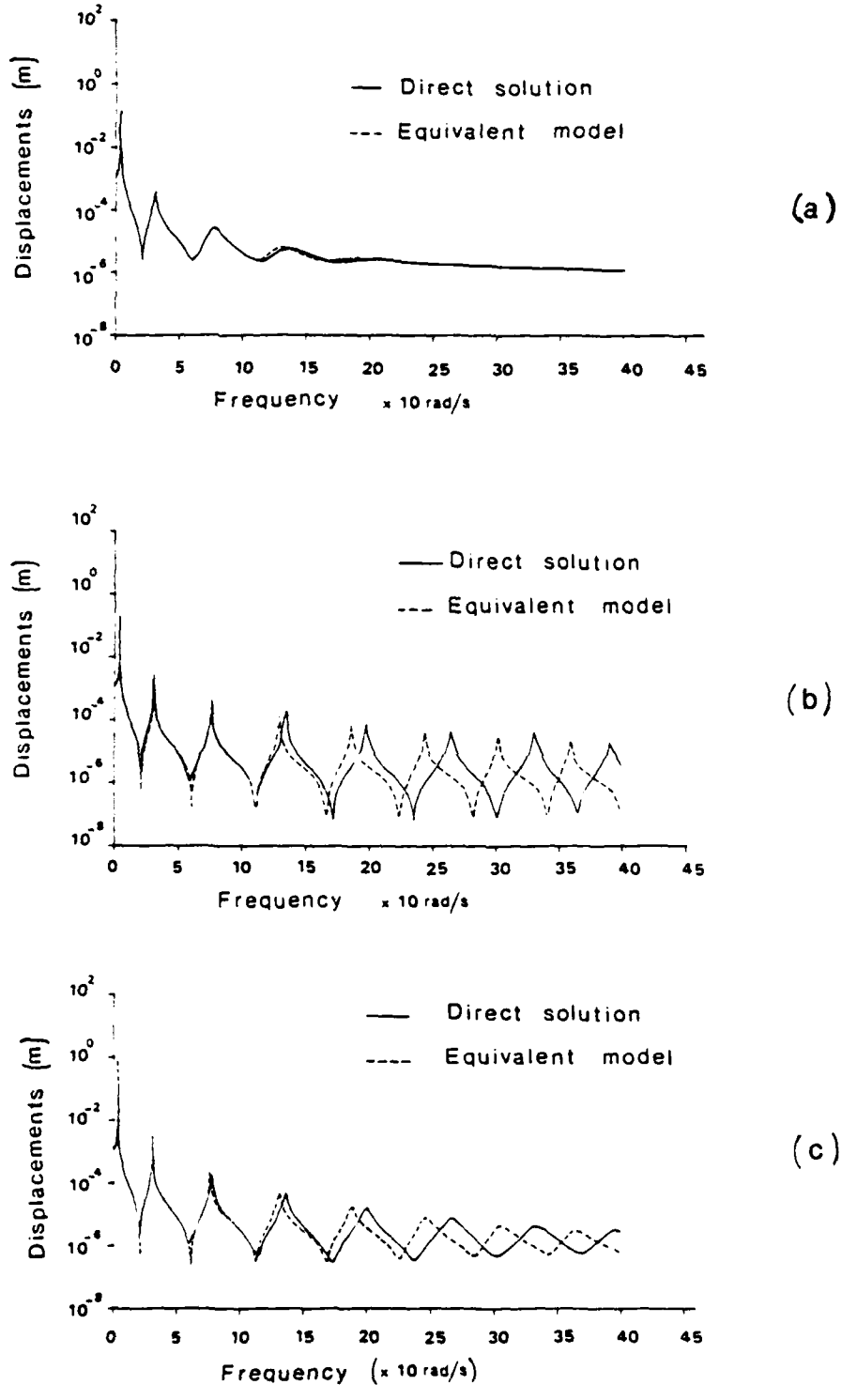

Figure 6: Steady state response of the simply supported truss: a) viscous damping, b) hysteretic damping, c) standard linear solid damping

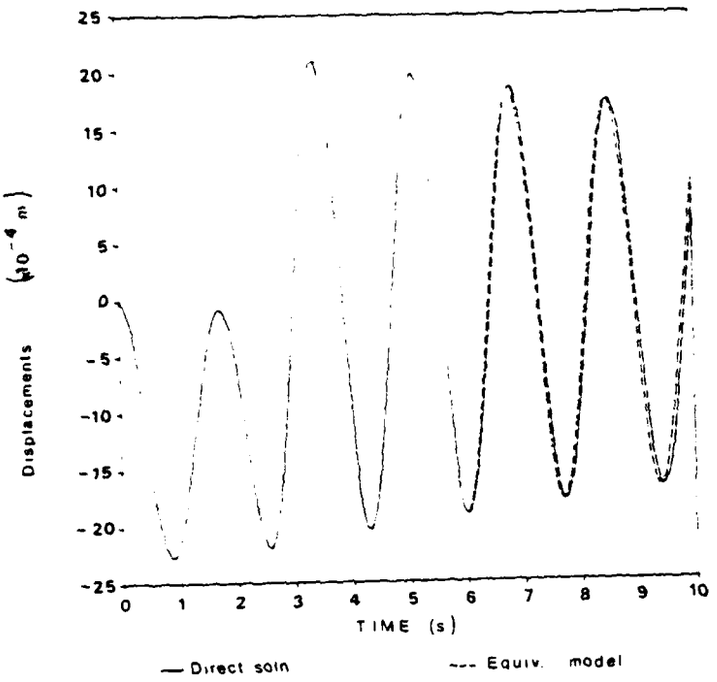

Figure 5: Transient response of the simply supported truss

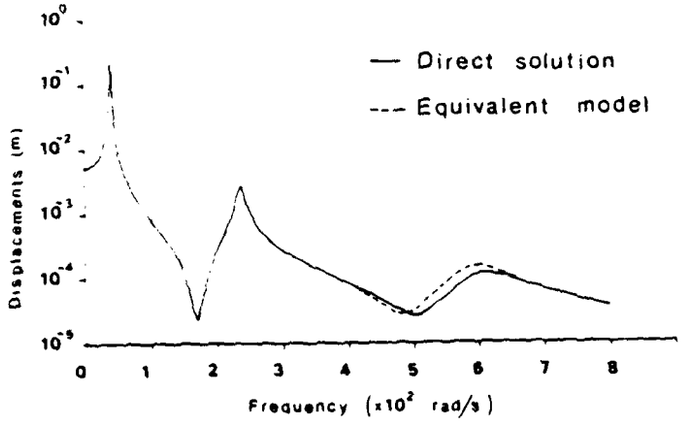

Figure 7: Steady state response of the lattice beam with triangular cross section

DETERMINATION OF RECEPTANCES OF LOCALLY DAMPED STRUCTURES

H. Nevzat Özgüven

Department of Mechanical Engineering
Middle East Technical University, Ankara, Turkey

1. INTRODUCTION

The mode superposition method is a useful tool in vibration analysis of structures. Receptances of a discretized model can most easily be determined by modal analysis if the structure is undamped or classically (proportionally) damped. When the damping is non-classical, the method necessitates the use of complex modal vectors [1-3], which increases the computational time required for both the eigensolution and the modal summation. For structures with frequency dependent internal damping properties (e.g., coated with viscoelastic materials), a different complex eigenvalue problem must be solved at each exciting frequency. Various approximate modal analysis methods, on the other hand, are available for the dynamic analysis of non-classically damped structures. Most of them require the solution of a real eigenvalue problem and then use the undamped modal data to predict the dynamic behaviour of the damped structure. Application of these approximate methods is usually limited by several factors such as level of damping or separation of modes. As the survey of these methods can be found elsewhere [for example, see 4 and 5], it need not be repeated here. Several authors have also discussed and compared the validity of various approximate methods [6-10].

In this work a method is proposed for the computation of the receptances of a non-classically damped structure from their undamped counterparts, which can easily be obtained from the undamped modal data. A numerical example is given.

2. THEORETICAL APPROACH

2.1 Modal Analysis

Consider a discrete model of a damped structure. The equation of motion can be written as

$$[M]\{\ddot{x}\} + [[K] + i[H]]\{x\} = \{F\} \qquad (1)$$

where [M], [K], [H] are mass, stiffness and structural damping matrices of the system respectively; {x} is the vector of generalized coordinates, {F} is the generalized forcing vector and $i=\sqrt{-1}$. The dot denotes differentiation with respect to time. The undamped modal data for the system under consideration can be obtained by solving the following eigenvalue problem

$$[K]\{\phi\} = \omega^2 [M]\{\phi\} \qquad (2)$$

Solution of equation (2) yields n undamped natural frequencies, ω_r^2, and n real modal vectors, $\{\phi^r\}$, where n is the order of the system. The orthogonality of the real modes with respect to the mass and stiffness matrices renders the dynamic analysis of the undamped system straightforward. The modal vectors of the undamped system can be normalized with respect to the mass matrix

$$[\phi]^T [M][\phi] = [I] \qquad (3)$$

$$[\Phi]^T [K] [\Phi] = [\omega_r^2] \qquad (4)$$

where $[\Phi]$ and $[I]$ are the modal and unit matrices, respectively, and $[\omega_r^2]$ is a diagonal matrix containing the squares of the undamped natural frequencies. The transformation

$$\{x\} = [\Phi] \{\eta\} \qquad (5)$$

uncouples the equation of motion of the undamped system in which case the equation of motion takes the form

$$\{\ddot{\eta}\} + [\omega_r^2] \{\eta\} = [\Phi]^T \{F\} \qquad (6)$$

The principal coordinates $\{\eta\}$ can be solved from equation (6) and substituted into equation (5) to yield the response to the excitation $\{F\}$. For a harmonic excitation of frequency ω, the response can be written as

$$\{x\} = \sum_{r=1}^{n} \frac{\{\Phi^r\} \{\Phi^r\}^T \{F\}}{\omega_r^2 - \omega^2} \qquad (7)$$

from which the receptances of the undamped system can be identified as

$$[\beta] = \sum_{r=1}^{n} \frac{\{\Phi^r\} \{\Phi^r\}^T}{\omega_r^2 - \omega^2} \qquad (8)$$

The classical damping case (i.e., in which the undamped modal matrix is orthogonal with respect to the damping matrix) does not introduce further complications: For a classically damped system the receptance matrix can be calculated from:

$$[\alpha] = \sum_{r=1}^{n} \frac{\{\Phi^r\} \{\Phi^r\}^T}{\omega_r^2 - \omega^2 + ih_r} \qquad (9)$$

where h_r is the modal damping and defined as

$$h_r = \{\Phi^r\}^T [H] \{\Phi^r\} \qquad (10)$$

In the conventional approximate method for the dynamic analysis of non-classically damped systems, equation (9) is used by ignoring all non-diagonal elements of the transformed damping matrix. However, the method has its drawbacks and its limitations as discussed in [7, 8, 10].

2.2 The matrix Inversion Method

Consider again the system described by equation (1). For a harmonic excitation of frequency ω it can be re-written as

$$[\,[K] - \omega^2[M] + i[H]\,]\,\{x\} = \{F\} \qquad (11)$$

where the inverse of the coefficient matrix can be identified as the receptance matrix of the damped system; that is

$$[\alpha] = [\,[K] - \omega^2[M] + i[H]\,]^{-1} \qquad (12)$$

Similarly, the receptance matrix of the corresponding undamped system, $[\beta]$, can be

written as

$$[\beta] = [\,[K] - \omega^2[M]\,]^{-1} \qquad (13)$$

Incorporation of equations (12) and (13) yields

$$[\alpha]^{-1} = [\beta]^{-1} + i[H] \qquad (14)$$

Premultiplying both sides of equation (14) by $[\beta]$ and postmultiplying by $[\alpha]$ yields the required relationship between $[\alpha]$ and $[\beta]$

$$[\beta] = [\alpha] + i[\beta]\,[H]\,[\alpha] \qquad (15)$$

or

$$[\beta] = [\,[I] + i[\beta]\,[H]\,]\,[\alpha] \qquad (16)$$

The receptance matrix of the damped system can then be written in terms of the undamped receptance matrix $[\beta]$ and the damping matrix [H] as

$$[\alpha] = [\,[I] + i[\beta]\,[H]\,]^{-1}\,[\beta] \qquad (17)$$

Alternatively, equation (16) can be solved for $[\alpha]$, which does not require a matrix inversion but the simultaneous solution of a set of complex equations. For local damping treatments, equation (17) can be partitioned to reduce the order of the matrix to be inverted. Furthermore, as the real part of the matrix to be inverted is the unit matrix, the computational effort required for inversion is reduced considerably.

It is also possible to derive equation (17) by using a substructuring approach, that is to say by insertion of a secondary system into the primary one via receptance coupling, basic principles of which has been given by Bishop and Johnson [11]. Such a technique was used by Hammill and Andrew [12] to calculate the effect of a small number of discrete damping sources upon particular receptances; the method was then extended by Özgüven [5] to determine the complete damped receptance matrix. In both works the effect of external damping sources are investigated. Using a similar technique and treating the internal damping as external forces acting on the undamped system, would again yield equation (17). However, the procedure would be more complex and it would involve physically somewhat meaningless mathematical operations, such as considering a negative element of the internal damping matrix as a negative external damper.

2.3 Locally Damped Systems

For a locally damped system, the damping matrix [H] can be partitioned as

$$[H] = \begin{bmatrix} [H_{11}] & [0] \\ [0] & [0] \end{bmatrix} \qquad (18)$$

where $[H_{11}]$ is the nonzero part of the damping matrix of order m. It can then be shown [5] that the damped receptance matrix can be put into the form

$$[\alpha_{11}] = [\,[I] + i[\beta_{11}]\,[H_{11}]\,]^{-1}\,[\beta_{11}] \qquad (19)$$

$$[\alpha_{12}] = [\,[I] + i[\beta_{11}]\,[H_{11}]\,]^{-1}\,[\beta_{12}] \qquad (20)$$

$$[\alpha_{21}] = [\beta_{21}] - i[\beta_{21}]\,[H_{11}]\,[\alpha_{11}] \qquad (21)$$

$$[\alpha_{22}] = [\beta_{22}] - i[\beta_{21}]\,[H_{11}]\,[\alpha_{12}] \qquad (22)$$

where subscripts 1 and 2 refer to damped and undamped regions, respectively. Thus the receptance matrix of the damped system can be obtained by inverting a single complex matrix whose real part is the unit matrix and therefore the effort necessary to invert it is comparable to that of inverting a real matrix of the same order. Furthermore, the order of the matrix to be inverted is just m, the value of which depends on the number of damped points in the discretized model.

For structures with both uniform and additional local damping, the damping matrix can be written as the summation of a proportional damping matrix and a non-proportional one in the form of equation (18). Then the matrix inversion method can again be used economically by considering only the non-proportional part of the damping in equation (17), and by taking the effect of the proportional damping into consideration in evaluating $[\beta]$ (i.e., by using equation (9) instead of equation (8) for the computation of $[\beta]$).

3. RESULTS AND DISCUSSION

The method is applied to a simple two degree of freedom system with

$$[M] = \begin{bmatrix} 5 & 0 \\ 0 & 10 \end{bmatrix} \text{ kg}$$

$$[K] = \begin{bmatrix} 2.05\ 10^6 & -2.50\ 10^5 \\ -2.50\ 10^5 & 2.50\ 10^5 \end{bmatrix} \text{ N/m}$$

$$[H] = \begin{bmatrix} 1.15\ 10^5 & -2.50\ 10^4 \\ -2.50\ 10^4 & 2.50\ 10^4 \end{bmatrix} \text{ N/m}$$

which may be considered as the combination of two classically damped systems having the loss factors $\eta_1 = 0.05$ and $\eta_2 = 0.10$, producing a non-classically damped system when combined. The undamped natural frequencies of the system are

$$\omega_1 = 147.58 \text{ rad/s} \quad \text{and} \quad \omega_2 = 642.82 \text{ rad/s}$$

The receptance matrix of the system is calculated at a number of frequencies including resonances by the method suggested, and then the results are compared with the exact values which can easily be obtained for a simple two degree of freedom system. The comparison of the results shows that the method suggested yields the *exact values* for both real and imaginary parts of the receptances at every frequency. Table 1 shows the calculated values of the receptances at several frequencies. The selected frequencies are the frequencies at which either the real part or the imaginary part or the modulus of the receptance shows a maximum.

Increasing the damping 10 times did not deteriorate the accuracy of the results, indicating that the method works for heavily damped systems as well. However, it should be noted that in the numerical example given the exact values of the undamped receptances are used rather than the truncated values, and this will not be the case when the method is applied for large structures. A continuing study investigates the effect of using truncated receptance values on the accuracy of the method. Also a numerical technique is currently under development to avoid the inversion process of the complex matrix in equation (17), trying to make the method economical even for systems with large damping matrices.

Table 1 - The computational values of the receptances

Exc. Freq. ω (rad/s)	α_{ij}	Real Part Re(α) (m/N)	Imag. Part Im(α) (m/N)
141	α_{11}	$0.9474\ 10^{-6}$	$-0.4255\ 10^{-6}$
	α_{12}	$0.3267\ 10^{-5}$	$-0.3211\ 10^{-5}$
	α_{22}	$0.2437\ 10^{-4}$	$-0.2598\ 10^{-4}$
145	α_{11}	$0.8362\ 10^{-6}$	$-0.7188\ 10^{-6}$
	α_{12}	$0.2292\ 10^{-5}$	$-0.5436\ 10^{-5}$
	α_{22}	$0.1605\ 10^{-4}$	$-0.4284\ 10^{-4}$
ω_1	α_{11}	$0.5815\ 10^{-6}$	$-0.8434\ 10^{-6}$
	α_{12}	$0.2720\ 10^{-6}$	$-0.6308\ 10^{-5}$
	α_{22}	$0.1273\ 10^{-6}$	$-0.4886\ 10^{-4}$
148	α_{11}	$0.5320\ 10^{-6}$	$-0.8452\ 10^{-6}$
	α_{12}	$-0.1127\ 10^{-6}$	$-0.6304\ 10^{-5}$
	α_{22}	$-0.2844\ 10^{-5}$	$-0.4870\ 10^{-4}$

5. CONCLUSION

In this paper a method of determining the receptances of a locally damped structure from their undamped counterparts is proposed. The method, in general, can be used to predict the receptances of any damped system. However, the inversion process restricts the economical application of the method to structures with small damping matrices. Yet, it is always possible to separate the damping matrix of a non-classically and fully damped structure into proportional and non-proportional parts. If the non-proportional damping matrix can be arranged and partitioned such that the non-zero part is of a small order, then the method can still be used economically to determine the receptances of the actual system from the receptances computed considering only the proportional part of the damping. A typical example of such a system is a locally coated structure with a proportionally damped base structure.

The method has several advantages: The frequency dependence of damping properties does not affect the computational time considerably, as the same eigensolution is used for all cases. Furthermore, the accuracy of the method depends only on the accuracy of the undamped receptances. In other words, the exact values can be obtained if the exact undamped receptances are known, regardless of the level of damping or the spacing of the natural modes of the structure. Indeed, the numerical example given shows that when the undamped receptances are calculated from the analytically computed exact modal vectors without any truncation, the damped receptance values found by the matrix inversion method are the exact values. Moreover, the method has the same accuracy at every exciting frequency unlike most of the approximate methods which provide acceptable accuracy only in a certain range of frequencies. However the accuracy of the method when using truncated receptance series has not been tested yet.

6. REFERENCES

1. R. W. TRAILL-NASH 1950 Aeronautical Research Laboratories Report SM 151. An analysis of response of a damped dynamical system subjected to impressed forces.

2. K. A. FOSS 1958 Transactions of the American Society of Mechanical Engineers, Journal of Applied Mechanics 25, 361-364. Co-ordinates which uncouple the equations of motion of damped linear dynamic systems.

3. A. L. KLOSTERMAN 1971 Ph.D. Dissertation, University of Cincinnati. On the experimental determination and use of modal representation of dynamic characteristics.

4. R. F. BALDACCI, A. CORSANEGO and A. DEL GROSSO 1979 Damping Effects in Aerospace Structures, AGARD Conference Proceedings No. 227 Numerical modelling of structures to account for internal damping.

5. H. N. ÖZGÜVEN 1982 Journal of Sound and Vibration 85, 383-395. Receptances of non-proportionally and continuously damped plates - reduced dampers method.

6. W. T. THOMSON, T. CALKINS and P. CARAVANI 1974 International Journal of Earthquake Engineering and Structural Dynamics 3, 97-103. A numerical study of damping.

7. R. W. CLOUGH and S. MOJTAHEDI 1976 Intrnational Journal of Earthquake Engineering and Structural Dynamics 4: 489-496. Earthquake response analysis considering non-proportional damping.

8. H. N. ÖZGÜVEN 1981 American Society of Mechanical Engineers Paper No. 81-DET-75. Modal analysis of non-proportionally damped mechanical structures.

9. R. W. TRAILL-NASH 1981 International Journal of Earthquake Engineering and Structural Dynamics 9, 153-169. Modal methods in the dynamics of systems with non-classical damping.

10. H. N. ÖZGÜVEN and S. E. SEMERCİGİL 1982 Proceedings of the First International Modal Analysis Conference, 662-670. Accuracy of modal approximations for dynamic response analysis of non-proportionally damped mechanical structures.

11. R. E. D. BISHOP and D. C. JOHNSON 1960 The Mechanics of Vibration. Cambridge University Press.

12. W. J. HAMMILL and C. ANDREW 1971 Journal of Mechanical Engineering Science 13, 296-301. Receptances of lumped-parameter systems containing discrete damping sources.

END

FILMED

DTIC